Spatiotemporal Dynamics of Ventricular Fibrillation in a Three-Dimensional Anisotropic Heart Model

by

John Robert Fitz-Clarke

Submitted in partial fulfilment of
the requirements for the degree of
Doctor of Philosophy

at

Dalhousie University
Halifax, Nova Scotia
July 2003

Your file Votre référence
ISBN: 0-612-83713-0
Our file Notre référence
ISBN: 0-612-83713-0

DALHOUSIE UNIVERSITY

DEPARTMENT OF PHYSIOLOGY AND BIOPHYSICS

The undersigned hereby certify that they have read and recommend to the Faculty of Graduate Studies for acceptance a thesis entitled "Spatiotemporal Dynamics of Ventricular Fibrillation in a Three-Dimensional Anisotropic Heart Model" by John Robert Fitz-Clarke in partial fulfillment for the degree of Doctor of Philosophy.

Dated: July 31, 2003

External Examiner:

Research Supervisor:

Examining Committee:

Departmental Representative:

DALHOUSIE UNIVERSITY

DATE: September 14, 2003

AUTHOR: John Robert Fitz-Clarke

TITLE: Spatiotemporal Dynamics of Ventricular Fibrillation in a Three-Dimensional Anisotropic Heart Model

DEPARTMENT OR SCHOOL: Physiology and Biophysics

DEGREE: Ph.D. CONVOCATION: October YEAR: 2003

Permission is herewith granted to Dalhousie University to circulate and to have copied for non-commercial purposes, at its discretion, the above title upon the request of individuals or institutions.

Signature of Author

Contents

List of Figures

List of Tables

Abstract

Ventricular tachycardia and fibrillation are potentially lethal heart rhythms that can cause sudden cardiac death. The spatial and temporal electrical dynamics and stability of these complex rhythms are not well understood. We employed computer simulation to study the mechanisms of VT and VF in reaction-diffusion media, and to examine correlates in the electrocardiograms. A simple coupled map lattice model of cardiac tissue was developed to explore spatiotemporal complexity, by quantifying entropy and Lyapunov exponents during phase transitions to deterministic chaos. This model allowed basic features of electrocardiograms to be derived from their dipole source maps. A new mathematical model based on the Luo-Rudy formulation was then developed to simulate dynamics of sodium, calcium, and potassium ionic currents (I_{Na}, I_{Ca}, I_K, I_{K1}, I_{to}) in human ventricular action potentials. This theoretical model was simplified to contain only the minimal number of currents necessary to capture the essential behaviour of endocardial, epicardial, and M cells, while retaining sufficient simplicity to permit large-scale computation in a whole heart. Propagation and stability of electrical waves was explored in one-, two-, and three-dimensional monodomain cellular arrays, and in an anisotropic biventricular heart. Reentrant circuits were induced in normal tissue, and evolved into two-dimensional spiral waves and three-dimensional scroll waves. Stability was altered by varying the action potential restitution curves to achieve solitary fixed or meandering spiral waves, which fractionated into more complex fibrillation. Several subtypes of VF and their simulated electrocardiograms were characterized. The nature of successful and unsuccessful defibrillation shocks were then examined. This work represents application of a multiple-component ionic model of human ventricular cells to VT and VF in a whole heart model, a theoretical study of body surface electrocardiograms during reentrant VT and VF, and an attempt to develop a thermodynamic theory of fibrillation based on statistical mechanics.

Abbreviations and Symbols

AF	atrial fibrillation
AP	action potential
APD	action potential duration
BCL	basic cycle length
CA	cellular automata
CL	cycle length
CML	coupled map lattice
DFT	defibrillation threshold
DI	diastolic interval
DAD	delayed afterdepolarization
EAD	early afterdepolarization
ECG	electrocardiogram
EG	excitable gap
ERP	effective refractory period
FE	free end of wave front
ISF	integrated safety factor
LR1	Luo-Rudy phase 1 model 1991
LR2	Luo-Rudy phase 2 model 1994
LRS	Simplified LR1 model developed in thesis
LV	left ventricle
ME	microelectrode
MAP	monophasic action potential
MVT	monomorphic ventricular tachycardia
PVT	polymorphic ventricular tachycardia
QP	quasiperiodicity
RV	right ventricle
SF	safety factor of conduction
SHV	Simplified Human Ventricular cell model
TdP	torsades de pointes
VF	ventricular fibrillation
VFT	ventricular fibrillation threshold
VT	ventricular tachycardia
WF	wave front
VW	vulnerable window

a_x, a_y, a_z	diffusion coefficient of conductance, rectilinear axes
a_L, at	diffusion coefficient of conductance, longitudinal and transverse
APD_o	minimum APD or intercept of restitution curve
APD_m	maximum APD or plateau of restitution curve
C_m	membrane specific capacitance
d	calcium channel gate inactivation
D	distance from heart to sites of equatorial ECG leads

D	conductivity tensor
E_{Ca}	calcium equilibrium potential
E_K	potassium equilibrium potential
E_{K1}	potassium equilibrium potential
E_{Na}	sodium equilibrium potential
f	calcium channel activation
f	frequency in cycles per time
f_{K1}	transmural modifier of I_{KT}
f_{K2}	transmural modifier of I_K
f_{K3}	transmural modifier of I_{to}
g_{Ca}	calcium conductance
g_{Na}	sodium conductance
g_K	potassium conductance
g_{K1}	potassium conductance
g_{to}	transient outward current conductance
h	sodium channel inactivation
$H(x)$	Heaviside operator: 0 if $x < 0$, 1 if $x > 0$
I_{Ca}	calcium current
I_{ion}	total ionic current
I_K	potassium current
I_{KT}	total potassium current
I_m	transmembrane current
I_m	peak strength of decaying shock
I_{Na}	sodium current
I_{stim}	stimulus current
I_{to}	transient outward current
I_X	potassium current
k	wave number
K	Kolmogorov entropy
L	wave length or circuit length
L_{crit}	critical ring size for reentry block
L_o	obstacle size
m	slope of restitution curve
m	sodium channel activation
N_A	number of active neighbours in CML model
N_c	number of core points or reentrant circuits
N_{crit}	critical ring size for reentrant circuit
N_D	number of discontinuities in binary string
p	transient outward current activation
P_i	probability of an event
Q_m	membrane charge in safety factor equation
R	refractory period
R	radius of heart cylinder
R_c	radius of gyration of cores
R_k	radius of observation point

R_m	membrane resistance in cable equation
s	transient outward current inactivation
S	entropy in general
S_C	entropy of cycle lengths
S_D	entropy of diastolic intervals
S_G	pattern entropy of core separations
S_M	conditional entropy
S_v	surface-to-volume ratio of cell
S_1	initial pacing-stimulus for induction of reentry
S_2	shock-stimulus for induction of reentry
S(f)	frequency spectrum
S(k)	wavenumber spectrum
S{S(f)}	entropy of frequency spectrum
t	time
t_v	time of vulnerable window
V	transmembrane voltage
V_{ecg}	voltage of ECG signal
V_m	maximum voltage of action potential
V_R	resting membrane potential
Vp_i	peak voltage of action potential
V_{range}	maximum minus minimum ECG voltage for lead set
V_{rms}	root mean square voltage of ECG
V_{th}	threshold voltage for action potential
V_{uo}	voltage constant in $f_\infty(V)$, controls restitution curve intercept
$W(R,\varphi)$	weighting function of dipoles for ECG calculations
W_f	rate of energy dissipation in ionic currents
X	potassium channel activation
X	departure of APD from APD_c in Hill equation
X_{ij}	activation variable for CML model
Y_{ij}	inactivation variable for CML model
Z	Boltzmann thermal partition function
β	fibre angle measured from horizontal plane
Δt	time step for numerical integration
ε	helical angle of fibre in ventricular wall
γ	characteristic length scale of wave
η	nondimensional radius of gyration of cores
φ	angle of equatorial latitude for ECG site
φ	tangential angle in polar coordinates of point in 3D heart
φ	relative phase of pacemaker cell
Φ	potential function for changes in N_c
λ	correlation length
λ	Lyapunov exponent
λ_i	Lyapunov spectrum
λ_L	membrane length constant, longitudinal direction

λ_t	membrane length constant, transverse direction
$\Gamma(r)$	correlation spectrum
μ	transmural factor for defining cell types
θ	conduction velocity
ρ	dipole strength in CML model ECG
ρ	axial coupling of cable model
ρ_L, ρ_t	bulk resistivity of tissue
τ	time constant of restitution curve, or of gating parameter
τ_m	time constant of membrane action potential foot
τ_{uo}	time constant of recovery of f gate in I_{Ca}
ν	nondimensional voltage threshold V_{th}/V_m
ξ	APD restitution curve slope at DI = 0
ζ	core spacing in CML model

Acknowledgements

"We are certainly not to relinquish the evidence of experiments for the sake of dreams and vain fictions of our own devising; nor are we to recede from the analogy of Nature, which is wont to be simple, and always consonant to itself." Isaac Newton.

"One of the principal objects of theoretical research in any department of knowledge is to find the point of view from which the subject appears in its greatest simplicity." Joshua Willard Gibbs, 1881.

"Theory can be useful, but it can also be a distraction. The key is to understand the problems and model them at the right level of abstraction." J. Doyne Farmer

The work presented here evolved over a period of twelve years, first as a medical student project, then an obsessive hobby, then graduate student research, and finally a Ph.D. dissertation. I owe gratitude to many people who provided me with guidance, support, and inspiration over these years. My thesis advisor, Dr. Milan Horácek, for introducing me to theoretical and quantitative cardiac electrophysiology, and for providing assistance, advice, and advocacy before and during graduate studies. The Dalhousie Medical Research Foundation for awarding me the Leo Alexander Studentship in Cardiovascular Research 1991-92, which allowed this work to begin in the summers during medical school. Dr. Drew Armour for stimulating discussions, and an open invitation to his lab where the humbling complexities of cardiac physiology were evident. Dr. Martin Gardner and Dr. Larry Sterns for introducing me to clinical electrophysiology and catheter ablation during a residency elective in the catheterization lab. Dr. John Clements for comments and encouragement. Mr. Brian Hoyt for assistance with computer resources. Dr. Bill Smith and Dr. Raymond Ideker for allowing me to spend an inspiring medical school elective observing experiments in ventricular fibrillation at the Basic Arrhythmia Lab at Duke University in 1993. My wife Anna and son Christopher for tolerating my frustrations and seemingly endless obsessive behaviour at the computer. Finally, I would like to thank the many patients I have met, and continue to meet, whose problems are constant reminders of the importance of medical research.

Chapter 1

INTRODUCTION

1.1 Introduction

Heart disease remains the leading cause of mortality in the developed world, accounting for perhaps 400,000 deaths annually in North America [148, 239], of which about half occur suddenly due to acute coronary events [361]. Although disease substrate develops slowly over many years, sudden cardiac death (SCD) can be triggered by a brief electrical disturbance if it destabilizes normal regular ventricular rhythm. Instabilities can grow if they occur within susceptible substrate, and ultimately cause loss of coherent contraction. The most common lethal rhythm seen at the time of attempted resuscitation is ventricular fibrillation (VF) [380, 393, 480], which frequently evolves from preceding ventricular tachycardia (VT) [28, 374]. Nonfatal atrial fibrillation causes substantial morbidity, and contributes to heart failure and stroke risk [268].

The vast majority of SCD cases occur without any warning, and are therefore virtually unpredictable [186]. Rates of successful resuscitation from out-of-hospital cardiac arrest are poor [147, 211], and efforts must be started within a few minutes to maintain any hope of survival [303]. Drugs are presently the main therapy for primary prevention of life threatening dysrhythmias, but so far their impact on mortality has been disappointing [65, 479]. Drugs used during cardiac resuscitation remain controversial due to inadequate understanding of the mechanisms of action, and insufficient clinical validation [138,

500]. Implantable defibrillators have been shown to be effective within a subset of high-risk patients fortunate enough to survive cardiac arrest [293, 357]. Innovative therapies are needed to prevent and control electrical instabilities in the heart to avoid transitions to VT and VF, and to facilitate defibrillation during resuscitation [457]. New developments to improve survival will require greater physiological insight into the fundamental mechanisms of cardiac electrical instabilities.

Cardiac dysrhythmias arise from events at the cellular level, or even molecular level [280], yet manifest as disrupted spatial propagation of electrical waves within the atria or ventricles on a macroscopic scale [10]. Although basic qualitative mechanisms of dysrhythmias have been known for years from electrophysiological mapping studies [230], the details of complex spatiotemporal wave activity within the three-dimensional anisotropic heart are not well understood. This is due in part to experimental limitations and controversies surrounding the interpretation of results [551], confounded by the highly dynamic behaviour and short lifetimes of assumed reentrant circuits [306]. There is still inadequate understanding of how electrical stability is influenced by changes to the passive tissue substrate [562], and by the multitude of active ionic currents [98], which may themselves be subject to disease and pharmacological alteration [60].

Many experiments in cardiac electrophysiology have focused on isolated cells, membrane patches, and ion channels, while others have involved larger scale mapping of tissues and whole hearts [576]. It is essential that an integrated approach be employed to studying arrhythmogenesis, combining insight into both local cellular dynamics and large-scale spatial propagation. Conclusions based on single cells might not be valid in multicellular tissues where propagation can introduce new and unexpected phenomena. The pitfalls encountered while extrapolating single cell studies to whole hearts without such an integrated approach was emphasized by Starmer: "I found that with each anti-arrhythmic process we had identified in isolated cells, there was an obligatory multicellular pro-arrhythmic process due to the associated effects of the propagating excitation wave" [472]. Clinical trials, such as CAST [57] and SWORD [517], have shown certain drugs previously assumed to be anti-arrhythmic to actually be pro-

arrhythmic, in conflict with expectations based on conventional concepts [458]. It has been suggested that virtually every anti-arrhythmic drug is potentially pro-arrhythmic [65, 106]. Drugs have a multitude of effects and interactions that can alter the arrhythmogenic substrate, some specific targets of which are summarized in Table 1.1.

Body surface electrocardiograms measured on the torso are useful in the diagnosis of most rhythm abnormalities, and indeed have become essential in clinical practice. The precise quantitative relationship between the measured body surface patterns and the detailed electrical dynamics within the myocardium are not well understood, due in large part to experimental difficulties in simultaneously measuring signals on the body surface and within the heart. Potentially useful information in electrocardiograms, both spatially over the torso [173], and temporally within complex time-varying signals [301], is disregarded in clinical practice, either because it cannot be reliably extracted, or because the physiological correlation with substrate activity is not known [510]. Novel methods of analysing VT and VF signals might allow extraction of important information that allows subtyping of these rhythms, which could impact therapeutic approaches.

Table 1.1: Components of the Arrhythmogenic Substrate

1. Sinus rate
2. Conduction pathways
3. Conduction velocity
4. Intracellular coupling
5. Firing threshold
6. Action potential duration
7. Action potential restitution
8. Enhanced automaticity
9. Triggered afterdepolarizations
10. Nonuniformity of repolarization
11. Autonomic effects
12. Electromechanical effects

This dissertation presents a study of the mechanisms of tachycardia and fibrillation, and their subtypes, by employing mathematical and computer models of excitable media. The main objective is to try to understand the nature of these electrical rhythms as spatiotemporal dynamical phenomena, and to explore the projections of their complex signals on the body surface.

We begin with a review of normal cardiac conduction and the basic mechanisms responsible for electrical instabilities and dysrhythmias. Limitations of experimental mapping techniques still prevent detailed understanding of conduction abnormalities. Existing mathematical models of cardiac cellular electrical activity, both physiological and phenomenological, are discussed. We then examine a simple coupled map lattice model that provides insight into the genesis of electrocardiograms, and allows exploration of wave stability, nonlinear dynamics, phase transitions, and methods for quantifying spatiotemporal complexity. This simple model exhibits surprisingly rich dynamics that should theoretically be a subset of dynamics in more detailed and complex heart models. All previously published cellular models with ionic currents are based on results of animal experiments. There are presently no mathematical models specifically developed to simulate human cardiac cells. A new model of ventricular action potentials will therefore be developed in the second part of this thesis, and will be calibrated to match existing human data in the literature. This human cellular model will be incorporated into one-, two-, and three-dimensional arrays of cells representing myocardial tissue, and the conduction properties will be examined. The model will then be implemented in three-dimensional ventricles. The spatial and temporal conduction properties will be studied as the model parameters are manipulated, and the resultant body surface electrocardiograms will be calculated. It will be shown that the dynamics of propagating electrical waves are complex and sensitive to small changes in ionic currents, hallmarks of nonlinear and chaotic systems. Dysrhythmias simulated in the model will be initiated and controlled by changing cellular parameters, and electrocardiographic patterns of ventricular tachycardia and fibrillation will be analysed.

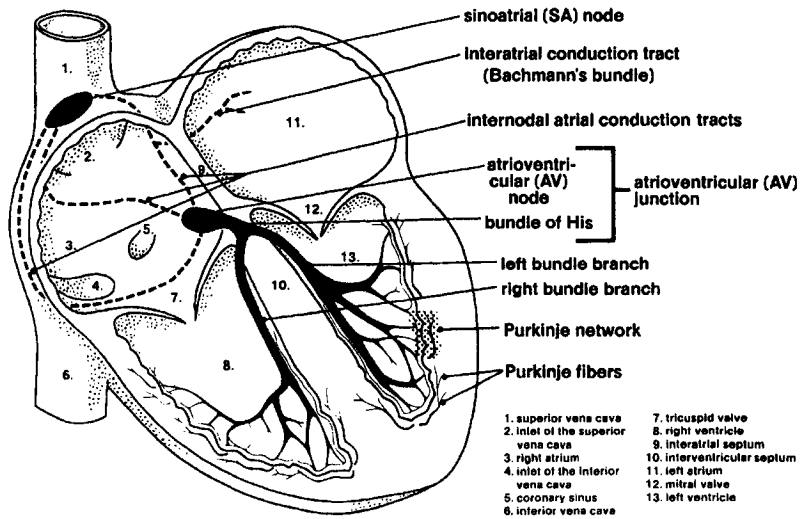

Figure 1.1. Electrical impulses in the normal heart originate in the sinoatrial node and pass through the atria and intrinsic conduction system to the ventricles (reproduced with permission [242]).

1.2 The Normal Heart

Normal electrical activity in the heart follows a stable repetitive sequence illustrated in Figure 1.1 throughout the entirety of life. Every second or so, an impulse is initiated within the spontaneously beating sinoatrial (SA) node and propagates as a wave across the thin right and left atria, causing these two upper chambers to contract. The impulse then passes from the bottom of the atrial septum through the atrioventricular (AV) node and then rapidly through the extensively branching His-Purkinje network to the left and right ventricles, causing these two thick muscular chambers to contract. The impulse dies out with the last contracting cell in this chain of events. Although this activity takes place within a three-dimensional heart, normal wave propagation is topologically equivalent to that which would occur on a one-dimensional cable. All cells involved recover their electrochemical states rapidly, and this unidirectional cycle repeats itself with the next SA nodal impulse. Each cell in the entire sequence normally fires once per cycle, ensuring a 1:1 correspondence between all cells during each beat. This normal sequence is called sinus rhythm, since all activity follows the SA node, whose intrinsic rate

determines the overall heart rate. Under normal conditions, sinus rhythm usually ranges between 60 and 100 beats per minute at rest.

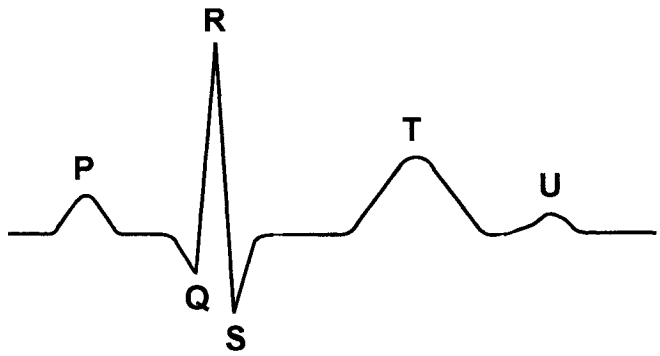

Figure 1.2. The normal body surface electrocardiogram for a single beat showing the P wave, QRS complex, T wave, and U wave.

An idealised body surface electrocardiogram (ECG) during normal sinus rhythm is shown in Figure 1.2. The P wave represents atrial activation beginning with SA node activation and ending when both atria are completely depolarised. The large-amplitude QRS complex is caused by depolarisation of the large ventricular mass. It is narrow, due to the sharp brief upstroke of the cellular action potentials, and the near-synchronous distribution of impulses throughout the rapidly conducting His-Purkinje fibre network. Ventricular repolarization produces the T wave, which lasts longer due to slow recovery of action potentials and due to local and regional spatial heterogeneity of action potential duration throughout the myocardium. The latter factor can produce a U wave, which is not always seen. Atrial repolarization in the electrocardiogram is of very low voltage, and is largely buried within the QRS complex. The notation of these waves was proposed by Einthoven who originally called them A, B, C, and D, but was concerned that additional earlier deflections might have to be added later, so renamed them starting at P [80].

Electrical activity in the heart can be mapped experimentally using several methods. Human endocardium is commonly mapped in clinical practice by transvenous catheters, but this technique is time consuming and usually confined to a few simultaneous

endocardial sites [188, 474]. The rhythm must be stable and repetitive to permit any type of extensive mapping as the catheter tip is moved to different locations. Epicardial mapping is possible during surgical thoracotomy by temporarily placing an electrode array over the heart surface, but is limited to studying only the two-dimensional external epicardium [73, 219]. Recently developed basket catheter devices allow two-dimensional endocardial mapping [294, 446], while intravascular catheters can map parts of the epicardium around the coronary sinus. Insertion of needle plunge-electrodes across the myocardial wall is presently the only method for obtaining three-dimensional maps [143, 561]. This method is obviously highly invasive and potentially damaging to the myocardium, and is therefore usually restricted to animal hearts. More recently, the development of voltage sensitive fluorescent dyes has allowed impressive high-resolution optical scanning of electrical activity over the epicardium [550], and across the wall of wedge preparations. Dye toxicity limits this technique to animal hearts. Surgical thoracotomy or Langendorff perfusion is required, and the results are again two-dimensional [133]. The ideal mapping technique that can produce three-dimensional electrical images noninvasively is much needed, but does not yet exist.

The only practical noninvasive method to measure cardiac electrical activity in humans is the body surface electrocardiogram, first employed by Einthoven in 1902 [41, 150]. Low voltage electrical signals are relatively easy to obtain, and represent the electrical field of the heart measured at a distance [193], either at several standard sites on the chest, or as time-dependent spatial maps over the entire torso [97]. Electrocardiograms aid in diagnosis of most dysrhythmias, but are measured at a distance from the heart and represent two-dimensional projections. Sparse spatial sampling, inevitable signal noise, and baseline drift limit reconstruction of the underlying three-dimensional myocardial dynamics [429].

1.3 Basic Arrhythmias

The conduction system of the heart seems simple in principle, but nonlinearities in the governing physical processes make action potential propagation sensitive to small local

variations, and open the possibility for rich stable and unstable dynamic phenomena [126]. Under pathological conditions, the electrical propagation sequence can be altered. Conduction in one region may be slowed or blocked, or a subset of cells may repetitively fire at a rapid rate. Either type of disturbance can cause wave fronts to alter their paths through the heart and disrupt stability. A small change at the cellular level can profoundly affect the global activation pattern. Stated most simply, a cardiac dysrhythmia results when the sequential 1:1 correspondence between the firing of each cell is broken.

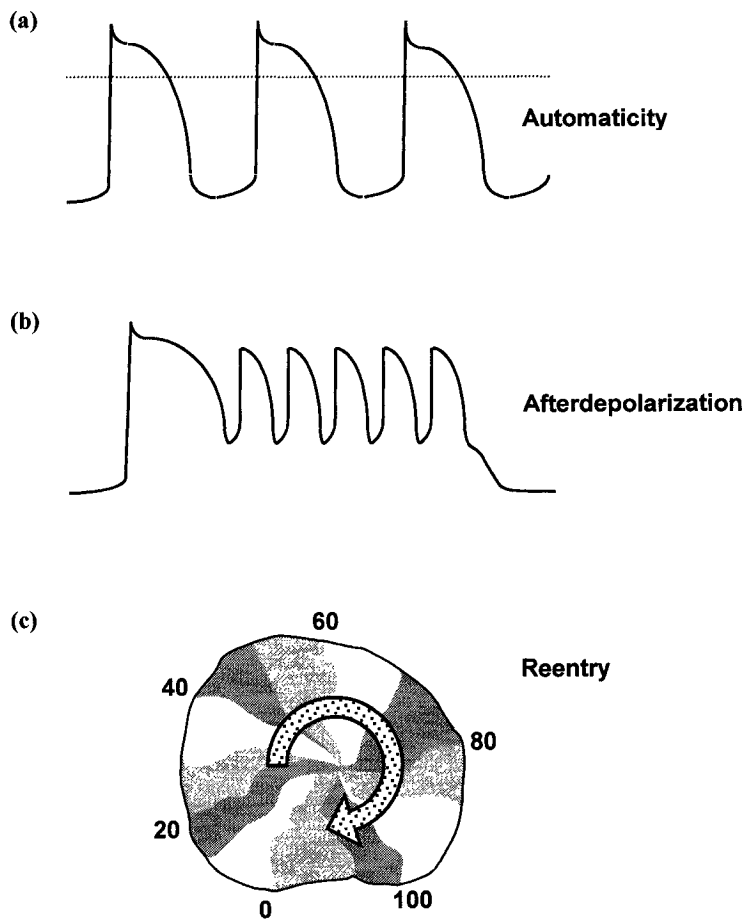

Figure 1.3. The three basic mechanisms of cardiac dysrhythmias resulting in repetitive firing are: (a) enhanced automaticity of an ectopic focus, (b) afterdepolarizations from a preceding action potential, and (c) reentry of propagation spatially around a closed path.

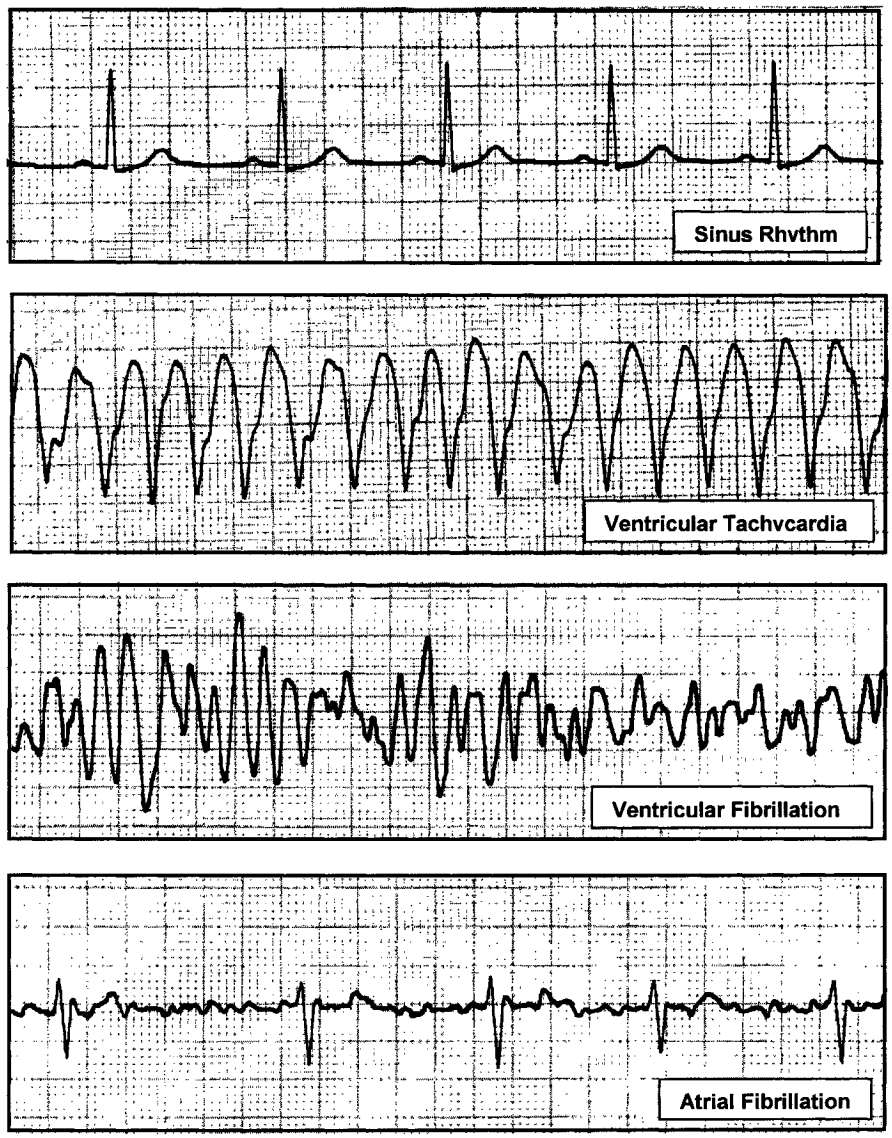

Figure 1.4. Normal sinus rhythm and some important cardiac dysrhythmias: ventricular tachycardia, ventricular fibrillation, and atrial fibrillation (reproduced with permission [242]).

It is generally agreed that there are three basic mechanisms by which dysrhythmias arise: (a) ectopic depolarization of an aberrant focus causing electrical waves to radiate from a fixed site [256], (b) repetitive depolarizations triggered within an incomplete action potential or shortly after a preceding action potential [548], or (c) spatial reentry of a

propagating wave front around a closed path causing reexcitation of cells along that circuit [120, 548]. These fundamental mechanisms are illustrated in Figure 1.3. Dysrhythmias are recognized in clinical practice by their characteristic rhythms and morphologies on the body surface electrocardiograms in a few standard leads. Some important examples are illustrated in Figure 1.4 and summarized below.

(i) ***Ventricular tachycardia (VT)*** results from rapid abnormal firing of ventricular cells. Any or all of the basic mechanisms just described may be involved, including rapid ectopic or focal activation [548], multiple afterdepolarizations [105], or a solitary large stable reentrant circuit [50, 139]. Although the transition from sinus rhythm to VT involves some form of electrical instability [403], VT is considered to be hemodynamically stable if cardiac output is maintained despite the rapid rate, and is not necessarily lethal. Conversely, if adequate ventricular filling between beats cannot be sustained because the diastolic interval is too short, cardiac output and blood pressure will fall [7]. Loss of consciousness, or even death, may follow if this type of VT is not corrected rapidly with drugs or electrical cardioversion [153].

(ii) ***Ventricular fibrillation (VF)*** is generally believed to consist of multiple complex wandering wavelets of turbulent electrical activity winding throughout the myocardium and preventing coordinated contraction [208, 252, 390, 480]. Despite the presence of ongoing electrical activity, cardiac output drops to zero and death follows within minutes unless the disorganized waves can be abolished by electrical countershock to allow the underlying sinus rhythm to return. VF is frequently the terminal event in death from cardiac disease, and from noncardiac diseases if there is sufficient metabolic derangement of the myocardium to destabilize conduction [361]. Although many experimental mapping studies have attempted to elucidate the spatial and temporal structure of VF, controversy still continues regarding whether VF represents random electrical activity or has underlying organization [29, 113]. Figure 1.5 shows a single-lead ECG obtained by the author from a patient during an attempted resuscitation from out-of-hospital cardiac arrest. This intriguing record was taken over a ten minute period, and shows several distinct patterns of VF. The physiological basis of these subtypes is not known, but may

have been influenced by progressive ischemia, administered drugs, and unsuccessful defibrillation shocks.

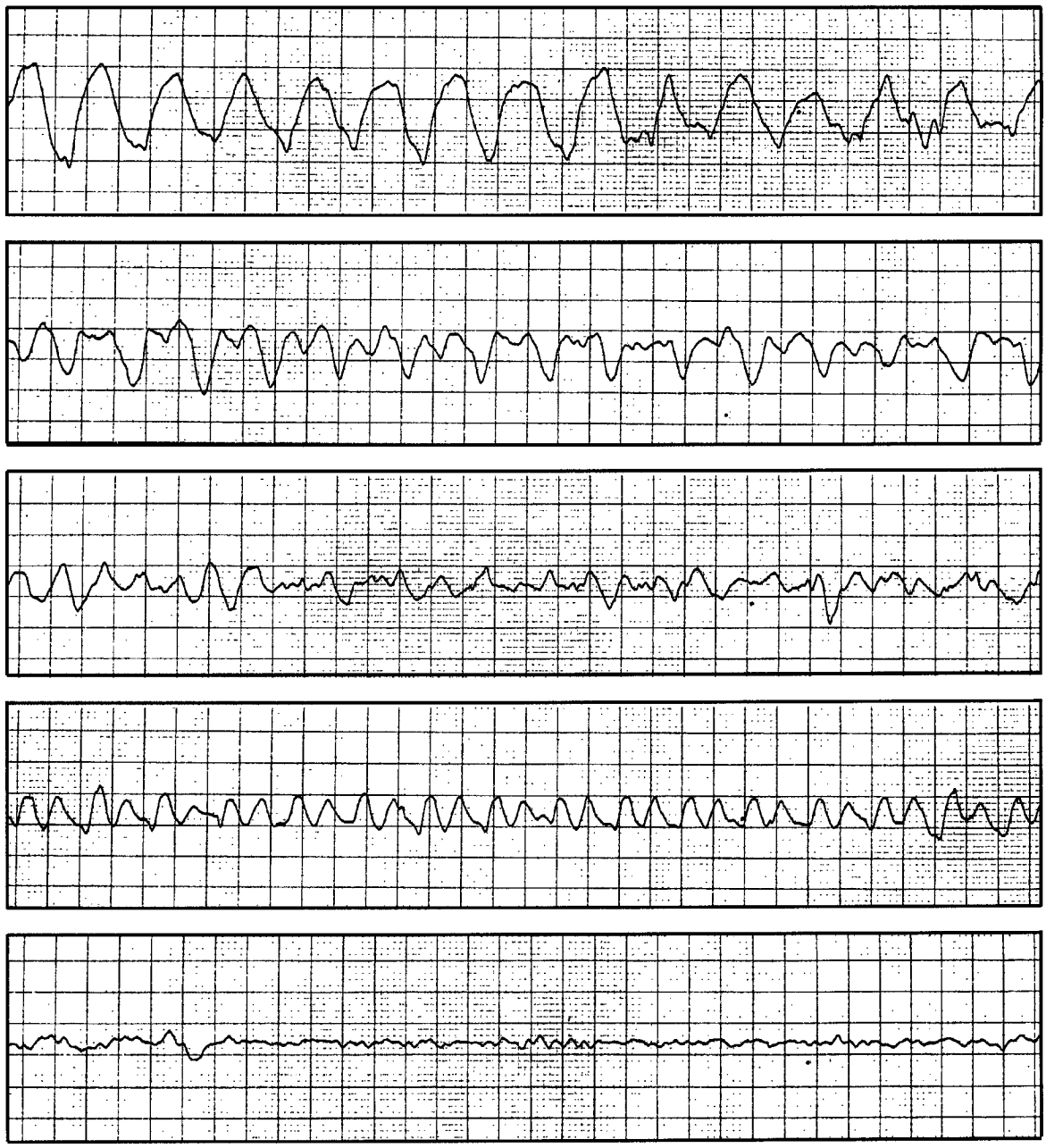

Figure 1.5. Single-lead electrocardiogram recorded from a patient in cardiac arrest during attempted resuscitation. Appearance of several different waveforms of ventricular fibrillation (VF) suggests the existence of VF subtypes exhibiting various amplitudes, frequencies, and morphologies which evolve over time. The physiological basis of these different patterns is not known.

(iii) ***Atrial fibrillation (AF)*** is analogous to VF with multiple wavelets of electrical activity wandering through the atria [516]. The regular SA nodal beats are completely blocked or suppressed by overdrive from irregular atrial waves, whose pattern and arrival times at the AV node determine rhythm. Since the ventricular rhythm is driven by the AV nodal rhythm, it is also irregular [456]. Unlike VF, AF is usually not lethal, because ventricular contractions can still continue, although with reduced efficiency. Complications of AF, however, can lead to significant morbidity [268]. Firstly, the ventricular rate can become too rapid to allow adequate diastolic filling and cardiac output can drop. Secondly, the loss of coordinated atrial contraction or "atrial kick" diminishes ventricular filling or preload, and results in about a 17% drop in cardiac output [356, 439]. This loss is especially significant if the patient already has compromised ventricular function, in which case AF can precipitate heart failure. Thirdly, poor atrial contraction can cause blood to stagnate and coagulate around the atrial walls and lead to thromboembolic stroke [432]. Drug therapies, like d-sotalol and amiodarone, used to prevent AF are frequently disappointing, and may introduce potentially serious side effects, including paradoxical ventricular dysrhythmias [517]. Electrical cardioversion is usually successful in restoring sinus rhythm, but AF frequently returns. Longer duration AF seems to be more difficult to reverse. It has been suggested that "AF begets AF", in reference to electrical remodelling of the atrial substrate that promotes its persistence [536]. This is likely a consequence of tachycardia-induced downregulation of membrane ionic channel expression [367]. When treatment fails, many patients are simply left to live with AF while on rate-controlling drugs and anticoagulation to minimize thrombus formation. Other therapies include AV node ablation with placement of a permanent ventricular pacemaker, and the surgical or catheter "maze" procedure which constrains wavelet path length to a size below that needed to maintain reentrant circuits [104]. A more recent option is catheter ablation of ectopic foci within the atria that appear to be responsible for initiating AF [254, 277]. Activity from these ectopic sites must be witnessed and recorded during clinical monitoring if the focus is to be accurately localised for ablation.

1.4 Cardiac Stability

Since cardiac cells behave individually as highly nonlinear electrical units, coupled with irregular geometrical and functional connectivity, it is intriguing to speculate on the stability of whole-heart conduction from the point of view of a nonlinear system. Figure 1.6 shows an hypothetical high-dimensional state space of heart electrical activity, and a corresponding bi-stable potential well. The number of states, and therefore dimension of this hyperspace, is equal to the number of cells multiplied by the number of dynamic variables defining each cell. Periodic sinus beats raise the state from the stable quiescent point in the normal well onto a trajectory, defined by the system dynamics, leading back to the resting point. Some small beat-to-beat variations might occur about this stable trajectory, similar to a ball moving from side to side as it rolls down a spiral channel. A benign premature beat or disturbance causes a small perturbation δ that recovers back to the stable attractor. Various pathological conditions, however, may push the state far enough away that the dynamics carry the trajectory across a separatrix ridge into an alternate basin of attraction. The state might settle into a periodic limit cycle of VT or a chaotic tangle of fibrillation. Unless interrupted by resuscitation, the VF attractor eventually decays into a deep well of asystole with progressive ischemia and death. Defibrillation shocks supply energy to raise the state back into the normal basin. Unsuccessful low-energy shocks fail to push the state across a barrier, or separatrix, and fibrillation returns. The two stable point attractors in this diagram, one in each basin, must actually be joined by a filament, since they both represent a state of complete rest.

We can define the "substrate of arrhythmogenesis" to be synonymous with the topology of this hypothetical multi-dimensional manifold that governs system response to electrical disturbances. Drugs alter the substrate by distorting the basins, and perhaps raising or lowering the separatrix barrier. This diagram is only conceptual, as no low-dimensional quantitative theory of such a complex state space currently exists [29, 269]. We must use simplified models to sample and explore this space by examining lower dimensional tangents or approximations to the manifold. There is a need to develop mathematical and computational tools for this purpose. Fortunately for our individual

longevity as humans, the basin of stability in the state space of a healthy heart is wide enough to recover from minor irregularities that occur in benign transient dysrhythmias. To a certain degree, this robustness is forced by local refractory behaviour that prevents reflection or reexcitation of impulses, and ensures 1:1 entrainment between the SA node and all other firing heart cells.

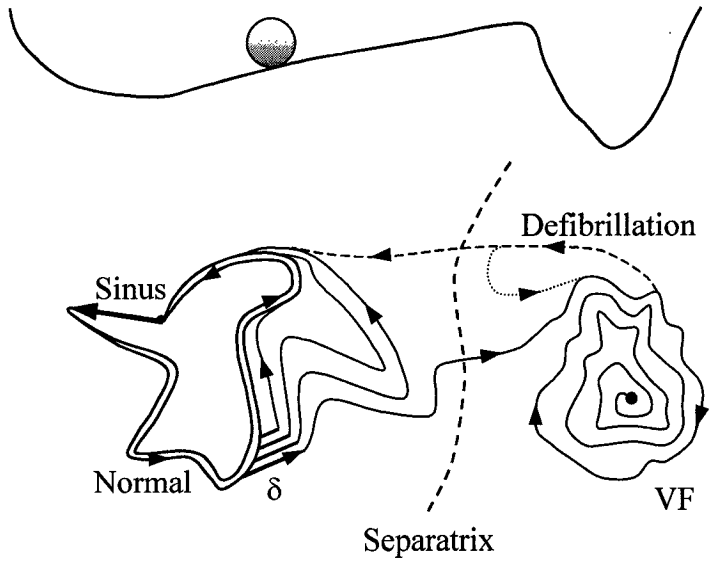

Figure 1.6. Basins of attraction in an hypothetical state space determine the stability of sinus rhythm and the transition to fibrillation. Sinus rhythm behaves like a stable limit-cycle oscillator, with irreversible fibrillation residing in a different region of the state space.

A general conceptualization of the various stages in the transition to cardiac dysrhythmias is summarized in Figure 1.7. It is beyond the scope of this dissertation to investigate all of these complex interactions, although the models developed here are capable of simulating a broad range of these phenomena. The main focus in this dissertation is on the stability and modification of induced reentrant dysrhythmias in normal cardiac tissue, in the absence of the abnormal physiological factors outlined herein. Since healthy hearts generally do not enter VT or VF spontaneously on their own, these rhythms will be induced artificially by various protocols such that their evolution and characteristics can be studied.

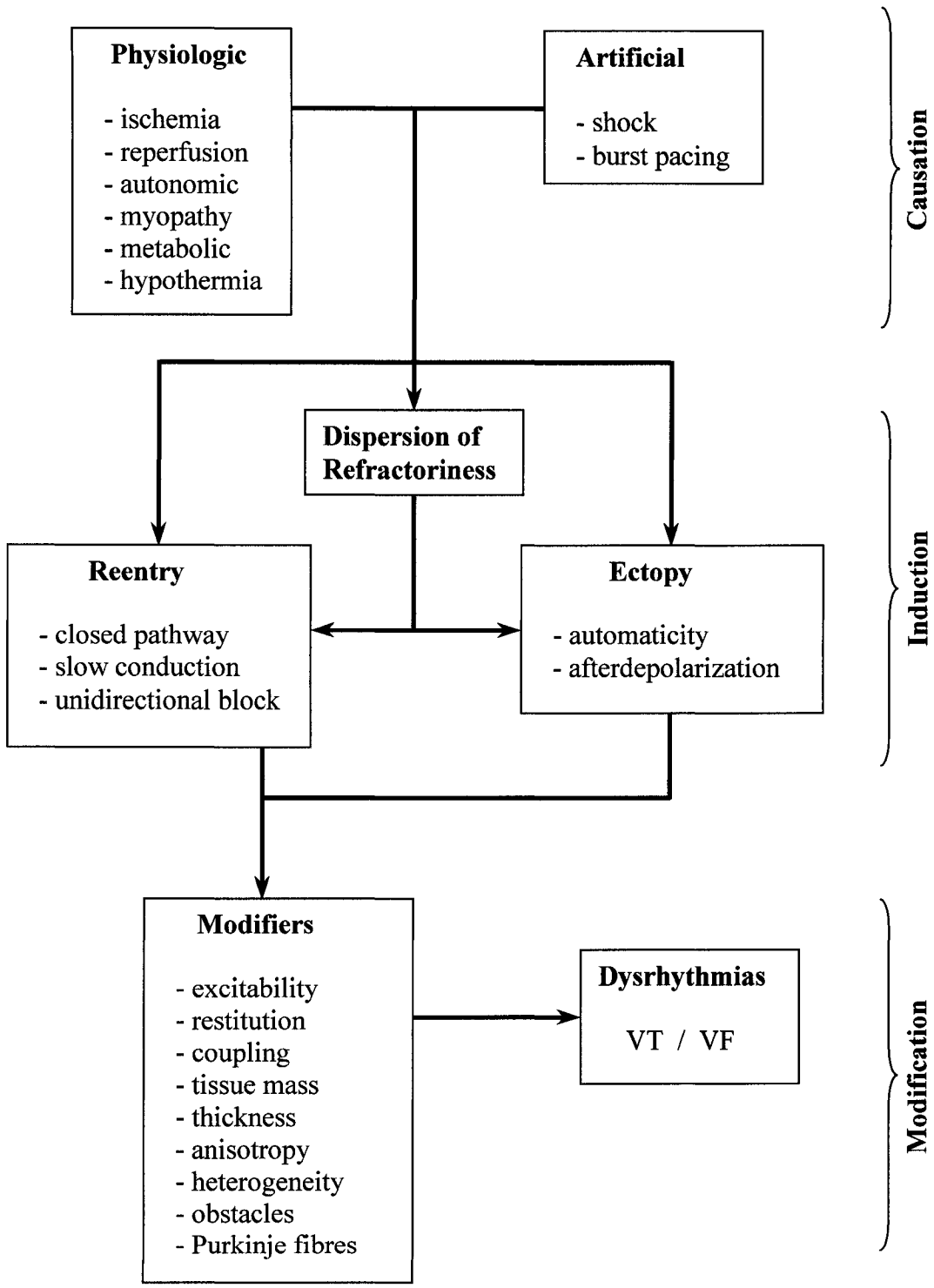

Figure 1.7. A general schema for conceptualizing the causation, induction, and modification of ectopic and reentrant cardiac dysrhythmias. The majority of studies in cardiac electrophysiology have focused on specific aspects of the multitude of interdependent relationships between the components of this diagram at various levels.

1.5 Objectives

Mathematical modelling and computer simulation are useful adjuncts for studying electrical activity in the heart [197, 388, 390, 510]. Models can consolidate existing knowledge, quantify relationships, generate novel perspectives, and help fill conceptual gaps that are inaccessible by experiment. The entire heart can be represented quantitatively as a three-dimensional electrical circuit, comprised of a large number of individual cellular elements accounting for ionic currents and intercellular coupling. A mathematical model of sufficient detail can be used to conduct "numerical experiments" by computer simulation under conditions that can be controlled and manipulated in ways that would be very difficult, or impossible, in real experiments. Some recent computer simulations of three-dimensional conduction and wave propagation in the heart, employing relatively primitive cellular models, have been used to simulate dysrhythmias [17, 33, 233, 388]. Validation of these types of models remains an ongoing problem, due to very limited experimental mapping studies on the whole-heart scale [359]. Inevitable gaps remain between the bottom-up engineering approach, based on theoretical principles, and top-down empirical experimentation.

This dissertation describes the development of two new theoretical models of reentrant dysrhythmias. The first is a simple two-dimensional coupled map lattice that retains only the most primitive features of action potential dynamics and cardiac conduction. Its simplicity allows a wide scope of investigation, and is used in particular to examine spatiotemporal complexity during fibrillation. The second model is a large-scale three-dimensional computer simulation of electrical activity within the ventricles. This model accounts for the dominant ionic currents responsible for ventricular action potentials in the anisotropic monodomain human heart. The objective is to study important cardiac dysrhythmias, including ectopic activation, reentrant circuits, and afterdepolarizations, particularly as they pertain to myocardial electrical wave dynamics of focal activation, and the stability of reentrant VT and VF. Electrocardiograms and body surface potential maps are simulated by forward-solution in a homogeneous infinite medium, and their relationship to underlying wave propagation is examined. The models developed here are

tools that will be used to investigate strategies for quantifying the spatiotemporal dynamics of propagating wave patterns, and the resultant body surface manifestations. The heart model might also assist in localizing arrhythmogenic foci to facilitate treatment by catheter ablation, and will be a useful adjunct in developing future innovative electrical, surgical, and pharmacological therapies of cardiac dysrhythmias [417].

All models to be discussed are based on normal myocardial tissue, whose behaviour must be understood to a reasonable degree before the role of specific disease processes can be investigated. Using the models developed here, it will be possible to resolve, with high resolution, the direct contribution of individual wave dynamics within the heart to the observed body surface electrocardiograms during simple and complex cardiac dysrhythmias.

The specific objectives of this work are as follows:

- Develop a three-dimensional computer simulation of electrical activity in the heart using reasonably realistic ionic models of human ventricular cell action potentials
- Simulate normal ventricular activation, and focal and reentrant cardiac dysrhythmias as wave propagation in anisotropic tissue
- Quantify the spatial and temporal patterns of wave propagation in the myocardium
- Study the influence of modifications to individual ionic currents on wave stability
- Calculate the resultant body surface potential maps and electrocardiograms
- Examine the contributions of intracardiac events to features in the electrocardiogram, by quantifying the spatial features of the body surface potential maps.

Some specific questions to be addressed are:

- How does restitution of action potential duration influence the spatiotemporal dynamics and complexity of fibrillation wave patterns?
- What information about myocardial electrical wave dynamics can be extracted from the body surface electrocardiogram?

- Can the body surface ECG distinguish between ventricular tachycardia originating from focal and reentrant sources?
- Is it possible to follow the transition from VT to VF as a bifurcation in spatiotemporal dynamics, or as a phase transition?
- Is there a continuum between the dynamics of VT and VF, and does this manifest in the electrocardiogram?

Chapter 2

CELLULAR MODELS

2.1 The Action Potential

The foundation of computational cardiac electrophysiology is the mathematical model used to represent the cellular elements. A variety of models covering a spectrum of complexity have been developed over the years, and will be reviewed in this chapter in order to gain perspective on existing modeling methods and their limitations. Each model describes the passive voltage-current relationship of subthreshold membrane, and the active voltage change during the action potential (AP).

Cardiomyocytes are long and slender cells connected in an organized matrix of electrically coupled parallel strands which form a functional syncytium [236, 471]. Active membrane-spanning ionic pumps separate charged ionic species into intracellular and extracellular compartments. Opposing ionic fluxes establish balance between charge and concentration gradients in a dynamic equilibrium to establish a transmembrane potential. This keeps the intracellular space about –90 mV relative to the extracellular space [60]. The exact value of the resting transmembrane potential depends on the ionic gradients, and varies between specific cell types and animal species [279]. Current injection into a cell from an external stimulus or an advancing depolarizing wave front raises this potential toward a threshold such that inward cationic currents, dominated by sodium and calcium, begin to exceed the smaller background outward currents carried by

potassium. As the balance is tipped to favour a net inward current, depolarization accelerates and the cell "fires" by rapidly depolarizing toward a positive potential. The fast inward current is dominated by a sodium spike lasting several milliseconds [435]. The resulting depolarization wave is largely responsible for sustaining propagation and also allows the calcium current to activate. The inward calcium current promotes further calcium release from internal stores, necessary to facilitate actin-myosin contractile interactions [9]. The inward currents inactivate at the positive potential, and the slower outward currents, carried by potassium, restore the cell back to its resting potential. The time course of these currents determines the action potential shape and duration which is traditionally divided into morphological phases illustrated in Figure 2.1.

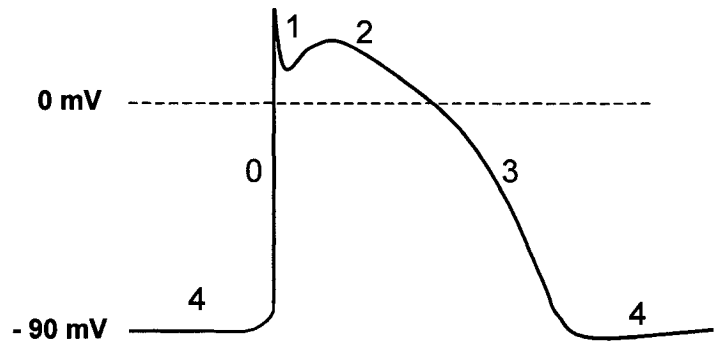

Figure 2.1. Morphological phases of the normal cardiac action potential.

Subsequent stimuli following an action potential elicit submaximal responses, unless time is allowed for complete recovery. The absolute refractory period (ARP) is the time during an action potential when no excitability can be elicited, and corresponds roughly to the phase 2 plateau. The relative refractory period (RRP), spanning into phase 3, is the recovery time beyond which the cell becomes excitable and can respond with an upstroke, though it may not necessarily propagate. The functional refractory period (FRP) is the earliest recovery time beyond which an elicited AP can propagate. Excitability refers to the ease with which an action potential can be produced, and is related to the threshold. Response refers to the amplitude of the resulting AP upstroke and is stimulus-

dependent. Restitution refers to the curve of action potential duration (APD) recovery over time. Standard restitution is the curve of APD as a function of diastolic interval (DI) elapsed from the tail of the preceding AP. Dynamic restitution is the curve of steady-state APD as a function of the pacing interval or basic cycle length (BCL). Conduction velocity also has a restitution curve as a function of DI or BCL.

2.2 Mathematical Models

Electrical activity of cardiac cells is essentially a physical process, and can therefore be described mathematically. Although ion channel kinetics appear to be stochastic at the molecular level [248], for modelling purpose, membrane behaviour may be considered deterministic. Stated most simply, each cell has a resting state and, if brought to a threshold, undergoes a transition to a firing state which it maintains for some duration, followed by recovery back to a resting state. If the cell is stimulated again during the refractory period (before complete recovery), the subsequent response is submaximal. Three categories of cellular model have historically been used to represent these processes with varying degrees of realism: cellular automata, relaxation oscillators, and ionic models.

2.2.1 Cellular Automata

The simplest mathematical models of excitable elements can be constructed with cellular automata (CA). First proposed by Ulam to von Neumann as a method for modeling algorithms of self-replication [490], cellular automata are the most primitive dynamic models. They are capable of implementing any Turing-computable algorithm, including simulation of a vast spectrum of spatiotemporal phenomena. Each element on a lattice holds one of a number of finite states which are permitted to change only at discrete time steps according to either deterministic or probabilistic state-transition rules based on the neighbour states. Rules acting locally give rise to global emergent properties on the lattice. Future state values of each cell *i* depend on the present values of the cell and those of a neighbourhood of cells *j* such that $X_{t+1}(i) = F(X_t(i), X_t(j))$. Although by definition

any numerical model is a type of cellular automaton by virtue of discretization in time and space, classically CA are intentionally constrained to a low number of states, sometimes as few as two. The theory of CA has been developed to a high degree, perhaps most notably by Wolfram [557, 559] who defined four subclasses of generic behaviour analogous to the fundamental types of attractors in nonlinear dynamics. Examples of CA models applied to biology include pattern formation, occular dominance stripes, animal coat markings, and ecosystem distribution [154]. Examples in physics include fluid dynamics, crystal aggregation, percolation in porous media, and phase transitions of condensed matter [507]. Many of these models have been used to examine emergent behaviour with self-organization, and to explore methods for quantifying complexity by analyzing changes in patterns, information content, and entropy [385, 556].

Applied to excitable tissue, CA models provide a simple formulation that attempts to retain only the most primitive features of cellular activation and recovery, yet allow much more rapid computation than partial differential equations. A block of tissue can be represented by a lattice within which each resting cell holds a value of zero, and upon firing, switches to a state of one for a predefined action potential duration. Such state transitions occur according to deterministic rules involving states of nearest-neighbour cells. Rules may be in the form of a look-up table, or as a series of conditional logic rules. Following a refractory period, which can assume a decreasing intermediate value or intermediate states, the cell returns to its resting state.

Wiener and Rosenbleuth described the first theoretical network model of cardiac conduction in 1946, using cellular automata with three states and constant propagation velocity [535] following Huygens principle. Flutter could not be induced in the model without the presence of anatomical obstacles. Moe revived this approach in 1964 to simulate heart tissue in a now classic model of atrial fibrillation employing a two-dimensional hexagonal cellular array with a resting state, firing state, and four refractory states [352]. Self-sustaining irregular vortices of reentry were reported, none of which were stable. Activity was described as being "turbulent rather than rhythmic and regular". A major finding was that multiple wandering wavelets resembling atrial fibrillation

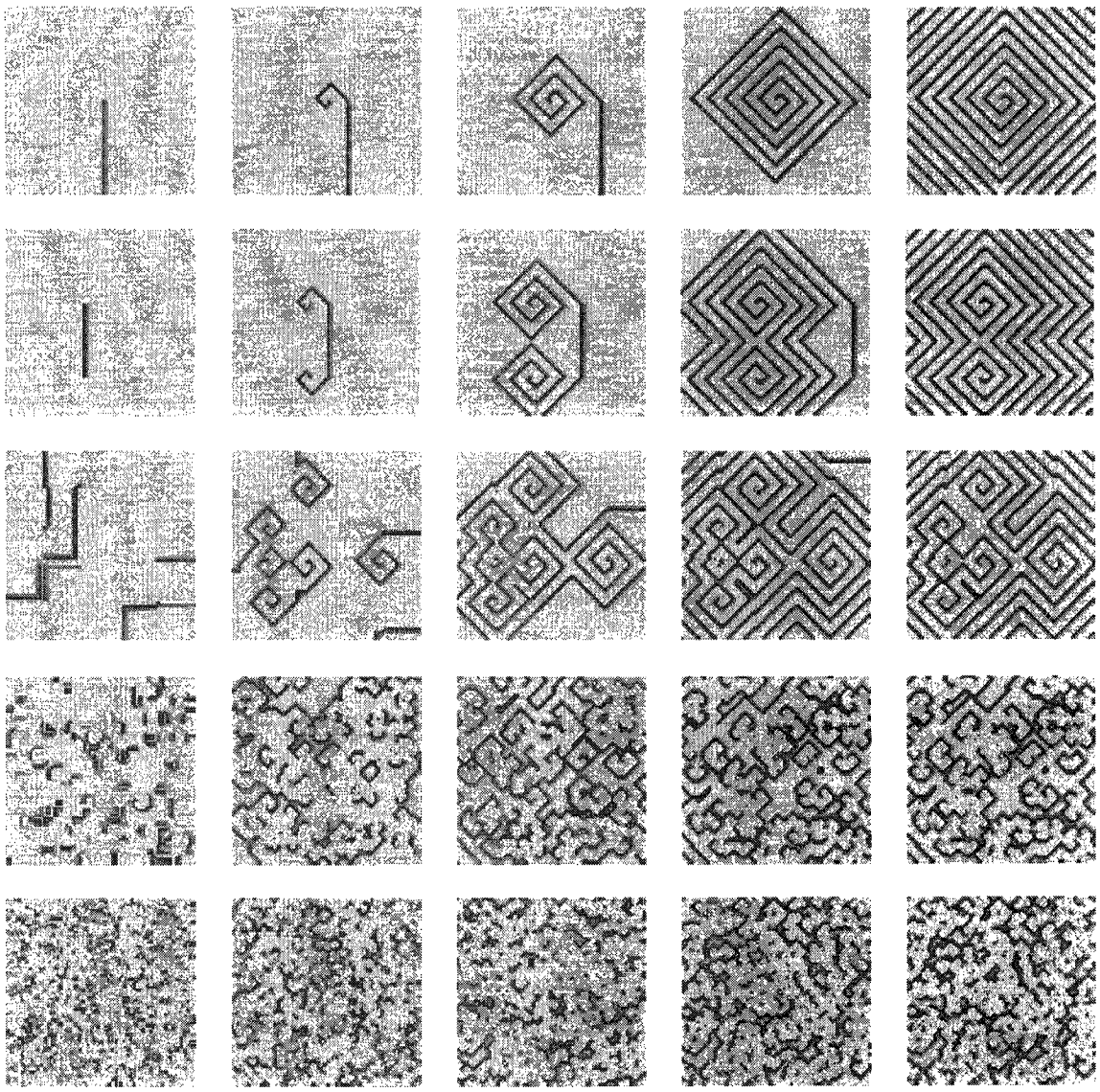

Figure 2.2. Spiral wave reentrant circuits develop from wave segments with free ends. Simple and complex patterns of fibrillation self-organize from random intial conditions and depend on the number of initial wavelets and their distribution. These simulations are based on a simple cellular automaton model to be discussed.

could be simulated, and their existence did not require anatomical obstacles or fixed spontaneous impulse generators. Two-dimensional models of self-organizing cellular automata, following a variety of specific local neighbour rules, are known to evolve into

fibrillation-like patterns [129, 276, 335, 518]. Several groups have used finite automaton models to simulate ventricular fibrillation by using random variables to define action potential durations [169, 192, 270, 351, 461]. These models demonstrate theoretically that increased dispersion of action potential duration can induce local reentrant circuits. This hypothesis has long been widely assumed, and has been confirmed by experiment mapping [52, 296, 298, 299]. Primitive CA models have been used to explore the stability of spiral wave reentry, and the role of action potential duration restitution [24, 249, 269].

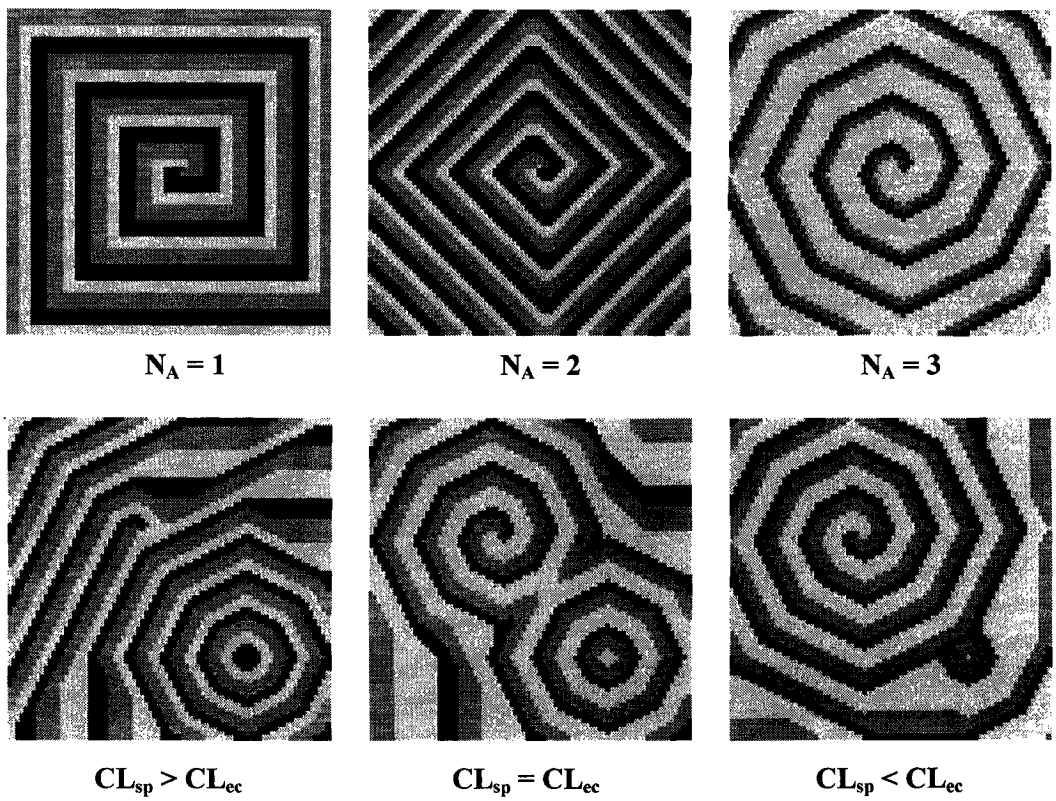

Figure 2.3. Wavefront curvature in a cellular automaton model depends on the minimum number of active neighbours N_A needed to excite each cell to fire (top). The spatial pattern of wave activity evolving with a reentrant spiral wave competing with an ectopic focus depends on the relative frequencies or cycle lengths (CL) of these two sources.

Figure 2.2 shows perhaps the simplest two-dimensional cellular automaton model that one can define based on rules chosen to mimic excitable myocardial tissue. The algorithm is shown in Table 2.1, and has similarities to that proposed by Greenberg and Hastings as

a model of genetic drift [212]. Each cell maintains a resting state X_{ij} of zero unless stimulated to fire by at least N_A of its immediate neighbours being in an excited state $X_{ij} > 0$ or above a threshold value $X_{ij} > X_{th}$. If the cell fires, its state X_{ij} changes from zero to a peak state value of APD (action potential duration) which counts down toward zero with each time step. Once the cell reaches zero, it must wait a predefined recovery time R (refractory period) until it is ready to fire again. The examples in Figures 2.2 and 2.3 show a 100 x 100 grid of elements with APD = 8 and R = 4. A stable spiral wave is induced artificially by introducing a partial wavefront with a free end, and backed by a row of refractory cells. Varying the minimum number of neighbours N_A between 1 and 3 causes a change in maximum wave front curvature, shown in the top row of Figure 2.3.

A second more interesting example, in the lower row of Figure 2.3, shows a reentrant spiral wave in the vicinity of a regularly beating ectopic focus. The spatial pattern and temporal behaviour of these two coexisting wave sources depends on their relative frequencies. In the left frame, the ectopic focus is beating slightly faster than the cycle length of the spiral wave, and tends to dominate the field. The centre frame shows both cycle lengths to be approximately equal. The right frame has a slower ectopic focus which is largely overdriven by the spiral wave. The wave source with the fastest frequency tends to suppress other sources, a common feature of coupled oscillators [111, 224, 541]. It is noteworthy that these two fundamentally different wave sources fail to annihilate each other in this model, and the frequencies are largely determined by the sum of action potential duration, refractory period, and diastolic interval: $f = 1/(APD+R+DI)$. If the frequencies of each source are only slightly different, such that each can produce sustainable waves, the ECG should at least transiently show quasiperiodicity, with the amplitude modulated by a beat frequency equal to this difference. The only interaction between cells in an automaton model is the binary decision to fire or not, based on the number of active local neighbours. There is no shortening of action potential, gradient of firing threshold, or dispersion relationship defining a change in conduction velocity with frequency. These latter properties are important in initiating instabilities and maintaining dysrhythmias [529].

As will be demonstrated later, fibrillation can evolve from a simple plane wave that splits into a complex field of multiple wavelets by a cascade of bifurcations, this being one of the fundamental routes to chaos. Behaviour progresses from simple to complex. An alternative route to a fibrillatory state is to start with the system overly-complex in a

Table 2.1: Finite Automaton Model Algorithm

Set initial condition X_{ij} Y_{ij}

For each time t = t + dt:

For each cell (i,j):

(1) Calculate cell voltages

$V_{ij} = (X_{ij} / APD_m) V_m$ Voltage $V_{ij} \propto X_{ij}$

(2) Count active neighbours $N_A = \Sigma (V_{ij} > 0.3 V_m)$ Maximum 8

(3) Update cell clocks

If $X_{ij} > 0$ then $X_{ij} = X_{ij} - 1$ Decrement firing clock if in AP

If $X_{ij} = 0$ then $Y_{ij} = Y_{ij} + 1$ Increment refractory period if resting

If $X_{ij} > 0$ and $N_A \leq 2$ then $X_{ij} = X_{ij} - 1$ Shorten APD of isolated firing cell

(4) Switch to firing state

If $X_{ij} = 0$ and $Y_{ij} \geq R$ and $N_A \geq 2$ then New firing APD

$X_{ij} = APD$ *

$Y_{ij} = 0$

If $X_{ij} = 0$ and $Y_{ij} \geq CL$ then Optional ectopic beat (cycle length CL)

$X_{ij} = APD$ *

$Y_{ij} = 0$

* where $APD = APD_o + (APD_m - APD_o)(1-\exp[-(Y_{ij} - R)/\tau])$

random state, with cells in different phases of firing and recovery far from equilibrium, and allow it to freely evolve or condense without external influence. Figure 2.2 shows this type of self-organization in the automaton model. The initial state is too complex to sustain itself in the medium, and the field attempts to settle to a less complex pattern that is sustainable, given spatial and temporal constraints inherent in the substrate. Interactions between neighbouring cells cause small phase shifts, that are on average locally convergent, causing a gradual dissipation of information. If there was no loss of information, it would be possible to run the system backwards by reversing time, and the initial condition would eventually be recovered [483]. Instead, dissipative systems can arrive at a given state by multiple routes, and reversal of time would result in ambiguity over the preceding state [222, 407].

The state is pushed over time toward an attractor, which in a continuous system can be a fixed point, a limit cycle, a quasiperiodic N-torus, or a chaotic tangle. The pattern may be a static or dynamic steady state constrained within a lower dimensional region of the state space, and is one of intermediate complexity between that of rest and randomness. The constraint of each cell to a finite number of possible states $\underline{S}$ within a finite $\underline{m}$ x $\underline{n}$ lattice means that there exists $d = \underline{S} \times \underline{m} \times \underline{n}$ possible states in the system, and that the behaviour follows a time-dependent trajectory through a d-dimensional state space. The methods of nonlinear dynamics and statistical mechanics can be introduced to quantify system behaviour, as will be demonstrated in a later chapter. We will also return to this simple model to examine spiral wave stability, and as a dipole source generator to assist in the interpretation of body surface electrocardiograms.

2.2.2 Hybrid Automata

Classical cellular automata switch abruptly between a small number of finite states. Discretization can introduce unwanted behavioural artifacts if one is actually attempting to represent a continuous excitable medium with overly-coarse resolution. Leon and Horacek introduced a hybrid continuous-discrete model of cardiac tissue in two- and three-dimensional media [308] to handle anisotropic conduction, and to overcome the

limitations of unrealistically abrupt state transitions to permit the smooth action potential morphology needed for calculating realistic body surface electrocardiograms.

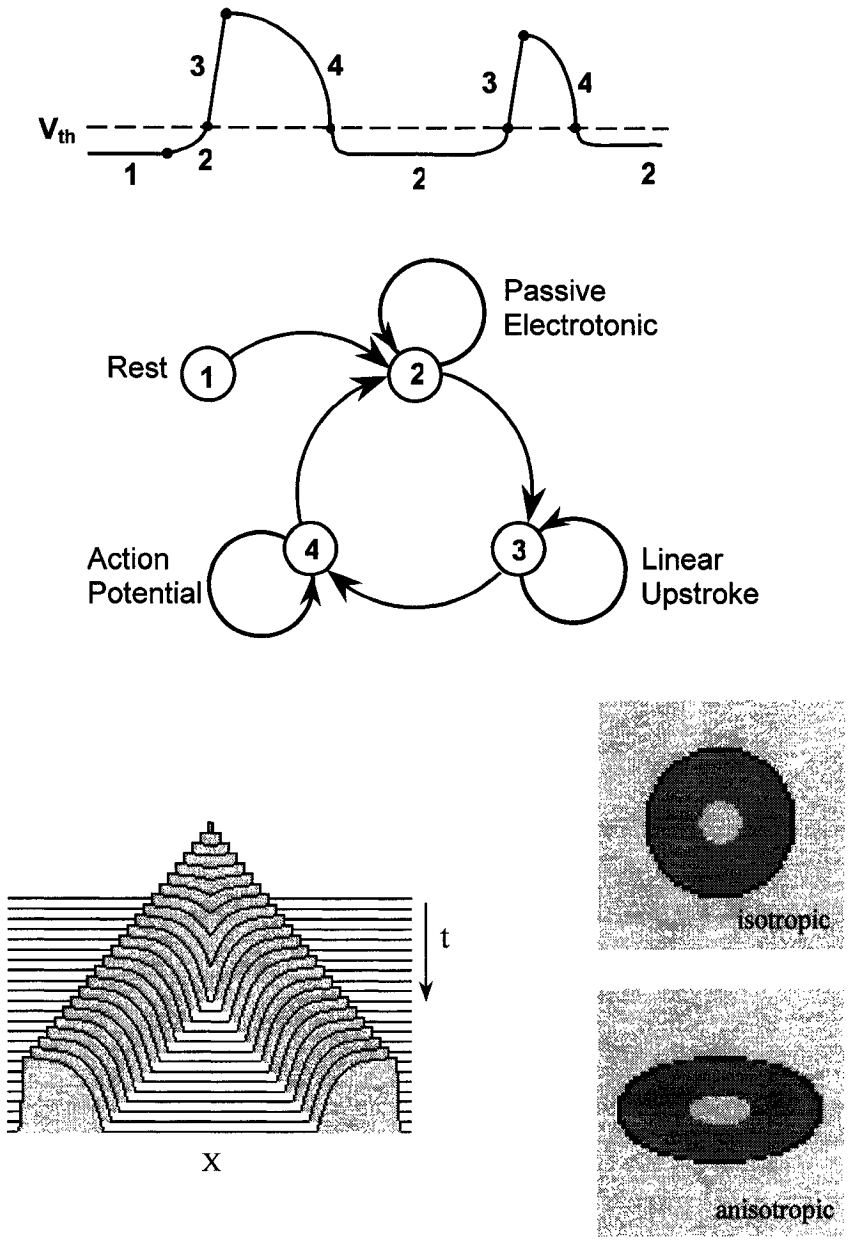

Figure 2.4. Hybrid automaton model showing subthreshold and suprathreshold states (top), and the state transition diagram (middle). Propagation of a single stimulus on a cable of cells results in a pair of action potentials radiating outward (lower left). The hybrid model allows isotropic or anisotropic action potential conduction, as shown by a single stimulus radiating outward in a two-dimensional field (lower right).

The Leon-Horacek hybrid automaton model is illustrated in Figure 2.4, which shows the state definitions and the state transition map. This model behaves as a continuous diffusion partial differential equation in state 2 when cells are below a threshold potential. When a threshold voltage is reached, the cell switches to state 3 with a constant upstroke velocity. When peak voltage is reached, the element behaves as a finite automaton for a predetermined duration, with a predefined action potential shape function taking over in state 4. As the cell recovers back below the threshold potential, the diffusion equation takes over again. Several minor variations of this model are possible, depending on the specific definitions of individual states. As few as two states will suffice if one incorporates the upstroke into the action potential profile. The resting state 1 in Figure 2.4 is not absolutely necessary, but reduces computational time early in the simulation by staying zero until a neighbour cell receives electrotonic current, at which time the state switches to 2. The examples show conduction along a one dimensional cable, and radial propagation in a two-dimensional sheet with isotropic and anisotropic conductivity.

The basic algorithm, modified from the original [369], is outlined in Table 2.2. The clock variable (nclock) can have two different meanings depending on the cell state, either counting down from a maximum value if the action potential is firing in state 3, or counting up from zero if the cell is refractory in state 2. There are only three state variables in the basic model: V(i,j,k), nstat(i,j,k), and nclock(i,j,k), allowing whole-heart simulation to be carried out efficiently. As with all models employing synchronous updating, dV/dt(i,j,k) must also be stored for time stepping. In Table 2.2 a few optional features are added to the basic model to expand its capabilites. Restitution of action potential duration APD = f(DI) can be added as an exponential function, but requires that APD(i,j,k) be stored so the profile function can be calculated for each time step. The threshold voltage V_{th} and the peak voltage V_{max} can be time-dependent, in which case the variable *nclock* effectively mimics recovery of the sodium channel. A simple linear ohmic ionic current can be added to improve subthreshold electrotonic interactions. External stimulation can force prolongation of the action potential by resetting the cell clock back an amount depending on stimulus strength. These new features improve realism and permit the model to simulate AP prolongation, decremental conduction, and

unidirectional block with an external stimulus or shock. The only additional stored variable in this case is $V_{max}(i,j,k)$. These modifications permit stimulus-induced reentry, as shown in Figure 2.5. This phenomenon will be discussed in a later section on reentry.

Table 2.2: Algorithm of Hybrid Automaton Model

For each time t = t + dt:

For each cell (i,j,k):

(1) Choose new state:

If (nstat = 1 and V* > 0)	nstat=2 (V* is any of 4 neighbours)
If (nstat = 2 and $V > V_{th}$)	nstat = 3 nclock=APD/dt
If (nstat = 3 and $V > V_{max}$)	nstat = 4 $V=V_{max}$
If (nstat = 4 and nclock = 0)	nstat = 2 nclock = 0 $V = V_{rest}$

(2) Calculate electrotonic current:

Evaluate V_{xx} ,V_{yy} and V_{zz} for Laplacian

Set stimulus current I_{stim} (optional)

$dV/dt = a_x V_{xx} + a_y V_{yy} + a_z V_{zz} + I_{ion} + I_{stim}$

(3) Update cells

If (nstat = 1)	nclock = nclock + 1	
If (nstat = 2)	V = V + dV/dt * dt nclock = nclock + 1	(electrotonic)
If (nstat = 3)	V = V + B * dt nclock = nclock – 1	(linear upstroke)
If (nstat = 4)	V = f(nclock, Vmax) nclock = nclock – 1	(action potential shape)

Options:	(1) $APD = a + (b - a)[1 - \exp(-nclock/\tau_1)]$	state 3 → 4 transition
	(2) $V_{th} = c + d \exp[-(nclock - ARP)/\tau_2]$	state 2 → 3 transition
	(3) $V_{max} = h\,[\,1 - \exp(-nclock/\tau_3)]$	state 2 → 3 transition
	(4) $I_{ion} = -g\,V$ (ohmic)	state 2 (subthreshold)
	(5) $nclock = nclock - p\,I_{stim}$	state 4 if stimulus on

The hybrid model has been implemented in blocks of tissue, an ellipsoidal left ventricle [309], and a human-heart geometry [370]. Computation proceeds rapidly and captures the essential behaviour of advancing wave fronts. Advantages of the hybrid model over the finite automaton model are the important ability to handle anisotropic conduction, and the option of reducing upstroke slope at short diastolic intervals to permit velocity restitution.

This type of model performs well in simulating intracardiac wave propagation during the depolarizing activation phase corresponding to the QRS complex of the body surface electrocardiogram. However, absence of electrotonic interactions in the model during most of the action potential, particularly phase 3 recovery, limits this type of model considerably if one is interested in repolarization dynamics during the T wave and simulating multiple beats encountered in VT and VF. Since it will not handle electrotonic interactions during the absolute and relative refractory periods, the present form has limited ability to simulate wave instabilities involved in dysrhythmias. This model also shares a problem with true automaton models, in that there is no mechanism to smooth spatial discontinuities introduced by stimuli or shocks. Dissipation of discontinuities by current diffusion can only take place during the brief intervals where the cells are subthreshold, and not while they are firing. In reality, neighbouring cells with disparate action potential durations exchange electrotonic current throughout their respective action potentials, such that the longer cell is shortened and the shorter cell is prolonged by small amounts to bring about a degree of smoothing. Since each automaton element in the domain changes according to individual clocks independently of its neighbours, elements retain memory of the past since the last state transition, and there is no mechanism for

transients and discontinuities to dissipate. Despite these limitations, the hybrid automaton model remained state-of-the-art for large-scale simulation for several years.

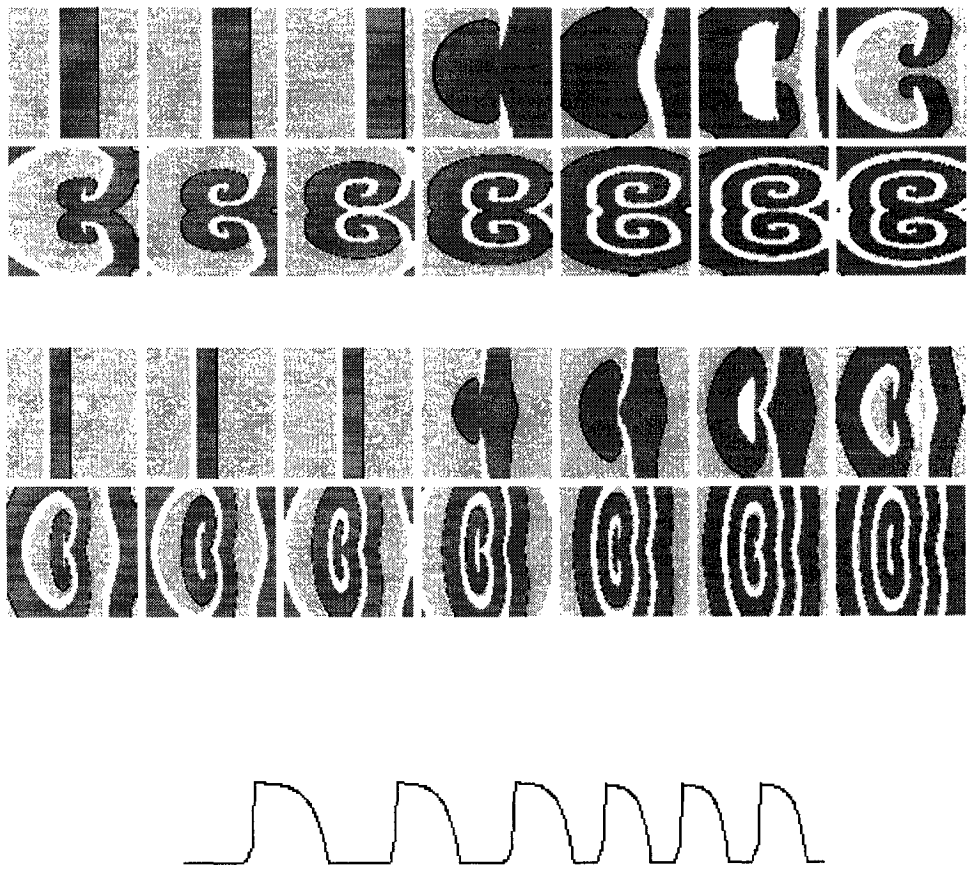

Figure 2.5. Stimulus-induced reentry in the hybrid model. A line stimulus S_1 delivered to the left edge of an 80 x 80 element field, followed by a spatially decaying shock S_2 to the centre of the field, results in retrograde block and formation of a spiral wave pair. Anisotropy is evident in these examples, with the fibre direction being horizontal (top) and vertical (middle). Action potentials are shown at bottom, sampled at one point over time and, above threshold, are simply defined as inverted exponential functions.

2.2.3 Relaxation Oscillators

Models based on differential equations have continuous variables that undergo smooth transitions, unlike those of finite state automata. Differential equation models of cardiac tissue have the essential topological features shown in Figure 2.6. The curve governing response during excitation has three distinct domains of alternating slope that may be

represented by a cubic or higher-order polynomial, or piecewise linear segments. There is a stable resting point, or attractor, at the resting membrane potential V_R intersected by a positive slope. Voltage pertubations away from this point cause a current favouring return to this point. Beyond a threshold potential V_{th} the sign of dI/dV changes and the current increases the voltage, pushing it away from this repellor. The rate of voltage change dV/dt determining action potential upstroke velocity depends on the magnitude of the current along this segment. The crossover point at V_m determines the peak voltage V_p and is a stable point. Recovery follows a trajectory in the V-I plane back to V_R according to an outward current. Subsequent action potentials occuring with incomplete recovery may follow different trajectories. All models to be discussed in the following sections retain this basic topology, despite varying levels of complexity.

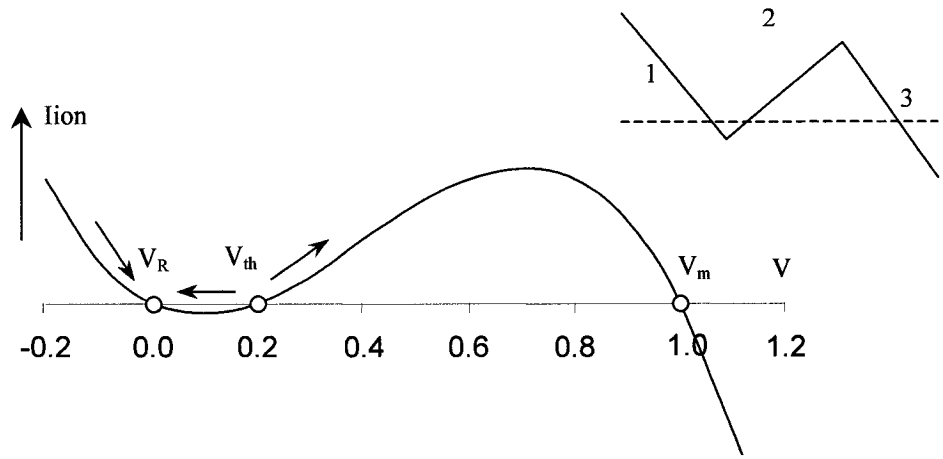

Figure 2.6. Topology of cellular excitation has three zeroes representing stable resting and peak voltages, and an unstable threshold. This curve can be a cubic or higher-order polynomial, a function based on ionic currents, or a piecewise linear function (inset).

Lord Rayleigh published an extensive treatise on the theory of sound in 1896 [416]. A particular interest in musical instruments inspired him to analyze self-excited vibration in reeds and bow strings which could be modeled by introducing nonlinear damping F(x) to the vibration equation. The choice of damping F(x) in this equation determines whether oscillations decay, remain stable, or are self-excitated.

$$\ddot{X} + F(\dot{X}) + \omega^2 X = 0 \qquad (2.1)$$

Van der Pol conducted experiments on spontaneous oscillations using an early radio transmitter built around a nonlinear triode tube [497]. By varying circuit parameters he was able to induce self-excitation and modify the shape and symmetry of the output waveform. He called this device a "relaxation oscillator", because each half-cycle was dependent on the charging of a capacitor [232]. The governing second-order differential equation approximates the stable linear version at small amplitudes, but becomes a limit-cycle oscillator with negative damping at larger amplitudes [489].

$$\ddot{X} + \alpha(X^2 - 1)\dot{X} + \omega^2 X = 0 \qquad (2.2)$$

Van der Pol and van der Mark in 1928 constructed an electrical circuit with three neon-tube oscillators of different frequencies coupled in series, and proposed this as a model of the beating heart with sinus node, atria, and ventricles [498]. This coupled oscillator model exhibits intervals of phase-locking and Wenckebach rhythms. Bonhoeffer later constructed a chemical iron wire model of axon propagation which could be represented by the same governing equations [482]. FitzHugh separated the single-variable van der Pol equation into a pair of first order differential equations in voltage V(t) and a second state variable W(t) controlling recovery [170], and showed that the phase plane of these two variables could be divided into a resting attractor with active or firing regions, an absolute refractory region, and a relative refractory region. FitzHugh also pointed out the topological similarity of this two-variable Bonhoeffer-van der Pol (BVP) model with the four-variable Hodgkin-Huxley nerve model [171] by introducing a transformation of variables. Nagumo constructed an electrical analogue of these equations employing a tunnel diode to give the cubic term [482]. The BVP model is now referred to as the FitzHugh-Nagumo (FHN) model, and is summarized in Table 2.3.

Table 2.3: FitzHugh-Nagumo Model

$$\frac{dV}{dt} = f(V) - W$$

$$\frac{dW}{dt} = \varepsilon(V)\,[g(V) - W]$$

$$g(V) = g_o\,(V - V_{OS})$$

(i) Cubic Version: $f(V) = a\,(V - V_R)\,(V - V_{th})\,(1 - V)$

(ii) Linear Version:

$$f(V) = \begin{cases} r\,(V - V_R) & \text{segment 1} \\ g_i\,(V - V_{th}) & \text{segment 2} \\ p\,(V - V_m) & \text{segment 3} \end{cases}$$

This FHN model has been the subject of numerous studies employing a variety of variations [102, 396, 491], the simplest being shown above. The nonlinear function f(V) is analogous to the excitatory current, and can be a cubic polynomial with three roots representing resting, threshold, and maximum potentials, or a piecewise linear function. The restoring current is analogous to W, and activates with a delay controlled by a time constant $\tau = \varepsilon^{-1}$ which may, in fact, be a voltage-dependent function [396].

For the purpose of illustration, the following parameter values are assigned: the resting potential $V_R = 0$, the threshold $V_{th} = 0.2$, maximum potential $V_m = 1$. The slope $r = -15$ represents the input resistance of the resting membrane, $g_i = 2$ is the conductance of the excitatory current analogous to g_{Na} of sodium, $p = -10$ is the membrane resistance at the action potential plateau. The excitation function f(V) is piecewise linear with three segments corresponding to the inset of Figure 2.6. The rate constant $\varepsilon = .05$ is the reciprocal of the time constant for the inactivation variable W that exponentially follows g(V), the effective outward current. The conductance $g_o = 4$ is analogous to g_K of

potassium. The optional offset voltage V_{OS} is a control parameter that is zero for normal ventricular and atrial cells having stable membrane with action potentials that must be stimulated to fire. If V_{OS} is given a small positive value such as 0.15, the intersection point of f(V) and g(V) changes from a stable attractor to a repellor, and the cell becomes an autonomously firing oscillator like a pacemaker. The phase planes for these two cases

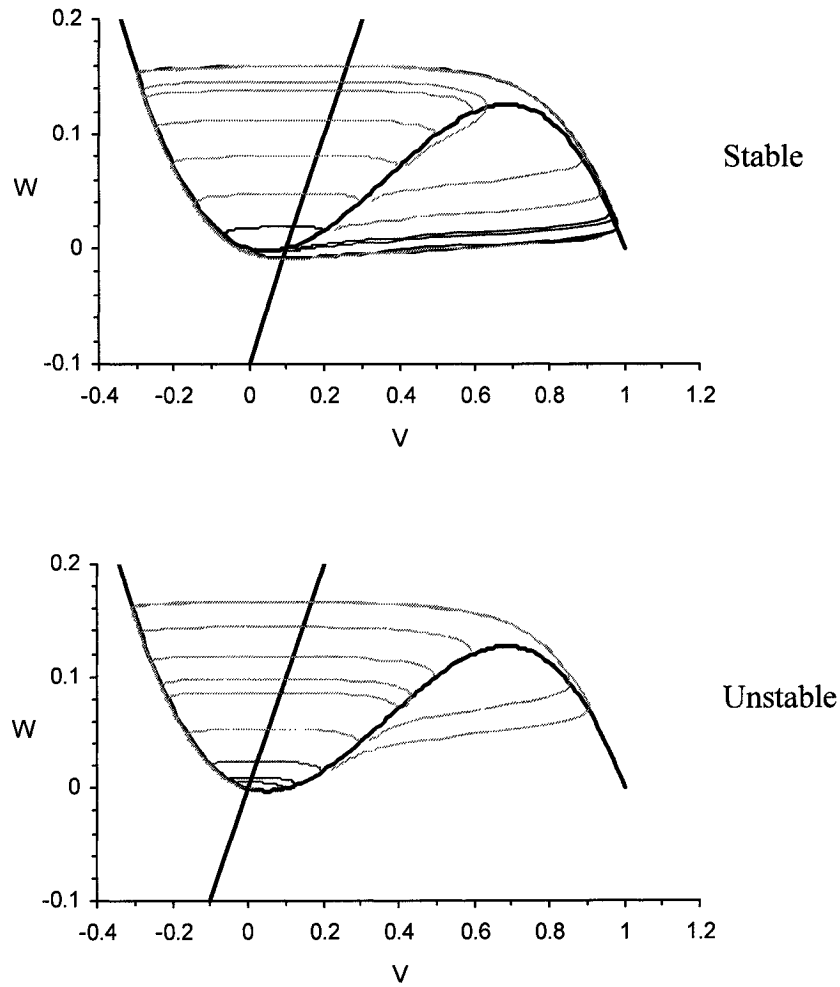

Figure 2.7. Phase plane for the FitzHugh-Nagumo relaxation oscillator model. The location of the intersection of the two nullclines, shown as thick lines, determines whether the resting point is stable, requiring a stimulus to induce firing (top), or unstable, producing limit-cycle oscillation (bottom) like a spontaneous pacemaker cell. These two modes of behaviour are apparent in the action potential trains in Figure 2.8.

are shown in Figure 2.7. Linear stability analysis can solve for the value of V_{OS} at which there is an abrupt change to spontaneous oscillation [45]. This occurs when there is a positive change in sign of the real parts of the eigenvalues of the Jacobian of the two-variable system of equations linearized at the point of interest. As V_{OS} is increased, the stable attractor becomes a limit cycle by a Hopf bifurcation. Figure 2.8 illustrates model behaviour of several versions. The action potentials in the basic FHN model tend to be somewhat square in shape, owing to unrealistic reactivation of the steep inward current f(V) during repolarization.

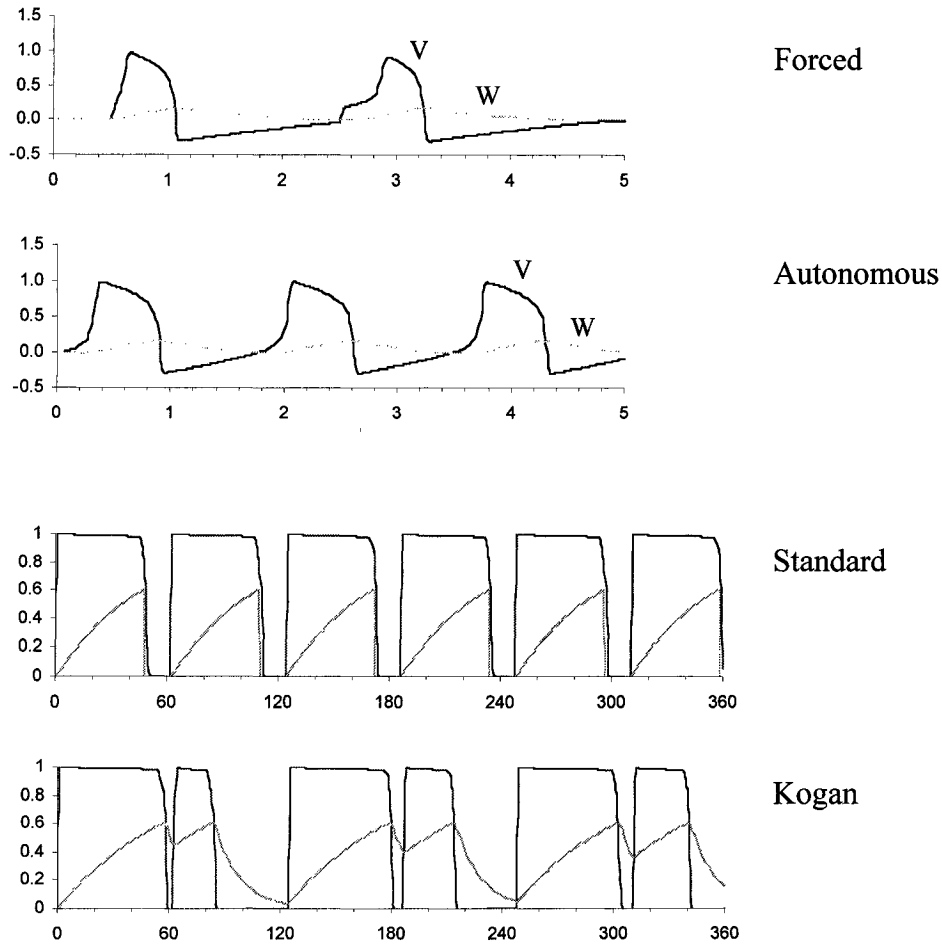

Figure 2.8. Action potentials of some variations of the FitzHugh-Nagumo model. The top two frames employ a cubic f(V), whereas the bottom two use piecewise linear functions resulting in a more square profile. The second frame shows a spontaneously oscillating pacemaker version, while all other models require an initiating stimulus. The bottom frame shows the Kogan modification to introduce APD restitution at rapid pacing rates.

Two-variable relaxation oscillator models exhibit relative refractoriness in the form of a higher stimulus theshold at incomplete recovery, but show no response refractoriness. In other words, a subsequent action potential, when elicited, is nearly identical in form to the preceding one. There is very little action potential shortening (restitution) for short recovery intervals. The original formulations of these models lack realistic action potential morphologies and restitution dynamics. They are nevertheless still useful as each requires only two variables: a transmembrane potential V, and a single time-dependent gating parameter W that controls recovery. The phase-plane trajectories (V,W) are readily plotted and analyzed providing insight into oscillatory behaviour, recovery, and overall stability [46].

Nonlinear phenomena are likely important in arrhythmogenesis [126, 542]. In particular, break-up of fibrillation waves may be a consequence of action potential alternans, quasiperiodicity, and chaos [189]. Since ambiguity of future state in a dynamic flow would arise if trajectories intersected in a state space, the Poincaré-Bendixson theorem of nonlinear dynamics states that any continuous system exhibiting bifurcations and chaos must have at least three state variables [449]. This gives rise to a three-dimensional or higher state space, where trajectories need never cross regardless of complexity. The two-state variable FHN model in its basic form cannot represent such behaviour without at least a third variable, consequently there is almost no restitution in the basic model. Kogan introduced modifications to the time constant ε of the slow variable of the FHN model according to the value of V and the sign of dw/dt, effectively making $\varepsilon(V)$ a third state variable, allowing for a limited degree of action potential duration restitution [285] shown at the bottom of Figure 2.9. The action potential profiles in the Kogan modification are still almost square because the inward current reactivates as the AP recovers, and since the inward current function f(V) is steep, there is an abrupt drop as the potential passes back over the zenith of the f(V) curve partway down. This phenomenon is physiologically unrealistic as the sodium current does not reactivate during action potential repolarization. It does not appear to be a simple matter to eliminate this problem and achieve a smooth action potential without introducing another state variable.

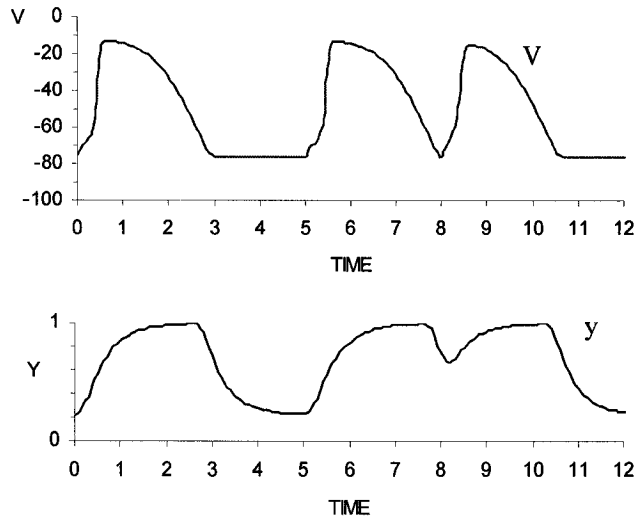

Figure 2.9. Original van Capelle-Durrer model with a single gating variable y(t). Action potentials are elicited by the first two current stimuli. There is no significant shortening of APD following the third premature stimulus at t = 8.

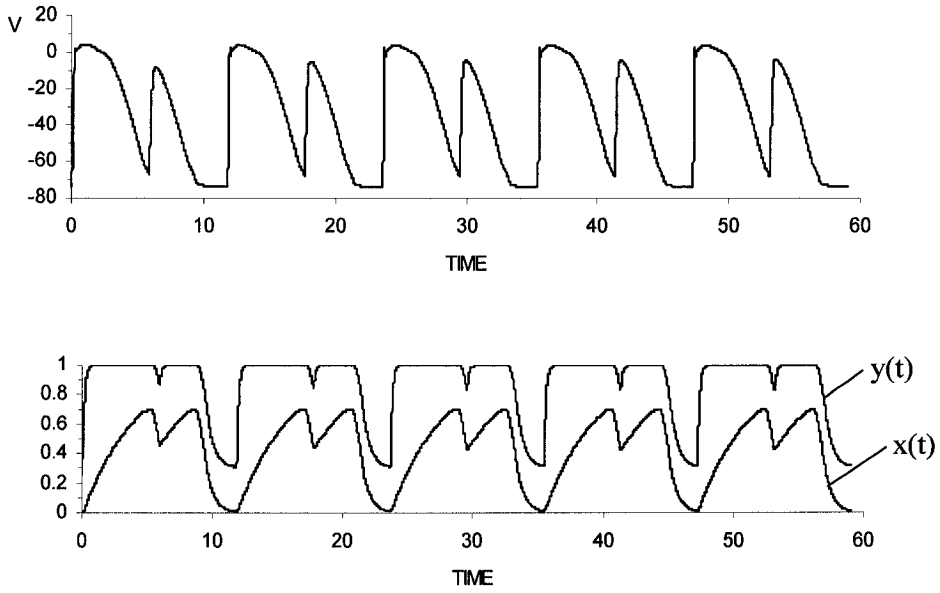

Figure 2.10. A modified version of the van Capelle-Durrer model described in the text. This version retains the original gating variable y(t) controlling the sodium current, and has a new state variable x(t) controlling the calcium current which gives restitution of action potential duration. The action potential morphology is more realistic, and alternans is seen to occur at the rapid pacing rate shown here.

An alternative two-variable model which is similar to the FHN model was developed by van Capelle and Durrer in 1980 [496]. This model, summarized in Table 2.4, uses a cubic activation function f(V) and a two-segment piecewise linear inactivation function to achieve action potentials with improved morphology. The most desirable feature of this perhaps under-utilized model can be seen by rewriting the original equations in terms of an inward current I_{in} and an outward current I_{out}, and the cubic activation polynomial f(V) in terms of resting potential V_R, threshold V_{th}, and peak voltage V_p. Unlike in the FHN model, the VCD model's inward current is inactivated by the multiplier (1 – y), and is therefore turned off rapidly after the upstroke. It recovers only after the action potential has almost reached resting potential, thus performing more like the true sodium current.

Table 2.4: Van Capelle-Durrer Model

$C \frac{dV}{dt} = I_{in} + I_{out} + I_{stim}$	$f(V) = .0035 (V - V_R) (V - V_{th}) (V - V_p)$
	$V_R = -74.5 \quad V_{th} = -64.3 \quad V_p = -11.2$
$\frac{dy}{dt} = [y_\infty - y] / \tau$	$y_\infty = 0.5 (V + 80)$ max range [0, 1]
$I_{in} = f(V)^* (1 - y)$	$g(V) = 0.5 (V + 80)$ if $V < -70$ $= 0.015 (V + 80)$ if $V > -70$
$I_{out} = g(V)$	$\tau = 0.5$

Figure 2.9 illustrates the behaviour of the original VCD model which, like the FHN model, lacks significant APD restitution. This is not surprising, since there are only two state variables. Action potential morphology is, however, substantially improved over that of the FHN model. Building on this basic VCD model, we can produce a remarkably good extension by introducing a simple modification to give it physiological currents I_{Na}, I_{Ca}, and I_K, and do so only by adding a third state variable x(t), complementing the existing state variables V(t) and y(t). The equations of this model, proposed here for

illustration only, are listed in Table 2.5, and the behaviour is shown in Figure 2.10. By comparison with the full ionic models to be discussed in the next section, sodium inactivation (1–y) here is analogous to h(t), calcium inactivation (1–x) here is analogous to f(t), and $I_K(V)$ is the voltage-dependent rectifier current. The time constants of y(t) and x(t) can be defined individually, allowing independent control of velocity and APD restitution. The cost of these improvements is the requirement for three state variables (V,y,x) rather than two (V,W).

Table 2.5: A Three-Variable Model

$$C \frac{dV}{dt} = I_{Na} + I_{Ca} + I_K + I_{stim}$$

$$f(V) = a (V - V_R) (V - V_{th}) (V - V_p)$$

$$a = .007 \quad V_R = -74 \quad V_{th} = -65 \quad V_p = 0$$

$$\frac{dy}{dt} = [y_\infty - y] / \tau_y$$

$$y_\infty = 0.05 (V + 80) \quad \text{range } [0, 1]$$

$$\frac{dx}{dt} = [x_\infty - x] / \tau_x$$

$$x_\infty = 0.05 (V + 70) \quad \text{range } [0, 1]$$

$$I_{Na} = f(V)^* (1 - y)$$

$$\tau_y = 0.15 \text{ or } 0.5 \text{ if } dy/dt < 0$$

$$I_{Ca} = -12^* (1 - x)\, y$$

$$\tau_x = 8.0 \text{ or } 4.0 \text{ if } V > -40$$

$$I_K = g(V)$$

$$g(V) = 0.6 (V + 80) \qquad V < -70$$
$$= 6 + .017 (V + 70) \qquad V > -70$$
$$= 7.2 + 0.5\, V \qquad V > 0$$

The apparent simplicity of these two-variable models belie their impressive capacity to exhibit rich dynamics open to mathematical analysis in one-, two-, and three-dimensional media. Relatively low computational requirements allow implementation in large-scale blocks of tissue, such that these types of models are the basis of most currently published whole-heart simulations employing reaction-diffusion kinetics [387, 510].

2.2.4 Ionic Models

Realistic physiological models incorporating individual ionic currents were not developed until Hodgkin and Huxley published their seminal model of the giant squid axon action potential in 1952 [229], based on the voltage clamp technique developed by Marmont [336]. The HH ionic model incorporates time-dependent and voltage-dependent sodium and potassium channel kinetics as differential equations. In 1962, Noble extended this concept to cardiac Purkinje fibres by formulating an inward rectifying potassium current, and later adding a slower calcium current to prolong the action potential [375]. Since the calcium current introduced at that time was admittedly unrealistic, further refinements were later introduced by McAllister, Noble, and Tsien [340], and by DiFrancesco and Noble [131]. The MNT model remains a commonly used description of conduction system Purkinje fibre. In 1977, following voltage clamp studies focussing on the calcium current, Beeler and Reuter introduced a model of the ventricular cell employing four currents [32], which remained the standard for modeling cardiac cells throughout the 1980's. This model is shown in Figure 2.11.

Complete recovery of membrane excitability following an action potential can take several seconds. A premature stimulus applied to a cell prior to complete recovery results in lower excitability and shorter action potential duration. Figure 2.12 shows the standard Beeler-Reuter model paced at a several basic cycle lengths. High frequency stimuli result in shorter action potential durations, owing largely to incomplete calcium channel recovery and incomplete potassium channel reactivation. The resulting steady state curve of APD versus basic cycle length (BCL) in Figure 2.11 is called the dynamic restitution curve. An alternative way to look at cell recovery is to plot the APD against the diastolic interval (DI) measured from the AP tail until delivery of a premature stimulus following a regular cycle train. This is called the standard restitution curve, and is only weakly dependent on the preceding cycle length. As a close approximation, APD depends on the recovery interval from the preceding action potential regardless of that cell's past history. Except for very short diastolic intervals, these curves can be reasonably approximated as the sum of two exponential terms [314]. Restitution in the BR model is a consequence of

slow recovery dynamics of calcium and potassium currents. Recovery of action potential amplitude is dependent on sodium channel recovery.

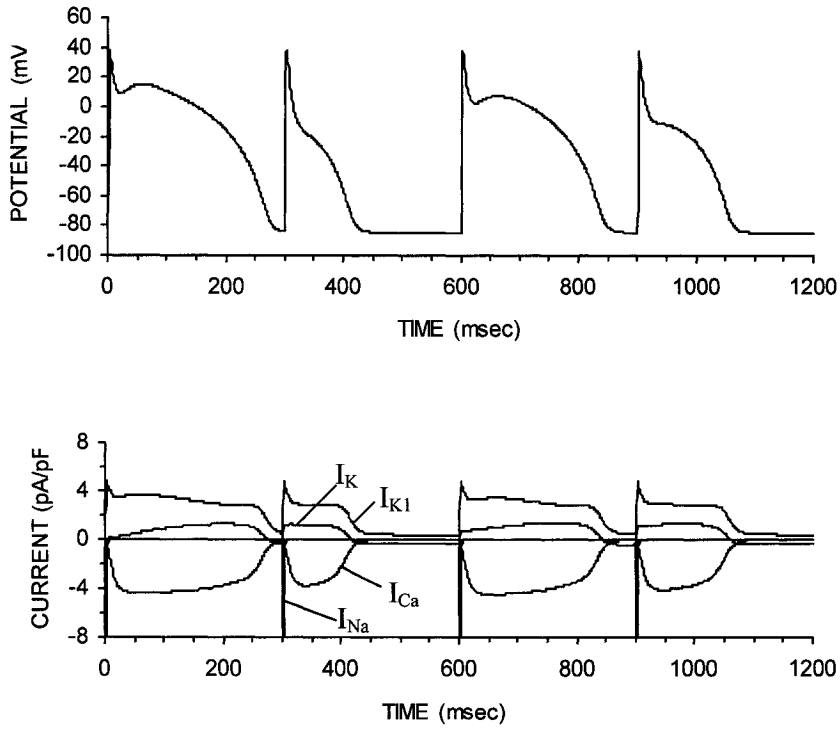

Figure 2.11. The standard Beeler-Reuter ventricular cell model and its ionic currents.

The BR model has several shortcomings. The very small membrane length constant and complex cellular structure of cardiac tissue prevented adequate voltage clamping at the time, and the large rapid sodium current could not be measured reliably. The sodium current kinetics from the Hodgkin-Huxley (HH) giant squid axon were therefore used. The chosen maximum sodium conductance in the BR model is several times smaller than that measured more recently in human ventricular myocytes [435]. The calcium current responsible for the action potential plateau lacks detail and was referred to simply as the "slow inward" current I_s. This current was modelled with simple HH kinetics, and does not account for calcium exchange between intracellular compartments [331]. Potassium currents, which were modified from those of the MNT model, are also overly simplified and higher than those seen in human cells, resulting in a relatively short APD. Some

important differences between tissue properties of giant squid axon and cardiac tissue are summarized in Table 2.6. Larger radius, lower resistivity, and higher sodium conductance all contribute to the higher conduction velocity seen in the giant squid axon.

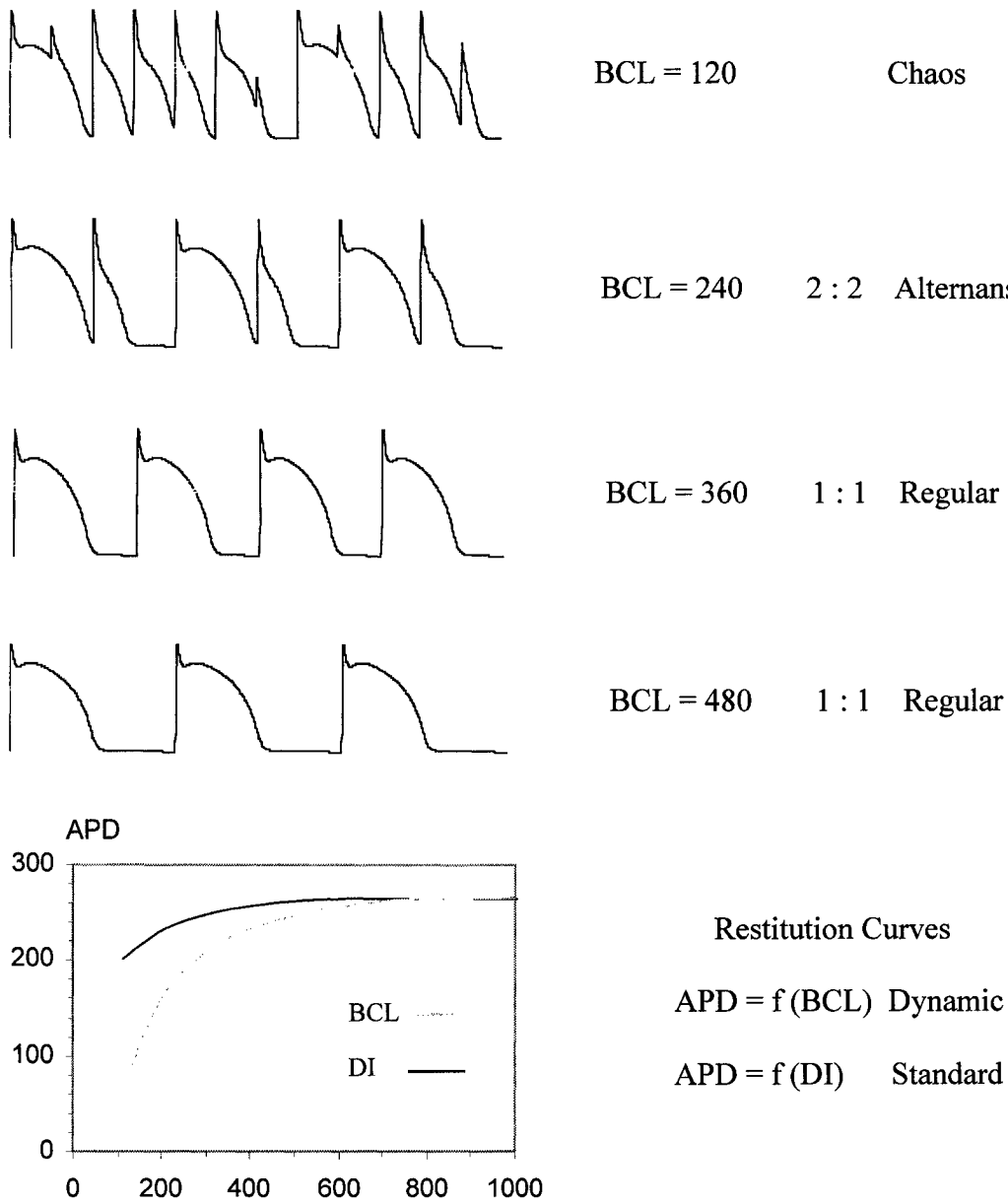

Figure 2.12. Pacing the Beeler-Reuter model at increasing rates results in various ratios of phase locking, from 2:1 alternans, through quasiperiodicity, to chaos (top). The dynamic restitution curve shows how action potential duration (APD) varies with pacing basic cycle length (BCL). The standard restitution shows how APD depends on the diastolic recovery interval (DI) since the previous action potential. Time units are in milliseconds.

Ebihara and Johnson [144], and Drouhard and Roberge [142] addressed deficiencies in the sodium current formulation by presenting modified versions of sodium current dynamics relevant to cardiac tissue. Luo and Rudy added several components to the outward potassium currents in their 1991 phase 1 model (LR1), while retaining the Beeler-Reuter calcium dynamics [329]. The Luo-Rudy phase 2 model (LR2) in 1994 added detailed multi-compartment intracellular calcium dynamics [330]. This model is currently the most detailed mathematical description of the ventricular action potential, and has been further modified to simulate action potentials in heart failure and ischemia. A useful feature of the LR1 and LR2 membrane models is an attempt to account for changes in extracellular potassium concentration. This is of particular importance during ischemia [149]. Varying $[K^+]_o$, even within the normal physiological range of 3.0 to 5.0 mM, causes significant changes in action potential properties. Supernormal excitability is also evident in this model, and is potassium-dependent [329].

Table 2.6. Comparison of Squid Axon and Cardiac Fibre

	Squid	Cardiac
Radius	0.238 cm	0.0008 cm
Resistivity	35 Ω cm	200 Ω cm
Sodium g_{Na}	120 mmho/cm^2	13 mmho/cm^2
Velocity	18 m/s	0.66 m/s

All the models discussed above are largely based on data taken from experiments on guinea pigs and other species whose cellular action potential duration and restitution properties do not necessarily correspond with human data. There is presently no cellular model specifically developed to represent human cardiomyocytes.

2.3 Cellular Black Box

Does the simulation of spatially propagating action potentials demand highly detailed cellular models? The answer to this question obviously depends on what is expected of the model. One can consider each element to be like a "cellular black box", since for the purpose of modeling electrical wave propagation, a cell or element may be considered to behave as an electrical device within a black box. The outside world sees only a voltage-current relationship, and need not be aware of the internal dynamics of the cellular model. Each element approximation sees only a current input from electrotonic influence of neighbouring cells or external stimuli, and adjusts itself internally to produce a voltage output seen by other cells as in Figure 2.13. As far as propagation within the global array is concerned, it does not matter what the detailed ionic mechanics are inside the cell, so long as the current-voltage relationship is determined. Simple models should suffice if one is concerned only with simulating the global transmembrane potential distribution V(x,y,z,t), as is the case for action potential propagation or ECG calculation. One must, of course, be aware of any limitations and the domains of validity, and be willing to accept simplifying assumptions.

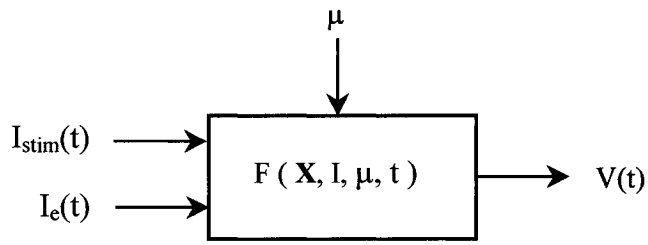

Figure 2.13. Each cellular element may be considered effectively a "black box" with an output voltage V(t) computed for a given current input. Internal dynamics F operate on a vector of state variables **X**(t), input electrotonic current I_e from neighbouring cells in the tissue domain, external stimulus or shock current I_{stim}, and a fixed parameter set μ.

2.4 Computational Limitations

A high-fidelity model for computer simulation would ideally contain cellular elements that correspond to the length scale over which properties can be assumed uniform, which would be smaller than individual cells themselves. All known ionic currents and intracellular and extracellular spaces would be included. Time steps would need to be chosen to capture the shortest events while maintaining numerical stability. To meet such resolution, a model would ned to have many millions of elements, and would require computational times that would vastly exceed any practical waiting period, even using the most powerful computing hardware presently available. The study of basic phenomena and interpretation of results also becomes difficult if one employs overly-complex models with too many variables. Virtually all computer models simulating any complex phenomenon face compromises, which necessitate simplifying assumptions. For a given computing power, applied to modeling cardiac electrophysiology, one must choose between defining detailed cellular models and defining complex geometry, as illustrated in Figure 2.14 with specific cellular models.

Most models described in this disseratation were run on a Pentium-based personal computer, including all cellular automata and coupled map lattices, and ionic models in single cells and one-dimensional cables. Ionic models in two- and three-dimensional geometries were run on an RS/6000 system (IBM Corp.) in the Department of Physiology and Biophysics. All programs and simulation software were written by the author, and graphics were produced by pixel-generating programs customized for this purpose.

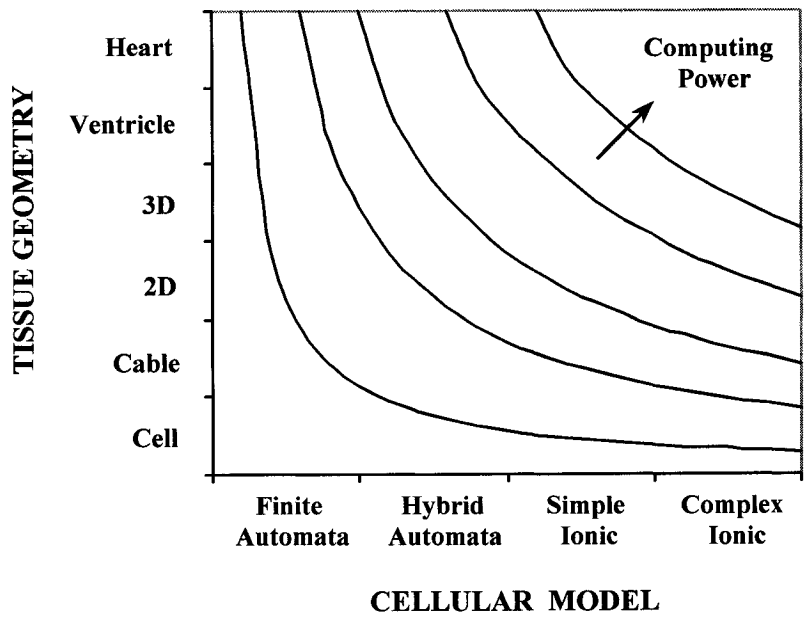

Figure 2.14. Limitations in available computing power determine the compromise between detailed cellular models and detailed tissue geometry. The curves are illustrative only, and not meant to be quantitatively accurate. The lower two contours are easily handled by personal computers, while the higher contours require a large mainframe computer or parallel processing supercomputer.

Chapter 3

COUPLED MAP LATTICE

3.1 Introduction

This chapter begins to explore the spatiotemporal structure underlying fibrillation using a simple two-dimensional coupled map lattice model (CML) that incorporates only the most basic features of excitable cardiac tissue. This simplified approach has several advantages over the use of more sophisticated ionic models. Complexity is reduced by defining only two state variables at each cell, one for firing and one for recovery. The rules governing individual cell behaviour are simple and can be adjusted independently of any specific cellular model. The salient roles of conduction velocity and action potential duration in the emergent spatiotemporal patterns can be explored. Restitution of action potential duration can be assigned any desired function APD = f(DI) without the added difficulty of tailoring complex ionic models to fit such a relationship. Statistical measures of complexity can be calculated relatively easily within a discrete medium. CML models, as proposed by Kaneko, have continuous state variables [263, 264], while closely-related cellular automata (CA) of cardiac tissue reported in the literature have discrete states [25]. Both types of models compute rapidly on a personal computer allowing large parameter spaces to be explored. Solitary and multiple spiral waves and ectopic foci will be simulated in a simple cylindrical heart geometry to explore the origins of complexity and the nature of phase transitions to fibrillation. We will use the model to analyse the origin of the electrocardiograms in fibrillation in a later chapter

Some basic questions to be addressed include:

How does spiral wave stability depend on action potential restitution?
What is the maximum density of spiral waves that can persist in a heart?
How do statistical measures of complexity depend on system parameters?
How do ECG patterns vary with size, location, and number of spiral waves?
Can the body surface ECG distinguish spiral wave from ectopic activation?

3.2 Algorithm

The components of discrete CML and CA models are the same as other dynamical systems: a state vector X(i), where i = 1...N; a state transition function $\omega(X)$ defining changes in X(i); and a fixed parameter set or external control μ. Whereas differential equation (DE) models evolve according to the vector of derivatives $dX/dt = f(X, \mu)$ integrated over small differentials, finite state models employ a discrete transition mapping $X(i+1) = \omega(X(i), \mu)$ from the present state to the next state, essentially mapping a discrete lattice domain onto itself at finite time intervals. Elements are called cellular automata (CA) if state variables are confined to discrete integers, whereas a coupled map lattice (CML) has continuous states as shown in Table 3.1. The differences in behaviour between CA and CML models may be subtle in many cases, since CA are essentially a subset of CML. CA models employ integer rather than floating point arithmetic, and require less computer memory. CML models, however, can exhibit chaotic dynamics within continuous states, unconstrained by the discrete states of a CA model [264].

Table 3.1 Comparison of Dynamical Systems

Model	Time	Space	State
DE	C	C	C
CML	D	D	C
CA	D	D	D

C = continuous D = Discrete

The algorithm for the CML model is shown in Table 2.2. Although extension of the model to three dimensions is relatively straightforward, investigations here will focus on a two-dimensional isotropic medium. The single state variable X(i, j) representing cell activation is set to zero if cell (i, j) is at rest. The cell fires if a threshold condition is reached, at which time X(i, j) is instantly set to its maximum APD value, which then counts down by one unit with each time step until arriving back at zero, thus defining the action potential. The cell voltage V(i, j) is proportional to this clock value, and is scaled to have a maximum value V_m. The resulting triangular AP profile is shown in Figure 3.1. The firing threshold is reached if at least N_A of its eight immediate lateral and diagonal neighbours are above a threshold voltage V_{th}. This switching criterion is essentially a discrete version of diffusive coupling. When the state X(i, j) returns to zero, an absolute refractory period R begins, and is counted up by one each time step by the variable Y(i, j). X(i, j) and Y(i, j) need not be separately stored variables, as both can occupy the same memory by assigning one to have a negative flag bit and taking the absolute value for computation, since X = 0 when Y > 0, and Y = 0 when X > 0.

An absolute refractory period R must expire before the cell becomes excitable again. This short interval prevents the repolarizing action potential tail from spuriously exciting neighbours by "backfiring" when spatial voltage gradients are large. Subsequent APD is determined by a restitution function APD = f(DI), where DI = Y(i, j) – R is the diastolic interval elapsed since the cell became excitable. This function is implemented by setting X(i, j) = f[Y(i, j) – R] at the time of firing, thus giving the APD shown in Figure 3.1. We have the option of defining all cells to have constant and spatially uniform APD, regardless of refractoriness, or more realistically, to recover with an assigned exponential time constant.

$$APD = f(DI) = APD_o + (APD_m - APD_o)\,(1 - e^{-DI/\tau}) \qquad (3.1)$$

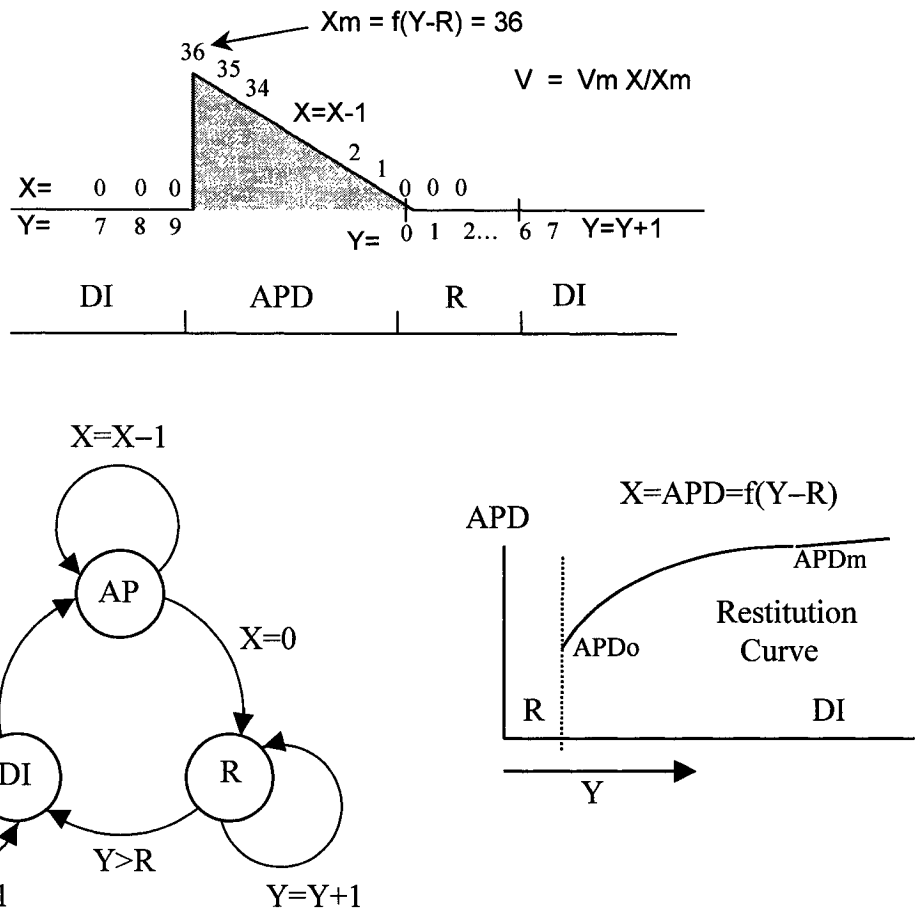

Figure 3.1. The basic Coupled Map Lattice model. An action potential is shown at the top along with the definition of states. The maximum value of X(i, j) is the APD. The diastolic interval DI does not begin until the refractory period R has elapsed. Recovery time Y counts up from the time X reaches zero at the end of APD. The restitution curve determines the next APD according to DI = Y – R. APD_o and APD_m are the intercept and maximum values of APD. Voltage is proportional to X(t) giving a triangular profile V(t).

Conduction velocity of a plane wave is uniform at one cell per time step, approximating Huygens principle of isotropic wave propagation independent of wave front curvature. Only the hybrid automaton model or continuous differential equation models can overcome these limitations, if one must account for velocity dispersion and anisotropy. Action potential shapes are triangular to maintain simplicity, although it is easy to assign some other template function V(nclock). The APD restitution curve is specified

independently of any ionic model, in our case taking on an exponential function. The model computes rapidly on a personal computer.

Table 3.2 Coupled Map Lattice Model Algorithm

Set initial condition X_{ij} Y_{ij}

For each time $t = t + \Delta t$:

For each cell (i,j):

(1) Calculate cell voltages

$V_{ij} = (X_{ij} / APD_m) V_m$ Voltage $V_{ij} \propto X_{ij}$

(2) Count active neighbours $N_A = \Sigma (V_{ij} > 0.3 V_m)$ Maximum 8

(3) Update cell clocks

If $X_{ij} > 0$ then $X_{ij} = X_{ij} - 1$ Decrement firing clock if in AP

If $X_{ij} = 0$ then $Y_{ij} = Y_{ij} + 1$ Increment refractory period if resting

If $X_{ij} > 0$ and $N_A \leq 2$ then $X_{ij} = X_{ij} - 1$ Shorten APD of isolated firing cell

(4) Switch to firing state

If $X_{ij} = 0$ and $Y_{ij} \geq R$ and $N_A \geq 3$ then New firing APD

$X_{ij} = APD$ *

$Y_{ij} = 0$

If $X_{ij} = 0$ and $Y_{ij} \geq CL$ then Optional ectopic beat (cycle length CL)

$X_{ij} = APD$ *

$Y_{ij} = 0$

* where $APD = APD_o + (APD_m - APD_o)(1-\exp[-(Y_{ij} - R)/\tau])$

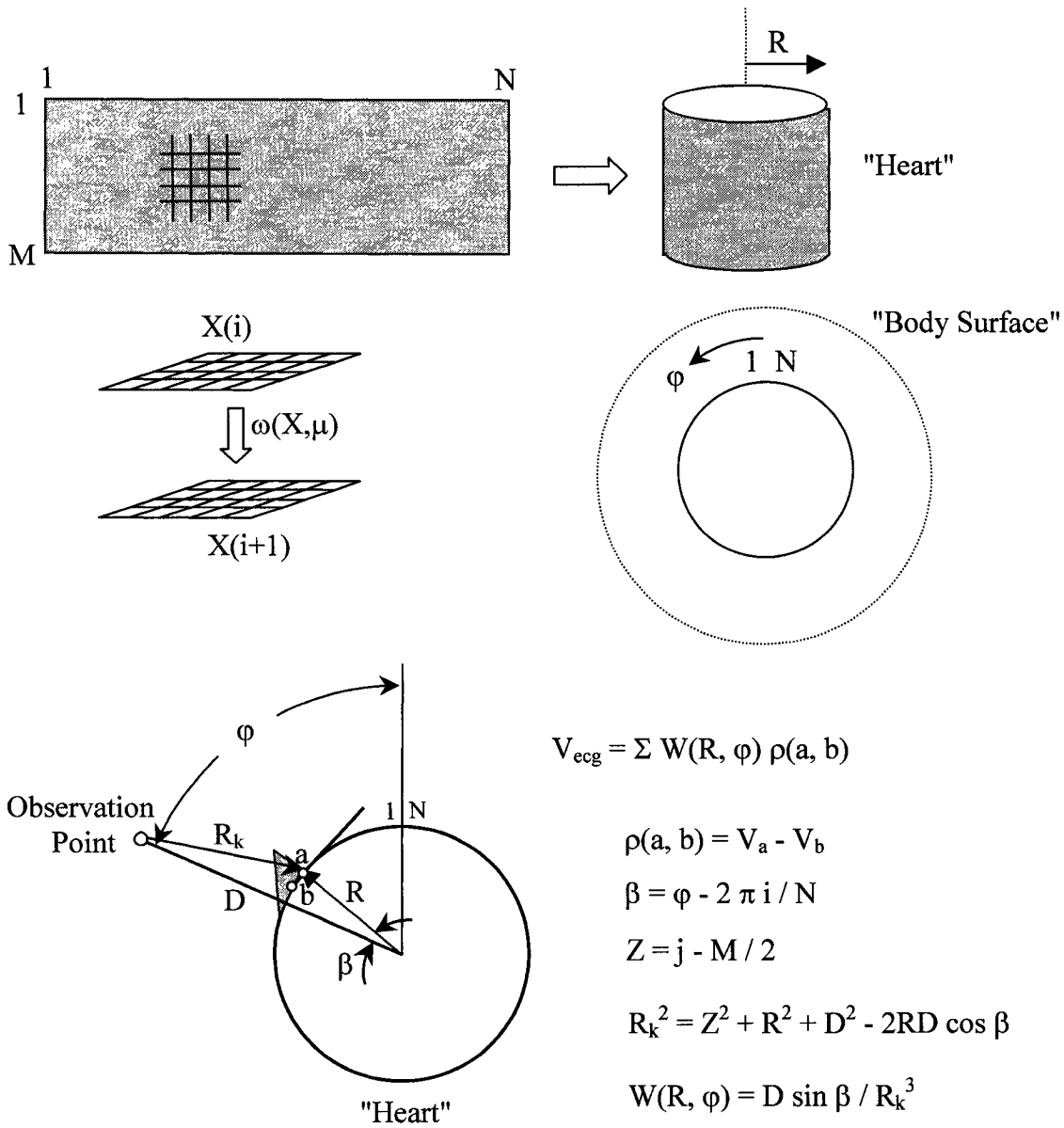

Figure 3.2. The NxM tissue domain is wrapped into a cylinder of radius R representing the heart. The body surface is idealized as a ring of radius D on which the ECG signals are calculated. The grid of states X(i, j) is mapped by the transition function $\omega(X, \mu)$ at each time step to determine the new states. The ECGs are calculated by summing dipole fields. Here the calculation is shown in two dimensions. The voltage difference between adjacent points a and b defines a single dipole $\rho(a, b)$ at surface point (i, j) on the cylinder within the shaded action potential shown. The component of the dipole vector tangent to the cylinder surface is resolved along the observation axis and divided by the distance R_k, which is determined by the cosine rule. This defines a spatial kernel function $W(R, \varphi)$ which varies as the inverse of R_k squared. φ is the location angle or longitude of the observation point relative to the tissue domain and is proportional to i.

For convenience, the model is implemented in arbitrary time and space units to permit unit incrementing and decrementing, but can be scaled into realistic units. If we assume that each time step equals 5 ms of real time, then a maximum APD = 60 units corresponds to 300 ms. APD scales as shown in Table 3.3. Plane wave propagation around a cylinder circumference of N = 150 space units takes 150 time units or 750 ms. If we assume a conduction velocity of 30 cm/s, a value between longitudinal and transverse velocites [420, 443] the cylinder circumference works out to 22.5 cm with a diameter of 7.2 cm, approximately the size of a real heart. Each spatial element is therefore 225 / 150 = 1.5 mm. The "heart" is then 150x50 units, corresponding to 22.5 cm of length and 7.5 cm of height. Higher spatial resolution can be easily obtained, but the above values are satisfactory for our purposes.

Table 3.3 Scaling of Model Time With Real Time

Model	Real
12 units	60 ms
16	80
20	100
24	120
28	140
32	160
36	180
42	210
48	240
60	300

Electrocardiograms V_{ecg} are calculated by summing the electrical potentials produced by each surface dipole as seen at a distant observation point within an infinite homogeneous volume conductor [193, 308]

$$V_{ecg} = k \int_H \frac{\nabla V \cdot \vec{r}}{r^3} dV \approx k \sum_{i=1}^{N} \sum_{j=1}^{M} \frac{\nabla V \cdot \vec{r}}{r^3} \qquad (3.2)$$

where $\nabla V \cdot r$ is the gradient of action potential field in the myocardium resolved along the vector r which extends from the surface point to the observation point. The integral is

evaluated over the heart volume H, which is a summation over the cylinder surface (i, j) in the CML model. The voltage gradient ∇V can be obtained numerically by taking each 2x2 cell-cluster and summing the vectors of the two voltage differences in the diagonal directions. Figure 3.2 shows an equivalent representation as a source dipole $\rho(a, b)$ for a cell pair centred at coordinates (a, b) in two-dimensions. In this special case, the voltage gradient can be calculated between each pair of cell neighbours, and resolved as a surface tangent vector along the observation axis by a dot product, and dividing the result by the third power of distance R_k between the source dipole and the observation point. V_{ecg} is the sum of all such contributions of individual dipoles to the field potential.

In preliminary simulations, the ECG observation points were placed in the same plane as the rectangular medium, but outside the tissue domain. The computed ECG's were found to be very sensitive to the sharp action potential wave fronts reaching the edge and abruptly terminating as they exited the domain. A similar phenomenon occurs in the heart at the instant when the ventricles become fully activated, and accounts for the abrupt drop of the RS segment of the QRS complex. Real ECG signals may also exhibit abrupt changes when wave fronts terminate at the basal boundary at the A-V ring. To avoid inappropriate dominance of these kinds of boundary effects in the two-dimensional model, the heart was idealized by wrapping the rectangular domain into a cylinder as shown in Figure 3.2, and placing the ECG observation points outside as body surface leads distant from the heart. This cylindrical heart is topologically like a thin shell single ventricle with a hole at the apex, and should be suitable for basic studies.

Since the ECG is a linear summation of individual dipole fields calculated according to Figure 3.2, we can resolve the direct contribution of each individual dipole source to a specific body surface lead by mapping the dipole distribution. In this manner, the detailed origin of each ECG point can be dissected to the cellular level if desired. For the 150x50 unit standard domain representing the heart, there are 7500 such dipoles with vector components oriented along the observation axis. $V_{ecg}(\varphi, t)$ at each time step t as seen at longitude ordinate φ on the equatorial ring is the sum of all positive and negative dipole contributions over the tissue domain.

Equation (3.2) can be rewritten in terms of the dipole strength ρ(a, b). Since the model is two-dimensional, each dipole contribution to the ECG can be multiplied by a weighting coefficient W(R, φ) that is inversely proportional to the cube of its distance from the observation site R_k, and proportional to the dot product of the circumferential tangent unit vector and the vector from the observation point along R_k. The full set of dipole weighting coefficients defines a kernel function shown in Figure 3.3, which when convolved with the dipole distribution gives the resultant ECG voltage.

$$V_{ecg} = \sum_{i=1}^{N} \sum_{j=1}^{M} W(R, \varphi)\, \rho(i, j) \qquad (3.3)$$

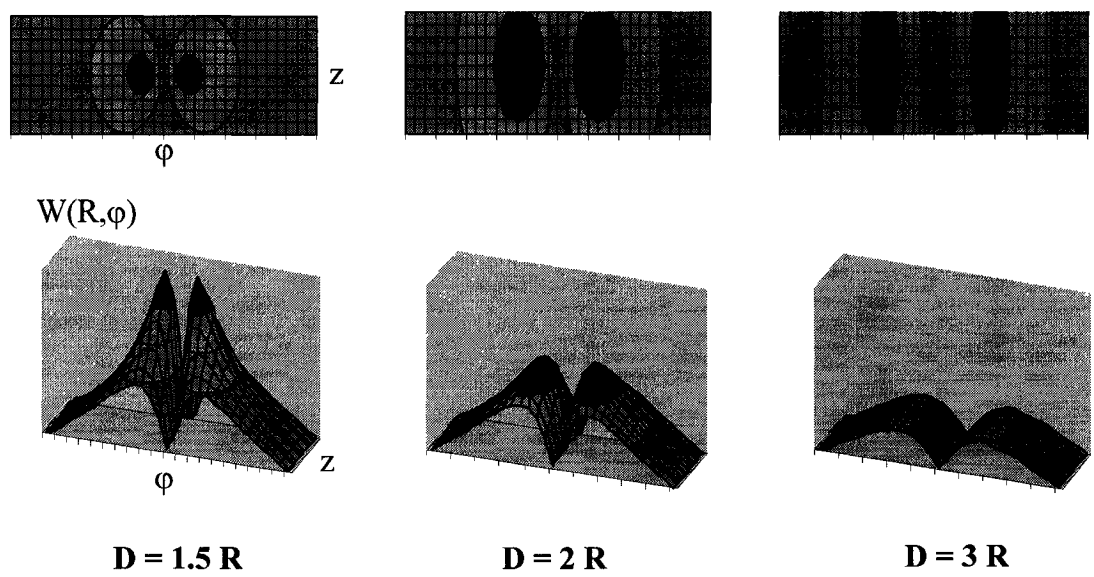

Figure 3.3. The dipole weighting function W(R, φ) may be visualized as a template on the cylinder surface fixed relative to the observation point. Maximum contributions to the ECG occur from dipoles within the two "gull wing" zones where the cylinder surface is tangent to the observation line vector. Contributions are maximally positive if the dipole points directly toward the observer as occurs under the peaks, the locations of which depend on the distance to the observation point. Templates are shown for observation points at increasing distances. No ECG contribution comes from the points nearest and opposite observation points at φ = 0 and 180 degrees, respectively, because the cylinder surface is perpendicular to the axis R_k at these points where the tangent angle β = 0. Dipole field contributions decrease with R_k^3.

Since the ECG of reentrant circuits is an integrated sum of dipoles undergoing periodic activation due to propagating circus movement, the frequency components of the ECG signal should theoretically be dominated by the periodicity of these reentrant circuits. The longest reentrant pathways should produce the slowest ECG waves, while smaller circuits should produce higher frequency contributions. These components can be extracted by calculating the distribution of cycle lengths (CL) over some time interval by defining an array to record time elapsed between action potential activations at each site, and constructing a histogram of these times. Likewise, since CL = APD + DI, we can also construct and monitor additional histograms for APD and DI. These should relate to the frequency content of the ECG signals determined by Fourier analysis.

3.3 Ectopic Activation

A regularly beating ectopic focus can be modelled by setting a small cluster of cells to fire at a regular cycle length as in Figure 3.4. The initiating site must be at least a 3x3 cluster to satisfy the neighbour rule with $N_A = 3$. Radial propagation produces expanding concentric rings, as expected. The body surface electrocardiogram map is shown at a distance D = 2R around an equatorial ring of 36 points at 10 degree intervals. The first ectopic beat produces a large negative ECG deflection directly over the ectopic site, where $\varphi = 90^{\circ}$, owing to the departing wave front upstroke defining dipole vectors that point away from this site. A large positive deflection appears at the ECG observation point diametrically opposite the ectopic site at $\varphi = 270^{\circ}$ where the dipole vectors converge. As more waves enter the domain with subsequent beats, the steep upstroke contributions become partially negated by the more shallow sloped repolarization segments of the radiating waves that produce smaller but more numerous opposing dipole vectors pointing toward the ectopic site. Multiple waves produce smaller ECG amplitudes than those seen with the initial solitary wave. A steady state is reached when the wave train fills the field.

The envelope of maximum ECG amplitudes measured circumferentially around the body surface ring for an ectopic focus shows two large maxima and two large minima spaced

at roughly 180-degree intervals, and several smaller peaks. The largest amplitude appears opposite the ectopic focus due to large radius wave fronts moving toward the far side producing a more coherent net dipole vector coinciding with the two peak zones under the W(R, φ) surface than the smaller radius near-field waves whose dipole vectors are more attenuated in different radial directions. Single lead ECG signals are approximately sinusoidal in time with the dominant frequency equal to that of the ectopic source. The space-time plot of V(φ, t) in Figure 3.4 shows this regular pattern.

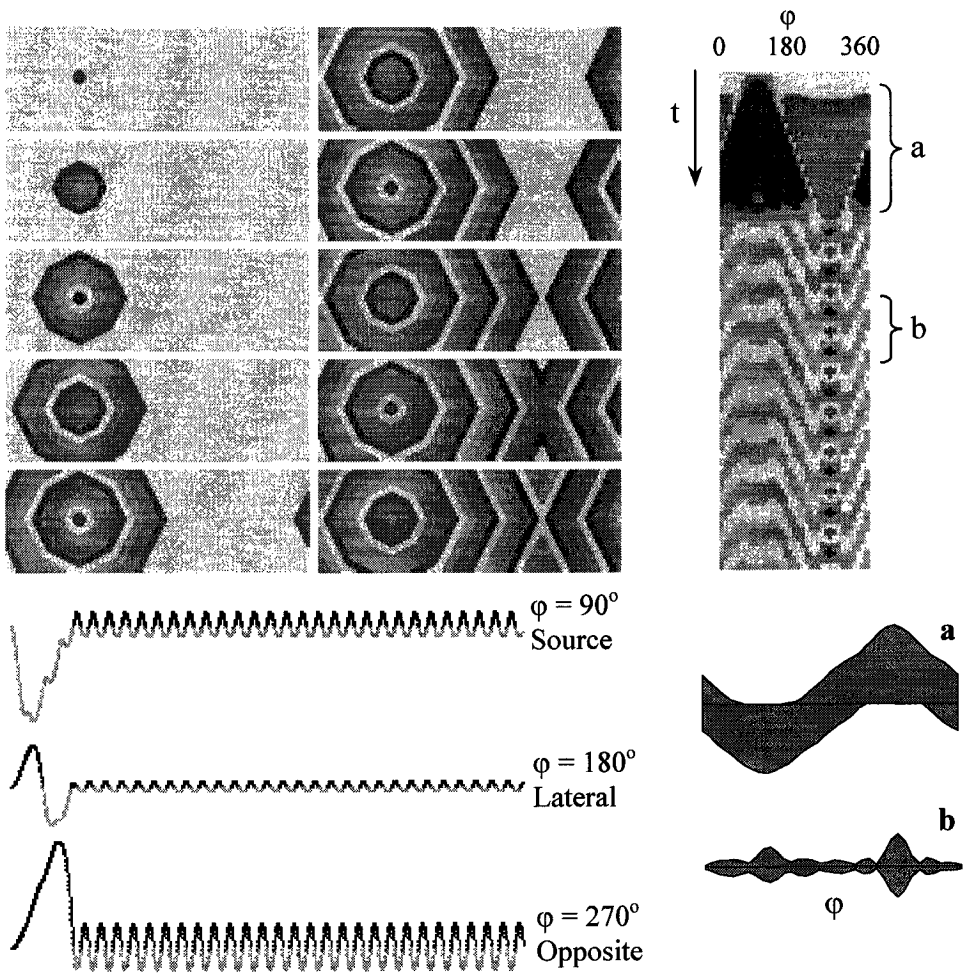

Figure 3.4. A single ectopic focus radiates a train of propagating action potentials which reach a steady state of concentric rings. ECG leads are shown over the focus (φ=90°), laterally (φ=180°), and opposite (φ=270°). The space-time plot of the ECG along an equatorial ring V(φ, t) at right shows the large initial deflections followed by smaller-amplitude oscillations in the steady state. The lower right silhouettes show the transient and steady state envelopes of maximum ECG amplitudes $V_{ecg}(\varphi)$ around the ring.

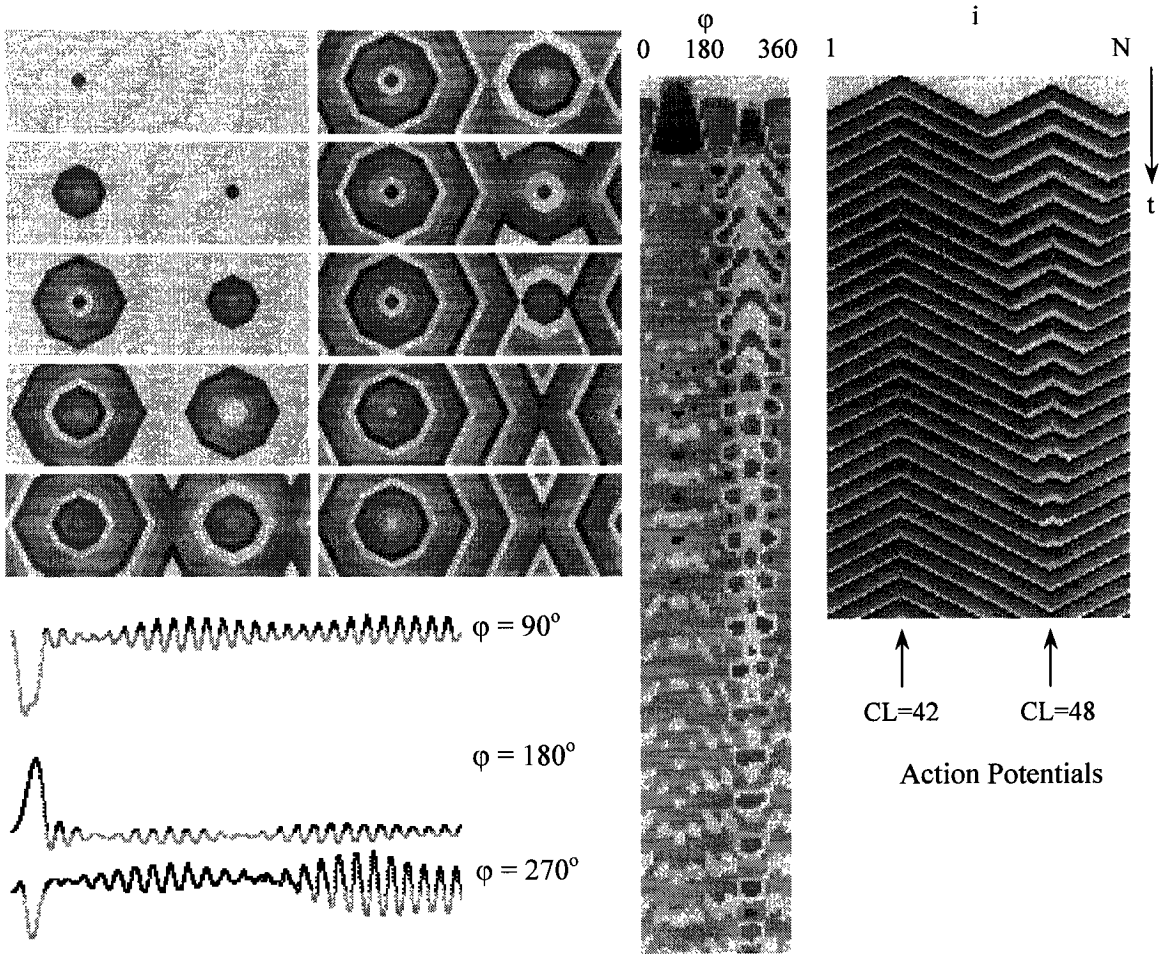

Figure 3.5 Two competing ectopic foci of different frequencies. The more rapid source at left with CL_1 = APD + DI = 42 gradually comes to dominate the field and blocks the slower focus with CL_2 = 48. The vertical plot at the far right shows the action potentials radiating out from their respective sources over time V(φ, t) at a horizontal slice j = 25. The chevron wave pattern of the slower source tapers until it is completely blocked, at which time the ECG space-time plot shown in the middle moves from a complex pattern to approach that of the single ectopic focus illustrated previously. An ECG pattern resembling polymorphic VT, or torsades de pointes, appears during the transient phase of the first 30 beats, until a steady state of a single ectopic focus is reached.

Multiple ectopic foci of fixed and varying frequencies have been simulated. The dipole template W(R, φ) allows prediction of the locations where the points of maximal ECG amplitude will lie, according to how well the dipole distribution ρ(i, j) multiples with W[R(i, j), φ (i, j)] so as to maximize the convolution integral of these two functions.

A simulation of two ectopic foci is shown in Figure 3.5. Two firing foci of dissimilar frequencies result in the fastest beating site dominating the field as was shown earlier in Figure 2.3. The slower focus has a slightly wider excitable gap that permits the waves from the faster focus to gradually penetrate its territory until it is largely overridden. Two competing ectopic pacemakers were originally proposed in 1966 as the mechanism underlying polymorphic tachycardia or torsades de pointes (TdP) [128]. A simple shell propagation model of TdP reported by Malik and Camm [332] demonstrated that the ECG amplitude showed beat frequency modulation resembling TdP only if the relative frequencies of the two foci were forced to vary as functions of time. The results in Figure 3.5, however, show that TdP patterns can arise from two foci of different frequencies that are fixed, but only during the transient phase. The ECG space-time plot of the competing pacemakers exhibits considerable complexity until a steady state is reached, beyond which the system dynamics merge with that of the single ectopic focus previously discussed. Other mechanisms of TdP, however, are plausible. Polymorphic VT may also arise from drifting spiral waves [207, 209].

3.4 Reentrant Circuits

The simplest reentrant circuit in a homogeneous field is a solitary spiral wave radiating outward from a phase singularity. Spiral waves in reaction-diffusion models [542] and simple cellular automata [270, 352] have been extensively investigated over the past several decades. Single or multiple spiral waves are considered to be the fundamental structures underlying VF and reentrant VT. There are numerous ways of achieving spiral waves in excitable media according to specifically chosen initial conditions or S_1-S_2 stimulation-shock protocols [547]. The easiest and most commonly employed initial condition is a linear row of cells having a free end near the centre of the domain, while backed by a refractory region to force unidirectional propagation away from the refractory region. Subsequent rotation around the pre-existing free-end singularity evolves into a spiral wave, as illustrated in Figure 3.6.

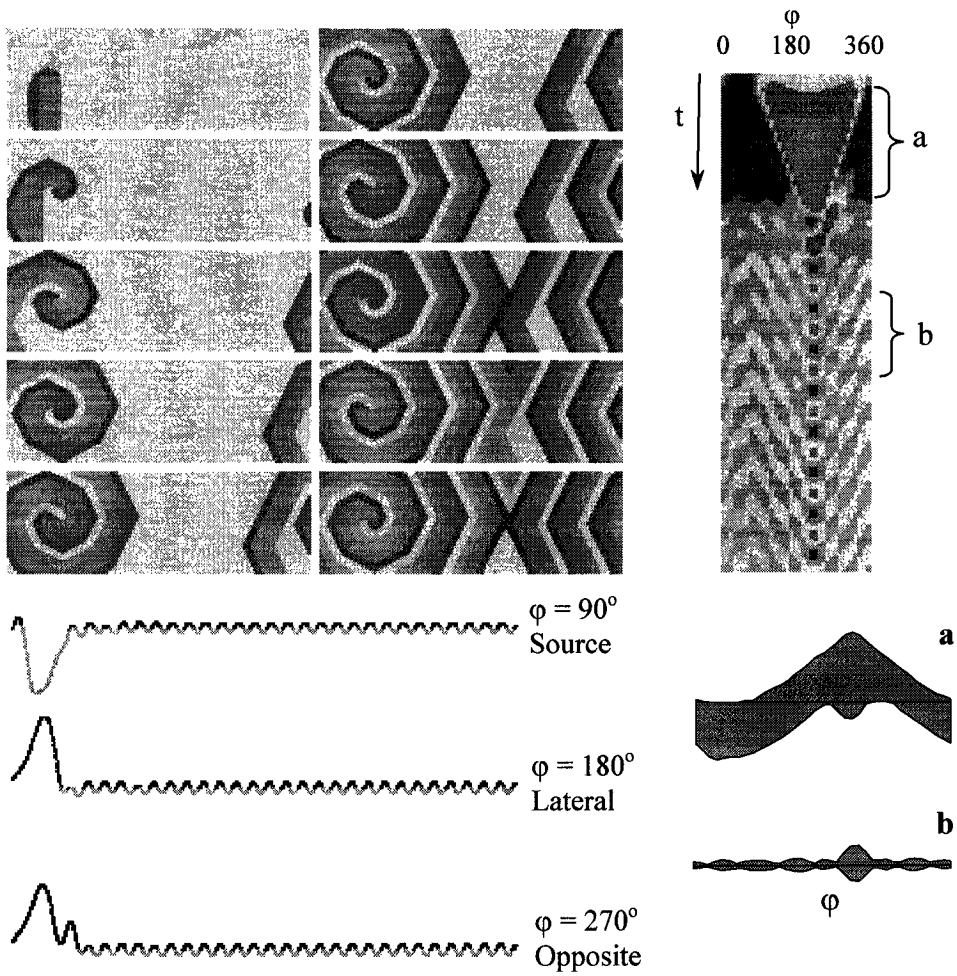

Figure 3.6. Reentrant circuit in the cylinder generated from a partial wave front with a free end backed by refractory cells. This initial condition rolls into a stable spiral wave if all cells have the same APD. ECG leads are shown over the core point and at 90 degrees. The space-time plot of the equatorial ring ECG map V(φ, t) is shown at right. Silhouettes of maximum ECG amplitude are again shown at right for the sampled regions a and b.

The ECG patterns of a spiral wave, as single lead signals and as a space-time plot, show some similarities to those of the ectopic source described previously, if the cycle lengths are equal. Both have steady state amplitude maxima at points directly opposite their respective sources on the heart. This is due to the greater dipole contributions from the converging large radius waves on the opposite side relative to those of the smaller radius departing waves over the initiating source. There are some important differences, however, in the precise shape of the wave forms, and in the locations of the ECG extrema

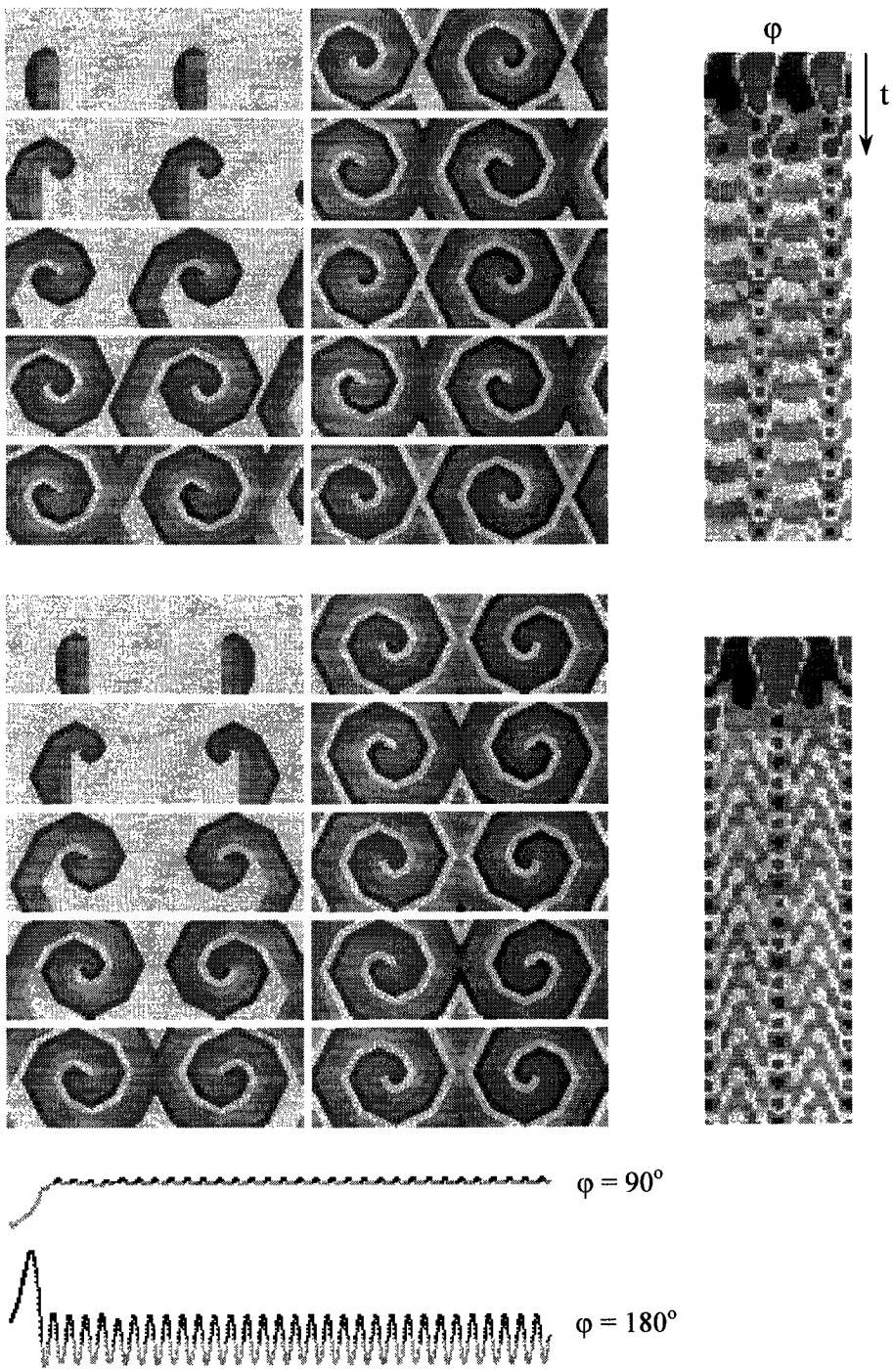

Figure 3.7 Spiral wave pairs. Both spirals have the same rotational sense (top) and opposite sense (bottom). Individual ECG leads are not shown for the top case, but are approximately sinusoidal in the steady state. Space-time plots of ECG maps show differences in extrema locations. The two leads show minimum and maximum amplitude ECG for the counter-rotating case, the former being almost isoelectric.

around the body surface. The spiral wave pattern exhibits a transient stage that lasts several cycles and eventually settles into an alternating zig-zag checkerboard pattern of extrema on the space-time plot, owing to radial asymmetry. These ECG extrema are spatially skewed relative to the more regular ectopic case. Asymmetry of the spiral wave pattern results in a tendency to dipole-field cancellation and consequent lower amplitude of the ECG relative to that of the ectopic source whose symmetric waves and dipole contributions to the ECG are directly additive on each lateral side of the heart. Two isoelectric amplitude minima are evident in the ectopic source, while multiple minima appear with the spiral wave. The latter also exhibits a more complex body surface space-time pattern. If we can extrapolate the results of this very simple model to a whole heart with any validity, it might be difficult to separate focal and reentrant types of monomorphic VT based on the ECG waveforms alone, although some distinguishing features are evident.

The next example shows a spiral wave pair where all APD = 36 are again assumed constant and uniform spatially with no restitution shortening at rapid cycle lengths. The top frame of Figure 3.7 shows the spiral pair with the same clockwise rotational sense with the two centres located equidistantly at 90 and 270 degrees on the cylinder, started simultaneously with no relative phase difference. The relative phase difference between the spirals can be adjusted by starting the second spiral with a delay varying between zero and the full cycle length depending on the phase difference desired. In other cases (not shown) the second wave was given a delay to introduce a phase lag between spirals. The computed ECGs are almost identical to each other, despite the phase differences between the spiral cores. The ECG is dominated by activity in the far field away from the core, where the spiral waves collide and produce a zone of irregular spatial pattern or interference, rather than within the spiral domain. This can be confirmed by defining masks to isolate two subregions: an "inner domain" that contains the pure spiral structure undisturbed by the far field, and an "outer domain" where the spiral structure becomes distorted or absent. The greatest change in the ECG is seen with the initial cropping, and each successive ECG in the cropped domain is very similar despite rotational phase shifts between each of spiral pair.

In virtually all simulations of ectopic and multiple spiral waves of constant frequency, there were irregular regions of ECG amplitude resembling the nodes and antinodes of standing waves. Isoelectric or low amplitude nodes tend to occur over or close to the core points, and antinodes of maximum amplitude occur roughly 90 degrees to the nodes. Spiral pairs rotating with the same sense on opposite sides of the domain produced larger ECG amplitudes than solitary spirals. Counter-rotating spiral waves of opposite sense produced yet larger peak amplitudes. Moving the cores of the counter-rotating pair closer together reduces the amplitude extremes in some cases, giving four or six nodes and antinodes of yet lower amplitudes. All ECG lead signals were approximately sinusoidal once a steady state had been reached. The frequency spectra of this ECG should be narrow-banded for the case of spatially uniform constant APD since all cycle lengths CL = APD + DI are nearly equal for the fully-developed wave fields. The peak frequency should correspond to the reciprocal of the cycle length, while the width of the peak is due to higher frequency components that would appear in the Fourier transform of the triangular action potentials. We will investigate this issues further in a later chapter.

Of clinical interest is the presence of small amplitude or isoelectric nodal points on the body surface maps in many of these simulations, most notably with spiral wave patterns that are reasonably fixed and stable. These nodes essentially represent a far-field interference pattern analogous to those seen in other types of wave phenomena involving radiation from two or more periodic sources. If actually present in real ECGs of VF, these nodal points would give theoretical foundation to reported observations in patients of "VF masquerading as asystole" in a subset of leads [158, 343], occurring in perhaps 2 to 3 percent of VF cases [109] leading to an incorrect diagnosis of asystole.

It is perhaps worth mentioning, as an aside, that unlike the logarithmic spiral defined by $r(\varphi)=r_0 \exp(K\varphi)$, which is identical when examined at all scales, the spiral waves of action potential propagation are not self-similar. A spiral wave cannot be self-similar, appearing the same at all scales and therefore lacking a characteristic length, if the wave thickness is everywhere equal owing to action potentials having constant duration independent of radius. A spiral can be self-similar only if the APD and R increase

indefinitely with radius. This would require that the APD restitution curve pass through the origin and extend linearly to infinity, or satisfy some other invariant function.

The ECG amplitude is also influenced by the total number of waves within the field, particularly waves occupying relatively large areas , such as large solitary waves, that can mount a coherent dipole contribution in a given direction. Fine fibrillation generally produces the lowest amplitudes due to the large number of wave fronts oriented toward and away from the observation axis tending to cancel each other within the peak regions of W(R, φ). Figure 3.8 shows action potential fields and their corresponding distributions of dipole sources W(R, φ) ρ(i, j).

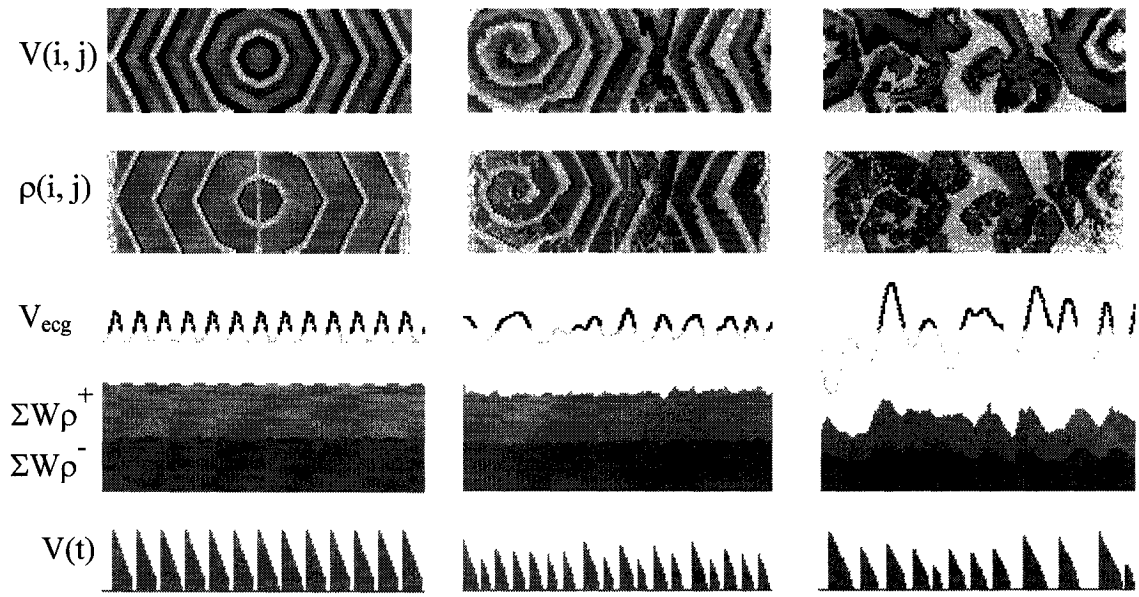

Figure 3.8. Spatial patterns of action potentials V(i, j) are shown in the top row for ectopic, spiral wave, and fibrillation. The corresponding field of dipole sources ρ(i, j) multiplied by W(R, φ) that contribute to V_{ecg} at observation point $\varphi=180^{\circ}$ is shown in the second row. Positive dipole contributions to Wρ are grey, while negative contributions to Wρ are black. $V_{ecg} = \Sigma$ Wρ is the sum of the positive and negative contributions and is shown on a magnified scale. Note that the positive and negative components are almost equal, and only a small difference determines the ECG. Largest contributions are from within the lateral gull wing zones where the cylinder surface is tangent to the observation line.

Adding more spirals to the domain, as shown in Figure 3.9, increases the ECG amplitudes if the reentrant circuits have the same period. The peak amplitude is even higher if the four spirals are symmetrically counter-rotating such that their dipole contributions are additive. Adding more spiral waves at higher densities eventually causes the ECG amplitudes to decrease as the dipole contributions tend to cancel on smaller spatial scales.

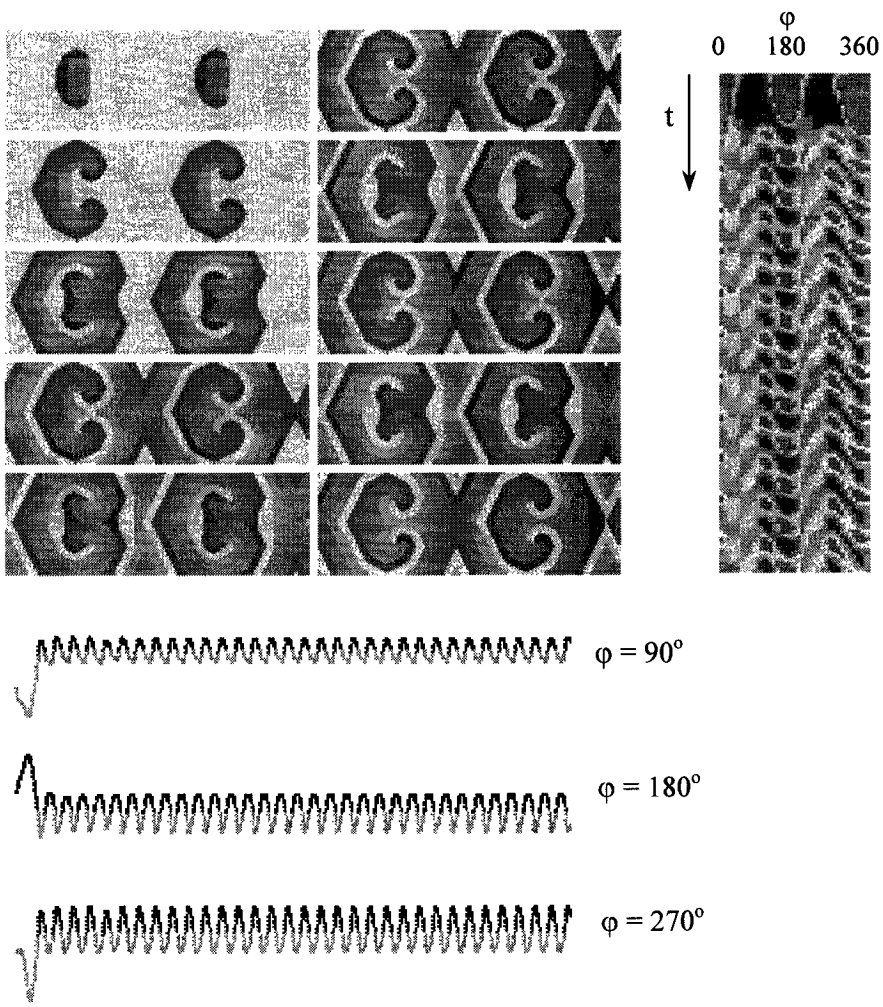

Figure 3.9. Four spiral waves of uniform APD = 36 result in ECG signals with the same frequency as the previous cases, but with a more complex equatorial body surface map. Contributions from the spiral pairs work together to produce larger amplitude signals.

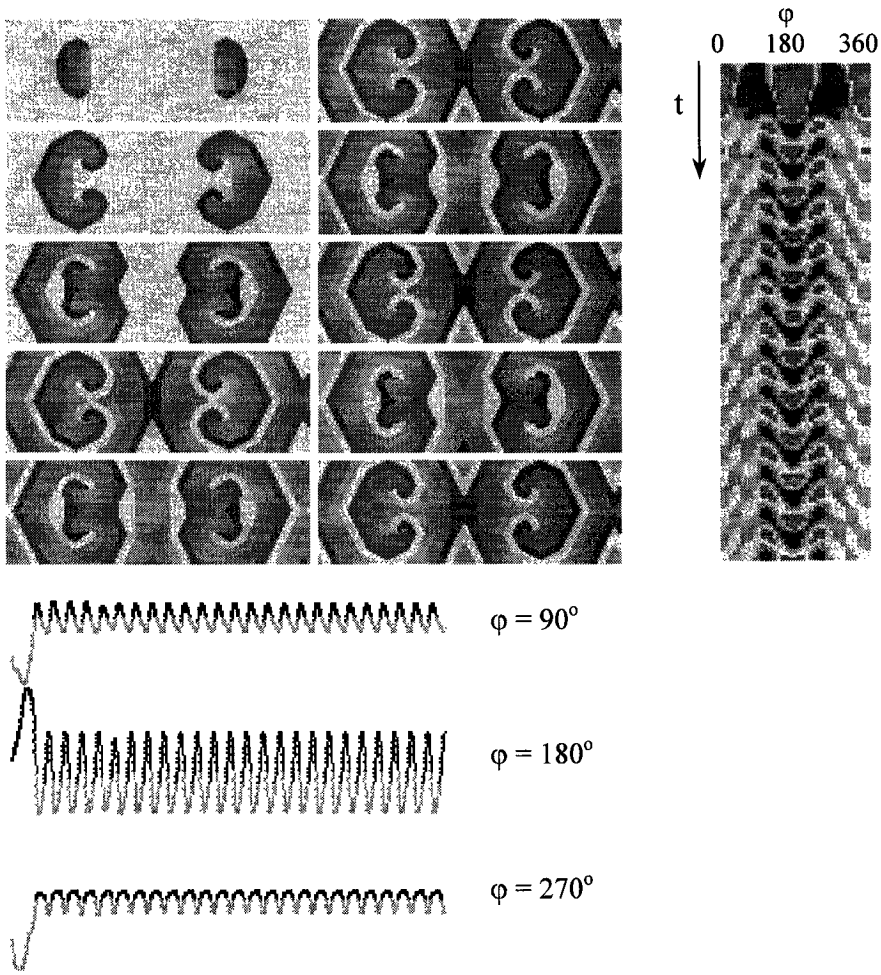

Figure 3.10. Symmetric counter-rotating spiral waves of constant APD = 36 produce a larger peak amplitude ECG than the previous case. Symmetry causes the wave fronts to be directly additive in their effects on the ECG, such that the greatest amplitude is over the observation point at 180°.

An example of fibrillation is introduced in Figure 3.11 evolving from a field of randomly firing "seeds" surrounded by random refractory zones. The system self-organizes by local interactions into multiple spiral waves centred at core points where there is juxtaposition of firing, intermediate, and resting states with sufficient space between such points to allow spiral wave evolution. This particular case has action potential restitution with APD_m = 36 and APD_o = 12. The pattern contains multiple reentrant circuits of many

frequencies producing a complex spatiotemporal body surface map. Long runs demonstrate no tendency to reach any regular pattern, except in a statistical sense. Another case of fibrillation is shown in Figure 3.12 where the complex field of irregular spirals waves is forced to become more regular by flattening restitution by raising APD_o from 12 to 36 while holding $APD_m = 36$. The ECG pattern of this particular subtype of fibrillation is regular and periodic. Fibrillation patterns will be explored in more detail in the next chapter.

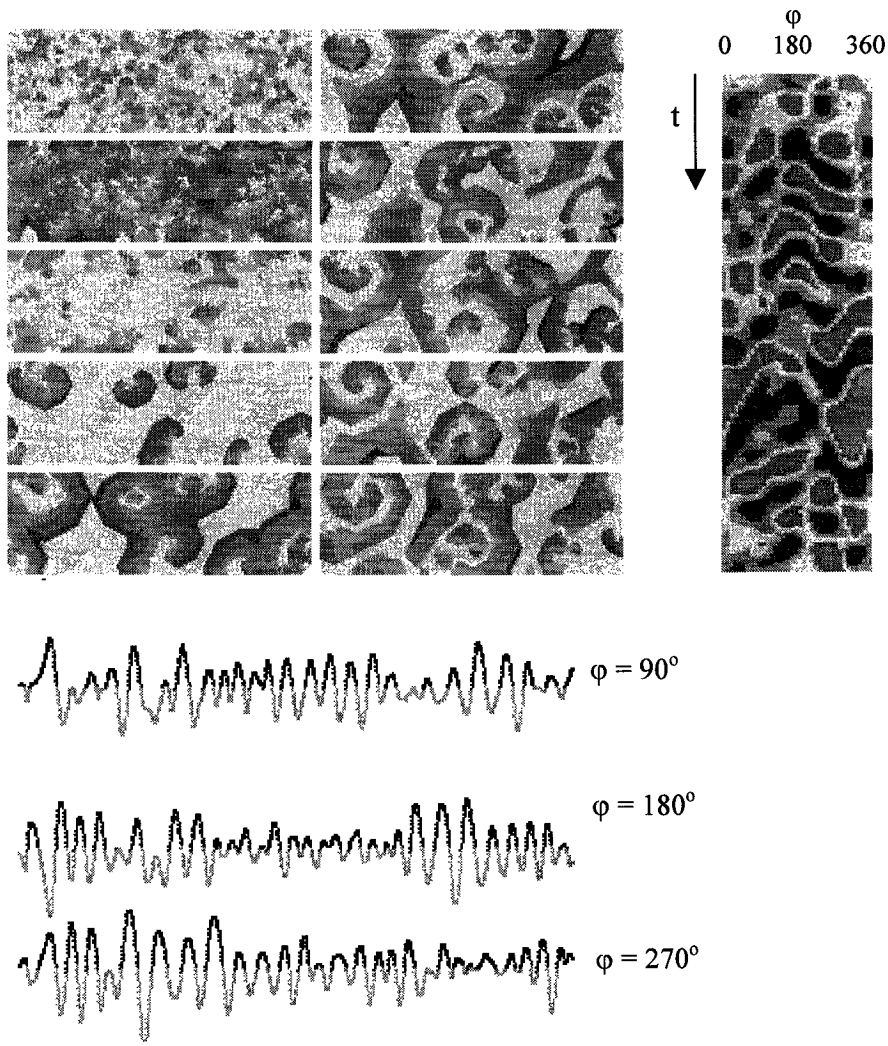

Figure 3.11. Fibrillation evolves from an initial condition where cells are assigned random states, like excited seeds, and settles into a complex pattern characterized by multiple reentrant circuits. The body surface map at right exhibits organized spatial and temporal periodicity appearing to contain many frequencies.

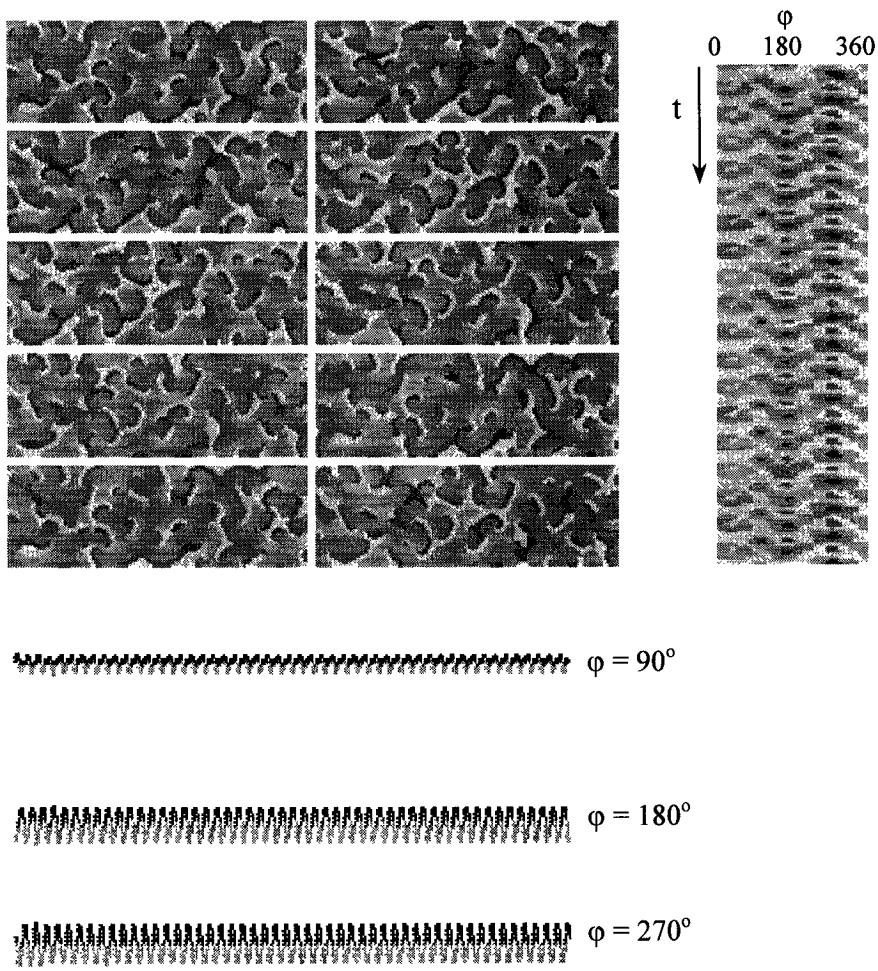

Figure 3.12. Fibrillation obtained from the previous case by raising the intercept of the restitution curve gradually until it is flat, such that all APD = 36. The core points are now fixed in location, and all cycle lengths are equal at CL = APD + R + DI. Since the ECG is the weighted sum of all dipoles which have equal CL, the ECG is perfectly periodic. The space-time plot at right shows this periodic pattern. The distribution of the ECG maximum amplitudes V(φ) should depend on the specific spatial pattern of core points.

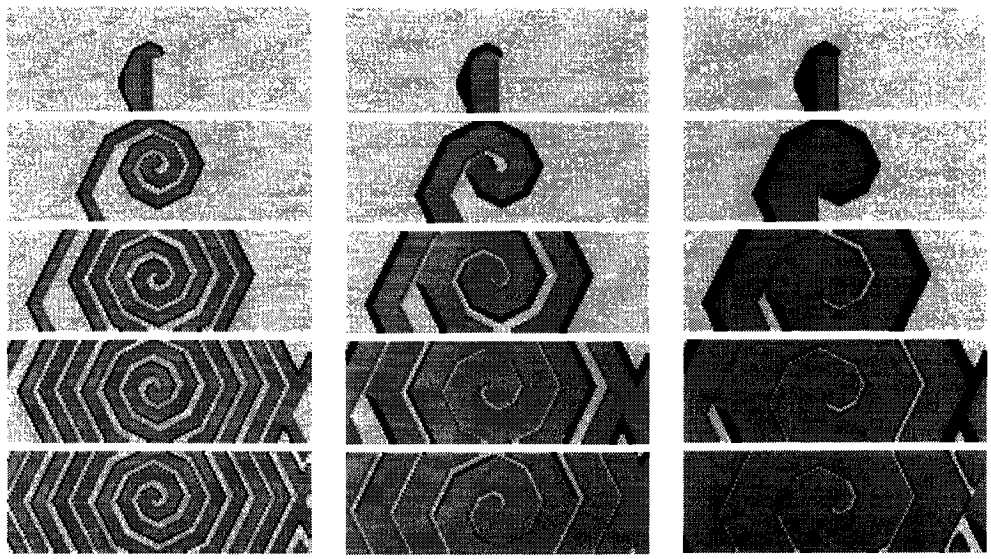

Figure 3.13. A solitary spiral wave, in this case generated by a line of firing cells with a free end, is stable when all APD are equal regardless of their duration. APD = 12, 36, and 60 from left to right.

3.5 Wave Stability

It has long been recognized that APD is shortened when a cardiac cell is given a premature stimulus [194, 313]. Nolesco and Dahlen proposed a graphic method to represent iterations of APD with each beat [374], that was applied to stimulated Purkinje fibres and ventricular tissue [45, 151]. Guevara et al. explored the patterns of bifurcations and phase-locking in clusters of paced heart cells [214, 215], pointing out the application of iterated Poincaré plots to these sequences. Driven ventricles show similar phase-locking patterns [444]. These concepts from nonlinear dynamics have since been applied to discrete [78, 79] and continuous [70, 259, 314] mathematical models of heart cells. Two-dimensional computer simulations of excitable cells having these properties have been used to explore the transition of spiral wave reentrant circuits into fibrillatory patterns. Karma demonstrated that an APD restitution curve slope greater than one is an important factor in promoting spiral wave instability and break-up [274]. Considerable

attention has since been directed at studying restitution properties of tissues and drugs and in theoretical models [24, 176, 286, 419, 523, 529].

Given suitable CML model parameters, a spiral wave can persist indefinitely, rotating in a steady state about a single phase singularity at its core, as already demonstrated in previous cases. Figure 3.13 illustrates the stability of a solitary spiral when all APD are constant. The CL are also constant, and the action potential train is regular. The diastolic interval is predictable at DI = CL – (APD + R). This case is shown in Figure 3.14, where the dynamics are determined by the intersection of this negative unity slope line with the restitution curve, which is essentially a flat line. If the restitution curve is given a positive slope, by lowering the intercept APD_o, the operating point changes accordingly. Perturbations of DI or APD away from this point dissipate after some small oscillations, as the dynamics return to this stable point. As APD_o is lowered further, the operating point suddenly becomes unstable to perturbation, and two stable points appear, as in the fourth frame of Figure 3.14. The action potential train then alternates between two APD values, having undergone a period-doubling bifurcation. The diagram illustrates how the APD and DI at any given time seek to find an equilibrium that depends on the fixed parameters CL, APD_m, and APD_o. A change in CL moves the equilibrium points resulting in a transient readjustment period. If the dynamics operate on a steep restitution curve slope, each successive action potential moves away from this point. If DI is forced to zero, the next action potential will block and a new pattern of 2:1 response is established. Every second action potential then fires with a new cycle length of 2 x BCL.

Changing the restitution curve in the two-dimensional model by lowering the intercept APD_o causes break-up into fibrillation, as shown in Figure 3.15. A mandatory criterion for spiral wave development and break-up is an advancing wave front somewhere and somehow developing a free end that must both persist long enough and have sufficient spatial separation from neighbouring waves to be able to roll up. Theoretically, spiral waves can multiply by a process of wave-breaking, whereby a continuous wave front gets pinched and blocks over a specific segment giving rise to two free ends that subsequently roll up into two daughter waves. These may then break into four waves, and so on, until

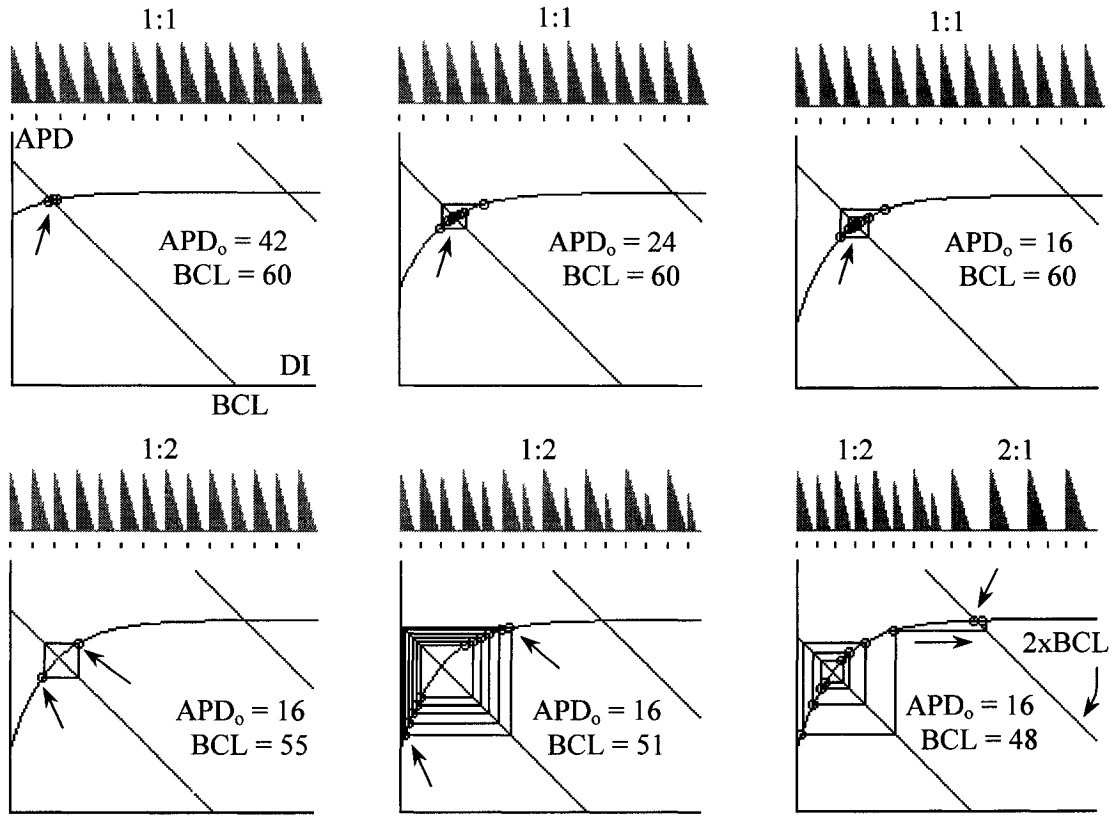

Figure 3.14. A regular action potential train in a single paced cell results when APD is constant, and is determined by the intersection of the restitution curve with the negative unity slope line of the cycle length CL. At shallow restitution slope m < 1 in the top row, the intersection point is stable, and iterations of APD with successive stimuli move toward this attractor. Here APD_m = 48 in all cases. In the bottom row, APD_0 = 16 and all intersections points fall on m > 1 so they are repellors. Alternans of APD develops for BCL > 50. Arrows show the asymptotically stable points. At BCL = 48, the APD values move away from the intersection until DI = 0, forcing a jump to the negative slope line of twice BCL. The ratios m:n shown at the top of each frame indicate the period of response (m) and the periodicity of the APD (n).

a limiting smallest scale is reached, analogous to viscosity limiting the smallest scale of fluid turbulence. This cascade of wave-breaking might be one route to fibrillation. This process has been observed in several types of ionic models [100, 274, 389, 529], and appears to be sensitive to the APD restitution slope. Wave break also occurs in the simple

CML model, notably in the absence of any reference to ionic currents. The stark simplicity of this model provides a unique perspective on the fundamental mechanism of wave break, since only a few simple variables are involved.

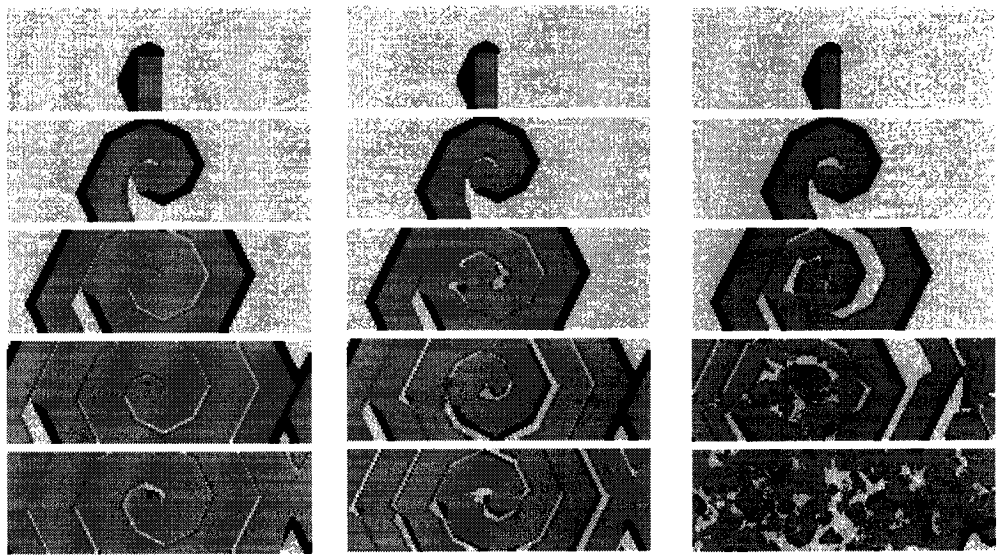

Figure 3.15. The spiral wave breaks-up when the restitution curve slope is increased by lowering APD_0 while the plateau $APD_m = 48$ is kept fixed. Oscillating instability of the excitable gap can be seen in the middle column, but remains bounded, while the instabilities grows until multiple regions of block occur in the right column.

Figure 3.16 shows a solitary spiral wave of constant $APD_m = 48$ which has reached a steady state. The restitution intercept APD_0 was then slowly decreased while the time constant $\tau = 10$ was kept fixed. As the slope increased, the wave front uniformity became increasingly sensitive to small perturbations of wave front curvature that gave rise to oscillations of amplitude along the wave front. Small differences in curvature between the advancing wave front and the preceding wave tail provide sufficient perturbations to initiate such instabilities. Fluctuations of diastolic interval δDI, manifesting within the excitable gap, result in fluctuations δAPD according to the slope of the restitution curve $m = \delta APD / \delta DI$ as shown in Figure 3.17. Perturbations are damped if $m < 1$, while differences in DI become magnified with each cycle if $m > 1$, eventually leading to instability and wave front block.

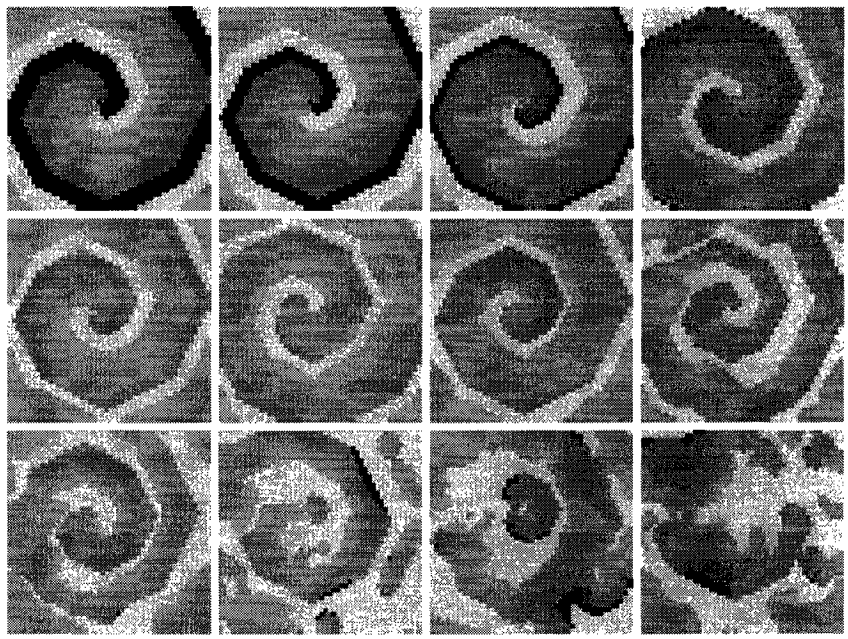

Figure 3.16. A spiral wave with all uniform $APD_m = 48$ is started from a steady state in the CML model. The restitution curve intercept APD_0 is gradually lowered from 48 to 16, increasing the slope at short diastolic intervals. The wave front develops amplitude oscillations which become unstable due to growth of small perturbations in the diastolic interval when $m > 1$. This finally leads to wave break and fibrillation.

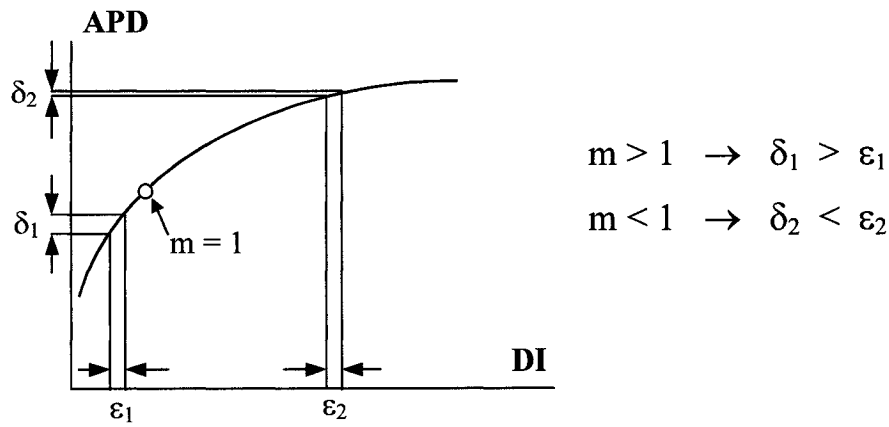

Figure 3.17. Small differences in diastolic interval DI between neighbouring regions lead to larger or smaller differences in action potential duration APD, depending on the slope of the restitution curve m at that specific point. After a few iterations through a region with $m > 1$, the differences can be large enough to dramatically alter the global dynamics.

Although this type of instability has been simulated in ionic models [189, 274, 389], and has become recognised in recent years, the CML model demonstrates a mechanism that is not immediately apparent in more complex models. The first wave break in the spiral occurs at the left region of Figure 3.16. By examining the space-time plot of a slice through the wave front shown in Figure 3.18, the reason for the instability leading to wave front block is apparent. There develops a critical point where the APD at one cell becomes progressively shorter while the neighbouring cell APD becomes longer. If the time delay, or dispersion of refractoriness, between the two neighbouring upstrokes grows to a sufficient magnitude, by the time the longer AP expires and becomes excitable again, the voltage of its shorter AP neighbour has dropped below threshold V_{th}. The long APD cannot be re-excited, and propagation fails. This mechanism of wave front block, whereby a propagating action potential decays to a voltage below its neighbour's firing threshold, is actually quite general. Block is most likely if this critical condition coincides

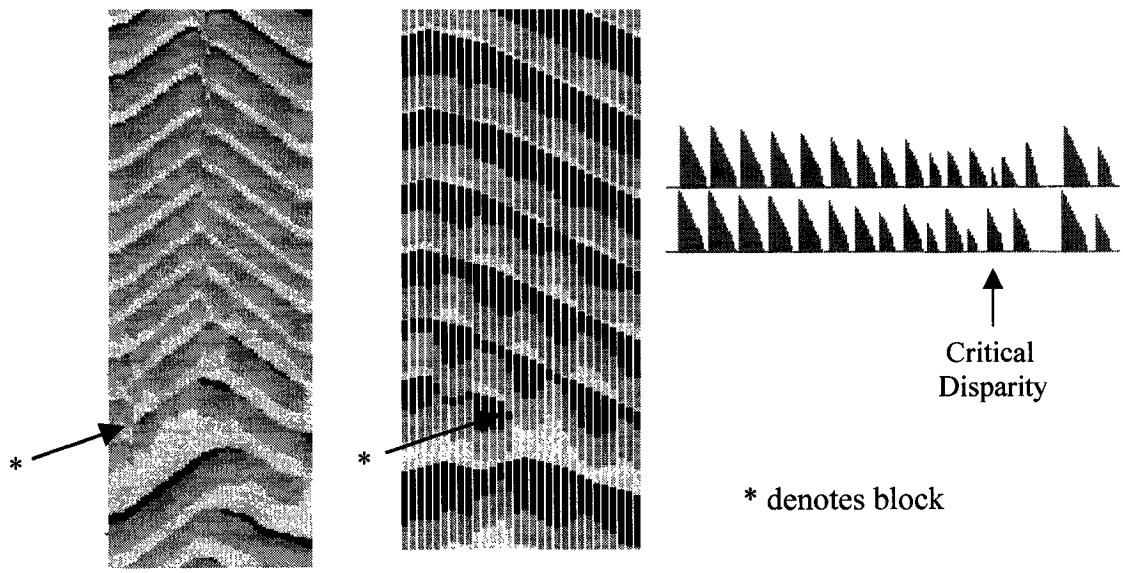

Figure 3.18. Space-time plots through centre of a spiral wave as the restitution curve becomes steeper. Growth of small perturbations and amplitude ripples are evident at left until wave front block occurs at arrow. The magnified plot at right shows wave break occurring in a separate simulation as one excited cell falls subthreshold at the arrow before its resting neighbour can be raised to its threshold. The action potentials of two neighbouring cells shown at right demonstrate growing disparity until block occurs.

with the oscillating wave front amplitude of the shorter APD cell being at its nadir. When expressed in these terms, it is not necessary to invoke arguments about ionic currents, except as they directly pertain to APD, DI, and V_{th}.

Figure 3.19 shows another spiral wave with $APD_m = 48$, $APD_o = 16$, $R = 4$, and $\tau = 10$ within a 50x50 domain. Maximum slope of the restitution curve is $\xi = (48-16)/10 = 3.2$ which is considerably greater than one. Irregularities slowly develop, first when the wave front encounters its tail and moves very close, leaving a small gap trapped at the core. This immediately establishes a disparity in diastolic intervals between neighbouring regions along the wave. As the wave rotates around 180 degrees, the diastolic disparity transformed through the restitution curve creates a disparity in APD. The difference is magnified if the restitution slope is greater than one. Each successive rotation creates a new wave ripple seen spatially along the excitable gap. Once the spiral wave becomes fully developed, these irregularities can be seen to extend along the entire wave front. If we imagine standing at the core and taking a walk outward along the wave front, we would see oscillations in the diastolic region or excitable gap, and consequent oscillations of the wave amplitude. Close to the core, the wavelength is small due to the small radius, but gets progressively larger, roughly in proportion to the radius. As the average curvature becomes less at greater radii, the amplitude of the oscillations becomes less dramatic. Consequently the histogram of diastolic intervals measured over periodic finite sampling intervals generally decays with DI, reflecting a predominance of short DI.

The spiral persists for a long time, over 40 revolutions, before it finally breaks up. Action potentials monitored at one cell, shown along the bottom, demonstrate obvious chaotic dynamics despite a long period of relative stability. Although spatial oscillations can be seen in the excitable gap throughout the simulation, these evidently remain subcritical for a considerable period of time and the spiral is stable despite being very irregular. The dynamics reside on a chaotic but well-confined attractor. This situation demonstrates that the mere presence of local chaotic dynamics does not guarantee global instability nor wave break. The eighth frame clearly shows amplitude oscillation along the wave front.

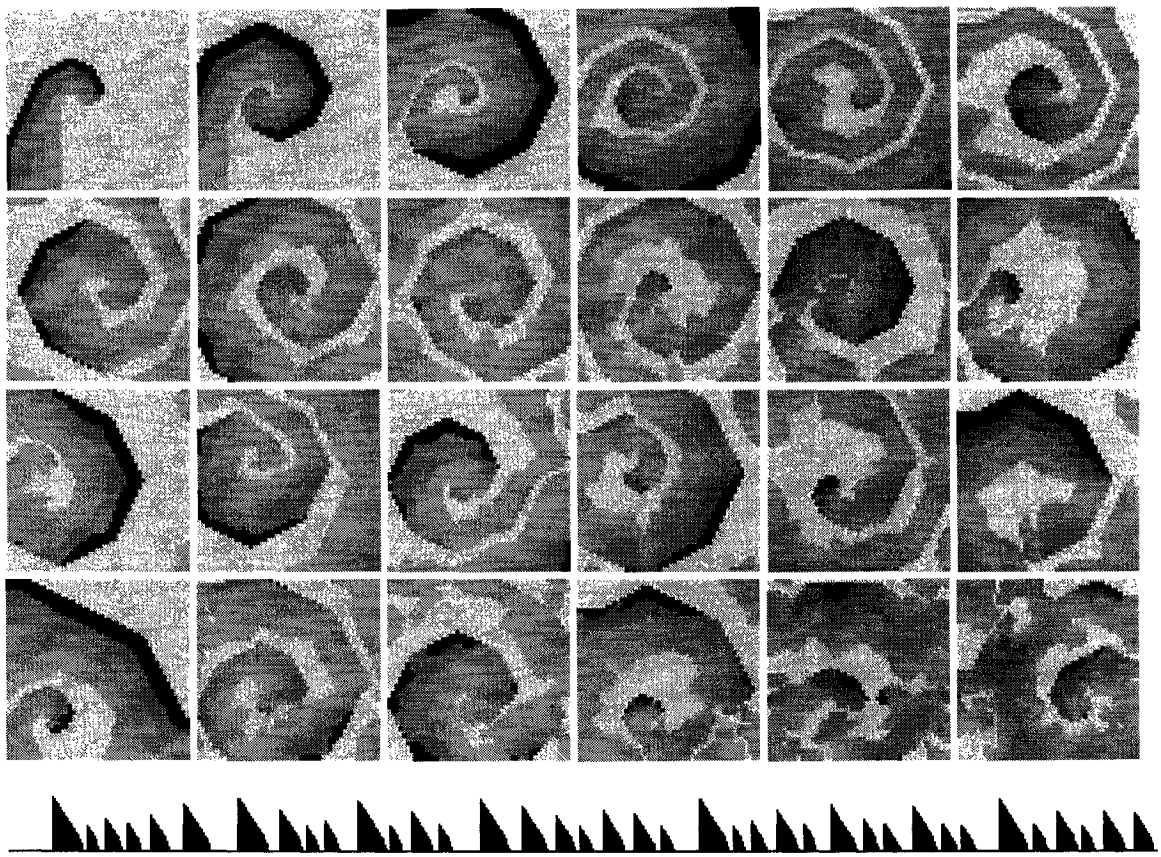

Figure 3.19. Spiral wave instability for fixed steep restitution is shown for a single wave started from a line segment. Although the maximum restitution slope m = 3.0 is much greater than one, over 40 revolutions were sustained with a long period of apparent global stability before local irregularities accumulated sufficiently to cause break-up. The action potential train shown along the bottom for a typical cell shows obvious chaotic dynamics.

The eleventh frame shows the wave finally being pinched off and breaking to reform into two core points. A cascade of successive wave breaking occurs shortly thereafter as a complex fibrillation becomes established in the remaining frames.

The parameter values defining the transition to instability were determined by multiple runs of a single spiral started from a line in a 50x50 bounded domain coupled map lattice with continuous states. During the initial roll up of spiral formation, the average APD tends to migrate from an initially high value down toward a distribution closer to APD_o, depending on the specific values of APD_o and APD_m. Initial conditions were therefore set

close to the mean with APD = 0.7 APD_o + 0.3 APD_m. It was found that stability of the single spiral wave was highly sensitive to the chosen initial conditions. Waves started from line segments sometimes blocked while meeting the tail on the first rotation, particularly when the APD was long and the reentrant circuit required a large circumference relative to the domain size. Other waves that survived early went on to break after a long time, while others drifted outside the boundaries. The initial conditions of refractoriness assigned to the regions at resting potential also had an influence on wave survival on roll-up. It is not surprising that sensitivity to initial conditions is an important issue, given the existence of chaotic dynamics locally despite globally stable behaviour. Simulations were run many times to seek a criterion of stability against wave break. Although it was difficult to discern a line of sharp phase transition, most cases of wave

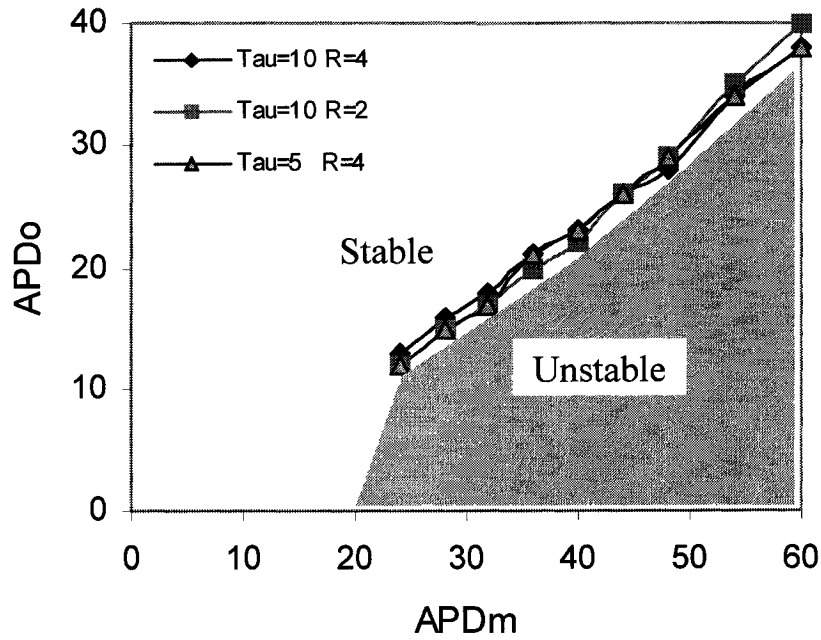

Figure 3.20. Effect of the action potential restitution curve on spiral wave stability and wave break. The boundary was determined by fixing the plateau APD_m and lowering the intercept APD_o in separate simulations until wave break occurred. Spiral waves were considered stable if they did not break within 2000 time steps, although they were irregular if $APD_o<APD_m$. Spiral waves became chaotic closer to the stability boundary, yet persisted without necessarily breaking. Results were relatively independent of restitution time constant τ and refractory period R. APD_m below 20 was found to be universally stable regardless of APD_o.

break occurred when APD_o was approximately a linear function of APD_m as shown in Figure 3.20. The stability boundary was approximately equivalent for $\tau = 5$ and 10, and R = 2 to 4. The linear approximation for the boundary line is $APD_o \cong 0.7\ (APD_m - 7)$.

3.6 Wave Block

Since wave break due to segmental wave front block is germane to the transition to fibrillation, it is necessary to understand wave block mechanisms in reentrant circuits. The simplest reentrant circuit is a one dimensional cable ring supporting unidirectional propagation. The CML model is easily reformulated into a closed ring by setting the domain height to M = 1, and N to the desired ring length. The firing rule is then modified so a cell fires if only $N_A = 1$ of its neighbours is above threshold V_{th}. The algorithm is otherwise identical with that previously described. Propagation is uniform and regular if the ring is large, but undergoes transient block and APD bifurcation at smaller sizes, with complete block at the smallest or critical size N_{crit}.

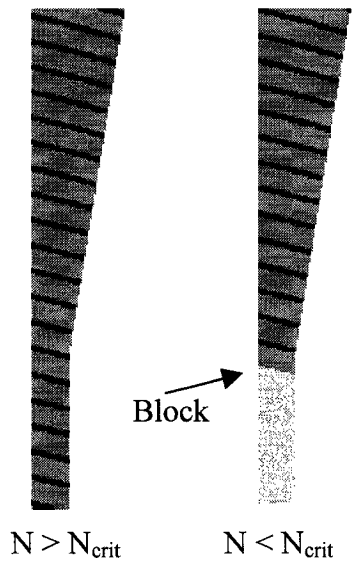

APD	Theoretical N_{crit}	Simulation N_{crit}
60	20	21
48	17	18
36	13	14
24	10	11
20	9	10
16	8	9

Figure 3.21. A one-dimensional cable ring with a single propagating action potential is gradually shortened until a critical length N_{crit} is reached, beyond which the wave front blocks against its own tail. This is the smallest possible size of a reentrant circuit. The table at right compares N_{crit} determined empirically by simulation, as shown in these examples, with that calculated theoretically by the equations described in the text, assuming $V_{th}/V_m = 0.3$.

Figure 3.21 shows a single wave of constant APD = 48 propagating around the cable ring given an initial length of N = 40. As the ring is gradually shortened, the critical length N_{crit} is reached, at which point the wave front impinges on its tail sufficiently to block. This is followed by loss of propagation and annihilation of all activity after remaining action potentials expire. This critical length is important because it determines the path length of the smallest possible reentrant circuits that can persist, and therefore the minimum allowable spacing between core points and the maximum density of fibrillation waves. There must exist a mathematical relationship $N_{crit} = f(APD, R, V_{th})$ for the special case of constant APD. For restitution where $APD_o \neq APD_m$ simulations show the APD distribution to migrate down toward a mean value that is close to APD_o, owing to relatively short diastolic intervals. The table in Figure 3.21 shows the critical ring length that just barely allows propagation for various values of constant APD determined empirically by ring shortening with R = 4 and $V_{th}/V_m = 0.3$.

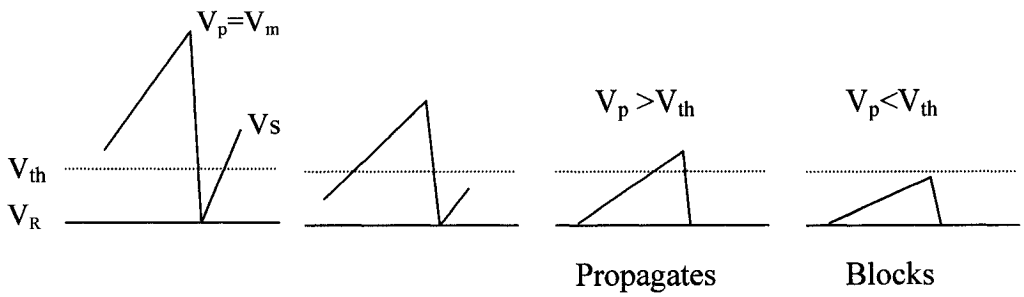

Figure 3.22. Block occurs when the action potential wave front impinges on its own tail leaving a solitary element in the circuit at resting potential V_R. This element must remain refractory until a time R elapses. Meanwhile the peak potential V_p falls from its initial maximum value of V_m. Propagation can continue only if V_p always stays above V_{th} while V_s falls below V_{th} and the resting refractory cell recovers. Otherwise the front will drop below the threshold before its preceding cell at V_s becomes excitable again.

Figure 3.22 shows an action potential profile along the ring cable when N is close to N_{crit}. There is a stage of rapid propagation at velocity θ around the ring followed by a stage of temporary block, as the wave front meets its tail and cannot progress until the blocking tail point recovers past its refractory period R to permit re-excitation. Complete block,

causing wave annihilation, occurs if the wave front has to wait excessively long, such that its voltage drops below V_{th} before its preceding neighbour tail point recovers past R. This marginal situation establishes an important theoretical criterion for wave block. Stated mathematically, the time for the front to fall from V_m to V_{th} must not exceed the time for the tail to fall from V_s to zero and clock the additional time R to become available for re-excitation. If $\dot{V}$ is the rate of voltage drop of the action potential, and the resting voltage is zero, then block occurs if

$$\frac{V_m - V_{th}}{\dot{V}} < \frac{V_s - 0}{\dot{V}} + R \qquad \dot{V} = V_m \frac{\dot{X}}{X_m} \tag{3.5}$$

Here V_s is the voltage at the tail point at the moment when the front point fires to V_m. It is determined by assuming that the voltage of the front drops from V_m to V_s during the time period N/θ over which the action potential propagates around the ring of length N and velocity θ.

$$\left(\frac{V_s}{V_m}\right) = 1 - \frac{N}{\theta}\frac{X}{X_m} \tag{3.6}$$

Simultaneous solution of these equations gives a reasonably close approximation to the function $N_{crit} = f(APD, R, V_{th})$, where X_m is the maximum value of X which is the average APD, and $X = 1$ is the rate of decrementing of state variable X.

$$N_{crit} \cong \theta\left(\frac{APD}{\dot{X}}\frac{V_{th}}{V_m} + R\right) \tag{3.7}$$

This expression shows that the critical ring size increases with APD, R, θ, and V_{th} and decreases with the peak voltage V_m. This equation performs well for constant APD as shown in Figure 3.23, where calculated N_{crit} is compared with simulation results for the shrinking ring at different V_{th}. Difficulties arise with this theory when restitution is added and APD is no longer constant. In particular, when $APD_o \neq APD_m$ the conduction

velocity θ can vary around the ring and throughout the cycle, especially when the circuit is small and the APD bifurcates into alternans or quasiperiodicity. The maximum possible value of θ is unity according to Huygens principle, but is usually much slower and nonuniform at smaller ring sizes. Simulations with restitution show empirically that θ actually decreases somewhat with both N and APD making the relationship determining N_{crit} much more complex. Despite the average APD being smaller, N_{crit} actually increases by a small amount at steeper restitution due to the emergence of alternans where two different APD that sustain on a ring segment occupy a larger space than two equal APD would of the same period. This alternans due to APD restitution is probably responsible in part for core point meander and nonuniform path length seen in two dimensional fields of fibrillation.

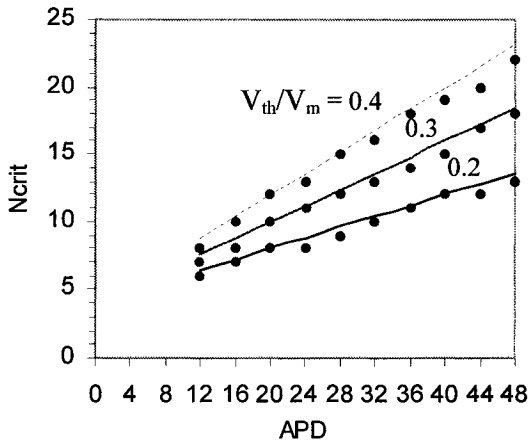

Figure 3.23. Critical ring size N_{crit} is the smallest possible one-dimensional path length on which action potentials can persist without blocking on their tails. N_{crit} depends on APD, θ, V_{th} and R. The points are from actual simulations on the shrinking ring, and the lines are from the theory in equation 3.7. Agreement is excellent. APD is in model units.

By extrapolation to two dimensions, one might conjecture that N_{crit} determines the minimum circumference of a reentrant circuit whose radius is half the minimum possible spacing between adjacent spiral waves. Of course the simplified analysis above based on a one-dimensional ring may not necessarily extrapolate cleanly to a two-dimensional medium where there is spatial electrotonic attenuation, and where all APD are not necessarily equal due to restitution.

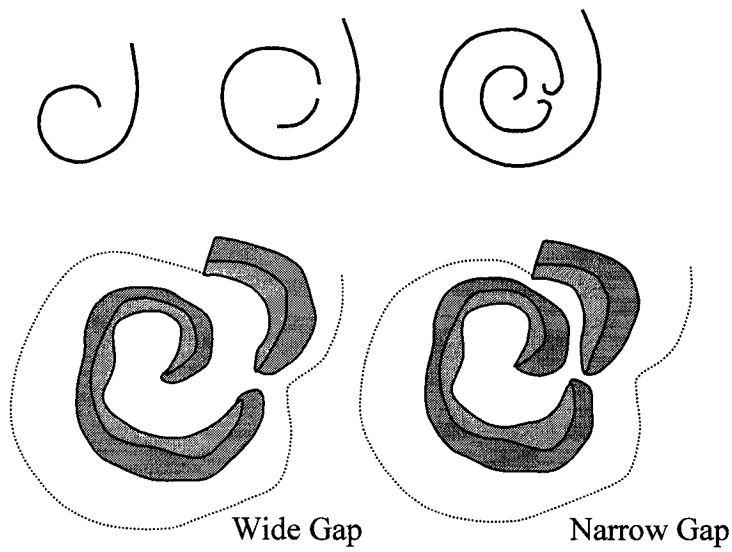

Figure 3.24. Wave break followed by roll-up into a new pair of spiral waves can only occur if there is adequate space in the diastolic gap to give the potential daughter waves opportunity to complete a revolution before being blocked. In the top illustration the original free end of the wave front completes a revolution and blocks the two new free ends from rolling up. The broken segment at bottom left has sufficient room to roll up and establish new spiral waves, unlike the case at lower right where the broken segment is too tight and will likely reunite and prevent daughter waves formation.

The mere occurrence of wave break does not guarantee that new reentrant circuits will develop and survive. Figure 3.24 shows an idealized spiral wave rolling up and breaking to form two new free ends under conditions previously described. These ends can evolve into a new pair of daughter waves only if there is sufficient space within the excitable gap for each new end to complete a half revolution in order to claim its territory before being blocked by the original mother wave as it completes another rotation within the same time period. This important requirement illustrates why the restitution slope criterion of $m > 1$ is necessary but insufficient to ensure break-up into fibrillation. There must not only be wave front block at some segment, but the diastolic intervals must become wide enough spatially, perhaps with oscillation, to fit the radius of a reentrant circuit of at least the critical ring size. It is reasonable therefore to conjecture that for any chosen APD_m and τ, the restitution intercept APD_0 that results in wave break and roll-up should be low

enough to produce a region with $m > 1$, and also admit a diastolic gap of width greater than the critical diameter of reentry $D_{crit} = N_{crit}/\pi$. The likelihood of wave break into fibrillation is therefore related to the conditional probability of both events occurring. This relationship between APD_m and APD_o at the fibrillation transition is embodied in empirically derived line in Figure 3.20.

3.7 Wavelet Capacity

Wave breaking is a route to smaller spatial structure. There must be a lower bound to the spatial scale of waves, otherwise activity would progress to fine grained totally random disorder. Presumably this is prevented by intracellular coupling and refractoriness that determine a limiting smallest spatial scale. We can attempt to establish higher densities of reentrant circuits in the domain to simulate progressively higher complexity fibrillation, either by defining initial conditions with more phase singularities or through dynamic evolution with wave breaking. What is the maximum number of reentrant circuits that can be sustained in a given area of medium, and how are they configured? This number is the wave capacity or maximum wave density, and represents the lower bound of spatial scale in a field of reentrant circuits.

Symmetry dictates intuitively that the maximum wave density occurs when core points lie on a regular periodic grid. If the action potential restitution curve is steep enough to force waves to alternate between being narrow and wide, then more narrow waves might intermittently fit between the wide waves allowing a greater total number of waves to exist in some spatially quasiperiodic pattern rather than in the regular periodic case. This problem is similar to that of determining the optimal packing of unequal sized molecules within a crystal lattice, however, it is more complex because waves are not static points but are dynamic structures in both space and time. Depending on the nature of the restitution curve, core points might move away from being fixed and instead trace circular or hypercycloidal trajectories such as those observed in ionic models [31, 40, 146, 412]. These have not appeared with clarity in CML model runs so far, although this issue has not been specifically investigated. This complex dynamical behaviour involving

core point meander further complicates the search for the spatiotemporal pattern of maximal wave capacity.

The duration with which a firing cell can potentially propagate its activity to a neighbour depends on the difference between the peak voltage V_m and the threshold voltage V_{th} as previously described. This difference defines a "voltage reserve" of the upstroke which determines the slowest possible conduction velocity. Although the maximum velocity cannot exceed one cell per time step by Huygens principle, much slower velocities are certainly possible. For example, consider very slow conduction with APD = 48, $V_m = 30$, and $V_{th} = 0.3V_m$. Once the cell fires, it can count down as many as (1 – 0.3) APD = 33 time steps without propagating and still be capable of exciting its neighbour, should that neighbour be temporarily refractory and then become excitable within that 33 time step window. Propagation in this case could theoretically be as slow as one cell per 33 time steps. More realistically, when action potentials are tightly packed and propagating around small scale circuits the APD would be shorter than APD_m due to restitution, and the slowest velocity would be higher than 1/33. The slowest possible velocity with the smallest possible APD and cycle length CL are the determinants of the smallest possible reentrant circuit path length $L = CL\ V_{max} = (APD_{min} + R) / V_{max}$. The actual limiting values depend on complex local interactions during propagation on the substrate and are not readily predictable without simulation. The case of the one-dimensional ring permits a theoretical solution as shown above, but the two-dimensional analogue is not as readily obtainable. The critical size of reentrant circuit in two dimensions must be determined empirically.

To investigate the capacity question empirically in two dimensions, we first establish an initial condition of periodic wave segments in an isotropic medium such that it evolves into a regular grid of counter-rotating reentrant waves. The APD can then be gradually lengthened while keeping it uniform throughout the entire field at each instant of time until the maximum stable wave density is achieved. The example shown in Figure 3.25 illustrates several stable wave patterns with APD = 24 on a uniform grid with a spatial periods of 25, 15, 10, and 5 units. The latter gives a maximum of $N_c = 120$ core points.

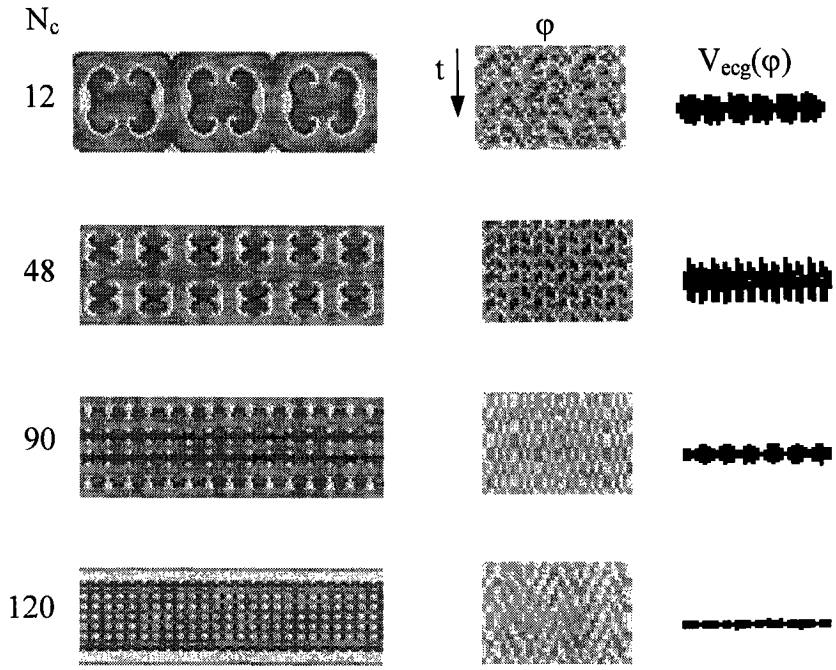

Figure 3.25. Regular grids of reentrant circuits are established with various periodicities. In each case APD = 24 such that N_{crit} = 10. Circuits remain stable even at very fine spacing, as shown in the bottom frame. The equatorial body surface maps in the middle column show fine spatial periodic patterns, and the envelopes of maximum amplitudes V(φ) are shown at right.

There is a relationship between the maximum spiral wave density, or minimum reentrant circuit size, for a given spatial periodicity of core points and the maximum APD that is sustainable in this circuit. Simulations were repeated on regular grids of spiral waves for different wavelengths of spatial periodicity to determine this relationship. The results are summarized in Figure 3.26, where ζ is the wavelength between core points, and the periodicity is twice this value due to the necessity of counter-rotating pairs. APD is the maximum action potential duration supported is this circuit without blocking. N_{crit} is the critical ring size for this APD derived from the one dimensional theory discussed earlier, and is shown for reference. A simple theoretical equation for the critical circuit size in two dimensions follows directly if we assume that the smallest reentrant path is a circle taken through elements just inside the periodic boundaries, since this "inside track" must

be part of the minimum wave front size $N_A = 3$ to ensure propagation. This criterion gives the equation for the minimum core point spacing ζ' of reentrant circuits in two dimensions where N_{crit} is the critical ring size equivalent to the path length.

$$(\zeta - 2)\pi \cong N_{crit} \propto \theta \left(\frac{APD}{\dot{X}} \frac{V_{th}}{V_m} + R \right) \tag{3.9}$$

The table in Figure 3.26 shows good agreement between the actual periodicity ζ of the grid defined in each simulation, and the calculated critical ζ_c based on the above equation using the maximum APD found to be sustainable in the simulation, thus validating this extension of the equation to two dimensions.

In terms of minimum size, the smallest reentrant circuits that could be achieved in simulations were on a grid with a pattern of repeats corresponds to a spatial period of 6x6 units giving $\zeta_c = 6$ and 250 core points. This could only be achieved by lowering parameters to $APD_{min} = 8$ and $R = 2$, which may be of theoretical interest, but are too small to be physiological for cardiac tissue. APD could however be increased up to about 65 when the spacing between core points was 10 units. By sketching an hypothetical array of arrival times in each cell on a grid, one might expect the smallest circuits to exist on 3x3 patches with a spatial periodicity of 4 units, but this does not turn out to be the case when actually tested in the model. These circuits are too small and fail to propagate because at a certain time within a cycle there is insufficient number of excited neighbours to maintain propagation into a very narrow isthmus of recovered tissue. The minimum number of neighbours rule $N_A \geq 3$ is violated at some point. The cell in the centre of the tiny 3x3 patch would also have to be a fixed phase singularity to permit a very small reentrant circuit to continuously revolve around it. This cannot be guaranteed with certainty unless the centre cell is persistently inexcitable in order to keep its location fixed. Fig 3.26 illustrates why the grid of smallest reentrant circuits in two dimensions must have a periodicity of 6 units to satisfy the $N_A \geq 3$ rule. Figure 3.27 compares the critical ring size and critical spiral wave core separation based on the one-dimensional ring theory and the two-dimensional extension described above. The close agreement

between theory and experiment suggests that the simple ring theory for N_{crit} gives a reasonable estimate of the critical circuit size for two dimensions.

ζ	APD	Ncrit	$\zeta_c = Ncrit/\pi + 2$
3 (3x3)	8	4.4	3.4
4	12	5.6	3.8
5	27	10.1	5.2
6	39	13.7	6.4
7	44	15.2	6.8
8	47	16.1	7.2
9	52	17.6	7.6
10	65	21.5	8.9

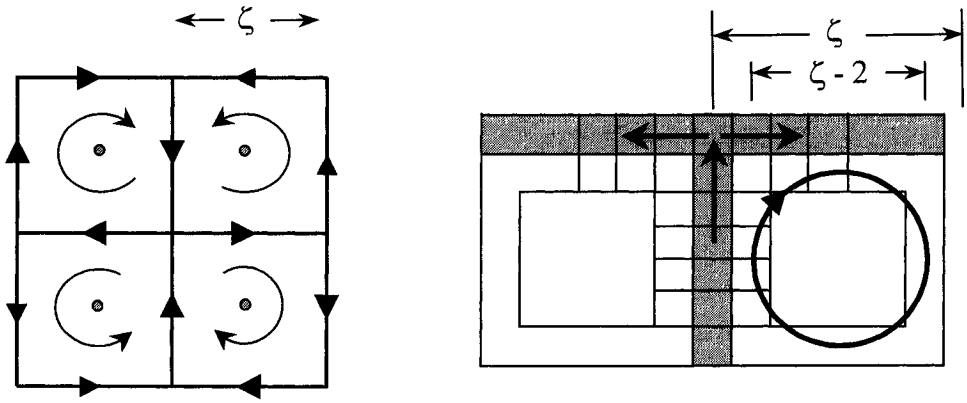

Figure 3.26. The smallest possible repeating unit in a regular grid of reentrant circuits is a square comprised of four counter-rotating circuits in a 2x2 configuration. If the size of each square reentrant circuit is ζ then the smallest path length taken during propagation approximates a square of size $\zeta - 2$, since the minimum width of the wave front must be $N_A \geq 3$ to ensure propagation by the minimum number-of-neighbours rule of state transition. If we assume that this path length approximates a circle of diameter $\zeta - 2$, then the one-dimensional ring theory gives an estimate for the critical size of the reentrant circuit in two dimensions. The table shows the actual unit size ζ in the simulation and the theoretical size ζ_c from the equation.

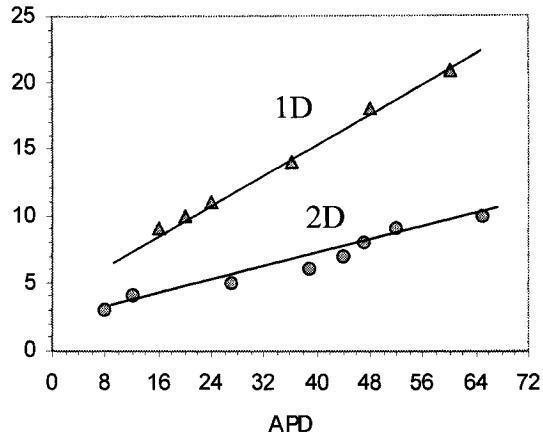

Figure 3.27. Comparison of minimum reentrant circuit sizes for one-dimensional ring (circumference) and two-dimensional spiral waves (diameter) determined empirically by simulation and by theoretical equations described in the text, which are validated by the good agreement. It should be noted that R=4 for the ring and R=2 for the spiral waves. The ratio between the two lines approaches π at larger APD, where R is less significant.

Obviously the scenario of densely packed reentrant circuits on a regular periodic grid is contrived and not likely to be achieved in real tissue. This case represents a theoretical lower bound on the characteristic size of small-scale fibrillatory patterns and on the smallest possible frequency components of the ECG. The specific values of spatial and temporal features in the model depend on the smallest chosen element or cell size, but the conclusions may be generalized. Obviously the greatest wavelet capacity in fibrillation theoretically should occur when reentrant circuits are smallest and most densely packed. Compatibility and symmetry dictate that, for an isotropic medium, the repeating pattern must be on a square grid with alternating clockwise and counter-clockwise circuits. A rectilinear grid would presumably be optimal in anisotropic media.

The next two chapters explore in greater detail the role of APD restitution on the evolution of spatiotemporal patterns of fibrillation in this model, and develop methods for quantifying complexity.

Chapter 4

THERMODYNAMICS AND COMPLEXITY

4.1 Introduction

For years the question has been posed as to whether fibrillation constitutes random or organized spatiotemporal activity [29, 127, 210, 269, 352, 549]. There must certainly be some degree of organization involved in VF, if for no more reason than the existence of electrotonic interactions that impart increments of phase synchronization between local neighbours. Given that a liquid can be obtained either by condensing a random gas, or by melting an organized solid, we can postulate that there exists two similar opposing routes to fibrillation that undergo a type of phase transition. At one extreme, we have seen how a simple wave breaks into multiple waves of greater complexity analogous to melting, presumably to some limit approaching randomness, but constrained by substrate properties. At the other extreme, initially random activity resembling that of a gas can self-organize into coherent fibrillatory waves through condensation. The thermodynamic analogy is that of intermolecular forces favouring organization and order through attraction competing with thermally-driven collisions favouring disorganization and disorder [238]. Figure 4.1 shows several patterns of fibrillation obtained by allowing an initially random field to self-organize.

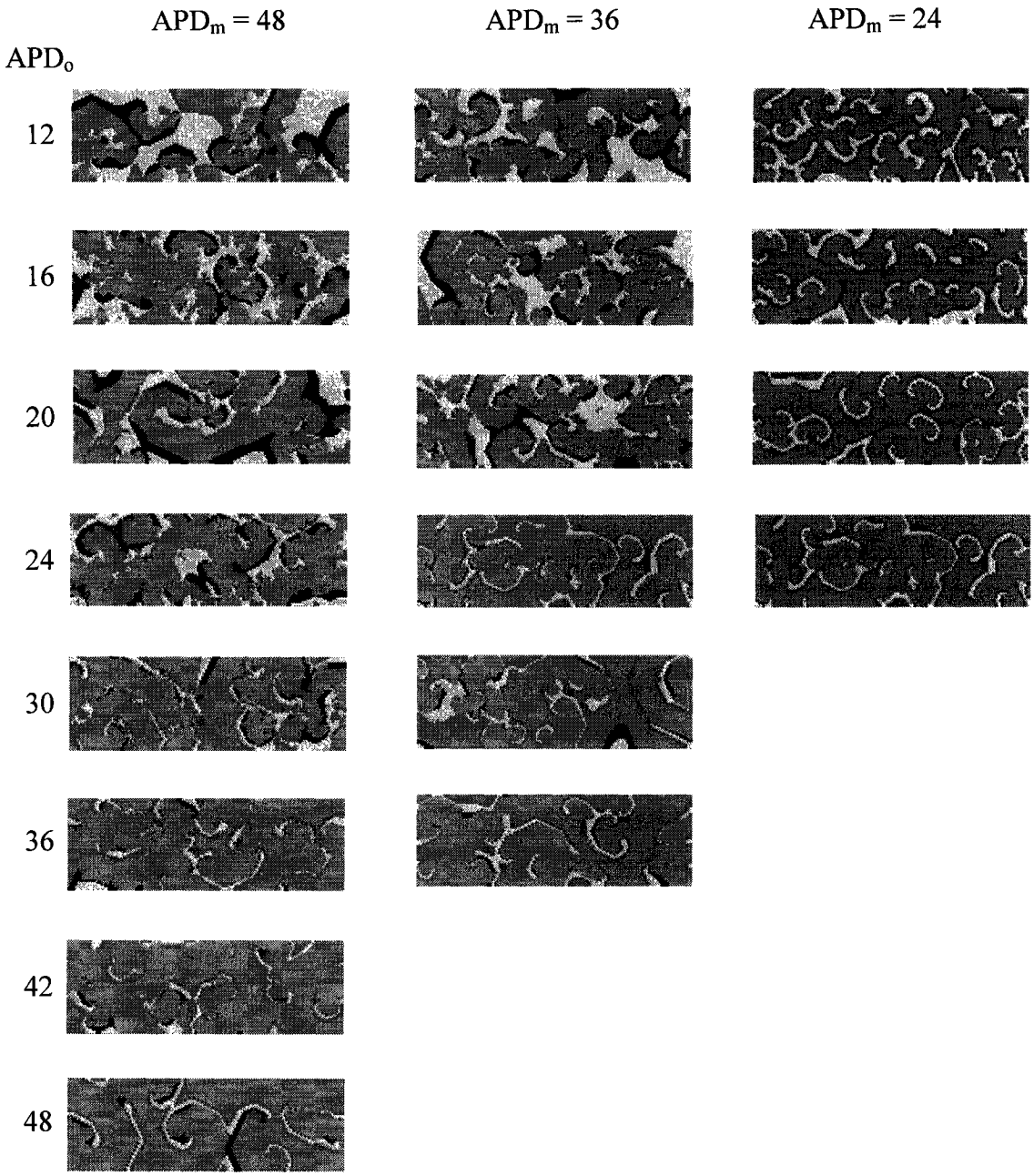

Figure 4.1. Composite showing the spectrum of fibrillation spatial patterns in the model for various values of the plateau APD_m and restitution intercept APD_o, with $\tau = 10$. Differences are evident in the characteristic size and uniformity of the waves, and the variability of the excitable gaps.

It seems natural to appeal to thermodynamics to seek insight into fibrillation. Phase transitions have been widely studied in spatially extended nonlinear systems [264, 302, 560]. The transition from regular sinus rhythm to complex VF is like a phase change from order to disorder, and is presumably associated with a change in some measure of total entropy. Clinically, we know that a small disturbance beyond some threshold can precipitate a transition to VF, suggesting that this direction is somehow energetically favourable [257], while the reverse process of defibrillation is relatively improbable spontaneously [431], generally requiring considerable energy to reverse artificially. These observations suggest that it might be possible to derive a thermodynamic theory of fibrillation within an idealized tissue model by quantifying the competing influences that govern the system dynamics. Before addressing thermodynamics in the strictest sense, however, we must bear in mind that energetically the heart is not a closed system. Energy is continuously replenished by metabolism which recharges cells after they fire, and can also be supplied iatrogenically by external stimuli or shocks. There is a large component of mechanical work done by contraction that would also need to be accounted in the first law of thermodynamics. Only at the time of death, when there is no intrinsic or extrinsic energy supply, does the heart approach a closed system. One must otherwise seek to apply methods of nonequilibrium thermodynamics to an open system [407].

4.2 Energy Potential

A system with no external influence tends to move toward a state of lower free energy as originally proposed by Gibbs [407]. At any given location, however, the decrease need not be monotonic, particularly if the system is spatially extended such that energy can be redistributed or partitioned. For our purposes, we propose a tentative definition of system energy by assuming that it is dissipated according to heterogeneity of spatial voltage. The system evolution tries to minimize the voltage gradients between cells by doing resistive work that is ultimately dissipated as heat. This is the behaviour of passive electrical circuits. The total of all gradients is proportional to the sum of the absolute values of all current increments between neighbouring cells. Mathematically, this is the volume integral of the conductance g times the voltage gradient squared according to Ohm's law.

$$W = \tfrac{1}{2} \int_V g\,[\,\nabla \cdot V\,]^2 \, d\forall \tag{4.1}$$

The one half term normalizes for the double counting of each neighbour pair as indices *i* and *j* reverse their roles during the integration or summation, and $\forall$ represents the tissue volume. Energy reaches zero only when the voltage field is homogeneous, as with complete quiescence or with synchronous firing of all cells. For practical purposes, we assume that resistance between elements is uniform and isotropic, and that all elements are of equal size. The energy equation then reduces to a volume summation of finite differences involving immediate neighbours *j*.

$$W = \tfrac{1}{2}\, g \sum_i^N \sum_j^M [V_i - V_j]^2 \tag{4.2}$$

A specific example employing a simple ionic model illustrates this concept. The two-variable model in Table 2.4 has a single inward sodium current and a single outward potassium current. Integrating the transmembrane current flowing down the instantaneous voltage gradient gives the potential energy function shown in Figure 4.2. This function is a bistable energy well with two resting points. A relatively small amount of energy must be supplied to overcome the threshold barrier, and allow the cell to fire by falling into the lower well representing the action potential peak. This second well of lower energy is also a stable attractor, unless there is a restoring current. The elevation drop is the energy lost, and has individual sodium and potassium contributions that dissipate small amounts of their respective stored Nernst potentials E_{Na} and E_K. If lost energy is not replenished, repetitive action potentials will run the system energy down like a marble rolling down a spiral track eventually depletes potential energy. This simple ionic model demonstrates that energy is dissipated independently in both the depolarization and repolarization phases, hence the use of the absolute-value operator in equation (4.2). This concept can be extended to any ionic model, provided that each and every ionic current is integrated over voltage as demonstrated for the Beeler-Reuter model in Figure 4.3.

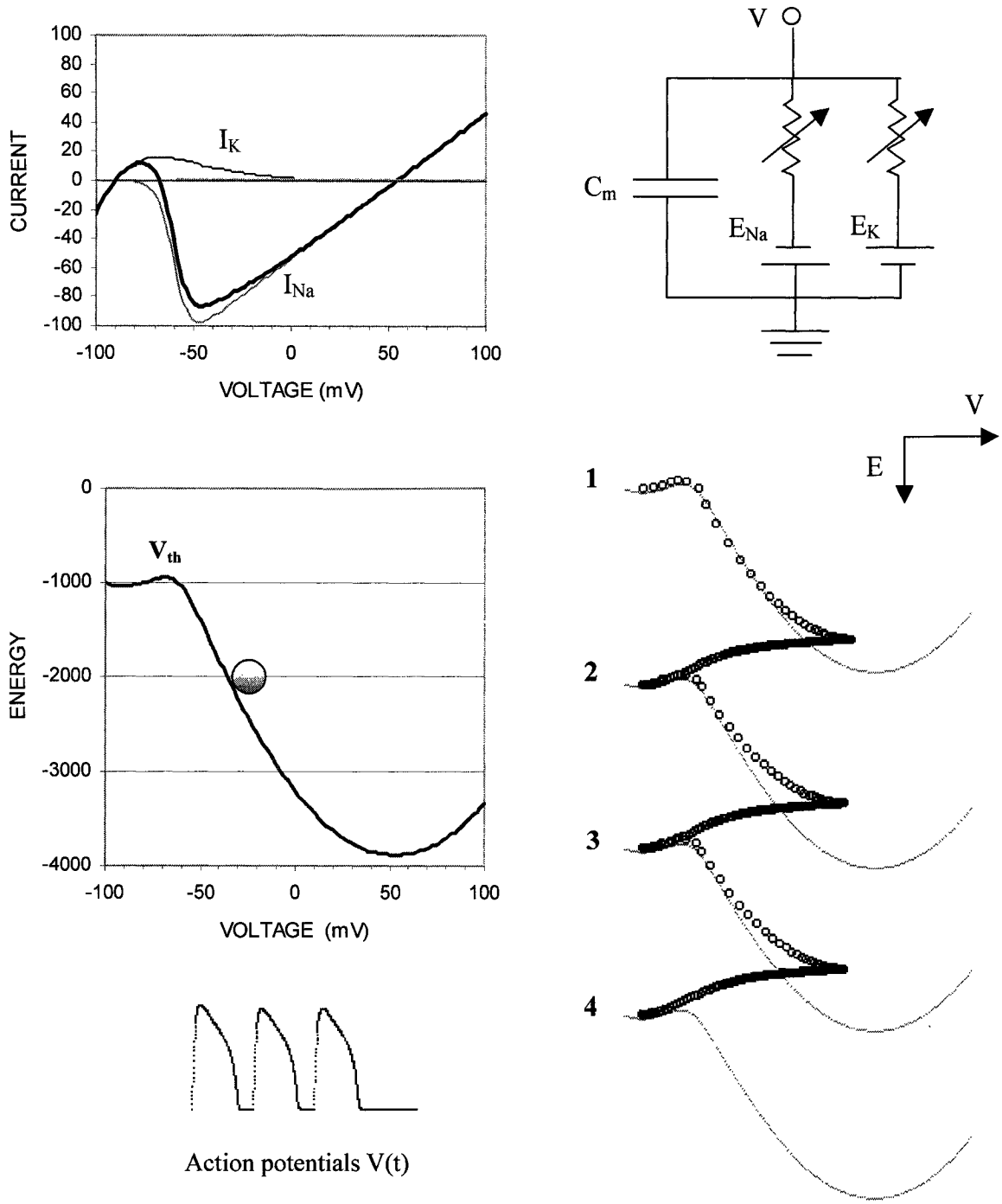

Figure 4.2. An energy potential for an excitable cell can be derived as shown in this simple example of a two-current model with I_{Na} and I_K for the circuit shown at upper right. The total current is integrated over voltage to give the potential-energy function, plotted as a bistable potential well containing a ball representing the state. When a threshold voltage is reached, the ball moves to a lower energy state. Repolarization moves it back, but this requires energy. Subsequent action potentials cause a cascade of falling energy.

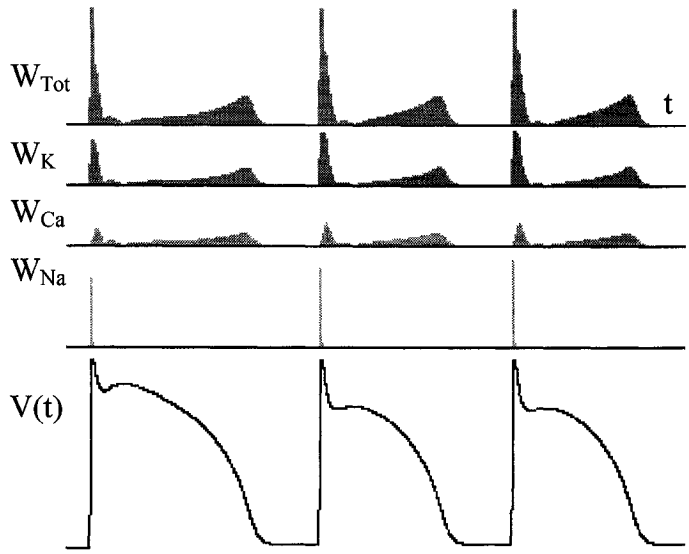

Figure 4.3. The rate of energy consumption during action potentials in the Beeler-Reuter model. Note that electrical work is done during both the depolarization and repolarization phases. The total energy loss is the area under the top curve. Each individual ionic current requires stored energy which is dissipated according to the voltage gradient and instantaneous conductance in Ohm's law. The concept is general for any number of currents; however, more currents obviously require more energy.

A physiological problem arises with this definition. As electrical energy of a cell is dissipated through surrounding resistance elements, it is continuously replenished by metabolism in an open system, such that a dynamic equilibrium of near constant total energy for each cell is maintained throughout life. By analogy, the marble in Figure 4.2 is lifted back up during or following each beat. Only when metabolism fails during ischemia does the total energy eventually run down to zero as intracellular potential energy stores become depleted. A more physiological definition of system energy would include the incoming flux from metabolism charging up the potential energy store. Such a model would need to calculate both the energy dissipated in electrotonic and ionic currents W_f and the total system energy E over time during simulations of normal and ischemic conduction, and account for any additional energy imposed by external stimulation or defibrillation denoted as W_{stim}.

$$W_f = \tfrac{1}{2}\, g \sum_{i}^{N} \sum_{j}^{M} |Vi - Vj|^2 \qquad (4.3)$$

$$E = E_o + \int_{t} k\,(W_{met} + W_{stim} - W_f)\, dt \qquad (4.4)$$

The integrand is the total rate of energy change relative to the initial value of E_o. The rate constant k depends on the capacity or effective "volume" of the energy compartment. As E gets very low with progressive ischemia, and approaches the energy $W_f dt$ being dissipated with each beat, the energy needed for propagation cannot be sustained and action potential propagation fails. The detailed events at the time of failure depend on how the remaining energy store is partitioned between maintaining upstroke and maintaining repolarization. Physiologically, this relates to how the diminishing potential energy, as transmembrane ionic gradients and ATP, choose between maintaining the sodium, potassium, and calcium equilibrium potentials that drive depolarizing and repolarizing currents. This complex bioenergetic issue of electrophysiological behaviour in low energy states will not be addressed here. We also cannot account for mechanical energy required for contraction, and therefore must assume that no mechanical work is done.

Accordingly, owing to quantitative uncertainty in the total energy balance, the first law of thermodynamics is not likely to be useful beyond the calculation of the rate of energy dissipation $W_f(t)$ by action potentials and propagation. Available energy stores are vastly larger than what is required for individual beats, and thus fibrillation can persist for many minutes, allowing hundreds of beats following total loss of coronary perfusion.

4.3 Entropy

A fundamental feature of many types of cellular automata and dissipative systems is the ability to self-organization [283, 490]. Asymptotic behaviour is generally independent of initial conditions, and depends only on the substrate lattice properties and the local rules. We have already seen how a state resembling fibrillation can be established in the medium by defining random initial conditions and allowing the field to spontaneously self-organize

according to its local rules. Clusters of activated cells mutually interact and condense into waves which persist due to the evolution of small-scale reentrant circuits or spiral waves. These waves are stable, so long as there always exists a point such that each of the three states (firing, refractory, and recovered) are in contact with each other, allowing activation to move from the firing cell into recovered tissue. This critical point is a phase singularity, since isochrones of all phases of the periodic cycle converge and rotate about this point like a pinwheel [543]. An additional minimum-number-of-neighbours criteria must also be satisfied to account for a threshold being reached. This latter constraint corresponds to the safety factor for conduction in continuous media, which pertains to the volume of source relative to sink needed to sustain propagation [125].

One approach to resolving the issue of fibrillation being random versus organized is to calculate the system entropy which quantifies the continuum between these extremes. Boltzmann originally proposed the statistical mechanical theory of entropy, to provide a molecular or microscopic explanation for the macroscopic description of thermal entropy proposed by Clausius [407]. Inspired by Darwin, he sought an "evolution equation" for matter. The concept of entropy is often illustrated by considering a box with a barrier across the centre dividing it into two equal compartments. Gas molecules occupy one side while the other side is empty. The respective concentrations on each side, expressed in arbitrary units, are one and zero. This initial state has order due to distinct partitioning. If the barrier is suddenly removed, the gas molecules can cross back and forth at random. Equilibrium is eventually established when the probability of a molecule moving out of one compartment is equal to that of a molecule moving in. A simulation of 100 particles with random crossing is shown in Figure 4.4. The equilibrium mean concentration is 0.5 with 50 particles on each side as expected. Owing to the system being dynamic or constantly in motion according to temperature, equilibrium can be defined in a statistical sense only, and must be measured over a finite time interval. Static equilibrium cannot exist, except at an infinitesimal moment. The number of combinations of placing N particles on each side gives rise to the statistical definition of entropy.

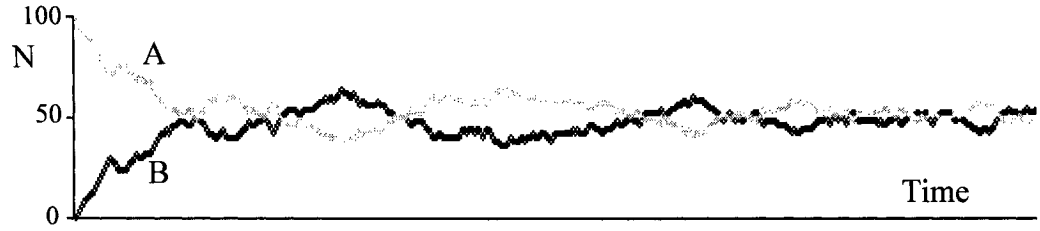

Figure 4.4 Chamber A initially has 100 particles and chamber B has none. After the partition is removed, the molecules are free to move back and forth at random between chambers. Eventually the mean number on each side is 50, and the concentration is 0.5. This is the configuration of equilibrium and maximum entropy.

Boltzmann recognized that in particle systems like gases, by number alone, there are far more possible disordered states than ordered states. Figure 4.5 shows the 16 possible states in a 4 bit binary string. The uniform states 0000 and 1111 are most ordered yet least likely, the probabilities of either being P = 2/16 or 0.125. The most probable states at any given time are those having two zeros and two ones, since these represent the maximum number of combinations, that being 6. The probability of one occurring is maximum at 6/16 or 0.375. Larger strings, in the limit, approach a binomial distribution of bit proportions according to Pascal's triangle. For any length of string having a binary alphabet, each bit having P = 0.5 gives the highest entropy because it has the greatest number of possible contributing states. A dynamical system moving randomly between states, without any preference in transitions, is therefore statistically far more likely to move toward disorder than toward order. Over a period of many state changes, this mostly unidirectional path to disorder is virtually assured by the law of large numbers. Once equilibrium is reached, the states tend to stay within a disordered subset of states, and the path followed becomes effectively irreversible because a route taken backward along the same path becomes extremely unlikely. This is the essence of the statistical mechanical interpretation of the second law of thermodynamics - that a system has a high probability of moving into disorganized states by virtue of their large number relative to that of organized states.

0 0 0 0
0 0 0 1
0 0 1 0
0 0 1 1
0 1 0 0
0 1 0 1
0 1 1 0
0 1 1 1
1 0 0 0
1 0 0 1
1 0 1 0
1 0 1 1
1 1 0 0
1 1 0 1
1 1 1 0
1 1 1 1

P(0)	P(1)	N	S = Σ P log(P)
1.00	0.00	1	1.00 log(1.00) + 0.00 log(0.00) = 0.00
0.75	0.25	4	0.75 log(0.75) + 0.75 log(0.75) = 0.81
0.50	0.50	6	0.50 log(0.50) + 0.50 log(0.50) = 1.00
0.25	0.75	4	0.25 log(0.25) + 0.25 log(0.25) = 0.81
0.00	1.00	1	0.00 log(0.00) + 0.00 log(0.00) = 0.00

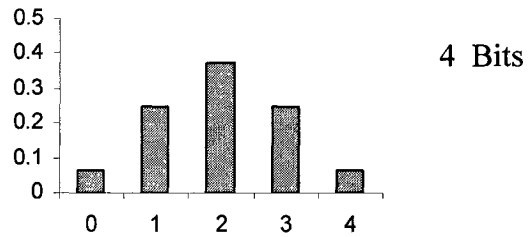

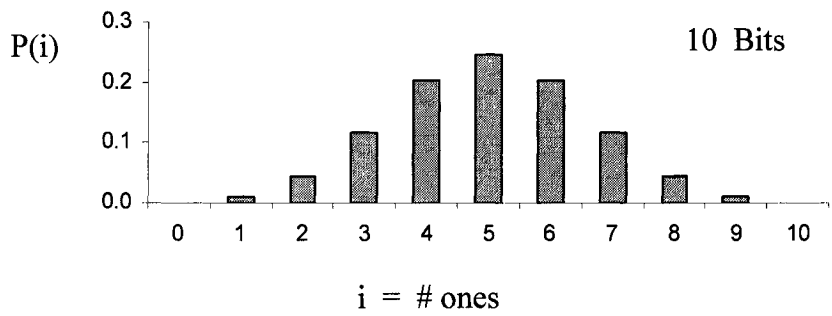

Figure 4.5. For a 4-bit string there are 16 combinations as shown. The most probable configurations are those with 2 zeros P(0) = 0.50 and 2 ones P(1) = 0.5 which account for 6 strings out of 16. These are the most likely strings to be recurrently visited, and are the states of maximum entropy where S_{max} = 1.00 for 4 bits. The digits 1, 4, 6, 4, 1 are given by Pascal's triangle, and can be generalized to any size of string, such as the 10 bit example shown, ultimately producing a binomial distribution in the limit of large numbers or long strings, provided that state changes are random. Non-random transitions, by contrast, give rise to order.

Now consider the same problem with a string of zeros and ones shown in Figure 4.6, where ones are black and zeros are grey. The ones are initially partitioned like gas molecules on the left half of the string. At each time step, two opposite bits chosen at random sites are changed to their complements, simulating a molecule moving from one site to another. After many iterations, eventually the number of bits in each state on each half of the string becomes equal, at a mean concentration of 0.5. This string could perhaps represent the state diagram of a piece of excitable tissue, where resting and firing action potentials hold states of zero and one respectively, and the two-dimensional field of cells is mapped onto a one-dimensional string. System entropy could then be calculated over finite time intervals based on sampled probabilities. Self-organization is implemented according to two rules. In the first case, if the two neighbouring bits are equal, the centre bit is set to the opposite value. In the second case, the centre bit is set to the same value. It is important to note that entropy *increases* when state transitions are random, for reasons previously discussed, but can *decrease* with self-organization, since element states change according to specific rules that are not random, favouring convergence to more organized states.

Within this context, it is easy to see that the initial condition is ordered and the final state is disordered, or that simplicity tends to move toward complexity. This might seem like a trivial statement, but it is not. It is actually much more difficult than first apparent to formally quantify the complexity of these patterns, or indeed that of any irregular spatio-temporal pattern. At issue are the precise definitions of simplicity and complexity, because there is no unique or absolute definition of these concepts. Can one even have a simple definition of complexity? Casti argues that complexity is an inherently subjective concept, depending on context [61], and that formally, it should be proportional to the number of inequivalent descriptions of the system an observer can make. Inequivalence means that observations cannot be transformed into one another by changing coordinates. Complexity increases with the number of possible descriptions, for example between bifurcations. This interesting philosophical issue is discussed elsewhere [61, 231]. Suffice it to say, for now, that many practical definitions of complexity can be devised, of which entropy is only one.

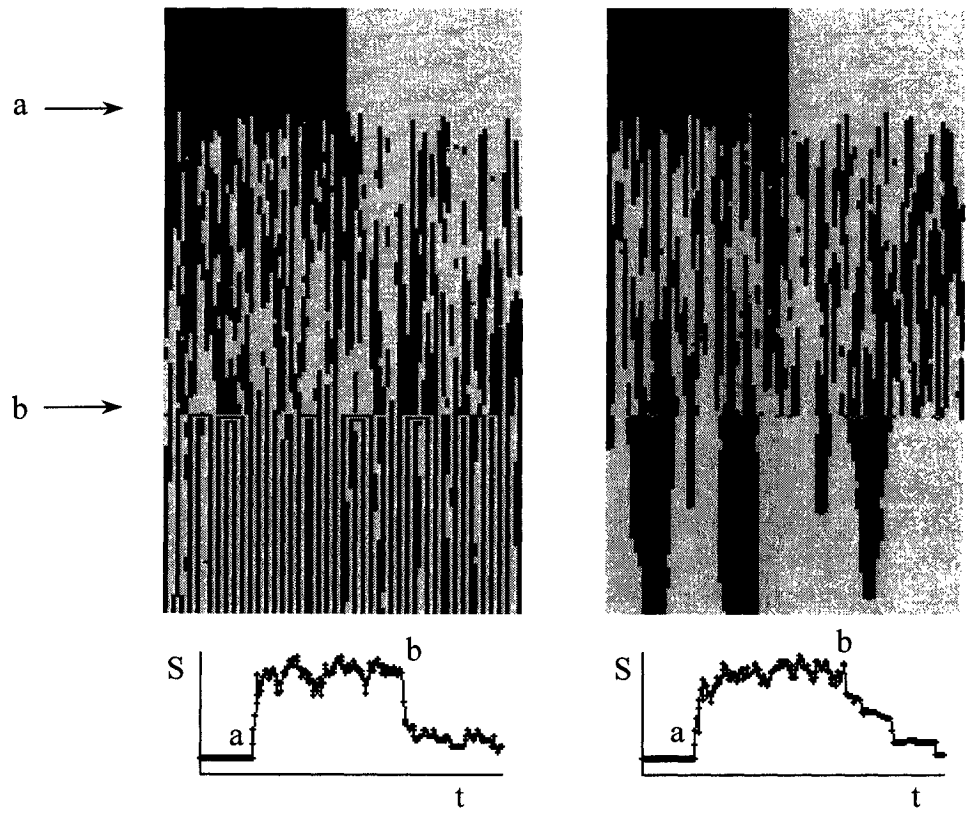

Figure 4.6 A string of 100 bits, initially partitioned like gas molecules on the left, is released at time "a". Random bit exchanges simulating molecule movement cause the pattern to evolve toward disorder. Entropy S, calculated from the distribution of same-bit cluster sizes, is shown at the bottom, and increases when spontaneous randomization is permitted. Two rules of self-organization are turned on at time "b" corresponding to anti-smoothing (left) and smoothing (right). In each case, self-organization decreases entropy.

The Boltzmann entropy equation is well known in statistical mechanics [238], and as pointed out by Shannon, is the amount of new information that one must provide at each instant in time to define the state of the system [400]. If there are a maximum number of possible states N, each with a probability of P_i for i = 1...N, then the entropy S is given by

$$S = -\sum_{i}^{N} P_i \log_2 P_i \qquad (4.5)$$

This measure defines the degree of predictability of future states in an evolving system. If the state is fixed, periodic, or otherwise perfectly predictable, then the probability of the next specific state being known is exactly one, and the entropy is zero. At the other extreme, if the system is perfectly random, then all states *i* are equally probable with P_i = 1/N, and the entropy takes on its maximum value of $S_{max} = -N\,(1/N)\log_2(1/N)$. The base of the logarithm is not important, but if the traditional base 2 is chosen, entropy takes on units of bits per time step, and may be directly interpreted as information.

The probability of occupying any specific state in a large system is extremely low. For example, consider only 50 cells that can take on two states: firing and resting. There are 2^{50} or about 10^{15} possible states in this small system alone. If we allow the existence of every state, the CML heart model with 7500 cells, each with perhaps 48 or more states if they were discrete integers, which they are not, has over 48^{7500} possible states! A real heart, with continuous states and far more cells, has vastly more possible states. Intercellular coupling and refractoriness reduce this to a much lower number of accessible or meaningful states, but the number of sites in the state space is still astronomical. It is obviously not practical to assemble a histogram of state visits during system evolution in order to calculate a true Boltzmann entropy based on possible microstates, even if we define wide bins corresponding to a very coarsely grained state space. The practical alternative is to define entropy based on collective properties, such as the probabilities of cells taking on specific values of APD, DI, or CL.

This entropy equation can be applied in various ways, quantifying order in a temporal sequence, a spatial pattern, or both as spatiotemporal activity [526]. We can define a temporal or point entropy of a specific cell by constructing a histogram of action potential upstroke times over a given sampling epoch spanning many action potentials, and determine the probabilities of the intervals between beats. For example, a periodic cell of cycle length CL = 40 time units has $P_{40} = 1$ and all other $P_i = 0$ giving S = 0, or perfect predictability. A beat-to-beat 2:1 alternans pattern might give $P_{30} = 0.5$ and $P_{50} = 0.5$, resulting in $S = -0.5\log_2(0.5) - 0.5\log_2(0.5) = 1.0$. Perfectly random activity partitions probabilities equally between N possible states, giving a maximum $S = -N(1/N)\log_2(1/N)$.

Examples of entropies for various histograms are shown in Figure 4.7. The top row shows sampling during a period of self-organization, while the bottom row was taken during spiral wave break-up at steep restitution. The maximum entropy for 100 bins, each having P(CL) = .01, during random activity for this case would be $S = -100\ (.01)\ \log_2\ (.01) = 6.64$, illustrating that these simulations have considerable organization, and are actually far from being random.

Entropy is a linear extensive quantity, which means that we can sum the entropies for each cell according to its state probabilities, and do so over all cells in the tissue domain to get a total spatiotemporal entropy. The longer the sampling interval, the more accurate will be the estimate of individual state probabilities. Entropy cannot be calculated as an instantaneous function of time, unless a moving average of a small sequence is followed. As the above definition of entropy is related to the width of the histogram of cycle lengths, one could alternatively define the degree of organization by the mean and standard deviation of the cycle length histogram. Entropy is more general, however, and directly related to information content, independently of any specific statistical distribution.

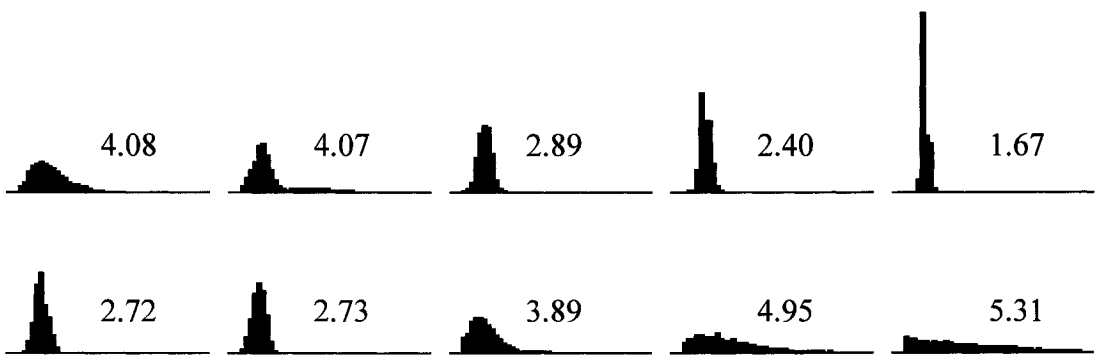

Figure 4.7. Entropy shown here is a function of the degree of order within the series of firing times for each and every element, and is related to the histogram of such events. The examples shown here are the probability distribution histograms P(CL) of cycle lengths taken from various simulations. The entropy of each is shown. Perfect predictability of a cycle length sequence would give P(CL) = 1.0 and S = 0, implying the existence of some regular pattern with a spike CL distribution. Random activity has the widest distribution of cycle lengths, and is associated with maximum entropy of 6.64. S is therefore related to the number and height of the histogram bins and uniformity of partitioning between them.

Since entropy is derived from the probability distributions, it says nothing about the specific sequence of events and how they might be related to each other in time. Action potentials might alternate regularly in a predictable 4:1 pattern, for example, or might have the same action potentials, but in a random order, as illustrated in Figure 4.8 for a constant cycle length. Both are identical statistically, in terms of the histograms p(DI) and p(APD), but the sequences are clearly different. Histograms for each are shown. An alternative form of the entropy equation, accounting for temporal order, can be defined using conditional probability. This can be referred to as conditional entropy S_M.

$$S_M = -\sum_{i}^{N} P(B|A) \log_2 P(B|A) \tag{4.6}$$

The term P(B|A) is the conditional probability of an event B occurring given that A has already occurred. If A and B are independent random events, and therefore uncorrelated, then P(B|A) = 1/N, identical to the probability of B occurring at random P(B) = 1/N giving $S = -N(1/N)\log_2(1/N)$, as before. At the other extreme, if any A is followed by a specific predictable B, due to a unique functional relationship between A and B, then P(B|A) = 1 and $P(B) \neq 0$. This gives $S_M = 0$. Calculation of these probabilities requires construction of an event matrix relating A and B to count of occurrences of (A,B) pairs, as in Figure 4.8.

Event A can be CL_i, APD_i, or DI_i, and event B can be the next CL_{i+1}, APD_{i+1}, or DI_{i+1}. This two-dimensional histogram is identical to the first return map of x(i+1) vs x(i) used in Poincaré plots to analyse bifurcations [304, 449]. The main difference between standard entropy S_C or S_D, based on p(CL) or p(DI), and conditional entropy S_M, based on P(B|A), is that the latter is based on a two-dimensional histogram whose projection along the B axis gives the one-dimensional histogram p(CL). S_M contains more information than S_C, and therefore also has a higher maximum. P(B|A) is the height of cell (A,B) divided by the sum of row A, while P(B) is the probability of events in column B. A perfectly regular sequence has a spike histogram with $S_M = 0$. Alternans gives two symmetric entries with $S_M = -2(0.5)\log_2(0.5) = 1$. A random sequence gives $S_M = -N(1/N)\log_2(1/N)$. Figure 4.9 shows the mapping of successive cycle lengths CL_i and CL_{i+1}. No relationship is apparent.

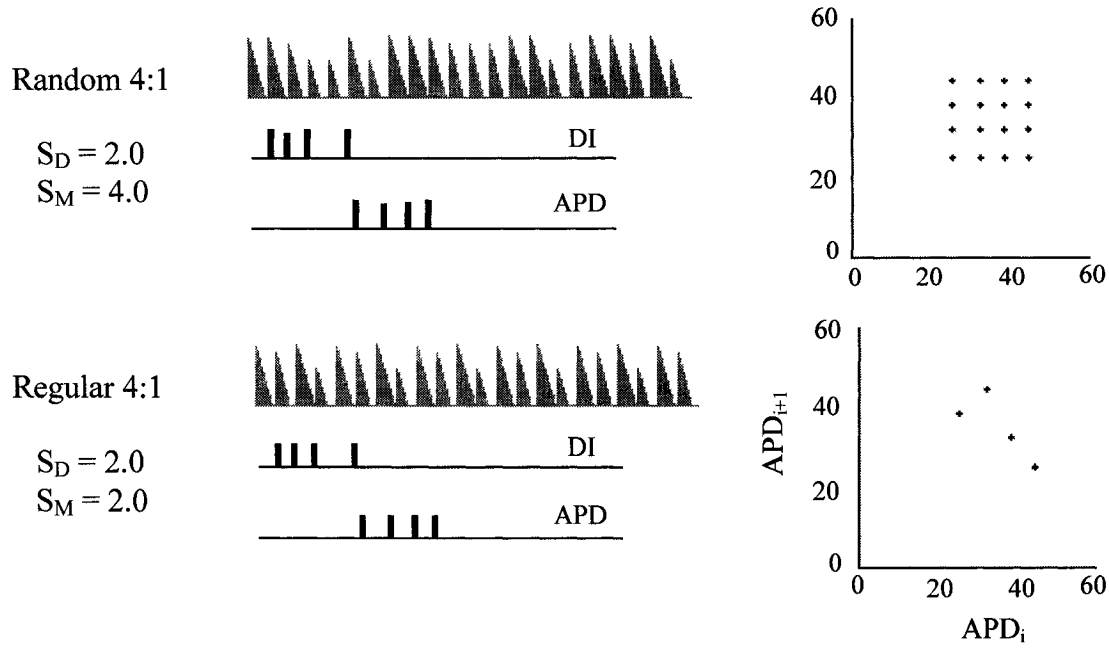

Figure 4.8. Comparison of standard entropy with conditional entropy. The top action potential sequence varies randomly between four values of DI and APD for a constant cycle length. Entropy of DI and APD is 2.0, based on the probability of 0.25 for 4 bins. The second sequence has identical DI and APD, but has a 4:1 periodic pattern. S_D cannot distinguish the regular from random temporal pattern because it is based on histograms alone which are identical for each case. Conditional entropy S_M is based on the conditional probability of APD_{i+1}, given the previous APD_i in the two-dimensional histogram at right. S_M captures the relationship within the DI and APD pair sequences better than S_D. S_M = 4.0 for 16 bins in the random case, and is 2.0 for the 4 bins in the regular case.

Figure 4.10 summarize many simulations with APD_m = 48 and APD_o varied from 12 to 48. Reducing APD_o lowers the average APD, and therefore lowers the total surface area occupied by action potentials. This increases the excitable gap, and therefore the width of the DI distribution. This in turn widens the CL histogram and increases DI entropy. DI and CL entropies remain almost identical to each other, except at very steep restitution where S_D may exceed S_c by a small amount because the DI distribution is unbounded, while the APD distribution is compressed by the APD_m plateau. The long upper tail of the DI histogram maps onto the flat plateau of the restitution curve, giving a small hump at the maximum value APD_m on the APD histogram.

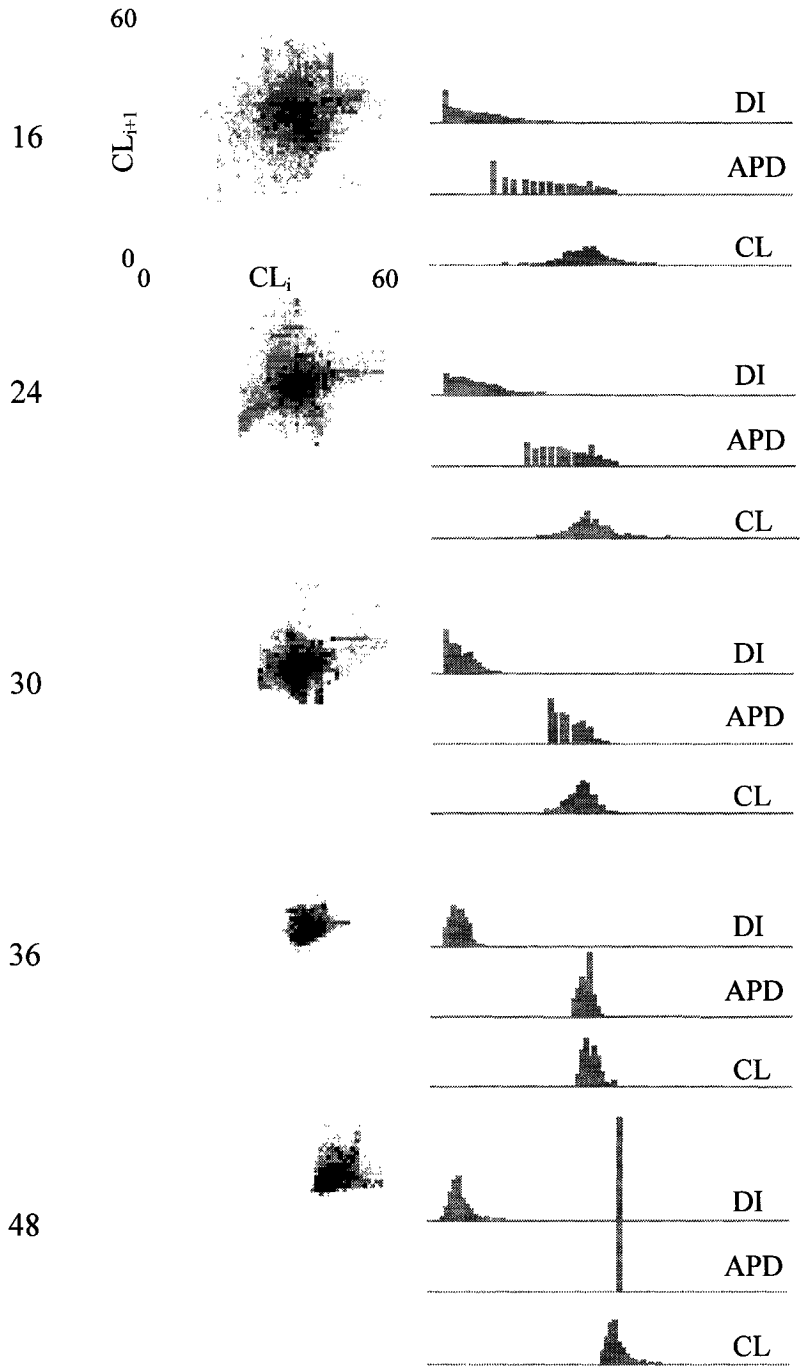

Figure 4.9. Event histograms showing p(DI), p(APD), and p(CL) for different restitution slopes APD_o = 16, 24, 30, 36, 48. The Poincaré plots comparing CL_i and CL_{i+1} at left show the degree of variability. No specific relationship between cycle length pairs emerges in these simulations. Most DI histograms have a peak at the shortest diastolic interval, corresponding to the refractory period R+1. The Poincaré plots, or return maps, can be used to calculate conditional entropy for CL, but even the simplest fibrillation with uniform APD_o = 48 has wide variability of CL, precluding any low dimensional attractor.

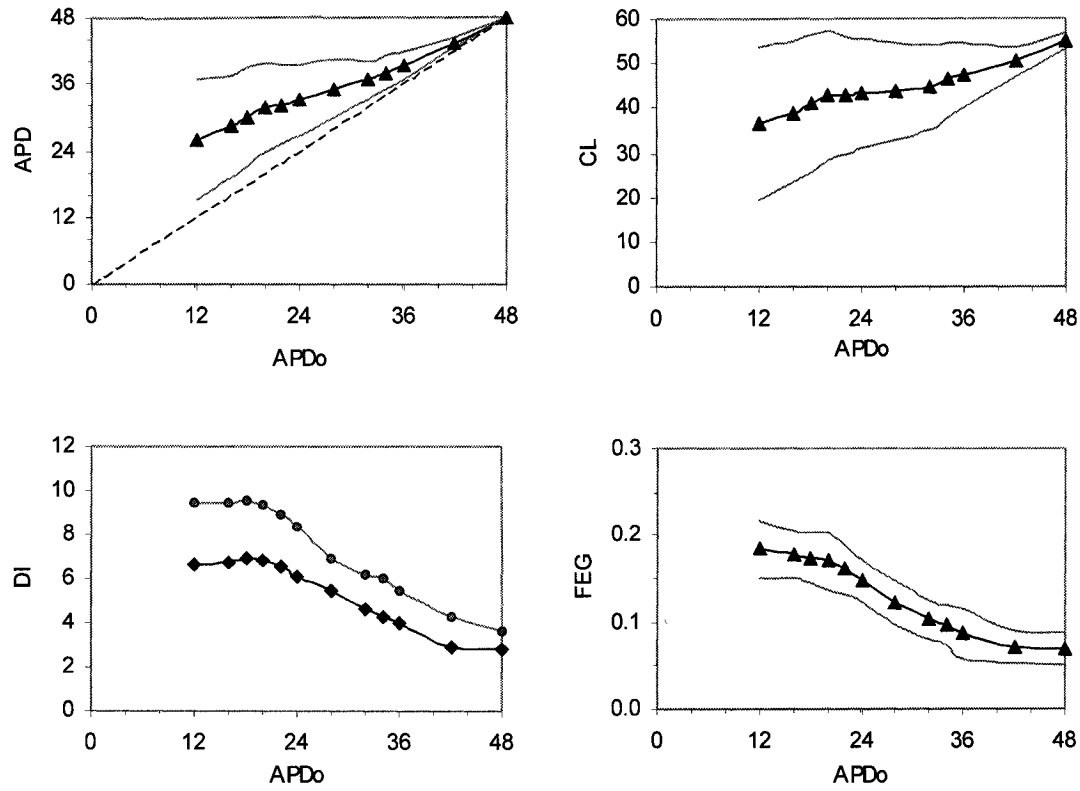

Figure 4.10. Effect of restitution on fibrillation APD, CL, DI, and excitable gap fraction F_{EG}. Mean values (black) and standard deviation (grey). Steep restitution lowers mean APD and CL, increases mean DI and F_{EG}, and increases variability of all quantities.

4.4 Lyapunov Exponents

Consider any point X_i in the N-dimensional state space at some arbitrary time t_o and a second point $X + \varepsilon$ separated by a very small distance ε in any direction. If the evolution of these two points is followed over time under the dynamics F(X), after some time interval $t - t_o$, the separation between these points will either diverge, remain the same, or converge. If the new distance grows exponentially over time, then λ is the Lyapunov exponent quantifying the growth rate [20].

$$F\{X(t)\} - F\{X(t - to)\} = \varepsilon e^{-\lambda (t - to)} \qquad (4.7)$$

Nearby points tend to converge if $\lambda < 0$, diverge if $\lambda > 0$, and have no tendency to separate or converge if $\lambda = 0$ as shown in Figure 4.11. In an N-dimensional state space there are N such values of λ, some of which may converge while others may diverge. The sum $\Sigma \lambda_i$ for i = 1..N represents the rate of volume change of an N-dimensional sphere of points around the initial condition. The Lyapunov exponent is therefore a measure of sensitivity to initial conditions or small perturbations along the trajectory of dynamic flow. Negative λ implies a stable system, insensitive to perturbations moving toward a fixed attractor such as a point or limit cycle, while $\lambda = 0$ implies neutrally stable behaviour, and a positive λ implies chaos. The complete Lyapunov spectrum λ_i of an N-dimensional system may contain values of both signs, implying simultaneous expansion and contraction of the initial condition sphere as it distorts along different axes of the state space. The sum of all λ represents the volume change of this set by Louiville's theorem [407], and is zero for conservative systems, and nonzero for dissipative systems like reaction-diffusion media.

Since the state space for X_i is usually bounded by limits on the variables, according to their physical meanings, this volume may oscillate in a limit cycle, or stretch and fold if the system is chaotic. Since transients following a perturbation may intermittently change signs and fluctuate, the strict definition of λ is based on the limit as $t \rightarrow \infty$, although in practice one must perform the calculations over some finite time interval [553].

Calculation of the complete Lyapunov spectrum for a given dynamical system can be computationally intensive if performed according to the first principles of its definition, especially if N is large [553]. For the special case of a discrete one-dimensional return map X(i+1) = F(X(i)), however, the calculation of λ is relatively straightforward and depends on the slope dF/dX of the function F(X) [269]. To calculate λ_i for i = 1..N, we can follow the changes in the components of X_i over time along each state space axis. Alternatively, if we know p(X), the probability distribution of X_i taking each and every value within the state space, evaluated over some finite but sufficiently long time interval to ensure convergence of the summation, we can calculate λ_i by integrating the conditional probability of λ_i for a specific value of X_i over the probability p(X) that X_i occurs [304].

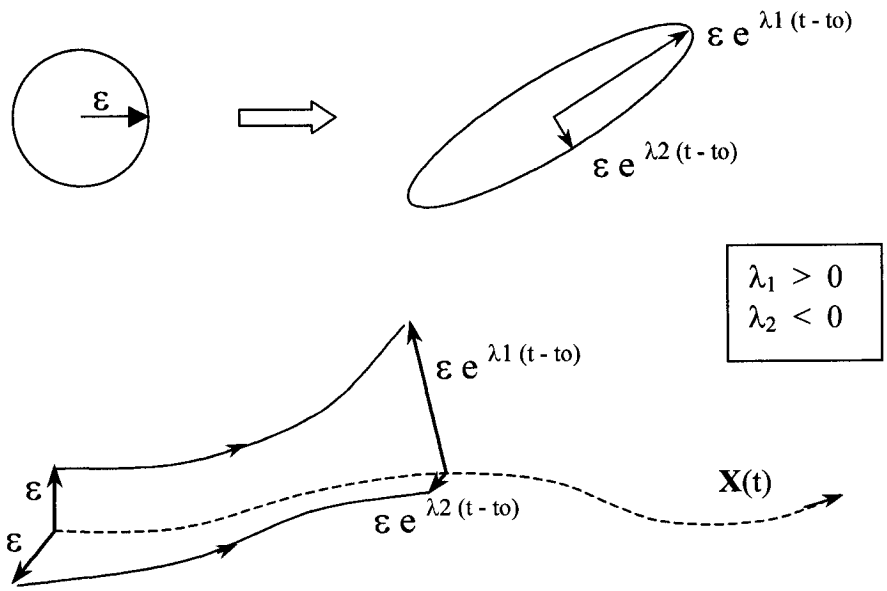

Figure 4.11. A cluster of state points within a small sphere distorts during system evolution. The Lyapunov exponent quantifies the rate of expansion or contraction of each state variable along its particular axis in the N-dimensional state space. The sum of the complete Lyapunov spectrum for all N state variables gives the rate of volume change of a small sphere of points surrounding the point of interest as the dynamics evolve. If all exponents are negative, the system is stable to perturbation. Positive exponents imply sensitivity to initial conditions and potential for chaos (Adapted from [20]).

$$\lambda = \int_X p(X) \log_e (dF/dX)\, dX \tag{4.8}$$

Applied to models of cardiac tissue, this function allows quantification of the sensitivity to initial conditions and presence of chaos during system evolution. We can define the discrete variable of the one-dimensional return map to be the diastolic interval DI between action potentials operating on itself through the restitution curve in repetitive activations:

$$\lambda_i = \sum_i p(DI_i) \log_e [(dAPD/dDI)_i]. \tag{4.9}$$

This equation is commonly applied to return maps such as the tent map and the logistic equation discussed in textbooks on nonlinear dynamics [20, 449]. The summation is over all occurrences of each DI within its histogram for many cycles. Since the restitution curve APD = f(DI) also influences the cycle length CL = APD + DI, the time sequence of DI values at each cell can be monitored to assemble the probability distribution p(DI). A long sampling time is required to build a reliable set of p(DI). To be pragmatic, we can instead take a shortcut by constructing p(DI) as an ensemble from all cells over some shorter interval. This simplifying assumption is a practical necessity; it is most accurate for a system which is ergodic, that is, having a tendency to eventually visit all possible states, these being combinations of DI, APD, and CL, such that the spatial and temporal distributions are equal [320]. This is a reasonable assumption, since all cells in the domain are identical and have equal likelihood of taking on any given state. The ergodicity assumption is validated empirically for APD and DI in Figure 4.12. Sampling over five cycle lengths generally produces reasonable convergence of the λ_i spectrum. If λ is divided by the mean CL, then the units are reciprocal time, otherwise it is dimensionless.

The presence of at least one $\lambda_i > 0$ implies an element of chaotic dynamics, or growing distortion along at least one state space axis. Obviously the sign of λ depends on the slope of the restitution curve m = dAPD/dDI according to equation (4.9). Positive exponents λ_i occur only if the slope m > 1. Figures 3.12 and 4.13 show how the restitution curve slope m determines whether variations in DI contract or grow according to how they map into variations in APD. The presence of at least one $\lambda_i > 0$ is a necessary, though not sufficient, condition for spiral wave break-up.

Short DI values map onto the high positive slope segment at steep restitution. Small differences in DI map onto larger differences in APD when the slope m > 1. Figure 4.14 shows the effect of restitution on chaotic dynamics, as quantified by the Lyapunov exponents calculated by equation 4.9. The sum of the positive and negative contributions is related to the volume change of a small element in the state space. The sum of the positive Lyapunov exponents gives the Kolmogorov entropy, which is another measure of

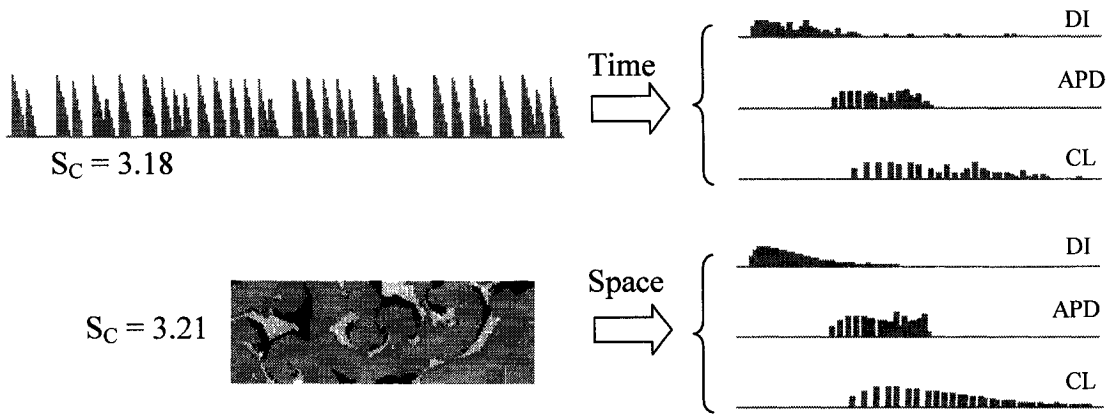

Figure 4.12. Validation of the ergodicity assumption. Event histograms were obtained by monitoring cycle lengths at one arbitrary cell over 3000 time steps (top), and also from all firing cells over the entire NxM field over a short time (bottom). Distributions and entropies for both cases are sufficiently close to validate the use of sampling over space to estimate single cell behaviour over a long time. This estimation technique is valid, because all cells have equal probability of taking on any given state, and the dynamics exhibit statistical stationarity for a given fixed parameter set.

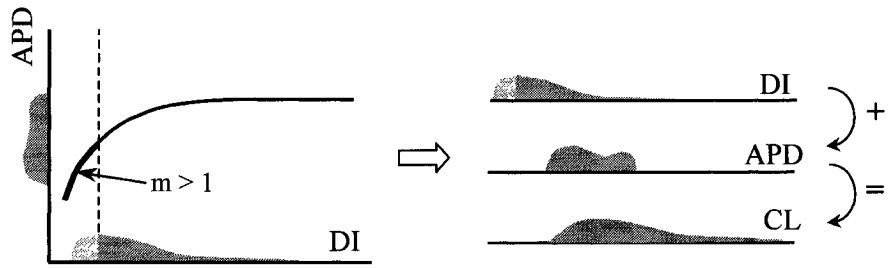

Figure 4.13. The histogram p(DI) determines the distribution p(APD) by mapping through the restitution curve. The cycle length distribution p(CL) is related to DI + APD + R = CL as shown at right. The distribution of DI is therefore the only independent variable amongst DI, APD, and CL. The tendency for spiral wave break-up into fibrillation is related to the proportion of p(DI) that falls under the region of the restitution curve where $m > 1$ (dashed line), as shown by the lightly shaded region of p(DI) and heavy curve segment. This relates to the Lyapunov exponent calculated by equation (4.9).

the degree of chaos [206]. Reducing the average APD, with consequent widening of the excitable gap (EG), gives rise to an increasing ratio of wave front to occupied action potential area, or "surface to volume ratio" of action potentials. By dimensional analysis, this defines a characteristic length of wave structure that becomes smaller at steeper restitution slopes.

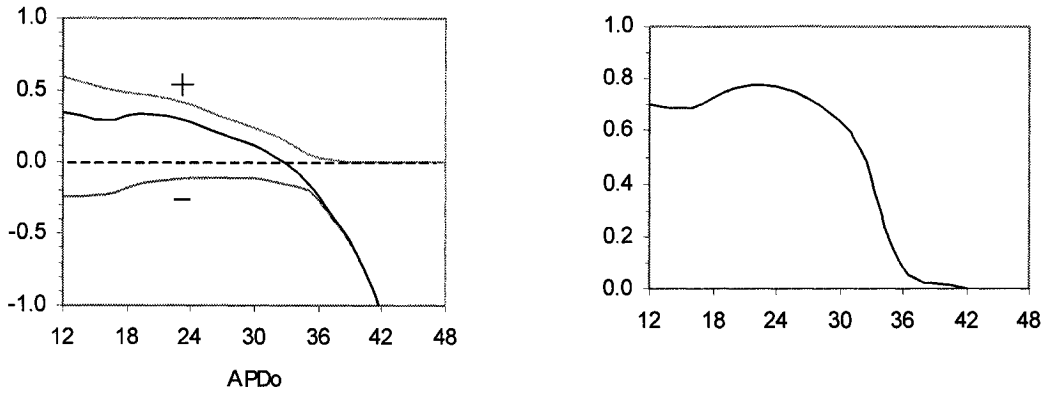

Figure 4.14. Lyapunov exponents are shown for various restitution slopes APD_o with $APD_m = 48$. Positive and negative contributions and the net sum are shown at left, while the proportion of positive contributions which is related to the Kolmogorov entropy is shown at right.

4.5 Nonlinear Dynamics

Dynamics is the study of time-dependent system stability and transitions between modes of behaviour. While the theoretical foundations were established by Poincaré over a century ago [398], pertaining to celestial mechanics [234], interest in nonlinear dynamics grew substantially in the latter half of the twentieth century with the ability to conduct digital computer simulation of nonlinear differential equations having chaotic solutions [199, 326], and discovery of the qualitative dynamics of period-doubling sequences of bifurcations in iterated equations as a route to deterministic chaos [162, 338]. For all but the simplest of spatially distributed systems, there is interaction between small scale local stability and instability, which can profoundly influence large scale global behaviour [449, 489]. Interaction between events on many scales is especially important in nonlinear

systems [19]. Biological systems have been a fruitful arena for discovering examples of these principles [198, 464]. A few salient concepts will be reviewed here as they apply to studying heart stability.

A system is completely defined by its state vector X(t), and its dynamics $dX/dt = F(X, \mu)$, where μ is the fixed parameter set or controlling constants. Behaviour evolves according to imposed initial conditions or external forcing. Fixed points exist where $F(X) = 0$. These points are attractors (stable) if nearby trajectories converge to them, repellors (unstable) if nearby points are pushed away, or saddle points (neutral) if trajectories approach from one direction and are pushed away in another direction. Stability is usually assessed by linearizing about the point of interest X_o, and examining the signs of the eigenvalues of the Jacobian determinant of $F(X - X_o)$ [489]. Attractors that are periodic orbits are called limit cycles. As the parameter set μ is varied, the attractor topology can change abruptly, introducing new fixed points or new paths on the attractor.

Since an N-dimensional state space is difficult to visualize and analyze, one can sample points at time intervals, as if flashing a strobe, and construct a lower dimensional set of points called a Poincaré section. If these points fall along a one-dimensional surface or line, and the sampling is regular, then the return map is simply $X(i+1) = F^1(X(i), \mu)$. The superscript "1" denotes that this is the first return. Iterating the process generates higher order return maps $X = F(F(X)) = F^2(X)$. The sequence of all such X(i) can settle to a fixed point, alternate in some pattern, or appear random, depending on F and μ. A periodic repeating sequence, such that $F^n(i) = F(i)$, is 2:1 if n=2, or more generally a ratio of m:n defines quasiperiodicity of m patterns within n cycles. The period becomes longer as $m \rightarrow \infty$ and $n \rightarrow \infty$, and the sequence begins to appear random, although it is not. In the infinite limit, the dynamics become chaotic [338], which by definition is complex dynamics that are deterministic and aperiodic [20]. Bifurcation analysis is the study of the changes in dynamics as parameters in μ are changed. Of particular importance are changes in fixed points $F(X, \mu) = 0$ and their stability.

The restitution curve of action potential duration during regular periodic stimulation is a return map $APD_{i+1} = f(APD_i)$ defining iterations of APD, which can be constant, periodic, quasiperiodic, or chaotic depending on the slope m [529]. Figure 4.15 shows the APD of a solitary isolated CML element paced at various cycle lengths. As CL is shortened, APD shortens gradually at first, then abruptly bifurcates into a 2:1 pattern. Successive bifurcations occur at the shortest CL's, revealing a few windows of chaotic action potential sequences where the entropy is high. This generic pattern of bifurcations in a return map paced at various rates was analysed in the logistic equation [162], and has been observed in paced cardiomyocytes [78, 215], paced ventricles [444], and cardiac action potential models [70, 214].

Relatively flat restitution, with plateau $APD_m = 48$ and intercept $APD_o = 42$, yields a simple bifurcation pattern, with all Lyapunov exponents negative and no chaotic windows. Steep restitution gives rise to several chaotic windows at the shortest cycle lengths. These coincide with positive Lyapunov exponents and increased entropy. The plots at right show the relationship between APD_{i+1} and the previous APD_i. Bifurcations cause dots to widen away from the diagonal. Results do not change significantly with simulations carried out in both one- and two-dimensional media. Figure 4.17 shows a composite of many simulations of a single paced cell. Shades of grey represent the largest APD when there are several APD's in the pattern. Each pixel row is a frame of APD = f(BCL), like those in Figure 4.16. The large fingers represent regions where $APD < 20$, and the left border of each finger is the bifurcation point where there is an abrupt transition to 2:1 periodicity. Faster pacing rates produce chaotic dynamics. Of particular importance is the sensitivity to small changes in BCL or APD_o in this region, showing that even very small differences in substrate between neighbouring subregions can give rise to local block initiating reentry.

What are the stable states of the heart and how do we define them? Quiescence is the simplest state, essentially a ground state where all $X(i) = 0$, fixed at the origin of the state space. This is the only known stable fixed point. Sinus rhythm is driven by a limit cycle oscillator at the sinus node. If we disregard systems driven by the sinus node or other supraventricular foci, then the only other sources that can initiate ventricular activity are

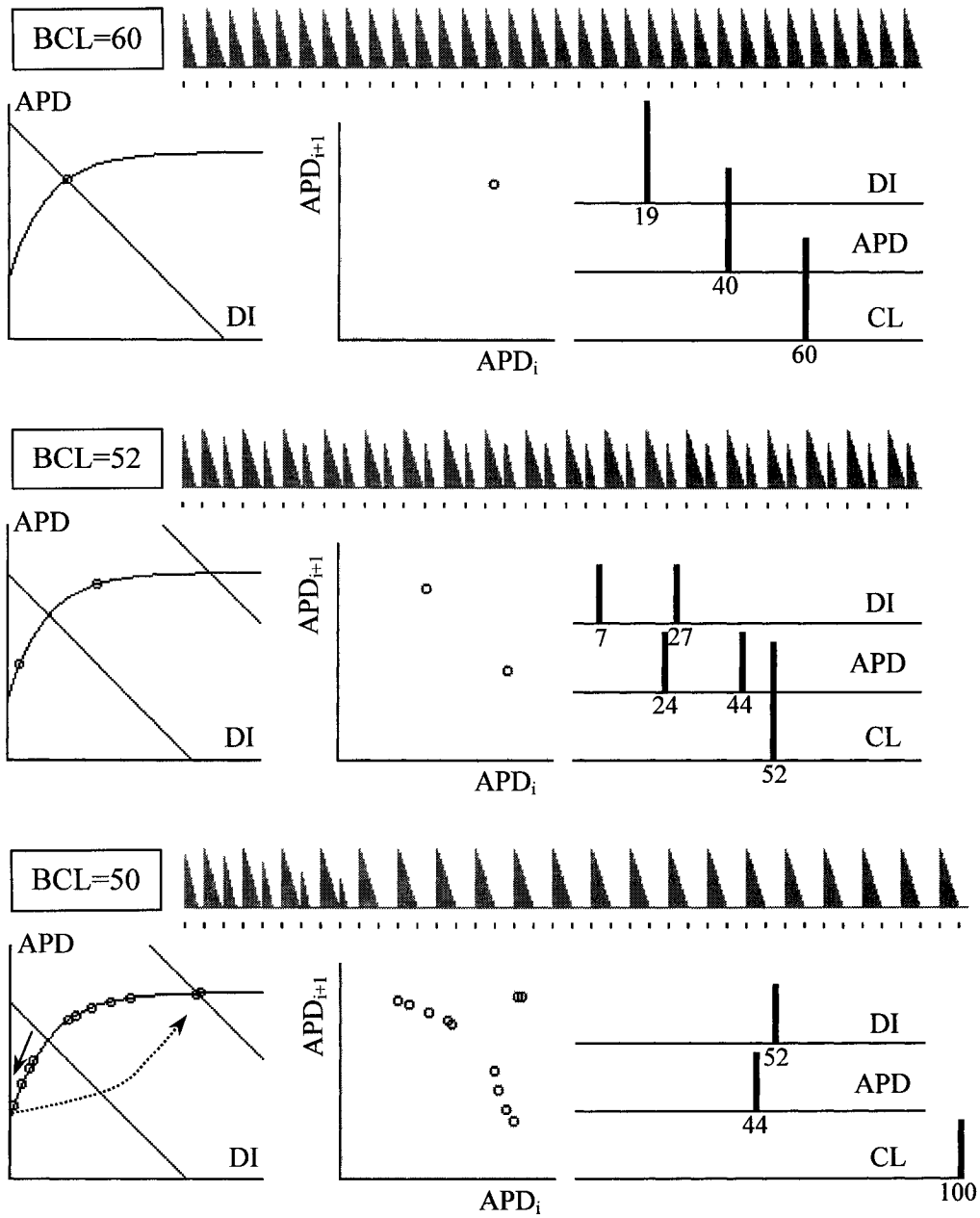

Figure 4.15. Single cell paced at a constant BCL = 60 (top). All action potentials fire with 1:1 response, since the intersection of the restitution curve and the negative unity slope line intersect where m < 1, and this point is stable to perturbation. At faster pacing, with BCL = 52 (middle), the intersection slope is m > 1, and a stable 2:2 response pattern develops with alternans between two APD. When BCL = 50 (bottom), the DI fall on a steeper slope where the intersection point is now unstable, and each successive APD is pushed away. Eventually, the shortest DI hits zero and the next action potential blocks, resulting in a 2:1 pattern developing where every second AP blocks, and the response period is BCL x 2.

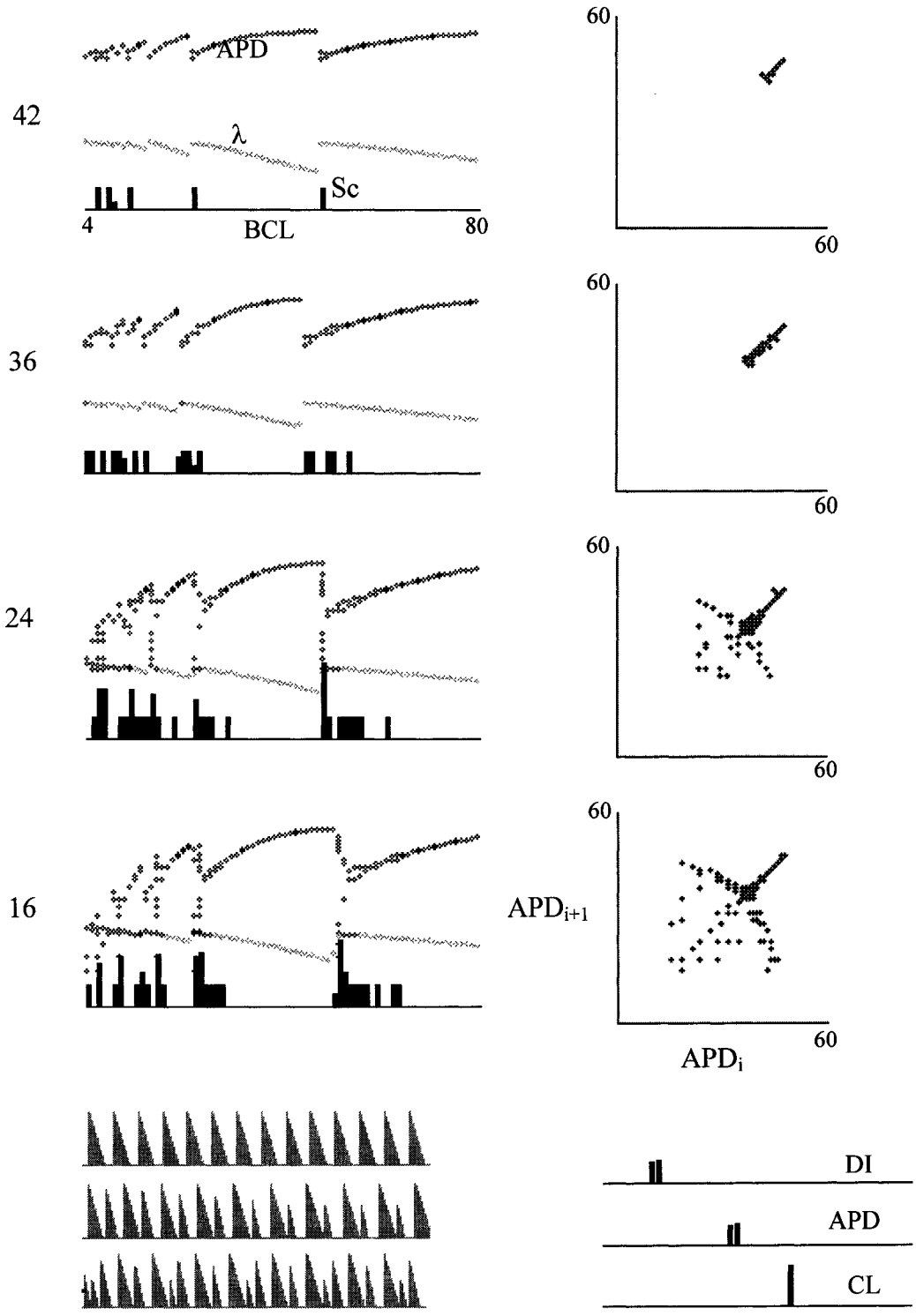

Figure 4.16. Single cell paced at regular cycle lengths CL_i. The restitution curve intercept APD_o is different for each of the four cases shown. Relatively flat restitution (top) produces windows of 2:1 APD alternans, while the steepest restitution (bottom) gives windows of chaotic dynamics. Lyapunov exponents and entropy are shown for each CL.

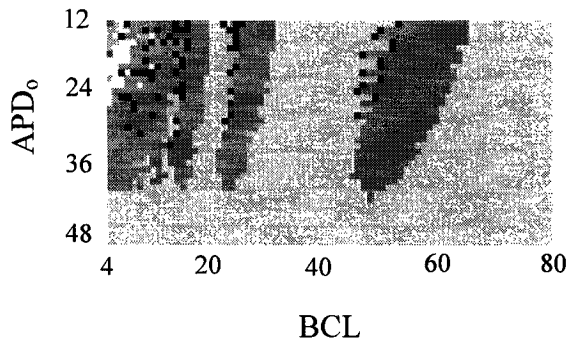

Figure 4.17. Composite diagram of maximum APD at different paced basic cycle lengths (BCL) and restitution, defined by APD_o for fixed $APD_m = 48$. Each pixel represents a separate simulation. Each pixel row is a bifurcation plot like those in Figure 4.15. Maximum APD is shown as light grey for the largest values APD > 40, darker grey for lower APD < 40. Black pixels represent the chaotic windows. Note that at the shortest BCL, very small changes in APD_o can give very different dynamics, owing to the complexity of this region containing embedded zones of quasiperiodicity and chaos.

ectopic pacemakers, driven by automaticity, afterdepolarizations, or reentrant circuits. If activity is regular and periodic, the state follows a limit cycle through a very high dimensional state space. A limit cycle can be stable or unstable, depending on whether or not it recovers its original trajectory after being subject to small perturbations. A single reentrant circuit or multiple circuits are both limit cycles. If the frequencies of multiple circuits are all equal, and all action potentials are regular of equal APD, then the cycle in the state space is a simple closed loop. If frequencies vary, the path might follow alternate loops.

It is noteworthy that since each axis of the state space represents an independent variable, it is the trajectory of the state vector representing the entire system at any given time that contains information about the spatial structure. For a cell paced at a constant BCL, the steady state DI and APD can be calculated as the intersection point of the restitution curve APD = f(DI) with the negative unity slope line representing pacing. Given BCL, the two equations are solved for DI and APD.

$$APD = APD_0 + (APD_m - APD_0)(1 - e^{-DI/\tau}) \quad (4.10)$$

$$BCL = APD + DI + R \quad (4.11)$$

It is useful to express this relationship in terms of the critical BCL for which the restitution slope is exactly one. This is shown in Figure 4.18. For any given APD_0, the upper curve is the BCL at which m = 1. Any BCL longer than this will give a stable train of constant uniform APD. Below this line, the APD can be nonuniform and be quasiperiodic. The bottom line is the lower bound on BCL, since we must have BCL ≥ APD + R, otherwise there would be no diastolic interval. Most importantly, the stability of APD at constant BCL pacing depends on the local slope m of the restitution curve in this region. If m < 1 then the point is stable, and all APD will settle to a fixed value. If m > 1, a small perturbation of APD or DI will cause oscillatory divergence of APD until block occurs.

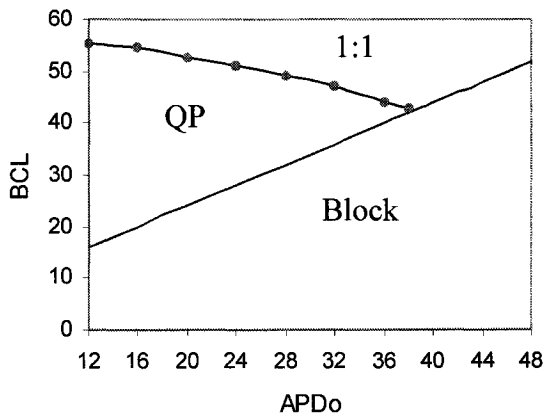

Figure 4.18. The role of BCL in determining action block. For a given restitution intercept APD_0, slow pacing above the curve gives uniform APD with 1:1 response. Below the curve, the restitution slope m < 1, and quasiperiodicity (QP) in APD with an n:m pattern of response becomes possible. The minimum BCL is the bottom line where BCL = APD + R, and DI = 0. The stimulus blocks below this line.

Figure 4.19 shows examples involving two solitary cells with $APD_m = 48$ and $APD_o = 24$ that are paced. The critical BCL is 51 for these specific parameters. In the first case shown at the top of the page, the two cells are paced at a subcritical rate of BCL = 54. The second cell is given a small perturbation by assigning it an initial APD smaller than that of the first cell by two units. In this stable regime, all APD converge to about 38. The bars at the top are the difference $\delta = |APD_1 - APD_2|$ due to the perturbation, which dissipates and directly demonstrates the negative Lyapunov exponent. The second case at the bottom of the page shows the identical conditions, but the pacing interval is now supracritical at BCL = 48. Note that the top cell has a fairly constant APD, since it is started close the equilibrium APD, but the perturbed cell below develops an oscillation. Finally APD exceeds BCL – R and the stimulus blocks. The difference δ in APD grows exponentially, demonstrating the positive Lyapunov exponent at this shorter BCL. These cases of single cell dynamics illustrate the fundamental mechanism of APD instability that leads to wave block during propagation.

A final important issue in these dynamics pertains to irreversibility and loss of information during system evolution. Once a cell fires in a CA or CML model, its future becomes determined and completely predictable: it will count down to zero for exactly APD time steps, at which point it will predictably switch to Y = 0. Once at rest, the refractory time Y is also predictable: it will count up by one each time step until it encounters a logical condition causing it to fire. Departures from predictability occur only when a logic rule is invoked that is not simply incrementing by one, but instead involves some sort of decision or divergent branching. Since this occurs in the CML model only at the state transition from rest to firing, new information enters the system only at the time of cell firing. Novelty enters only at the wave front, and the increase in information should be related to the amount of the wave front that passes through the region of the restitution curve where the slope $m > 1$.

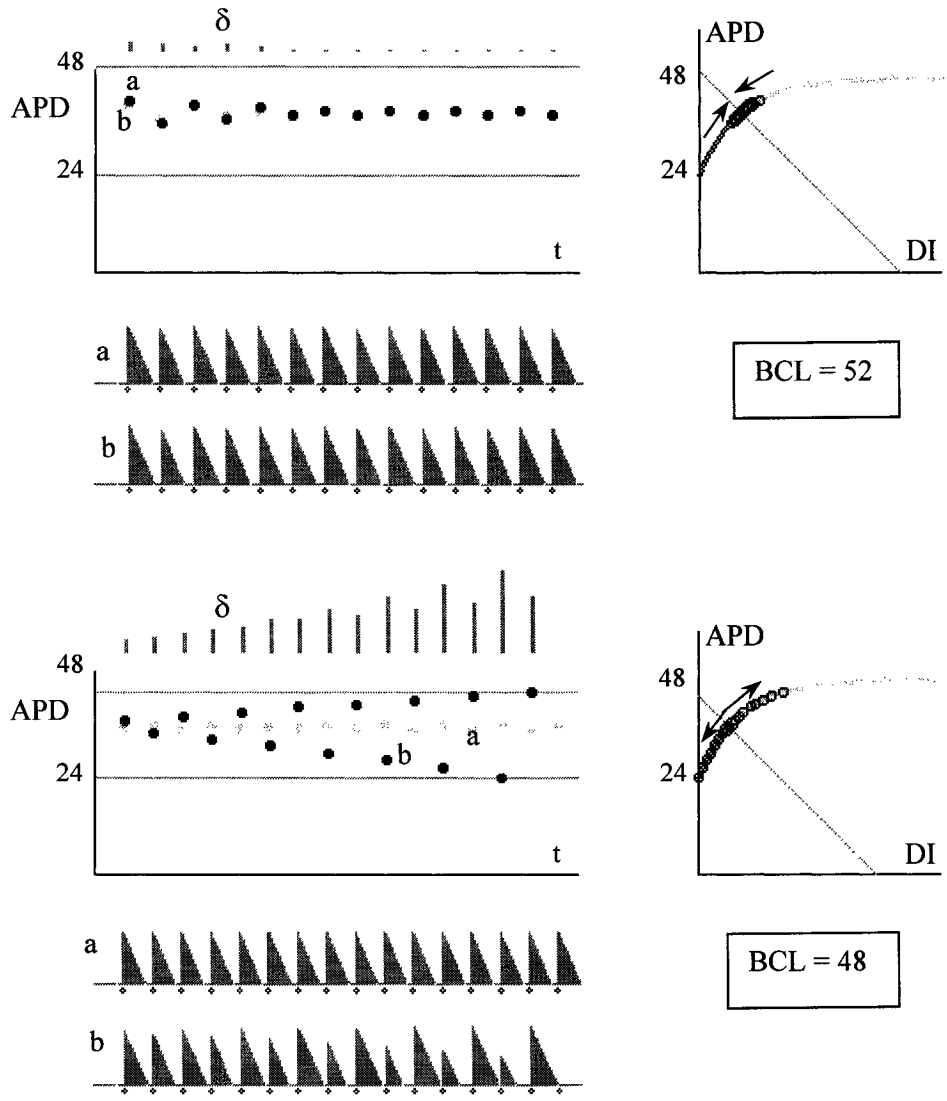

Figure 4.19. Single cells paced at constant BCL = 54 (top) and BCL = 48 (bottom). For both $APD_m = 48$ and $APD_o = 24$. Slow pacing at top gives 1:1 response. Faster pacing at bottom case blocks. The dots represent the APD of two separate paced cells having a very small time delay of 2 units between them. The slope $m < 1$ keeps the restitution intersection point stable, and the difference dissipates. The separation δ decays, directly demonstrating the negative Lyapunov exponent. The separation δ, in the lower case, grows due to the positive Lyapunov exponent. Block would lead to wave break according to Figure 3.13.

Clearly the temporal behaviour of fibrillation in terms of DI, APD, and CL distributions can be quite complex. All measures of complexity increase at steeper restitution. The next chapter will focus on spatial patterns of fibrillation waves and core points, and examine quantitative measures of spatial complexity.

Chapter 5

PATTERNS OF FIBRILLATION

5.1 Spatial Complexity

The need to measure and quantify spatial distribution and geometrical patterns arises in many branches of science [107]. Point processes are those that relate to patterns of regular or irregular points, such as condensation nuclei, pores in amorphous media, or the distribution of galaxies in space. Fibre processes are those that relate to lines or curves, such as dislocations in crystals, cracks in rocks, or domain boundaries. The fields of spatial statistics, stochastic geometry, and fractal geometry have been developed to quantify the characteristics of irregular and random sets [475]. Simple metrics for quantifying point processes include the intensity or density, equal to the number of points per unit volume, and the pair correlation which quantifies similarity over various distances. A completely random set of points in space has a density with a Poisson distribution [527]. These, as well as more recently developed metrics like the Minkowski functional, have been applied to quantifying Turing patterns in reaction-diffusion media [345].

Since any point on the body surface ECG is essentially determined by the spatial pattern of intracardiac electrical activity, we need quantitative measures of the spatial distribution of cardiac sources. Specific measures should relate to the spatial distribution, including

central tendency and uniformity or clustering of reentrant circuit core points. This chapter will focus on methods to quantify the spatial distribution of waves and core points during fibrillation, and will examine the effect on these patterns of changing APD restitution properties. Specifically, we will develop quantitative measures of spatial complexity that represent the distribution of reentrant circuits by the locations of their core points within a two-dimensional tissue domain. This will allow the spatial order and disorder of the core pattern to be followed during wave evolution. Ultimately, we are interested in developing metrics that can correlate spatiotemporal dynamical patterns of wave activity in the myocardium to the corresponding ECG patterns measurable on the body surface.

Core point distribution should be static or periodic when close to an equilibrium state, and dynamic or chaotic when far from equilibrium, where the system wanders through its state space transiently visiting local attractors, while its trajectories are mixed or reinjected by proximity to saddle points. Figure 4.1 demonstrated several examples of spatial patterns during fibrillation, and the role that APD_m and APD_o play in their determination. Clearly, a single number with one degree of freedom cannot uniquely represent a complex spatial pattern having many degrees of freedom. Any useful spatial metric must be defined such that it classifies a large number of higher information patterns having some common feature. This is the essence of descriptive statistics.

How does one begin to quantify spatial patterns? Considering the simplest example of a binary string, one measure of complexity would be the number of discontinuities N_D between neighbouring bits. A bi-partitioned domain "..111000.." has the minimum $N_D = 1$, while the opposite extreme case with an alternating pattern "..010101.." has the maximum number of discontinuities $N_D = N/2$, and the smallest characteristic length of one unit. Both of these patterns have obvious order or sequence predictability. In a random string, like the one-dimensional binary Boltzmann gas previously discussed, N_D grows from its initial value to a mean value lying between the extremes of the two cases defined above. N_D is a rough measure of the degree of order, but is not particularly useful because it says nothing about the actual pattern, and is not maximum for random disorder which must contain the greatest information.

Alternative order metrics could be chosen, relating to the distribution histogram of cluster sizes of bit neighbourhoods having a common value. For example, the alternating pattern "..010101.." has a spike histogram at 1 unit because that is the size of each bit cluster, while "..00110011.." has a spike at 2 units, "..100100.." has spikes at 1 and 2, and so on. The bi-partitioned field described earlier has a single histogram spike at a cluster size of N/2. A completely random field contains many cluster sizes L, and therefore would have a broad histogram approximating a power law $N = a L^{-\beta}$, resulting in a fractal distribution where there is no characteristic length scale. In a random field, small clusters are common while large clusters are rare, analogous to Zipf's law of word size distribution in text [334]. The information entropy calculated from these probability distributions would reflect the degree of pattern predictability in the respective bit strings. Entropy would be zero for all the regular patterns having solitary spike histograms, and would be maximum for the random pattern.

In principle, these concepts of measurement can be extrapolated and applied to the CML model of excitable tissue by developing more sophisticated numerical algorithms for pattern quantification based on discontinuities and domain sizes. The binary string might represent the state diagram of a piece of excitable tissue, where resting and firing action potentials hold states of zero and one respectively, and the two-dimensional field of cells is mapped onto a one-dimensional string. More generally, one could have multiple states within each action potential, rather than binary states, although, as described earlier, the number of combinations within the domain strings would be extremely large. In two dimensions, there is greater difficulty defining both the distribution of discontinuities, since they are irregular curves, and the distribution of cluster sizes which can be highly irregular patches. The temporal patterns of cardiac activity are also highly dynamic, being periodic, quasiperiodic, or chaotic.

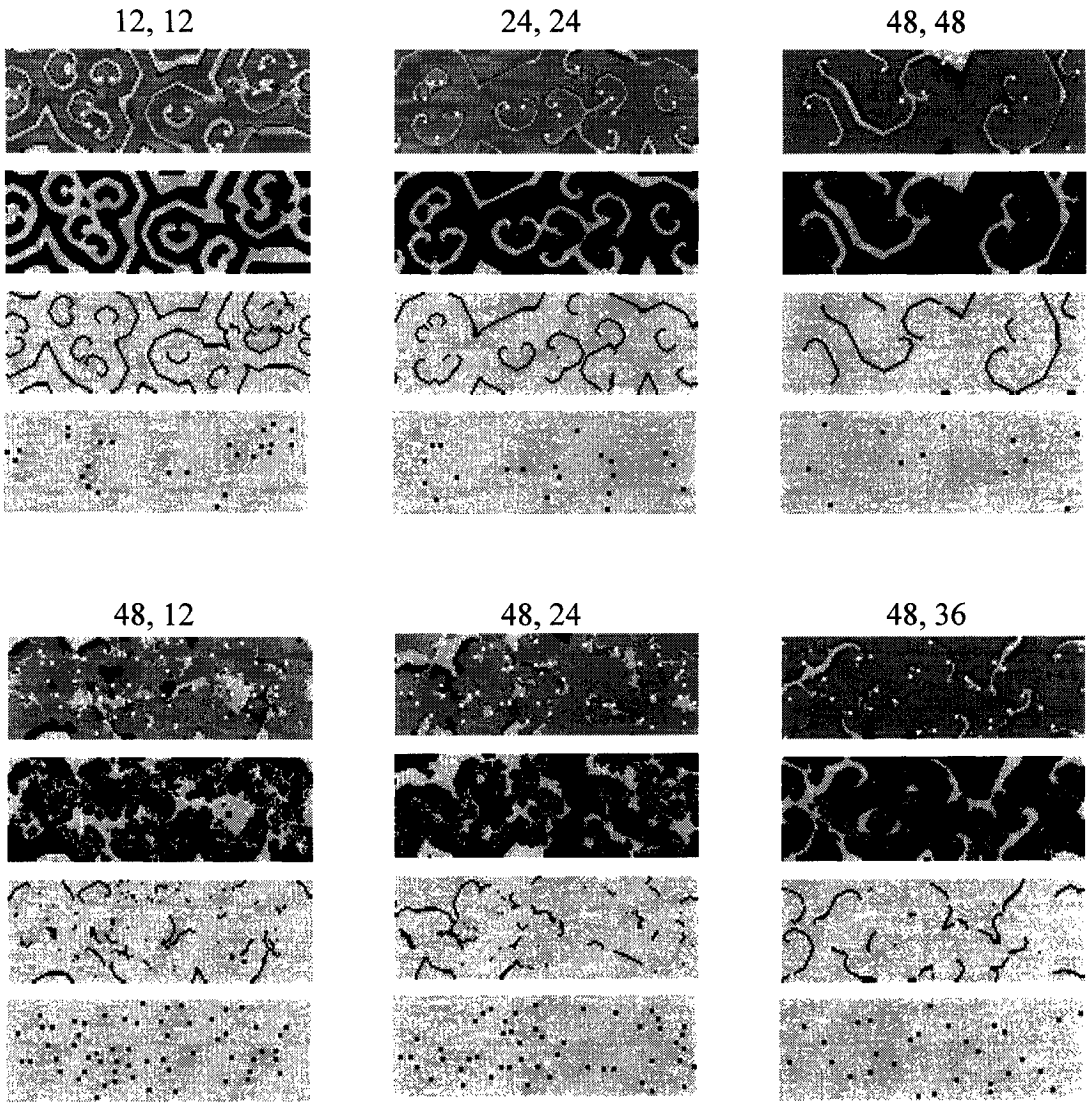

Figure 5.1. Fibrillation wave patterns V_{ij} in the top row are transformed into lower dimensional representations for spatial analysis. The second row is a binary map where black bits are the action potentials $V_{ij} > 0$. The third row shows only the wave front $V_{ij} = V_{max}$. The bottom row shows the reentrant circuit core points with the waves removed. Numbers above each frame are APD_m and APD_o.

Figure 5.1 shows frames of fibrillation converted into simplified forms that can be used to quantify pattern complexity. In the first case shown, the action potentials are converted into binary states: 0 if $X_{ij} = 0$, and 1 if $X_{ij} > 0$. The direction of propagation or rotational sense is lost in this transformation. A second possibility is to retain only the line of the wave front by giving it a value of one, while all other bits are zero. The resultant field appears greatly simplified, but actually little information about the wave pattern is lost. The total volume of the wave front is proportional to the energy dissipation, as described in the previous chapter. Another option is to discard the waves altogether, and retain only the core positions, which represent a vortex field. The simplest such case would be a solitary wave having one core point. This particular pattern is invariant to translation and rotation, although one could further define the rotational sense by −1 or +1, and arrive at a representation similar to that of the frozen Ising model of ferromagnetism [341]. Patterns arising from multiple core points also need to be defined. We will return to this issue later in defining pattern entropy based on the spectrum of core separation distances.

5.2 Correlation

The correlation length and time are the intervals in space and time over which a subsystem can be considered essentially independent of other subsystems. The correlation time gives an estimate of the time interval over which the initial condition still influences evolution. If many length scales are involved, one could quantify the spatial pattern based on an assumed power law occupancy of boxes versus box size over several length scales, the exponent being the Hausdorff dimension [160, 334]. This metric performs best if there is some degree of self-similarity over several orders of magnitude, as with fractal sets or even random spacing, but is less useful for the relatively sparse densities of cores that are typically encountered in fibrillation simulations. Likewise, the correlation dimension is another commonly used parameter, but suffers the same lack of utility if there is not a wide range of length scales within the spatial pattern [334].

The spatial correlation might be a more useful metric, being the spatial analogy of the time-delay autocorrelation [449]. It measures the degree of similarity of points separated

by given distances, and is evaluated by taking the product of some activation function Z(X) at two points corresponding to X(i) and X(i+r), separated by a distance r, and summing all such products over the spatial domain:

$$\Gamma(r) = \frac{1}{N} \sum_{i}^{N} Z(i)\, Z(i+r). \qquad (5.1)$$

The activation function Z(i) can be defined in various ways. The simplest choice is the normalized voltage $Z(i) = V(i)/V_m - 1$, since the mean of Z(i) must be zero. N is the total number of pairs summed for a given separation r. By definition, $\Gamma(r) = 1$ for $r = 0$, since each point has perfect correlation with itself, while $\Gamma(r)$ generally decreases with distance and approaches zero for widely separated points. Random activity has $\Gamma(r)$ dropping rapidly from one to zero at $r = 1$. A periodic plane wave has periodic $\Gamma(r)$ of wavelength r. Correlation is often used in statistical physics to quantify phase transitions and critical phenomena [300] in spatially-extended media, and has been applied in fibrillation mapping studies [30, 438].

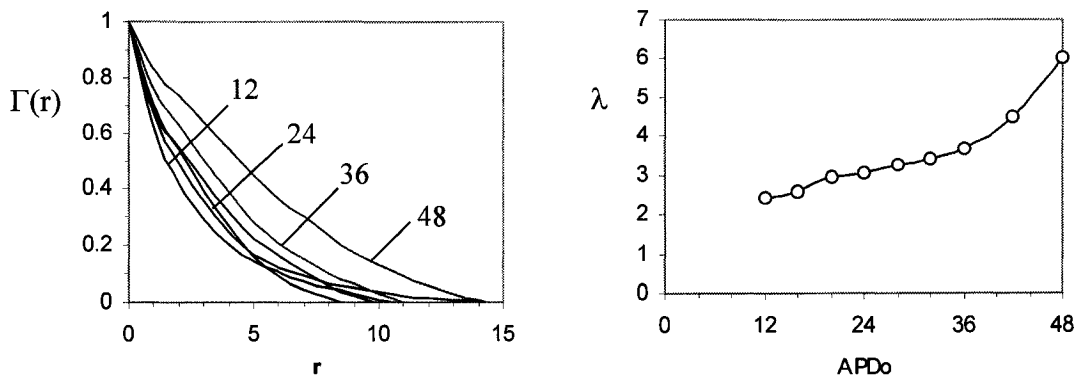

Figure 5.2. Spatial correlation spectra $\Gamma(r)$ are shown for various static spatial patterns of voltage V_{ij} averaged over 100 time units (left). The correlation length λ is the space constant for the best fit exponential curve (right), and increases with APD_o as expected. This reflects an increased wave size. $APD_m = 48$ for these cases.

Figure 5.2 shows the correlation spectra $\Gamma(r)$ for various APD_o. The correlation length can be defined as the point of zero crossing L_o, or as the space constant of exponential decay λ [30]. The correlation spectrum for a spatially regular spiral wave has a second peak corresponding to the wavelength when correlation is measured orthogonal to the wave. This peak does not appear in any of these fibrillation simulations because there are multiple waves oriented in many directions, whose contributions to the summation tend to cancel. While correlation can be calculated from a static pattern at any point in time, a mean value must be taken over some time interval to eliminate oscillations of action potential duration during spiral wave behaviour over short intervals. Calculated correlation lengths λ in Figure 5.2 range from 2.4 to 6.0, and increase with longer APD as expected. On the prior assumption that each spatial unit equals 1.5 mm, these λ values correspond to 3.6 to 9 mm respectively, similar to those measured experimentally [30]. This suggests that the CML model elements are of sufficient resolution to capture the characteristic details of fibrillation. The relative constancy of λ over the lower range of APD_o, can be explained by the fact that point pairs sampled along a highly fractionated wave front span a large distance r from zero upward, and prevent a specific wavelength between fronts from being discerned. For example, if two sampling points happen lie transversely along the same wave, the correlation will always be close to one regardless of the wavelength. The correlation length does not appear to be highly specific to APD_o in our model, and has very limited utility for larger scale pattern quantification due to considerable variability over time, relative insensitivity to small changes with APD_o, and disappointing ability to distinctly classify dynamics.

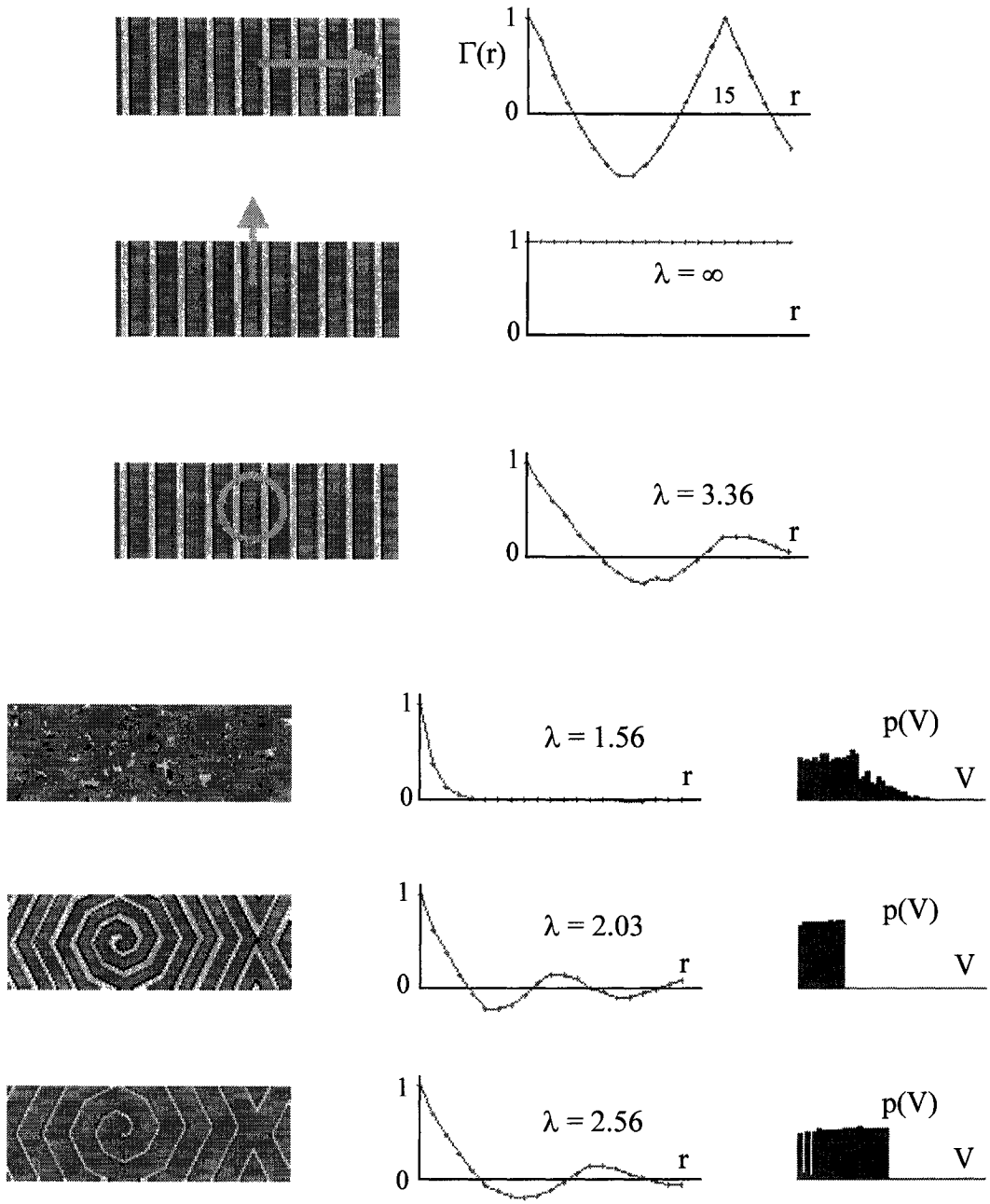

Figure 5.3 Spatial correlation spectra Γ(r) of a set of plane waves is periodic perpendicular to the wave fronts, and unity parallel to the wave front, if measured along a one-dimensional line (top). The two-dimensional correlation is based on distance from the reference point, shown in the third frame for one particular radius r. Correlation of complex or near-random patterns decays rapidly with distance, while spiral waves decay with oscillation due to wave periodicity. The histograms of field magnitude V_{ij} are shown at right, and tend to be flat for constant APD where all V are equally represented.

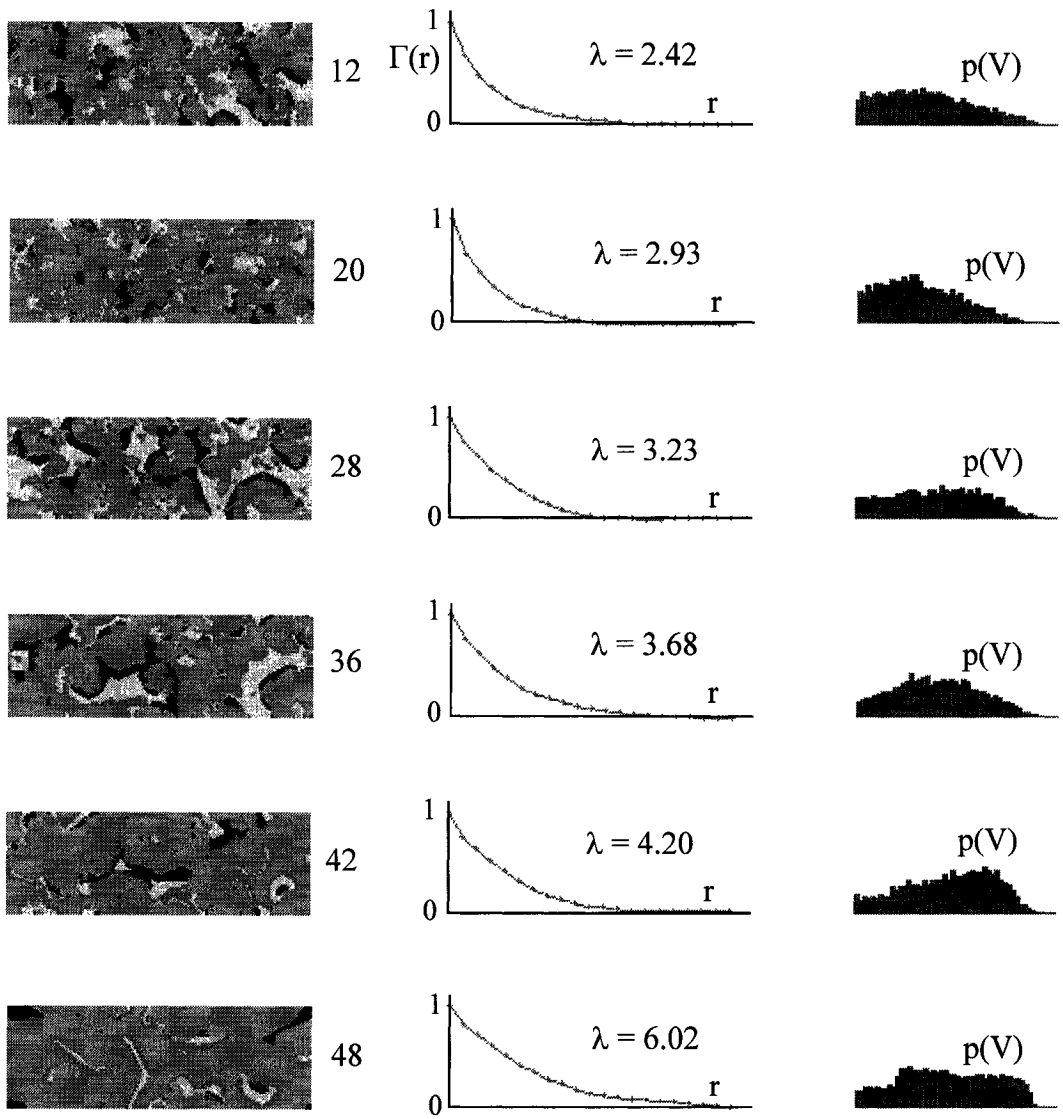

Figure 5.4. Spatial correlation Γ(r) for various patterns of fibrillation with $APD_m = 48$ and restitution controlled by APD_o, as indicated by the number to the right of the frame. Steeper restitution yields finer spatial structure as expected, and results in a shorter correlation length λ. Histograms p(V) of field magnitude V_{ij} are shown at right for each spatial pattern, and show a rough tendency to skew to higher V at longer APD_o.

5.3 Centroid

The simplest metrics of spatial distribution of points are the location of the centroid and the radius of gyration. The cores can be considered to be like point masses attached to the heart surface, and the centroid or centre of mass can be calculated as shown in Figure 5.5, and projected back onto the cylinder surface. The magnitude of the central tendency of core points is related to the radius R_c. If the points are equally distributed around the domain, the centroid will be on the cylinder axis where $R_c = 0$, and there will be no central tendency. If the points are clustered into a small region, the centroid projects into the centre of the cluster, and the radius R_c approaches the cylinder radius R. R_c is the radius of gyration of the point mass distribution. The metric $\eta = R_c/R$ defines the degree of core point clustering, while (x_η, y_η) is the centroid projection on the cylinder surface. By following $\eta(t)$ and $N_c(t)$ over time, we can monitor variability of the core point pattern.

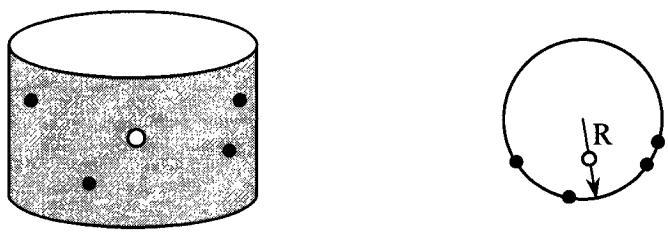

Figure 5.5. The spatial distribution of core points can be represented by its centroid. Cores are like point masses on the cylinder surface. The centre of mass is calculated in three-dimensional space as shown by the open circle at right, and projected back onto the surface to give its location on the heart shown by the white circle at left. The distance from the cylinder axis to the centroid is the radius of gyration R_C , which defines the degree of point clustering by the dimensionless ratio $\eta = R_C / R$.

5.4 Pattern Entropy

Spatial complexity can be defined by a spatial or pattern entropy S_G according the probability p(d) of core pairs having separation d at a particular moment in time [319]. A regular pattern on a periodic grid should approach $S_G = 0$, while a random pattern should

have high pattern entropy. This measure says nothing about the details of the spatial structure. Figure 5.6 shows two examples of pattern entropy according to this particular definition based on the probability distribution of the spacing between nearest neighbour pairs.

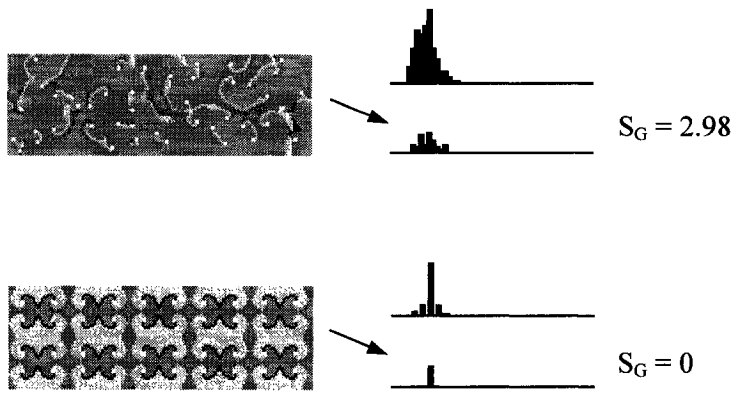

Figure 5.6. Pattern entropy S_G is based on the static spatial distribution of core points, as defined by the histogram of separations between nearest neighbours shown at right. The top histogram in each frame shows separations summed over a time interval, while the bottom histograms are a single point in time for the picture shown. The first case has a nearly random pattern of cores, which approximates a Poisson distribution p(d) between nearest neighbours. The second case shows reentrant circuits on a regular grid with a spike histogram. The smaller spikes next to the peak are due to core points drifting in small circles with each revolution. The regular grid has entropy $S_G = 0$.

Figure 5.7 shows several examples of fibrillation quantified by the core point distribution. The top frame in each set shows the fibrillation pattern V_{ij} and the middle frame shows the core point distribution. The centroid of the cores is indicated by a small circle. A Voronoi tesselation, shown at the bottom, is generated by starting at each core point and moving radially outward, like a crystal growth front away from a nucleus, until domain boundaries are established [327]. These tessellated subdomains are the regions within which each core point has its own spiral wave at that particular time. The spectra of nearest neighbour separation p(d) for each core point is used to calculate the pattern entropy S_G shown.

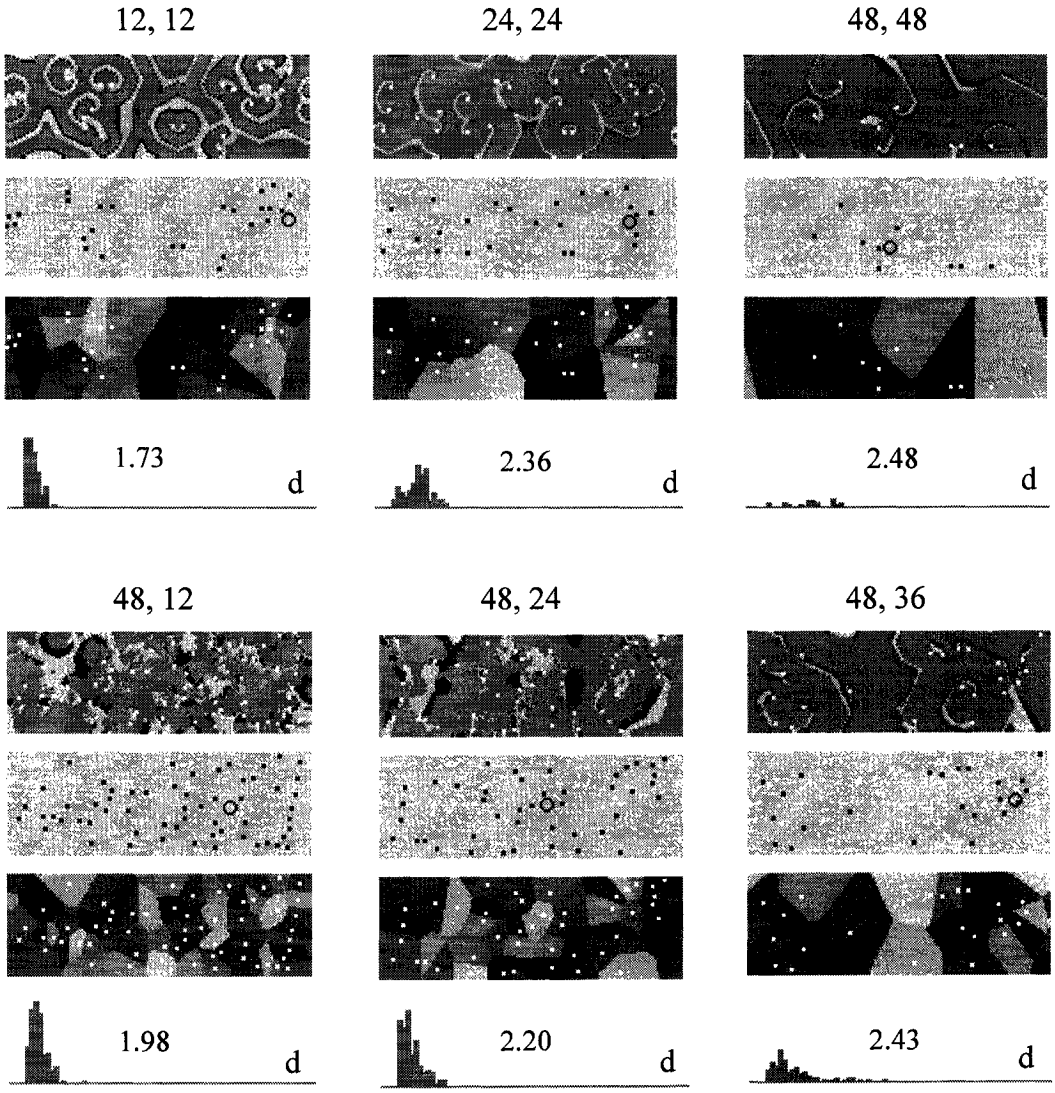

Figure 5.7. Fibrillation with constant APD (top), and with restitution (bottom). The core points for the reentrant circuits are highlighted in the action potential field Vij, and shown isolated in the second row. The centroid of the core point spatial distribution is shown as a small circle. The third row shows the Voronoi tesselation of the core point field, indicating the territory "owned" by each core point, within which each associated spiral wave operates. The histograms are of nearest neighbour separation, and are used to calculate the pattern entropy S_G indicated above each. Higher density of core points N_c forces shorter separation distance, and narrows the histogram lowering pattern entropy.

5.5 Characteristic Length

Dimensional analysis provides a natural measure of the characteristic length of wave activity, this being the area of firing cells divided by the wave front length. Expressed mathematically, $\gamma = \Sigma\ [H(X_i - V_m)]\ /\ \Sigma\ X_I$ where H(z) is the Heaviside operator that is zero for negative argument z and one for positive z. For a plane wave, γ equals the spatial wavelength, while for a radiating circular wave γ equals half the radius. There is a close inverse correspondence between γ and the rate of energy dissipation W_f in Figure 5.8, as both are dependent on the wave front volume. Energy is dissipated by firing cells most rapidly at small length scales, like dissipation in fluid turbulence. The rate of energy dissipation is calculated by Ohm's law in equation (4.2): $W_f = \Sigma\ |Vi - Vj\ |^2 / (2V_m^2\ NM)$, where the summation is over the four immediate neighbours j.

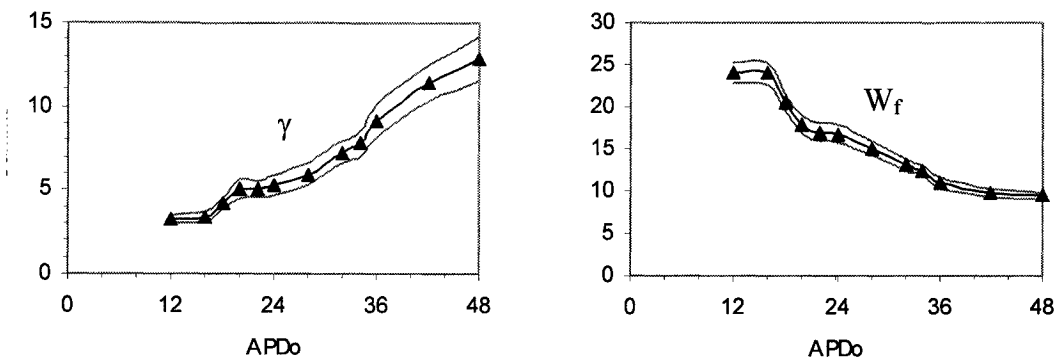

Figure 5.8. The characteristic length scale of fibrillation γ is shown (left) with mean and standard deviation for various restitution slopes APD_o with constant $APD_m = 48$. Higher APD_o results in a longer mean APD producing a larger spatial wave size. The rate of energy dissipation W_f of the action potentials (right) is related to the total area occupied by action potentials, and is roughly inversely related to the characteristic wave size. Energy is dissipated most rapidly in smaller waves which have a larger relative wave front surface to volume ratio.

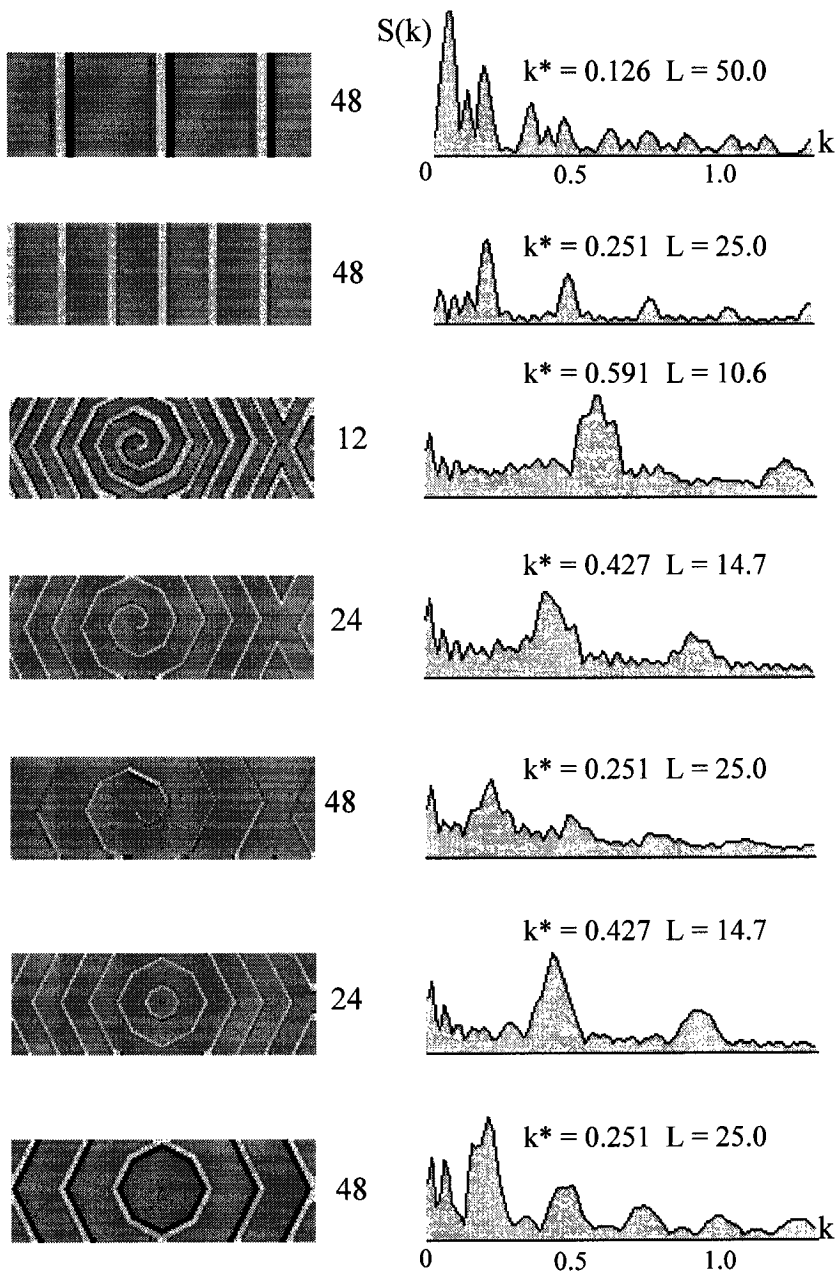

Figure 5.9. The wavenumber spectrum S(k) is calculated by Fourier transforming the single time frame of the wave field V_{ij}. Examples are shown for plane waves (top), spiral waves (middle), and ectopic foci (bottom) for each constant APD shown. The spectra are mean values calculated over one-dimensional longitudinal samples V_I, averaged over all slices j. The spectral peak at k* corresponds to the dominant characteristic reciprocal wave size $L = 2\pi/k^*$, with some additional contributions from higher harmonics, most evident in the plane waves.

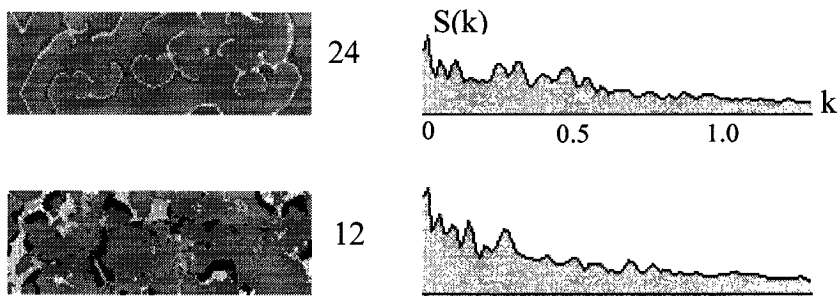

Figure 5.10. Wavenumber spectra S(k) for a solitary frame of fibrillation with APD = 24 (top), and APD_o = 24, APD_m = 48 (bottom). Due to the high variability of S(k) over time, mean values of the spectra averaged over many time steps fail to clearly discern a dominant characteristic length of fibrillation.

5.6 Wavenumber Spectra

The wavenumber spectrum S(k) is the spatial analogue of the frequency spectrum, and is obtained by Fourier transforming the spatial pattern V_{ij}. For any wavenumber k, the effective wavelength is $L = 2\pi/k$. Examples are shown in Figures 5.9 and 5.10, where the spectra are calculated along the long axis of the domain V_i, i = 1..N, and averaged over all j. The first frame shows three waves with APD = 48 traversing the cylinder. A peak is seen at k = 0.126, corresponding to the wavelength L = 50. Higher harmonics are evident. The three spirals show peaks at respective wavenumbers that decrease with APD, and determine the characteristic wavelength. It is especially noteworthy that the two radiating ectopic patterns have spectra S(k) that are virtually indistinguishable from those of the spiral waves with the same APD.

The fibrillation patterns shown in Figure 5.10 have highly variable spectra which change rapidly over time. The organized fibrillation pattern with APD = 24 has what appears to be a rough peak, but the more complex pattern with APD_m = 48 and APD_o = 12 is much more irregular with many peaks. A purely random pattern should have a wavenumber spectrum that approaches an inverse power law $S(k) \propto 1/k$, analogous to the 1/f distribution of Brownian noise [448].

5.7 Routes to Fibrillation

Fibrillation can be established in the model by two opposite routes previously discussed: a single wave breaking into many waves, or a randomly disordered initial condition self-organizing or condensing. For the purpose of illustration, the standard fixed parameter set will be retained for the 150x50 cylinder domain: APD_m= 48, R = 4, and τ = 10. Restitution is manipulated by lowering the intercept APD_o, which is considered a control variable. The case of APD_m = 48 and APD_o = 16 started from a spiral is shown in Figure 5.11. The spiral breaks progressively into fine fibrillation, since APD_o is less than the critical value of 32 determined an earlier chapter. In this simulation, there is a period of slow core point growth, some of which reattach and annihilate before rolling up, followed by a relative burst of core point growth once a few rotating centres become sustainable. Following break-up, there is a transient interval of convergence or re-organization. A few rare cases approaching spontaneous defibrillation were seen (not shown), particularly at the steepest restitution. As waves break, the surface-volume ratio increases as a finer structure evolves, while the cluster metric R_c approaches zero, indicating near-uniform spatial distribution of cores with no dominant clusters. Chaos becomes visually evident in the action potential train. The Lyapunov spectrum becomes clearly dominated by positive exponents shown in black, although a minority are negative shown in grey. The sum is most frequently positive for this case indicating potential expansion of nearby trajectories in the state space provided that small neighbouring disparities exist. The sum of the positive Lyapunov exponents shown in black gives a close approximation to the Kolmogorov entropy K which is the rate of increase of information [205]. Chaotic systems have $K > 0$.

Most simulations have a transient period that is very irregular prior to some dynamic steady state being reached, which may be quiescence, periodicity, quasiperiodicity, or seemingly random chaos. True randomness cannot exist in this model because all dynamics are purely deterministic. There are no stochastic or probabilistic variables in the model. Table 5.1 summarizes the metrics used to quantify spatiotemporal dynamics. These metrics can in principle be applied to three-dimensional heart simulations, but algorithm

development would obviously require greater effort, particularly because reentrant circuits in three dimensions are probably filaments that can twist and meander [165].

Figure 5.12 shows another case with the same parameters $APD_m = 48$ and $APD_o = 16$, however, started with a random initial condition. R_c stays close to zero as expected, indicating widely spread core points. Following some fluctuations during self-organization, all system variables settle to the same average values seen with the previous example, confirming that these two opposing routes to fibrillation lead to the same asymptotic behaviour. The dynamics become independent of the initial conditions, as all information from the past is eventually lost due to dominating positive Lyapunov exponents.

Entropy S_D of diastolic intervals is related to the width of the DI histogram. The DI distribution p(DI) must be considered an empirical outcome, since there is no theoretical means of predicting it without actual simulation. If most $DI < \tau$, the APD are largely determined by the steep-sloped segment of the restitution curve, whereas if much of p(DI) $> \tau$, the APD histogram becomes truncated for higher DI that map onto the flat part of the restitution curve, as shown earlier in Figure 4.13. In the former case, $S_D \cong S_C$, while for the latter case $S_D > S_C$. The histograms and entropies of APD and CL are directly related to the DI histogram mapped through the restitution curve, and are therefore not necessarily independent variables. The main point to be emphasized is that, once the restitution curve is fixed, the spatiotemporal DI distribution is the main determinant of the dynamics. Its histogram p(DI), or measures of it like S_D, embody important information about system behaviour that might be potentially useful. Unfortunately, there is no way to reliably extract p(DI) experimentally without great technical difficulty. It is particularly noteworthy that the DI histograms in simulations with steep restitution show wide "dispersion of refractoriness". This property is usually attributed to cellular or substrate heterogeneity [52, 217, 298], and is typically modelled with random variables [269]. In our case, however, all dynamics are purely deterministic. It is not necessary to invoke noise or stochastic variables to get this type of dispersion demonstrated in Figure 4.9 for different restitution slopes.

Table 5.1. Summary of Monitored Complexity Metrics

N_c = Number of core points or phase singularities of reentrant circuits.

η = Core point centroid radius R_c/R indicates cluster vs uniform-random spatial distribution. Varies from 0 (random) to 1 (clustered).

S_G = Instantaneous spatial entropy of core pattern of nearest 2 neighbour separation. 0 if $N_c \leq 2$ and grows with N_c, especially if spacing very nonuniform. Reaches high value at low N_c only if regular spacing.

S_D = Entropy of diastolic interval DI histogram p(DI).

S_C = Entropy of cycle length CL histogram. Indirectly embodies DI pattern (spatial core) and restitution.

S_M = Conditional entropy based on probability of a second cycle length being related to the first.

W_f = Energy dissipation. Sum of all voltage gradients squared. Indirectly related to the number of cells in firing state at any given time.

γ = Ratio of total number of firing cells in the domain divided by wave front size. This gives a characteristic length of wave like a volume-surface area ratio.

p(X) = Number of cells in each state range histogram. Shows total number of cells in action potentials and by subtraction also shows total surface area of excitable gap EG. Integration over sampling time interval gives Lyapunov number which is related to Lyapunov exponent.

p(DI) = Diastolic interval histogram

p(APD) = APD histogram, directly related to p(DI) through restitution curve.

p(CL) = CL histogram, determines S_C.

λ = Lyapunov spectrum and sum.

$\Gamma(r)$ = Correlation spectrum

λ = Correlation length

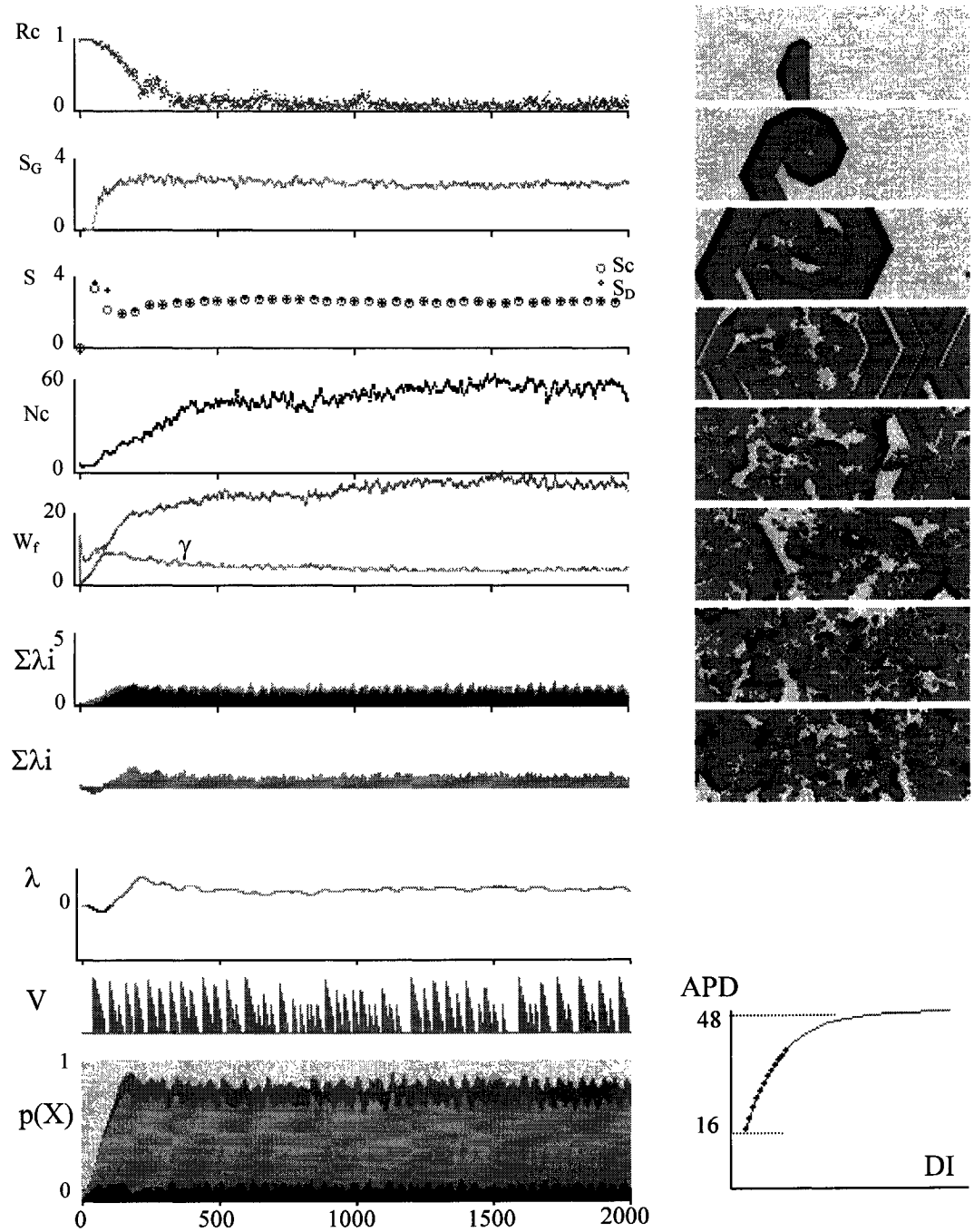

Figure 5.11. Simulation of spiral wave evolution and break down under APD_m=48, APD_o=16. Restitution curve is shown at the bottom right. Time period of 2000 units corresponds to 10 seconds of real time. Fine fibrillation develops, since the restitution curve is very steep. A plateau of approximately 60 reentrant-circuit core points is reached. The sum of positive Lyapunov exponents is shown in black over the grey negative sum.

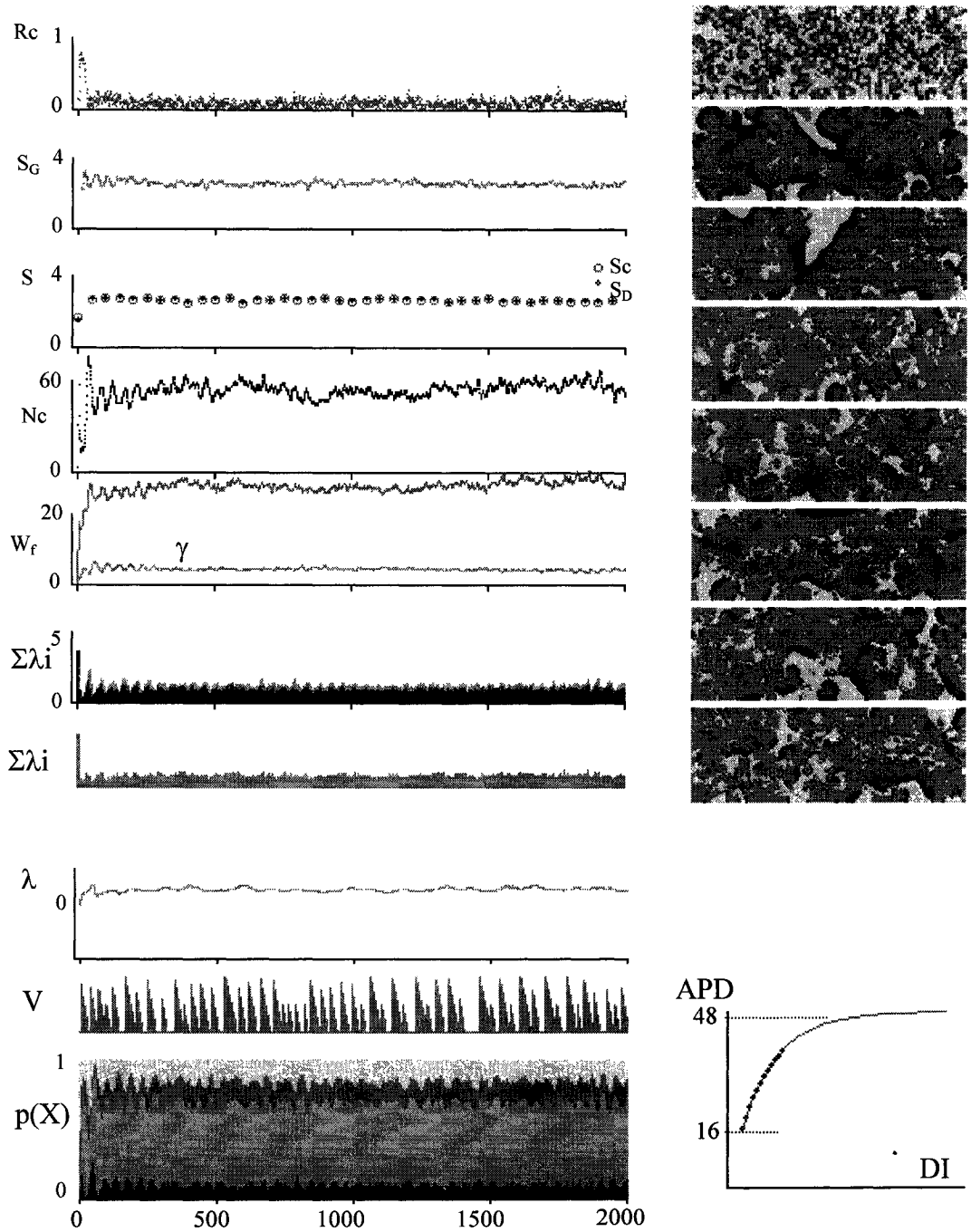

Figure 5.12. Same parameter set as previous example with APD_m=48, APD_o=16; however, initial condition is random and the system self-organizes into fibrillation. It is noteworthy that a statistical steady state is reached with the same measured values as the previous example, despite this case being started from an overly-complex initial condition. This case is like freezing, whereas the previous case was like melting. Both cases dissipate their transients and information through irreversible dynamics.

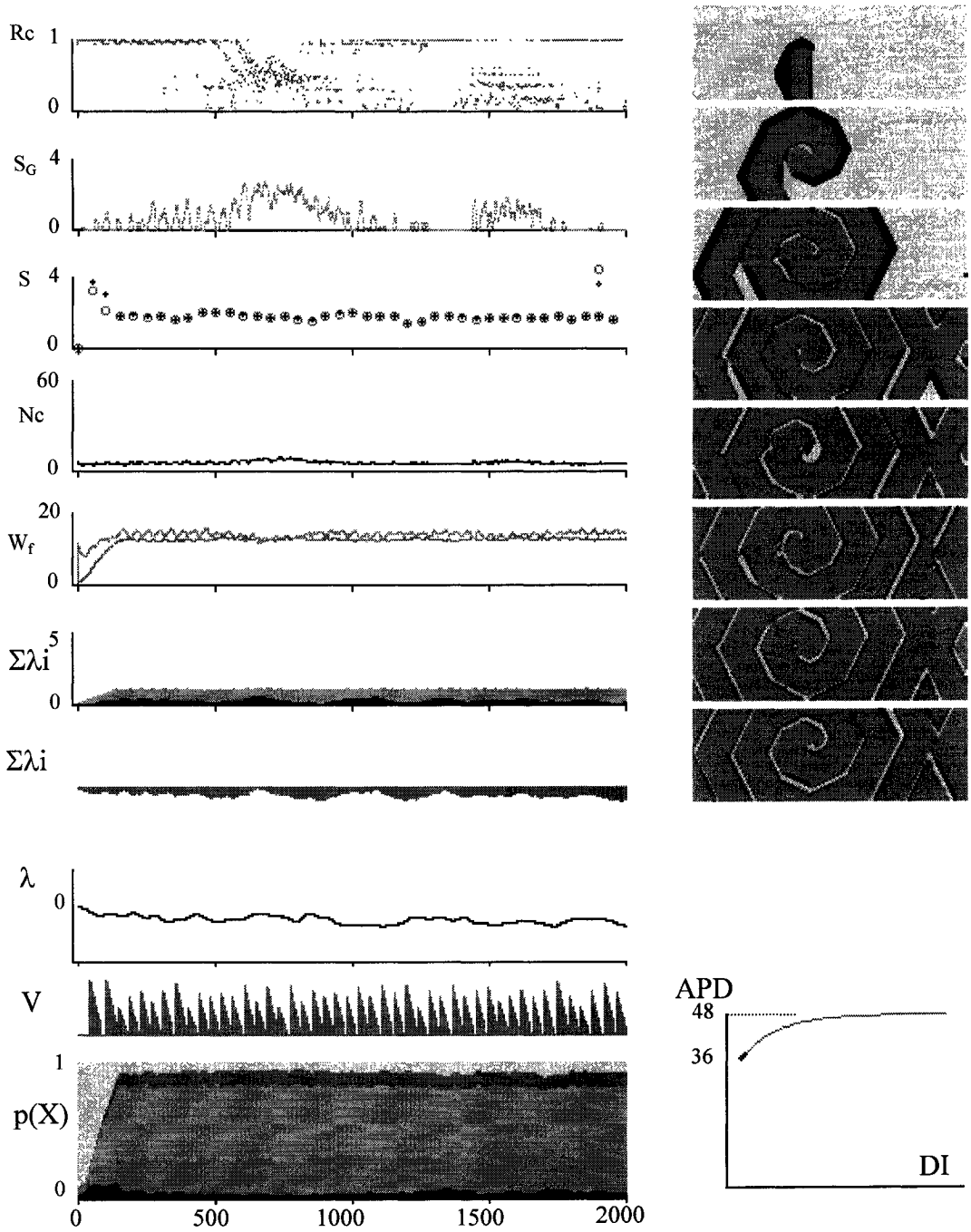

Figure 5.13. APD_m=48 and APD_o=36, yeilding a relatively shallow restitution curve started from a single spiral. The spiral remains stable and does not break, despite some irregularities that introduce noise into R_C and S_G. The dark spot on the restitution curve shows only a very small region with slope m >1, insufficient to give rise to any chaotic dynamics. The Lyapunov exponent λ remains negative throughout.

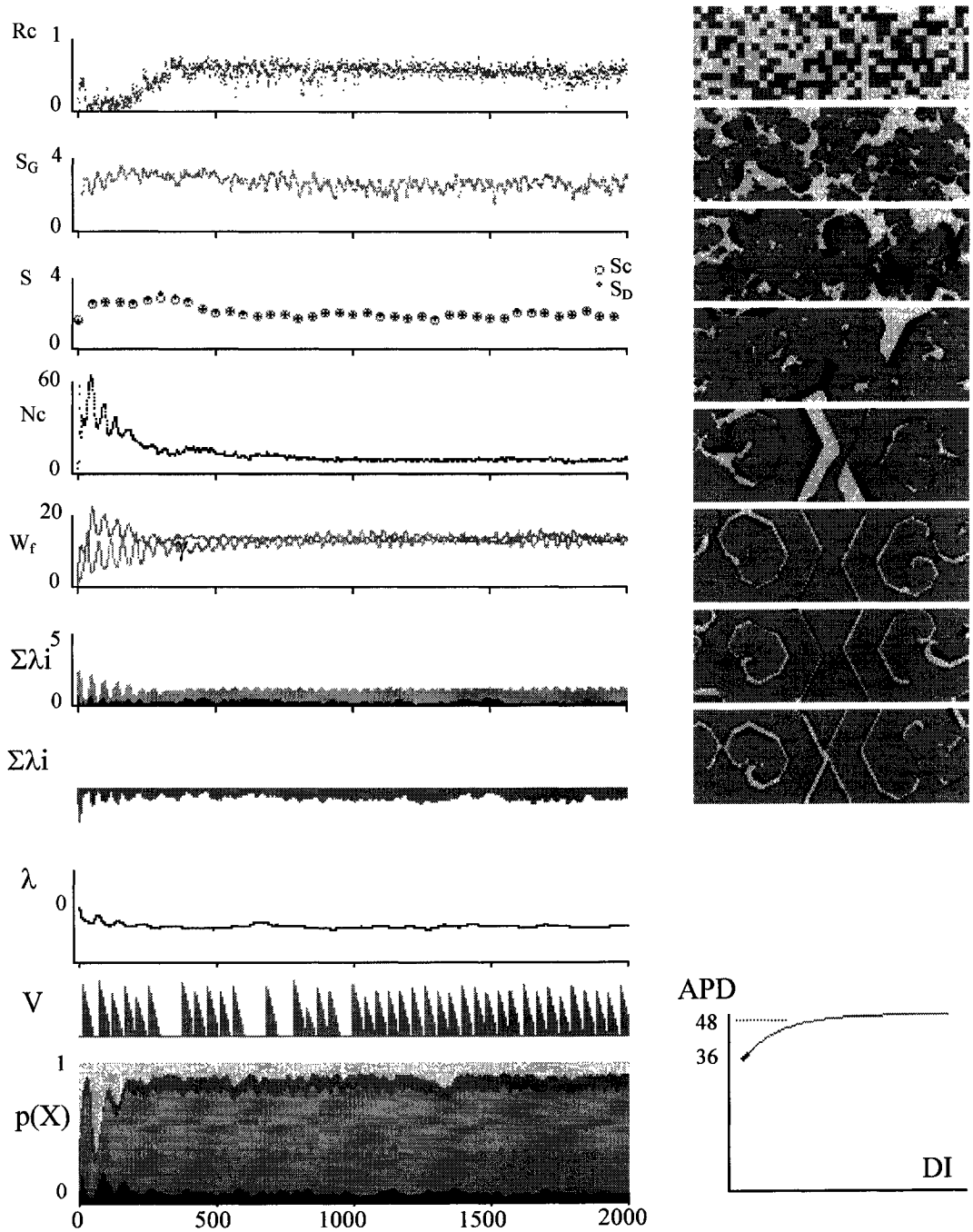

Figure 5.14. APD_m=48 and APD_o=36, started from a random initial condition. The pattern self-organizes into nine reentrant circuits with relatively large waves. The statistical parameters are essentially the same as those in the previous figure, except for R_C and S_G which depend on the number of core points.

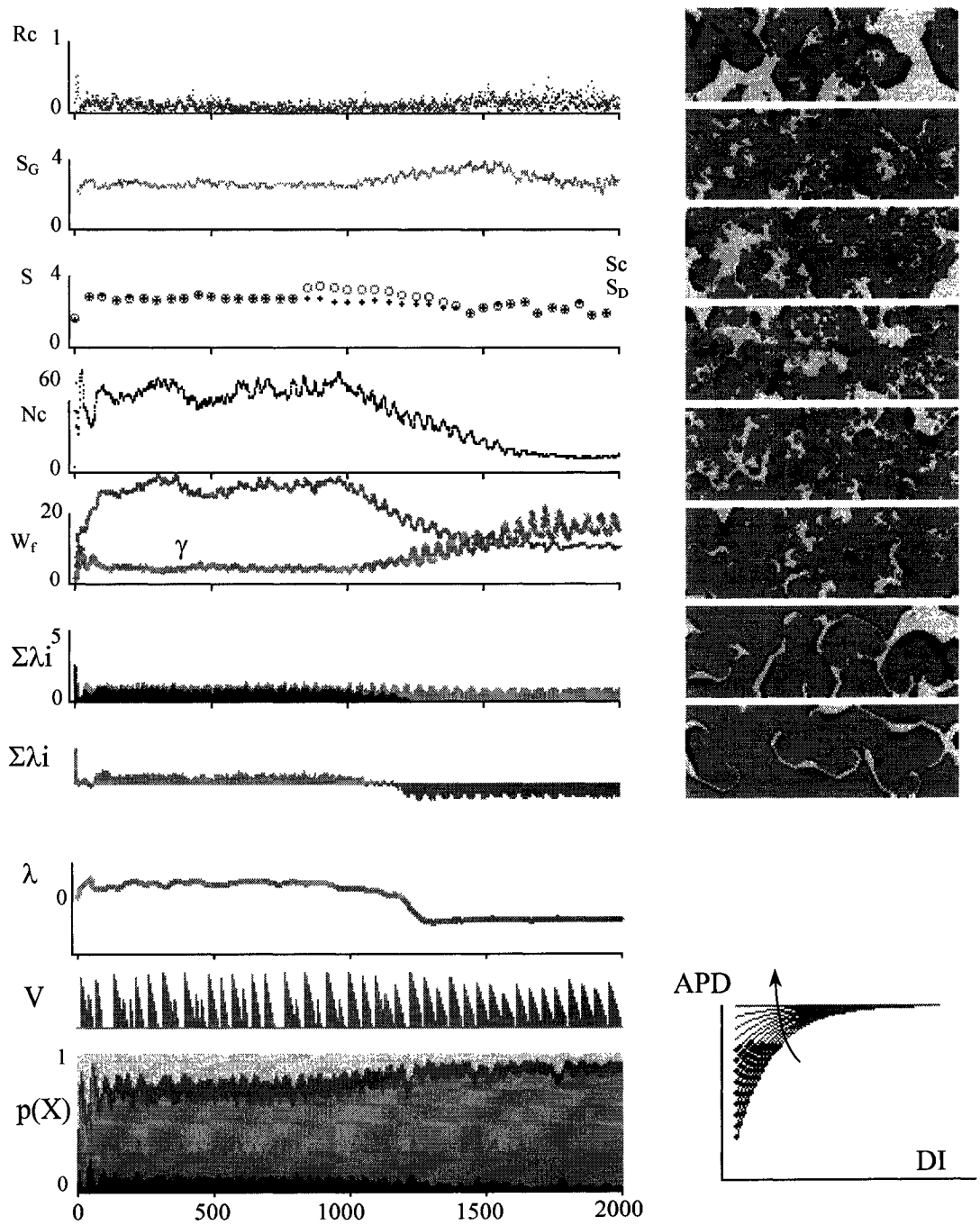

Figure 5.15. Flat restitution self-organizes into fibrillation poorly, due to the large critical ring size and a tendency to annihilate. A stable field is established here instead, by starting with $APD_m = 48$ and $APD_o = 16$, and then gradually flattening restitution until $APD_o = 48$. The usual distribution of fine complex waves condenses into a lesser number of more regular waves whose cores become locked into a stationary pattern.

Figure 5.13 shows a spiral developing with $APD_o = 36$. The restitution curve is relatively flat, and very little activity falls onto the region of the curve where $m > 1$, as shown by the very small thick segment. The Lyapunov exponents are all negative. The action potential train becomes nearly regular after a transient period, and wave break does not occur. Figure 5.14 shows a simulation with the same parameter set, but started from a random initial condition. Asymptotic behaviour is the same, with $N_c = 9$ rather than one.

As the intercept point APD_o is lowered to steeper restitution, the core points start to show some local spatial oscillation, as reflected in the R_c and S_G traces, which are the two purely spatial metrics of the static core pattern monitored at each time step. Wave break finally occurs around $APD_o = 24$. The spatial pattern breaks up into multiple waves, and N_c rises to approach a plateau of about 35 core points, suggesting a maximal wavelet capacity. The Lyapunov exponents under these conditions are still mostly positive. The cluster centroid metric R_c moves toward zero as fully developed fibrillation fills the domain with near-uniformly spaced widespread core points. Slow fluctuations of R_c indicate that core points continue to drift, and a steady state is not reached. The action potential train is clearly chaotic.

The Lyapunov exponents and their sum become maximally positive, and the Kolmogorov entropy is maximum, when $APD_o < 24$ as shown in the previous chapter. This finding is due to the DI histogram widening such that more cells find their DI becoming longer due to the widening excitable gap, and therefore find themselves under the more shallow plateau of the restitution curve where $m < 1$. The net result is that steepening restitution, concurrent with a widening diastolic interval distribution, gives rise to the Lyapunov exponent λ reaching its maximum positive value at high, but not maximal, restitution curve steepness. Once again, this demonstrates that maximum positive λ is not equivalent to maximum chaotic dynamics of the system, at least in this discrete medium. It is only necessary that the sum of the Lyapunocv spectrum $\Sigma \lambda > 0$ when waves do finally break and chaos ensues.

Lowering the intercept further to $APD_o = 20$ produces fully-developed chaos. Virtually all measures of activity are highly irregular. Entropy is high, fluctuating around mean values of $S_D = 3.02$ and $S_c = 3.50$. While we still have $\Sigma \lambda > 0$, its value has dropped to 0.25. The more significant role of negative exponents in the Lyapunov spectrum contribute to intermittent coalescence and break-up of waves, as seen in alternating slope regions of the $N_c(t)$ plot. Although probably unrealistically low, when pushed below $APD_o = 12$, incidences of spontaneous defibrillation are seen due to the very wide excitable gaps. Although spontaneous defibrillation is exceedingly rare in real hearts, perhaps even non-existent under physiological conditions, we are left to wonder if it could potentially occur at extremely steep restitution, as demonstrated here if such conditions actually existed in real hearts.

When restitution is relatively flat with $APD_o > 40$, maximum slope $\xi < (48–40)/10 = 0.8$. A spiral wave is difficult to establish because the wave front wants to follow the preceding wave tail down and off the domain without breaking. To establish a field of fibrillation with flat restitution, one must allow a random field with steeper slope m to self-organize, and then gradually flatten the restitution curve until $APD_o = 48$. Figure 5.15 shows $APD_m = 48$ and $APD_o = 16$ allowed to run for 800 time units or 4 seconds. The restitution curve is then gradually flattened by increasing APD_o to 48. Several predictable changes take place, including a drop in entropies S_D and S_C, core point coalescence resulting in decreased N_c, and an increase in the length scale γ of the waves. Entropy S_D becomes relatively small and stable around 2.2, regardless of the number of core points. As the restitution slope m passes through one, the Lyapunov exponents changed sign from positive to negative, and the action potential train becomes more regular. The bottom frame, showing states p(X), indicates narrowing of the excitable gap at the top in light grey, and less volume of wave front shown as the thin black area at the bottom. Surprisingly, despite all APD being equal and the core points being fixed as indicated by the near-constant spatial entropy S_G, the diastolic intervals remain irregular and the system does not settle into any steady state. This is probably a numerical artifact due to the unit decrementing of states being too coarse to allow complete dissipation of irregularities.

Although wave patterns are stable with very narrow DI, APD, and CL histograms, even some very long runs with constant APD failed to demonstrate complete dissipation to periodicity. This suggests that it might be difficult for a pattern of several reentrant circuits to settle into a purely monomorphic VT, even with flat restitution, unless the diastolic intervals, and therefore cycle lengths, can become fairly uniform.

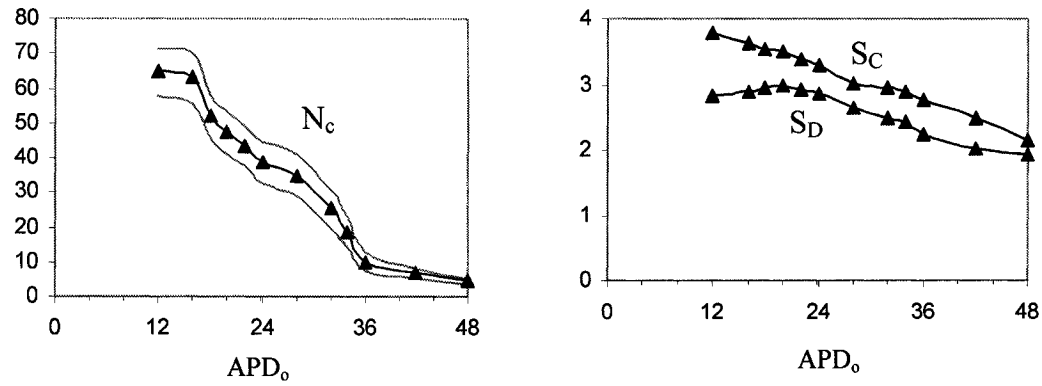

Figure 5.16. Effect of restitution on fibrillation mean core point or reentrant circuit number N_c (left), and two measures of entropy: spatiotemporal DI entropy S_D and CL entropy S_C. Steeper restitution with lower APD_o produces more reentrant circuits with finer spatial scale and generally higher entropy.

5.8 Strength of Fibrillation

The transition from a spiral wave to fibrillation through wave break involves a "fibrillation threshold" (VFT) being crossed. At the onset of fibrillation, there is a brief interval where a wave front segment blocks, as was illustrated earlier in Figure 3.24, and two free ends are established. The resulting two new core points can either grow in strength to become independent spiral waves, or mutually annihilate by recombination. For a new spiral wave to survive, the wave front must maintain its ability to excite the cells ahead without exhausting itself and blocking. In the core region, the front is pressed against its own tail, which temporarily impedes propagation. Failure occurs if the peak voltage of the action potential at the wave front drops below threshold as it waits for the tail to recover enough to fire again. In the CML model, the strength of the wave front is therefore the "voltage

reserve" by which the peak voltage V_p exceeds the threshold V_{th}. We can define a quantitative index of spiral wave strength by calculating this difference within the core point 2x2 cell cluster, and normalizing it against the largest possible difference $V_m - V_p$. A global measure of fibrillation strength is the integrated safety factor (ISF), which we define as the sum of all safety factors for each reentrant circuit.

$$ISF = \sum_{i}^{Nc} (Vp_i - V_{th}) / (V_m - V_{th}) \qquad (5.2)$$

This metric is made nondimensional by the denominator, such that the individual core safety factor is zero if V_{pi} drops to V_{th}, and is maximum of one if V_{pi} equals V_m. ISF is zero if there are no reentrant circuits, and increases with core number N_c. ISF becomes positive above the VFT, with the onset of spiral wave VT or VF, the magnitude indicating how far the dynamics are away from spontaneous defibrillation. It should be mentioned that ISF applies only to reentrant circuits, and is not the same as the more commonly described safety factor (SF) for normal wave front conduction, which will be defined later.

Figure 5.17 shows a histogram of individual safety factors for each core point, placed in descending order, for a few examples of fibrillation. The ISF is the sum of all such spikes over the range of N_c. Of note is the virtually ubiquitous presence of at least a few strong core points in each case, represented by the largest spikes. This indicates that these examples of fibrillation are relatively robust, and far from spontaneous defibrillation.

As a final note, lowering the threshold for cell firing V_{th} allows more reentrant circuits to develop during fibrillation. The standard threshold value chosen for most simulations is $V_{th}/V_m = 0.3$. Complex near-random activity is seen below 0.2. A plateau of larger scale structure is seen around 0.4. Figure 5.18 shows the effect of changing V_{th} and the restitution slope on the average number of core points. Note that N_c is highly variable when V_{th} is high, and is nearly constant when V_{th} is low. This figure will be the foundation for the next chapter, which attempts to define fibrillation as a phase transition.

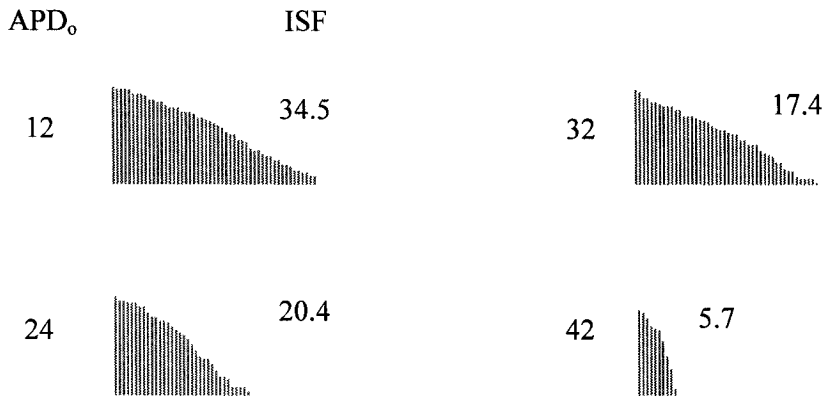

Figure 5.17. Histograms of safety factors for reentrant circuits of fibrillation shown for various APD_o with APD_m = 48. Each spike represents a separate reentrant circuit, the height of which is the safety factor for that specific core point. There is considerable heterogeneity of core point strength throughout the field of fibrillation, as indicated by the highly variable safety factors. Weak core points are at the tail of the distributions, and are most likely to self-terminate. At least a few circuits for each case have maximum strength, indicating that these examples of fibrillation are quite robust. The integrated safety factor (ISF) is shown for each case, calculated as the total volume of the histogram.

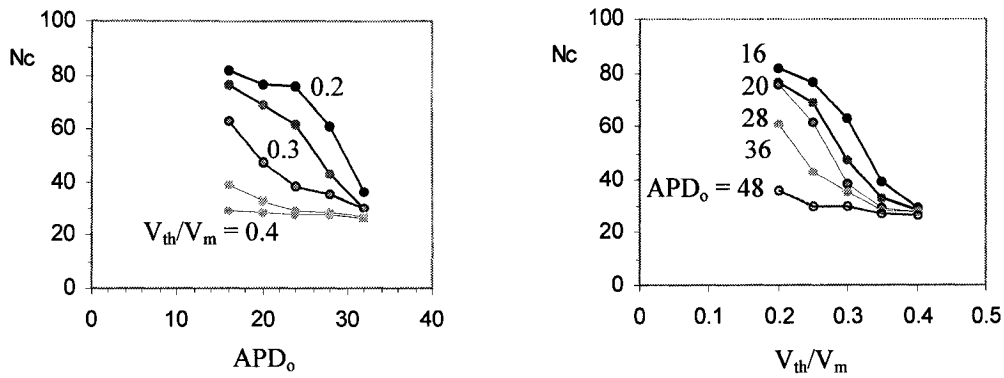

Figure 5.18. Influence of changes in the cell firing threshold V_{th} on the equilibrium number of reentrant circuits N_c. Lowering the threshold allows more circuits to develop. The left figure shows contours of V_{th} and the right figure shows contours of APD_o.

Chapter 6

PHASE TRANSITIONS

6.1 Equilibrium

Although microscopic states in thermal or physicochemical systems are not generally predictable, mean values can be described by thermodynamic variables which obey equations of state at equilibrium. Systems with many particles must be characterized by various mean values and probabilities [238]. From a functional perspective, fluctuations of individual element microstates allow continuous exploration of the global state space of non-equilibrium systems, and relaxation into the most favoured states, if any exist, that are accessible to the dynamics. Phase transitions between states of matter are associated with clearly defined changes in molecular order. In thermal systems, macroscopic order changes as the balance between attractive and repulsive intermolecular forces undergoes a distinct shift. Some well-studied examples of phase changes involving spatial patterns include the spontaneous formation of periodic Bénard convection cells in heated fluids [4], magnetization of ferromagnetic materials below a critical temperature, as idealized in the Ising model [341], and melting and vapourization of solids. We can hypothesize that the onset of cardiac fibrillation is a phase transition governed by cell dynamics competing between local convergence and divergence. Interactions between excitable cells occur through electrotonic currents, which promote state convergence by diffusion and

dissipation of irregularities, while state divergence is a consequence of nonlinearities in active ionic currents resulting in restitution-driven instability.

Phase transitions within distributed systems of cooperative elements are distinguished by an abrupt change in some measurable order parameter, while an independent control is changed. The input control is usually temperature in thermal systems, but it can be other state variables. There is no unique definition of the order parameter for physical systems in general, but for a specific application it should be chosen to quantify some essential feature of the structure related to new properties. Most commonly it is a simple scalar, but it can be a multi-component quantity or vector. Classic examples in statistical mechanics, pertaining to phases of matter, include density differences in liquid-gas systems, polarity of magnetic subregions, orientation of liquid crystals, and spatial correlation of patterns [238].

As a specific hypothesis, let us propose that reentrant wave activity will undergo one or more phase transitions in the cardiac tissue CML model as the action potential restitution curve slope is changed. An independent control parameter, analogous to temperature, is the action potential slope factor ξ, defined as the slope of the restitution curve at DI = 0. The influence of a second control parameter, related to the firing threshold voltage ν, will also be explored.

$$\xi = (APD_m - APD_o)/\tau \tag{6.1}$$

$$\nu = V_{th}/V_m \tag{6.2}$$

The first parameter ξ is zero for flat restitution or constant APD; $\xi = 1$ for the intercept slope being one; and $\xi > 1$ if the restitution slope is steeper than one. If APD_m and τ are both constants, as previously assumed, then APD_o can substitute for this parameter. The second parameter ν accounts for the likelihood of the threshold condition being met. One

might expect, intuitively, that instability and wave-break would be most likely if ξ is high and ν is low.

Order parameters that embody spatial wave patterns as dependent variables should be capable of identifying phase transitions. What are the unique characteristics of fibrillation that relate to spatial or temporal order? Simulations of wave-break suggest that, at the very least, there must be an increase in the number of spiral waves, as measured by the number of core points N_c, this being the simplest order parameter. Since $N_c(t)$ can undergo considerable variability during fibrillation, as waves intermittently break and coalesce, a mean value must be taken. Since the focus in this dissertation is on the normal heart, we will not deal with the separate issue of fibrillation initiation by factors such as ischemia or triggered activity [72, 257, 403], outlined in Figure 1.7, that promote regional block, but will instead assume that a solitary spiral wave has already formed by some unspecified mechanism of symmetry-breaking. To be specific, we will consider a single stable spiral wave with $N_c = 1$ to be like a solid phase, and the transition by wave-break to $N_c > 1$ to be like melting into a liquid phase. Melting occurs when N_c increases and cores become mobile, while freezing occurs when N_c decreases to a fixed value and a stable spatial pattern becomes locked-in. Freezing can occur through slow annealing or rapid quenching, depending on how quickly control parameters are changed relative to the relaxation time constant of the system response [508].

Entropy might seem like an obvious measure of order. The most appropriate definition of system entropy is probably that based on the distribution of diastolic intervals p(DI), since this relates to the other entropies, S_A and S_C, which are constructed from their respective distributions p(APD) and p(CL) through the restitution curve. The only truly independent entropy measure is that derived from p(DI). Fluctuations in DI experienced by each element individually, and in the system as a whole, suggest a functional analogy with the distribution of molecular velocites in a gas where the width or dispersion of p(DI) is like molecular kinetic energy that serves to permit state space exploration. Simulations of the model show that the DI distribution is very narrow if $APD_o = APD_m$ and becomes wider

according to the APD difference, although Figure 4.21 showed that there is not an abrupt change. Highly ordered and tightly wound spiral waves, and dense fibrillation wave patterns, are associated with a narrow p(DI), while complex highly disordered patterns with wide and variable excitable gaps result in a wide p(DI) distribution. Both the entropy of p(DI), and the standard deviation σ_D of p(DI) about its mean, are measures of system order, although neither identifies a sharp phase transition.

A third measure of system order is the spatial correlation discussed earlier. This measure is commonly used in statistical mechanics to quantify phase transitions, as ordered subregions emerge from a disordered background during crystalization or freezing [300]. The correlation length for random spatial or temporal patterns is very short, while that for order patterns is much longer, as illustrated in Figure 5.2.

What spatiotemporal quantities determine if two types of fibrillation are equivalent? This is an important question because different subtypes of fibrillation might have diagnostic or prognostic significance, and might respond differently to therapies. Strictly speaking, runs of fibrillation cannot be equivalent unless they are identical, but for practical purposes subtypes can be defined according to their conformity to some degree of dynamical similarity. Subtypes must be functions of at least APD_o and APD_m, which through their dynamics determine p(DI), N_c, and spatial patterns. Static measures taken at one time instant are not necessarily representative of the overall dynamics because oscillations in fibrillation patterns span some larger period related to cycle lengths. Useful metrics must be averaged over several cycles. To be clinically useful without invasive instrumentation, these metrics would need to be correlated with quantities measurable in the body surface ECG.

Thermodynamics seeks to find relationships between average values of a relatively small number of state variables at equilibrium. It is not a simple task to derive an exact thermodynamic theory of fibrillation because the system is usually far from equilibrium, and there are no known governing conservation laws in a dissipative system that would

allow the derivation of a suitable analytical Hamiltonian governing microstates [238]. The model that we seek here will, by necessity, be phenomenological, with equilibrium defined in a statistical sense only.

Figure 6.1 shows the state diagram for a generic pure substance like water. The three thermodynamic state variables are pressure P, volume V, and temperature T. If volume is expressed as density, all variables are intensive quantities independent of mass, and the equation of state is $F(P, \rho, T) = 0$. An analogy to cardiac tissue is proposed in Table 6.1. Restitution slope is the main independent control variable, affecting stability and acting upon all cells, and therefore behaves like temperature. The number of core points N_c divided by the domain size gives the reentrant circuit density $\rho = N_c/ (NxM)$, analogous to mass per unit volume. An increase in firing threshold V_{th} can reverse spiral wave break-up, just as changes in pressure can reverse the effects of changes in temperature. This suggests that the firing threshold $\nu = V_{th}/V_m$ is analogous to pressure. An equation of state for the cardiac tissue model would therefore have the form $F(\nu, \rho, \xi) = 0$. The search for this function involved running many long simulations, under various initial conditions and parameter changes, to delineate regions of behaviour that define the mean relationship between ν, ρ, and ξ. The equation of state obtained is shown by the curves in Figure 5.21, which define a three-dimensional surface analogous to that in Figure 6.1.

Table 6.1: Thermodynamic State Variables in Cardiac Tissue

Matter			Cardiac	
Temperature	T	.....	Restitution	ζ
Density	ρ	.....	Core density	ρ
Pressure	P	.....	Threshold	ν

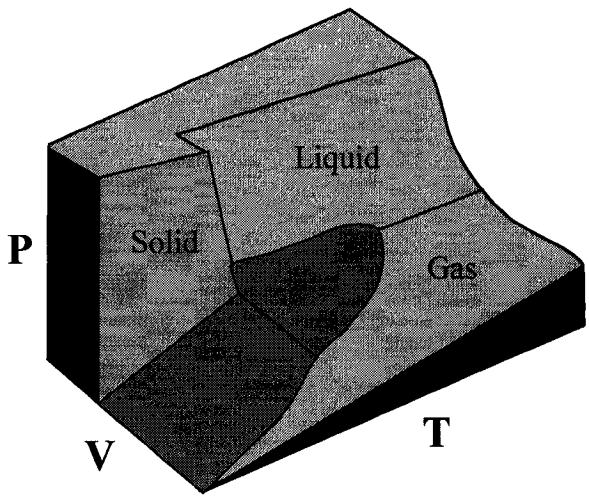

Figure 6.1. Phase diagram for a generic pure substance like water, showing the surface of equilibrium between pressure, volume, and temperature.

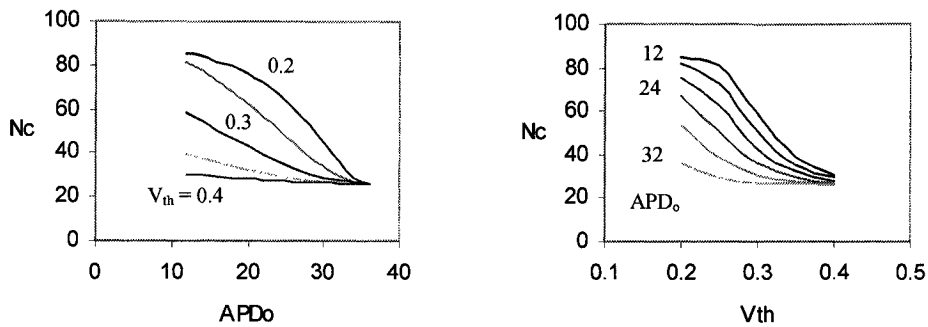

Figure 6.2. A function representing the equation of state $N_c(APD_o, V_{th})$ is fit to the mean N_c obtained from the CML model summarized in Figure 4.23, and fit to a Hill equation with a chosen exponent a = 2.

An approximation to this empirically-derived equilibrium equation of state can be fit to the surface $N_c = f((APD_o, V_{th})$, defined by the curves in Figure 5.23. A modified Hill equation provides a reasonable fit:

$$N_c = N_{co} + cX^a / (1 + (bX)^a) \tag{6.3}$$

where

$$X = APD^* - APD_o$$
$$APD^* = 34$$
$$N_{co} = 32$$
$$a = 2$$
$$b = 0.1 \exp(-(V_{th} - 0.2)/.07)$$
$$c = 0.7 \exp(-(V_{th} - 0.2)/.045).$$

The equation is valid only for $X > 0$ where $APD_o < 32$. The exponent $a = 2$ was chosen *a priori* as the best fit integer, and parameter fitting was done visually rather than formally. A good fit was obtained. There is no known underlying physical or theoretical reason why a Hill equation should be used. The choice is simply based on the sigmoidal appearance of the curves derived by simulation. This function is plotted in Figure 6.2, and closely matches Figure 5.17 obtained as a composite from many model simulations. While the general form of this equation for N_c was chosen prior to the parameter fit, its dependence on a power of X gives it properties compatible with a critical point in a second order phase transition. This issue will be explored in a later section.

6.2 Non-Equilibrium

A thermal system undergoes a first order phase transition when it develops a double potential well allowing coexistence of two states within a finite temperature range, as shown in Figure 6.3. At the critical temperature T_c, the free energy is equal between both

phases. There are two wells above T_c, one of which is less favoured and gives rise to a metastable point, while only one of the pure phases can exist below T_c. The free energy potential surfaces of each phase overlap, producing a discontinuity in the slope at the transition temperature T_c. In thermal systems, this slope is the entropy and the difference between the surface ordinates is the latent heat [569]. An abrupt jump can occur from one phase to the other if T is moved away from T_c. An example is the ice-water transition. Supercooled water can remain in a liquid phase well below the freezing point under ideal conditions, and abruptly turn to ice if a nucleus is introduced. There is a zone of suppressed transformation characterized by overlapping metastable branches, and giving rise to hysteresis if the temperature is cycled.

By contrast, a second order phase transition always has one well, allowing only one phase to exist at any given temperature. The smooth potential surfaces meet and terminate at the transition line. They are continuous in slope instead of intersecting, and there are no metastable branches. This transition is typically characterized by the sudden emergence of increased complexity and self-similarity, with power-law correlation of properties in the transition zone [300]. First and second order transitions can be visualized as sections through a cusp catastophe, as shown in Figure 6.4 [570].

Figure 6.5 shows the phase transition from a solitary spiral into fibrillation as the order parameter $\xi = (APD_m - APD_o)/\tau$ is varied by lowering APD_o. If a uniform spiral is allowed to reach a perfect steady state, and then is subject to a very slowly decreasing APD_o, it can persist for a long time without breaking. Any perturbation will grow into an instability if a small irregularity is introduced, like an ice crystal introduced into supercooled water. The growth rate is especially rapid at steep ξ. This observation hints at the existence of a first-order phase transition with metastability, or hysteresis in a second-order transition. To test these possibilities, APD_o was lowered at various rates and spatiotemporal order was monitored by the changes in width of p(DI), which grows with increasing disorder. By clamping $APD_m = 60$ and imposing a very slow rate of change of ξ, one can lower APD_o to 15 before wave break occurs. A more rapid change of ξ brings

on wave-break sooner. By plotting $N_c = f(APD_o)$ for a given APD_m the region of disordered fibrillation can be separated from that of the ordered solitary spiral. Routes of wave-break and coalescence or solidification can be followed as trajectories through the diagram. A composite over several different examples with constant APD_m is shown in Figure 6.6.

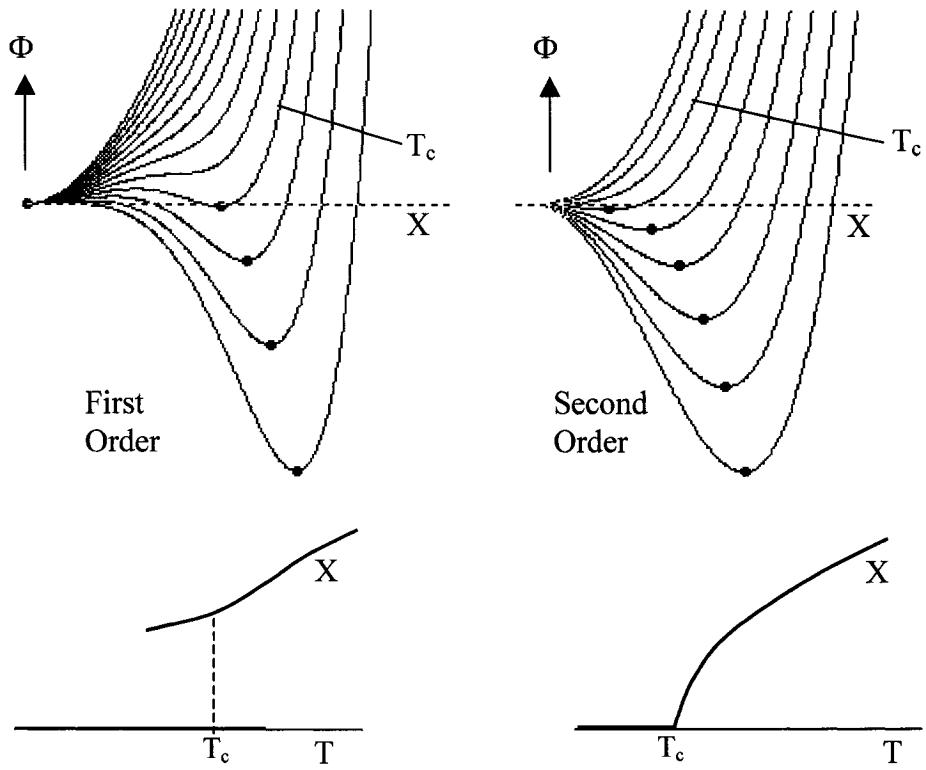

Figure 6.3. A first order phase transition is characterized by region with two stable states giving rise to metastable branches (left), while a second order transition is continuous with only one stable state (right). T = temperature, X = order or density, Φ = free energy. Above the critical temperature T_c in a first order phase transition, a second potential well emerges abruptly allowing co-existence of two phases at a given temperature. In a second order phase transition, a single potential well emerges at T_c, and only one phase can exist.

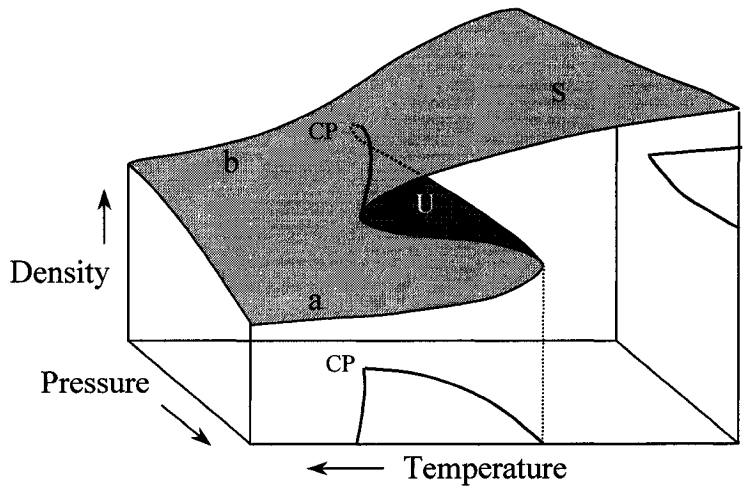

Figure 6.4. First and second order phase transitions can be conceptualized as sections through the surface of a cusp catastophe, illustrated here for a substance like water. A first order transition occurs at pressures above the critical point (CP) along line "a" where there is a metastable region with two overlapping equilibrium points, while a second order transition along line "b" is smooth below CP. Surfaces are stable (S) or unstable (U) as shown. A bifurcation into two stable solutions occurs at the critical point.

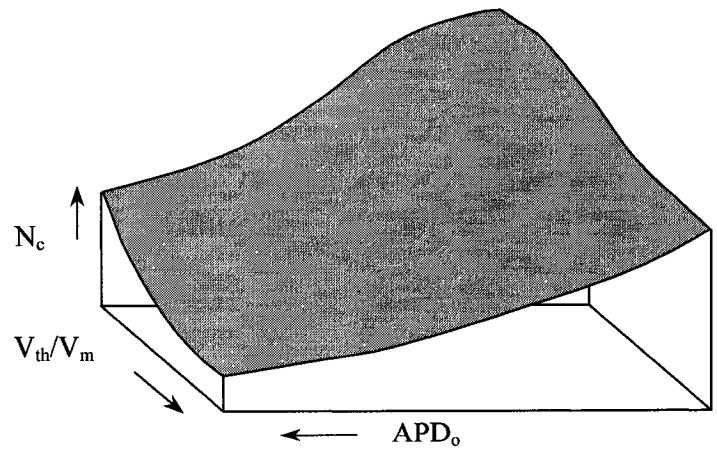

Figure 6.5 The equilibrium phase surface $N_c(APD_o, V_{th})$ for the CML fibrillation model is smooth, and corresponds most closely to a second order phase transition. There are no known metastable regions. This surface fits the Hill equation (6.3).

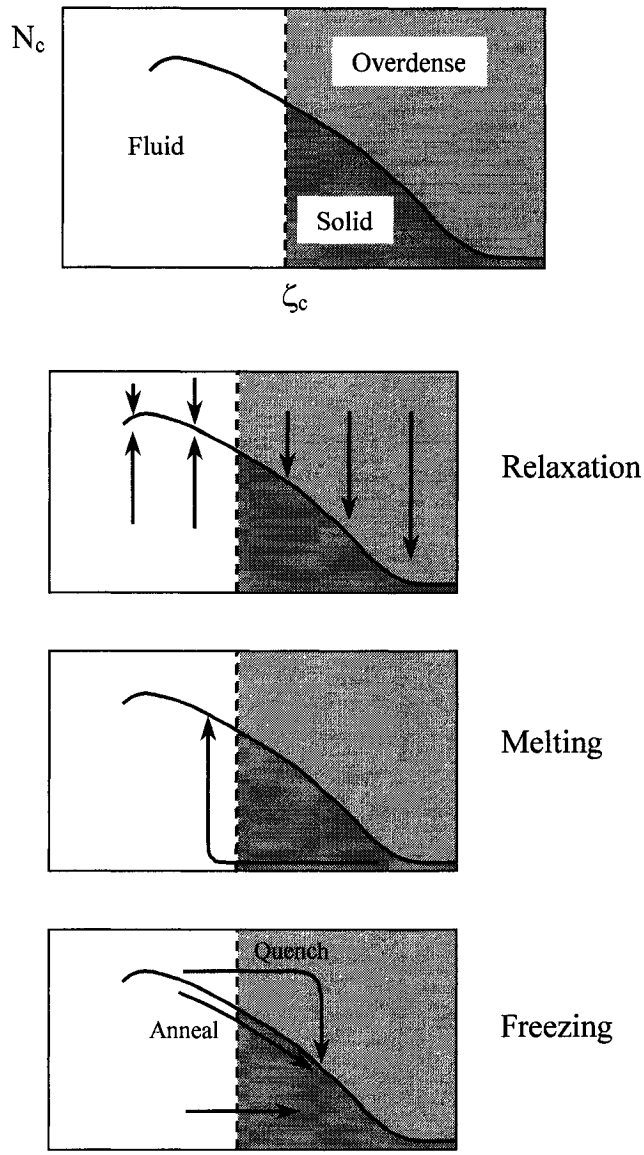

Figure 6.6. Phase diagram for the system. The transition parameter $\zeta = (APD_m - APD_o)/\tau$ along the abscissa is analogous to temperature, and core point number along the ordinate is like density. As restitution is made steeper, by lowering APD_o below a critical value corresponding to ζ_c, the system "melts" and spiral waves break up and multiply in a free or fluid phase. As APD_o is raised again, the system "freezes" back into a solid pattern with fixed core points. A rapid freeze is like quenching, while a quasi-equilibrium slow change is like annealing.

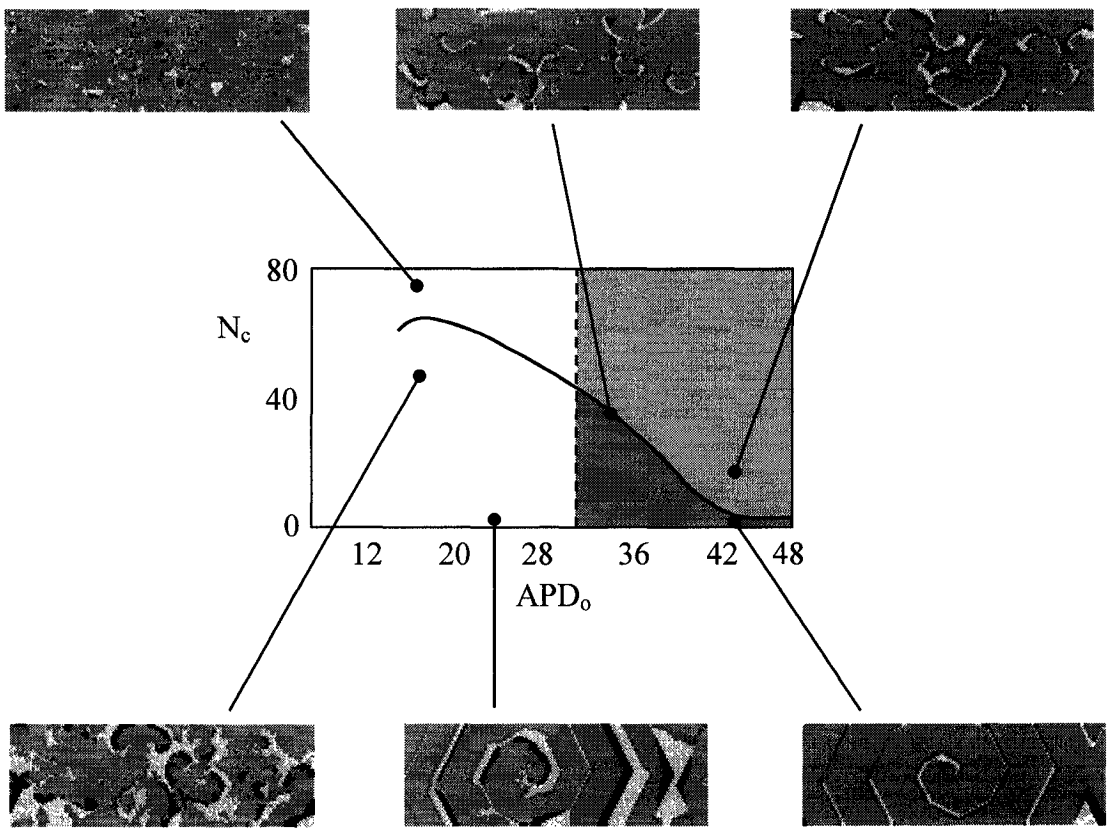

Figure 6.7. Subtypes of solitary spiral VT and multiple spiral VF map onto the phase diagram according to the combination of restitution APD_o and the number of cores N_c. The curve represents the equilibrium mean N_c for a given APD_o. Configurations located below the line will break-up if $APD_o < 32$, and those above the line will self-organize to a lower N_c.

6.3 Markov Population Model

We have seen that wave break occurs below about $APD_o = 32$ for the standard value of $APD_m = 48$, and is more rapid at lower APD_o where restitution is steeper. Wave break is also more likely when N_c is high, as waves are more crowded together and irregularities are more likely to be magnified by nonlinearities leading to local block. Coalescence is seen to occur above a critical N_c and increases with shorter APD_o. Higher N_c causes more crowding of waves whose cores are more likely to come into proximity and cancel as the narrow isthmus between them blocks. These opposing processes suggest that a competition exists between birth by wave break and death by coalescence. A simple stochastic population model is proposed to account for this balance that determines $N_c(t)$:

$$dN_c/dt = \text{core birth rate} - \text{core death rate} \tag{6.4}$$

$$= f(APD_o, N_c) - g(APD_o, N_c)\,. \tag{6.5}$$

In statistical mechanics this is called a master equation, and determines changes in probabilities of events. The proposed functions f and g are shown in Figure 6.8. To implement this equation in a Monte Carlo simulation, the functions f and g are considered to be probabilities. Two uniformly distributed random variables Xi and Yi, between 0 and 1, are generated at each time step. If $Xi < f$ then $N_c = N_c + 1$, accounting for core point birth, and if $Yi < g$ then $N_c = N_c - 1$ accounting for core point annihilation. Time stepping from an initial condition specifying APD_o and N_c gives the time series $N_c(t)$, which is close to that seen in the deterministic CML simulations. The intersection of the curves where $f(APD_o, N_c) = g(APD_o, N_c)$ determines the equilibrium value of N_c for a given APD_o. The stochastic nature of changes in N_c produces a dynamic rather than static equilibrium, particularly when APD_o is low and f and g are both nonzero. An example of the Markov model simulation of $N_c(t)$ is shown in Figure 6.9, which resembles that from the CML model.

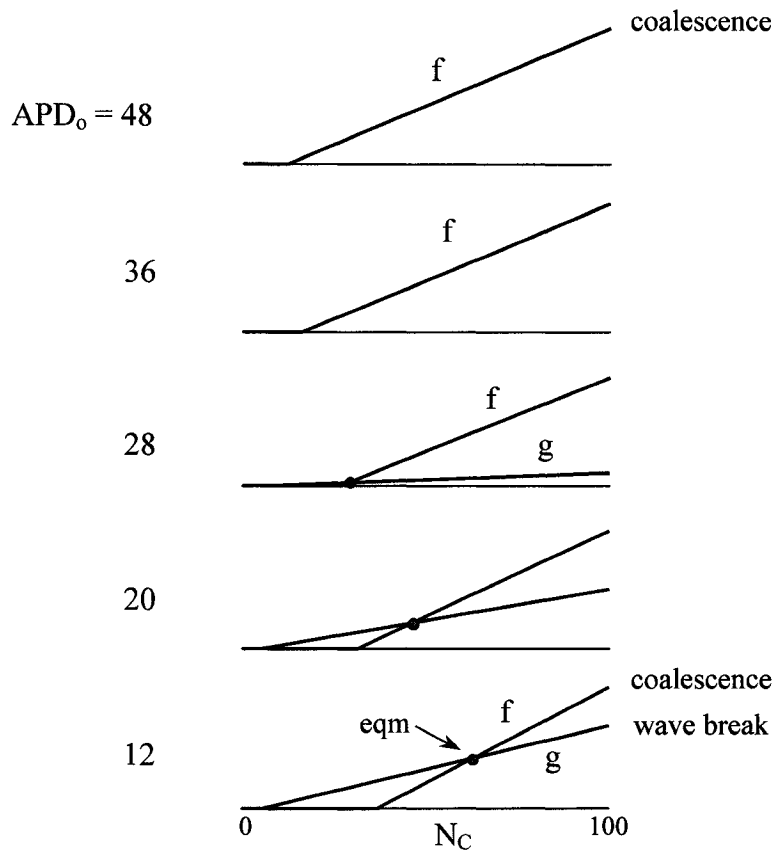

Figure 6.8. Probability functions determining wave break and wave coalescence in the population model according to the number of cores N_c at each time step. The function $f(N_c, APD_0)$ determines the rate of wave coalescence, which is greatest at high densities and drives N_c down, while $g(N_c, APD_0)$ determines the rate of wave break, which occurs below $APD_0 = 32$ and drives N_c up. The intersection point, where $f = g$, gives the mean N_c or equilibrium N_c where, for a given APD_0, these processes are on average balanced. The integral of the difference $(f - g)$ gives the potential function Φ governing changes in N_c.

Since f and g are the positive and negative processes driving changes in N_c, we can define a potential function or free energy surface by integrating the difference $f - g$. This function defines a surface $\Phi(APD_0, N_c)$, whose topology determines the regions of stability. The surface is shown in Figure 6.10, and is derived by the following equation:

$$\Phi\,(APD_0, N_c) = \int (f - g)\, dN_c. \qquad (6.7)$$

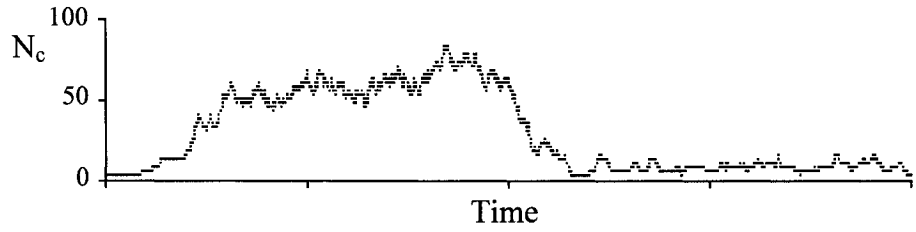

Figure 6.9. Implementation of the Monte Carlo model as described in the text produces a time series representing the number of core points $N_c(t)$.

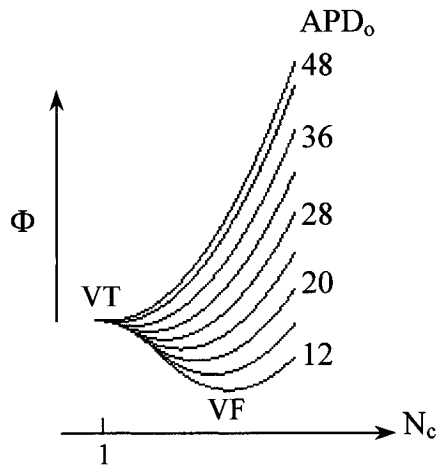

Figure 6.10. A potential function is derived from the population model. For each APD_o there is a curve whose slope is the net driving influence for changes in N_c. The composite of all such curves defines a surface $\Phi(APD_o, N_c)$ whose ordinate is in arbitrary units of the functions f and g, but related to the free energy. A marble placed on the surface will seek the lowest point, which for VT is $N_c = 1$, and for VF is in the basin where $N_c > 1$. APD_o determines the stability and equilibrium N_c.

If at any time N_c is too high to survive, coalescence will dominate and the operating point will roll down the hill until it reaches a flat section where it will stop as N_c reaches a stable value. If N_c is too low, and a mechanism of wave break can occur, then N_c will grow. This can only occur if $APD_o < 32$, the critical value where the surface Φ transforms into a concave basin. The basin nadir determines the equilibrium value of N_c for a given APD_o. The number of core points changes according to the slope of the potential function.

$$\frac{dNc}{dt} = K\frac{\partial \Phi}{\partial Nc} \tag{6.8}$$

In actual fact, the basins where $APD_0 < 32$ must be chaotic attractors, and might best be imagined as fuzzy or jiggling moving surfaces, comprised of multiple unstable trajectories passing near saddle points, forcing the operating point to move chaotically about the mean values shown. This surface is a three-dimensional representation of the phase diagram in Figure 6.6, and is shown in Figure 6.11.

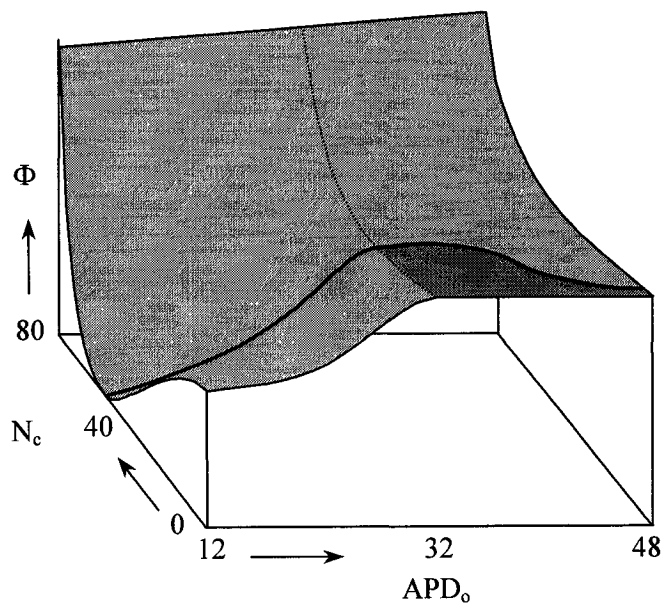

Figure 6.11. Phase diagram of the CML model redrawn as a potential surface. Wave break occurs below the critical APD_0, indicated by the dashed line, which also demarcates the boundary of the concave basin of fibrillation. Note that the dark region above the critical APD_0 at low N_c is a actually a flat surface where there is no driving force for wave break, and the state is stable.

A first-order phase transition requires the existence of two basins at any given APD_o, corresponding to two coexisting phases. The barrier between them would vanish as the control parameter APD_o is changed, as in Figure 6.3. This particular topology, found from the population model, suggests that the VT-VF transition is most similar to a second order phase transition, since at any given time there is only one basin with one stable attractor.

Note that if reentrant VT happens to be a solitary reentrant circuit with $N_c = 1$, it is stable only if initiated under conditions where $APD_o > 32$, because in this regime there is no driving force for wave break, and VT can persist. In other words, there is no incentive to move the marble above $N_c = 1$, since it is on a flat part of the surface. The zone of stable VT is therefore a line along $N_c = 1$ intersecting with the region $APD_o > 32$. Simulations show that it is possible, however, for N_c to be as high as 30 while still in the stable zone where $APD_o > 32$ without experiencing wave break. Topologically, the line of $N_c = 1$ crosses a saddle point where VT goes from being stable to unstable as APD_o is lowered. The flat region, with $N_c > 1$ and $APD_o > 32$, represents a field of multiple stable spiral waves that neither breaks nor coalesces, such that a fixed number of spirals N_c persists unchanged. One could debate whether dynamics in this zone should be called VT or VF, since the ECG pattern would be regular and monomorphic. While theoretically possible in the model, this state would have a low likelihood of occurrence in a real heart because multiple stable spiral waves would not likely initiate *de novo* within this zone, and if $APD_o > 32$, there could not be growth of N_c by wave break. In other words, we could speculate that this region of the phase space might not normally be accessible by typical dynamics in a real heart. VF occurs in the model when $APD_o < 32$, and the dynamics are forced to migrate into the concave basin where wave-break becomes active, and ultimately competes with coalescence as N_c grows. Since the surface is smooth and continuous in the model, there is no abrupt transition or separatrix between VT and VF. Accordingly, these rhythms, which are normally considered distinct entities in clinical practice, actually constitute a continuum. Within this theoretical conceptualization, it is not clear if and why VT and VF should be considered separate or distinct phenomena, except as pertains to different N_c.

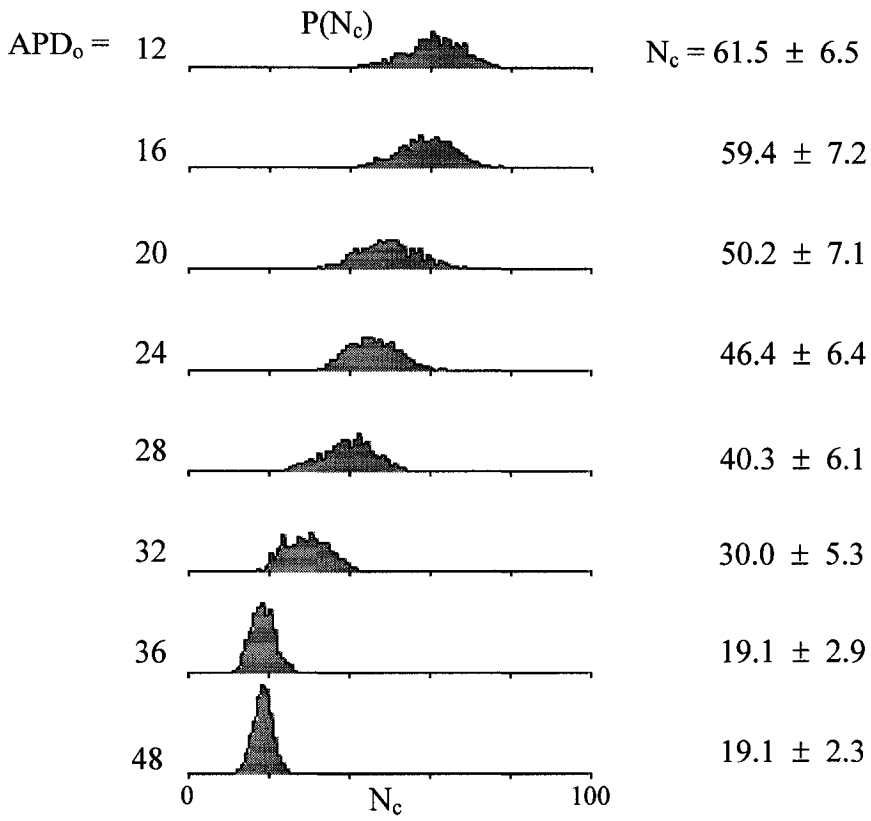

Figure 6.12. The number of core points $N_c(t)$ during fibrillation in the CML model, at various restitution slopes APD_o, is shown at left. Random initial conditions were allowed to self-organize to a statistical steady state before the N_c time series was collected. The numbers at right are the mean and standard deviations of the $p(N_c)$ distributions. The fluctuations in $N_c(t)$ are due to competition between wave break and coalescence. Note that the distribution is more narrow at lower APD_o.

We can carry the statistical mechanical interpretation further by attempting to account for fluctuations of N_c within the basins, which are shown in Figure 6.10, as derived from the CML simulations of fibrillation. Fluctuations can be estimated in thermal systems by defining a partition function that decays exponentially, and represents the probability of finding molecules at various energies. In our case Z decays with the order parameter φ.

$$Z = B \exp(-\beta\varphi) \tag{6.9}$$

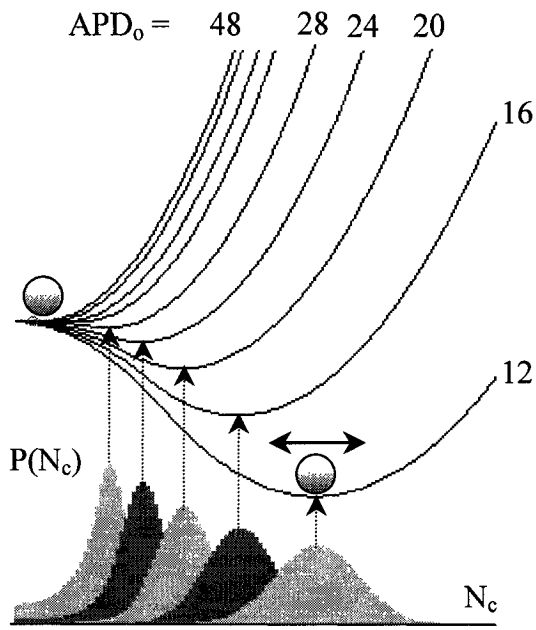

Figure 6.13. The potential surface $\Phi(N_c, APD_o)$ governing changes in core number N_c conceptually contains a marble seeking the lowest available point. Wave break and coalescence determine the equilibrium or mean N_c according to restitution slope controlled by APD_o. Variability of $N_c(t)$ depends on an effective "temperature", which is modelled below by probability distributions that are functions of APD_o. Lower APD_o is like a higher temperature that causes more vigouous activity and greater variability in N_c.

This function can be multiplied by the potential function Φ to give the probability distribution of states $p(N_c)$. The constant β in thermal systems is the product of the Boltzmann constant and temperature kT, which influence the magnitude of fluctuations in the order parameter φ, causing it to increase with temperature. The order parameter in our case is N_c, and the coefficient B normalizes the probability distribution so the total area is equal to one. In our case, we do not know what the effective "temperature" of fibrillation means, but the unknown parameter β determines the width of the N_c probability distribution. It would not be unreasonable to assume that the "temperature" is either APD_o, or at least some function of APD_o, since this vital parameter determines much of the system behaviour. Figure 6.13 shows the probabilities calculated according to the product

$p(N_c) = Z\Phi$ with the "temperature" function chosen empirically as $\beta = 0.5 + 0.2*(32 - APD_o)$ to give more wave breaking at lower APD_o, consistent with the wider distribution of N_c seen in the simulations shown in Figure 6.12. This equation for $p(N_c)$ is valid only in the wave break region where $APD_o < 32$.

6.4 Landau Theory

If we are willing to temporarily assume that the phase transition from VT to VF is second order, then we can pursue a more formal derivation of the potential function through further application of statistical mechanics. Landau in 1937 proposed a phenomenological theory of thermodynamic stability pertaining to second order phase transitions, noting that symmetry was broken at a critical value of the order parameter φ [250], that for our purposes is analogous to N_c. The potential surface equation can be assumed to be a polynomial expansion in powers of φ that is independent of the details of the system or of the phase transition [493]. This assumes that there is a saddle point in the potential surface at the phase transition. The details of a specific system are embodied in the coefficients. Application of Landau theory to the CML fibrillation model provides quantitative insight into the behaviour of the VT-VF transition under these assumptions. Briefly, the potential $\Phi(APD_o, N_c)$ can be expressed as a polynomial in the order parameter N_c where the coefficients a and b are functions of APD_o that remain to be determined.

$$\Phi = \Phi_o + \{ -h N_c + 1/2\, a N_c^2 + 1/4\, b N_c^4 + \dots \} \qquad (6.10)$$

The equilibrium values of N_c are found at the minima of Φ where $\partial\Phi/\partial N_c = 0$ and $\partial^2\Phi/\partial Nc^2 > 0$. At this point there is no driving force to change N_c. Specifically, if $h = 0$ and $a, b > 0$ then the only solution to equation (6.10) is $N_c = 0$, the quiescent state corresponding to asystole, or the topologically symmetric state of a wave front in normal sinus rhythm. A nontrivial solution is obtained if instead $a(APD_o) < 0$ and $b(APD_o) > 0$. The minimum free energy of the surface then occurs at:

$$N_c^2 = - a(APD_o) / b(APD_o). \quad (6.11)$$

If we now assume that $a(APD_o)$ is a power series in the displacement of APD_o from its critical value, previously assumed to be $APD_c = 32$, then $\chi = (APD_o - APD_c)/ APD_c$. If b is constant near APD_c then

$$a(APD_o) = \alpha \chi + \beta\chi^2 + \ldots \quad \alpha > 0 \quad (6.12)$$

It follows from equation (6.10) that in the vicinity of APD_c, the equilibrium N_c varies as the square root of $APD_o - APD_c$, with the critical exponent being 0.5, since $N_c \propto \chi^{0.5}$ at the phase transition. This relationship is shown in Figure 6.14, superimposed on the actual measured mean $N_c(APD_o)$. The fit is not perfect because the actual potential surface from the CML model is not a true polynomial, but has a flat region above APD_c indicated by the "solid" zone in Figure 6.11. Since this is a perturbation expansion, it is most valid close to the point where $\chi = 0$ or $APD = APD_c$. The potential surface derived heuristically by the Markov model can be approximated to such a function, where the coefficients a and b relate somehow mechanistically to the probability distributions of core point spacing and interactions. Analytic functions could, in principle, be derived in more detail for various thermodynamic constants, stability criteria, and power-law scaling at the critical point of the phase transition. Extension of the theory would allow the full weight of formal statistical mechanics theory to be brought to the problem on a level beyond that already described. Useful parallels might then be drawn with other similar physical systems. The details of this analysis is beyond the scope of the present work.

Finally, the potential surface $\Phi(APD_o, N_c)$ should be considered to have a barrier between $N_c = 0$ and $N_c = 1$, which runs along the entire APD_o axis. Normal sinus rhythm, with relatively long cycle lengths, produces stable propagating wave fronts with insufficient curvature or substrate heterogeneity to induce block or wave break. Propagation stability without reentrant circuits is therefore ensured, such that in the normal heart $N_c = 0$. A relatively high barrier must be crossed by the marble before a reentrant circuit can

spontaneously develop and proceed to establish a reentrant VT having $N_c = 1$. Presumably, ischemia or other pathological processes in the heart somehow lower the height of the barrier, such that a relatively small disturbance can precipitate VT or VF, particularly if the restitution curve is steep. The model structure presented so far does not allow for a transition from $N_c = 0$ to 1 to account for these important initiating events. Such modifications would ultimately allow better conceptualization and topological interpretation of the usually ill-defined "fibrillation threshold".

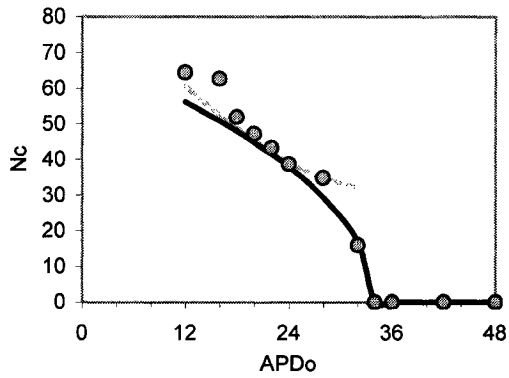

Figure 6.14. A comparison of mean $N_c(APD_o)$ from the CML model (circles) obtained from a solitary spiral wave with $APD_m = 48$. Below about $APD_o = 32$ the wave breaks into many waves. The approximated Landau equation predicts a square root relationship for N_c below $APD_o = 32$ (black line). The Hill equation discussed earlier (grey line) shown for $V_{th}/V_m = 0.3$ also gives a reasonably good fit, but is valid only for $APD_o < 32$.

It should be possible to develop a more comprehensive statistical mechanical theory of fibrillation than that presented so far. Ideally, we should seek closure by relating the macroscopic free energy surface, thus far derived phenomenologically, to the underlying microscopic cellular dynamics. This is usually done in statistical mechanics by formulating a Hamiltonian of the individual particle interactions, which are energy-preserving in a conservative system, and relating them to the polynomial coefficients of the potential surface using Landau theory [238, 568]. It is not immediately clear how this theoretical process might relate to dynamics in the cardiac CML model, but the issue is worthy of further development. Some progress to a better theory might be realized by

considering that wave break is not a simple function of APD_o, but is dependent in some complex manner on the spatial pattern of waves or core points which determines the statistical distribution of the diastolic intervals. This in turn influences the magnification of instabilities through the restitution curve, as previously described.

Stabilization of waves through coalescence, on the other hand, is dependent on the proximity of neighbouring core points whose statistical distribution could be more rigorously defined. We have also assumed that spiral break-up occurs at a critical value of APD_o corresponding to a critical restitution slope similar to a melting temperature. Simulations show empirically that this is not a sharp transition, but there is really a somewhat fuzzy boundary of APD_o that separates stable and unstable waves. Within this zone surrounding the critical APD_o, wave fronts block over small segments, but sometimes reconnect without progressing to the genesis of daughter waves, suggesting an occasional type of intermittency. This unstable-to-stable transient is responsible, at least in part, for the approximated critical $APD_o = 32$ being slightly lower than the expected value of 34 where the restitution curve region with slope $(APD_m - APD_o - R)/\tau > 1$ first appears.

The transition to fibrillation is an instability that must have similarities to instabilities in other spatially-distributed physical systems [108], particularly those that involve coupled oscillators that self-organize into complex patterns [204, 271]. The phase transition is one example. A comparison with hydrodynamic stability might be insightful. Transient wave block that recovers without wave break, occurring around the critical APD_o, has similarities to intermittency, seen in the transition from laminar flow to turbulence around the critical Reynold's number. As velocity increases in laminar pipe flow, bursts of turbulence first develop when $Re > 2300$, but are ultimately suppressed due to dominating viscous stability. Beyond $Re > 2800$, inertial instability dominates, and fully developed turbulence can persist [454]. This transition to turbulence is promoted by three factors: velocity fluctuations in the incoming flow, boundary surface roughness, and the adverse pressure gradient. Stability of this flow is analysed by solving the Orr-Sommerfeld

equation derived from the Navier-Stokes equations [454], the solution of which resembles a phase diagram with a stable region. It is tempting to hypothesize that fluid fluctuations are like irregularities in the cardiac wave front, and surface roughness is like substrate APD heterogeneity. Pressure gradient does not have a clear analogy. The turbulent transition occurs through intermittency, similar to that emerging in a one-dimensional return map, which progresses to chaos as the control parameter is increased [263]. Spatiotemporal intermittency is one recognized route to chaos [265] that might be relevant in the transition to fibrillation. The Ginzburg-Landau equation is another theoretical example, having both diffusion and instability terms, whose solutions exhibit phase transitions and spatiotemporal chaos [281]. Defect-mediated turbulence [99] appears in models of coupled oscillators, representing chemical reactions or convection, through spontaneous self-organization into patterns resembling fibrillation [124, 563]. Spinodal decomposition is another mode of phase transition that also produces fibrillation-like patterns during growth of co-existing phases along interface boundaries [202].

In conclusion, the simple population model and its potential surface, as developed so far, suggest that VT and VF are just opposite ends of a continuum of possible states, in terms of number of reentrant circuits. If this is true, we should be able to follow the transition of spatiotemporal cell dynamics, and the resultant ECG signals, across the continuum from one extreme to the other as APD_0 is lowered or raised. We might then be able to account for the entire spectrum of ECG subtypes, from simple large-amplitude monomorphic VT through to more complex low-amplitude polymorphic VF. This will be the subject of the next chapter.

Chapter 7

FIBRILLATION ELECTROCARDIOGRAM

7.1 Background

The body surface electrocardiogram is the only practical means, in most clinical settings, for obtaining information about the electrical state of the myocardium. It is noninvasive and adequate to diagnose most basic heart rhythms. A single lead is usually all that is required to monitor a patient's rhythm and distinguish sinus rhythm from VT and VF in order to initiate cardiac resuscitation, when indicated. Efforts to extract more information from ECG signals of VT and VF, beyond their simple recognition, have so far not been fruitful. Attempts have been made to characterize the VF signal by various statistical parameters, including mean frequency, amplitude, and scaling exponents [48, 83, 318], however, no measures of VF characteristics have yet been incorporated into clinical practice. The complexity of these signals suggests that they are rich in information. The challenge is to determine precisely what these signals, both temporally and spatially, might be able to reveal about the electrical behaviour of the myocardium.

Kac, in 1966, asked: "Can we hear the shape of a drum?" [262], referring to the general problem of finding the inverse solution of the source distribution, given a set of remotely measured signals. The analogous question relevant here is: "Can we hear the shape of fibrillation?" by measuring a set of remote ECG signals. If subtypes of VT and VF can be

better discerned and characterized, opportunities might arise for improved therapies. Precisely what information about electrical activity in the heart can we extract from the time series of a single lead of VT or VF? What further information might several leads add? Is it worthwhile to examine the entire spatiotemporal signal set from multiple lead body surface mapping during VT or VF, if such data was available clinically? Could such information influence clinical diagnosis or treatment of subtypes of tachyarrhythmias? These questions have not yet been answered, but need to be pursued since the ECG is the only accessible measurement of VF in practice, and embodies all the three-dimensional system dynamics transformed onto a two-dimensional surface. This chapter explores the relationship between intracardiac events and the features of the ECG signals generated by subtypes of simulated VT and VF, as various system parameters are varied within the cylinder heart CML model.

7.2 Ectopic

The simplest ECG that can be generated by the CML model is that due to a periodic source, either a repetitively firing ectopic focus or a solitary fixed spiral wave. For an ectopic focus of fixed frequency radiating concentric waves, the only relevant variables are the APD and the firing frequency, equal to the reciprocal of the cycle length. Since CL = APD + R + DI, the maximum frequency occurs when DI = 0. The role of both CL and APD on the ECG and body surface map is shown for various constant APD in Figure 7.1. The ectopic beat produces an ECG peak that radiates outward on the body surface from the source point. The largest amplitude occurs opposite the focus, while the amplitude is smallest a short distance on either side of the focus. When CL is kept constant at 52, there are some differences in the ECG time signals for APD = 16, 24, and 48, although these are subtle. Most notably, the equatorial peaks opposite the focus are sharper and more narrow for the shorter APD. The frequency spectra, obtained by Fourier transforming the time series for these cases, exhibit a solitary spike at $f^* = 1/CL$ (not shown), and are virtually indistinguishable, except for a slightly smaller peak and lower energy for the shorter APD. This suggests that, while the CL can be easily estimated from a narrow banded ECG frequency spectrum, it is unfortunately not possible to extract any

estimate of APD from this information alone, even in this simple case. The ECG frequency spectra around the cylinder, originating from an ectopic focus, are shown in Figure 7.2, and are narrow as expected. The CL histogram (not shown) is a solitary spike at CL = 42. The peak frequency is 1/42 = 0.024 which, assuming each time unit is 5 ms, corresponds a period of 210 ms and a frequency of 4.76 Hz.

The effect of changing the ectopic cycle length with constant APD = 24 is shown in Figure 7.2. The ECG amplitudes are smaller for the higher frequency sources, since more waves with cancelling dipole contributions fit in the domain. It is also noteworthy that the lowest amplitude spatial regions around the ectopic foci are wider at the higher frequencies. All cases are shown after a steady state has been reached, after which the initial waves have expanded to fill the domain.

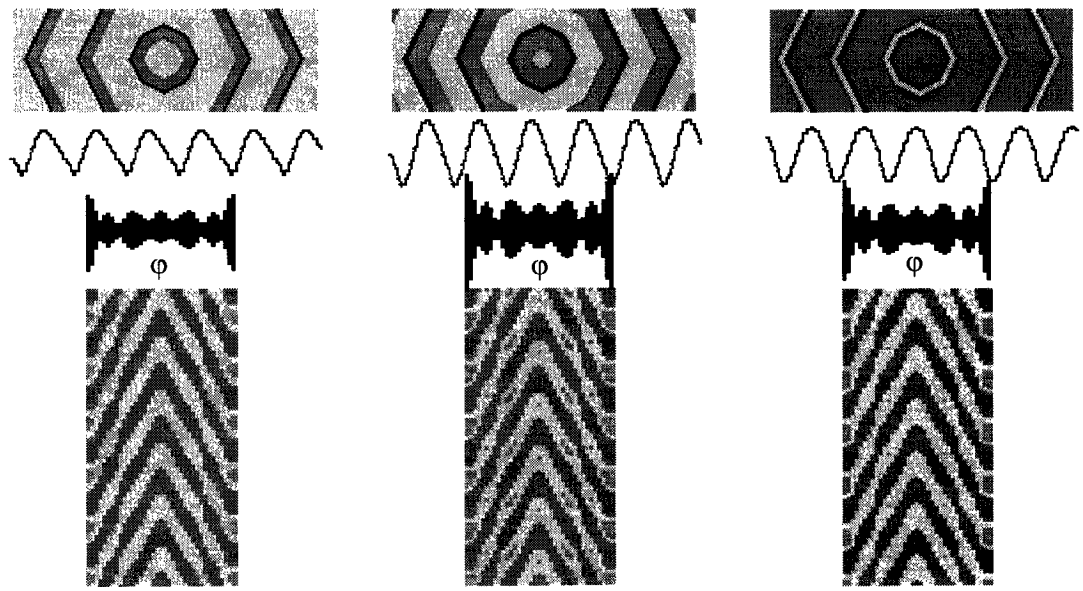

Figure 7.1. Ectopic focus radiating waves at CL = 52 (top). The role of APD = 12, 24, 48 is minimal in the single ECG lead measured directly over the focus, shown below the wave field. The envelope of maximum ECG amplitudes around the equatorial ring is somewhat larger for the longer APD. The body surface time-space maps are also remarkably similar, exhibiting small amplitude differences only.

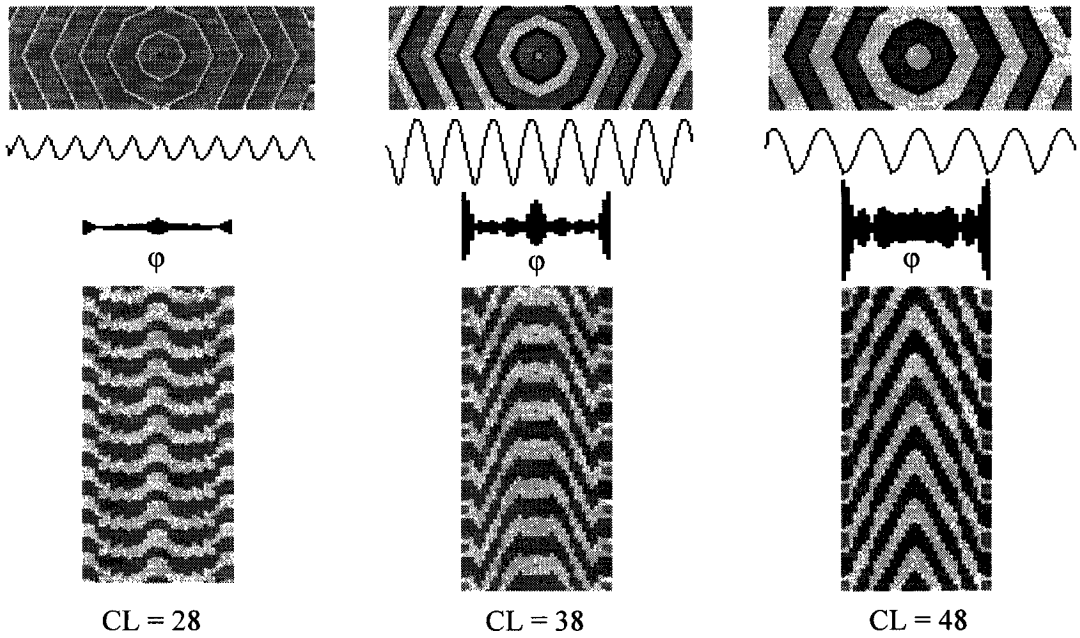

Figure 7.2. Ectopic focus with constant APD = 24 radiating waves at various CL = 28, 38, 48. The role of CL on the ECG is quite significant, much more so that of than APD. The amplitude of the single lead, measured directly over the focus, is smallest for the shortest cycle lengths where there is greatest cancellation of wave contributions to the ECG. The envelope of maximum ECG amplitudes around the equatorial ring is largest for the longer CL. The body surface time-space maps are quite different for each CL, in terms of relative amplitudes and spatial phases.

The ECG pattern of an ectopic source with APD = 36 and CL = 42 is shown in Figure 7.2. The time signals give rise to narrow-banded frequency spectra in all leads, with a peak frequency at $f^* = 1/CL$. The amplitude envelope of the equatorial leads is smallest at the most rapid frequency due to interference and partial cancellation of the dipole contributions of multiple concentric waves. In all cases, the maximum amplitude occurs opposite the ectopic source.

When a regularly beating ectopic focus occurs in the presence of restitution, where $APD_o < APD_m$, the ectopic cell can fire as soon as its refractory period R has expired, even at steep restitution. Consequently, DI is always close to zero, and since APD is nearly constant at APD_o, there is little opportunity for aperiodicity, quasiperiodicity, or chaos to

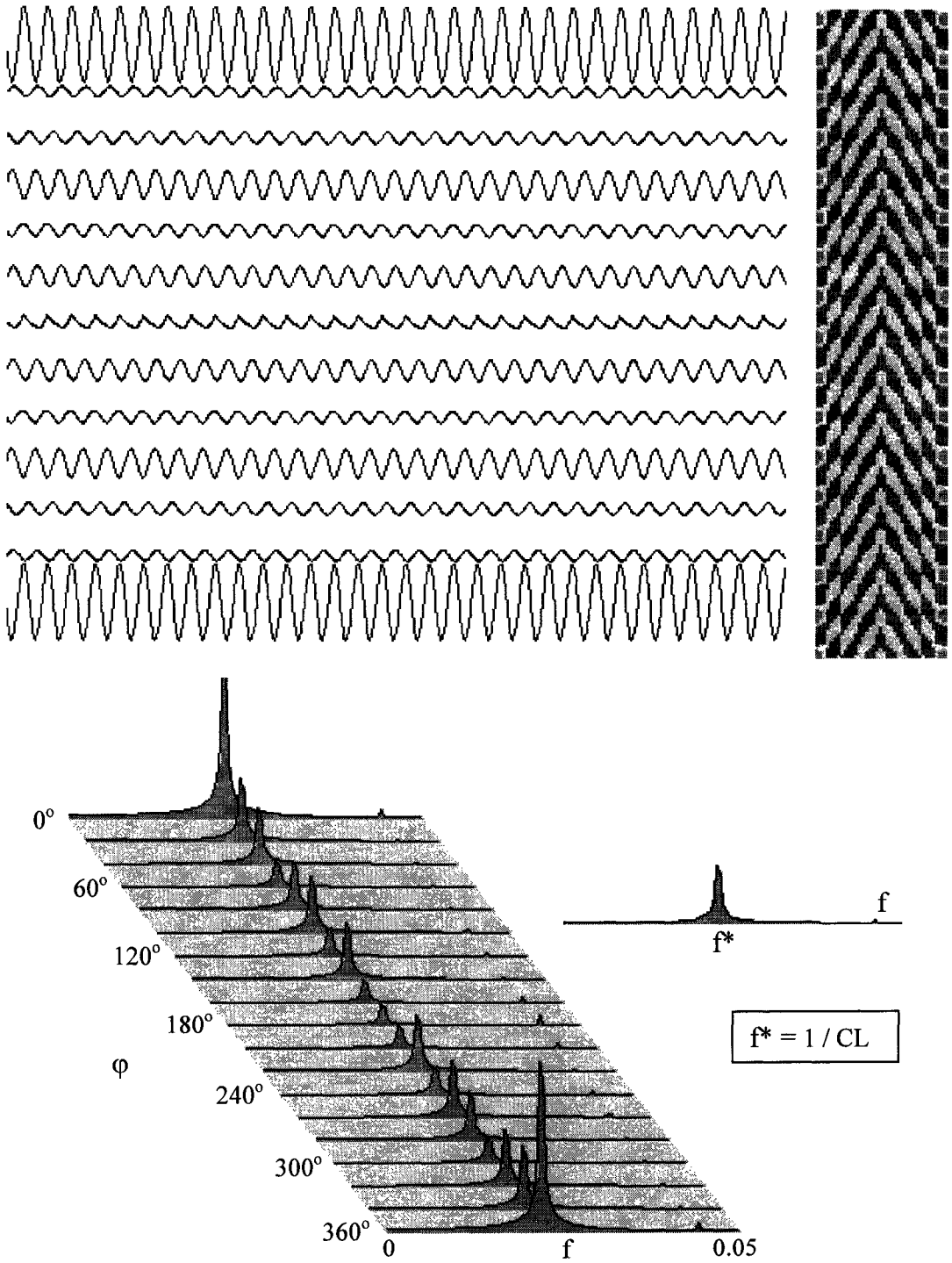

Figure 7.3. Ectopic focus with constant APD = 36, CL = 42. Equatorial ECG leads are shown at 30° intervals along with the complete body surface map space-time plot (top), the frequency spectrum for each lead (bottom), and the average spectrum (right).

develop from an ectopic focus when DI is constant. All APD and cycle lengths are also constant, giving a perfectly periodic ECG. The main variable affecting this ECG is the cycle length, which is close to $1/(APD_o + R)$, and since APD migrates down toward APD_o, this controls the dominant frequency of the ECG. Once APD settles to a constant value, the restitution curve plays no role and there is no significant difference from the previous cases described. In summary, these are the ECGs of monomorphic VT driven by an ectopic focus.

7.3 Reentry

Can the ECG of a reentrant circuit be distinguished from that of an ectopic focus? We will examine a solitary spiral wave with constant APD. When the APD in the model is constant and below about 30, the core remains stationary. All DI are approximately equal giving a monomorphic ECG. At higher APD, however, the diastolic interval or excitable gap becomes spatially nonuniform, and fails to settle to a single value. This causes the core to move within a small region. The failure of small DI transients to dissipate entirely might be a numerical artifact from the discrete nature of the model. The ECGs for these cases of reentry are polymorphic, due in part to drifting of the core within a small area.

In order to re-establish a monomorphic pattern due to a fixed spiral wave, the core was anchored by a small inexcitable obstacle. This keeps the DI constant, and forces all cells to have constant CL. If the obstacle is chosen to be small enough, it anchors the spiral wave, but the artificial core does not affect the ECG. This allows a uniform excitable gap to be re-established, and also prevents wave break and core point movement, even for cases of very steep restitution. An undesirable side effect of using an obstacle anchor is that, for a constant propagation velocity, the cycle length is determined by the obstacle circumference rather than the natural dynamics of the core. Figure 7.4 shows the ECGs of a single spiral wave for various constant APD with the core being anchored.

To specifically compare ectopic monomorphic VT with that of reentrant sprial wave VT, it is necessary to keep the source frequency and APD equal for both cases. A comparison

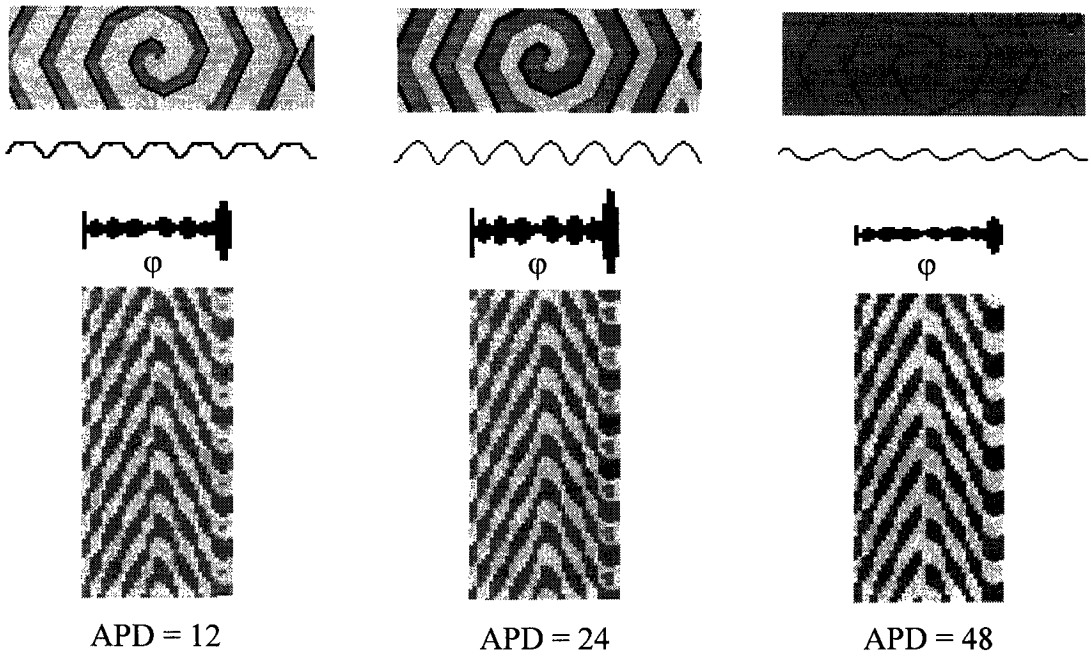

Figure 7.4. Spiral wave radiating waves at CL = 52 (top). The role of APD = 12, 24, 48 is again minimal, as can be seen in the single ECG lead measured directly over the focus shown below the wave field. The envelope of maximum ECG amplitudes around the equatorial ring is somewhat smaller than that for the ectopic focus. It is largest at intermediate APD. The body surface time-space maps are also very similar.

is shown in Figure 7.5. Here a small 3x3 obstacle anchors the spiral wave to prevent drift, and gives CL = 42 for the chosen APD = 36, the same two parameters used in the previous simulation of the ectopic focus. The ECG similarities between these two mechanisms of monomorphic VT are perhaps more striking than any differences. The similarities are in the ECG amplitudes, which are both maximal opposite their respective sources, and the presence of four peaks around the heart equator. There are some small differences. The ectopic focus produces a slightly higher ECG amplitude, which has a slightly more prominent "dome and dagger" morphology in the smaller leads, while the spiral wave tends to produce a more sinusoidal shaped ECG in most leads. The locations of the amplitude peaks are slightly shifted around the heart equator relative to those of the ectopic focus. The averaged frequency spectra are almost identical for the two cases, except the ectopic focus has a higher mean amplitude peak and contains more energy.

These simulations and others run at different frequencies show that there are no strikingly obvious characteristics that would allow easy visual distinction between focal and fixed reentrant monomorphic VT based on the ECG signals alone, despite this model being stripped to its greatest simplicity. This issue has important clinical implications, however, because these two entirely different mechanisms of VT cannot generally be distinguished from each other, yet their optimal management is different. The time series must be subject to more detailed analysis in order to extract more information that would allow these two fundamental types of VT to be separated by ECG monitoring alone.

7.4 Fibrillation

Fibrillation can be established in the model either with constant APD or with restitution $APD_o < APD_m$. We will first consider cases with constant APD. Figure 7.6 shows three examples of fibrillation with APD = 24 shown after self-organization from different random initial conditions. In each case, the DI and CL histograms are virtually identical (not shown), but the body surface ECG space-time plots are obviously quite different, indicating differences in the spatial distribution of core points. The repeating spatial pattern indicates that the core points are fixed in location. Since the number of possible core point spatial combinations and patterns are astronomical, even for the core point numbers N_c encountered in the model, on the order of N_c factorial, we must deal with ECG characteristics statistically.

The first issue is whether there is a difference in ECG characteristics between a solitary spiral and a field of multiple spirals when APD is constant and the CL distribution is identical, such that the only difference is the number of core points N_c. In other words, can the ECG signals distinguish solitary spiral "VT" from multiple spiral "VF" when all other conditions are equal? Compare the simulation with APD = 36 having $N_c = 1$ started as a single spiral in Figure 7.5, with a that of multiple spiral field allowed to self-organize from a random field, settling to $N_c = 10$ in Figure 7.7. Both runs produce virtually identical histograms, with mean DI = 6.8 and CL = 42.8. The APD distribution p(APD) is a spike at 36. The DI entropy is similar at about 1.7 for both cases, independent of N_c.

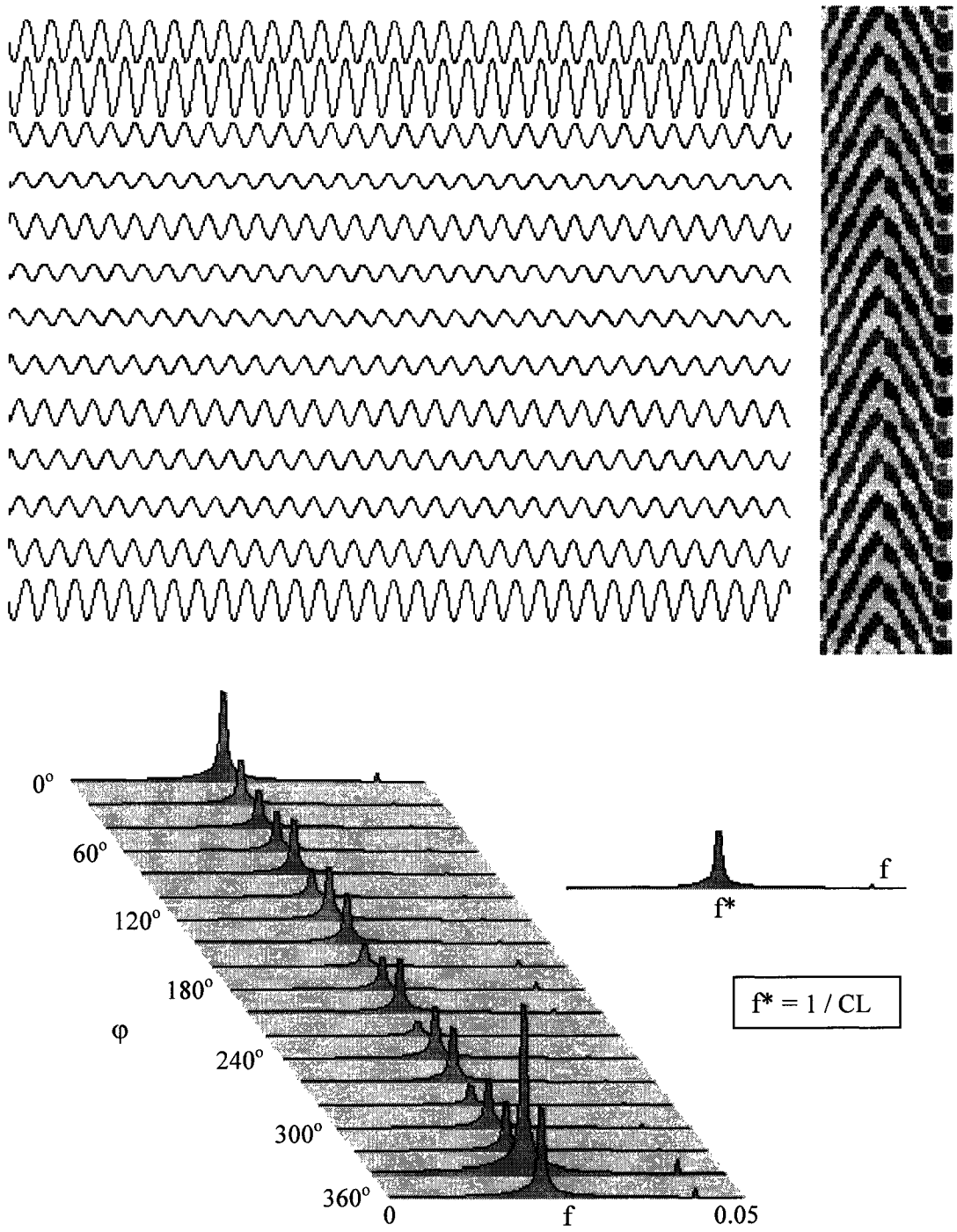

Figure 7.5. Solitary spiral wave with constant APD = 36, CL = 42. Equatorial ECG leads are shown at 30° intervals along with the complete body surface map space-time plot (top), the frequency spectrum for each lead, and the average spectrum (bottom). The similarities with the ectopic case in Figure 7.3 are noteworthy.

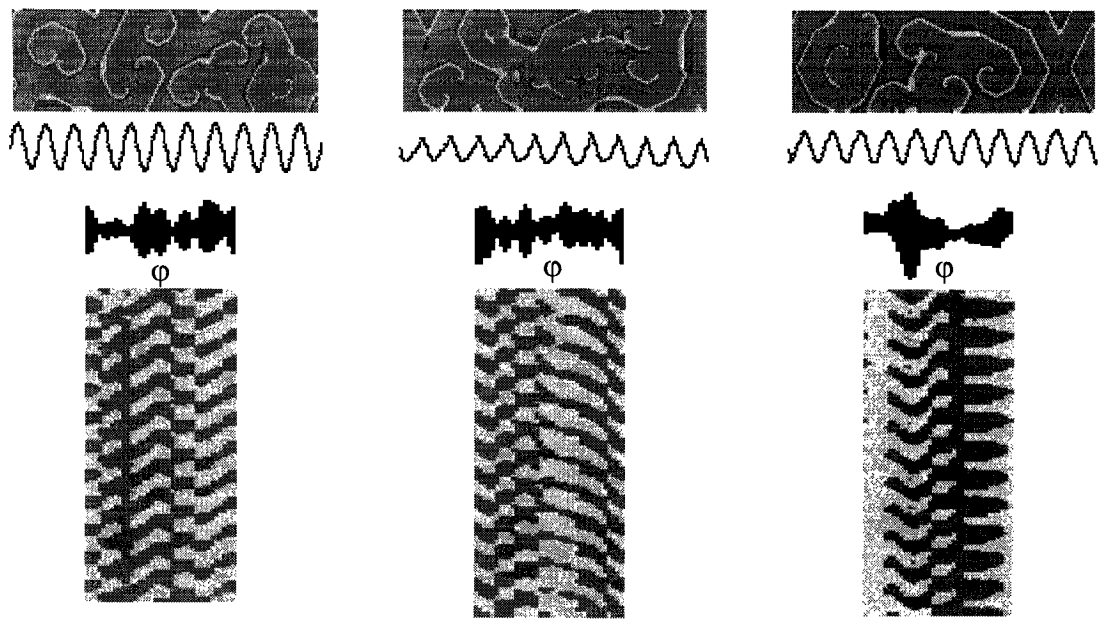

Figure 7.6. Multiple spiral wave fibrillation with APD = 24 self-organized from different random initial conditions. The frequencies of the ECG signals are the same, but the spatial patterns are different, as can be seen in the envelopes of maximum ECG amplitudes around the equatorial ring and the body surface time-space maps.

Figure 7.8 summarizes the ECG characteristics for the ectopic source, solitary spiral, and multiple spiral fibrillation for these cases with APD = 36. The solitary spiral ECG leads have an average V_{rms} = 9.69 [range 2.07 - 26.52], while that of the multiple spirals has a similar mean, but much lower range V_{rms} = 11.7 [range 7.79 - 17.52]. Multiple spirals evidently attenuate the dipole contributions to any given lead, producing a generally lower range of ECG amplitude. The frequency spectra of these two cases are also very similar. This is not a surprising finding given that the CL histograms are essentially the same. Since the time signals are similar, except for amplitude, the only distinguishing feature between these two cases, where N_c = 1 and N_c = 10, is the spatial pattern of the ECG over the body surface. Although no major characterizing features are obvious, solitary spirals tend to produce their peak amplitudes on the body surface opposite the core point, and their lowest amplitudes in a zone over the core. Multiple spirals, like fibrillation, produce a less consistent spatial pattern with less amplitude variation between leads.

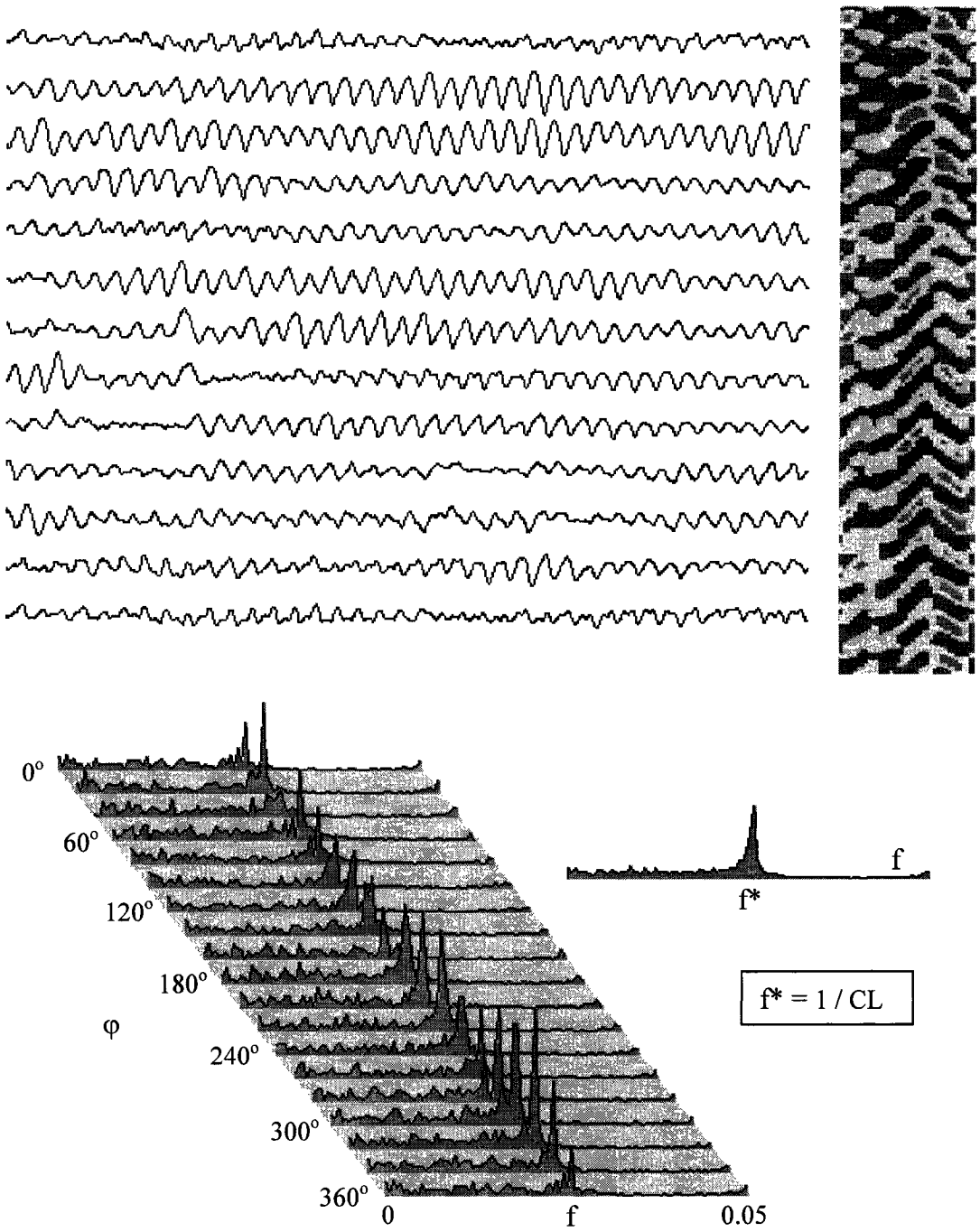

Figure 7.7. Multiple spiral wave fibrillation with constant APD = 36. Equatorial ECG leads are shown at 30° intervals along with the complete body surface map space-time plot (top), the frequency spectrum for each lead, and the average spectrum (bottom). Amplitudes are lower than the solitary spiral case due to dipole attenuation from more waves around $N_c = 10$. Spectral energy at low frequencies is due to core point drift.

If we now introduce APD restitution, such that $APD_0 < APD_m$, there will be dispersion of DI, APD, and CL, as seen previously in the histograms of Figure 4.9. This begs the question of whether restitution-induced APD dispersion, due to a nonuniform DI, widens the CL histogram, and therefore adds more frequency components to ECG spectrum. In other words, we would expect the ECG spectrum to be wider at lower APD_0. To investigate this question, while controlling for spiral wave drift and break-up at steep restitution, a small obstacle was placed at the core to ensure the clean solitary spiral did not break up at short APD_0. Runs were then repeated at various APD_0 with $APD_m = 48$.

Solitary spiral "VT" ECGs are shown in Figure 7.9, sampled at 10 degree intervals around the body surface equator, for a spectrum of APD_0 from 48 down to 32 where the wave remains stable without breaking. Fibrillation ECGs with APD_0 from 48 down to 12 are shown in Figure 7.10. The ECG signals are narrow-banded at flat restitution with $APD_0 = 48$, while there is vigorous wave break at lower APD_0 where the ECG signals are highly irregular. The space-times plots indicate relatively stable fixed patterns at higher $APD_0 > 32$, and highly dynamic patterns at lower $APD_0 < 32$.

Frequency power spectra S(f) averaged over 36 leads for $APD_0 = 12$ to 48 are compared with the cycle length histograms p(CL) in Figure 7.11. Both are widest at low APD_0, and become narrow as restitution is flattened toward maximum $APD_0 = 48$. Peak frequency f* is clearly discernible down to $APD_0 = 28$, but disappears at steeper restitution, where it becomes difficult to characterize any preferred frequency. Differences in peak frequency are generally fairly minimal. Peak frequency $f^* = 0.025$ corresponds to $CL = 40$. The central tendency of CL histograms are easier to quantify. Ideally, we would like to be able to measure the frequency spectrum of the body surface ECG signals and infer the CL distribution in order to quantify intracardiac activity. Given the wide dispersion of S(f), this does not seem possible based on averaged frequency spectra.

ECG amplitudes were compared for VF at various restitution slopes. Random initial conditions were allowed to self-organize as usual, and once a statistical steady state appeared to be established, ECGs were obtained in 36 equatorial leads. The root mean

square (rms) amplitudes were calculated for the time series of each individual lead and for all lead data sets combined, and are shown in Figure 7.12. As APD_o was raised, the rms amplitude for all leads decreased then increased, with a minimum appearing around 32 to 40. The rms amplitude of the largest lead increased considerably beyond APD_o = 36. The range of rms amplitudes was fairly narrow at lower APD_o and became large at higher APD_o. This finding reflects the tendency of highly dynamic VF to spread its energy around all leads at low APD_o because there is no preferred spatial pattern. At higher APD_o, the spatial pattern tends to be much less variable, as core points tend to lock into fixed locations causing specific leads to become favoured according to the positions of underlying relatively stationary and coherent spirals.

	Ectopic	Spiral	Fibrillation
N_c	1	1	10
S_C	0	1.08	1.73
S_D	0	1.72	1.79
μ_C	42.0	42.8	42.8
μ_D	6.0	6.8	6.7
V_{rms}	9.69	9.69	11.70
V_{rms} min	2.06	2.07	7.79
V_{rms} max	25.07	26.52	17.52
V_{rms} Δ	23.02	24.45	9.54

Figure 7.8. Characteristics of ectopic, spiral, and fibrillation for the same APD = 36. Mean DI μ_D and mean CL μ_C are similar for the solitary spiral and multiple spirals. There are essentially no significant differences in ECG amplitudes or distribution between the ectopic focus and the spiral wave. V_{rms}min and V_{rms}max are the minimum and maximum values of the ECG sampled over all leads. Fibrillation has a similar mean V_{rms} averaged over all leads, but much less heterogeneity of individual lead V_{rms} due to greater dipole attenuation from multiple waves moving in many directions.

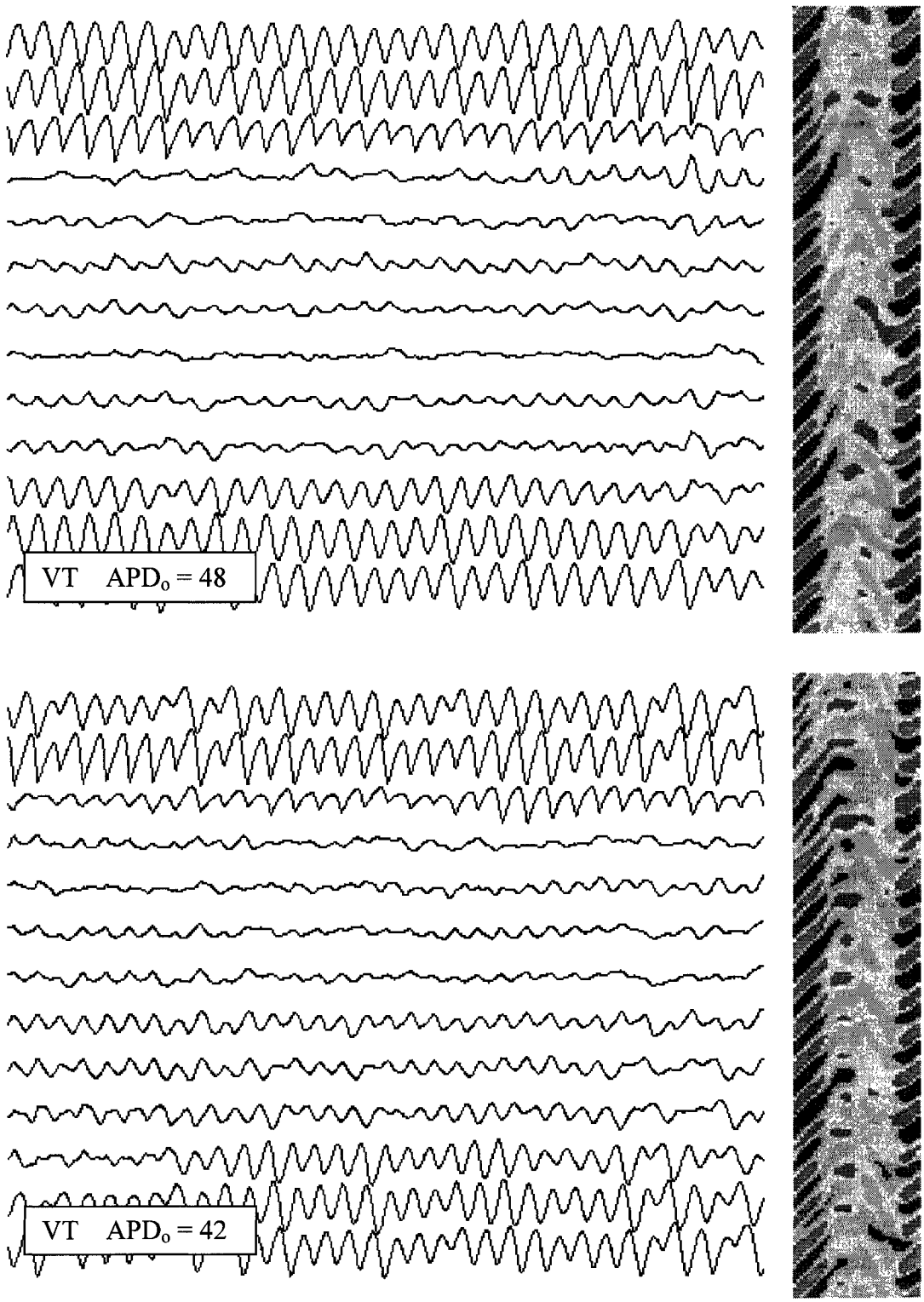

Figure 7.9 (a). ECG of solitary spiral "VT" with $N_c = 1$. $APD_m = 48$, $APD_o = 48, 42$.

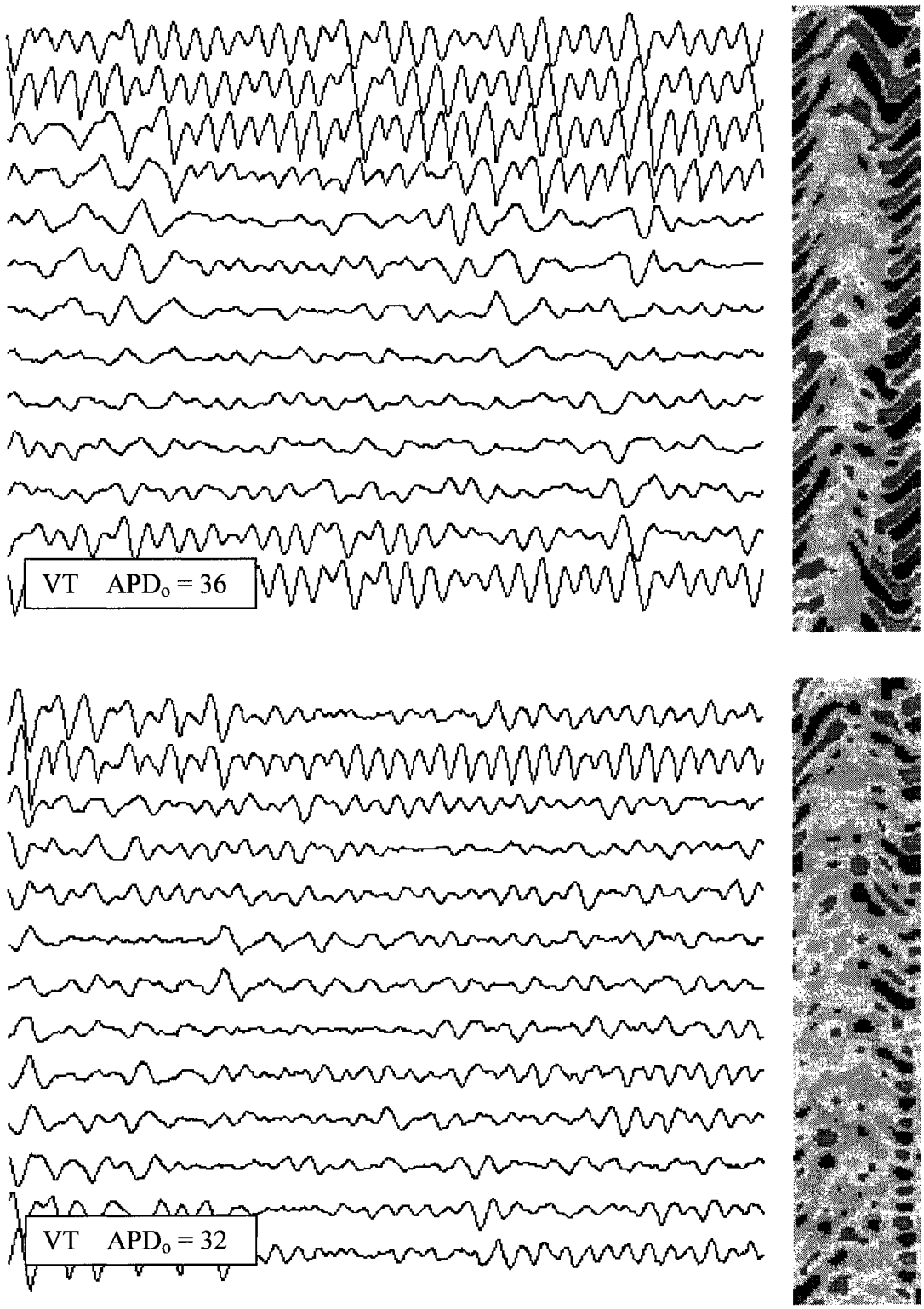

Figure 7.9 (b). ECG of solitary spiral "VT" with $N_c = 1$. $APD_m = 48$, $APD_o = 36, 32$.

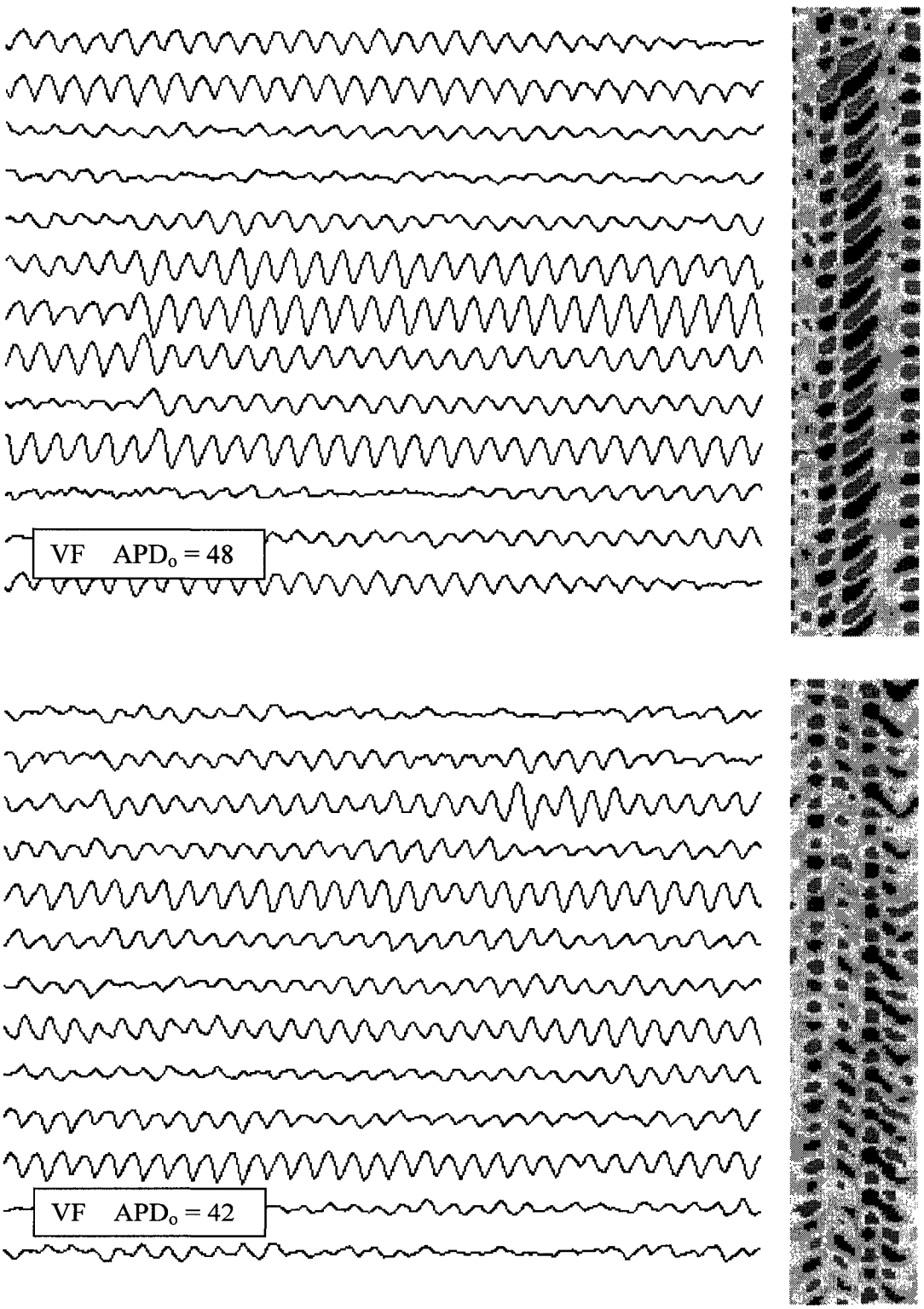

Figure 7.10 (a). ECG of multiple spiral "VF" with $N_c > 1$. $APD_m = 48$, $APD_o = 48, 42$.

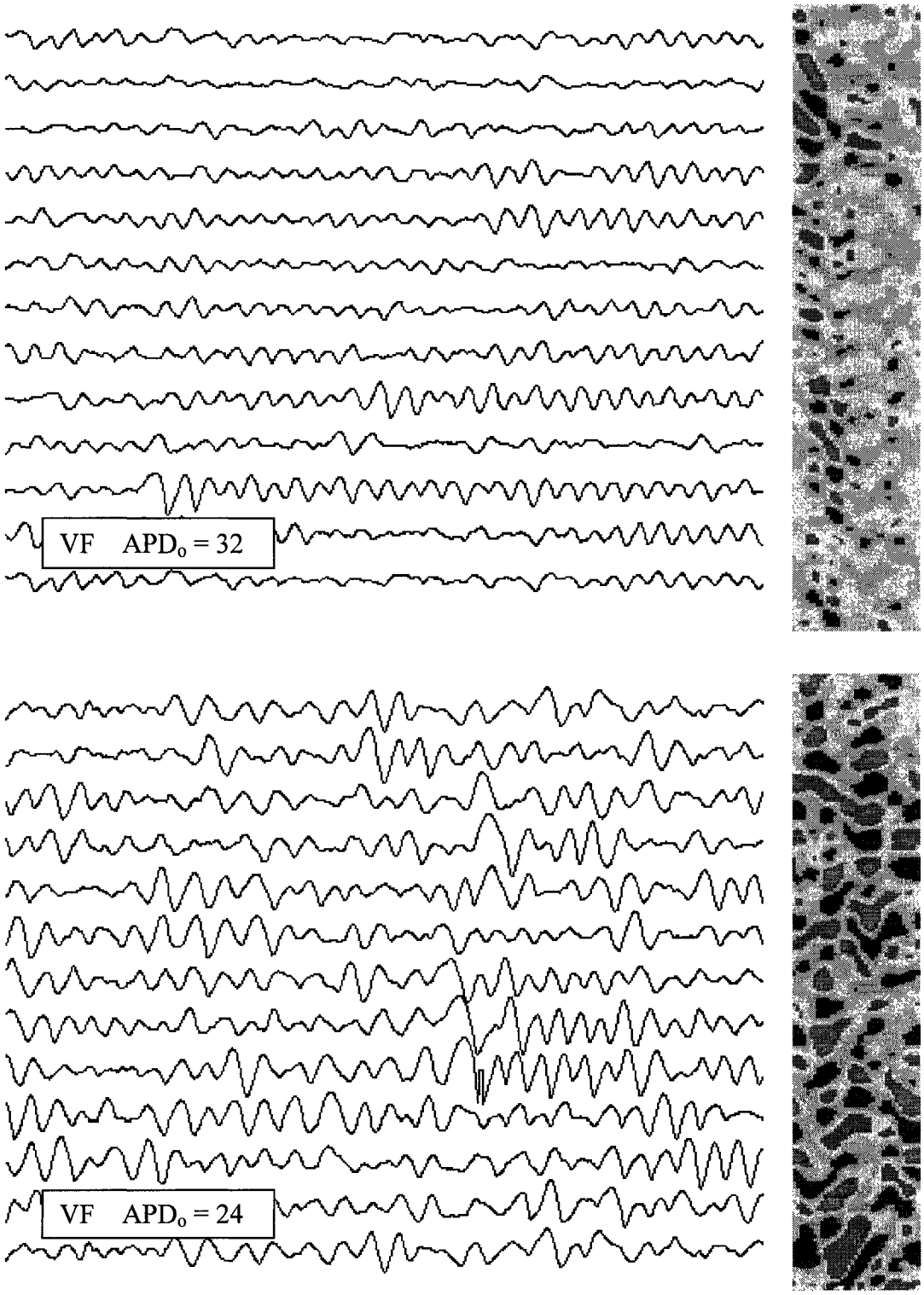

Figure 7.10 (b). ECG of multiple spiral "VF" with $N_c > 1$. $APD_m = 48$, $APD_o = 32, 24$.

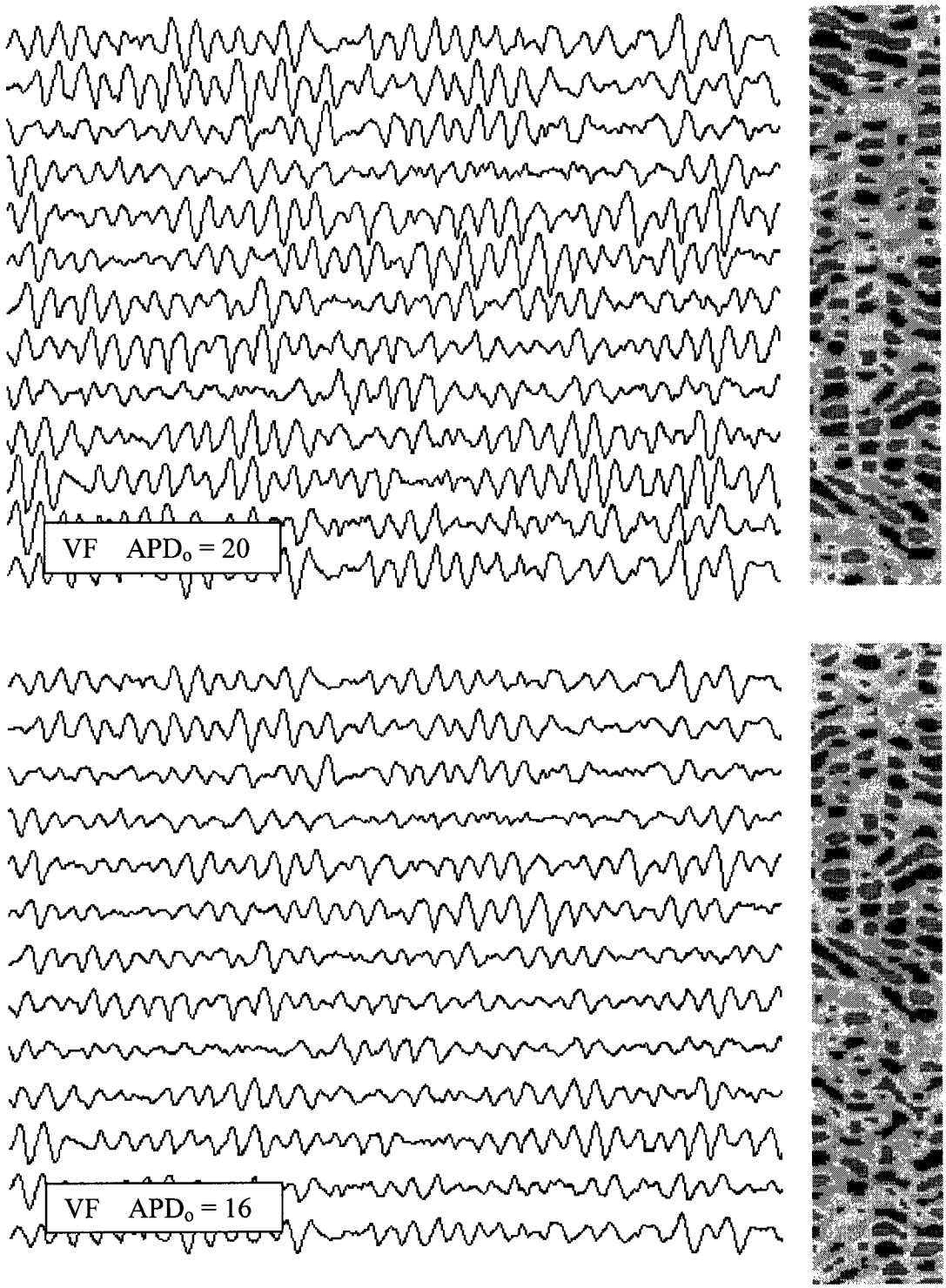

Figure 7.10 (c). ECG of multiple spiral "VF" with $N_c > 1$. $APD_m = 48$, $APD_o = 20, 16$.

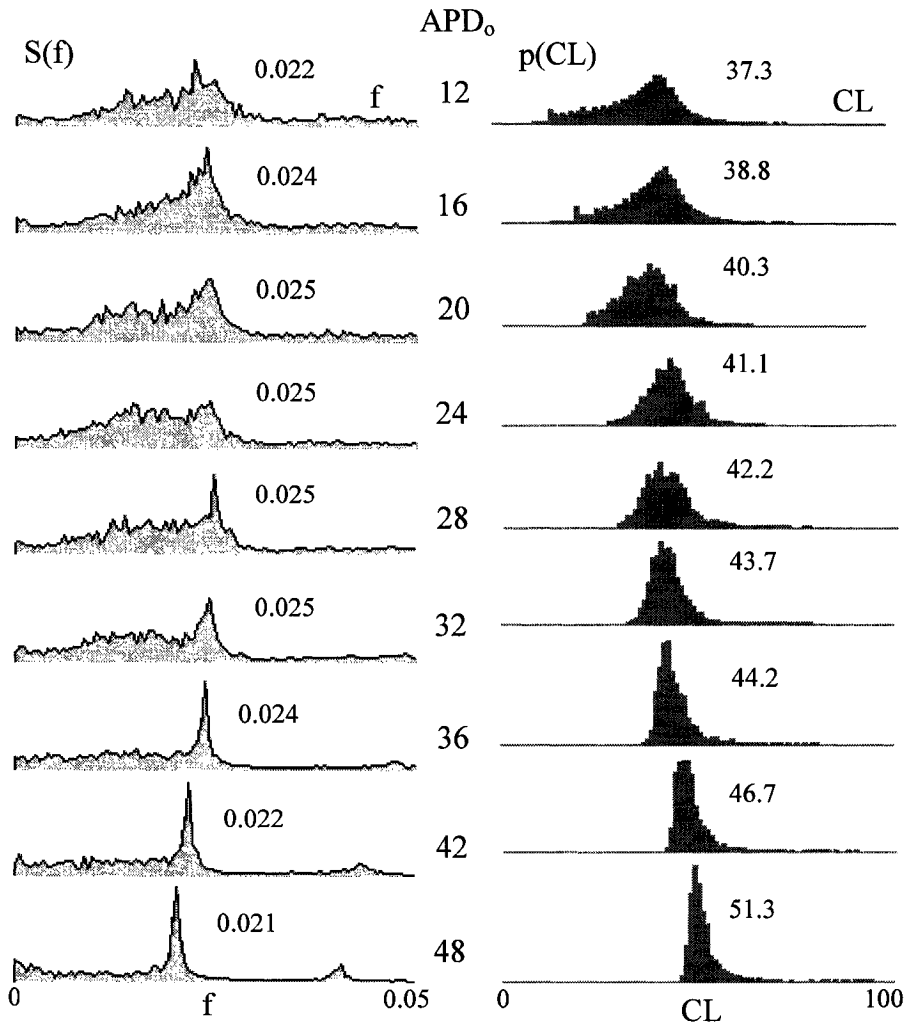

Figure 7.11. Frequency spectra of the ECG from multiple spiral VF averaged over all 36 leads for each APD_0 on the body surface (left). The corresponding CL histogram for each APD_0 from the heart (right). Longer APD_0 produces more organized wave activity with a more regular wave pattern approaching periodicity. This is associated with a more narrow CL histogram and a narrow-banded frequency spectrum. At steeper restitution, the distributions are both wider. Higher mean CL corresponds to lower peak frequency. The peak frequency f* (left) and mean cycle length CL* (right) are shown.

Exactly how does the CL histogram generated within the heart relate to the frequency spectrum of the ECG measured on the body surface? We have already seen that the peak frequency for a regular solitary source is simply $f^* = 1/CL$. This is intuitively obvious for a single frequency corresponding to a spike CL histogram. If more frequency components

are present, does the spectral width relate to the CL width? Conversely, a spike in the ECG frequency spectrum, along with a stationary body surface map, must imply that constant APD is being generated from a fixed focus, but exactly how does the CL histogram relate to the frequency spectrum of the ECG?

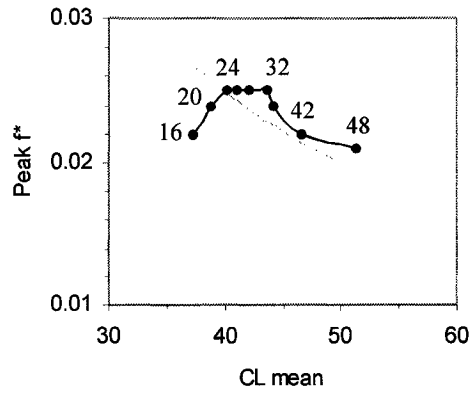

Figure 7.12. Relationship between peak frequency f* of the ECG signal of VF for various APD_o (labels) are compared with the mean cycle length CL* (black). The expected peak frequency is f = 1/CL* (grey). The agreement is not good in the low frequency range due to considerable spectral energy dispersion shown in Figure 7.11. Peak frequency f* in the ECG is, therefore, not necessarily a good predictor of the mean CL*, according to this model.

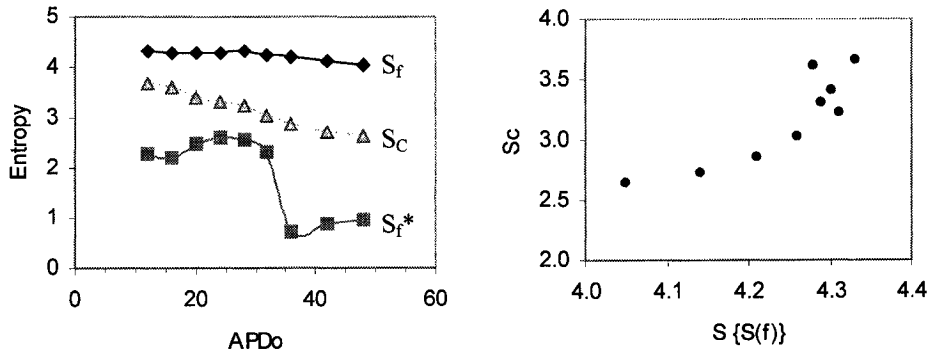

Figure 7.13. Width of both the frequency spectrum S(f) and cycle length histogram p(CL) are expressed as entropies, as functions of APD_o (left). The entropy of S(f) is shows little change with APD_o, while S_c is the entropy of CL, and decreases with APD_o. Modified entropy S_f*, presented for illustration, was calculated by truncating the lowest 10 percent of the spectral energy to enhance the contributions of the spectral peaks. Entropy of S(f) does show a relationship with Sc (right), but the range of spectral entropy $S\{S(f)\} = S_f$ is very narrow, ranging between 4.0 and 4.4.

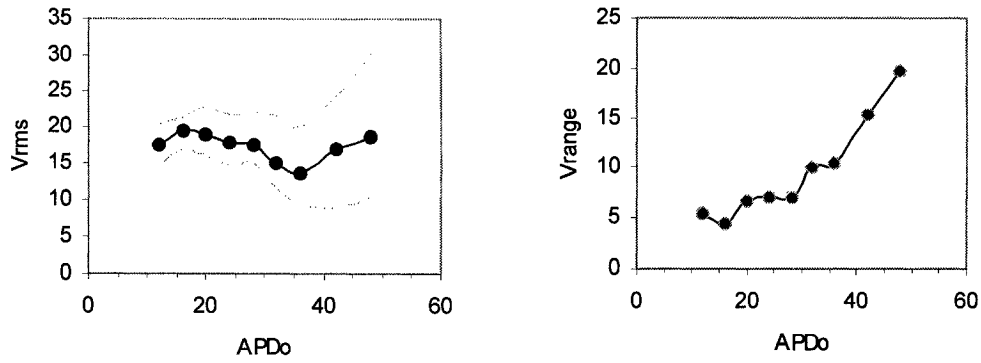

Figure 7.14. The ECG amplitude expressed as the mean of V_{rms} of the 36 leads shown as a function of APD_0 (left). The maximum and minimum V_{rms} of individual leads is shown by the grey lines. The difference is called the V_{rms} range, and is shown enlarged (right).

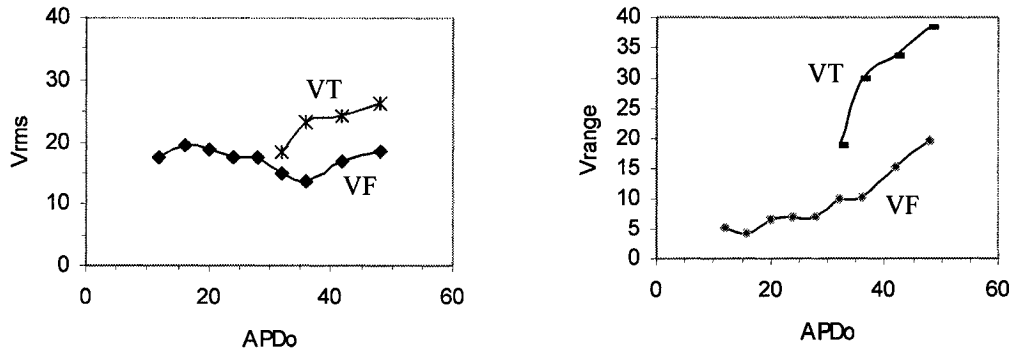

Figure 7.15. The mean of V_{rms} averaged over 36 leads (left), and the V_{rms} range (right) of all individual leads are shown for VF and VT (left). The range is much higher for VT than for VF.

Specifically, does the CL histogram entropy correlate with the ECG frequency entropy? Figure 7.12 shows the entropies of the CL histogram p(CL) and the frequency spectrum S(f). Unfortunately, the spectral entropy is not sufficiently specific to APD_0 to permit a good relationship. Perhaps there are better mathematical methods of signal processing to compare CL histogram complexity with ECG complexity. The methods of nonlinear dynamics, such as embedding dimension, various fractal dimensions, or measures of power law scaling [449], might be useful for relating these measures, but will not be addressed here.

Figure 7.14 shows how ECG amplitudes V_{rms} change with APD_o. There is not a unique relationship between V_{rms} and APD_o that would allow prediction of APD_o based on measured V_{rms}. The range, or difference between minimum and maximum V_{rms} of individual leads, however, does change substantially with APD_o. This suggests that the V_{rms} range might be the best body surface predictor of intracardiac APD_o. Figure 7.15 shows the V_{rms} range for both single spiral VT and multiple spiral VF, as functions of APD_o. VT clearly has a larger amplitude and a clear functional relationship. The ECG of fibrillation has a low amplitude range at short APD_o, where wavelets are very small, because the dipoles from positive and negative slope segments of the spatial action potential profile are closest together. The respective dipole contributions to the ECG voltage tend to cancel because of the vanishing difference in distances R_k in the denominator of the ECG equation (3.2). The largest ECG amplitude should occur when the spatial wave structure has a much larger scale such that, at the points of ECG extrema, there exists a dominance of either positive or negative dipole contributions, but not both simultaneously, within the lateral peak $W(R, \varphi)$ zones. Figure 7.14 shows the effect of spiral waves of various APD_o on the ECG amplitudes. The maximum ECG tends to decrease as the wave structure is made smaller.

Some important questions remain unanswered. Based on body surface ECG measurements, how can we determine the location of the source foci? This will require application of matrix-based inverse solution techniques. Is it possible to extract the CL histogram from the ECG? This has not yet proved to be possible using the CML model, due to poor specificity of p(CL) for given S(f). Furthermore, might we somehow get DI or APD from derived CL data, if such information were available? If we could somehow better determine the CL histogram from the frequency spectrum, could we then extract information about APD restitution? Can we get the APD and DI histograms? There might not be a unique relationship to determine APD characteristic if we are only given CL, and therefore determination of APD might not be possible. Perhaps the spatial BSPM can help resolve the ambiguities somehow through calculation of the inverse solution. More work will be needed to help resolve these issues.

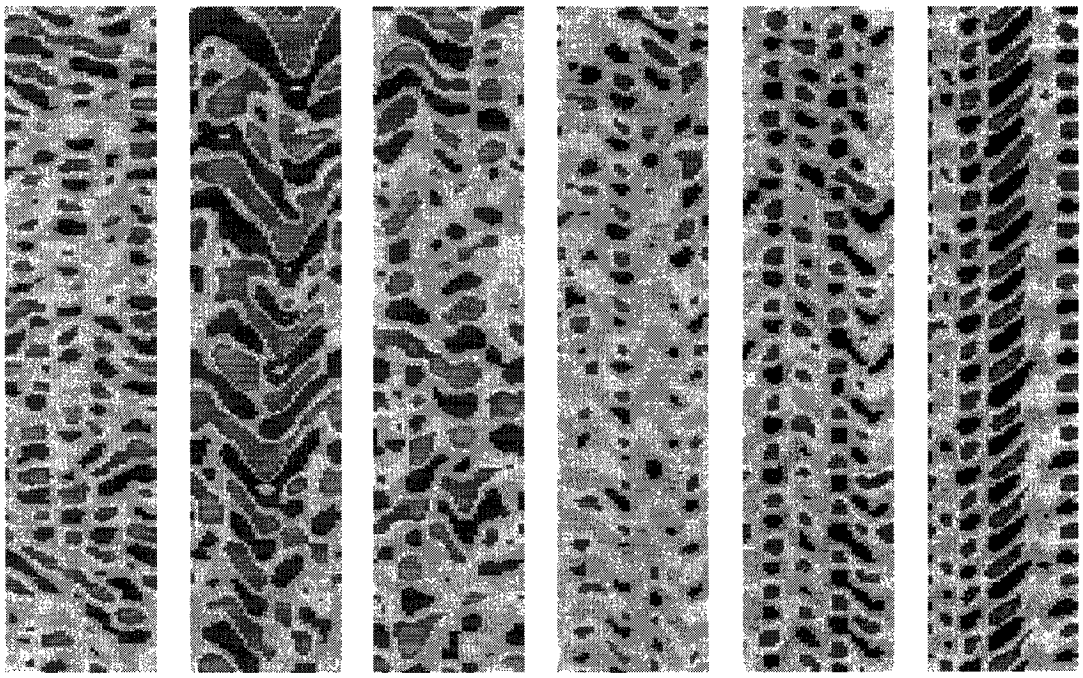

Figure 7.16. Spatiotemporal patterns of the body surface electrocardiograms of VF for fixed $APD_m = 48$, and various APD_0 as labelled. Note that $APD_0 = 20$ gives the largest characteristic size of the ECG pattern. The spatial pattern appears "locked-in" for the cases where $APD_0 > 32$, shown in the last three frames at right.

7.4 Obstacle Anchoring

An obstacle within excitable tissue has the potential to capture a reentrant circuit and become a centre of rotation around which an advancing wave front can revolve and stabilize [245, 495]. Such an obstacle might be a pre-existing infarct or region of ischemia, or a hole like a blood vessel. This possibility was recognized in 1920 when Lewis mapped wave activation moving around the great vessels of the dog atrium [313]. Since then it has been assumed that most cases of monomorphic VT are due to reentry around some such anchoring structure [50, 139, 404], although in practice it is difficult to prove this conjecture without invasive mapping.

The CML model can be used to investigate the role of an inexcitable obstacle on wave behaviour. For a constant isotropic propagation velocity, the obstacle circumference determines the rotation period and cycle length, regardless of APD. A smaller obstacle allows a higher frequency of rotation with shorter CL to develop, as shown in Figure 7.17. The APD and DI that emerge are determined by the compatibility condition that they must sum to this value of CL. The values of APD and DI can be found where the restitution curve intersects the unity negative slope line that meets both axes at CL + R, as was shown in Figures 3.14 and 4.15. If this intersection point falls on the segment of the restitution curve with slope < 1, the reentrant circuit behaviour is periodic and stable. If the slope is >1, the rotation period might be constant, but is unstable to perturbation and can potentially break into quasiperiodicity. We would then expect to see a transition from monomorphic to polymorphic VT, which would occur through a bifurcation.

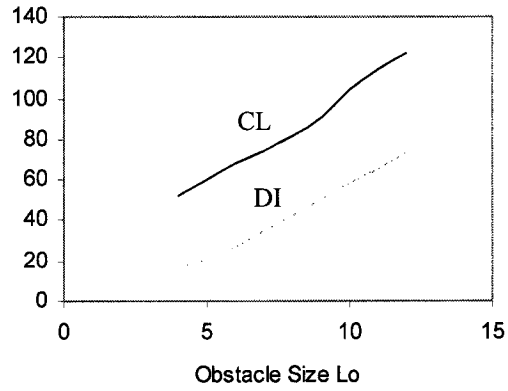

Figure 7.17. A square inexcitable obstacle at the core anchors a spiral wave with APD_0 = 20. The obstacle size L_o determines the perimeter, which in turn controls the rotation period CL and diastolic interval DI. These influence APD through the restitution curve. APD remains essentially constant, without bifurcation, down to a 4x4 obstacle, below which APD irregularity develops.

When a solitary spiral was established around obstacles of various sizes from 3x3 to 16x16 at various restitution slopes characterized by APD_0, the rotation period CL is a linear function of the obstacle size L_o, and therefore circumference, indicating a constant propagation velocity around the hole. If APD and CL are constant during wave rotation

around the obstacle, the ECG should approximate a sine wave with a period equal to CL = APD + DI + R. The exception would be at short CL with steep restitution, where small obstacles give low APD_o. We can predict where the bifurcation in APD would occur at short DI by referring back to Figure 4.17 showing the critical CL, below which APD breaks away from 1:1 morphology into alternans. This line is redrawn in Figure 7.18, along with the lines of cycle length dependence on obstacle size $CL = f(L_o)$. ECGs that depart from sine waves should appear where CL falls below the solid curve for a given obstacle size L_o, indicating the onset of APD alternans.

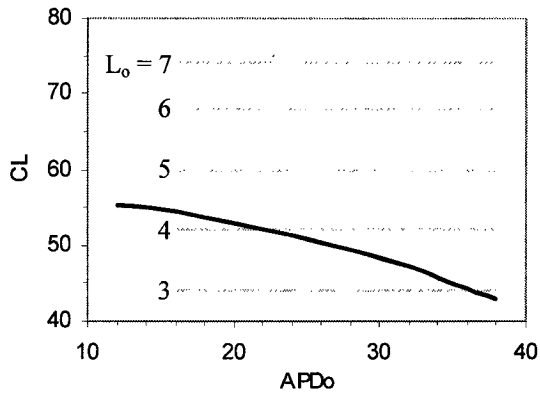

Figure 7.18. The solid curve shows the boundary based on restitution curve slope m = 1, below which APD bifurcates into alternans. If the rotation period CL of a spiral wave travelling around a square obstacle of size L_o is above this line, all APD are equal and the ECG should approximate a sine wave. If CL falls below this solid line, which occurs only for the smallest obstacles at steepest restitution, the resultant ECG should show some irregularity in morphology due to APD nonuniformity. According to this diagram, this occurs for $L_o = 4$ below $APD_o = 22$, and for $L_o = 3$ below $APD_o = 35$.

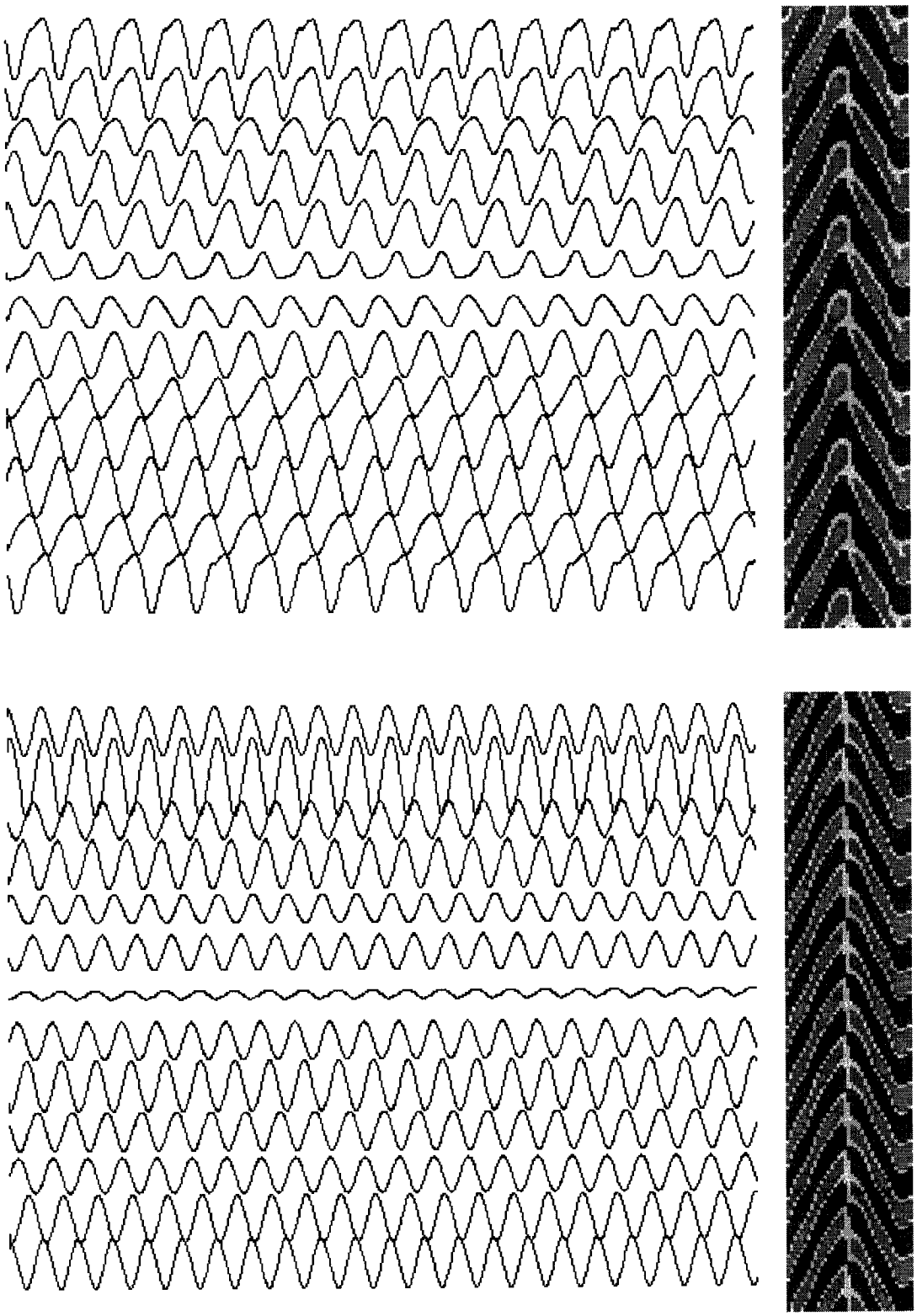

Figure 7.19 (a). Solitary spiral rotating about a 3x3 and 6x6 obstacle. $APD_o = 20$.

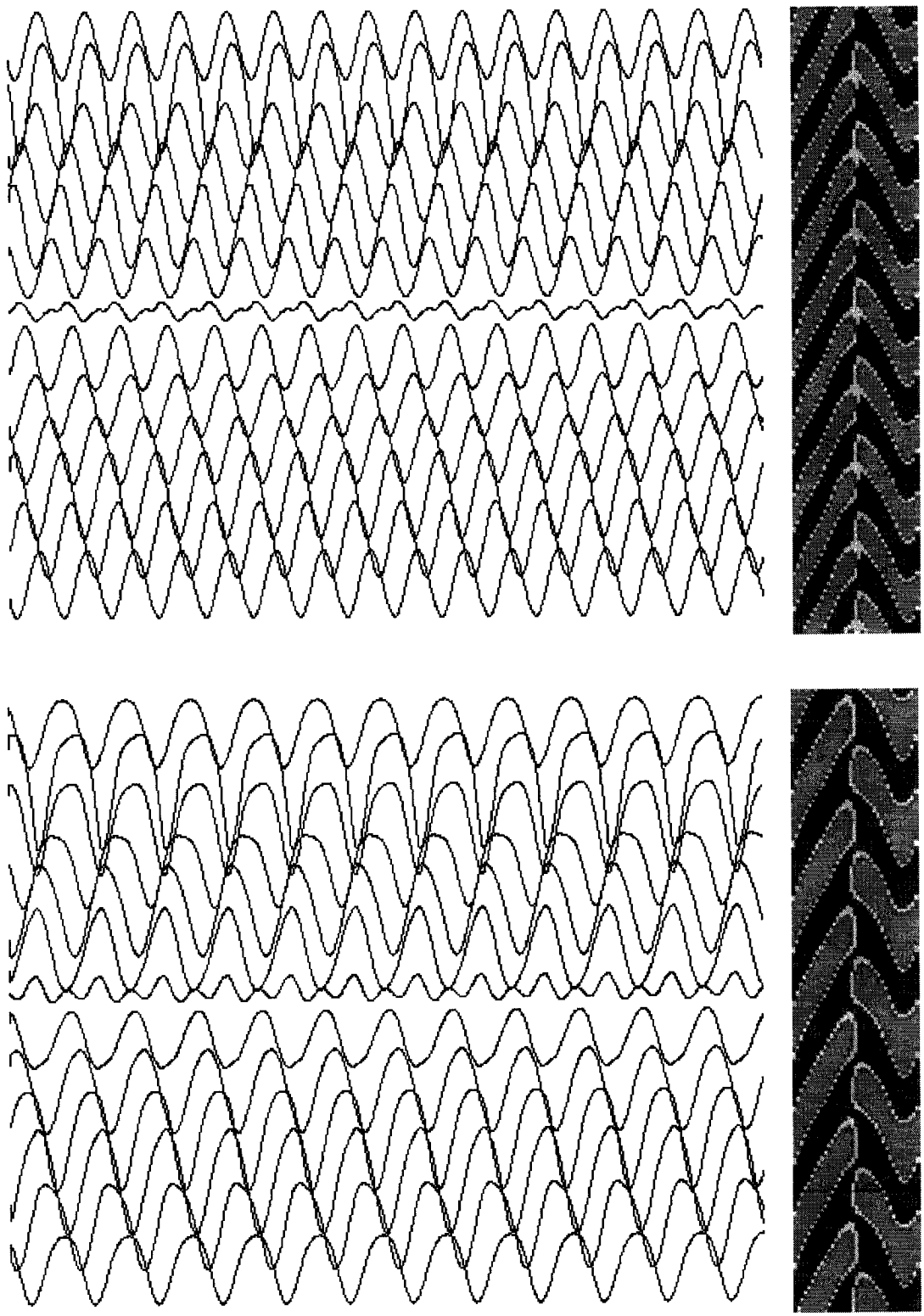

Figure 7.19 (b). Solitary spiral rotating about a 9x9 and 12x12 obstacle. $APD_o = 20$.

L_o = 3x3 L_o = 6x6 L_o = 12x12

Figure 7.20. Solitary spiral of "VT" rotating about square obstacles of sizes shown. Large obstacles have long diastolic intervals which keep APD nearly constant on the restitution curve, and produce uniform spirals. The smallest 3x3 obstacle has a short cycle length giving a diastolic interval that falls under the steep slope of the restitution curve. This causes the APD to undergo alternans, giving an irregular wave width. For all cases shown $APD_m = 48$ and $APD_o = 20$.

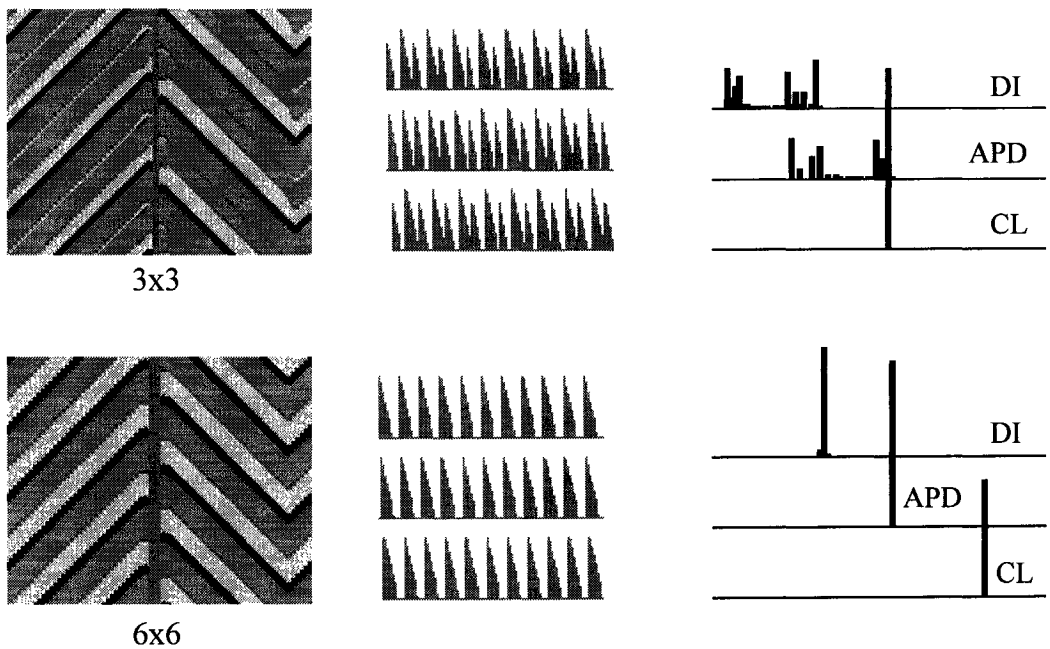

Figure 7.21. Spiral wave rotating around a square obstacle 3x3 (top) and 6x6 (bottom). Space-time plots at left are taken horizontally through the mid-field where j = 25. The 2:1 pattern of APD is evident for the small 3x3 obstacle, while APD is constant for the 6x6 obstacle. Action potentials are shown in the middle for three sites near the obstacle. The histograms at right show the APD to be constant for the larger obstacle, while APD splits into multiple values for the smaller obstacle due to steep restitution slope.

Figure 7.19 shows the ECG signals from the 36 equatorial leads of a solitary spiral wave rotating about square obstacles ranging in size from 3x3 to 12x12. Most ECG signals of

"VT" resemble sine waves, with some asymmetry evident in a few leads. There is an obvious trend toward lower frequencies when obstacles are larger, owing to longer cycle lengths. Frames of the corresponding action potential fields V_{ij} for each are shown in Figure 7.20. The spiral waves are regular, except at low $L_o = 3$ where the short diastolic interval operating through steep restitution with $APD_o = 20$ allows APD irregularity to manifest on the steep slope. It is noteworthy that all of these ECG signals of VT are monomorphic with fixed amplitude. The steady-state histograms are very narrow for DI, APD, and CL. There is no occurrence of polymorphic VT originating from this type of rotation about an obstacle in this idealized model.

Figure 7.21 shows space-time plots of the voltage Vj(t) across the mid-field at j = 25. The larger 6x6 obstacle has nearly uniform APD, DI, and CL, as seen in the histograms and action potential plots. The smaller 3x3 obstacle has irregular action potentials due to the short diastolic intervals. The action potential plot shows 2:1 alternans in the DI and APD plots, although the cycle lengths are uniform. It seems that the dynamics encounter a bifurcation point as the obstacle is made smaller, and the histograms of DI and APD split into multiple values. The question of greatest interest is whether or not the ECG measured on the body surface can discern this bifurcation originating from qualitatively different wave dynamics in the heart.

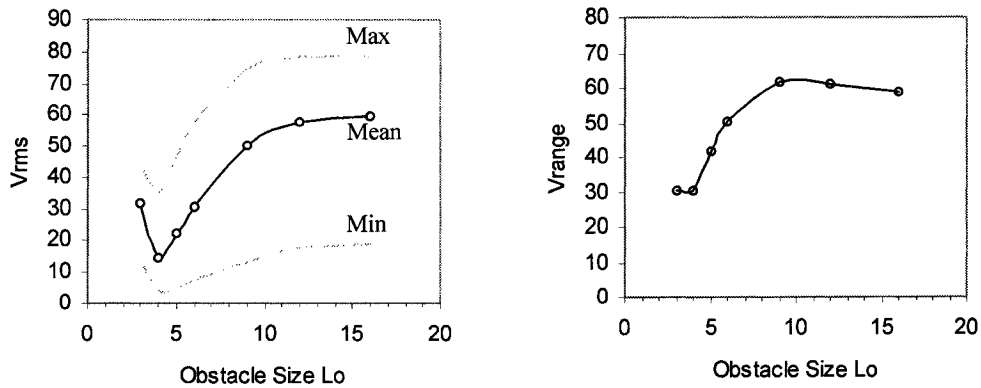

Figure 7.22. Role of obstacle size L_o on the ECG amplitudes of spiral wave "VT" for $APD_o = 20$. Mean V_{rms} (left) for all 36 leads and the total range (right) are shown.

The characteristics of the 36 lead ECG signals are summarized in Figure 7.22 for the spiral wave around obstacles ranging in size from 3x3 to 16x16. There is a clear trend to larger mean amplitude and larger overall range between leads as obstacle size increases. The exception is the smallest 3x3 which has a larger amplitude than expected. This is due to the large alternans width of APD at short CL preventing the trend to shorter APD with smaller obstacles. In other words, the bifurcation illustrated in Figure 7.21 abruptly expands the cycle length to 88 from 44, as would be expected according to the linear relationship in Figure 7.17. This departure in CL can be seen in Figure 7.23.

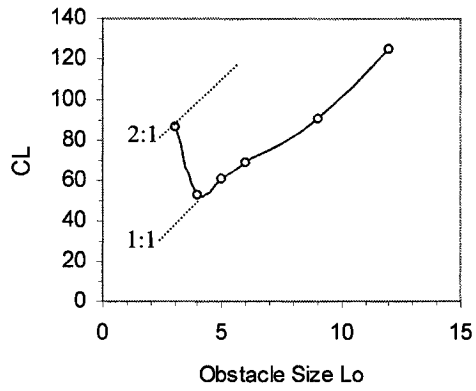

Figure 7.23. The role of obstacle size L_o in determining the cycle length CL of a rotating spiral wave with $APD_o = 20$. Only the smallest 3x3 obstacle exhibits sufficient width of APD alternans to block the monotonic decrease in CL, and there is a jump to a 2:1 APD pattern at twice the cycle length. This manifests in the dominant frequencies of the ECG series in Figure 7.19.

Remarkably, the clear transition of spatiotemporal dynamics in the tissue domain between the 3x3 and 6x6 obstacles, which actually occurs between 3x3 and 4x4, does not clearly manifest in the ECG. Subtle variation can be seen in the ECG time series, but most importantly there is no polymorphic VT generated by the irregular APD for small obstacles. The reason can be explained in part by recalling that the intersection point of the negative unity slope line of CL in Figure 4.15 will only fall on the steep slope of the restitution curve if CL is small relative to τ, and APD_o is much lower than APD_m to give a slope > 1 segment. Irregular wave fronts, occurring near the core region or obstacle,

make only a small contribution to the overall ECG signal, which is dominated by the more coherent larger radius waves in the far field. Polymorphic VT is further prevented in this model by the wave front velocity being constant and independent of APD. This tends to keep the wave fronts parallel in the spiral, whereas, if velocity restitution were present, as would be likely in real tissue, the wave fronts would develop a degree of spatial oscillations that would introduce oscillations in the excitable gaps contributing additional frequency components to the ECG.

Prior to the foregoing analysis, we felt that aperiodic or quasiperiodic dynamics around the core might generate polymorphic VT if there was both steep restitution and a small obstacle to achieve a short CL. Very low APD_o, however, increases the likelihood that wave irregularities away from the core region can become unstable and break into VF. Polymorphic VT or torasade de pointes does not occur due to a reentrant circuit rotating around a fixed inexcitable obstacle in this model, except perhaps only during an initial transient period. Since the model does not exhibit velocity restitution, which likely plays a role in the transition to chaotic dynamics [529], these simulations would need to be repeated in a more detailed two or three dimensional ionic model to better resolve the conditions conducive to polymorphic VT by a reentrant mechanism.

Monomorphic VT (MVT), polymorphic VT (PVT), and VF can generally be classified subjectively based on inspection of ECG morphology alone. As has been shown, there is a tendency for ECG amplitude to be lower at higher N_c. The distinction between PVT and VF, however, becomes somewhat arbitrary here since some observers might choose to define VF simply as the existence of multiple waves with $N_c > 1$, regardless of their global stability, while others might claim that dynamic instability should be present before labelling a rhythm VF. The issue is whether VT and VF should be defined and classified based on substrate-level wave dynamics or on ECG morphology. We favour a mechanistic definition based on the number of waves: if $N_c = 1$, the rhythm is VT, while if $N_c > 1$ the rhythm is VF, regardless of its stability. The mechanisms of reentrant circuit stability and persistence are essentially the same between the two rhythm classifications, only the number of waves is different.

This CML model is obviously a gross simplification of real cardiac tissue, and some phenomena cannot be captured. Velocity restitution that might be important to spiral wave instability is not considered [408], although spiral wave break-up occurs in the CML model in its absence. Vortex shedding with detachment of reentrant circuits has been reported in tissue as waves pass around obstacles having edges of very small radius of curvature [55], particularly under conditions of low excitability ionic models.

This chapter concludes the investigation of VT and VF dynamics in the CML model. The remainder of this dissertation involves the development of a more detailed and realistic ionic model of cell dynamics and implementation in a three dimensional heart. This more sophisticated model will be used to explore some of the phenomena described thus far in the CML model.

Chapter 8

VENTRICULAR CELL: A NEW MODEL

8.1 Model Objectives

This chapter describes the development and calibration of a new ionic model of the human ventricular action potential that will be used in large-scale simulations involving spatial propagation. Before developing a new cellular model, existing ventricular cellular models must be examined. Some of the simpler models were seen in previous chapters. Here the focus will be on more complex ionic models that will be judiciously simplified to permit more rapid computation and reduced storage essential to large-scale simulation in a whole heart. The objective is to develop a parsimonious model that captures the essential features of cell behaviour with only minimal sacrifice when compared with the more complex cellular models. Specifically, the model must retain the following essential properties:

(1) Realistic action potential morphology V(t)
(2) Employ dominant transmembrane currents (I_{Na}, I_{Ca}, I_K, I_{K1}, I_{to})
(3) Allow reasonably physiological interpretation of state variables
(4) Capture desired features of cellular behaviour including:
    - upstroke amplitude
    - action potential duration

- supernormal excitability
- effective refractory period
- action potential duration restitution
- conduction velocity
- regional heterogeneity

(5) Retain minimum number of stored dynamic variables for each cell
- 5 state variables (transmembrane potential and 4 gating parameters)

(6) Allow modifiable cellular properties to account for:
- regional heterogeneity (endocardium, M cell, epicardium)
- distinct tissue types (atrium, ventricle)
- changes in ionic concentrations

The cellular model must also be implemented in a coupled lattice of reasonable spatial resolution to simulate propagation within tissue, and in addition must:

(1) Propagate in one-, two-, and three-dimensional tissue

(2) Propagate in three-dimensional anisotropic heart geometry with 1-mm resolution,

(3) Exhibit basic arrhythmogenic mechanisms to include:
- automaticity
- reentry
- afterdepolarizations,

(4) Simulate specific arrhythmias:
- ventricular ectopy
- monomorphic VT
- polymorphic VT
- ventricular fibrillation

(5) Exhibit myocardial dynamics and body surface electrocardiograms comparable with experimental results reported in the literature and on file.

A salient point in these objectives is that, unless one is investigating the role of multiple individual ionic channels, one need not employ highly sophisticated models that

exhaustively account for the multitude of known currents. Cellular models can be simplified to a few variables, yet still capture the essential features of action potential morphology and propagation with less computational demand. Such a parsimonious approach is central to this thesis.

8.2 Simplified Cell Model

Existing mathematical models of ventricular action potentials were developed around the results of animal experiments. Ionic currents in these models are based on measurements in myocytes of several species including guinea pig, rat, dog, and rabbit that may not necessarily be valid in human myocytes. Several recent experimental studies have begun to examine human ventricular and atrial tissue obtained from biopsies, surgical cannulation sites, or explanted hearts that are in various stages of disease. Other studies have involved dissociated cells *in vitro* that may not represent the behaviour of coupled cells in whole tissue preparations. Such differences in methodologies and inconsistencies between studies pose difficulties to the development of an accurate standardized model of human action potentials.

The general approach that will be taken here begins by first examining the original 1991 Luo-Rudy phase 1 model (LR1). This model has six gating parameters or state variables (m, h, j, d, f, x) that must be stored and integrated at each time step in addition to the cell potential V. It will be shown that this model can be simplified to a reduced model, which will be called LRS ("Luo-Rudy Simplifed"), with four gating parameters (h, d, f, x) by first reformulating the sodium current. This condensation will result in only a small change in behaviour as compared with the original model. Since the equations for the gating parameters and time constants in the original formulation are expressed as lengthy functions of $\alpha(V)$ and $\beta(V)$, they will be simplified to retain the same behaviour, yet allow adjustments to be made more intuitively for specific objectives. Where possible, gating variables will be expressed as Boltzmann functions, and time constants will be expressed as piecewise linear or Gaussian functions. The choice of parameters for these simplified functions is based on a visual best-fit between the original functions and the

new approximations. The considerable additional complexities of calcium handling in the more recent Luo-Rudy phase 2 model [330] will not be incorporated in the models to be developed in this dissertation, as the computational requirements are much higher, and several more variables would need to be processed and stored. The LRS model presented here is intended to mimic the full LR1 model [329]. It is summarized in Table 8.1.

Table 8.1 Simplified Luo-Rudy Model (LRS)

$I_{ion} = I_{Na} + I_{Ca} + I_{KT} + I_K$

$I_{Na} = g_{Na}\, m^3 h\, (V - E_{Na})$

$m^3 = 1/(1+ \exp(-(V+32)/4))$
$dh/dt = (h_\infty - h)/\tau_h$
$h_\infty = 1/(1+\exp((V+70)/3.3))$
$\tau_h = 0.16 + 25\exp(-((V+66)/15)^2)$
$= 2\,\tau_h$ if $dh/dt > 0$ (recovery)

$I_{Ca} = g_{Ca}\, d\, f\, (V - E_{Ca})$

$dd/dt = (d_\infty - d)/\tau_d$
$df/dt = (f_\infty - f)/\tau_f$
$d_\infty = 1/(1+\exp((V+25)/-9))$
$f_\infty = 1/(1+\exp((V+24)/7))$
$\tau_d = 8 + 25\exp(-((V+23)/35)^2)$
$= 16$ if $V > 10$
$\tau_f = 100+0.8(V+25)$
$= 100+7.0(V+25)$ if $V>-25$

$I_{KT} = I_{K1} + I_{KP} + I_B$

$I_{K1} = g_{K1}\, K_{1\infty}\, (V - E_{K1})$
$I_{KP} = .018\, Kp\, (V - E_{K1})$
$I_B = .039\, (V+60)$
$K_{1\infty} = 1.3\exp(-(V-E_{K1}+9)/18) - .02$
$= 0$ if $V > -35$
$Kp = 1/(1+\exp-(V-7.5)/6))$

$I_K = g_K X_i X (V - E_K)$

$X_i = .11 + .89 \exp(-(V+100)/40)$
$= 1$ if $X_i > 1$
$dX/dt = (X_\infty - X)/\tau_X$
$X_\infty = 1/(1+\exp((V+25)/-13))$
$\tau_X = 630\exp(-((V+25)/55)^2)$ $V > -25$
$= 210 + 420\exp(-((V+25)/35)^2)$ $V < -25$

$g_{Na} = 13$ $dt = 0.1$ ms
$g_{Ca} = .09$
$g_K = .282 \text{ sqrt}([K]_o/5.4)$
$g_{K1} = .6047 \text{ sqrt}([K]_o/5.4)$

$E_{Na} = RT/F \ln([Na]_o/[Na]_i) = 54$
$E_{Ca} = 74$
$E_K = RT/F \ln(([K]_o + .01833\,[Na]_o)/([K]_i + .01833\,[Na]_i))$
$E_{K1} = RT/F \ln([K]_o/[K]_i)$
$RT/F = 8.314*310/96.487 = 25.67$

Istim1 = 20 dts = 2 ms
Istim2 = 20
$[Na]_o = 140$
$[Na]_i = 18$
$[K]_o = 4.0$
$[K]_i = 145$
C = 1.0

Vmax = 35

This four-parameter LRS model reproduces behaviour of the original six-parameter LR1 model quite closely, but does so with less complexity. Its purpose is to demonstrate the possibility of achieving comparable behaviour between an existing complex model and a simplified version. Simulated action potentials of the full LR1 model are shown in Figure 8.1, along with the contributing ionic currents. Comparison is made in Figure 8.2 with the LRS model at various pacing intervals. Dynamics are very similar, with only subtle departures owing to accumulation of very small differences within the highly nonlinear

regions of the model. The simplified LRS model appears to capture the behaviour of the full LR1 model reasonably well.

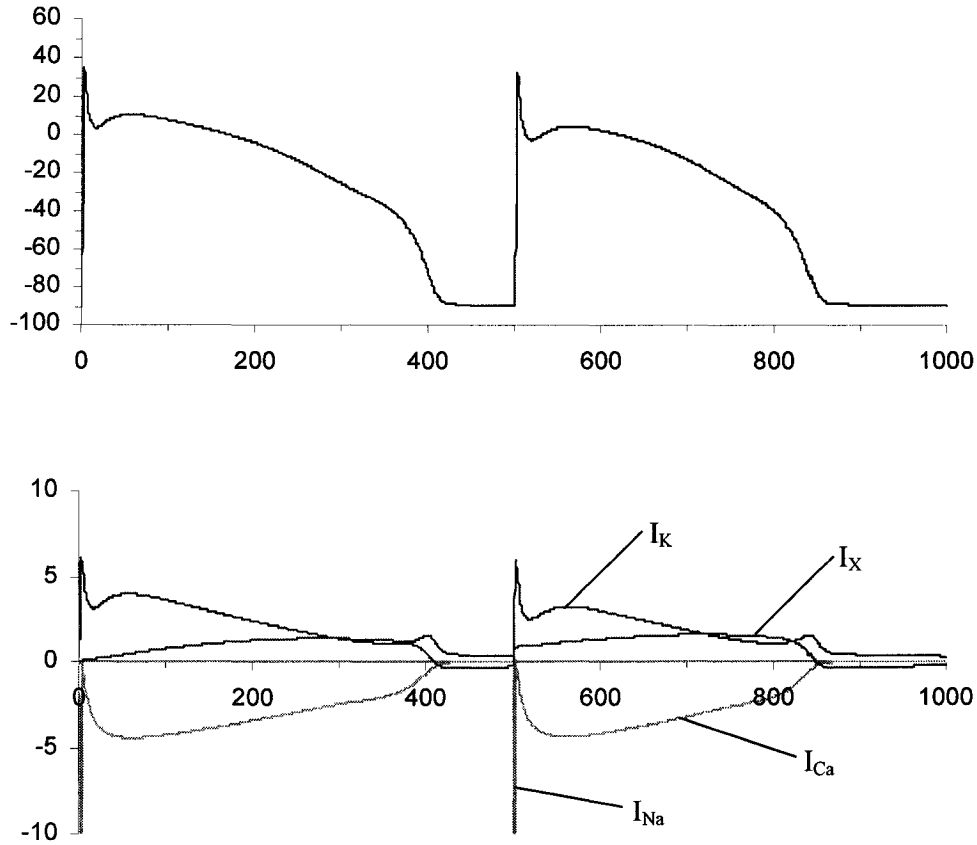

Figure 8.1. Standard Luo-Rudy 1 models of ventricular action potential paced at 500 ms intervals. Transmembrane potential is shown at the top and contributing ionic currents are shown below.

The LRS model will next be used as a departure point in developing an adjusted four parameter model of human ventricular action potentials, which will be called the SHV model ("Simplified Human Ventricular"). This new SHV model will be used for all subsequent simulations of ventricular dysrhythmias. A similar approach for developing a simplified atrial cell model will follow in a later chapter. The following sections examine the formulation and performance of the SHV model in Table 8.2.

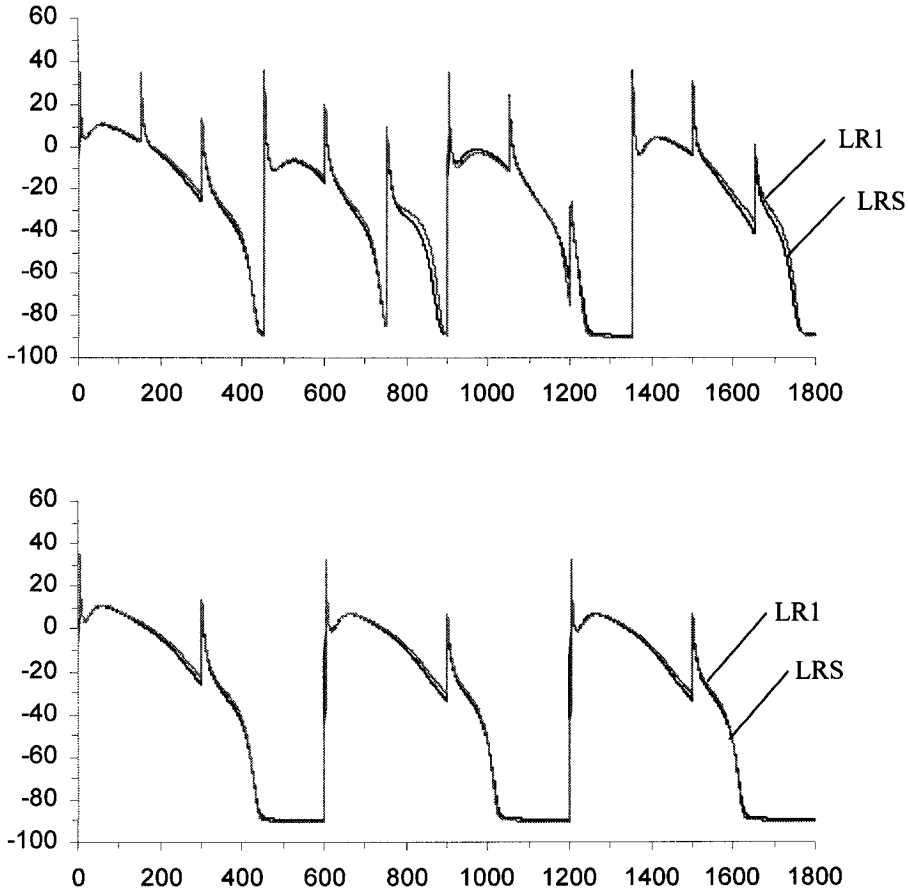

Figure 8.2. Comparison of the standard LR1 model with the simplified LRS model. Action potentials are shown for a single cell paced at 150 ms (above) and 300 ms (below). Differences between models are negligible, even at rapid pacing where chaotic dynamics are evident.

Table 8.2. Simplified Human Ventricular Model (SHV)

$I_{ion} = I_{Na} + I_{Ca} + I_{KT} + I_K + I_{to}$

$I_{Na} = g_{Na}\, m^3 h\, (V - E_{Na})$

$m^3 = 1/(1+ \exp(-(V+32)/4))$ *
$dh/dt = (h_\infty - h)/\tau_h$
$h_\infty = 1/(1+\exp((V+70)/3.3))$ *
$\tau_h = 1 + 25\exp(-((V+66)/15)^2)$ *
$= 3\ \tau_h$ if $dh/dt > 0$ (recovery) *

$I_{Ca} = g_{Ca}\, d\, f\, (V - E_{Ca})$

$dd/dt = (d_\infty - d)/\tau_d$
$df/dt = (f_\infty - f)/\tau_f$
$d_\infty = 1/(1+\exp((V+5)/-7))$ *
$f_\infty = 1/(1+\exp((V+24)/7))$ *
$\tau_d = 8 + 15\exp(-((V+23)/35)^2)$ *
$\tau_f = 240 - 140\exp(-((V+0)/30)^2)$ *
$= \tau_{fr}$ if $df/dt > 0$ (recovery) *
$\tau_{fr} = 350$ (range 100 - 1000) *
$d = d_\infty$ if $dd/dt > 0$ (faster upstroke) *

$I_{KT} = I_{K1} + I_{KP} + I_B$

$I_{K1} = .5\, g_{K1}\, f_{K1}\, K_{1\infty}\, (V - E_{K1})$ *
$I_{KP} = .012\, f_{K1}\, Kp\, (V - E_{K1} - 60)$ *
$I_B = .009\, f_{K1}\, (V+60)$ *
$K_{1\infty} = 1/(1 + \exp(-(V - E_{K1})/18)$ *
$Kp = 1/(1+\exp(-(V-10)/10))$ *

$I_K = g_K\, f_{K2}\, X_i\, X\, (V - E_K)$

$X_i = .11 + .89 \exp(-(V+100)/40)$
$= 1$ if $X_i > 1$
$dX/dt = (X_\infty - X)/\tau_X$
$X_\infty = 1/(1+\exp((v+16)/-9))$ *
$\tau_X = 100 + 900 \exp(-((V+70)/35)^2)$ $V < -70$*
$= 1000$ $V > -70$*

$I_{to} = g_{to} f_{k3} p_\infty (1 - d) (V - E_K)$ *

$p_\infty = 1/(1+\exp((V-10)/-5))$ *

$dd/dt = (d_\infty - d)/\tau_d$
$d_\infty = 1/(1+\exp((v+5)/-7))$ *
$\tau_d = 8 + 15\exp(-((V+23)/35)^2)$ *

$g_{Na} = 13$ mS/cm^2 dt = 0.2 ms
$g_{Ca} = .08$ mS/cm^2 dx = .1 cm
$g_K = .28$ sqrt($[K]_o$/5.4)
$g_{K1} = .61$ sqrt($[K]_o$/5.4)
$g_{to} = .067$

$E_{Na} = RT/F \ln([Na]_o/[Na]_i) = 54$ mV
$E_{Ca} = 70$ mV
$E_K = RT/F \ln(([K]_o+.01833\ [Na]_o)/([K]_i+.01833\ [Na]_i))$
$E_{K1} = RT/F \ln([K]_o/[K]_i)$
$RT/F = 8.314*310/96.487 = 25.67$

$f_{K1} = 0.80$ endo	0.80 Mcell	0.85 epi	(modifies I_{KT})
$f_{K2} = 0.2$	0.05	0.2	(modifies I_K)
$f_{K3} = 0.1$	0.8	1.0	(modifies I_{to})
$\tau_{fr} = 350$	500	350	(I_{Ca} recovery)

$I_{stim1} = 20$ dts = 2 ms
$I_{stim2} = 20$
$[Na]_o = 140$
$[Na]_i = 18$
$[K]_o = 4.0$
$[K]_i = 145$
$C = 1.0$

$V_{max} = E_{Na}$ *

* indicates a change from the LRS model

8.2.1 Sodium Current

The fast inward sodium current is responsible for action potential upstroke and propagation. This channel has been a target for class I antiarrhythmic agents, including procainamide and lidocaine, and has been linked to genetic defects causing dysrhythmias

in the long QT syndrome. The sodium current modeled by the original Hodgkin-Huxley formulation [229] is $I_{Na} = g_{Na}m^3h(V - E_{Na})$. This may be visualized as an ohmic current modified by the activation gate m and the inactivation gate h, each varying between 0 and 1. E_{Na} is the sodium reversal potential from the Nernst equation. Technical difficulties, owing to a small membrane length constant and rapid activation, prevented accurate voltage clamp studies of I_{Na} on multicellular cardiac tissue for over two decades. Early ionic models of cardiac tissue, including the McAllister-Noble-Tsien 1975 [340] and Beeler-Reuter 1977 [32] formulations, used the giant squid axon current basically unmodified, except for much lower values of g_{Na}. Colatsky and Tsien in 1979 [94] were eventually able to achieve satisfactory voltage clamping of rabbit Purkinje fibre allowing DiFrancesco and Noble in 1984 [131] to formulate improved equations for the sodium current. The slower inactivation and recovery phase of I_{Na} were not captured well. Ebihara et. al. in 1980 [144] were able to voltage clamp spherical clusters of cultured chick heart cells, and demonstrate that a g_{Na} of 23 mS/cm^2 was required to account for the peak value of I_{Na}, much higher than the g_{Na} of 4 mS/cm^2 used by Beeler and Reuter. Ebihara and Johnson [144] reformulated the Hodgkin-Huxley equations for h_∞ and τ_h to more closely match these experimental results. Drouhard and Roberge [142] reformulated m_∞, h_∞, τ_m, τ_h once again as a compromise based on several more studies on rat ventricular cells. More recent Markov models of the sodium channel attempt to account for individual ion channel kinetics by simulating probabilities of transitions between several open and closed states [86, 325]. These models closely reproduce HH kinetics, but with some interesting and more realistic features that appear to better match patch clamp results [248]. The models developed here, and to be described in this dissertation, retain the HH approach, and are satisfactory for most practical purposes.

The time constant τ_h controls the rapid inactivation of I_{Na}. Since τ_h must control rapid inactivation and also control the slow recovery of h, Beeler and Reuter felt the activation-inactivation process could not be simulated with a single time constant. They were forced to introduce a second recovery variable j with slower dynamics. The resulting modified equation $I_{Na} = g_{Na}m^3hj\ (V - E_{Na})$ with three gating parameters has been used more recently in detailed models by Luo and Rudy [329, 330], who use the EJ formulation of m_∞, h_∞,

j_∞, τ_m, τ_h, τ_j. Three state variables m,h,j, in additions to the transmembrane potential V, must be carried during the numerical simulation of I_{Na}.

Sakakibara et al. [435] have recently used a whole cell patch-clamp method to study I_{Na} in human ventricular cells obtained at surgery. Their work remains one of the few studies of the human ventricular sodium current, and was conducted at room temperature. The threshold was found to be about –60 mV, and peak I_{Na} occurred around –30 mV. An earlier study by Bustamante and McDonald [53] on the sodium current in human atrial cells at room temperature found similar results, with peak I_{Na} to be around –30 mV, and $V_{0.5}$ for h to be about –75 mV.

The variable h inactivates rapidly during the action potential upstroke, and largely determines the duration and spatial width of the I_{Na} spike. To achieve rapid deactivation of h, yet slow recovery seen experimentally, Beeler and Reuter introduced the slower variable j, as previously described. To reduce computer storage requirements, we will instead represent the product h*j by one stored variable, with acceptably small error, by introducing rules based on the sign of dh/dt. Accordingly, a rapid time constant τ_h is employed for deactivation when $dh/dt < 0$, since j is sufficiently close to 1, and slower time constant is used for recovery, when $dh/dt > 0$. Therefore, h used here approximates the product h*j in the original model. A comparison confirming this similarity is shown in Figure 8.3. The I_{Na} employed thus requires calculation of a purely voltage-dependent fully activated current $g_{Na}\, m_\infty^3\, (V - E_{Na})$ at each time step, which is then modulated by the single stored variable h. Consequently, three stored variables m, h, and j used in the original formulation have been reduced to one stored variable h:

$$I_{Na} = g_{Na}\ h\ m_\infty^3\ (V - E_{Na})\ . \qquad (8.1)$$

We can avoid introducing j by using a longer τ_h during recovery, as previously described, and employ a prolongation factor, such that $\tau_h = 3\tau_h$ during recovery. In other words, τ_h is calculated from the basic equation in Table 8.2, but is further multiplied by 3 if $dh/dt > 0$, which occurs during recovery. The prolongation factor of the recovery time constant was

chosen to be 3, since this is the ratio of τ_h/τ_j in the BR and LR models, and also gives a peak time constant of about 75 ms, which is close to the peak of the fast component of recovery measured at -90 mV by Sakakibara [435]. The functions $h_\infty(V)$ and $\tau_h(V)$ are shown in Figure 8.4. Maximal depolarization V_{max} of the action potential upstroke is determined by the sodium current, which cannot drive V beyond its own reversal potential E_{Na}. Since overshoot can occur as an artifact during numerical time stepping, V must be constrained to not exceed a maximal value, set to E_{Na} in the model.

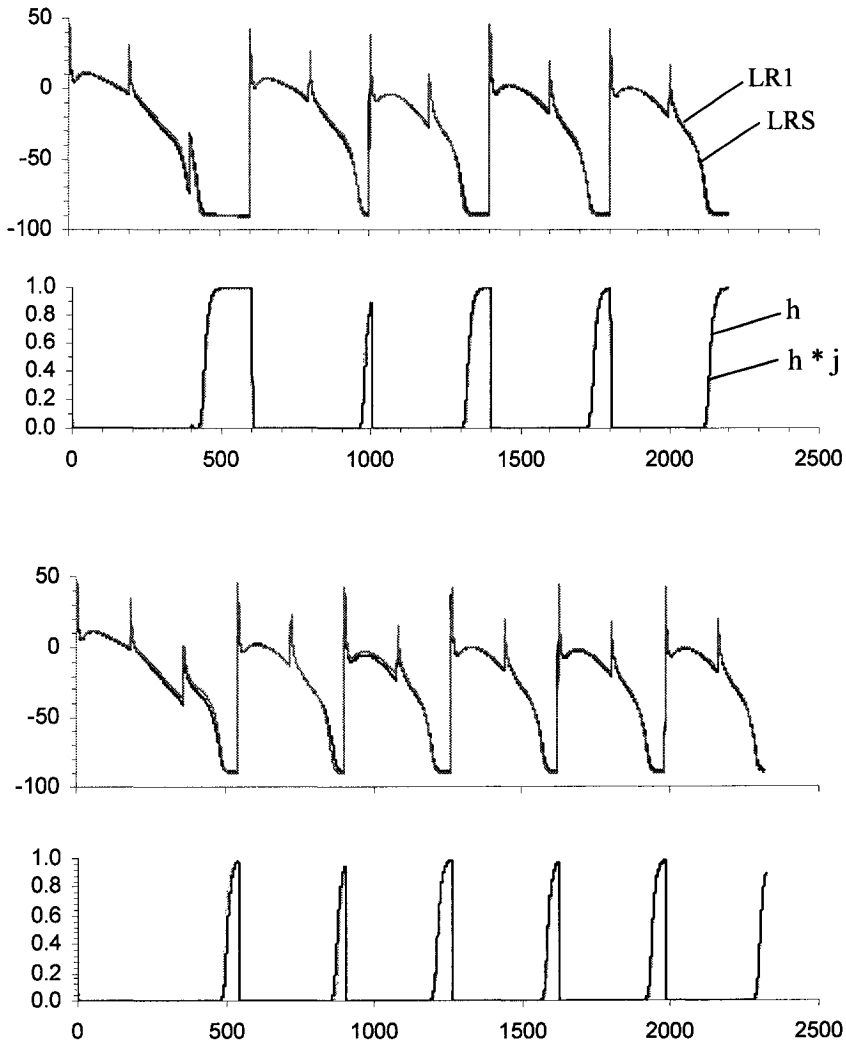

Figure 8.3. The function h(t) in the simplified LRS model approximates the product h(t)*j(t) in the original LR1 model by using a time constant that depends on the sign of dh/dt. The approximation appears to be valid, as the curves are indistinguishable. This eliminates the need for the extra state variable j(t).

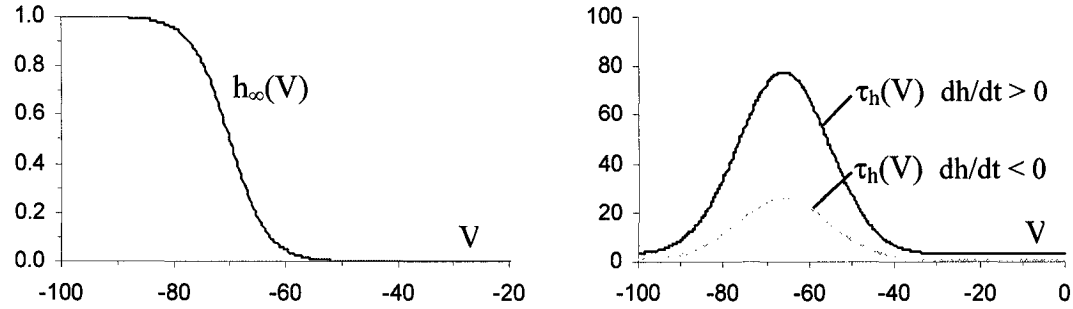

Figure 8.4. The gating parameter h(t) controls the time-dependent inactivation and recovery of I_{Na}. The steady-state function $h_\infty(V)$ is shown at left. The time constant τ_h is shown at right. τ_h is rapid for inactivation (grey), when $dh/dt < 0$, and is slow for recovery (black), when $dh/dt > 0$. Recovery is three times slower than inactivation.

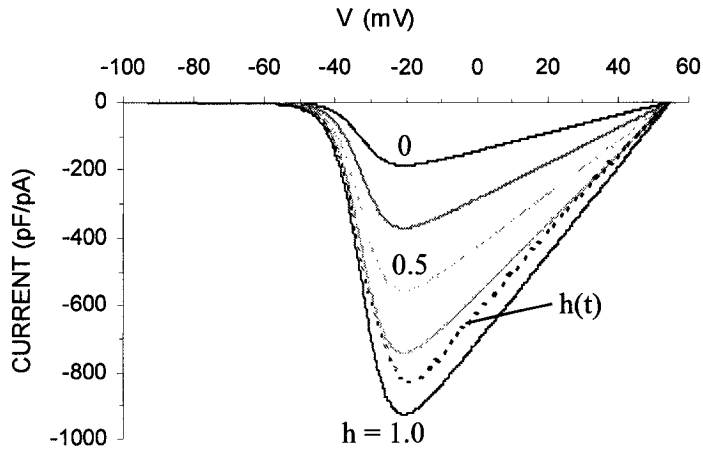

Figure 8.5. Steady-state V-I relationship for I_{Na} and its dependence on h. Maximum value occurs when h=1. The actual trajectory followed during an action potential upstroke depends on how h(t) changes, and is shown by the dashed line, which travels from h = 0 at resting potential to h = 1, as V increases to its maximum value.

Simplifications are introduced here to the I_{Na} model, such that storage only of V and h are necessary. Owing to the time constant for changes in m being very short, on the order of 0.3 ms, replacement of the variable $m^3(V,t)$ with its steady state time-independent function $m_\infty^3(V)$ introduces acceptably small error and allows larger time steps to be used in the numerical integration. The function $m_\infty^3(V)$ may further be approximated by a two-

parameter Boltzmann function. Accordingly, we retain $V_{0.5}$ = –32 mV and k_m = 4 for the SHV model, giving a peak I_{Na} at about –35 mV, matching a curve fit to $m_\infty^3(V)$ used in the Luo-Rudy models. This choice of constants ensures complete inactivation of I_{Na} at normal resting potential. The resulting steady state V-I relationships for h = 0 to 1 are shown in Figure 8.5. For $h_\infty(V)$ we choose $V_{0.5}$ = –70 mV and k_h = 3.3, which is steep enough to ensure that I_{Na} inactivates completely at rest. The time constant of inactivation τ_h is retained from the EJ formulation used in the LR1 model, and corresponds well with the fast component measured by Sakakibara et al. [435], approaching about 25 ms.

8.2.2 Calcium Current

The basic form of the inward calcium current in the BR and LR1 formulations is similar to that of I_{Na}, but has a more positive threshold and much slower kinetics. The gating variable d(t) activates relatively rapidly during depolarization, and f(t) inactivates slowly.

$$I_{Ca} = g_{Ca}\, d\, f\, (V - E_{Ca}) \tag{8.2}$$

Studies of the human ventricular L-type calcium current are few in number, but fairly consistent in their findings [37, 98, 317, 346]. Thresholds are around –40 to –33 mV, peak steady-state I_{Ca} occurs between 0 and +10 mV, and the reversal potential is around +50 to +60 mV. T-type calcium channels have not been found in human ventricular or atrial tissue. The gating variables d and f have been measured in human ventricular myocytes. $V_{0.5}$ of d was found to be –4.2 mV [346], –4.8 mV [317], and –0.14 mV [36]. Slope factors were, respectively, 7.0, 6.2, and 8.2. $V_{0.5}$ of f was found to be –23.5 mV [346], –28.5 mV [317], –24.6 mV [37] with slope factors of 7.8 and 5.5. Time constants for d and f correspond approximately to the fast and slow components respectively of I_{Ca} recovery [346].

For the proposed SHV model, the activation $V_{0.5}$ of d is raised from the LR1 value of –25 to –5 mV, which has the effect of raising the action potential plateau to more realistic values around +10 mV for human ventricular cells, and is close to the above measured

values. The slope factor for d is approximated as 7 based on the above values. Since I_{Ca} activates more rapidly in ventricular cells than in the BR or LR1 simulations, we propose setting $d = d_\infty$ to achieve rapid upstroke of I_{Ca}, consistent with other models, and to permit better definition of the transient outward current I_{to} that immediately follows the upstroke in epicardial cells. The steady-state calcium current $g_{Ca}\ d_\infty\ (V-E_{Ca})$ has a threshold around –35 mV and a peak around 0 mV, consistent with the I_{Ca} voltage clamp results discussed earlier. The reversal potential E_{Ca} will be set to +70 mV. The above functions are illustrated in Figure 8.6.

As in previous models, I_{Ca} inactivation in the SHV model is controlled by f. $V_{0.5}$ for f_∞ will be set to –24 mV with a slope factor of 7 consistent with the voltage clamp data discussed above. Recovery of f is a determinant of subsequent action potential duration. This constant carries special importance as we may consider $V_{0.5}$ for f_∞ to be an adjustable parameter that controls the intercept of the APD restitution curve. For example, shifting $V_{0.5}$ for f to a more negative value achieves greater inactivation of I_{Ca} and a shorter subsequent APD at small diastolic recovery intervals. This concept will be discussed in more detail in a later section on restitution.

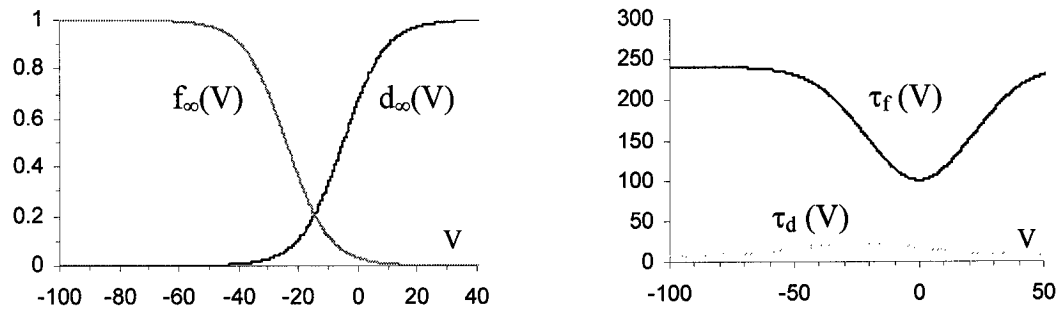

Figure 8.6. Gating kinetics of the activation variable d(t) and inactivation variable f(t) that control the calcium current I_{Ca}. Steady-state $d_\infty(V)$ and $f_\infty(V)$ are shown at left and the time constants τ_d and τ_f are shown at right.

The recovery of f(t) during diastole is governed by the time constant $\tau_f(V)$, which also influences action potential duration. In several studies of isolated human ventricular

myocytes, this parameter has consistently demonstrated both fast and slow components, each with a U-shaped voltage dependence. In one study carried out above -20 mV, the fast τ_f varied between 12 and 124 ms, and the slow τ_f varied between 133 and 3124 ms [346]. Within this voltage range, two other studies found the fast component for τ_f to be relatively voltage-independent, around 10 to 20 ms, with a mean slow component varying between 80 and 250 ms [37]. Recovery of I_{Ca} appears to be biexponential, with time constants of 65 and 638 ms at -80 mV [317]. These results are similar between normal cells and those from failing hearts.

Action potentials measured in isolated cells are typically longer than those measured in intact beating hearts. The reason for this discrepancy is not clear, but might involve the absence of electrotonic interactions in isolated cells, or the presence of artifacts due to specimen preparation and artificial perfusate. Electrotonic current from neighbouring cells influences modifies APD by adding either a depolarizing or repolarizing current that prolongs or shortens APD, respectively, by adding to or subtracting from the total ionic current. To keep the APD shorter and more consistent with *in vivo* measurements in intact hearts, it is necessary to either shorten I_{Ca} or increase outward currents. In one version of this model we chose the former option, and for baseline action potentials we nominally set τ_f to be 120 ms in the SHV model. This is in the range of the measured slow component, and allows a reasonable fit of simulated action potentials to those reported in the human RV endocardium shown in Table 8.3. Prolonging τ_f to match voltage clamp data more precisely would result in the APD being unrealistically long in whole-heart simulations. The choice of a constant τ_f = 120 ms during inactivation is a minor departure from voltage clamp data, but serves as a free parameter, and is intended to force the baseline APD to match measured values in intact hearts as reported in the literature. In a second version, we assigned τ_f to be an inverse Gaussian function ranging from 240 ms to a nadir of 100 ms at 0 mV, approximating voltage clamp data. During recovery of f, we assign τ_f = 350 ms to give a longer time constant to match measured human restitution curves of *in vivo* catheter-based studies. We can consider τ_f and $V_{0.5}$ for f to be control parameters that can be adjusted to manipulate APD restitution, as these

functions determine the dominant time constant and intercept, respectively, of the restitution curve.

The complex nature of I_{Ca} and its regulation have been investigated in animal cardiomyocytes, and more advanced mathematical models have been proposed. Most notable is the Luo-Rudy phase 2 model [330], which employs a third gating variable f_{Ca} which inactivates I_{Ca} according to the concentration of intracellular calcium released from internal stores. This variable provides negative feedback control to close the calcium channel. Despite the added complexity of this and other more detailed calcium models, action potential restitution properties measured in cells or whole hearts are still not necessarily captured accurately. Modifications to these more complex models, for the purpose of addressing simple basic questions, also becomes more difficult. As will be shown later, restitution properties can be incorporated and modified quite satisfactorily in simpler models without such additional complexity of calcium dynamics. To maintain parsimony and avoid further computational demand, f_{Ca} will be set to 1.0, effectively ignoring the role of intracellular calcium effects on the action potential.

While the physiological role of calcium currents is to facilitate mechanical contraction, the primary electrical role of the calcium current in the action potential is to maintain the plateau and control APD. The simpler formulation of I_{Ca} here allows enough flexibility to handle action potential restitution satisfactorily. Propagating wave dynamics involving reentrant circuits is largely dependent on interactions between the action potential upstroke and recovery tail, neither of which are strongly dependent on the details of I_{Ca}.

8.2.3 Rectifier Current

The dominant outward repolarization currents are carried by potassium, and are targets for class III antiarrhythmic agents. Many potassium channels have been identified in cardiac tissue [463]. Defects in genes coding for potassium channels appear responsible for some dysrythmias associated with long QT syndrome [152]. Although other potassium currents might await discovery, the total time-independent potassium current

I_{KT} in the Luo-Rudy LR1 model is made up of three components which are each functions of voltage and extracellular potassium concentration $[K^+]_o$. Despite very brief time constants in these component currents, measured in voltage clamp experiments, there is practically no time dependence of I_{KT}. This summated potassium current can therefore be computed at each time step, and no integration or storage of gating variables is required.

$$I_{KT} = I_{K1} + I_{KP} + I_B \tag{8.3}$$

The dominant current component is I_{K1}. The LR1 equation for I_{K1} was derived from the guinea pig data of Sakmann and Trube [437]. Relatively few studies of I_{K1} have been conducted on human cells, owing to difficulties in accessing healthy tissue. The human studies of ventricular tissue that are available are fairly consistent qualitatively, showing a negative-slope conductance region and tapering current at positive voltages [11, 38, 287, 288, 501]. It is difficult to compare these studies quantitatively, since several types of inconsistent units are used. The curves tend to be similar qualitatively, but peak amplitudes cannot be compared. Koumi et al. [288] examined I_{K1} from human, feline, and guinea pig atrial and ventricular myocytes, and found the slope-conductance characteristics were remarkably similar between these species, although amplitudes varied. Their results for human ventricular myocytes are consistent with those measured by Varro et al. [501].

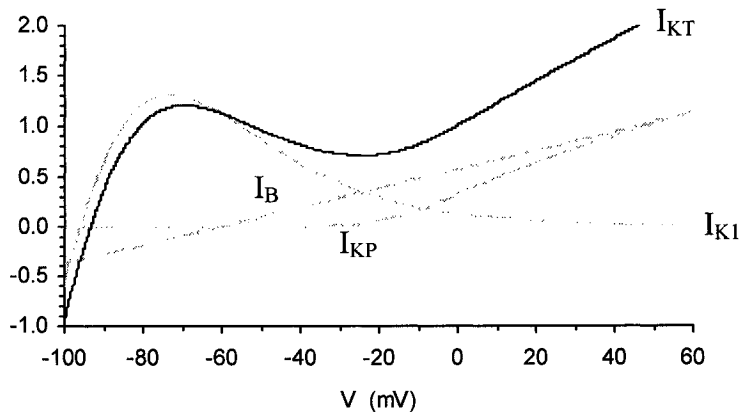

Figure 8.7. Time-independent potassium currents I_{K1}, I_{KP}, I_B, and the total I_{KT}.

The I_{K1} formulation from the LR1 model is modified here for the SHV model and further simplified. The additional background current I_B is retained from the LR1 model, although modified, since it is analogous to the linear residual current observed in two studies of human ventricular total time-independent outward current [287, 288]. I_{KP} activates and dominates at relatively positive voltages, and is essential to induce repolarization at the peak of action potential, especially in endocardial cells that lack a significant transient outward current I_{to} to serve this role. Konarzewska et al. [287] called this the sustained current I_{sus}, since it appears as a steady state current following voltage clamp I_{to} transients, and is purely voltage dependent. The effect of I_{KP} or I_{sus} is much more prominent in atrial cells where it has also been called the sustained outward current I_{so}. I_{K1} becomes steeper with increased $[K^+]_o$ following a square root relationship, and the reversal potential shifts in a more positive direction [22]. These potassium currents are shown in Figure 8.7.

8.2.4 Delayed Rectifier Current

The outward delayed rectifier current I_K is carried by potassium, and is time-dependent according to an activation variable which can be called X(t), and a nonlinear inactivating function $X_i(V)$. Both are voltage dependent.

$$I_K = g_K X_i X (V - E_K) \tag{8.4}$$

The I_K formulation of the LR1model is largely based on rabbit myocyte data of Shibasaki [329], while I_K in the Beeler-Reuter model is adapted from the MNT Purkinje fibre model [340]. At least two separate delayed rectifier currents, a rapid component I_{Kr} and a slow component I_{Ks}, have been identified experimentally in animal hearts [441]. The presence and magnitude of these two currents varies considerably between species [503].

Data on I_K in human tissue is relatively rare. Veldkamp et al. [504] performed voltage clamp studies on human ventricular cells and found evidence for only the rapid I_{Kr} component, which had a Boltzmann $V_{0.5}$ of –29.9 mV and an activation time constant of

101 msec at 30 mV. There was no apparent slow I_{Ks}. Iost et al. [247] described the kinetics of I_{Kr} in undiseased human ventricular myocytes, and demonstrated fast activation and slow inactivation. The activation $V_{0.5}$ was –5.7 mV, which according to Veldkamp [503] should be corrected to about -16 mV, and the time constant was 31 ms at 30 mV. The deactivation time constant was 600 ms at –40 mV. No current-voltage relationship was given. Beuckelmann et al. [38] also found the delayed rectifier current to be barely detectable in undiseased human donor hearts, however most dissociated cells obtained were from the mid-myocardial layer where M cells are most abundant, and might not be representative of endocardial or epicardial cells. Koumi et al. [288] found repolarization of action potential in human ventricular myocytes to be independent of frequency, suggesting little if any influence from any time-dependent rectifier current. Konarzewska et al. [287] also found the delayed rectifier current to be small or absent.

While evidence for I_K appears inconsistent, these investigators have pointed out that I_K blockers have been shown to prolong the APD in human papillary muscle and to prolong the QT interval in patients. This circumstantial evidence suggests that there might be significant functional I_K channels including I_{Ks} [44, 287]. The only reported finding of I_{Ks} in human myocytes is that of Li et al. [315].

It remains unclear if there is much contribution from a delayed rectifier current in the human heart. If I_{Ks} does indeed exist in the human ventricle, it would in conjunction with I_{Ca} be responsible for the restitution of action potential duration at long diastolic intervals and long basic cycle lengths. Since we do not yet have consistent and reliable information on these currents, only one effective current I_K with a long time constant is retained in the SHV model, with an amplitude selected to match target action potential durations. The activation $V_{0.5}$ is set to –16 mV as suggested by Veldkamp [503]. Inactivation Xi(V) is retained from the LRS model. The time constant curve for $\tau_x(V)$ resembles that of canine myocytes, but shifted such that the peak is at a lower voltage of –70 mV, and the positive arm reaches a lower asymptote of 100 ms. These adjustments result in rapid activation when V is high, and slow recovery at low voltages consistent with the findings of Veldkamp [504].

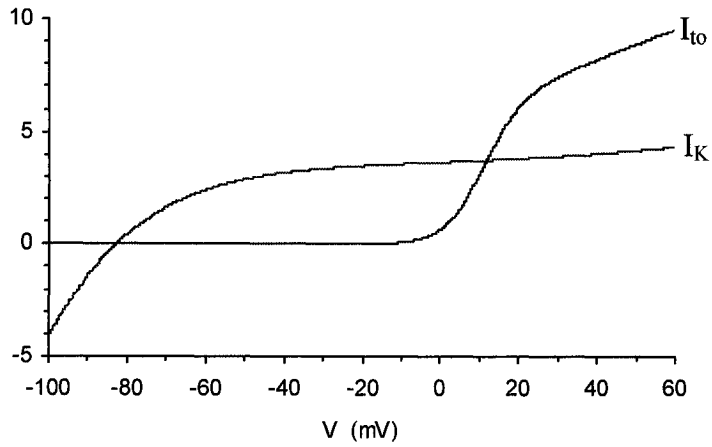

Figure 8.8. Time-dependent potassium currents are the delayed-rectifier current I_K and the transient outward current I_{to}. Steady-state values are shown. The former is modified by the gating variable X(t), and the latter is modified by p(t) as described in the text.

8.2.5 Transient Outward Current

Some action potentials have a characteristic "spike and dome" morphology, particularly those of ventricular epicardium, mid-myocardial M cells, and some atrial cells. Other action potentials, notably in endocardial cells and some atrial cells, have a smooth monotonic decrease during phase 2 repolarization. A brief early transient outward current I_{to} carried by potassium causes partial phase 1 repolarization, and is responsible for the "spike and dome" morphology of epicardial and M cells. This characteristic feature attributed to I_{to} has been observed in cells from several species, including human. Although once attributed to chloride, I_{to} appears to be carried by potassium, and can be modeled with Hodgkin-Huxley kinetics. This current seems to be important in simulating accurate action potential morphology and regional heterogeneity. However, neither the basic LRS model, nor the original LR1 model that it mimics, contain I_{to}.

The functional role of I_{to} in the heart is not clear, and has been the subject of speculation. Since the time course of I_{to} overlaps with activation of the sodium and calcium currents, this transient outward current effectively slows the peak effect of these inward currents,

and determines the degree of immediate phase 2 repolarization. This influences the plateau potential, which impacts on the degree of calcium and potassium current activation, and can therefore influence the APD, calcium influx, and contractility. Experimental application of the I_{to}-blocker 4-aminopyridine produced only a small change in APD. Computer simulations of the action potential by Priebe and Beuckelmann [406] failed to show much difference in APD, with and without I_{to}. There is evidence that I_{to} receives α-adrenergic modulation, and might be important in autonomically induced arrhythmias. Pacing induces rate-dependent downregulation of I_{to}, suggesting a role in cardiac memory [424]. The transmural gradient of I_{to} has been implicated in differences in refractoriness between epicardium and endocardium, differences in T wave morphology, the Osborne J wave in hypothermia [565], and selective depression of the epicardium in ischemia [328].

Although two components to this current have been identified in canine ventricle, a fast I_{to1} and a slow I_{to2}, a single current I_{to} will be used in the present SHV model to maintain parsimony. Adequate behaviour can be captured with a single component, and accurate modeling of two separate components would require additional stored variables with little gain in overall dynamical behaviour. The following form will be assumed.

$$I_{to} = g_{to}\, p\, s\, (V - E_K) \tag{8.5}$$

This current activates above -20 mV, and increases approximately linearly with V [11, 38, 287, 364, 454]. Since I_{to} appears to be carried by potassium, the reversal potential will be assumed equivalent to E_K, although it has been measured in failing hearts at the more positive value of -65 mV [363]. Activation of human ventricular I_{to} has $V_{0.5}$ values that vary considerably between studies: 9.7 mV (epi) and 23.1 (endo) [531], 16.7 [363], -8.9 (epi) and -7.8 (endo) [287], 11.8 [11], 25.7 (epi) and 31.6 (endo) [364], 20.6 [532]. Some of these differences might reflect varying degrees of diseased state of explanted hearts. Corresponding inactivation $V_{0.5}$ values are: -31.9 mV (epi) and -25.3 (endo) [531], -34.5 [363], -36.3 (epi) and -33.0 (endo) [287], -30.5 [11], -9.5 (epi) and -17.6 (endo) [364], -21.4 [532].

Since activation of I_{to} is rapid, and we would prefer to avoid adding new state variables, it will be assumed in the SHV model that p activates immedately upon upstroke, and is equal to its steady-state value p_∞, with the time constant effectively being zero. The half activation $V_{0.5}$ is given an intermediate value of +10 mV, within the range of the above studies. If, for convenience, the inactivation variable s is assigned $V_{0.5}$ of –5 mV, then we can define s = (1 – d), where the activation variable d from I_{Ca} is used as a surrogate variable to avoid further computer storage. Since p_∞ is not time-dependent, the resultant gating product p_∞ (1 – s) causes a transient current pulse that activates rapidly on upstroke and inactivates in parallel with activation of I_{Ca}. These choices place the foot of I_{to} activation around –20 mV, consistent with experiments. The measured inactivation time constants of I_{to} are 61ms [11], 37.6 ms [501], and 35.6 to 48.4 ms [532]. Recovery of I_{to} measured in human ventricle is largely monoexponential with short time constants of: 22 to 39 ms [531], 41 ms [363], 9.1 [364], 18 to 25 ms [532]. By comparison, the model τ_d, which will control I_{to} inactivation, is between 8 and 23 ms. Using τ_d to control recovery of s in the SHV model gives a time constant at rest of about 9 msec. Consequently, the notches of epicardial and M cells are preserved even at short diastolic intervals. The peak amplitude of I_{to} is set to 10 pA/pF, consistent with reported values in epicardial cells. Although the substitution of d for s is not a perfect replacement, performance appears to be reasonable, and computational demand is not increased.

After the SHV model development was completed, a simplified human ventricular cell model was published by Bernus et. al. [34]. Their modelling approach followed a similar process to ours. The more detailed model of Preibe and Beukelman [406], based on available voltage clamp data from human cells, was simplified to incorporate six state variables, rather than the five used in the SHV model. The Bernus model simplifies the sodium current product h*j by a variable v^2 that is similar to our h(t). Their calcium current also activates rapidly by a variable similar to our $d_\infty(V)$. As in the SHV model, potassium currents are combined into time-dependent and time-independent components. The extra state variable in the Bernus model is assigned to the transient inward current I_{to}. Although a formal comparison between the SHV model and the Bernus model has not yet been conducted, the two models appear to be remarkably similar, despite being developed

independently around the same time. It is not entirely surprising that other models of human ventricular action potentials would be under development elsewhere because a general philosophy of cellular model parsimony is necessary at this time to allow large-scale computation of action potential propagation in a whole heart.

8.3 Human Action Potentials

Human action potential characteristics can be measured experimentally *in vivo* only to a limited extent. The majority of such studies have involved the RV endocardium due to its easy accessibility by transvenous catheter during clinical investigation. A few studies have examined the LV endocardium by catheter, and even fewer have measured the epicardium during cardiac surgery. Explanted Langendorff whole-heart preparations have also been examined. Some of these studies used microelectrodes, while others employed suction monophasic action potential recording (MAP). These differences in methodology, pacing rates, diseased substrate, temperature, physiological and pharmacological milieau, and the overall variability between studies, compound the difficulty in defining standard human action potentials for the purposes of mathematical modeling.

Cellular properties also vary spatially throughout the myocardium, exhibiting differences in local electrophysiological properties and responses to pharmacological agents. These regional variations in action potential behaviour might influence electrical wave propagation and stability, and may be important in arrhythmogenesis and control. The most notable regional differences are those between epicardial and endocardial cells. Mid-myocardial M cells, with long action potentials at slow pacing rates, have also been found in rat, guinea pig, canine, and human ventricles. Several studies in animal specimens have examined differences in ionic currents between these distinct cell types, although relatively few studies have focussed on human tissue.

Table 8.3 shows a summary of several studies measuring human ventricular action potentials. This table is not meant to be exhaustive, as there is a vast literature on human electrophysiological studies that holds more information on action potential durations.

The purpose of this table is to show the considerable variability in measured APD, and to establish approximate target values to calibrate the mathematical model being developed. Only two studies could be found that reported APD values from the human LV that also specified endocardial or epicardial locations. The remainder of published APD studies examined only the RV endocardium accessed by transvenous catheter. No published data could be found on RV epicardial action potentials. For the purposes of the model being developed, one must define epicardial and endocardial action potential characteristics. The results in Table 8.4 are the achieved targets of APD and restitution in the SHV model, following titration of the baseline parameters.

Regional and transmural differences in action potential duration depend on differences in ionic currents. Most studies comparing epicardial and endocardial cells have involved voltage-clamping of tissue from animal species. Litovsky and Antzelevitch [322] proposed that the transient outward current I_{to}, found predominantly in epicardial cells, was responsible for the differences seen in morphology of action potentials. This current causes the partial repolarization notch during phase 2 prior to the plateau [13], and appears to have a substantial effect on shortenting of APD, as seen both experimentally and in mathematical modeling. This current is prominent in the epicardial cells, but almost absent in endocardial cells of many species [13], including humans [362]. Simulations of the SHV model show that the presence of I_{to} shortens APD.

Konarzewska et al. [287] found I_{K1} to be similar in human LV subepicardial and RV subendocardial ventricular myocytes, although measurements were not made above –60 mV. Liu et al. [323] found I_{K1} to be about 10% lower in canine endocardial cells as compared with epicardial cells. Furukawa et al. [185] found the amplitude of I_K to be about 47% lower in feline endocardial cells, with similar voltage dependence exhibited between epicardial and endocardial cells. The difference was considerably less in I_{K1}. Antzelevitch et al. [13] found much less distinction in canine ventricular cells. No other studies quantifying regional differences of I_{K1} or I_K in human cells could be found in the literature. Curiously, a few studies have shown human epicardial cells, which are

characterized by prominent I_{to}, to actually have longer APD's than endocardial cells [394].

For modeling purposes, separate parameter sets will be defined for epicardial, endocardial, and M cells. To account for regional action potential differences, the currents I_{to}, I_{K1}, and I_K are modified in the model by dimensionless coefficients fk1, fk2, and fk3 respectively, which vary from 0 to 1 to control regional differences in current density. The action potential characteristics in Table 8.4 have been chosen assuming I_{to} to be very smallest in endocardium, I_K to be uniform transmurrally, and I_{K1} to be largest in the epicardium.

The behaviour of mid-myocardial M cells with long action potentials can be simulated satisfactorily by lowering I_K and I_{K1}. We found that accounting for the long time constant of restitution also required extending the recovery τ_f from 350 to 500 ms, which allows good fit to the restitution curve for cycle lengths up to 2 seconds. The spatial distribution and coupling of these cells throughout the ventricles have not yet been adequately defined by experiments reported in the literature. At this time, one can only make assumptions regarding M-cell distribution for the present simulations, pending better experimental elucidation of their properties. The role of M cells in arrhythmogenesis appears to be important mainly, at slower heart rates. During tachyarrhythmias like VT and VF, the action potential duration of M cells approaches those of endocardial and epicardial cells and the differences become less significant.

The final version of the proposed SHV model, shown in Table 8.2, differs substantially from the original LR1 model. The proposed modifications to LR1 are necessary to incorporate the aforementioned changes to I_{Na}, I_{Ca}, I_{K1}, I_K, and I_{to} in an attempt to model human ventricular cells with a reasonable degree of computational parsimony. Model conductances, gating parameters, and time constants have been adjusted through simulations, such that action potential behaviour approximates human data where available in the literature. This SHV cellular model is sufficiently flexible that action potential and restitution properties can be easily modified for specific applications.

Table 8.3 Restitution of Action Potentials Measured in Human Heart

Location	Method	BCL	APD_{90}	Reference
LV endo	ME	1000	378	[195]
LV endo	MAP	594	239-273 min	[180]
		833	306-336 max	
LV epi	MAP	618	247-320	[180]
		741	270-330	
RV endo	MAP	400	225	[307]
		600	265	
RV endo	MAP	400	280-300	[355]
		600	270-290	
		1000	290-400	
RV endo	MAP	300	218	[447]
		400	231	
		600	260	
RV endo	MAP	400	216	[178]
		600	272	
		1000	328	
RV endo	MAP	300	210	[434]
		400	236	
		600	270	
RV endo	MAP	400	220-250	[182]
		600	230-260	
		1000	240-270	
RV endo	MAP	300	220	[371]
		400	240	
		600	270	

ME	Microelectrode in resected tissue specimen
MAP	Monophasic action potential by suction catheter
APD	Action potential duration, ms
BCL	Paced basic cycle length, ms

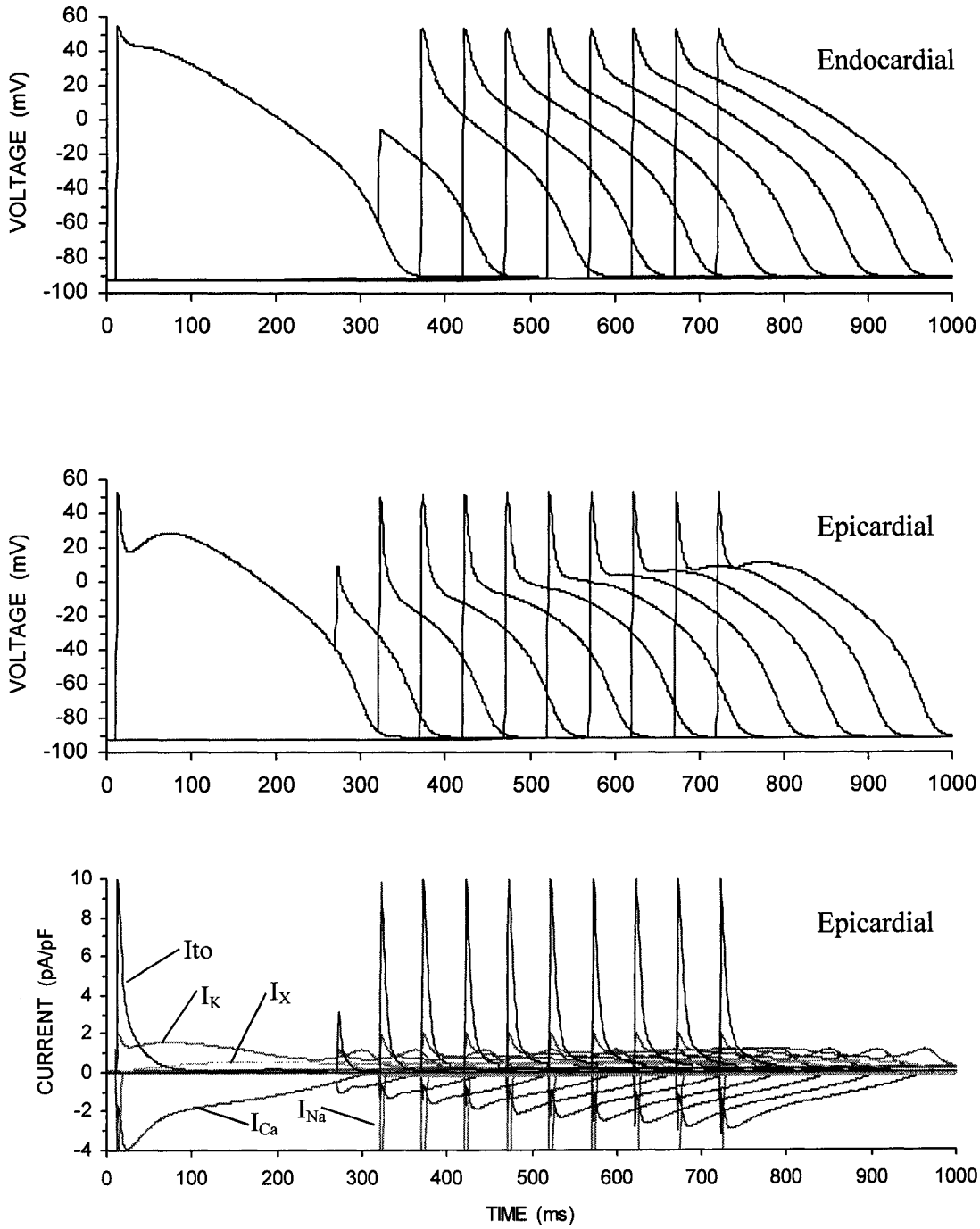

Figure 8.9. The SHV model of human ventricular action potential showing epicardial, and endocardial cell voltages and ionic currents for the epicardial cell.

Table 8.4 Restitution of Action Potentials Simulated by SHV Model

BCL	Endo*	Cell*	Epi*
200	177		161
300	211	234	188
400	239	269	213
600	282	325	256
800	310	365	284
1000	326	393	301
2000	350	443	325
5000	354	452	329

* APD_{90} at 90% repolarization. APD are for steady pacing

8.4 Model Performance

Action potentials V(t) are calculated by numerically integrating the charging of the membrane capacitance by the total ionic current and any external stimulus current injection

$$I_{ion} = I_{Na} + I_{Ca} + I_{KT} + I_K + I_{to} \tag{8.6}$$

$$C_m \frac{\partial V}{\partial t} = I_{ion} + I_{stim} \tag{8.7}$$

Currents are expressed per unit area in $\mu A/cm^2$. C_m is the specific membrane capacitance chosen to be 1.0 $\mu F/cm^2$ in accordance with previous mathematical models. This value of capacitance is based on measurements by Weidman in 1955, and is consistent with more recent measurements [501]. Since C_m is set to exactly 1.0 $\mu F/cm^2$, membrane currents can also be expressed in pA/pF, which facilitates comparison with voltage clamp literature. I_{stim} is the externally applied depolarizing stimulus current. Sample action potentials for endocardial and epicardial cells are shown in Figure 8.9, along with their contributing ionic currents. The effect of external potassium concentration $[K^+]_o$ on SHV endocardial action potentials is shown in Figure 8.10 and Table 8.5.

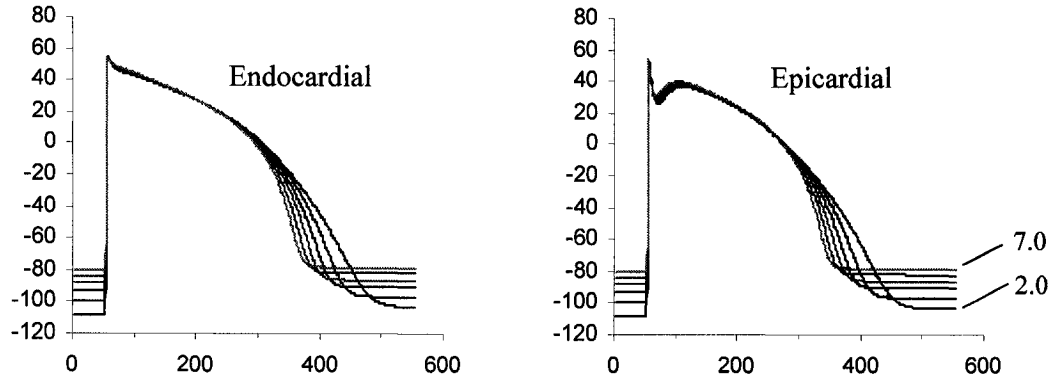

Figure 8.10. Effect of extracellular potassium concentration $[K^+]_o$ on the endocardial (left) and epicardial (right) cell action potentials. Raising $[K^+]_o$ from 2.0 to 7.0 mEq/L increases outward currents I_K and I_{KT}, which shortens the APD and depolarizes the resting potential.

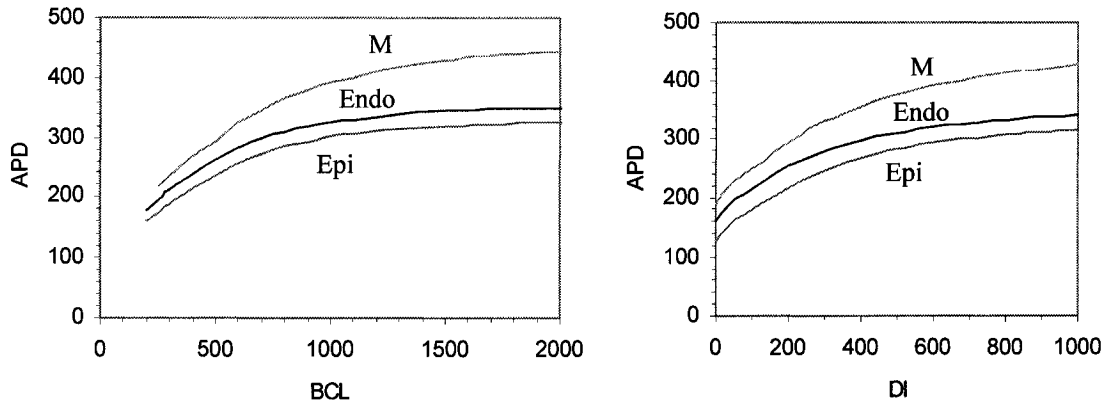

Figure 8.11. Restitution curves of action potential duration for the SHV model simulating endocardial, epicardial, and M cells. Dynamic restitution (left) shows steady-state APD for a constant paced basic cycle length BCL. Standard resitution (right) shows APD of a single action potential following a diastolic recovery interval DI.

Table 8.5. Effect of Extracellular $[K^+]$ on Resting Potential and Threshold

$[K^+]_o$	APD Endo	APD Epi	V_R	I_{th}
2.0	397.4	368.6	-108.4	21.2
3.0	370.8	344.2	-99.9	18.1
4.0	354.4	329.2	-93.3	15.6
5.0	343.2	319.2	-88.0	13.6
6.0	338.2	315.0	-83.6	11.8
7.0	328.6	306.0	-79.8	10.6

8.4.1 Restitution

Restitution refers to the recovery of action potential duration (APD) following preceding action potentials (AP). There are two types of restitution curves: standard and dynamic. The standard restitution expresses APD as a function of diastolic interval (DI) measured from the preceding AP tail. In practice, a train of constant pacing S_1-S_1 action potentials is followed by a varying test S_1-S_2 diastolic interval. Dynamic restitution expresses steady state APD as a function of a constant pacing interval S_1-S_1 called the basic cycle length (BCL).

Standard: APD = f [DI]

Dynamic: APD = f [BCL]

The restitution curves for the nominal SHV model are shown in Figure 8.11, illustrating the role of pacing interval and diastolic recovery on APD. The magnitude of the calcium-channel closing gate f at the time of action potential upstroke is an important determinant of subsequent APD. Small f at the time of upstroke initiation results in low subsequent I_{Ca} magnitude and short APD. Fully recovered f at the time of upstroke gives maximal APD. The intercept of the restitution curves APD = f[DI] and APD = f[BCL] are dependent on the minimum f value. Figure 8.12 shows how restitution curves can be manipulated by changing two parameters: $V_{0.5}$ for f determines the intercept at short APD, and the

recovery time constant τ_f determines the effective time constant of restitution. The time constant τ_x also plays a small role at the longest recovery intervals, depending on the magnitude of I_K contribution to the action potential.

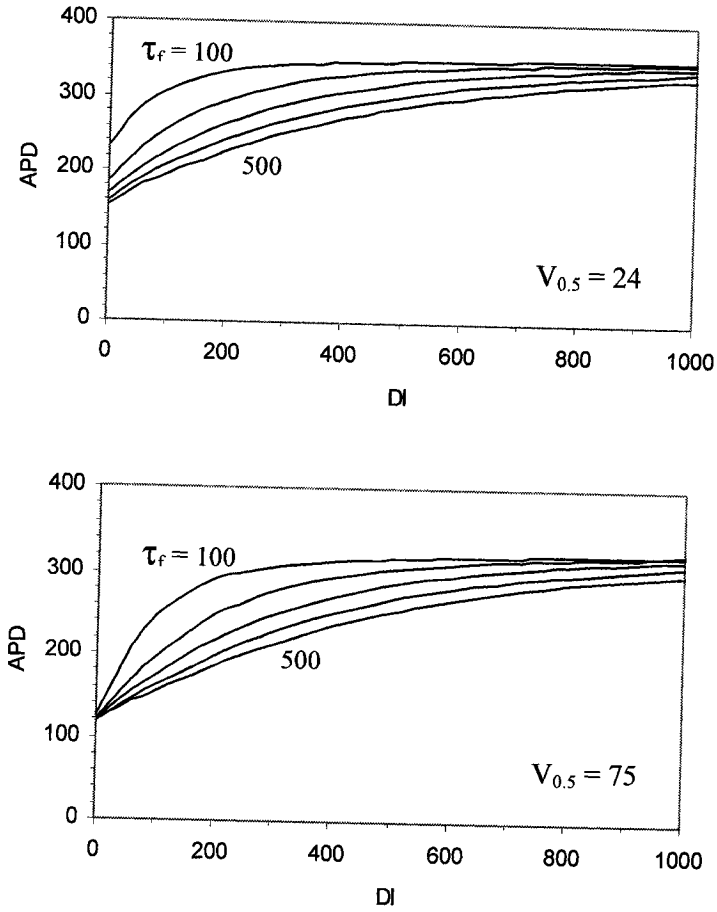

Figure 8.12. Changes in the time constant for f control the effective time constant of the APD restitution curve. Shifting $V_{0.5}$ for the inactivation variable f(t) controls the intercept of the APD restiution curve. Each curve is for different τ_f shown in 100 ms intervals, for $V_{0.5}$ = 24 (top) and $V_{0.5}$ = 75 (bottom). These two variables are like control parameters that can alter the APD restitution curve intercept and time constant as desired.

8.4.2 Threshold

The action potential threshold can be defined as the minimum stimulus current I_{th} necessary to cause the cell to fire. The threshold voltage V_{th} is that reached at the end of the stimulus interval corresponding to I_{th}. These definitions are sensitive to what one defines as the precise moment of firing, a somewhat arbirary moment during a continuous upstroke. We define the threshold to be the point where dV/dt becomes positive at one time step dt beyond the end of the stimulus interval, regardless of the amplitude of the subsequent action potential. This definition is appropriate for solitary cells for the purpose of comparison under different conditions and stimulus protocols. An alternative definition might be the minimum current impulse needed to initiate propagation. This scenario will be addressed in the next chapter. Stimulus current thresholds for the SHV model are shown in Figure 8.13 as functions of recovery interval from the previous action potential, measured from the time V passes below -80mV. The effects of varying extracellular potassium concentration $[K^+]_o$ is also shown.

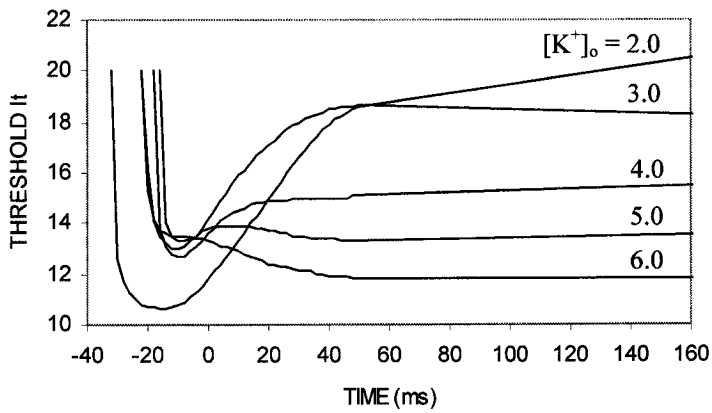

Figure 8.13. Firing threshold of a single cell in the SHV model for 2-ms stimuli. Stimulus current I_{th} depends on the diastolic recovery interval DI and the potassium concentration $[K^+]_o$. Note the presence of greatest supernormality at low $[K^+]_o$.

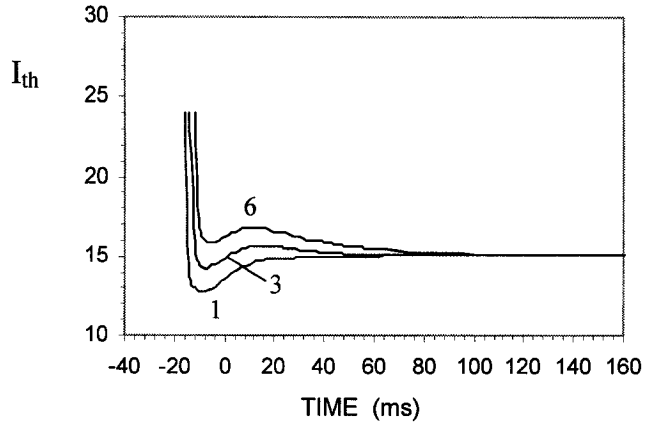

Figure 8.14. Supernormality, seen as an early dip in the current threshold, is enhanced by fast sodium channel recovery. If h(t) recovers faster than V(t) repolarizes, firing requires less ΔV to reach threshold. Time scale is relative the action potential tail at V = –80 mV. The numbers for each curve are the prolongation factor for the time constant of recovery of h, the nominal value being 3. $[K^+]_o = 4.0$.

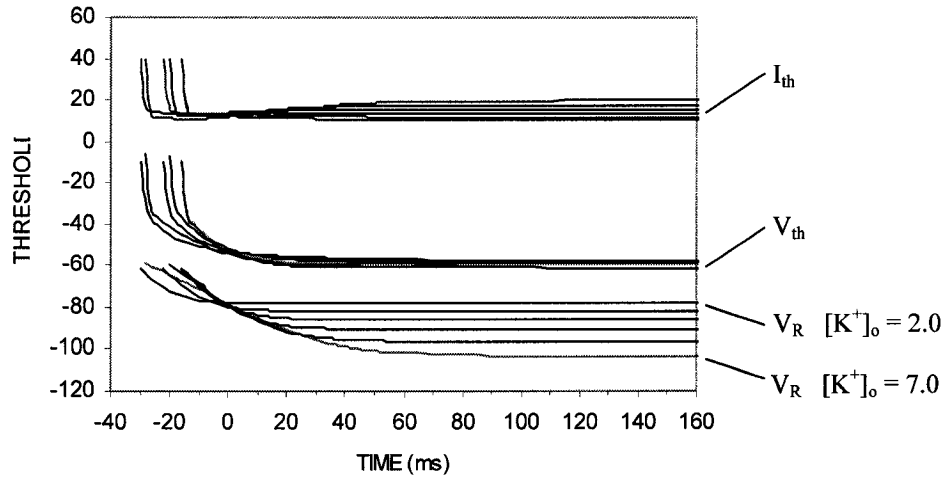

Figure 8.15. Membrane voltages prior to stimulus delivery V_R are shown at bottom versus recovery interval from the point where V = –80 mV for different values of $[K^+]_o$. Voltages V_{th} after the 2-ms barely-threshold stimulus are shown in the series just above. The corresponding current thresholds I_{th} are shown at top, which are equivalent to those in Figure 8.13.

8.4.3 Supernormality

It was first demonstrated in Purkinje fibre that near the end of action potential repolarization the threshold for subsequent firing is briefly reduced below the value for completely rested tissue [79]. Ventricular tissue appears to behave similarly [117]. While demonstrated experimentally in cellular preparations, any practical importance of this interesting phenomenon to arrhythmogenesis has not been demonstrated. As will be shown later, weak defibrillation shocks give rise to new activation wavefronts and unidirectional block within the supernormal window where the stimulation threshold is lowest. This window may prove to be important to the mechanisms of fibrillation and defibrillation shocks. The present SHV model exhibits supernormality as illustrated in Figure 8.13. This occurs because the voltage threshold recovers faster than the action potential voltage, allowing the difference between these curves to be lowered transiently. Supernormality is therefore greatest at low potassium concentations, because action potential recovery is slower, and is enhanced by faster recovery of sodium channels, which lowers the voltage threshold curve as in Figure 8.14. The voltages before and after the delivery of a threshold current stimulus are shown in Figure 8.15.

8.5 Automaticity

Cardiac cells usually remain close to resting potential, unless stimulated to threshold by an external current. Automaticity refers to an excitable cell spontaneously depolarizing away from the resting state according to its own intrinsic dynamics in the absence of any external stimulus. Pacemaker cells in the SA node rely on this phenomenon for their normal function, and may rely on a slow depolarizing current I_f [132]. Many cardiac cells experience slow automaticity at long diastolic intervals in the absence of any driving current, as with ventricular escape beats in bradycardia or complete A-V block, but are usually prevented from doing so by overdrive from normal sinus rhythm. Dysrhythmias can arise when abnormal automaticity at a specific site causes an ectopic focus to undergo spontaneous diastolic depolarization and fire rapidly, initiating a propagating wave. The LR1, LRS, and SHV models are completely passive during recovery, being

pulled monotonically to resting potential by the dominant outward currents, and do not exhibit such behaviour. An additional pacemaker current I_f could be added [132] to simulate diastolic depolarization, but is not essential. Automaticity will occur in any of these ionic models if an inward current, such as I_{Na} or I_{Ca} recovers sufficiently to depolarize and re-excite the cell before it reaches resting potential. This will occur with the sodium current if the $V_{0.5}$ for m^3 is shifted to a slightly more negative potential. In the SHV model we can achieve automaticity by choosing 37 mV with a slope factor of 6, and shifting I_{K1} 5 mV in a positive direction. These adjustments simultaneously raise the resting potential and lower the threshold potential. An example of this automaticity is shown in Figure 8.16. The frequency of firing is sensistive to small shifts in $V_{0.5}$ or g_{Na}. These changes convert the stable attractor at resting potential into a repellor, giving rise to a limit cycle oscillator. This phenomenon will be useful for simulating premature beats or focal VT.

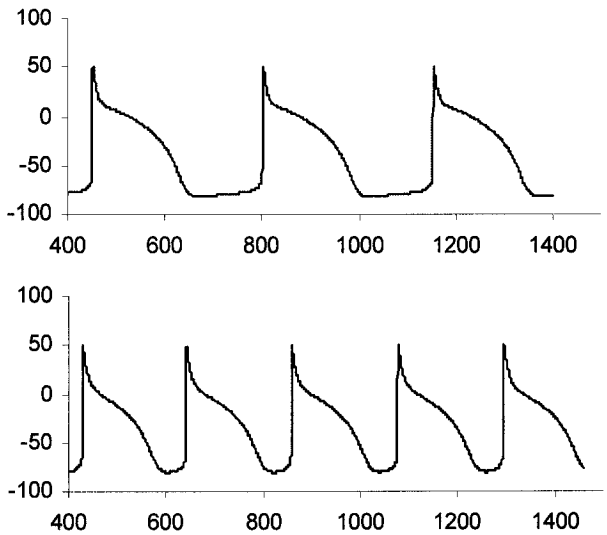

Figure 8.16. Automaticity is achieved in the SHV model by shifting the $V_{0.5}$ for $m^3(V)$. This feature is useful for simulating ectopic foci. The degree of voltage shift controls the magnitude of the diastolic depolarizing current and therefore frequency of oscillation.

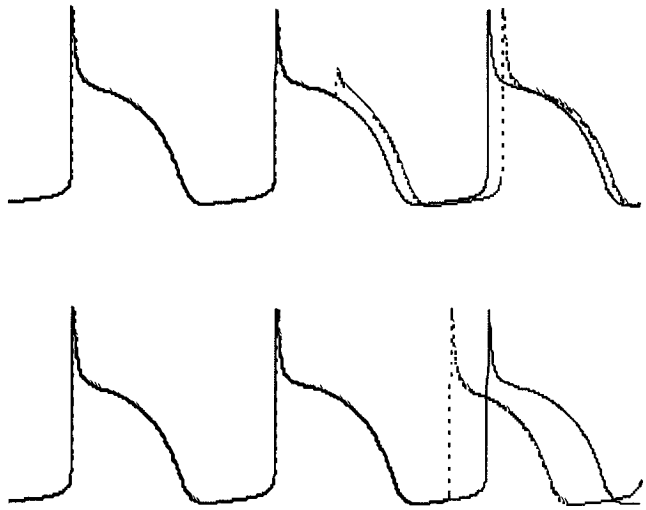

Figure 8.17. Phase resetting for pacemaker cells with automaticity. A stimulus delivered prior to the action potential upstroke advances its phase, causing it to fire earlier (top). A stimulus delivered later, after sodium current recovers enough to fire, retards the phase.

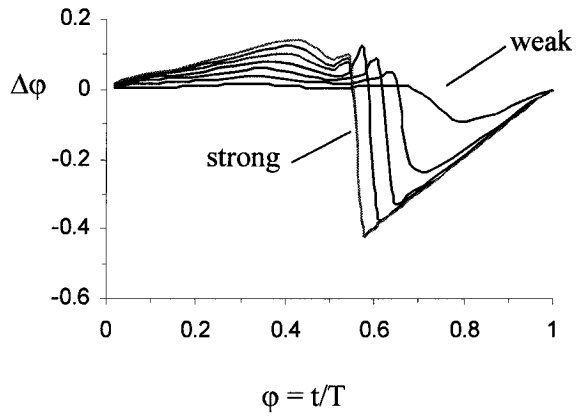

Figure 8.18. Phase resetting curve for a cell with automaticity. Relative phase φ is measured with respect to the undisturbed upstroke of a regular train of period T. A single stimulus delivered at φ changes the phase of the subsequent train by Δφ. Note that early stimuli retard the phase $\Delta\varphi > 0$, while those beyond about $\varphi = 0.55$ give rise to a new upstroke that effectively advances the phase with $\Delta\varphi < 0$. Stronger stimulus intensities cause earlier and larger phase shifts.

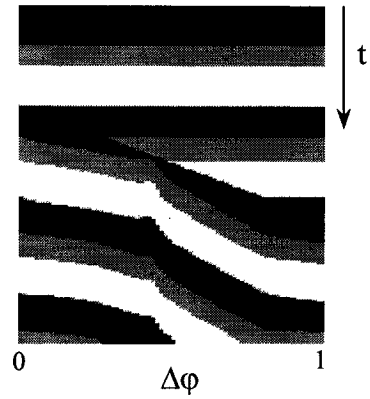

Figure 8.19. Space-time plot of a cell with automaticity. Time evolves down the ordinate axis. Relative phase of stimulus delivery φ is along the abscissa. Action potentials are shown in black. If φ = 0, the cell fires regularly like a pacemaker. As φ is advanced, the action potential is at first prolonged, and the phase is advanced. Eventually, a new action potential is evoked where the dark band splits.

An external stimulus delivered to a pacemaker cardiac cell will reset its phase. Since the action potential is prolonged if stimulated late in repolarization, the subsequent rhythm is reset with a delayed phase shift. Conversely, a stimulus given prior to the action potential, during the late diastolic period, advances the rhythm by causing premature firing. This biphasic behaviour is demonstrated in Figure 8.18, which shows the phase response for various stimulus strengths. The number of action potentials does not change with weak stimuli, only the relative phase of each is altered. As the stimulus strength is increased, however, the shifts become progressively greater, such that at a critical time and strength there is an abrupt transition from a phase lag to a phase lead, as the stimulus time moves into a region of sufficient recovery that a new action potential can be initiated. The total number of action potentials, over a given time, is therefore increased by one (type 1 phase resetting). These have been called type 0 and type 1, depending on whether or not a cycle is effectively lost as the stimulus phase is smoothly varied through a complete cycle. Winfree has explored the behaviour and general theory of biological oscillators, phase resetting, and the role of phase singularities in the stimulus strength-time space [541, 542]. The phase resetting curve (PRC) shown in Figure 8.18

demonstrates that stimuli delivered during the action potential have only a small effect on inducing a phase lag. Beyond a critical point, near the tail, the phase shift changes sign, and the action potential train is advanced. Stronger stimuli cause greater advancement, since they can reach threshold earlier. This critical point of sign reversal is related to the time of onset of sodium channel recovery. Figure 8.19 shows action potential pacemaker periodicity, as stripes of different shades plotted vertically downward over time. Across the top are various relative phases at which the external stimulus is delivered. It can be seen that the weak stimulus advances the phase of the next action potential by a small amount, but the number of waves is preserved. As the stimulus strength is increased, the phase shift δ eventually moves through the entire cycle length T and resynchronises, with resultant loss of a cycle. If these plots were stacked on top of each other, one would obtain a three-dimensional "time crystal" described by Winfree [542]. In the centre would reside a singularity, or point of phase ambiguity. Best explored an oscillating form of the Hodgkin-Huxley equations, and found two "black holes" at a critical stimulus time and strength such that the spontaneous rhythm could be annihilated [36]. The cell dynamics are effectively pushed into a hole in the state space where it no longer knows its phase, and therefore cannot fire.

8.6 Afterdepolarizations

Cardiac cells do not normally fire unless stimulated by currents from neighbouring electrotonic interactions or external stimulation. Under abnormal conditions, however, a cell can spontaneously depolarize via its own internal dynamics, giving rise to a source of focal beats [12]. While automaticity occurs following recovery to resting potential, early afterdepolarizations (EAD) occur during the action potential phase 3 or 4 before reaching resting potential [258]. Delayed afterdepolarizations (DAD) occur at resting potential following recovery. Unlike automaticity that is independent of previous action potentials, afterdepolarizations occur only after a preceding action potential has somehow "primed" the intrinsic cell dynamics for further spontaneous firing. The extra beats may be singular or occur in salvos of repetitive firing. The mechanisms responsible for EAD's and DAD's are not well understood, but probably involve internal calcium overload, forcing calcium

exit to drive an inward depolarizing sodium current via a Na^{+}-Ca^{++} exchanger [514]. Accurate simulation of EAD's and DAD's based on these assumptions would involve further model complexity incorporating internal calcium compartments, more gated currents, and increased computational demand [571].

During repolarization, the net outward current exceeds the net inward current. An afterdepolarization will occur whenever any phenomenon within the cell dynamics causes reversal of current, such that the net inward current dominates once again before the cell has recovered. While there may be several possible ionic mechanisms capable of EAD induction, premature depolarization can be simulated within the present model by a mathematical adjustment. Since the depolarizing current in the model is predominately sodium, EADs can be induced in the model simply by shifting the h recovery curve $V_{0.5}$ from -70 mV to a slightly more positive potential of -60 mV, thereby achieving spontaneous depolarization during phase 3 recovery. Shortening the Boltzmann constant for h from 3.5 to 2.5 sharpens the EAD upstroke. Shifting $V_{0.5}$ for f from -75 to -55 mV and shortening the time constant for f recovery to 25 ms results in faster calcium current recovery and increases the duration of each EAD action potential. Introduction of these changes causes spontaneous EAD activity in endocardial cells when $[K]_o$ falls below about 2.6 mM. At this concentration, the opposing outward potassium currents are too weak to prevent EAD formation. Owing to the lowest repolarizing potassium currents being in the endocardium and M cells, EADs tend to originate from these locations and may propagate through the ventricular tissue. While these adjustments designed to induce EADs are phenomenological and might not be physiologically correct, they do produce realistically appearing EADs that can be easily modified for the purpose of simulating EAD propagation and the electrocardiograms of resultant arrhythmias. Examples are shown in Figure 8.20 for a single cell with spontaneous EADs. Lowering the external potassium concentration decreases the repolarizing currents and allows the sodium current to reactivate and depolarize the cell. This modification could be used to simulate ectopic depolarization as a cause of torsades.

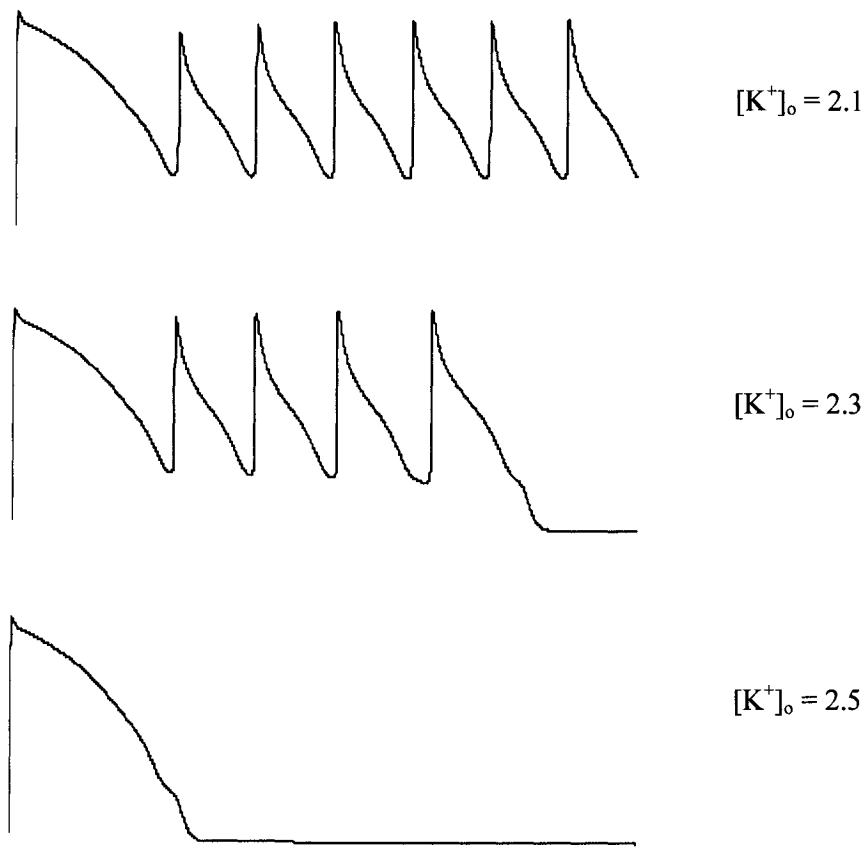

Figure 8.20. Examples of early afterdepolarizations in the SHV model resulting from shifting the recovery of I_{Na} to establish a balance toward a net inward current during phase 3 recovery. EADs do not occur unless $[K^+]_o$ is lowered to 2.5, at which point a repolarization bump is evident. At $[K^+]_o$ of 2.3, several repetitive beats occur, but terminate when I_K builds up, while below 2.1 the beats continue indefinitely.

8.7 Model Limitations

Obviously any model that simplifies a real system has limitations within subdomains of behaviour. The art of modeling involves achieving specific pragmatic objectives, while eliminating unnecessary complexity, and at the same time maintaining awareness of the compromises and limitations. A main limitation of the SHV cellular model involves simplifications to the ionic currents. In particular, calcium dynamics are overly simplified and ignore intracellular calcium. Some ionic currents are missing, in particular the I_{NaCa} exchanger, and the fast and slow potassium rectifiers I_{kr}, $I_{ks,}$. Regional heterogeneity of properties may be inaccurate since there remains uncertainty of the correct spatial distribution of I_{to}, I_{K1}, $I_{K,}$ within the myocardium. Finite discretization of the medium inevitably introduces small numerical errors due to coarse time steps and spatial grid size. These are not serious limitations if the model serves its intended purpose, which is to model the essential behaviour of cardiac tissue parsimoniously. Adding additional ionic currents and higher resolution is still feasible, but comes with higher computational cost.

Chapter 9

WAVE PROPAGATION

9.1 Tissue Electrical Properties

Myocardial contraction can be induced by a single stimulus delivered almost anywhere within the ventricles. Activity spreads away from the stimulus site throughout the syncytium by rapid electrical wave propagation. Optimal hemodynamic efficiency probably requires activation in a specific sequence, this presumably being the normal sequence that starts at three endocardial sites and is completed within 120 msec [143]. This time interval is brief, due to the rapidly conducting His-Purkinje network, and corresponds to the duration of the QRS complex of the electrocardiogram.

The availability of electrotonic current to excite cells and maintain propagation depends on intercellular electrical coupling, which is directionally-dependent in the anisotropic medium. Cell-to-cell coupling is facilitated by low-resistance gap junctions between cells. The effective coupling resistance must, therefore, lie between these values. Attempts to measure bulk resistivity of tissue have yielded inconsistent results [402, 427]. Nevertheless, coupling conductances can be chosen for the present simulation, based on the assumed parameters in Table 9.1, that give reasonable conduction velocities. The equivalent electrical circuit for the membrane is not a passive RC circuit, but rather contains elements with variable transmembrane conductance shown in Figure 9.1. The definitions of length constant λ and time constant τ are therefore valid only under

subthreshold electrotonic conditions, as these values become voltage- and time-dependent at potentials above threshold. They can be derived by linearizing the ionic model equations to get their values at any given potential. The effective membrane resistance R_m can be considered to be the ratio of dI_{ion}/dV_m taken at resting potential. This value can be determined analytically by differentiating the expression for the ionic current, with gating parameters held fixed at resting values, to obtain what would be a rather complicated expression. An easier, though less insightful, solution is obtained numerically by simply perturbing the membrane with a small input current clamp ΔI_{ion} = 0.05 $\mu A/cm^2$, and measuring the responding small voltage change ΔV_m, which turns out to be 0.21 mV for the basic SHV model. This approximated numerical derivative gives a membrane resistance at rest of 4200 Ωcm^2. The time constant of the action potential foot and the longitudinal length constant can be calculated by applying linear cable theory as

$$\lambda_L = \{ R_m / (\rho_L S_v) \}^{1/2} = \{ 4200\ \Omega cm^2 / (250\ \Omega\ cm * 2000\ cm^{-1}) \}^{1/2} = 0.92\ mm$$

$$\lambda_t = \{ R_m / (\rho_t S_v) \}^{1/2} = \{ 4200\ \Omega cm^2 / (750\ \Omega\ cm * 2000\ cm^{-1}) \}^{1/2} = 0.53\ mm$$

$$\tau_m = R_m C_m = 4200\ \Omega cm^2 * 1.0\ \mu F\ cm^{-2} = 4.2\ ms\ .$$

The conductance expressed as a diffusion coefficient is given by

$$a_L = 1 / (\rho_L S_v) = 1 / (250\ \Omega\ cm * 2000\ cm^{-1}) = .00200\ k\Omega^{-1} = 2.00\ \mu S$$

$$a_t = 1 / (\rho_t S_v) = 1 / (750\ \Omega\ cm * 2000\ cm^{-1}) = .00067\ k\Omega^{-1} = 0.67\ \mu S\ .$$

The length constants for passive membrane of 0.92 and 0.53 mm mean that electrotonic voltage spread decays approximately e-fold at these distances, and propagation should be possible on a grid of 1-mm elements. A small sacrifice in propagation fidelity might be expected in the transverse direction, owing to its shorter λ_t and the relatively large element size of 1 mm; however, the membrane is not passive. Active currents can magnify the potential gradient and facilitate propagation, despite short space constants.

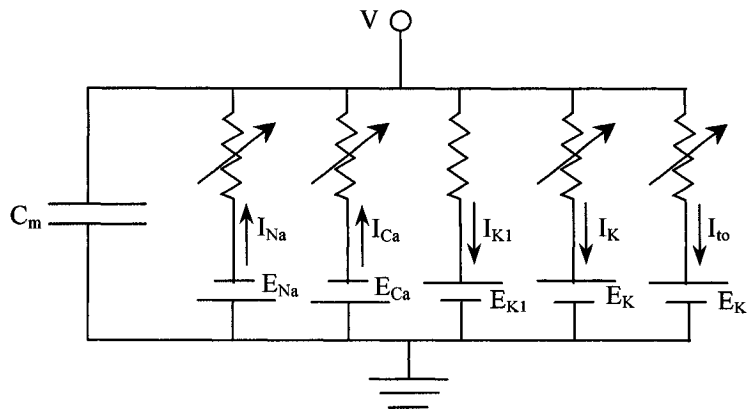

Figure 9.1. Equivalent circuit representation of a membrane patch of the SHV model.

Hunter et al. [240] obtained approximate analytical solutions to propagation of the action potential by reformulating the one dimensional cable equation with a travelling wave solution of the form $V = f(x-\theta t)$. They assumed the total ionic current during the upstroke to be various polynomials of degree n, with zeroes at V_R, V_{th}, and V_{max}. By defining η to be the potential above resting, such that $\eta = V - V_R$, the ionic current can be approximated as $I_i = g\,\eta\,[1 - (\eta/\eta_{th})^n]\,[1 - (\eta/\eta_{max})^n]$. It can be shown for the simplest cubic case, where $n = 1$, that velocity v and length constant λ satisfy

$$v^2 \propto g\, a_x\, C_m^{-1}\, f(SF)$$

$$\lambda \propto g^{-1/2}\, a_x^{-1/2}\,.$$

Conduction velocity v is therefore inversely proportional to the square root of the axial conductance a_x, under the assumption of polynomial $I_i(V)$. The parameter g is analogous, but not equal, to the sodium conductance. In the LRS and SHV models, during the upstroke (before I_{Ca} and I_K activate), $I_i(V)$ is approximately $I_{Na} + I_{KT}$, which does not fit a low-order polynomial function. It is, therefore, not possible to derive an analytical

expression for the dependence of velocity v on sodium conductance g_{Na} without considerable difficulty. Such a functional relationship would likely be complex, and is more readily determined numerically. By approximating the potential during upstroke to be a higher order function involving the HH variable m^3, it has been shown that v should be relatively insensitive to g_{Na}, except at very low values [240]. Velocity is also related to the safety factor of propagation SF, which will be discussed in the next section. Wave front curvature influences velocity in two and three dimensions, by adding additional electrotonic load in the lateral directions [159].

Table 9.1. Conduction Constants Used in the Model

Assumed Parameters:

ρ_L	250 Ω cm	Bulk resistivity (longitudinal)
ρ_t	750 Ω cm	Bulk resistivity (transverse)
S_v	2000 cm^{-1}	Cell surface-volume ratio
C_m	1.0 μF cm^{-2}	Membrane capacitance

Calculated Parameters:

R_m	4200 Ω cm^2	Membrane resistance
λ_L	0.092 cm	Length constant (longitudinal)
λ_t	0.053 cm	Length constant (transverse)
τ_m	4.2 ms	Time constant foot
a_L	.00200 $k\Omega^{-1}$	Conductance (longitudinal)
a_t	.00067 $k\Omega^{-1}$	Conductance (transverse)

Axial conductance values must be chosen for use in the models. Table 9.2 gives a summary of several studies measuring conduction velocity in ventricular tissue. Values vary considerably depending on tissue types, but do fall within reasonable ranges. These velocities will be used as a standard for comparison with simulations later, and provide a rationale for selecting the ratio of anisotropy for model tissue. One must be aware,

however, that velocities measured on the epicardium can be higher than true conduction velocities, depending on the apparent angle of the wave front relative to the epicardial surface. Arisi et al. [15] found transverse velocities as high as 33 cm/s and longitudinal velocities up to 120 cm/s during normal activation of the dog heart, perhaps due to this virtual-velocity effect. Wave front velocity will equal conduction velocity only if the vector normal to the wave front is colinear with the vector of the measured velocity. Otherwise, apparent velocity is equal to the true wave front velocity divided by the cosine of the angle between these two vectors.

Table 9.2 Mean Conduction Velocities From the Literature

Tissue	Species	Orientation	Velocity	Ratio	Reference
Papillary m.	Canine	Longitudinal Transverse	47 - 52 cm/s 14 - 20 cm/s	3.1	[469]
Epicardium	Canine	Longitudinal Transverse	58 25	2.3	[420]
Trabeculum	Calf (25°C)	Longitudinal Transverse	48 16	3.0	[92]
Ventricle	Canine	Longitudinal Transverse	7 - 71 8 - 20		[443]
Ventricle	Canine	Longitudinal	63		[141]
Endocardium	Canine	Longitudinal Transverse	98 25	3.9	[360]
Intramural	Human	Oblique	46 cm/s		[143]
Ventricle	Rabbit	Longitudinal Transverse	65 cm/s 20		[445]

9.2 Cable Model

The classic model for a one-dimensional cable was first proposed by Thompson in 1855, as a means for predicting voltage decay due to leakage in a transatlantic telegraph cable, and solved using a method developed by Fourier. Weber later solved the cable equation in cylindrical coordinates using a Bessel function series in 1873. The cable equation was given credence when Hodgkin and Rushton found it provided a good fit to subthreshold electrotonus measured in crustacean nerve axons. The voltage clamp circuit, developed by Cole and Marmont, provided experimental foundation for Hodgkin and Huxley to mathematically model action potential propagation in the giant squid axon using the cable equation. Aidley reviews and discusses many of these historical developments [5]. The advent of the digital computer permitted numerical solutions to the electrotonic equations, including ionic models, by Cooley and Dodge [96] using a trapezoidal integration scheme, and by Joyner et al. using the Crank-Nicholson [261]. The mathematical theory of one-dimensional cable conduction was reviewed by Spach and Kootsey [468], and by Hunter et al. [240] who developed approximate analytical solutions. Henriquez has more recently reviewed the theory of propagation [225].

The one-dimensional cable equation for action potential propagation is classified as a reaction-diffusion equation. It is nonlinear, owing to terms in the ionic current model.

$$C_m \frac{\partial V}{\partial t} = a_L \frac{\partial^2 V}{\partial x^2} + I_{ion} + I_{stim} \qquad (9.1)$$

$$I_{ion} = I_{Na} + I_{Ca} + I_{KT} + I_K \qquad \text{LRS model}$$

$$I_{ion} = I_{Na} + I_{Ca} + I_{KT} + I_K + I_{to} \qquad \text{SHV model}$$

These equations must be solved numerically by a time stepping simulation, due to nonlinearity of the components of I_{ion}. The implicit Crank-Nicholson method of numerical integration is inherently stable, and converges if element discretization is fine enough. Figure 9.2 shows action potential propagation of the original six-parameter LR1

model along a cable with various element sizes and time steps. The main effect of simplifying the sodium current, by removing the time constant for m, is a faster conduction velocity. When the sodium conductance g_{Na} is lowered to compensate, the agreement between the LR1 and the simplified LRS models is excellent.

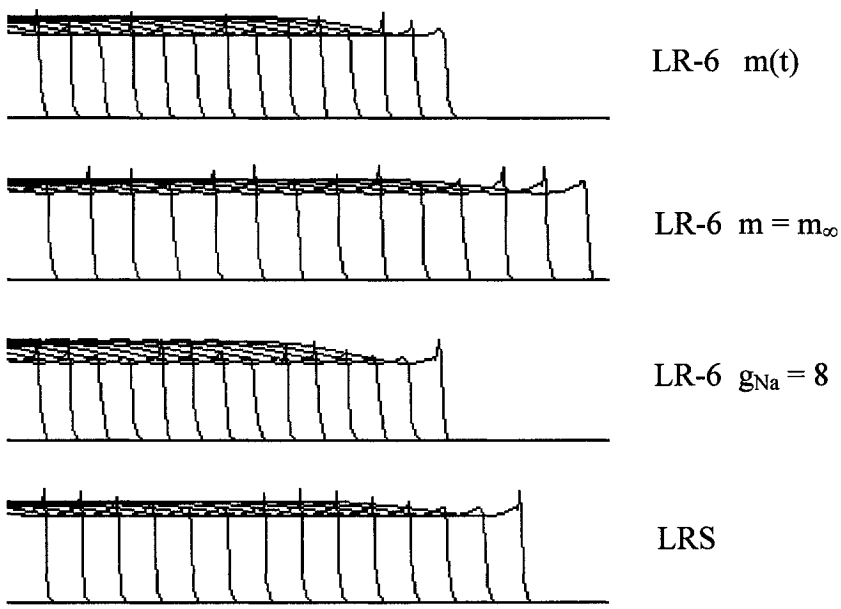

Figure 9.2. Comparison of action potential spatial profiles during propagation along a 10-cm cable. The original six-parameter LR6 model with g_{Na} = 13 is shown at top. Modifying the upstroke gating parameter to be only voltage-dependent m(t) = m_∞, simplifies the model, but as shown in the second frame, results in a faster propagation velocity. We can compensate for this side-effect by lowering the sodium conductance to g_{Na} = 8, as shown in the third frame. The bottom frame shows the simplified four-parameter LRS model, which performs in agreement with the six-parameter model at top. The cable equation is integrated using the Crank-Nicholson method. Δx = 0.05 cm and Δt = 0.002 ms.

In anticipation of larger-scale three-dimensional simulations to be run later, a simple forward-stepping Euler method will be used for most numerical integration. This decision allows avoidance of the additional complexities of higher order predictor-corrector algorithms or implicit methods, and should be acceptable if time steps Δt are sufficiently short.

$$V(t+\Delta t) = V(t) + \frac{\partial V}{\partial t}\Delta t \tag{9.2}$$

$$\frac{\partial^2 V}{\partial x^2} = \frac{V_{i+1} - 2V_i + V_{i-1}}{\Delta x} \tag{9.3}$$

Figure 9.3 shows propagation of epicardial and endocardial SHV action potentials along a 10-cm cable with $\Delta x = 0.05$ cm and $\Delta t = 0.2$ ms, using forward step Euler method. Ends are sealed with no-flux boundary conditions $\partial V/\partial x = 0$. A 2-ms point stimulus $I_{stim} = 20$ $\mu A/cm^2$ is applied to one end. Conduction velocity, with the above parameters, is about 56 m/s, consistent with that measured experimentally along longitudinal fibres.

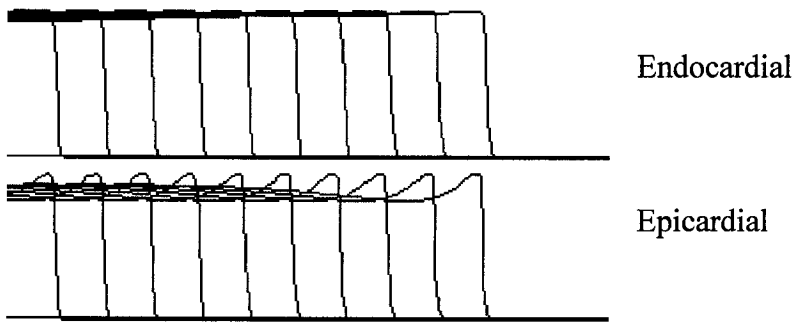

Figure 9.3. Action potential propagation along a 10-cm cable with the SHV membrane model for endocardial cells (top), and epicardial cells (bottom) with $g_{Na} = 13$, using a forward-stepping Euler method. The spike-and-dome morphology is evident in the epicardium. Conduction velocity is approximately equal for both tissue types.

9.2.1 Velocity

Figure 9.4 shows the effects of varying coupling a_L and sodium conductance g_{Na} on conduction velocity v in the cable. One should theoretically see $v \propto a_L^{1/2}$ [240]. The voltage change between relatively coarse 1-mm elements can be very large during the AP upstroke, and occasionally violate this relationship. With the objective of achieving large scale three-dimensional simulation, this potential failure of velocity to scale correctly

with conductance will be accepted, since conductances will be not be varied once they are chosen. The main consequence of this limitation is that the anisotropy ratio of conductances will be close to that of the velocities, rather than the velocities squared. One must exercise caution in interpreting results if conducting simulations involving changes in intracellular coupling.

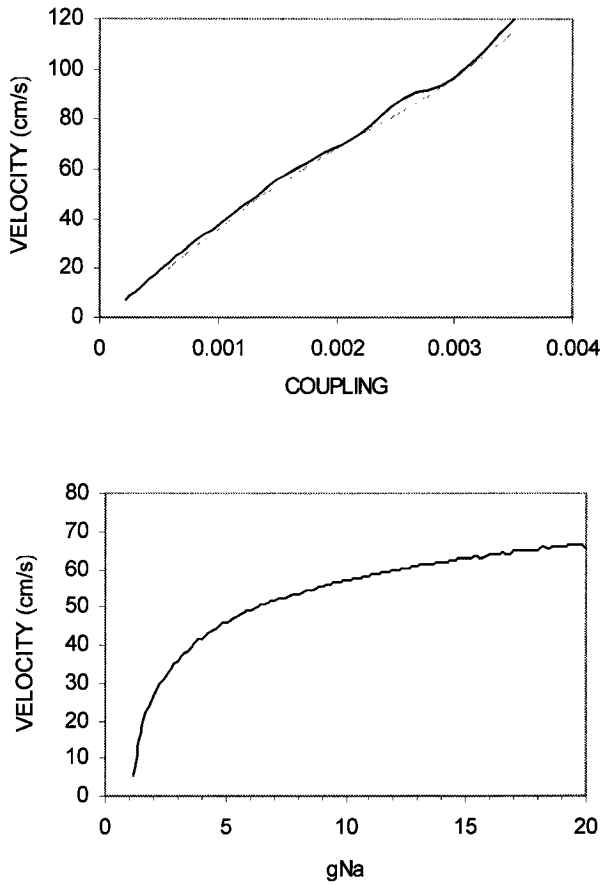

Figure 9.4. Effect of axial coupling (top) and sodium conductance (bottom) on velocity of propagation along a cable using the SHV model. The two lines in the top figure represent endocardial (thin line) and epicardial (thick line) cells, which show little difference in conduction velocities.

9.2.2 Safety Factor

Continuous propagation requires that each cell supply sufficient current to excite its downstream neighbour, while sustaining its own action potential under this load. The degree to which a cell can supply current exceeding the minimum necessary for

conduction can be quantified by a parameter called the safety factor (SF) for conduction. There have been several mathematical formulations of SF proposed [125, 240, 310], although some have been criticized [452]. Here the approach of Shaw and Rudy is followed [452]. The safety factor can be loosely defined as the ratio of source current that the cell loses, both to its downstream neighbours and to the membrane capacitance as V changes, divided by the amount of sink current received by upstream neighbours. To avoid difficulties incorporating the strength-duration relationship of current stimuli as these integrals are evaluated, Shaw and Rudy instead defined SF to be the ratio of the respective charges, or integrated currents, over the time interval that the membrane receives charge during the action potential upstroke. SF may be calculated by the following equation, where the integrals are evaluated over the time that $\int Q_m \, dt > 0$.

$$SF = \frac{Q_c + Q_{out}}{Q_{in}} \qquad (9.4)$$

$$= \frac{\int I_c \, dt + \int I_{out} \, dt}{\int I_{in} \, dt}$$

where

$$I_c = C_m \frac{dV}{dt}$$

$$I_{out} = \frac{V_i - V_{i+1}}{\rho S_v (\Delta x)^2}$$

$$I_{in} = \frac{V_{i-1} - V_i}{\rho S_v (\Delta x)^2}$$

$$I_m = I_{in} - I_{out}$$

$$Q_m = \int I_m \, dt$$

Normally there is little difference between Q_{in} and Q_{out}, except for the time lag of propagation, and there are nearly identical areas under these curves. The SF is then dominated by the influence of the substantially larger Q_c. During robust conduction, the

AP upstroke is brisk and capable of sourcing a large capacitive current, giving SF > 1. Under conditions of weaker conduction, Q_c becomes smaller and SF approaches 1. When SF = 1, conduction cannot proceed, velocity reaches zero, and block occurs. Q_c is largely obtained from the ionic current I_{ion}, which is dominated by the sodium current I_{Na}. SF is therefore dependent on both the axial coupling ρ, which determines Q_{in} and Q_{out}, and the sodium conductance g_{Na}, which influences Q_c. Reducing either of these variables sufficiently will cause conduction block. In two- and three-dimensional propagation, wave front curvature also influences the local current density [159], and plays an additional more complex role in determining the safety factor.

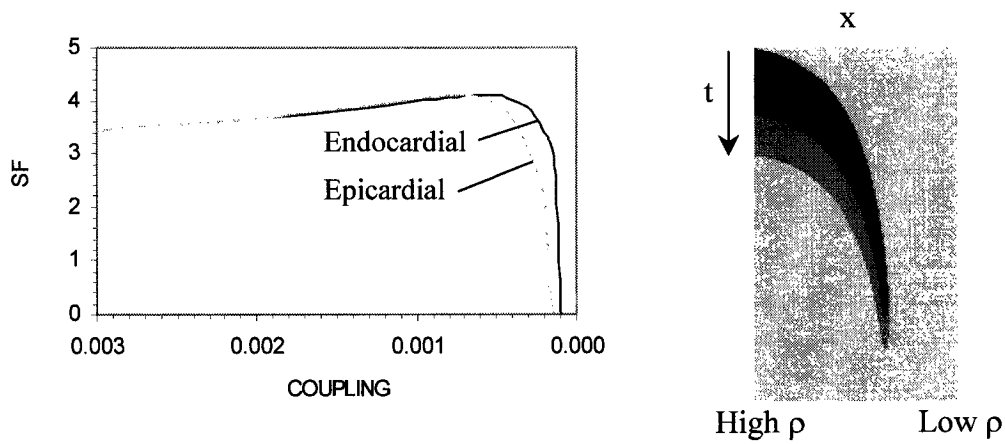

Figure 9.5. Safety factor of conduction along a one-dimensional cable as a function of axial coupling for endocardial and epicardial cells (left). The frame at right shows a space-time plot of an action potential propagating along a cable, from left to right. There is a gradient of decreasing conductivity pre-existing on the cable. Propagation fails or blocks when the wave front reaches the location where the safety factor SF = 1.

To illustrate the development of conduction block, and establish the SF for normal conduction, a modified cable model is introduced using the SHV formulation. A stimulus is applied at one end, where x = 0, and a gradient of diminishing axial coupling, $\rho(x) = \rho_1 + (x/L)(\rho_2 - \rho_1)$, and hence gradient of safety factor, is defined down the cable. Here ρ_1 = 3.0 μmho and ρ_2 =.03 μmho. Action potential conduction proceeds quickly at first, due to low-resistance coupling, but eventually reaches a critical point where the safety factor drops to 1.0 and block occurs. Figure 9.5 shows a space-time plot of this situation.

Velocity is the slope of the activation front, which drops to zero at the point of block. The conduction velocity and safety factor are shown as functions of the axial coupling ρ, derived from this simulation with $\Delta x = 0.1$ cm. The SF drops to 1.0 around $\rho = 0.1$ μmho for the endocardium, while for normal conduction, with $\rho = 2.0$ μmho, SF is about 4.1. The relationship between conductivity and block is likely sensitive to the nature of discretization, and is subject to numerical error in simulations with overly coarse media.

9.3 Sheet Model

The cable equation can be extended to a two-dimensional sheet of cells. Fibre anisotropy is incorporated by defining separate longitudinal and transverse conductivities a_L and a_t.

$$C_m \frac{\partial V}{\partial t} = a_L \frac{\partial^2 V}{\partial x^2} + a_t \frac{\partial^2 V}{\partial y^2} + I_{ion} + I_{stim} \tag{9.5}$$

In the one-dimensional cable model, the length constant λ is defined by the passive electrotonic spread, such that voltage V decays as $\exp(-x/\lambda)$ from a point stimulus. For the analogous two-dimensional isotropic case, where $a_L = a_t$, the passive membrane response to a point stimulus is, instead, proportional to the Bessel function $(1/\lambda)K_o(r/\lambda)$. Analytical solutions will not be discussed further here, since the membrane is not passive, and numerical simulation is required for solution.

More generally, fibre angles can be varied throughout the domain by expressing the electrotonic current in terms of the anisotropic conductance tensor D [95].

$$C_m \frac{\partial V}{\partial t} = \nabla \cdot D \nabla V + I_{ion} + I_{stim} \tag{9.6}$$

where

$$\nabla \cdot D \nabla V = a_T (V_{xx} + V_{yy}) + (a_L - a_T)(s_x^2 V_{xx} + s_y^2 V_{yy} + 2 s_x s_y V_{xy})$$

$$s_x = \cos \varphi$$

$$s_y = \sin \varphi$$

The angle φ is the deviation from the x axis within the x-y plane, and V_{xx}, V_{yy}, and V_{xy} represent the partial derivatives. In the isotropic case, where $a_L = a_t$, the wave front propagates outward as an expanding circle. With anisotropy, the wave front is an ellipse, with semi-major axis parallel to the principal axis of the conductivity tensor. The aspect ratio of the elliptical front depends on the ratio of the conductivities. Figures 9.6 shows radial conduction from a stimulus at the centre of a square sheet of 41x41 elements, with $\Delta x = 0.1$ cm for isotropic and anisotropic cases. Higher curvature slows velocity, due to current sink in the lateral directions. Lower coupling or conductivity slows propagation.

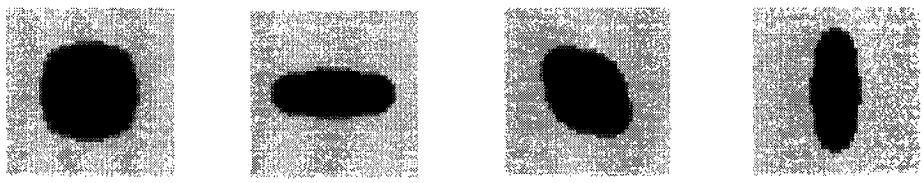

Figure 9.6. SHV action potentials propagate radially outward from a single stimulus in the centre of a two-dimensional sheet of 41x41 elements. The wave front is circular when the sheet is isotropic (left), and elliptical when it is anisotropic (right), shown here for three different fibre directions.

9.4 Block Model

The propagation equation in three dimensions, assuming symmetry in the transverse directions is relatively straight forward:

$$C_m \frac{\partial V}{\partial t} = a_L \frac{\partial^2 V}{\partial x^2} + a_T \frac{\partial^2 V}{\partial y^2} + a_T \frac{\partial^2 V}{\partial z^2} + I_{ion} + I_{stim} \qquad (9.7)$$

More generally, however, the fibre orientation is not along a cartesian axis, such that the electrotonic current must be derived in terms of the anisotropic conductivity tensor [95]:

$$C_m \frac{\partial V}{\partial t} = \nabla \cdot D \nabla V + I_{ion} + I_{stim} \tag{9.8}$$

The electrotonic current term $\nabla \cdot D \nabla V$ is derived by first transforming the conductivity tensor D^* from cartesian coordinates (x, y, z), where the longitudinal conductivity a_L is along the z axis, to a new coordinate system D with its principal axis along the fibre. The transformation matrix P is a function of angles φ and γ, which vary with location [91].

$$\mathbf{D} = \mathbf{P}^{-1}\, \mathbf{D}^*\, \mathbf{P} \tag{9.9}$$

$$\mathbf{D}^* = \begin{pmatrix} \sigma_t & 0 & 0 \\ 0 & \sigma_t & 0 \\ 0 & 0 & \sigma_l \end{pmatrix} \qquad \mathbf{P} = \begin{pmatrix} \cos\varphi \cos\gamma & \cos\varphi \cos\gamma & -\sin\varphi \\ -\sin\varphi & \cos\varphi & 0 \\ \sin\varphi \cos\gamma & \sin\varphi \sin\gamma & \cos\varphi \end{pmatrix}$$

After evaluating equation (9.9), followed by the gradient and divergence operations, one obtains a lengthy expression involving spatial derivatives of V, φ, and γ [91]. These can be denoted as: V_x, V_y, V_z, V_{xx}, V_{yy}, V_{zz}, V_{xy}, V_{xz}, V_{yz}, φ_x, φ_y, φ_z, γ_x, γ_y, γ_z. If we further assume that the spatial derivatives of φ and γ are relatively small, compared with those of V, then the resulting expression is greatly simplified, and does not involve first derivative terms of V:

$$\begin{aligned} \nabla \cdot D \nabla V = {} & a_T (V_{xx} + V_{yy} + V_{zz}) + \\ & (a_L - a_T)(s_x s_x V_{xx} + s_y s_y V_{yy} + s_z s_z V_{zz}) + \\ & 2 (a_L - a_T)(s_x s_y V_{xy} + s_x s_z V_{xz} + s_y s_z V_{yz}) \end{aligned}$$

$$s_x = \cos\varphi \cos\gamma$$

$$s_y = \sin\varphi \cos\gamma$$

$$s_z = \sin\gamma.$$

Examples of anisotropic propagation will be presented in the next chapters.

Chapter 10

VENTRICULAR ACTIVATION

10.1 Idealized Geometry

A three-dimensional model of the right and left ventricles, to be used for whole-heart simulations, is presented in this chapter. Ellipsoidal sections were synthesized and joined to approximate the size and thickness of the human heart. Anisotropic fibre angles were assigned to each element on a three-dimensional rectilinear grid denoted by coordinates (i, j, k). While more detailed human [184, 237, 347] and canine [8, 33, 368] heart geometries derived from digitized anatomical sections have been used in other heart models, the idealized ellipsoidal shape employed here keeps the geometry simple and reproducible, and is sufficient for the purposes of this study.

10.1.1 Size and Shape

Human heart dimensions obviously vary among individuals, and are also dependent on the instantaneous contractile state. Myocardial wall thickness can increase as much as 25% from diastole to systole. The heart dimensions chosen for the present computer model are based on reported autopsy specimen mid-contraction averages for normal human hearts [241], and are summarized in Table 10.1.

The LV was generated from a thick hemi-ellipsoidal shell with concentric internal and external surfaces. The RV was similarly generated, and truncated to fit onto the LV with parallel semi-major axis separation, as in Figure 10.1. The base of the heart, at the AV ring, was truncated by about 1 cm to avoid having to define complex valve geometry. This biventricular geometry was then parsed into cubic elements. Element size was set to 1 mm to obtain an 81 x 77 x 81 element block comprised of 214,580 active cells. The active cells represent 42.5% of the block. The remaining elements, within the rectangular block, but outside the heart domain, are set to be null cells, and do not participate in computation.

Table 10.1 Dimensions of Human Ventricles

RV	thickness	8 mm
	Length	76
	diameter	76
LV	thickness	16 mm
	length	80
	diameter	64
Axial separation		1.0 cm

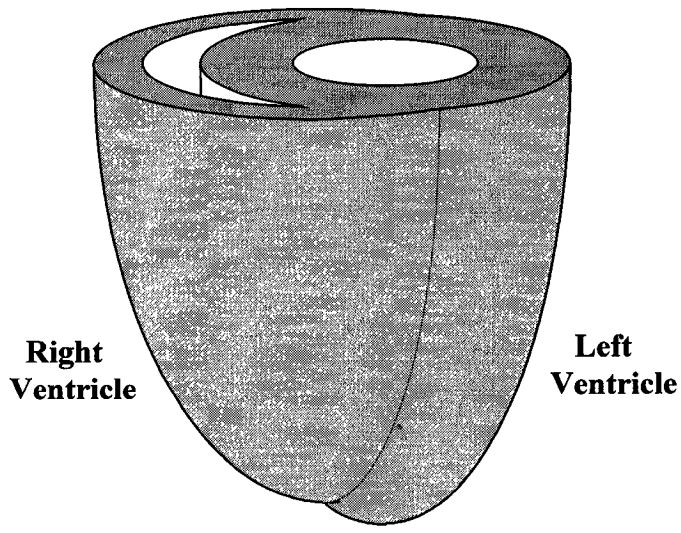

Figure 10.1. The basic ellipsoidal biventricular model drawn to scale.

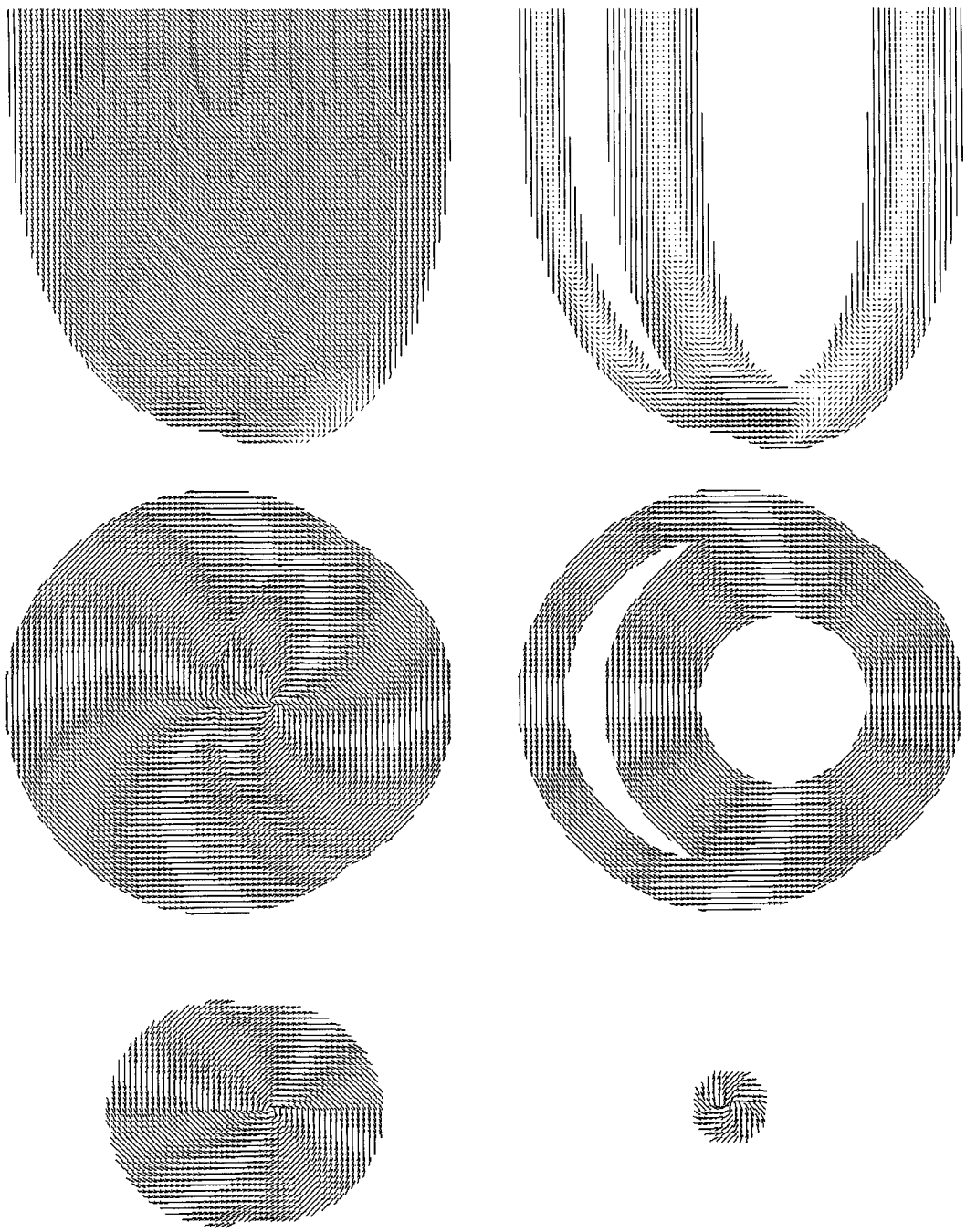

Figure 10.2. Fibre orientation in the biventricular model, shown at several transverse slices. The top frames show the epicardial surface and a coronal section. Middle frames show the apical and basal views. Bottom frames show transverse slices close to the apex.

10.1.2 Fibre Angles

The ventricular myocardium is a continuous muscle mass with fibres wound such that they spiral toward the apex and form a gradient of fibre angle across ventricular walls [477]. The model representation is shown in Figure 10.2. Histological studies show the fibre angle distribution to be approximately linear, but actually slightly sigmoidal, across the wall, varying from about –60 to 60 degrees depending on location [213]. There is a tendency to somewhat greater angles at the papillary muscle in some locations, up to 90 degrees at the papillary muscle root [175]. Angles increase during diastole in some, but not all, regions [478].

To maintain simplicity within the biventricular model, fibre angles across the wall were varied from $\beta_i = -60^o$ at the endocardium to $\beta_o = 60^o$ at the epicardium. Fibre angles were first defined on these surfaces only, and then multiplied by a longitudinal parameter function $f_b(z)$ which equals one at the base where fibre angles are maximum away from the x-y plane, and progressively decreases toward zero, to lie flat in the x-y plane, as the apex is reached.

$$\beta = f_{bi}\,\beta_i \qquad \text{(endocardium)} \qquad (10.1)$$
$$\beta = f_{bo}\,\beta_o \qquad \text{(epicardium)}$$

where
$$f_{bi} = \text{sqrt}\,[\,1 - z^2/c_i^2\,]$$
$$f_{bo} = \text{sqrt}\,[\,1 - z^2/c_o^2\,]$$

Fibres angles β throughout the thickness of the LV and RV were interpolated between the surface values by Laplacian smoothing. This considers fibre angle to be analogous to the electrical field between plates of a capacitor. Boundary conditions of β_i applied to the RV and LV endocardium, and β_o applied to the entire epicardium, were assigned. Smooth interpolation was achieved by modifying the main electrical propagation simulation, which solves the reaction-diffusion equation for transmembrane potential V, to solve instead the diffusion equation $d\beta/dt = a\nabla^2\beta$ to a steady state giving $\nabla^2\beta = 0$. The ionic

and stimulus currents were set to zero, and the simulation was run until a steady state was reached. This solution to the Laplace equation ensures a smooth distribution of fibre angle $\beta(i,j,k)$ throughout the entire three-dimensional myocardium.

The circumferential angle φ was calculated as the tangential angle in polar coordinates of the concentric fibre layer, rotated by an additional angle ε representing the degree of helical twist towards the longitudinal axis as the apex is approached. Twist becomes progressively tighter at the apex. Semi-major ellipsoidal axes for the RV and LV were centred at (x_c,y_c). Maximal helical angle ε_{max} at the apex was set to 60^o to match the visual appearance of fibres in histological studies [167, 213].

$$\varphi = \tan^{-1}[(y - y_c)/(x - x_c)] + \varepsilon \qquad (10.2)$$

where $\varepsilon = \varepsilon_{max} f_f$

$$f_f = 1 - [\,1 - z^2/c^2\,]^{1/2}$$

Smooth interpolation of φ throughout the myocardium was achieved by the same technique described above, by assigning boundary conditions of φ to the endocardium and epicardium. The Laplace equation $\nabla^2\varphi = 0$ was then solved by the simulation, as previously described, to yield the full distribution of φ throughout the myocardium. Figure 10.2 shows the final anisotropic biventricular model with fibre orientation. The smoothed layered concentric shells can be seen. These elements are available for cell-type assignment to account for transmural and regional ionic current heterogeneity. It is noteworthy that there is a dominant convergence of fibres to the LV apex, and there is also a secondary locus nearby on the RV, consistent with histology [175].

10.1.3 Transmural Heterogeneity

Ionic currents, and therefore cellular properties, vary regionally within the heart, most notably across the ventricular wall, but also from apex to base. One consequence of this heterogeneity is that the endocardial APD is usually longer than that of the epicardium. This transmural gradient of APD affects the repolarization sequence, and contributes to T wave and U wave genesis [12]. Theoretically, T waves should be of opposite polarity to the QRS complex (discordant), and have the same integrated area as the QRS complexes, if all action potentials are identical. In reality, T waves are usually concordant with the QRS complex because the vector representing spatial voltage gradient reverses during recovery. The APD is also prolonged in the mid-myocardial layer, due to M cells that have a long APD, particularly at low heart rates. The exact APD distribution throughout the heart is not presently known, and has been technically difficult to determine. Limited studies suggest that M cells exist within both the LV and RV, and may be more dense closer to the endocardium [13]. Better determination of the M cell distribution is essential to the development of more accurate whole heart models that simulate repolarization dynamics.

Curiously, early mapping studies across the ventricular wall, using transmural plunge electrodes, failed to identify any prolonged activation within the mid-myocardium of intact hearts [1], despite this being the case with *in vitro* tissue preparations [13]. M cell action potentials become especially distinct at long pacing intervals that exceed those seen in sinus rhythm [13]. One mapping study, in whole hearts, showed that the latest cells to activate tended to be the earliest to repolarize, regardless of pacing site. This suggests that APD is not necessarily a fixed function of location, but might depend on the spatial activation sequence. These results lead one to speculate that, in addition to regional ionic current differences, electromechanical factors during contraction might be involved in modulating action potential duration [181].

Rogers et al. found that APD on pig RV and LV were equal at several cycle lengths and during VF [422]. The same finding was noted in dogs, although I_{to} was smaller in the left

ventricular epicardium [130]. Canine right ventricular mid-myocardial layers have higher potassium currents I_{to} and I_{KS} than the left ventricle [513]. Differences in electrophysiological properties and restitution between the right and left ventricles in human hearts have not been reported.

To be specific, we have assumed that transmural gradients of I_{KT}, I_K, and I_{to} exist across the ventricular wall, and increase linearly from endocardial to epicardial surface. Despite the possible existence of regional differences, epicardial and endocardial cells were assigned uniform properties over their respective surfaces in both ventricles. This gradient of properties allows T waves to be simulated, and might also be an important modifier of wave stability during reentry. M cells, when added, were defined in the middle layers of one or both the left and right ventricles. Since we do not know the correct M cell distribution, we have explored three candidate configurations. To account for this spatial heterogeneity of action potential behaviour, the ellipsoidal model was assigned a dimensionless factor μ, ranging from zero to one, that was used to define contours of the cell type layers. Smoothing and interpolation throughout the ventricles was achieved, once again, by solving the Laplace equation $\nabla^2\mu = 0$ with these boundary conditions by the method previously described. The factor μ was then used to define the cell layers by regionally modifying the ionic membrane model. Assignment of specific cell types allows accounting for the ventricular gradient. The M cell layer was defined within a specified range of μ. The baseline configuration and the three test configurations A, B, and C, are shown in Figure 10.3, with their resulting cell-type layers.

10.2 Activation Sequences

The bundle branches and Purkinje fibre conduction system are absent in this heart model. While it is not a difficult task to incorporate these features, using a branched cable network model similar to that previously described for one-dimensional propagation, we have left the intrinsic conduction system out, and focused only on conduction phenomena confined to the ventricles. Activation can be initiated by individual point stimuli or by regional shocks covering larger areas. The transmembrane potential V at each cell changes according to the sum of ionic currents, stimulation or shock currents, and electrotonic current from neighbouring cells.

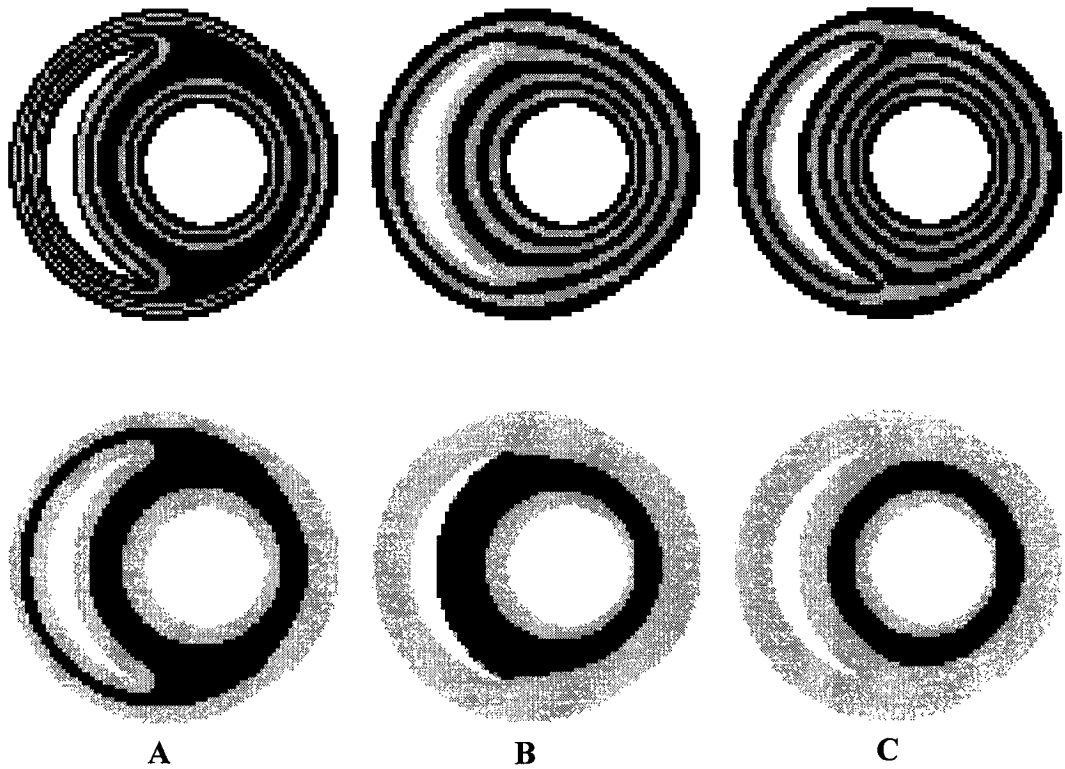

Figure 10.3. Cell properties were assigned according to location within the ventricular walls, and varied from endocardium to epicardium. Cell type contours for the three configurations (A to C) tested, as derived from Laplace smoothing, are shown in the top row. The M-cell layers for each are shown below. These contours determine the action potential duration in the absence of electrotonic interactions.

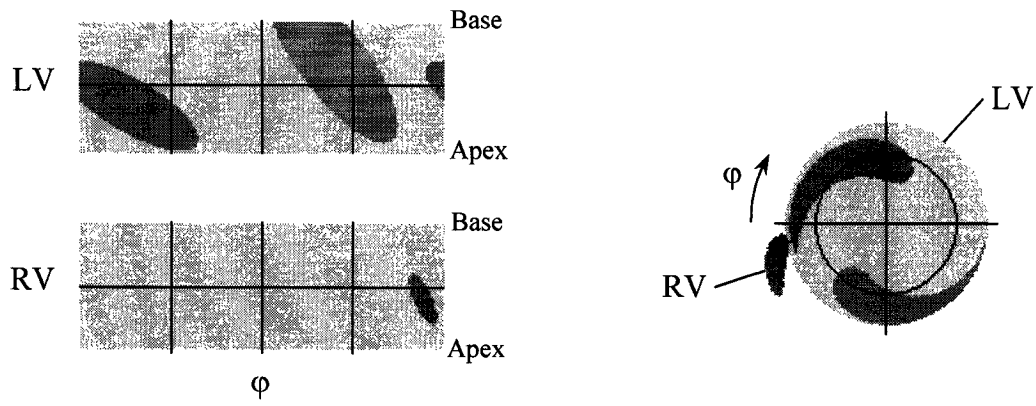

Figure 10.4. Endocardial activation due to sinus rhythm was simulated by applying patch-stimuli to the endocardium, approximating the insertion of the Purkinje fibres. Insertion sites are idealized as elliptical patches defined on Mercator projections of the RV and LV endocardial surfaces, and mapped back onto the heart. The figure at right shows a view of the endocardium looking toward the apex showing the fascicle insertions.

Sinus rhythm was approximated by applying stimuli to the endocardial surfaces in a sequence to mimic activation by the Purkinje fibres. The detailed maps of human heart activation obtained by Durrer [143] remain a unique resource for model calibration that, to our knowledge, have not been repeated or extended. These maps show earliest activity appearing within two approximately elliptical patches on the LV endocardium, opposite one another, corresponding to the two fascicles of the left bundle, and another on the RV endocardium, just above the apex. This sequence was approximated in the biventricular model by defining three elliptical patches of activation. The two endocardial ellipses in the LV were given helical twist, by defining the tangential angle of the semi-major axis of the ellipse to skew as a linear function of z, as shown in Figure 10.5. Activation isochrones of this idealized sinus rhythm are shown in Figure 10.6. Repolarization sequences are shown in Figures 10.6 to 10.8 for the various M cell configurations in Figure 10.3.

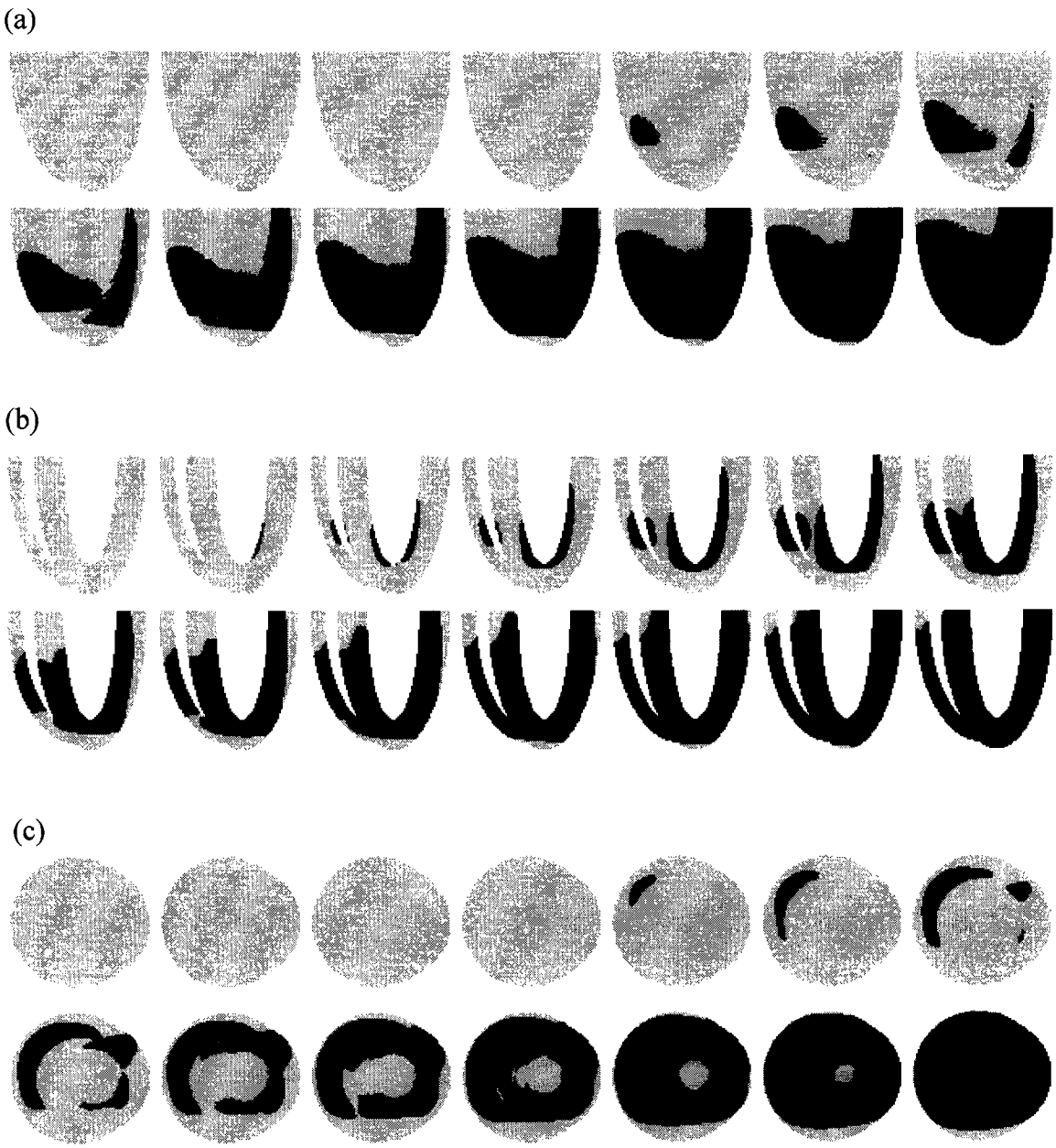

Figure 10.5. Normal sinus rhythm was simulated by externally activating endocardial regions corresponding to three bundle-branch insertion sites. Frames are shown at 10-ms intervals. (a) Anterior epicardial view, showing break-through near the RV anterior septum and LV free wall. (b) Coronal view, showing propagation outward from the endocardial sites. (c) Apical view of activation. (d) Basal view at first horizontal layer. (e) Transverse view through a slice at midlevel, showing activation. (f) Repolarization at the same level. Note that repolarization fronts in this case closely follow the activation fronts, suggesting the existence of near-constant APD throughout the myocardium, despite heterogeneity of properties across the wall.

(d)

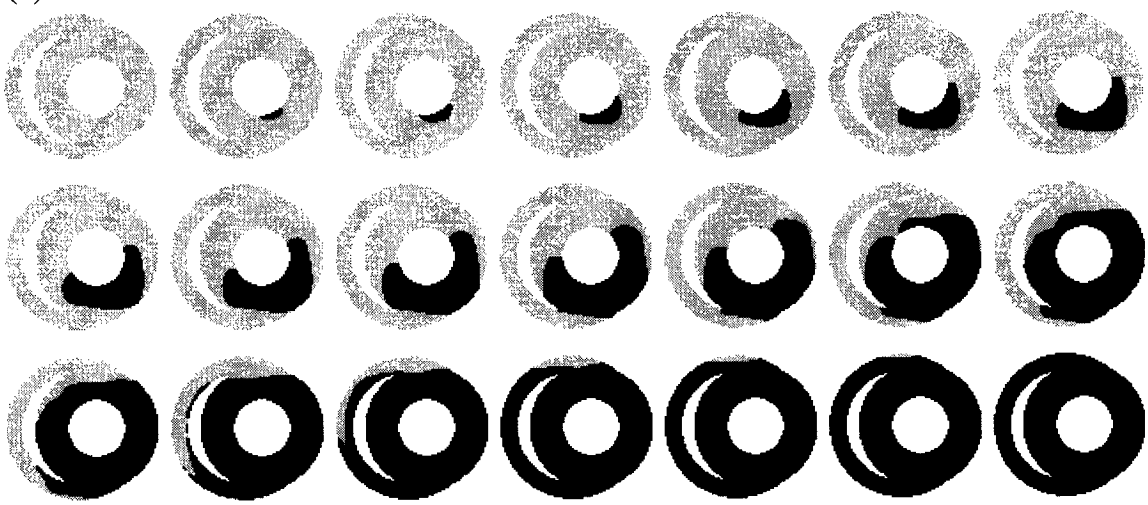

(e)

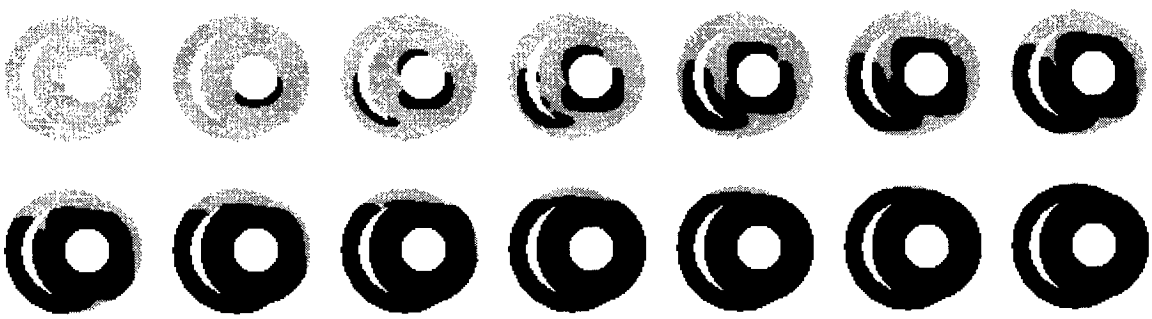

(f)

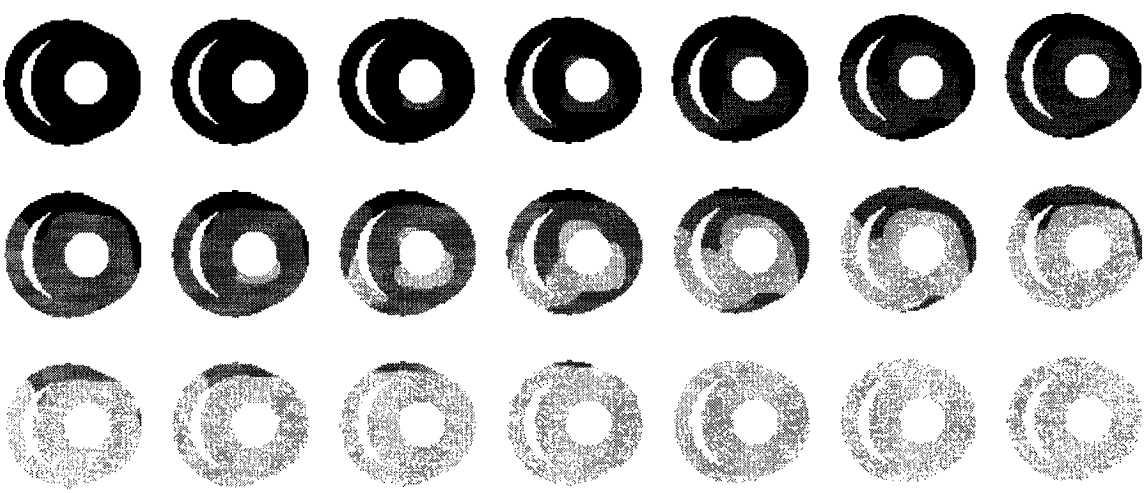

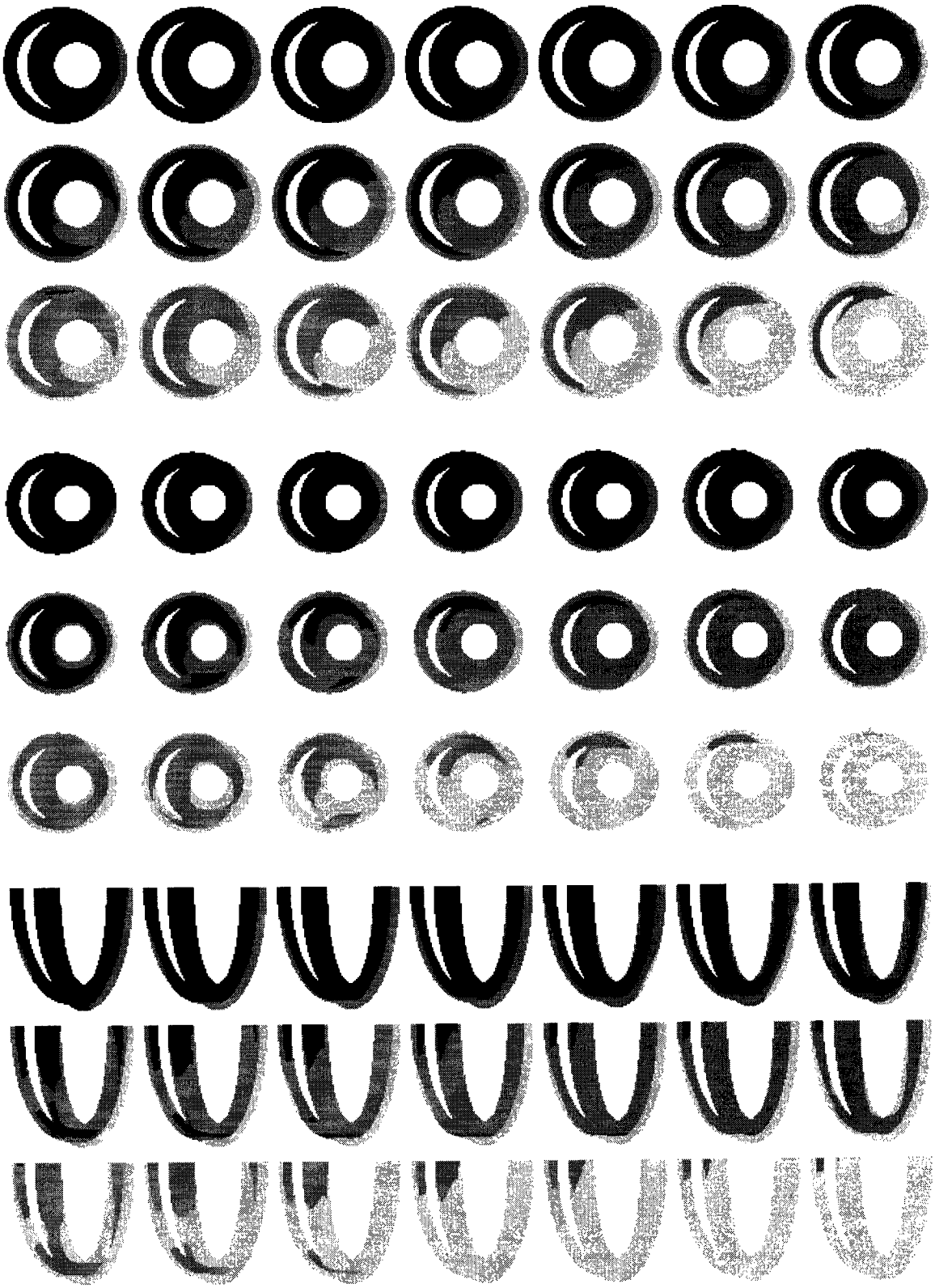

Figure 10.6. Repolarization of M cell configuration A.

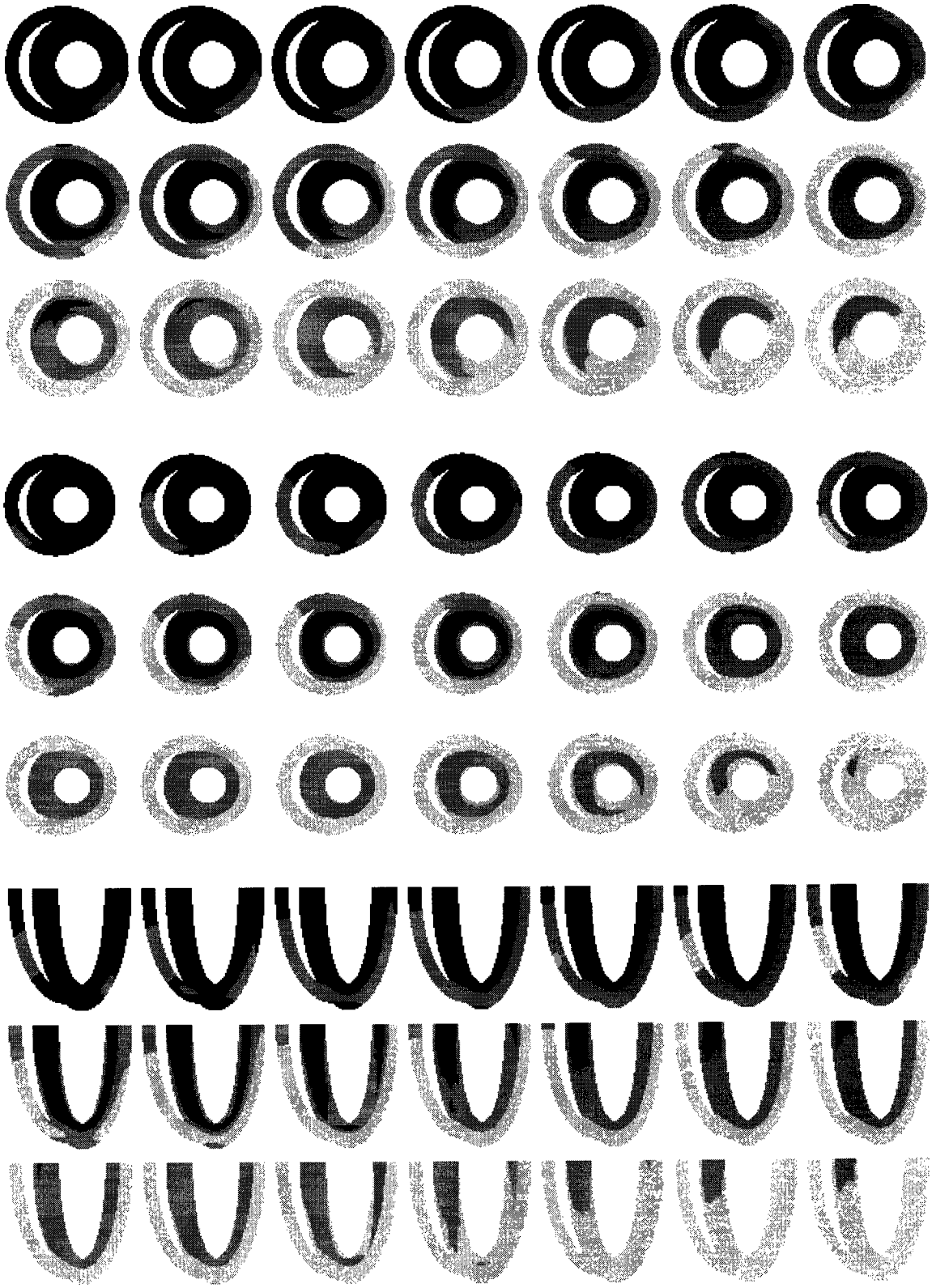

Figure 10.7. Repolarization of M cell configuration B.

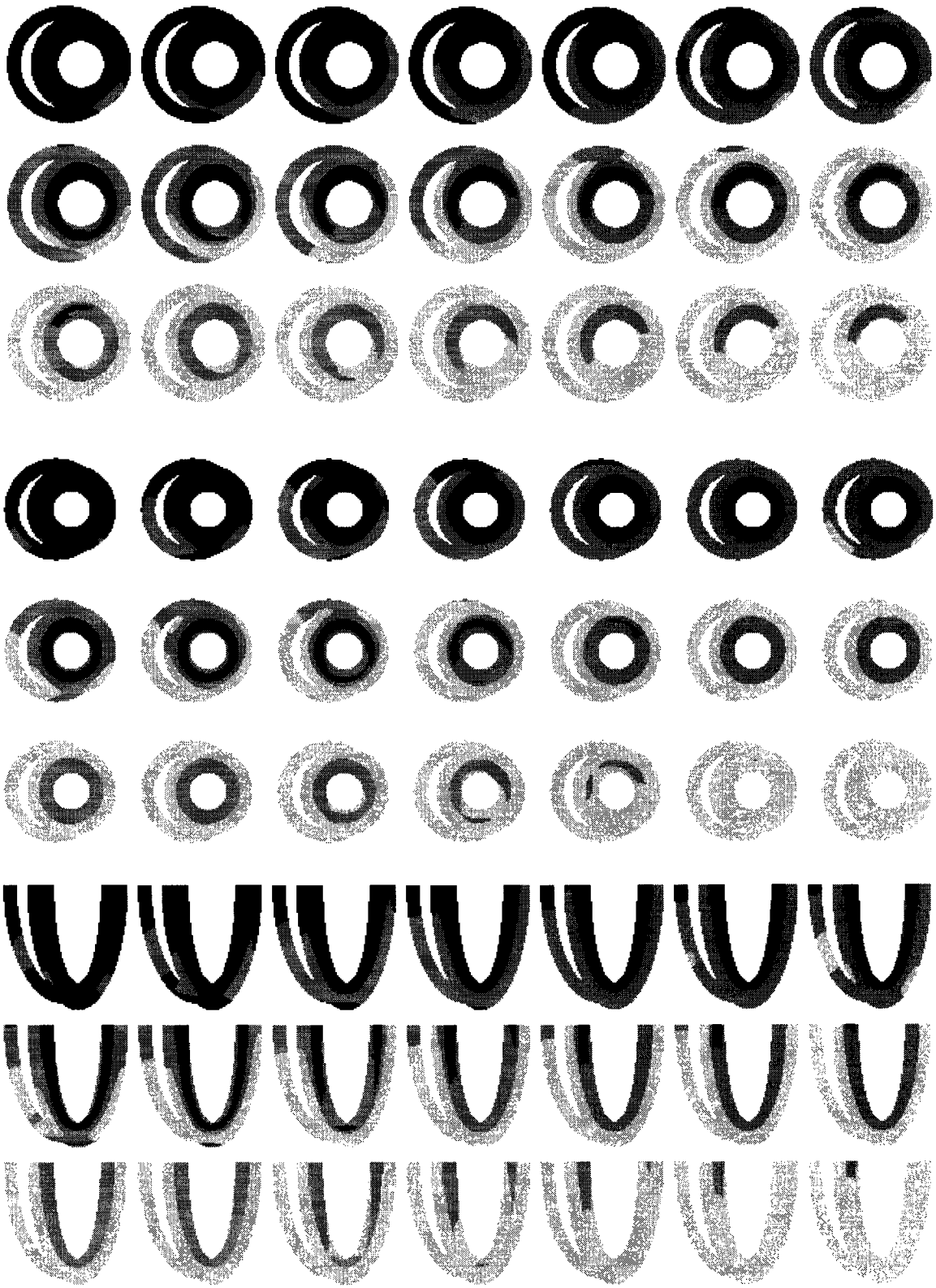

Figure 10.8. Repolarization of M cell configuration C.

10.3. Electrocardiogram

The body surface electrocardiogram (ECG) is the electrical field generated on the torso by all sources and sinks within the three-dimensional volume conductor of the heart. An exact derivation of the ECG field requires the solution of a boundary value problem - essentially the Poisson equation subject to the geometrical boundary conditions pertaining to the heart, lungs, and a no-flux current condition on the body surface. The problem is usually formulated in terms of Green's function [193].

A simplified approach of Leon and Horacek will be used here [308], assuming that the body is contained within an infinite homogeneous volume conductor. This allows the body surface potential to be calculated as the sum of the fields due to each effective dipole, without the need to satisfy boundary conditions or perform any matrix operations. The ECG potential V_{ecg} is the sum of all dipole currents, each of which is proportional to the voltage gradient over the cell membrane, and to the component of the anisotropic conductance tensor evaluated at the cell location. The equation for ECG calculation for isotropic media is:

$$V_{ecg} = a \int_H \frac{\nabla V \cdot \vec{r}}{r^3} d\forall \approx a \sum_{j=1}^{M} \frac{\nabla V \cdot \vec{r}}{r^3}$$

where H is the volume of the heart and $\underline{a}$ is a coefficient related to the volume conductivity. The analogous expression in anisotropic media is more complex [308]:

$$V_{ecg} = a_t \int_H \frac{\nabla V \cdot \vec{r}}{r^3} d\forall + (a_l - a_t) \int_H \frac{(\nabla V \cdot \underline{a_l}) \underline{a_l} \cdot \vec{r}}{r^3} d\forall$$

which reduces to [308]:

$$= a_t \sum_{i=1}^{N} F_l / r^3 + (a_l - a_t) \sum_{i=1}^{N} F_o / r^3$$

where

$$F_o = (x - x_e) F_2 + (y - y_e) F_3 + (z - z_e) F_4$$

$$F_1 = (x - x_e) \partial V_x + (y - y_e) \partial V_y + (z - z_e) \partial V_z$$

$$F_2 = s_x s_x \partial V_x + s_x s_y \partial V_y + s_x s_z \partial V_z$$

$$F_3 = s_y s_x \partial V_x + s_y s_y \partial V_y + s_y s_z \partial V_z$$

$$F_4 = s_z s_x \partial V_x + s_z s_y \partial V_y + s_z s_z \partial V_z$$

$$r^3 = [(x - x_e)^2 + (y - y_e)^2 + (z - z_e)^2]^{1.5}$$

$$s_x = \cos \gamma \cos \varphi$$

$$s_y = \cos \gamma \sin \varphi$$

$$s_z = \sin \gamma$$

The summation is over all points (x, y, z) in the heart, and (x_e, y_e, z_e) is the observation point or fixed electrode. Angles φ and γ specify the fibre orientation, as previously described; ∂V_x, ∂V_y, and ∂V_z represent the partial derivatives from the gradient operator; and a_l and a_t are the longitudinal and transverse conductivities. This solution should be a reasonable approximation to the true ECG that would be obtained from the full Green's-function method, however, the amplitude is underestimated due to the absence of equivalent image sources that would be required to match the no-flux boundary conditions omitted here. The effects of conductivity inhomogeneities within the chest are also not considered, but these effects are likely minimal [415]. These limitations are acceptable if we consider amplitudes derived from this equation to have arbitrary units, and to be compared only by their relative values.

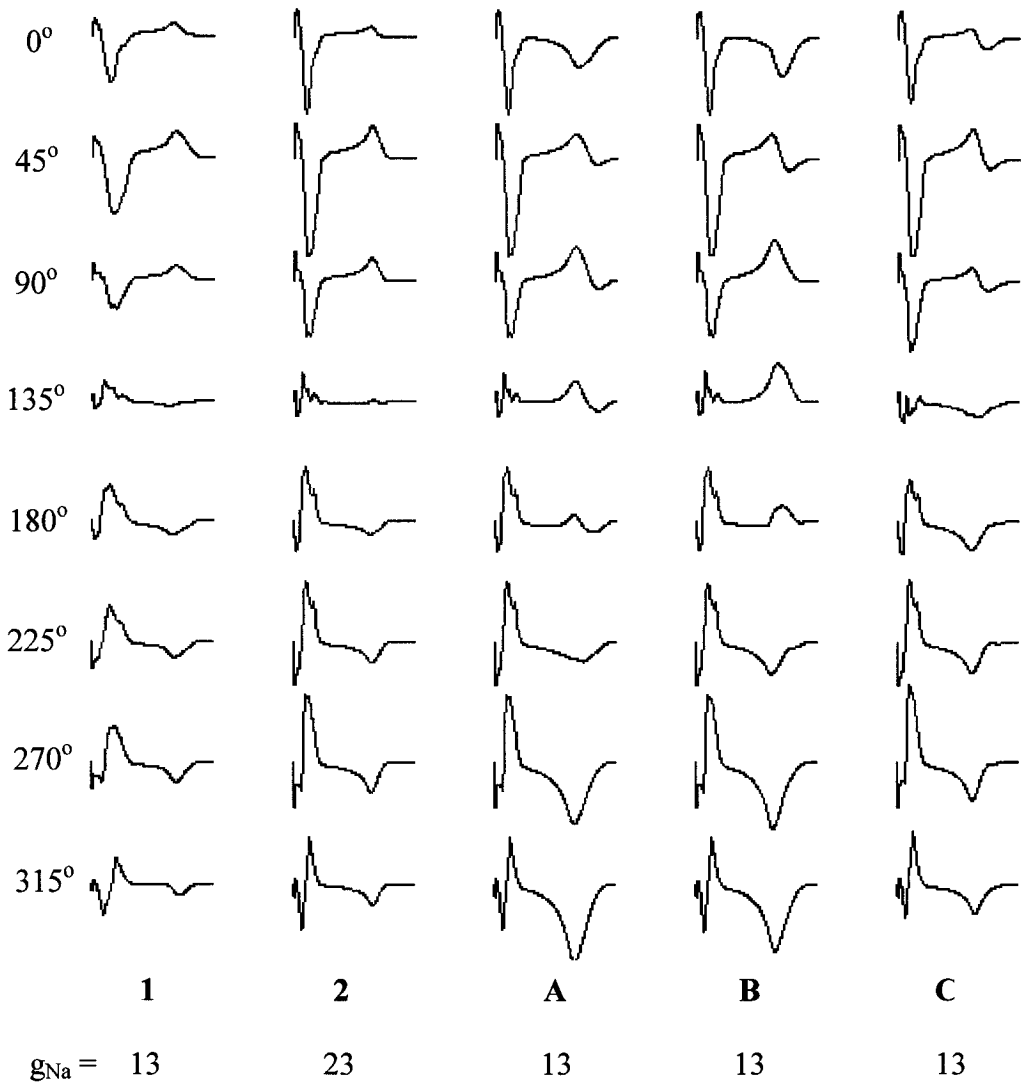

Figure 10.9. Single beat 8-lead equatorial electrocardiograms for each configuration of simulated sinus rhythm, showing the QRS complexes and T waves. Initiation was from endocardial patches stimulated to simulate the sequence of normal sinus rhythm. Cases 1 and 2 have a ventricular gradient, but no M cells. Cases A to C have the different M cell configurations as shown in Figure 10.3. T wave morphology is particularly sensitive to these differences in regional cell properties.

10.4 Recovery and T Waves

While ventricular activation sequences corresponding to the QRS complex have been mapped in human [143] and canine hearts [1, 466], much less information is available on the recovery sequences responsible for the T wave. The main reason for this limitation is the technical difficulty of recording, with confidence, the much smaller voltage gradients that occur during repolarization. T wave genesis is generally believed to be due to the repolarization wave being opposite (discordant) to that of the depolarization wave [2, 103, 376]. Repolarization in the model simulation is evident in Figures 10.6 to 10.8, and essentially follows the sequence of depolarization over the epicardium, since perfect uniformity of APD over this cell layer has been assumed in the model. Burgess et al. [51] and Abildskov et al. [1] found the canine epicardial recovery sequence to be closely correlated with the excitation sequence, confirming that the APD was fairly uniform over the epicardium.

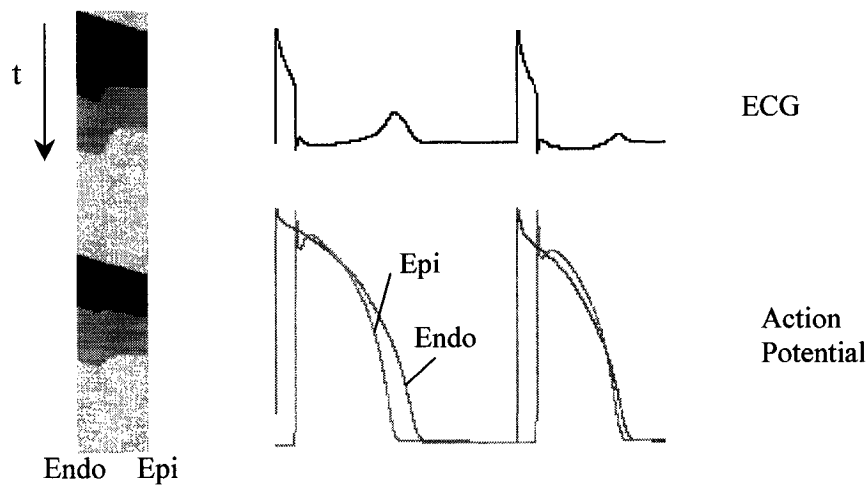

Figure 10.10. Origin of the ECG and T wave in a cable model representing a section from endocardium to epicardium. Activation causes the QRS complex. During the action potential plateau, there is very little gradient between cells, and the ECG is relatively flat. The T wave occurs during repolarization when the voltage gradient reverses. The M cell layer, located close to the endocardium, also contributes to the gradient reversal.

Since the main objective of this work has been to model tachy-arrhythmias, such as VT and VF, we have not required a His-Purkinje conduction system that would be necessary if we were modelling the precise sequence of conduction during normal sinus rhythm. We can approximate sinus rhythm, as previously described, by applying a series of external current stimuli, with times and locations on the endocardium chosen to mimic the initial endocardial sites of activation that would result if the conduction system were present. This addition allows both the QRS complexes and T waves to be modelled, once the initial activation pattern is placed on the endocardium. The activation sequence proceeds from endocardium to epicardium, and recovery is from epicardium to endocardium, as seen in human catheter studies [179, 180]. Figure 10.10 shows how the ECG depends on voltage gradients. In this case, an action potential propagates along a 17-element cable of 1-mm elements, simulating a section across the ventricular wall from endocardium to epicardium. An M cell layer spans layers 3 to 8, and is given properties (f_{k1}, f_{k2}, f_{k3}, τ_{fr}) shown in Table 8.2. The epicardial APD is shortest, so repolarization reverses direction, as evident in the action potential profiles. This causes the T wave to be positive giving results consistent with mapping of the LV wedge preparation by Antzelevitch et al. [566].

T wave alternans (TWA) refers to the 2:1 periodic alternation of the electrocardiogram T wave between two morphologies [455]. First recognized by Lewis shortly after the introduction of the ECG by Einthoven [312], alternans was later found to be a risk factor for sudden cardiac death [414]. Cohen et al. found TWA to develop following coronary ligation in canine hearts, and its presence correlated with a lower threshold for VF induction [3, 426]. Sensitive ECG recordings can measure TWA clinically, and have confirmed the associated risk of VF [156]. Growing interest in applying nonlinear dynamics to cardiac rhythm analysis followed after Guevara et al. demonstrated action potential alternans, quasiperiodicity, and chaos in isolated myocytes stimulated *in vitro* at increasing rates [214, 215]. These observations led Kaplan et al. [270] to hypothesize that T wave alternans might be manifesting the first bifurcation in a period-doubling cascade leading to higher-dimensional chaotic VF. They were not able to discern any further bifurcations in ECG signals of VF, however, beyond the first 2:1 transition [269]. Further

work is needed to define the distribution of M cells and APD across the ventricular walls and throughout the heart in order to simulate more accurate repolarization.

10.5 Model Limitations

The main limitations of this ventricular geometry are:

(1) Spatial resolution has been limited to 1-mm elements, although it is easily modifiable to smaller elements with higher computational cost.

(2) Absence of an intrinsic Purkinje fibre conduction system requires that all activation be initiated by external stimuli.

(3) The idealized shape as ellipsoidal shell ventricles has been chosen to allow basic wave behaviour to be studied without the additional complexities of the irregular shaped heart. Simulations can be carried out in the future using this cellular model within a more realistic anisotropic human heart geometry developed by Hren and Horacek [237].

(4) The precise distribution and heterogeneity of cell types throughout the myocardium, especially that of M cells, is not known and must be assumed until better information becomes available.

Chapter 11

TISSUE MODELS OF REENTRY

11.1 Historical Background

Irregularities in pulse rate were recognized long before their physiological origins were understood, and were given terms such as "delirium cordis" and "pulsus irregularis perpetuus" [172, 228]. Cardiac rhythm abnormalities were believed to be solely due to spontaneous ectopic impulse initiation [123] until McWilliam proposed in 1887 that "peristaltic contraction" could re-excite pathways over which a wave had already passed [344]. McWilliam worked with many animal species, ranging in size from birds to cattle, and observed that rhythm irregularities in small hearts would often spontaneously terminate, while large hearts sustained fibrillatory movement indefinitely. Such was the first suggestion of a critical mass being required to sustain fibrillation.

In 1906, Mayer demonstrated circular re-excitation in tissue ring preparations cut from invertebrate medusa bells, and noted that a contractile wave could be induced to propagate around the ring [339]. These studies were repeated in rings cut from turtle hearts. Mayer also pointed out the relationship between refractory period, conduction velocity, and path length. Mines repeated these studies in 1914 with ring preparations from tortoise hearts, and proposed that block along one pathway and the presence of a return pathway was a necessary condition for reentry to occur [350]. Mines suggested that this type of circular excitation was responsible for fibrillation. Around the same time,

Garrey was carrying out similar experiments in atrial tissue independently, and proposed the same reentry hypothesis for cardiac arrhythmias [187]. He was the first to propose that atrial fibrillation was caused by a "contractile maelstrom" of reentry, and that differences in local tissue refractoriness might maintain these circuits in the absence of "natural rings". Garrey further showed that fibrillation persisted in smaller cut tissue segments, and therefore did not likely originate from ectopic foci. In 1920, Lewis induced, by faradic stimulation of the canine right atrium, a "mother wave" circulating around the vena caval orifices, and was able to apply recording electrodes to capture part of this sequence [313]. He was able to show that conduction velocity was slower in repetitively excited tissue. This was the earliest experimental model of atrial flutter, although some controversy followed as to whether or not the results represented true circus movement. Rosenbleuth and Garcia-Ramos in 1947 confirmed with six electrodes that circus movement was indeed underlying atrial flutter in the dog heart [425].

The simplicity of these ring models contrasted with the difficulties faced proving these hypotheses in intact hearts. Wiggers in 1930 carried out studies of ventricular fibrillation induced by a carefully timed premature stimulus in canine hearts [540]. There appeared to be a "vulnerable window" of time during which the second stimulus could induce VF. Wiggers defined four stages of VF based on cinematography [537]. The first undulatory stage lasts a few seconds and is followed by a second convulsive stage lasting 15 to 40 seconds. The third tremulous stage lasts 2 to 3 minutes followed by a final atonic stage with contractile failure.

Based on a cellular automaton model, Wiener and Rosenblueth in 1946 claimed that flutter or fibrillation could not be induced without anatomical obstacles [535]. These authors mentioned the possibility of rotating spiral waves, but only around an opening. Moe et al. formulated a cellular automaton computer model and demonstrated that reentry might be possible without an anatomical obstacle [352]. Two decades would pass until Allessie et al. in 1977 proved this concept by inducing circus movement in the rabbit atrium, and using multiple surface electrodes confirmed that reentry could occur around areas of functional block in the absence of anatomical obstacles [10]. The central

core proved to be normal excitable tissue in the refractory state of its cycle. This type of reentry has become known as the "leading circle" concept. These investigators also emphasized that the wavelength or minimal size of the circuit is given by the product of conduction velocity and the effective refractory period.

11.2 Mechanisms of Reentry

What are the minimum criteria necessary to establish reentry? First, there must exist a closed path available to support continuous propagation. A one-dimensional closed ring is therefore the simplest possible geometry that can sustain reentry. A stimulus applied at any point on a uniform ring will propagate bidirectionally around the ring since wave fronts will follow any available path into excitable tissue. Activity extinguishes only when there is no further excitable tissue available, either because a domain boundary is reached, or because the wave front encounters refractory tissue, has nowhere to go, and blocks. If block extinguishes propagation at part, but not all, of a wave front then the remaining segment can invade retrogradely into a new pathway that becomes available when the blocked region recovers. Garrey and Mines both recognized these essential requirements for reentry - an alternate pathway and unidirectional block.

Extending this concept more generally into two and three dimensions, it is worth reiterating that reentry becomes possible whenever a wave front is blocked over a partial segment. Any process that breaks a wave front leaving a free end will cause a reentrant circuit to establish itself around that free end point as shown in Figure 11.1. The end point can follow the boundary of a hole or inexcitable obstacle, as suggested in early studies, but can also occur within continuous tissue. In the latter case, a spiral wave develops about a point in two dimensions, or a scroll wave develops about a filament in three dimensions. Winfree has discussed the topology of these concepts [542].

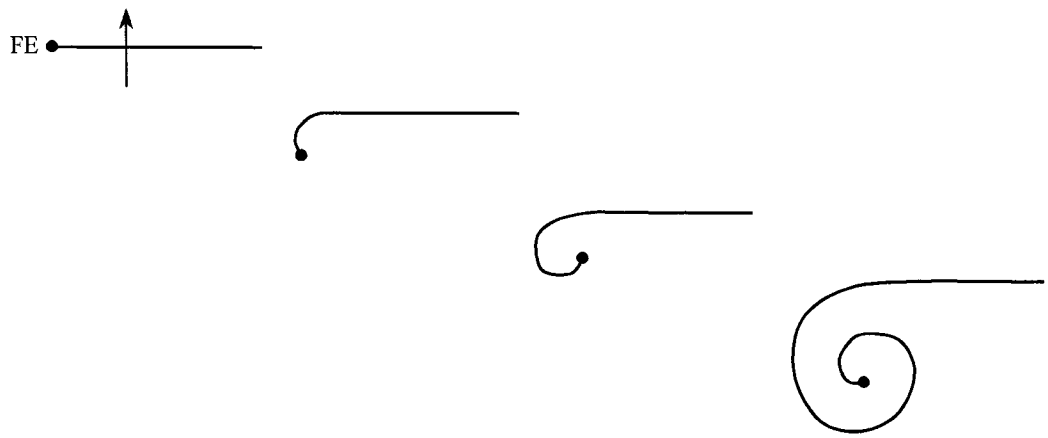

Figure 11.1. A free end (FE) of a propagating wave front adjacent to excitable tissue will naturally roll-up into a spiral wave. The creation of free ends is fundamental to the origin of reentry, and is usually a consequence of block over a wave front segment. The free end is a point in two dimensions and a filament in three dimensions.

An advancing wave front cannot transform into a reentrant circuit without there existing a region of at least transient conduction block. This basic requirement can be illustrated by examining propagation of a wave front over a piece of tissue in Figure 11.2. The plane wave encounters a region of inexcitability and blocks while the remainder of the wave advances. A free end is established on the wave front and runs along the boundary of the blocked region, tracing what is typically called an "arc of conduction block". If the blocked region then recovers excitability after the surviving wave segment has passed, the free end can begin to advance into newly excitable tissue. The natural behaviour of the tip is to roll up into a spiral wave if sufficient space is available.

The second row of frames in Figure 11.2 shows how this wave phenomenon can be approximated on a tissue ring domain representing conduction around a functional or anatomical obstacle. In this case the wave front would normally advance down the ring taking both pathways arms in unison. For reentry to occur, the wave front must return up one arm to complete a continuous closed path. Such a reversal requires block at some point in the circuit to permit the antegrade arm to become a retrograde arm.

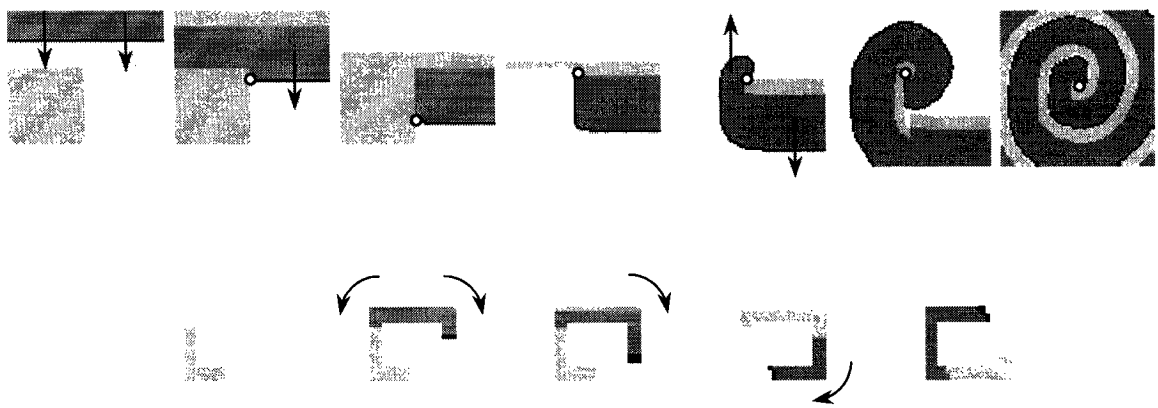

Figure 11.2. Reentry can be established in a two-dimensional sheet of tissue (top), by placing a region of transient inexcitability in the path of the advancing wave front. The wave blocks over part of its length, immediately creating a free end (circle) that follows the blocked region. If the block is only transient, the free end can propagate into excitable tissue, once the block is released, and form a reentrant circuit, which develops into a spiral wave. The arrows indicate how the left-arm ultimately converts from downward to upward propagation. The second row (bottom) shows the same simulation, but with the square domain masked to expose only a ring, approximating a reentrant circuit. Ring models, reduced to one-dimensional cables, provide a simple means to study reentry and block.

11.3 Stimulus-Induced Block

Fibrillation typically occurs in hearts with abnormal or diseased substrate exposed to ischemia, metabolic derangement, or autonomic influences. To establish fibrillation in normal or "healthy" tissue and heart models studied here, we must induce it artificially by external stimulation, or by transient alteration of tissue substrate, such that at least one region of unidirectional block is forced. A point or patch stimulus, delivered within the refractory zone of an action potential wave, will achieve this result, provided that it occurs at the right place and time, within the vulnerable window [543].

Stimulus-induced block has been studied theoretically in cable ring models by several investigators to elucidate the nature of the "vulnerable window", within which a stimulus

can induce reentry [413, 472, 473]. Figure 11.3 illustrates this phenomenon in a cable ring of SHV endocardial cells. The cable is given an initial stimulus S_1 at location i_1, which causes an action potential to propagate bidirectionally around the ring. A second stimulus S_2 is delivered at time t_{S2} to a point in the refractory zone i_2, located on the action potential tail. If t_{S2} is too early, falling within the absolute refractory period, the stimulus is ineffective and blocks bidirectionally. If t_{S2} is too late, the stimulus gives rise to new waves that propagate bidirectionally outward. If applied within a narrow window, the stimulus will propagate in the retrograde direction only, and block in the antegrade direction. This vulnerable window lies on the action potential tail, and can be defined in terms of either the critical time interval or the corresponding critical space interval.

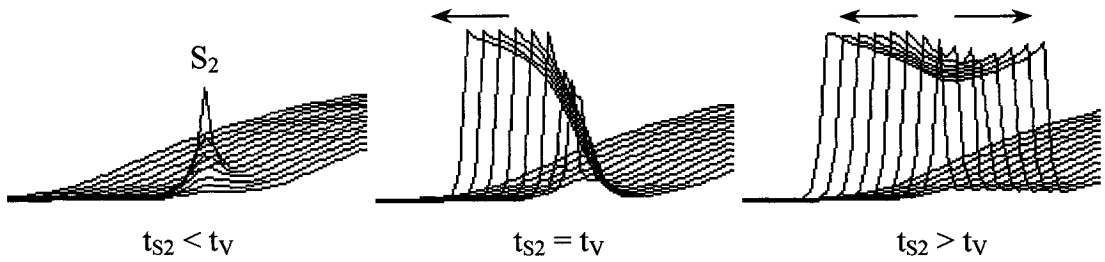

Figure 11.3. A current stimulus S_2 is delivered to a point on the tail of the action potential at time t_{S2} on a cable of SHV endocardial cells. The result depends on how t_{S2} relates to the time of the vulnerable window t_V: bidirectional block if $t_{S2} < t_V$ (left), unidirectional block if $t_{S2} = t_V$ (middle), or bidirectional propagation if $t_{S2} > t_V$ (right).

The mechanism responsible for unidirectional block within the vulnerable window (VW) is illustrated in Figure 11.4. Basically, success or failure of stimulus-induced propagation depends on the ability of the sodium current to reach its threshold and source enough ionic current to its neighbouring sinks to maintain a safety factor greater than one. The vulnerable window must occur where there is a spatial gradient of h(x), within the region where $0 < h(x) < 1$. Initial depolarization at point i_2 causes $h(i_2)$ to inactivate back to zero, which enhances the asymmetry of h(x) around the stimulus point. If S_2 raises i_2 above its threshold, then inward I_{Na} will activate and overcome the outward residual potassium currents. As activation begins to propagate bidirectionally, the antegrade front encounters

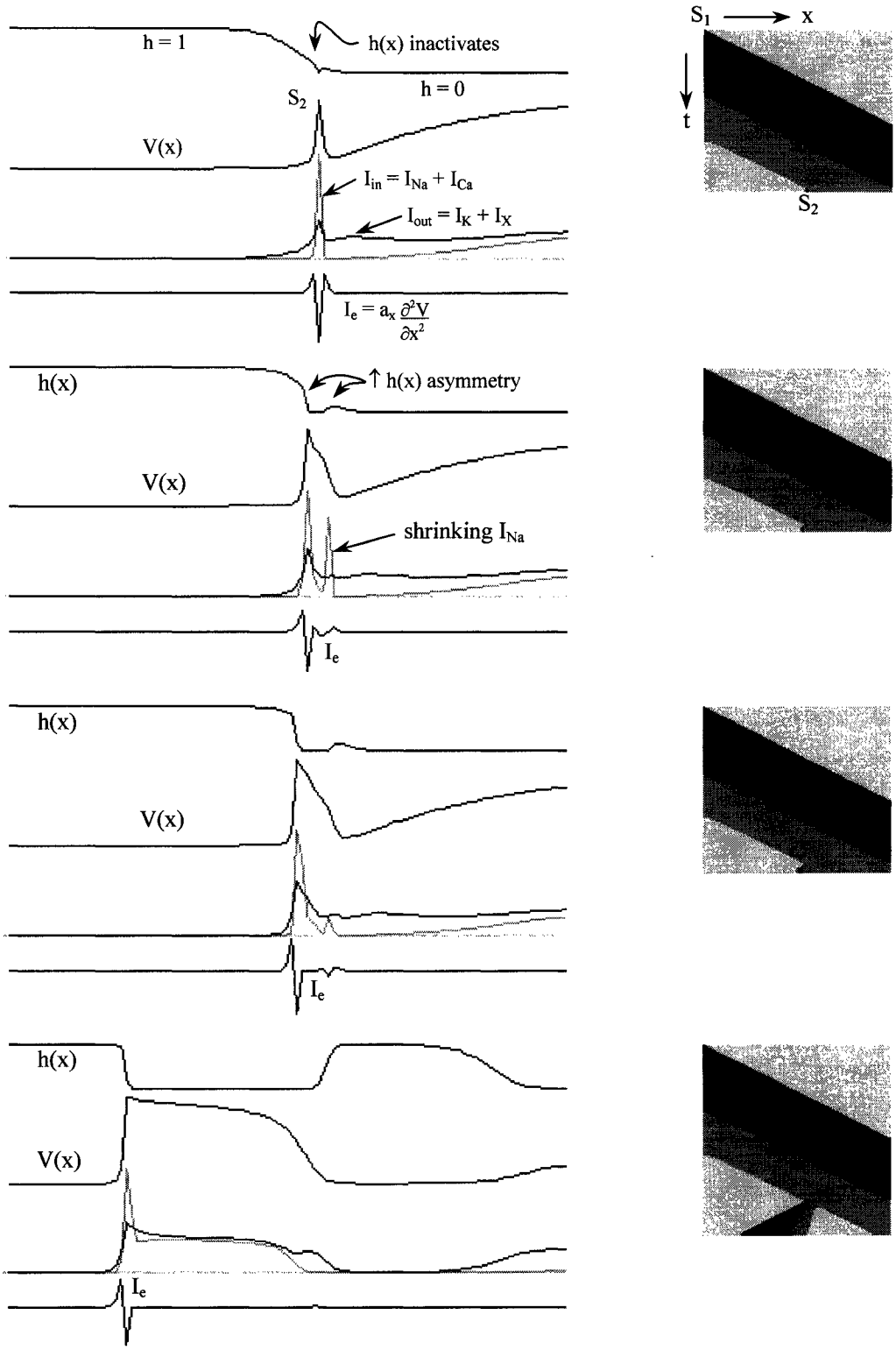

Figure 11.4 Stimulus-induced unidirectional block within the vulnerable window is illustrated at four different times in a cable of SHV endocardial cells. Space-time plots are shown at right for each frame. See text for discussion.

a higher firing threshold than the retrograde front, due to the larger outward current in that direction. While retrograde propagation proceeds easily, the antegrade front tries to mount the receding action potential tail, causing the baseline or resting potential at the wave front to depolarize a small amount, which progressively inactivates h(x) in its neighbourhood. At the same time, growing asymmetry in V(x), around the stimulus point, diminishes the electrotonic current $I_e = a_x \partial^2 V/\partial x^2$ on the uphill or antegrade arm, which becomes more pronounced until I_e is eventually insufficient to reach threshold, and block occurs. Remarkably, a similar vulnerable window mechanism of unidirectional block also occurs in simpler relaxation oscillators like the FitzHugh-Nagumo model and the van Capelle-Durrer model, where there is a similar critical gradient of recovery of the respective excitation variables [496].

Quan and Rudy implemented a Beeler-Reuter model in a ring with high-resistance intercalated disks, and demonstrated that a point stimulus applied within the vulnerable window (VW) could induce unidirectional block, causing a solitary wave to perpetuate around the ring [413]. The width or duration of VW increased with higher sodium conductance, and with increased axial resistivity. Starmer et al. examined a similar ring model, but without intercalated disks, employing both FitzHugh-Nagumo and Beeler-Reuter membrane dynamics [473]. This model showed the VW to decrease with increased sodium conductance, in contrast to the Quan-Rudy results, and to increase with higher potassium conductance.

11.4 Tail Block

An established reentrant circuit can block if the wave front encroaches too far onto its own tail. This process appears to be fundamental to wave break, which requires that part of the wave front blocks, leaving one or more free ends, as previously discussed. Insight into the mechanisms of tail block might reveal useful strategies to prevent or terminate reentry.

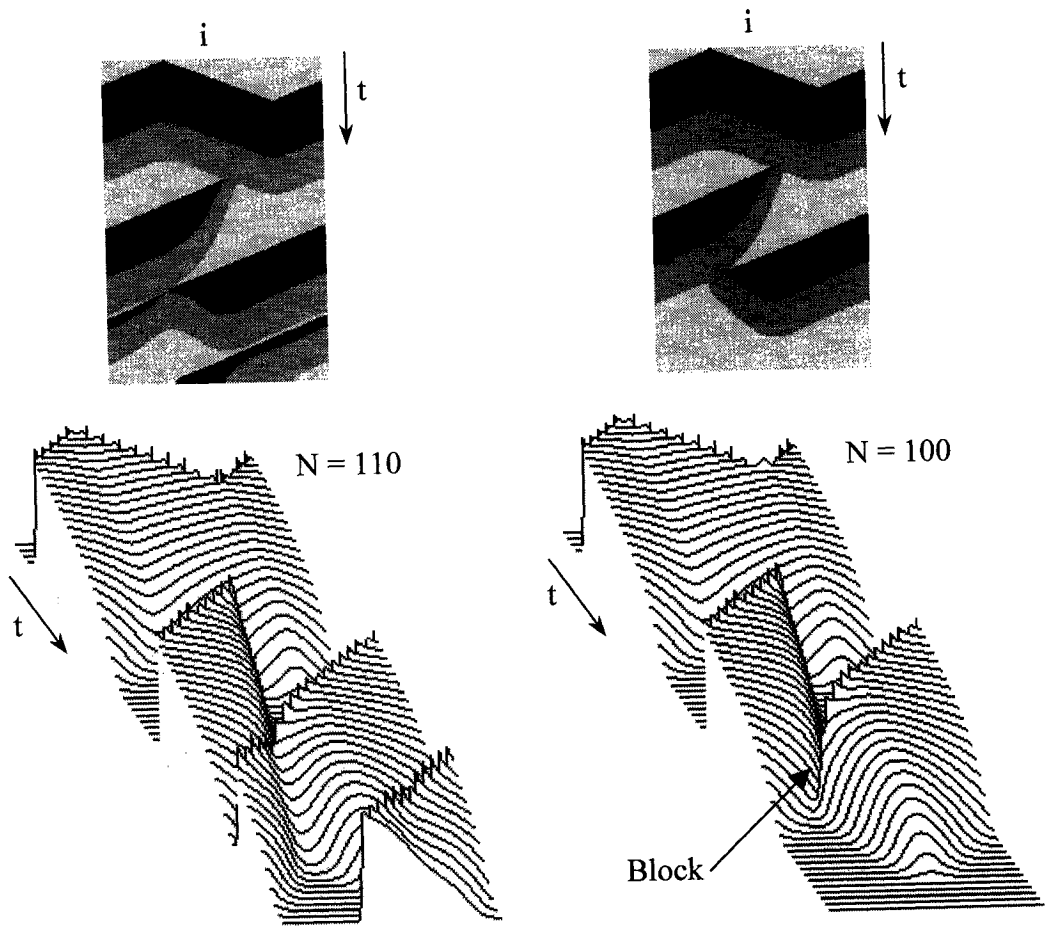

Figure 11.5. Critical ring size. Time-space plot of action potentials propagating on a ring of SHV endocardial cells. A first stimulus S_1 causes the AP to propagate in both directions. The second stimulus S_2 at the AP tail results in a new AP that blocks in the retrograde direction and survives in the antegrade direction. If the ring is large enough, with N = 110 mm, the AP can continue to circulate indefinitely (left), but if the ring is too small, with N = 100 mm, the AP blocks against its own tail (right). The critical ring size for this particular parameter set is 107 mm. $g_{Na} = 13$, $g_{Ca} = 0.08$, $g_K = 0.80$, $g_X = 0.20$, $g_{to} = 0.10$, $a_x = .002$, $\Delta x = 1$ mm, $tS_2 = 372$ ms.

Figure 11.5 shows a ring of 110 endocardial SHV elements of 1-mm size coupled with $a_L = .0020$ mmho. An S_1 stimulus initiates an impulse that propagates around the ring in both directions, and extinguishes by collision on the opposite side. A second stimulus S_2 applied to the vulnerable window causes antegrade block and retrograde propagation. The resulting wave travels around the ring indefinitely, provided that the ring size L is larger

than a critical size L_{crit}. In this case, propagation sustains if L > 106 mm, but below this critical length, the action potential catches up to its own tail and blocks, as shown in the second frame. The critical length depends on the conduction velocity θ and the effective refractory period (ERP). Assuming that all APD are equal, the critical length can be approximated as $L_{crit} = \theta \times ERP \approx \theta \times APD_o$. This expression assumes that the ERP is minimum, corresponding to the restitution intercept APD_o. In reality, smaller ring sizes cause APD to vary from cycle to cycle, depending on the nature of both the APD and velocity restitution curves [410, 509]. Ionic conductances and substrate coupling determine velocity and APD, as previously discussed. Accordingly, L_{crit} must be shorter for weaker coupling a_x, and lower sodium conductance g_{Na} because these lower the velocity. L_{crit} is longer for increased g_{Ca} and decreased g_K and g_X, since these changes increase the APD and ERP.

The degree to which the leading edge can encroach upon the tail to shorten L_{crit} depends on the firing threshold, which is a function of g_{Na} h(x), and g_K, as previously discussed. The mechanism involves decremental conduction, similar to that occurring with antegrade block in the vulnerable window. Figure 11.6 shows an action potential on the ring catching up to its tail. The wave front moves at velocity θ_1, which is greater than the preceding tail velocity θ_2. As the front mounts the tail, the foot rises, causing partial inactivation of h(x), which further decreases I_{Na}. At the same time, the front experiences a more depolarized threshold, due to greater outward currents encountered. If the front does not slow enough to match the tail velocity, both I_{Na} and the peak voltage progressively diminish, causing the electrotonic current I_e to likewise fall. Eventually the shrinking I_e cannot lift the wave front to meet a rising threshold, and block occurs.

A more detailed analysis is shown in Figure 11.7. The action potential tail propagates to the left at velocity θ_1. It carries with it translating templates representing the threshold voltage V_{th} and the peak voltage V_{max}. The second action potential arrives at a faster velocity θ_2. The inset shows the wave front entering the mouth of the shaded template, and ultimately approaching the intersection of V_{th} and V_{max}. Block occurs when the wave front jams itself into the wedge weakening the electrotonic current below its threshold.

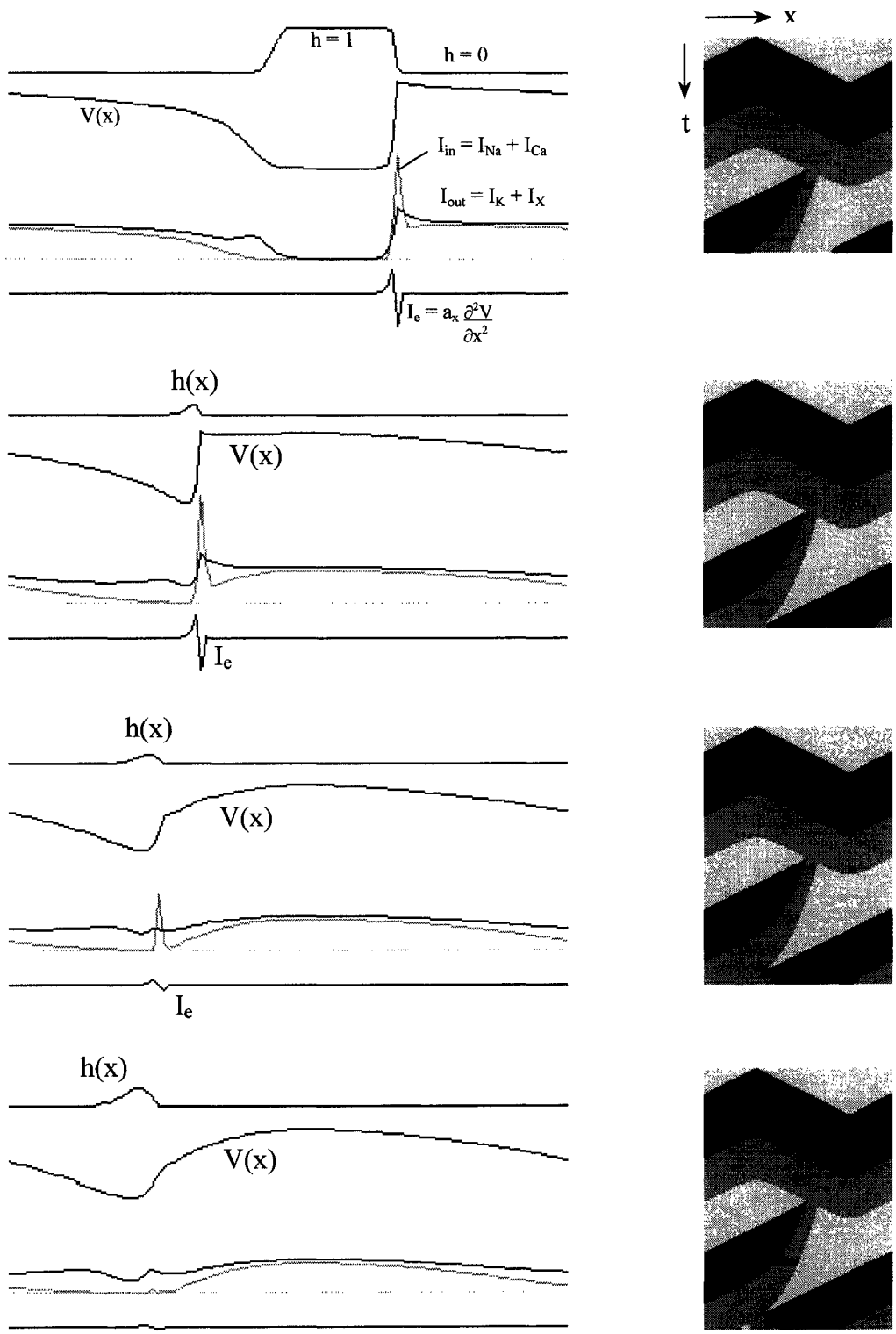

Figure 11.6. An S_2 stimulus induces a reentrant circuit around a cable ring of SHV endocardial cells, as previously described. The ring is too short and allows the wave front to catch up to its tail and block. See text for discussion.

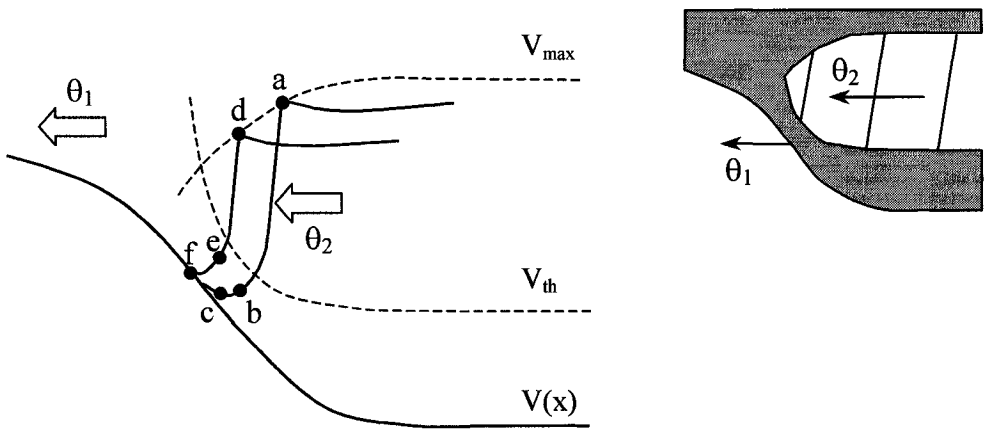

Figure 11.7. The wave tail moves left at velocity θ_1, while the front catches up at velocity θ_2. Points a-c determine the electrotonic current at point b, which raises b above threshold V_{th} to become point d. The peak voltage V_d is reduced compared with V_a, while at the same time, the threshold is now higher near point e. The electrotonic current at the new foot point e, determined by voltages at points d-f, is lower that that of the previous foot point b. Provided that $\theta_1 > \theta_2$, this decremental conduction behaves as if the front moves into the wedge of a template attached to the tail, and terminates as shown in the inset.

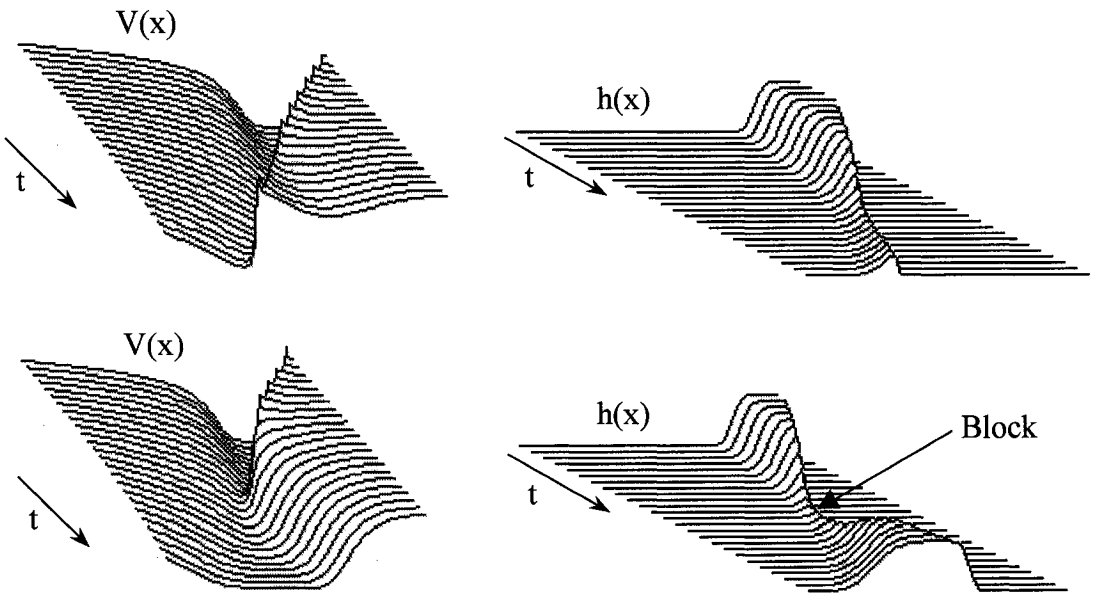

Figure 11.8. Space-time plots of an action potential front catching up to a preceding tail. Propagation is from right to left. Voltage V(x, t) is shown in the left frames, and the corresponding excitability h(x, t) of I_{Na} is at right. In the top row, the AP meets the tail and matches its velocity to avoid block. In the bottom row, the cable is just below its critical length, and the AP blocks against the tail. Note that $h(x) > 0$ within the excitable gap, and falls below a critical size at the time of block.

The recovery time course of both V_{th} and V_{max} depend on the recovery of h(x, t), since this controls I_{Na} dynamics determining excitability and response. When $\theta_2 > \theta_1$, h(x) gets squeezed between the front and the tail until it can barely sustain propagation, as shown in Figure 11.8. This analysis raises a fundamental question: why doesn't the wave front just slow down to match the tail velocity so it does not block, like a tail-gating car that must reduce its velocity as it approaches a slower vehicle to avoid a collision? In other words, under what conditions is $\theta_1 > \theta_2$? Insight into this process might suggest a means to prevent block by ensuring that the front slows to $\theta_1 = \theta_2$ as the tail is approached. To answer this question, we must further examine the wave front dynamics in the tail region. Figure 11.9 shows an action potential where the front and the tail do not necessarily translate at the same velocity. The space-time plot shows that there must be a spatial gradient of APD to permit the tail velocity difference $\theta_1 \neq \theta_2$.

$$\theta_2^{-1} = \theta_1^{-1} + \frac{\partial(\text{APD})}{\partial x} \qquad (11.1)$$

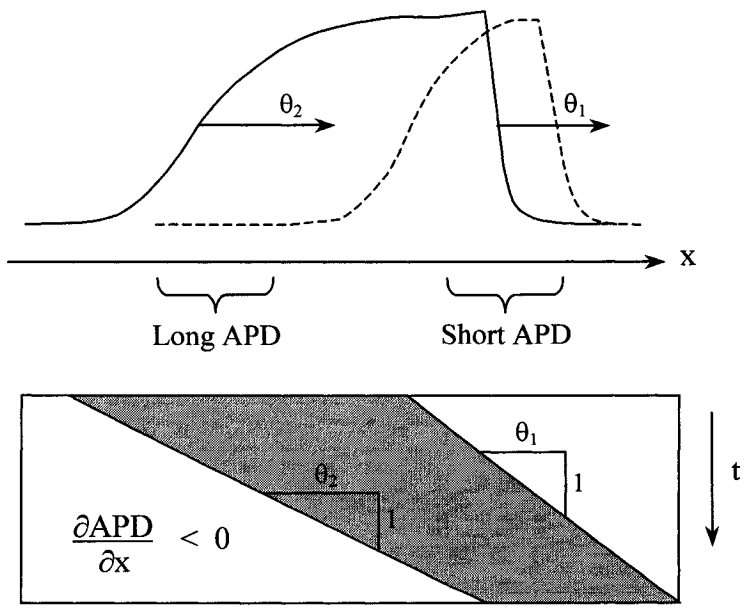

Figure 11.9. The relationship between θ_1 and θ_2 depends on the underlying spatial distribution and gradient of APD(x), according to equation 11.1. An action potential entering a region of negative APD gradient experiences an increase in tail velocity.

There are two possible origins of an APD gradient: anatomical and functional. An anatomical gradient occurs due to fixed spatial heterogeneity of cellular properties, such as that across the ventricular wall involving differences in endocardial, epicardial and M cells. A functional gradient arises due to APD and velocity restitution where there is a gradient of diastolic interval DI(x). This causes what is typically called "dispersion of refractoriness". Both of these gradient-generating processes can coexist, giving rise to considerable variability of wave front and tail velocities, manifesting as complex wave dynamics.

11.5 Spiral Waves

Extending the concept of stimulus-induced reentry to two dimensions, Winfree [543] predicted theoretically that a two-stimulus S_1-S_2 protocol should induce reentry by establishing topological conditions necessary for the formation of a phase singularity, which must lie at the core of a spiral wave reentrant circuit. Although speculative at the time, this mechanism was proposed as an explanation for shock-induced fibrillation described by Wiggers [540], and was confirmed experimentally in a patch of canine heart by Frazier et al. [183]. The counter-rotating spirals predicted by Winfree's theory were later observed transiently in the canine epicardial maps obtained by Chen et al. [75].

An initial wave front propagates across the tissue of heart, induced either by a train of regular S_1-S_1 pacing, or by normal sinus rhythm via the His-Purkinje system. This establishes a spatial gradient of refractoriness. A second stimulus S_2 is then delivered to a different site, within a carefully chosen time window during recovery of the action potential. The resulting second wave blocks in the antegrade direction, but propagates freely in the retrograde direction, thereby establishing a reentrant circuit. The two free ends, created at the boundary of the block zone, roll into a reentrant spiral wave pair in two dimensions. A more complex scroll wave develops about a filament in three dimensions.

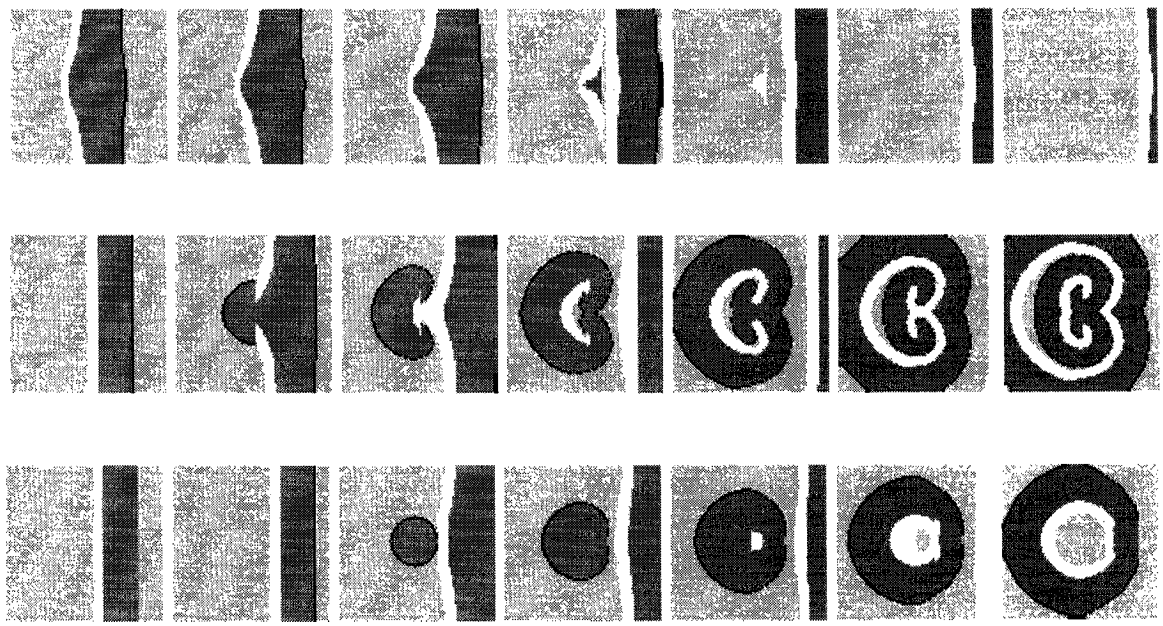

Figure 11.10. Reentry-induction in two dimensions. A priming stimulus S_1 applied to the left boundary causes a plane wave to advance across the 80 x 80 field. A circular shock stimulus S_2 is applied over the action potential tail. If the stimulus is too early (top), the action potential is simply prolonged. In the vulnerable window (middle), the wave front induced by the shock blocks in the antegrade direction, but propagates radially in the retrograde direction. A pair of counter-rotating spiral waves evolve around the free ends of the blocked wave front. A late stimulus (bottom) induces a new radiating wave without block. The hybrid automaton model is used for demonstration here, since the mechanism of block is relatively clear. The lightest shade is the relative refractory zone.

A simple example of this process is simulated in Figure 11.10, using the modified hybrid automaton model described earlier in Table 2.2, which perhaps most clearly demonstrates the mechanism of unidirectional block in a two-dimensional tissue domain. The initial "priming" plane wave, originating from a stimulus S_1, advances across the field and leaves a gradient of refractoriness in its wake. Action potentials are prolonged by a premature depolarizing shock S_2 spanning a small region over the repolarizing tail. This gives rise to a new action potential wave front, which propagates backward into well recovered tissue, but cannot advance forward due to the region around the tail remaining refractory. If the premature stimulus or shock is delivered during phase 2 of the action potential, it has little effect because it is too early. A stimulus during phase 3 prolongs the

AP, but again fails to initiate a new wave if too early. At the opposite extreme, a stimulus delivered too late, in well-recovered phase 4 tissue, propagates bidirectionally. Within the vulnerable window, the stimulus gives rise to unidirectional block allowing retrograde propagation only. This phenomenon occurs in both relaxation oscillator models [473] and ionic models [413]. It appears to be a fairly ubiquitous feature of nonlinear reaction-diffusion media, independent of the specific model chosen. Theoretically, the size of the vulnerable window, expressed either as a spatial width or a time interval, depends on both the stimulus timing and strength. Winfree described the vulnerable window as being a "bull's eye" within the stimulus time-strength plane [542]. An example of shock-induced reentry in the ionic SHV model is shown in Figure 11.11.

Once an initial spiral wave is formed, it will begin to experience front-tail interactions similar to those described on the cable ring. The spiral wave is stable under conditions of relatively flat APD restitution in Figures 11.11 and 11.12. Steepening the APD restitution curve, in Figure 11.13, causes tail block and wave break, which leads to fibrillation. In this case, restitution was steepened by shortening the calcium current recovery time constant τ_{uo} from 100 ms to 50 ms.

In the simple CML model, the restitution slope is determined by one parameter; however, there are many ways to manipulate and control the restitution curve in ionic models. Figures 11.14 and 11.15 show the effects of changing some SHV model parameters. The time constant of the restitution curve is largely determined by the time constant τ_{uo} of I_{Ca} recovery. Although it might not be physiologically realistic to manipulate τ_{uo}, this variable provides a convenient control parameter. Reducing calcium conductance g_{Ca} flattens restitution and shortens the plateau APD. Increasing potassium conductance g_K also shortens the plateau APD. While the effects of these ionic parameters on APD are rather obvious, the effects on the firing threshold and velocity restitution are not so apparent. It is therefore difficult to immediately predict how parameter changes in ionic models will affect wave stability and spiral wave break-up to fibrillation, without actually carrying out the numerical simulations. There is not yet a comprehensive theory that can predict break-up.

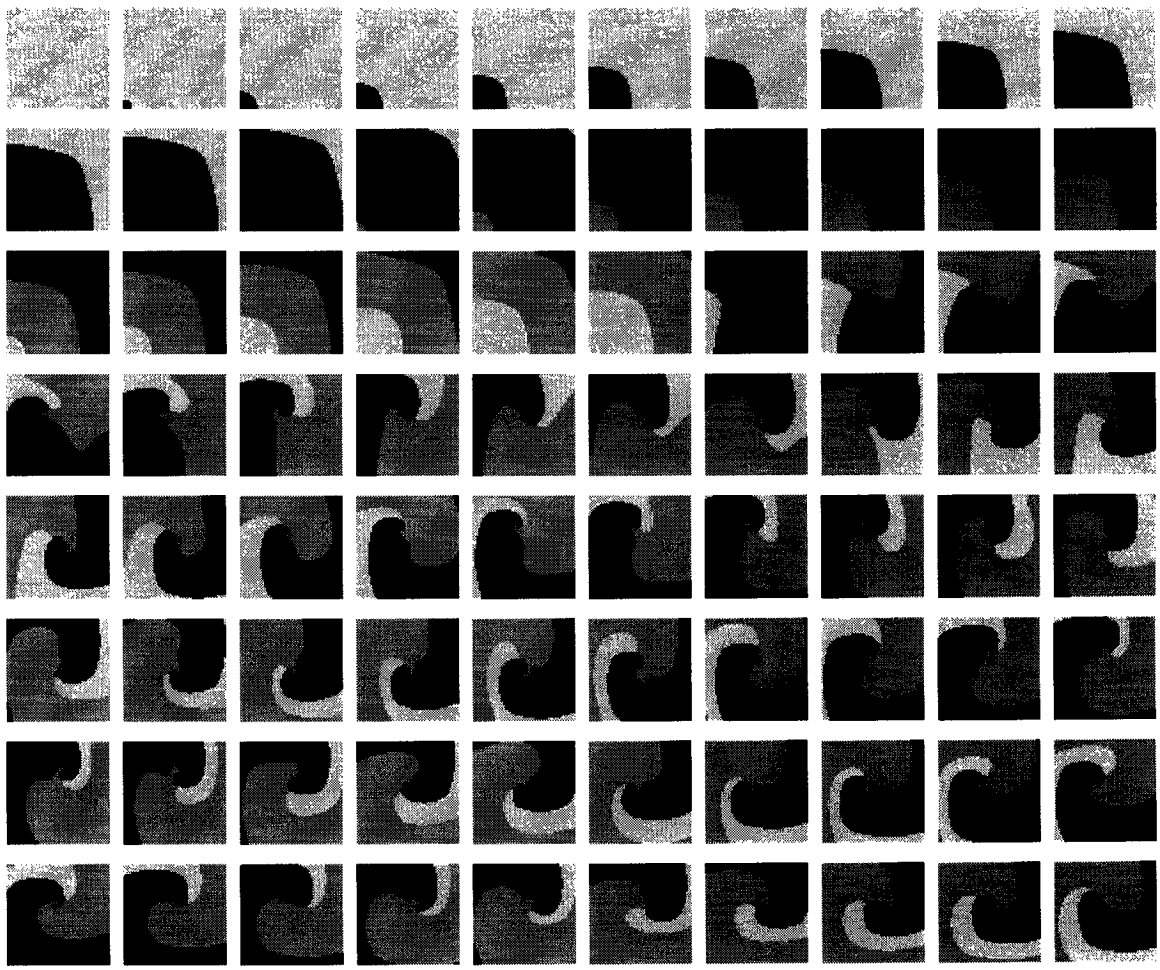

Figure 11.11. A two-dimensional sheet of 51 x 51 SHV epicardial cells corresponds to a 5 x 5 cm patch of tissue. Reentry is induced by an S_1-S_2 stimulus protocol. A point stimulus S_1 is applied to the lower left corner at t = 0, causing a wave to propagate outward. A second stimulus S_2 is applied, as a radially decaying shock, to the lower right corner at t = 260 ms. A spiral wave of reentry evolves, and is stable for the chosen parameters. The core point actually traces a hypercycloidal trajectory. Frames are 10 ms apart. The domain is isotropic with $a_x = a_y = 0.0020$. Restitution is relatively flat due to g_{Ca} being lowered. Parameters are $g_{Na} = 13$, $g_{Ca} = 0.03$, $g_K = 0.05$ $g_X = 0.20$, $g_{to} = 1.00$, $\tau_{uo} = 350$ ms, $V_{uo} = 24$ mV, $\Delta x = 1$ mm.

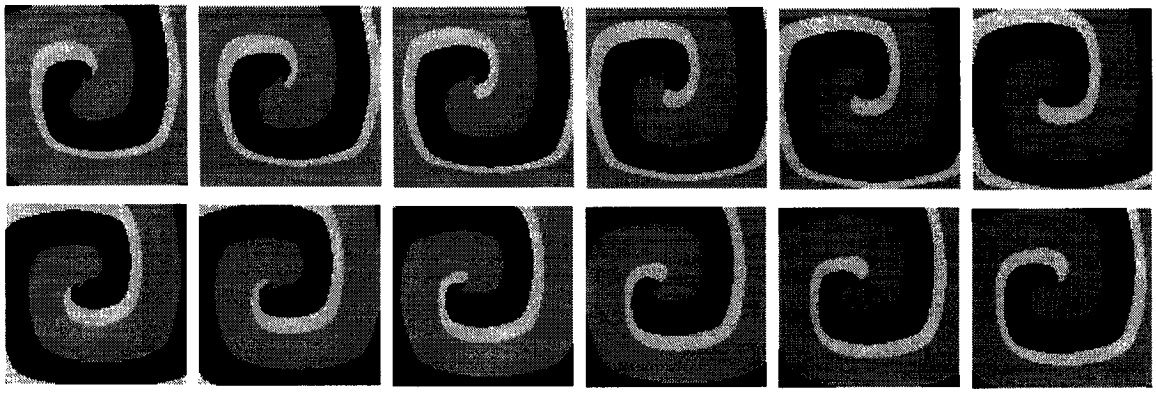

Figure 11.12. Stable spiral wave in a 100x100 sheet of SHV epicardial cells equivalent to a 10x10 cm patch. $a_x = a_y = 0.002$, $g_{Na} = 13$, $g_{Ca} = 0.08$, $fk_1 = 0.85$ $fk_2 = 0.2$, $fk_3 = 1.0$, $\tau_{uo} = 100$ ms, $V_{uo} = 75$ mV, $\Delta x = 1$ mm. The excitable gap settles to become fairly uniform.

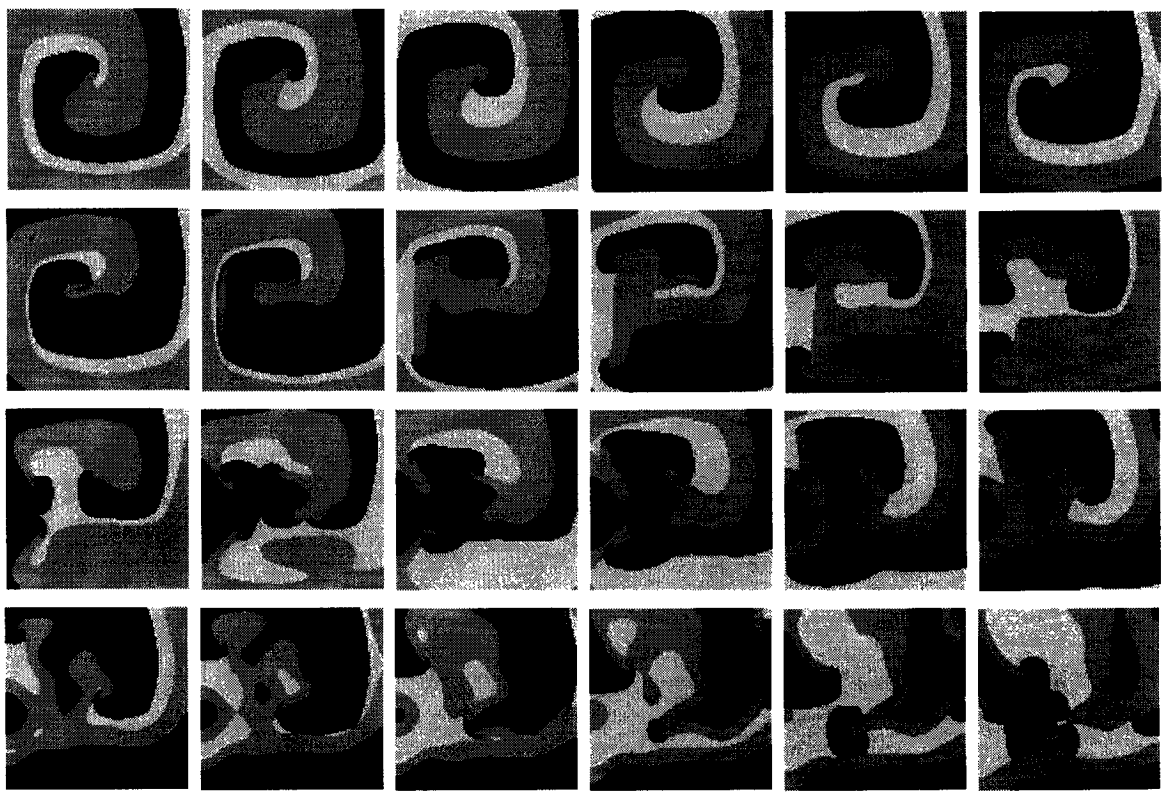

Figure 11.13. The same initial conditions as in the previous figure, but τ_{uo} is lowered from 100 ms to 50 ms, resulting in a steeper restitution curve slope beyond a critical value. The spiral wave becomes unstable and breaks into complex fibrillation. The critical event is wave front block, seen in frames 9 and 10. Head-to-tail interaction, combined with irregularity in the excitable gap, causes the path-length to fall below the critical ring size. Three meandering core points can be seen to evolve in the later frames.

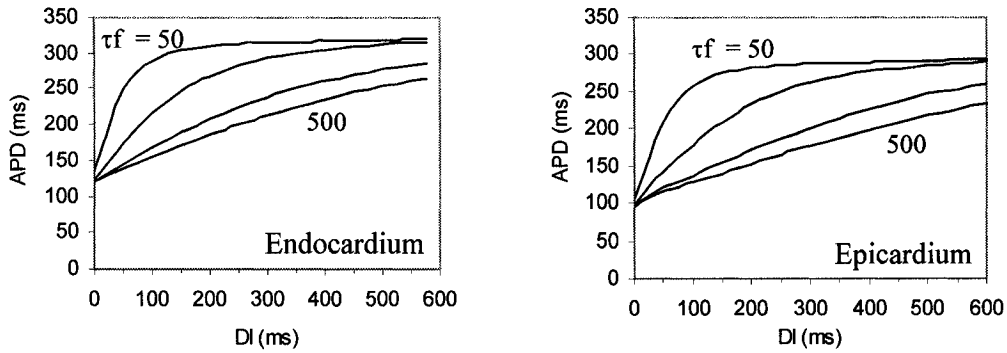

Figure 11.14. The restitution curve of the SHV endocardial (left) and epicardial (right) cells with the standard parameters, but with the recovery τ_f = 50, 150, 350, 500 ms. The slope m > 1 occurs only when τ_f < 100, and short diastolic interval DI. It is within this regime that spiral waves theoretically could become unstable and break up. $[K^+]_o$ = 4.0.

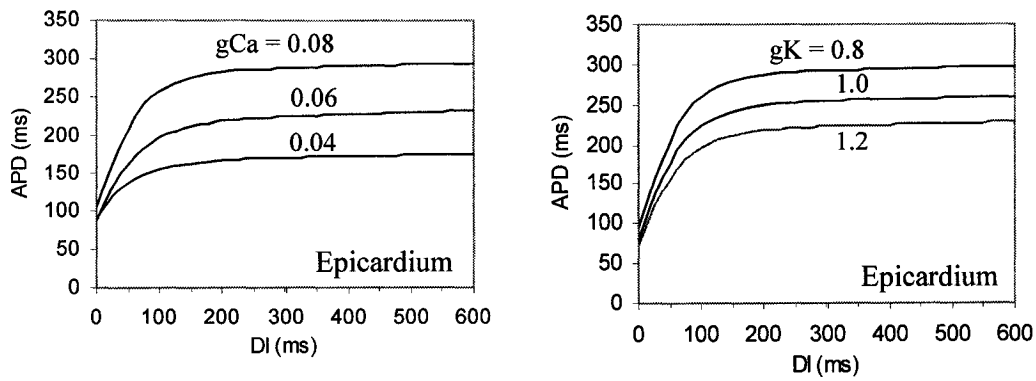

Figure 11.15. Restitution curves for epicardial cells for various g_{Ca} (left) and g_K (right). APD shortens if g_{Ca} decreases or g_K increases. The recovery τ_f is 50 ms for these examples. Note that changes in g_K have relatively little effect on the slope or intercept. APD can be decreased to 80 ms by raising g_K by 20%, and yet lower by larger increases.

Simulations suggest that spiral wave break-up occurs when there is a disparity of wave front and wave tail curvature, such that the front can partially block and produce core points. There are nine possible combinations of wave front and tail curvature during interactions, as shown in Figure 11.16. It is only those interactions with $\kappa_F > \kappa_T$ that can potentially block. We could define a block parameter $\sigma = \kappa_F - \kappa_T$ that must be positive

for the wave front to block and break. This is a necessary, but not sufficient, condition. We must also consider that wave front velocity is modified by curvature through upstroke current sinking into the lateral electrotonic load. Convex curvature slows the wave and concavity increases velocity. The velocity correction factor has been shown to be simply proportional to the curvature. Velocity of a curved front is $\theta(\kappa) = \theta_p - a\,\kappa$ where θ_p is the plane wave or cable velocity, and κ is the local curvature [190].

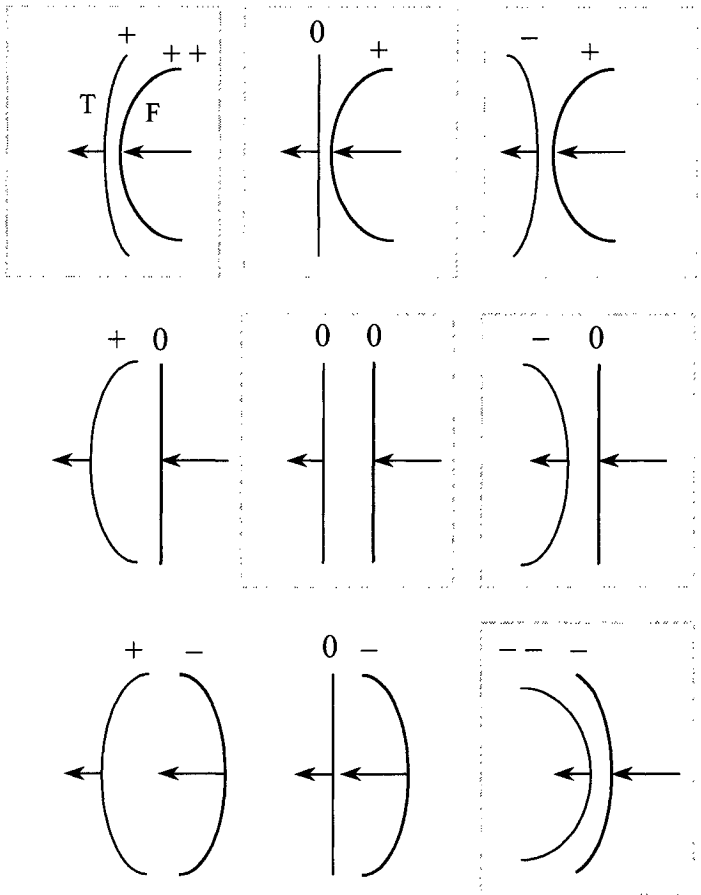

Figure 11.16. A wave front catching up to a wave tail can block over a partial segment and break only if there is a difference of curvature at the contact point. Considering three classes of curvature (+, 0 , –) for each of the front (F) and tail (T), there are nine combinations of interactions as shown. Of these, it is only those with curvatures $\kappa_F > \kappa_T$ that can experience a segment of block (grey boxes). The special case of $\kappa_F = 0$ and $\kappa_T = 0$ in the centre (dashed box) can block only over its entire length, and is representative of the one-dimensional cable.

11.6 Cycle Length

Since a spiral wave radiates outward from its core, all cells in its territory must fire in 1:1 correspondence with the same period or cycle length. Figure 11.17 illustrates how the wave front must spatially adjust its velocity and curvature to satisfy this constraint. What determines the cycle length of a spiral wave? By considering a small ring around the core singularity, we can see that the orbital period is the product of velocity and ERP on the circuit, or more precisely, the path integral of this product around the ring, if properties are nonuniform. For example, if conditions are such that the conduction velocity is very slow and ERP is very short, the minimum or critical path length will be small, and the core will appear to be almost stationary. If velocity or ERP are increased, the core point must begin to move around the local area to permit all neighbourhood cells to fire for their respective APD. This requirement gives rise to hypercycloidal or "flower petal" meander described by others [31, 412, 472].

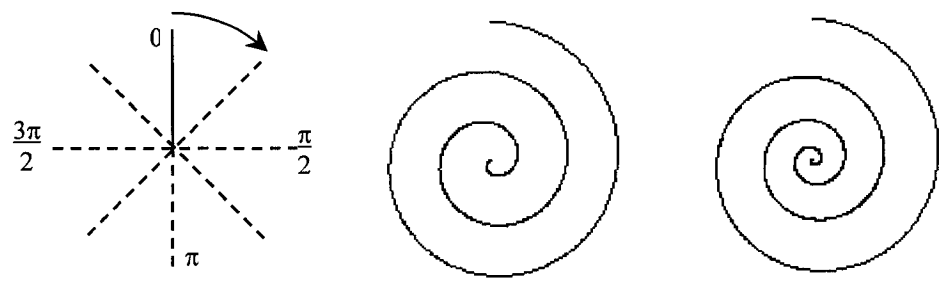

Figure 11.17. A wave front propagates around a phase singularity. Straight wave fronts require that velocity increase in direct proportion to radius (left). In reality, velocity reaches a plateau value away from the core, and curvature develops. Velocity is constant and independent of curvature in the uniform spiral (middle). For comparison, velocity increases as a power law of radius in the self-similar Archimedean spiral (right). The specific relationships between cycle length, curvature, and velocity determine the shape of the wave. Cardiac spiral waves most closely resemble the middle case in isotropic media, but velocity must decrease with curvature due to electrotonic load. Only the wave fronts are shown. The APD restitution curve determines the wave thickness (not shown).

The shortest possible ERP corresponds to APD_0, located at the intercept of the restitution curve where DI = 0. This minimum APD never falls below about 100 ms for the typical SHV parameters, and this occurs when the gating variable f is most fully inactivated, such that $I_{Ca} \approx 0$. The only way to achieve even shorter APD is to increase the potassium rectifier current I_K by raising g_K or $[K^+]_o$. This manipulation shortens APD, but at the same time raises the firing threshold.

11.7 Stability and Restitution

How can spiral wave break be prevented to avoid the transition to fibrillation? Karma first showed theoretically that steepening the slope of the APD restitution curve induced spiral wave break up [274]. Other model studies have come to the same conclusion [529]. Panfilov more recently showed that a higher APD restitution slope was required in two-dimensional media compared with three dimensions [389]. The reason for this apparent difference is not clear.

Riccio et al. examined standard restitution (SR) and dynamic restitution (DR) of normal and drug-treated canine ventricle [419]. In this study, the slope of DR was greater than one, while that of SR was less than one. Verapamil reduced the slope of both curves below one, stabilizing reentry. Procainamide reduced the SR slope only, and had no effect on the DR slope. This did not affect stability of reentry. Procainamide failed to prevent pacing-induced VF, while verapamil converted existing VF into a periodic rhythm. These results suggest that the DR slope $m > 1$, and not the SR slope, is involved with spiral wave break-up. Verapamil has also been shown to convert complex VF into stable VT in the rabbit heart [525].

Figure 11.18 shows three spirals created by the S_1-S_2 protocol. Wave stability depends on the APD restitution curve slope, which in these cases is controlled by altering the calcium conductance g_{Ca}. The wave is stable, with a uniform excitable gap at shallow restitution, when $g_{Ca} = 0.06$. At $g_{Ca} = 0.10$, the excitable gap becomes irregular, but the wave does not break. At $g_{Ca} = 0.12$, the wave finally breaks and fibrillation develops. The

mechanism of break can be seen as partial front-block due to curvature disparity of the first type in Figure 11.16, combined with velocity mismatch due to a functional APD gradient. This allows the front to overtake the tail and block. Two new free ends are created giving birth to daughter waves. The basic mechanism underlying this process is shown schematically in Figure 11.19. Any radial section through a hypothetical uniform spiral wave reveals a spatially regular wave train. The equilibrium APD and DI of the uniform spiral are determined by the intersection of the negative unity slope line at the cycle length CL, as previously illustrated in Figures 3.14 and 4.19. The main difference between sections a and b is a phase lag equal to the sector angle. A perturbation, such as a small APD prolongation δ, applied to the wave tail on section b causes a slight phase shift of the wave train. This is equivalent to momentarily shifting the unity slope CL line left by δ. If the restitution slope $m < 1$ at the intersection, the perturbation is damped, and the spiral is structurally stable. If $m > 1$, a ripple develops in the excitable gap, which grows and works its way around the gap, as demonstrated with the CML model in Figure 3.16. Ultimately, the growing curvature and velocity disparity causes block by the mechanism discussed earlier and illustrated in Figure 11.7. Figure 11.20 shows a closer examination of the third sequence of Figure 11.18. This example reveals the mechanistic similarity of two-dimensional block with that of the one-dimensional cable.

According to this simple theory, spiral wave break up should occur when the restitution slope m is greater than one. Factors other than APD restitution slope, however, are likely involved. It stands to reason that if the cycle length is perfectly regular, disparity of neighbouring cells can grow by the instability illustrated in Figure 11.19. In reality, cycle lengths are not perfectly periodic. While the critical APD restitution slope m for break up does seem to be close to one, variations in conduction velocity probably dampen or exacerbate perturbations, and complicate the picture. We have not specifically examined this effect, nor have we accounted for changes in intercellular coupling, anisotropy, wall thickness, and fibre rotation. Some of these issues will be examined in the next chapter, which deals with three-dimensional fibrillation in the anisotropic heart.

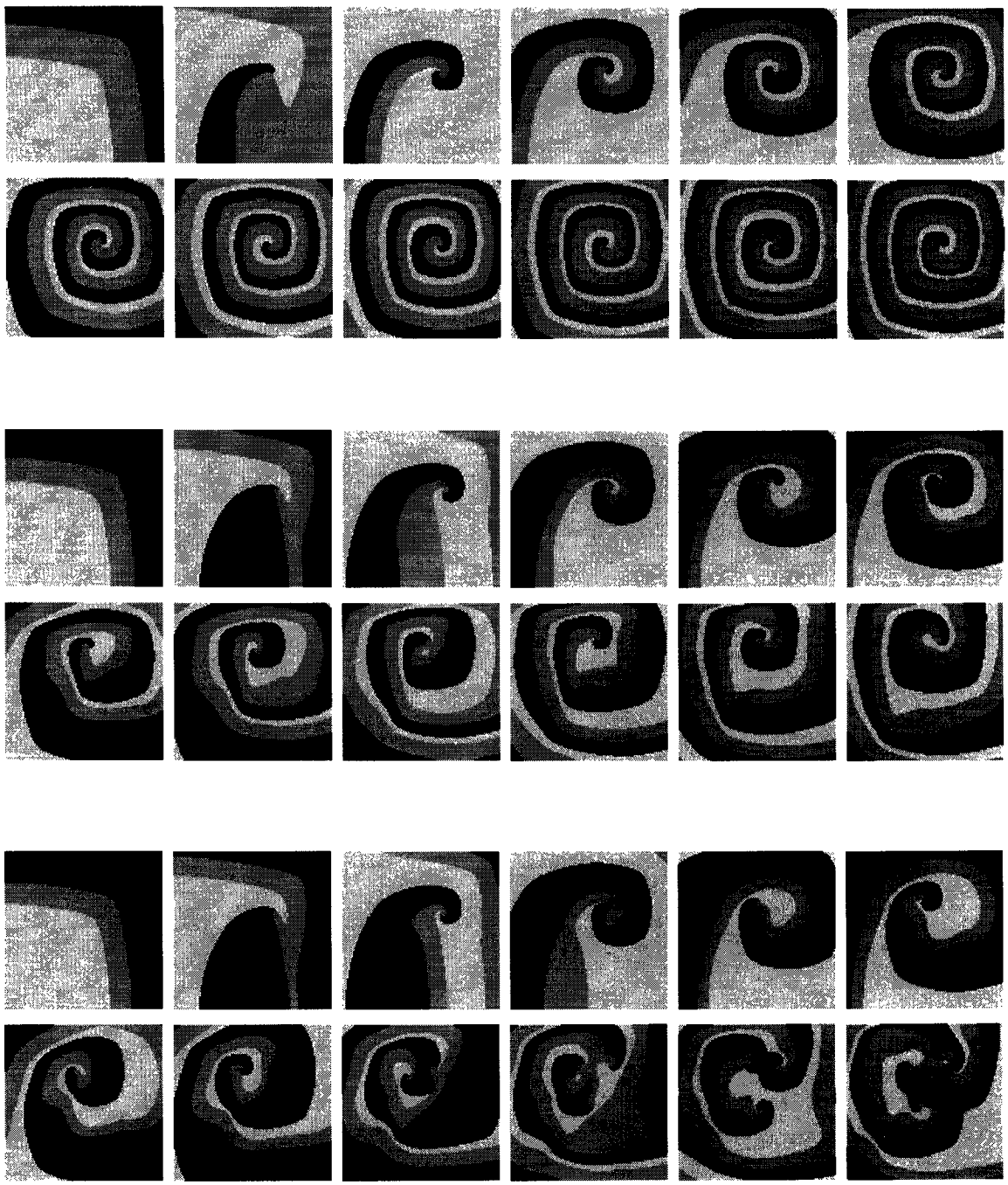

Figure 11.18. The role of restitution slope on the stability of a spiral wave using the SHV membrane model. An S_2 shock initiates a reentrant circuit in these 20-ms frames. The APD restitution curve slope is manipulated by changes to the calcium conductance. g_{Ca} = 0.06 (top), 0.10 (middle), and 0.12 (bottom). Flatter restitution stabilizes the spiral, while steep restitution causes break-up to fibrillation.

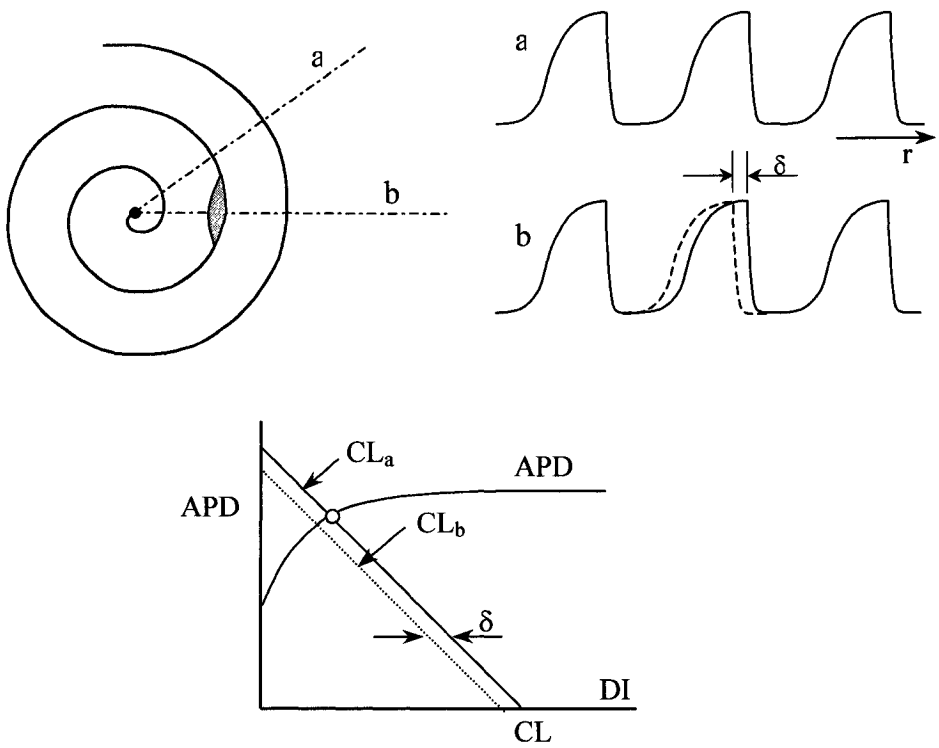

Figure 11.19. An idealized spiral wave radiates outward at uniform velocity (upper left). Sampling along sections a and b show regular action potentials (upper right) of constant cycle length CL = APD + DI. This situation corresponds to the equilibrium point (circle) in the bottom figure, where the APD restitution curve intersects the negative unity slope line (bottom). CL is determined by dynamics at the core, which in turn dictate APD and DI, which are constant for all cells. A perturbation δ occurs on the wave at section b to retard the front or delay the tail. This introduces a decrease in DI for the next action potential, which is thereby shortened by the amount that the unity slope line shifts to the left (dashed line). If the slope m <1, the perturbation decays and the spiral wave remains stable, although perhaps distorted. If m > 1, the perturbation is unstable and grows with cycle, manifesting as ripples in the excitable gap. The wave front and tail velocities are no longer equal, and tail block becomes possible by the mechanism previously described for the cable. Wave break ensues giving rise to fibrillation.

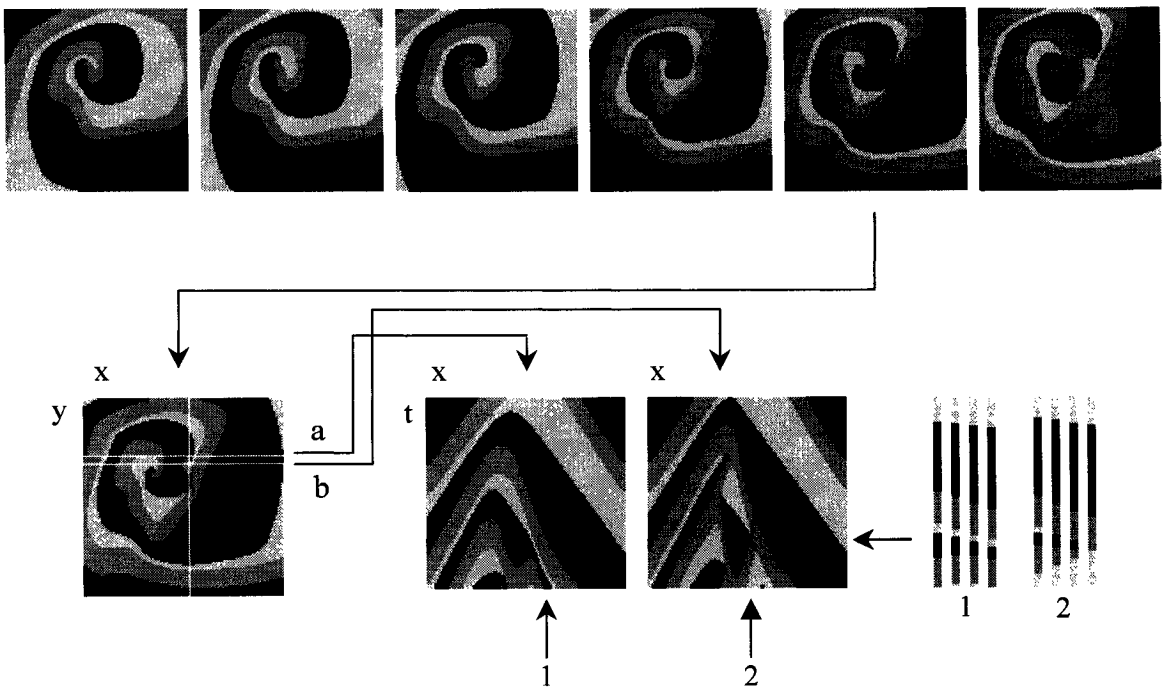

Figure 11.20. A rotating spiral wave in the sequence (top), shown in 20-ms frames, breaks in the last two frames to initiate fibrillation. The critical event is block of one segment of the wave front at the point of contact with the preceding tail. By sampling V(x, t) along the two sections shown at left, on either side of the point of block, it can be seen that the wave front is able to continue propagating along the upper slice "a", but blocks in the lower slice "b". By examining the time-space plots V(x, t) shown for each of the two slices, block is evident in the panel at right, indicated by the arrows at the bottom. The wave front block on its tail is similar to that seen in the cable model below the critical ring size. If we now dissect further to look at the action potentials at the specific cells in and around the point of block, we can see the difference between the wave front segment that survives, and the segment that blocks due to velocity disparity.

Chapter 12

VENTRICULAR ARRHYTHMIAS

12.1 Ventricular Ectopy

An impulse spreading radially outward from an ectopic focus is the simplest ventricular dysrhythmia. An ectopic beat occurring during normal sinus rhythm usually causes a premature contraction followed by a compensatory pause until arrival of the next normal sinus beat. In a review of this phenomenon, Janse discusses terminology and argues that these impulses should be called "premature ventricular beats" (PVB) [256]. These beats are common in both healthy and diseased hearts, and are usually benign. There has long been concern, however, that premature beats occurring during ischemia, or in the presence of cardiomyopathy, might initiate VT, which would deteriorate to VF. The well-known Cardiac Arrhythmia Suppression Trial (CAST) examined the use of class Ic sodium channel blockers in the post-myocardial infarction period, and found premature beats to indeed be well suppressed, but higher mortality was clearly seen in the treatment group as compared with the placebo group [57]. Evidently, the less frequent PVB's that did occur were more lethal, perhaps due to some sort of concomitant substrate change induced by the drug that brought other electrophysiological mechanisms into play. The reasons for this adverse clinical outcome are not yet clear, and have been the subject of considerable speculation [386, 472].

The exact cause of a specific ectopic impulse cannot generally be determined without high-resolution mapping, but theoretically can involve any or all of the three fundamental

mechanisms previously discussed: automaticity, afterdepolarization, or reentry. In the preceding discussion of the coupled map lattice model, it was shown that periodic radiating impulses can originate from either a spontaneously beating focus or closely spaced counter-rotating reentrant spirals. In both cases, waves merge within a short distance producing coherent radiating waves in the far field. Solitary spiral waves are topologically distinct from ectopic foci, since the wave fronts are not closed loops or surfaces, although they do generate radiating waves similar to those of ectopic foci if observed a few wavelengths away from the central core. Ectopic beats occurring during ischemia appear to be predominantly focal and not reentrant [403]. This might be fortunate, as reentrant circuits tend to persist, while ectopic foci tend to be transient, provided they do not trigger other dysrhythmias. Waves radiating from an ectopic focus, however, can block as they enter a region of depressed conduction, due to ischemia or refractoriness from a preceding action potential, allowing reentrant circuits to germinate at the newly-formed free ends .

An ectopic beat can be simulated most easily by applying a current stimulus to the desired site. Figure 12.1(a) shows an action potential wave radiating from the anterior epicardium at vertical ordinate z = 34 mm, hereafter defined as the equatorial level. The repolarizing tail wave follows the same isochrones as depolarization, since the cellular properties in the epicardial layer are uniform. Some small differences are evident due to electrotonic interaction from curvature. Complete depolarization of the heart takes about 200 ms. Transverse sections at the level of the ectopic site are shown in Figure 12.1(b) during activation and recovery. The simulated equatorial ECGs and body surface maps are shown in Figure 12.1(c). Equatorial leads are displayed at 20-degree intervals, illustrating the large negative deflection that occurs over the ectopic site due to wave departure, and the positive deflection in the reciprocal leads. The body surface potential maps are displayed at 20-ms intervals, showing the ECG potentials sampled over a 10-degree grid on a sphere of radius 12 cm centred at the midpoint of the heart.

An ectopic focus at the same co-ordinates as the epicardial above case, but on the endocardial surface, is shown in Figure 12.2. Epicardial breakthrough takes about 70 ms,

and occurs simultaneously at two sites, due to the relatively flattened wave front meeting the curved epicardial surface at two points. The repolarization sequence is again quite similar. The apical and transverse views show that posterior breakthrough occurs shortly after anterior breakthrough, because anisotropic conduction around the ventricle is faster along the fibres than that across the wall. The ECG leads show a small initial positive peak, due to transmural conduction toward the anterior surface, followed by the larger negative deflection. Amplitudes from the endocardial ectopic beat are generally smaller than those from the epicardial ectopic site.

An ectopic beat originating at the apex is shown in Figure 12.3, giving rise to a wave that propagates upward to the base. Conduction across the right ventricle takes slightly longer than that over the left ventricle because the apex is located slightly to the left side of the heart. The ECG amplitudes are smaller than those of the equatorial ectopic beats because the wave front dipole vectors point to the equatorial observation sites at highly acute angles. The body surface maps show a negative wave moving up the body surface sphere, in direct correspondence with the propagating wave front on the heart.

A series of spontaneous ectopic beats is simulated in the SHV cellular model as illustrated in Figure 12.4. Shifting the sodium excitation curve $m^3(V)$ more negative, and shifting the potassium current $I_{K1}(V)$ more positive, causes spontaneous phase 4 diastolic depolarization and automaticity. A solitary ectopic focus radiates a regular train of action potential waves from the anterior epicardium in Figure 12.4(a). The train of spontaneous action potentials from the focus is shown along with those induced in a neighbouring cell. Slow diastolic depolarization, that gradually reaches threshold, is evident in the ectopic cell. By contrast, the neighbouring cell is driven to threshold by the larger electrotonic current, and therefore activates more rapidly. The action potential of the neighbour cell is shortened somewhat by electrotonic interaction such that the tails of the neighbour cells tend to become more synchronized despite different upstroke times. The ECG leads at various radial locations above the heart equator are also shown. Figure 12.4(b) shows a sequence of 10 ms frames of the resultant body surface maps on a sphere, and a space-time plot of potentials along the equatorial ring. Periodicity is evident.

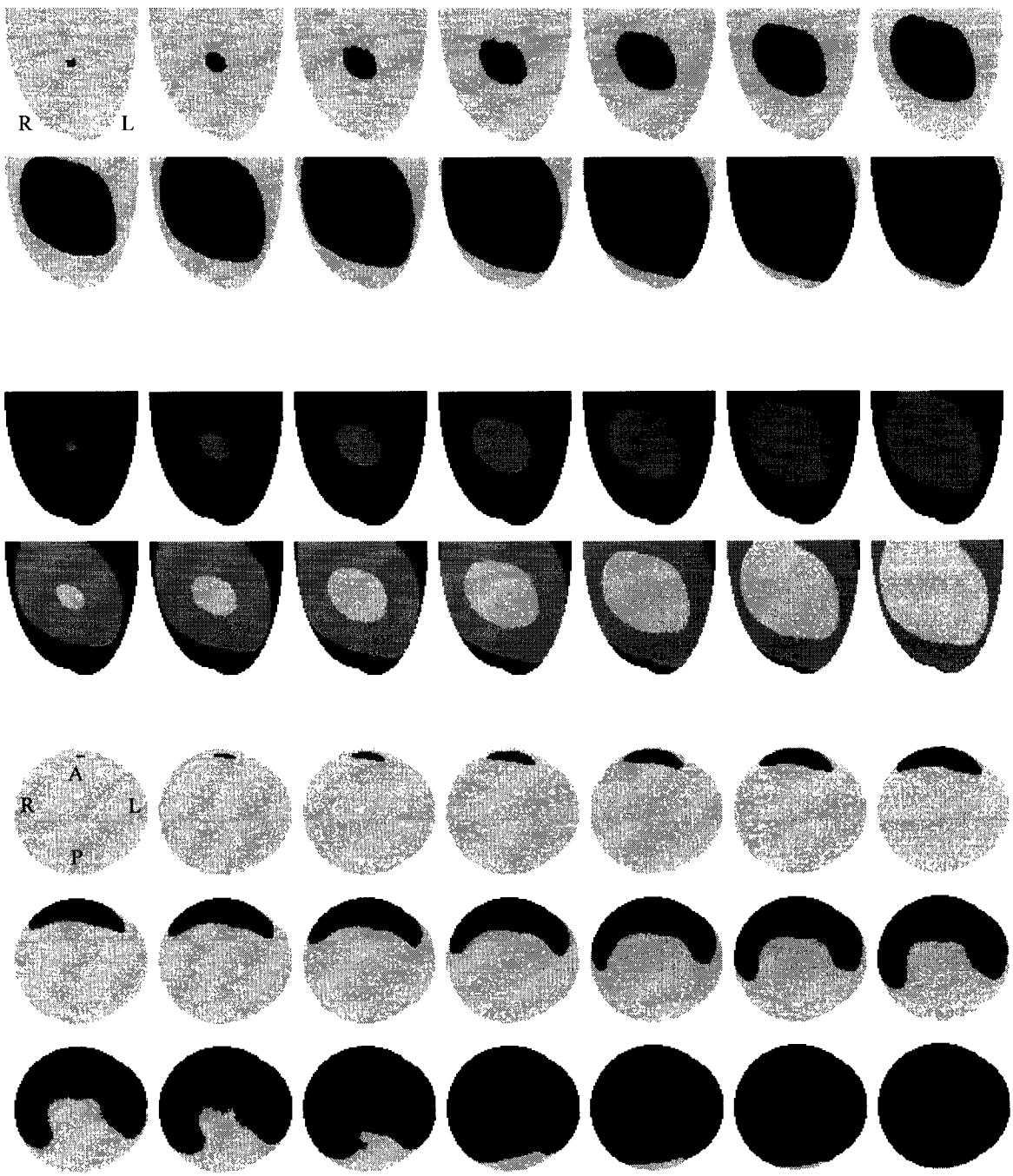

Figure 12.1(a). Activation from a single ectopic beat originating from a focus on the anterior epicardial surface shown at 10 ms intervals. Depolarization (top), repolarization (middle), and apical view (bottom). Symbols denote orientation: A = anterior, P = posterior, L = left ventricle, R = right ventricle. Resting potential (light), moderately depolarized (grey), fully depolarized (black).

Figure 12.1(b). Transverse sections through the heart during the ectopic beat at the anterior epicardium. Activation (top) and recovery (bottom) sequences are nearly identical, with the exception that electrotonic interactions alter recovery to a small degree, particularly near the end. Cellular properties f_{k1}, f_{k2}, and f_{k3} in this case vary linearly across the wall.

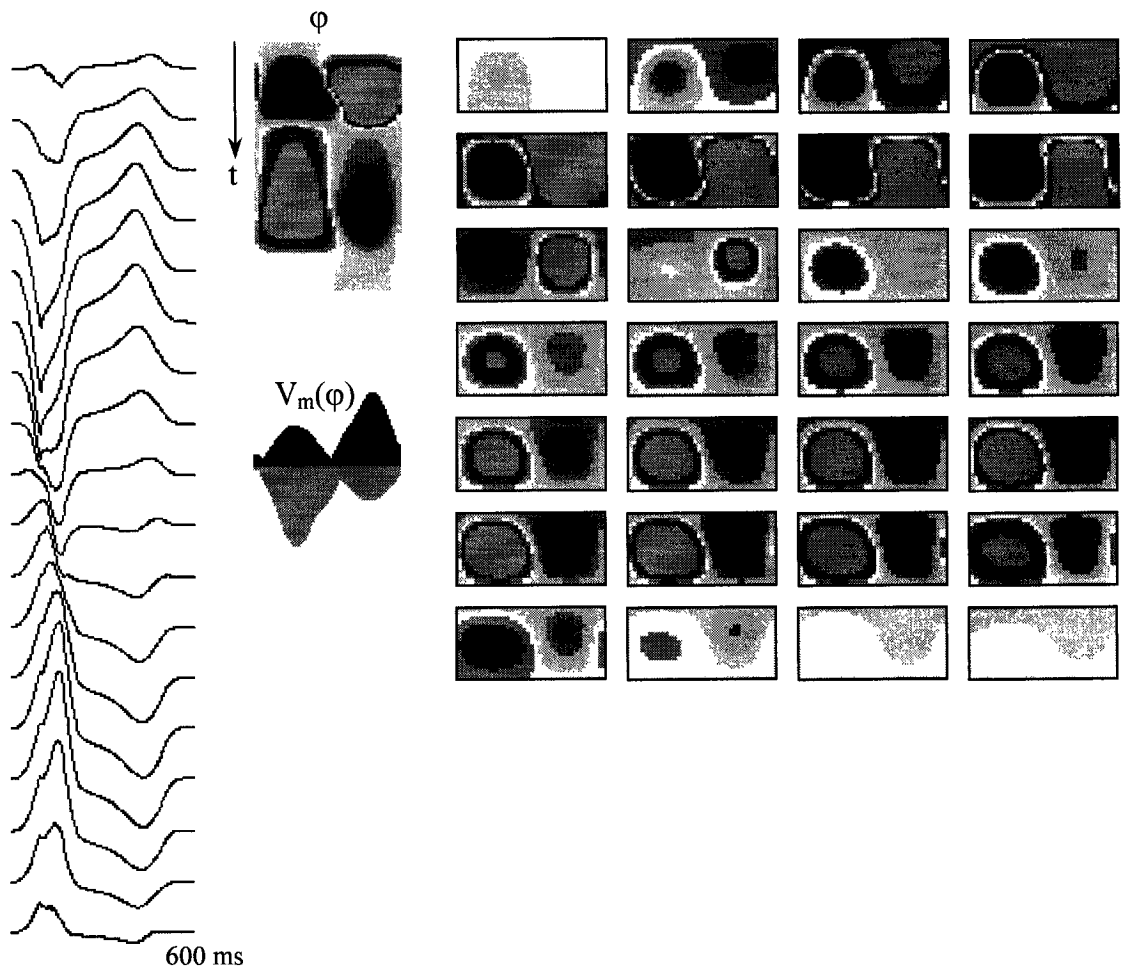

Figure 12.1(c). Electrocardiograms resulting from activation initiated at the anterior epicardium ectopic focus, as measured around an equatorial band at 20 degree intervals (left). A large negative deflection occurs over the focus, around $\varphi = 90^{\circ}$, due to wave departure. A positive deflection appears on the opposite side, around $\varphi = 270^{\circ}$, as waves approach this area. The space-time plot (middle top) shows the dominant peaks. The envelope of positive and negative peak ECG voltages $V_m(\varphi)$ is shown beneath. The full body surface potential maps, in 20-ms frames (right), represent the ECG potentials at 10-degree intervals of latitude and longitude on a Mercator projection of a sphere surrounding the heart.

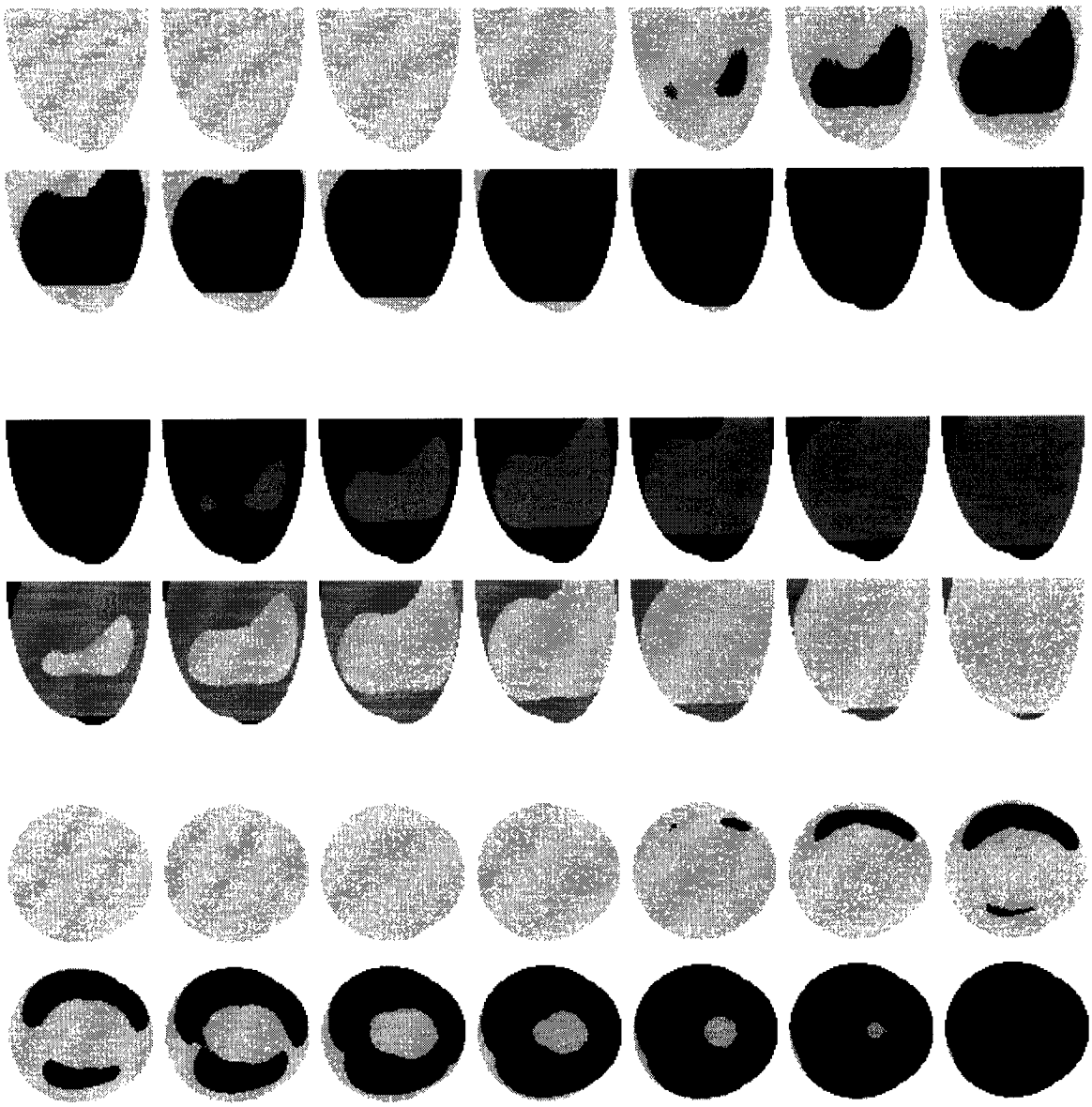

Figure 12.2(a). Activation from a single ectopic beat originating from a focus on the anterior endocardial surface is shown at 10-ms intervals. Depolarization (top), repolarization (middle), and apical view (bottom). Resting potential (light grey), depolarized (black).

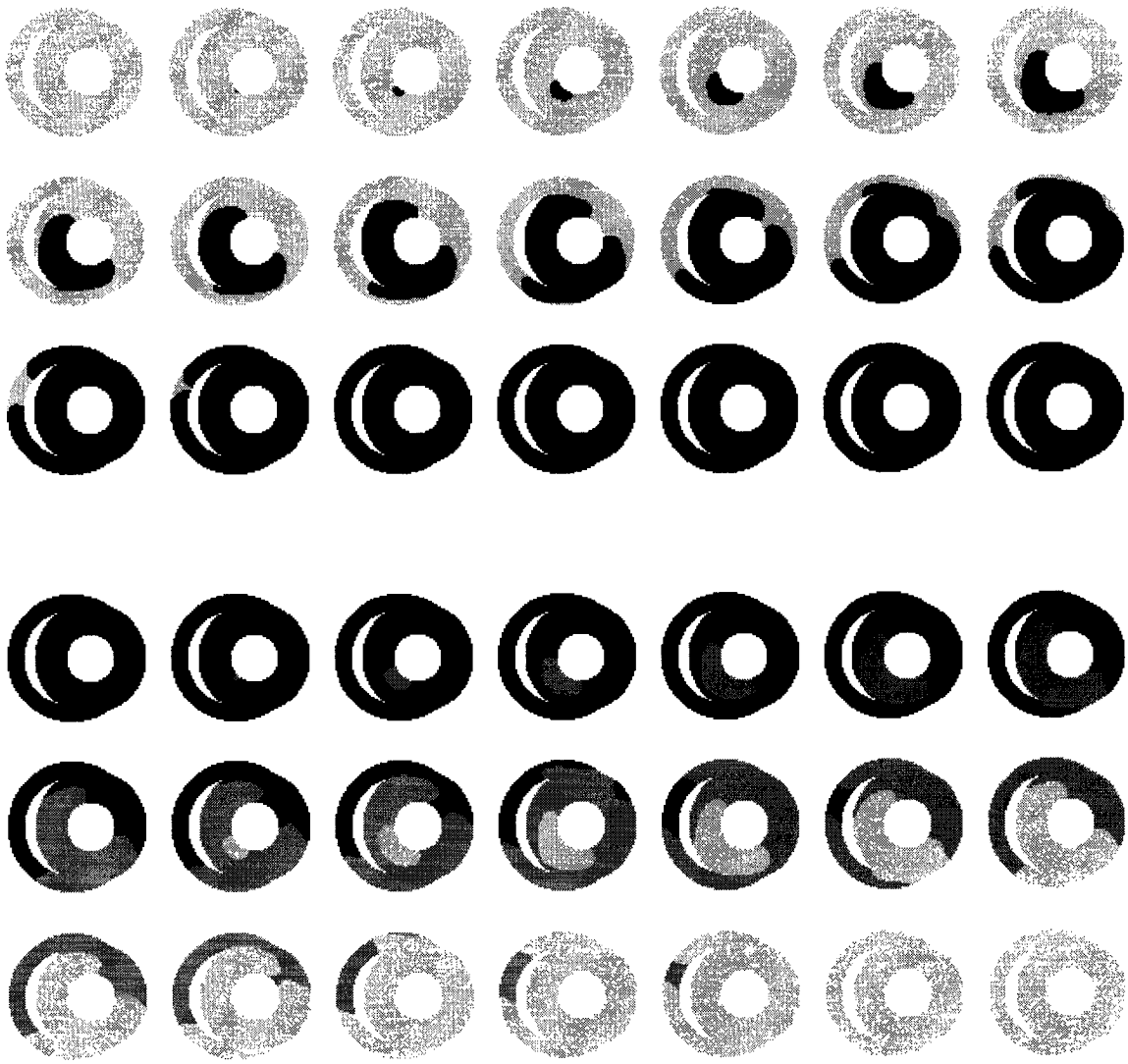

Figure 12.2(b). Activity on transverse sections through the heart during the ectopic beat at the anterior endocardium. Cellular properties f_{k1}, f_{k2}, and f_{k3} vary linearly across the wall for this case.

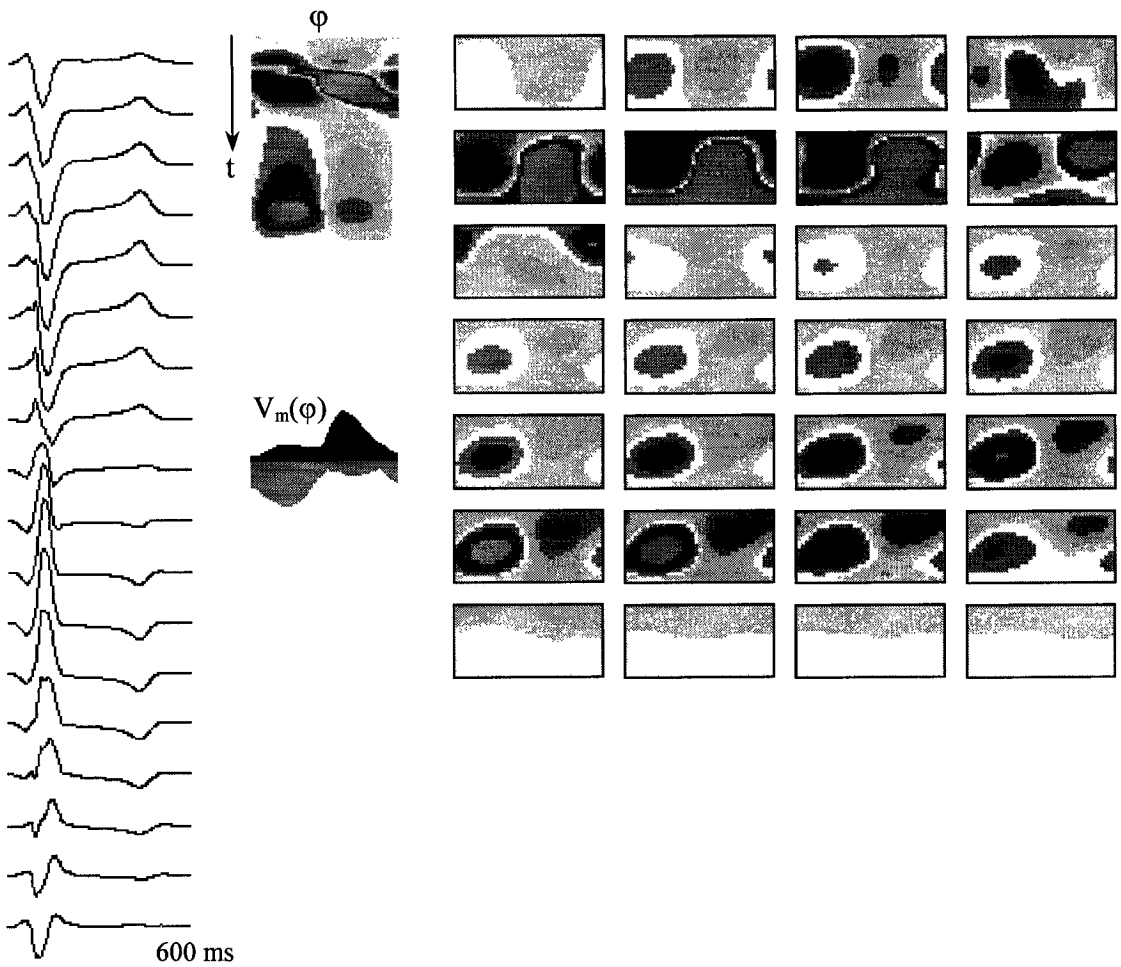

Figure 12.2(c). Electrocardiograms resulting from activation initiated at the ectopic focus at the anterior endocardium, as measured around an equatorial band at 20 degree intervals (left). Compared with the epicardial case, a small positive deflection occurs over the focus at $\varphi = 90^{\circ}$, due to transmural wave approach before the larger negative deflection. Amplitudes are smaller than those for the epicardial case due to more attenuated wave front dipole vectors. The space-time plot (middle top) shows the dominant peaks. The envelope of positive and negative peak ECG voltages $V_m(\varphi)$ is shown beneath. The body surface potential maps in 20-ms frames (right) are at 10-degree intervals of latitude and longitude on a sphere surrounding the heart.

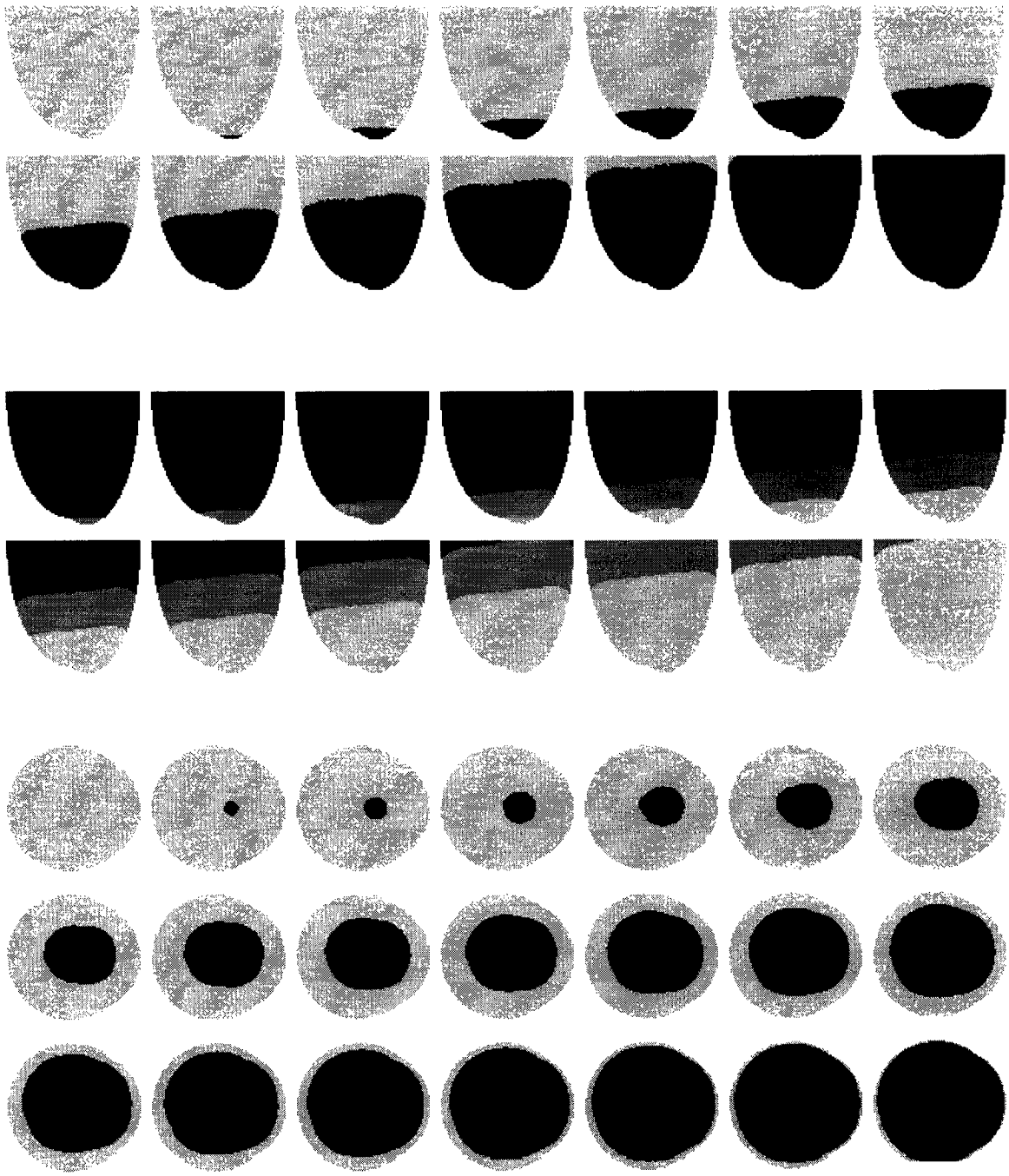

Figure 12.3(a). Activation from a single ectopic beat originating from a focus at the apex epicardial surface, shown at 20-ms intervals for the anterior views, and 10-ms intervals for apical views. Depolarization (top), repolarization (middle), and apical view (bottom). Resting potential (light grey), depolarized (black).

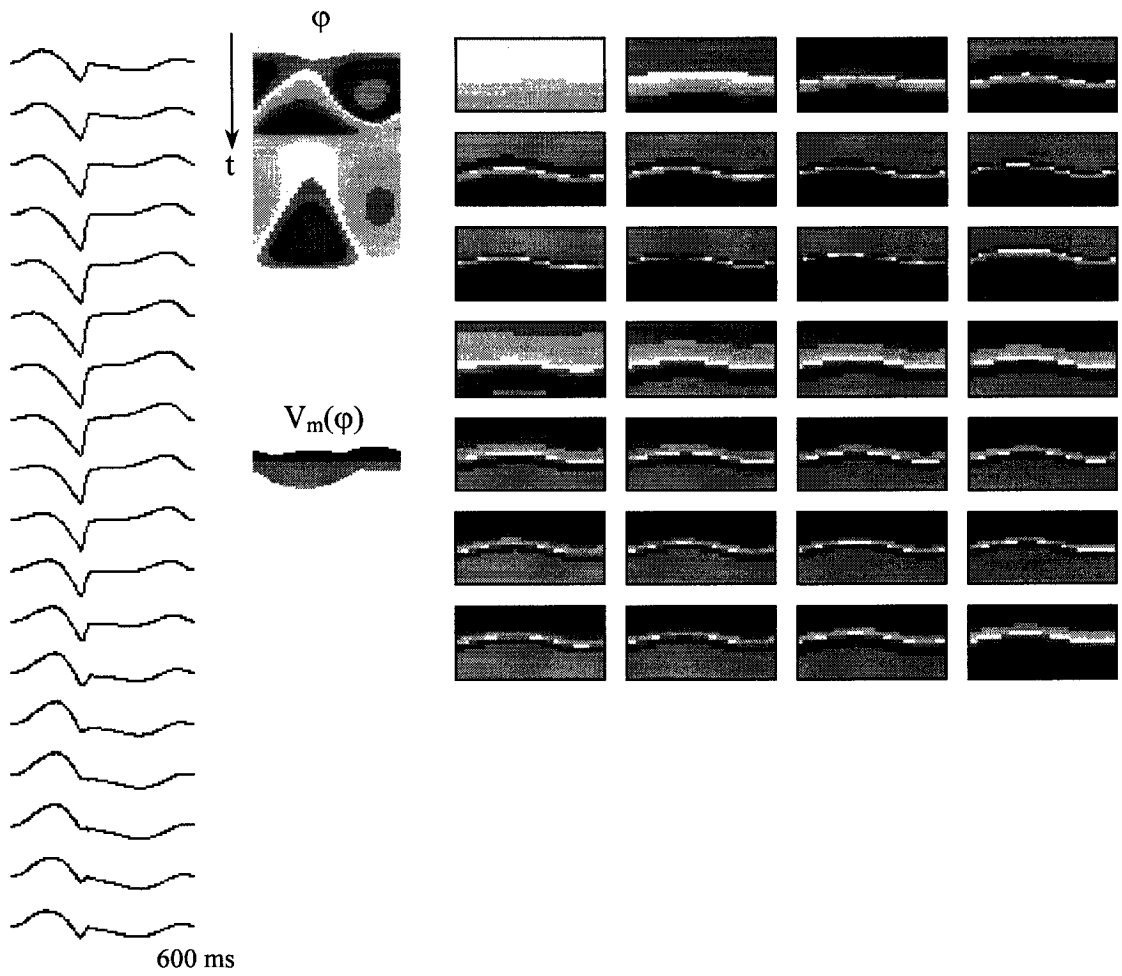

Figure 12.3(b). Electrocardiograms resulting from activation initiated at the ectopic focus located at the epicardium, as measured around an equatorial band at 20-degree intervals (left). An initial small positive deflection is seen in all leads due to wave approach from the apex. Maximum negative amplitude occurs over the apex, and amplitudes over the equator are relatively smaller. Asymmetry in equatorial leads is due to slower conduction up the right ventricle from the off-centre apex, and is apparent in the apical view in the previous figure. The space-time plot (middle top) shows the dominant peaks. The envelope of positive and negative peak ECG voltages $V_m(\varphi)$ is much smaller than those from the equatorial ectopic foci previously illustrated. The body surface potential maps, in 20-ms frames (right), are again at 10-degree intervals of latitude and longitude on a sphere surrounding the heart.

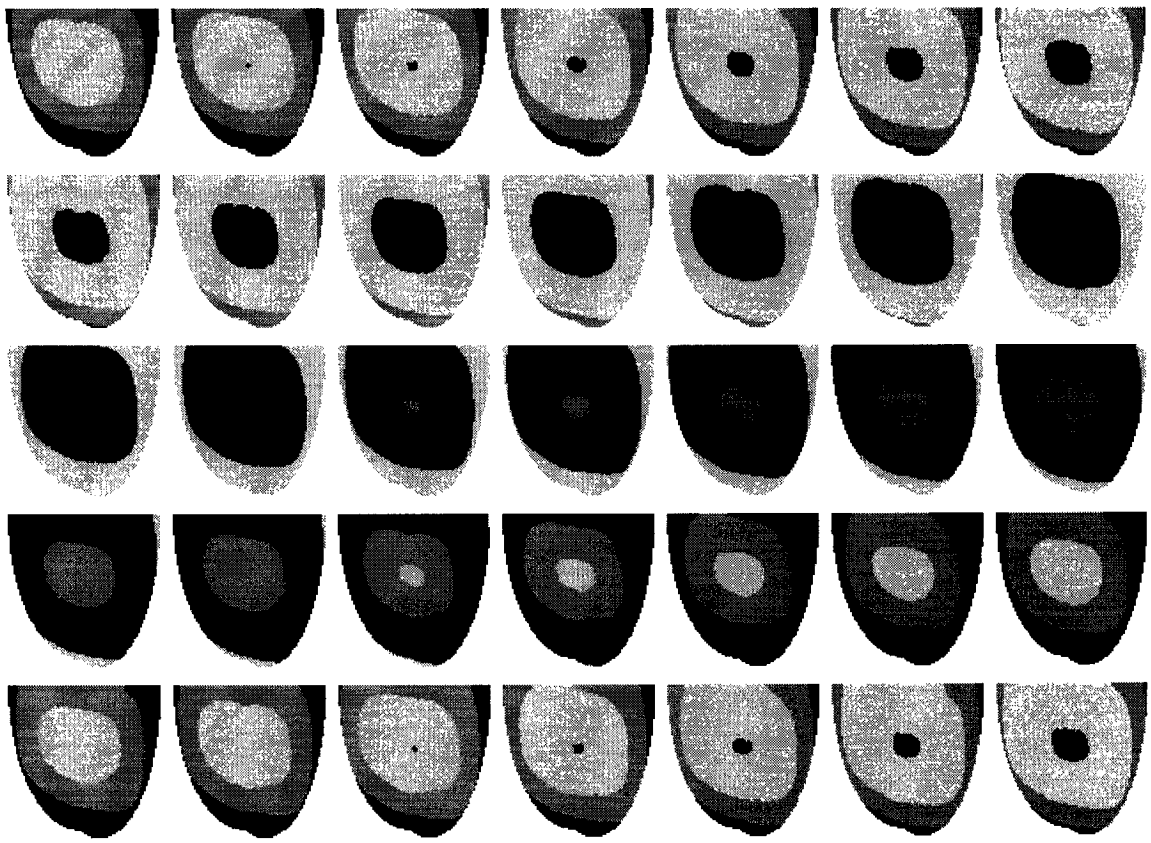

Figure 12.4. Anterior epicardial view and transverse section during an ectopic beat originating from a focus on the endocardial surface.

12.2 Ventricular Tachycardia

Ventricular tachycardia (VT) is, by definition, a rapid rhythm of ventricular origin. Any or all of the three fundamental dysrhythmia mechanisms can be involved, according to mapping in canine [290, 418] and human hearts [139, 548], involving transmural [122, 140] or intramural pathways [290, 404]. Transient runs of VT are often seen during myocardial infarction and during coronary reperfusion. These beats are likely focal in nature [404, 548, 561]. Afterdepolarizations can also cause focal VT, but may be more likely to cause polymorphic VT, owing to beat-to-beat variability of the action potential morphology during repetitive salvos [152]. Reentrant circuits are generally considered the most likely candidates for fixed persistent VT, since they can anchor around obstacles of depressed excitability [96, 139, 196]. The core points of reentrant circuits can meander in space, and might be responsible for at least some cases of polymorphic VT [440].

Figure 12.5(a) shows a solitary spiral wave rotating around a point on the anterior LV wall. To ensure stability without spiral wave break-up, it was necessary to flatten the APD restitution curve by lowering the calcium current from 0.10 to 0.06. The core point is relatively stationary, although some drift is evident upon close examination. In a longer run (not shown) the core point drifted slowly toward the apex, if initiated on a more curved region of the ellipsoidal surface. This drift may have been influenced by surface curvature or fibre anisotropy, but this has not been further investigated. The equatorial ECG leads and body surface map are shown in Figure 12.5(b). Figure 12.6 shows a solitary spiral wave rotating about the apex. The cell parameters are the same as in the previous case, but the initial conditions were changed to place the core point at the apex. Some variability is seen in the action potential spatial thickness because the restitution curve is not completely flat. The ECG and body surface maps are also shown. Core point meander within a small subregion is evident, and this meander causes a small amount of variability in the ECG. If the core point is firmly anchored by defining a small inexcitable plug at the core region, the ECG should be stabilized to become monomorphic.

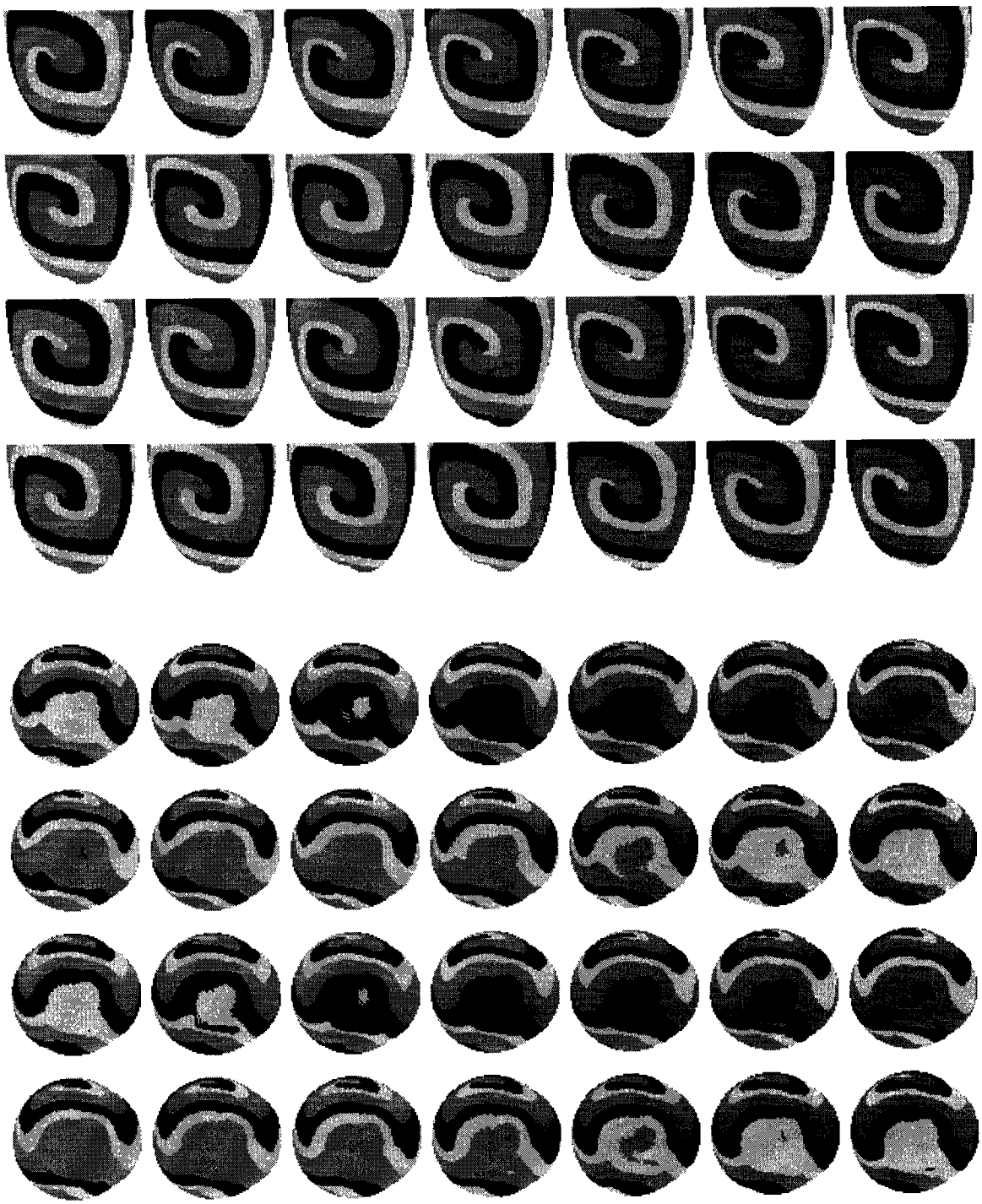

Figure 12.5(a). Anterior and apical epicardial views of a solitary spiral wave reentrant VT rotating about a point on the anterior epicardium.

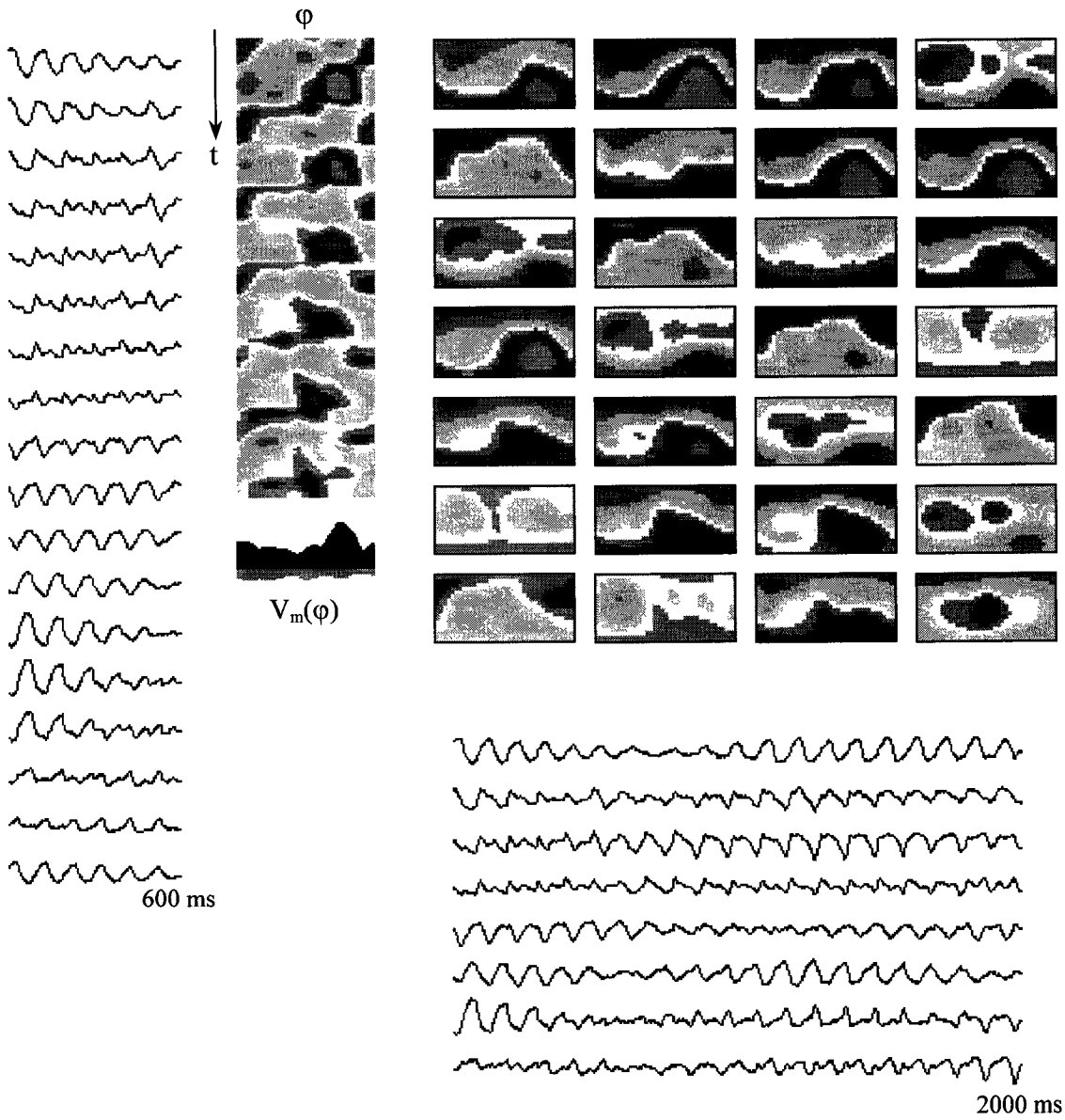

Figure 12.5(b). Electrocardiograms corresponding to the anterior solitary spiral, as measured around an equatorial band at 20-degree intervals (left) for 1000 ms. A small amount of locally confined core drift gives rise to a weak polymorphic ECG. Maximum negative amplitude occurs over the spiral core, and maximum positive amplitude occurs at the opposite side. The space-time plot (middle top) shows the dominant peaks. The body surface potential maps in 20-ms frames (right) are again at 10-degree intervals of latitude and longitude on a sphere surrounding the heart. The ECGs from a longer run of 2000 ms are shown at bottom right at 45-degree intervals.

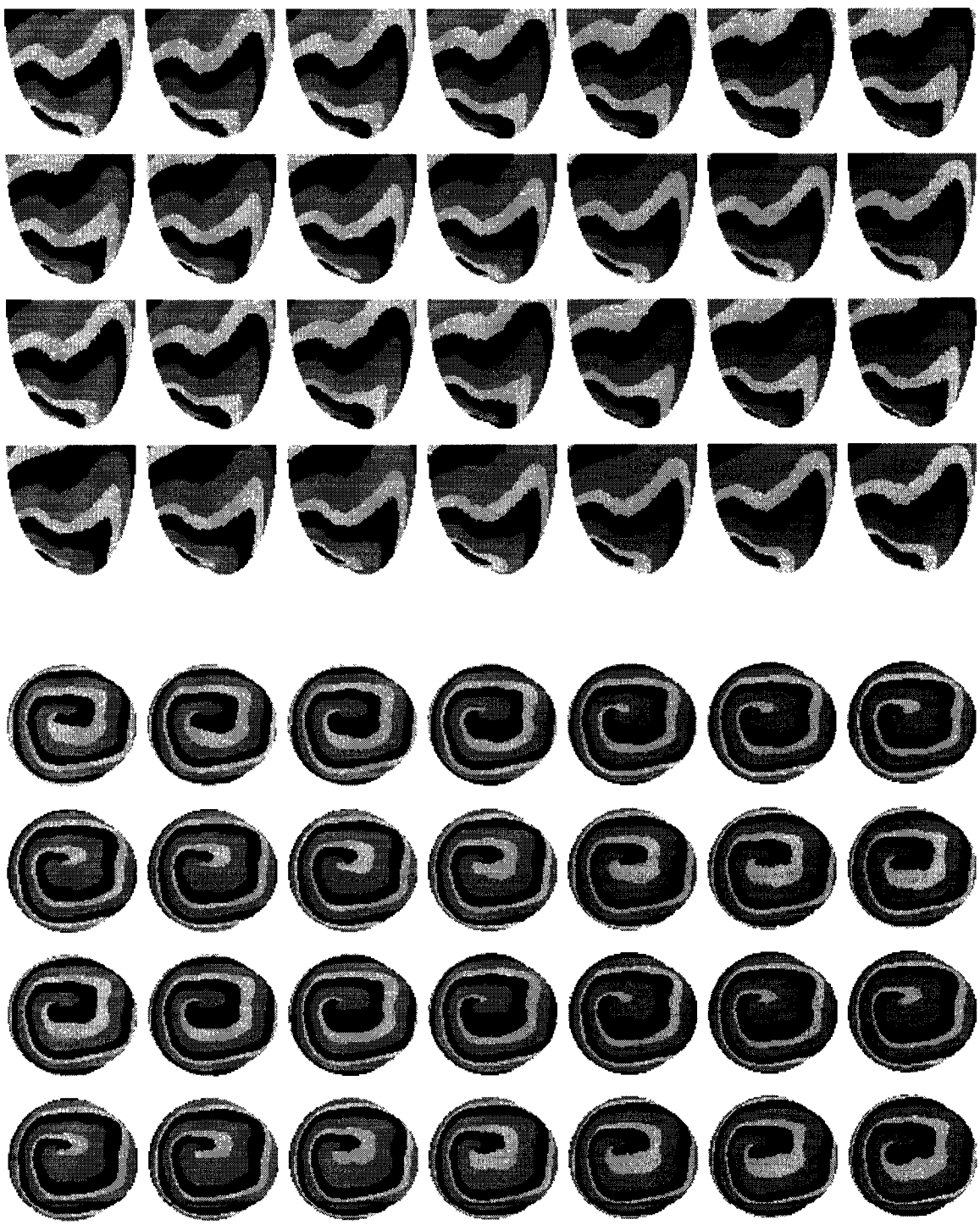

Figure 12.6. Anterior and apical epicardial views of a solitary spiral wave reentrant VT rotating about a point at the epicardial apex.

Dessertenne reported observations in 1966 on a group of patients experiencing syncope associated with runs of VT lasting 5 to 15 seconds and spontaneously stopping, often to recur in multiple paroxysms [152]. It was noted that many of these patients had a prolonged QT interval and some degree of atrio-ventricular block. VT appeared to occur either with a ventricular premature beat followed by a long coupling interval, or with ventricular bigeminy. The recorded electrocardiograms exhibited a unique form of VT, characterized by apparent twisting of the electrical axis of the peaks around an imaginary isoelectric line. Dessertenne called this rhythm "torsades de pointes" (TdP), or twisting of the points, a term which was formally adopted in 1978 for this specific type of polymorphic ventricular tachycardia.

The pathogenesis of TdP is not well understood, and still subject to speculation [514]. Several mechanisms have been proposed including two separate ectopic foci with different frequencies [26], a slowly wandering reentrant circuit [209], and a series of repetitive afterdepolarizations [12]. All of these mechanisms are plausible. TdP was originally believed to be caused by two competing ectopic foci with different periods that alternately control rate [462]. Accordingly, the ECG would be expected to have a fluctuating amplitude, with a beat frequency equal to the difference between the ectopic frequencies. D'Alnoncourt tested this theory in isolated porcine hearts by pacing the LV and RV simultaneously at different frequencies [112]. An ECG resembling TdP was indeed obtained, but only if the stimulation frequency of one site was continuously varied sinusoidally. Malik and Camm also found, in their simple computer model of two competing ectopic foci, that the imposed frequency had to be varied with time in order to obtain such a pattern [332].

12.3 Ventricular Fibrillation

Experimental mapping studies show ventricular fibrillation (VF) to be consistent with multiple reentrant circuits [69, 306], presumed to be analogous to vortex filaments seen in chemical media [542] and computer simulation [164, 409], although mapping limitations have so far prevented direct visualization of these three-dimensional structures

in actual myocardium. Despite VF appearing to have a degree of underlying organization [29, 113, 210], reentrant circuits, or surface rotors, are rarely seen clearly in mapping studies of three-dimensional myocardium [218, 421, 423], due to meander and complexity of epicardial break-through patterns. Rotors cannot usually be followed beyond one or two rotations. Gray et al. [210] found that less than one fifth of phase singularities could be followed for even one complete rotation. Up to 10 rotations have been observed after chemical ablation of the subendocardial layer [69], which produces a functionally two-dimensional medium. Rogers et al. were able to track one rare reentrant circuit around 18 rotations in a pig heart [423]. The actual number of reentrant circuits in VF is not clear. Gray et al. demonstrated that a single meandering rotor, rather than many, can give rise to an irregular ECG of VF. Extra frequency components in the ECG appeared to be due to a Doppler effect arising from meander. This finding argued against the hypothesis of Winfree that a critical thickness of myocardium was necessary to produce VF [545].

VF can be established in the computer model by the two-stimulus protocol [543]. Figure 12.7(a) shows an initial S_1 stimulus delivered to the base of the right ventricle causing an action potential wave to pass across the heart. An S_2 shock is then delivered to the apex at time t = 460 ms, resulting in re-excitation of the refractory zone followed by formation of a pair of counter-rotating reentrant circuits, one of which is seen in the anterior view. The induced spiral waves are unstable for the assigned SHV parameter set, and break-up into VF occurs after one or two rotations. This mechanism of VF-induction in the canine heart was first demonstrated by Chen et al., who confirmed that scroll waves could be induced in normal hearts [75, 453]. Other studies have also induced reentry by this mechanism [23]. Intramural reentry can be seen on close examination of the model simulation in Figure 12.7(c).

Figure 12.7(d) shows the anterior epicardial views of VF activity, filtered to show only the action potential upstrokes (activation) wave fronts. These highly dynamic patterns are very similar to those measured by Witkowski et al. using voltage-sensitive optical dyes [550], which they displayed in colour as voltage derivatives rather than as absolute

voltages. The close correspondence between their images and the simulations shown here probably constitute the best available validation of the model with experimental maps. Spiral wave segments can be followed between the time frames shown, but it is difficult to track the survival of any given reentrant circuit beyond a few rotations, due to dynamic complexity and core meander, consistent with reports based on epicardial maps [423, 453]. Since the wave fronts are scroll waves rotating around filaments in three-dimensions, epicardial break-through can falsely appear to be focal, as seen in frame 14 of Figure 12.7(d) where two rings appear on the surface, originating from wave propagation inside the wall, and subsequently radiate outward. Epicardial focal patterns such as these are sometimes seen during VF [69, 550], giving the appearance of ectopic activation. It is also interesting to note that the effect of fibre anisotropy on preferred direction of conduction can be seen in these epicardial images, in both anterior and apical views. This correspondence has been demonstrated in mapping studies [423].

Table 12.1 gives a summary of ECG frequency characteristics of VF measured in a number of studies from the literature. There is considerable variability of dominant frequency (FrD), depending on species and elapsed time. This literature survey was done to see if there was a tendency for VF to have specific values of FrD that would be useful for model validation. As can be seen, however, there is no such gold standard. This further highlights the need to understand conceptually, or theoretically, why VF can have such a broad range of characteristics.

Many simulations of VF have been carried out using the anisotropic SHV-biventricular model under different parameter sets. For the purposes of foregoing discussion, we will define six subtypes of VF obtained by varying g_{Na}, g_{Ca}, g_K, g_X, τ_u, and V_{uo}. The chosen parameters are summarized in Table 12.2. The latter two parameters control the intercept and time constant, respectively, of the APD restitution curve, as was illustrated previously in Figure 8.12. Examples of anterior epicardial maps of VF are shown in Figure 12.8, along with definitions of nomenclature for each case. The three-letter code for each case is based initially on subjective appearance, but will be formalized later.

Figure 12.7(a). VF can be induced in the model by delivering a stimulus to the RV base (not shown). As the repolarization tail passes across the heart, a shock is applied to the apex, as shown in the third frame from left in the top row. A phase singularity is established, around which a spiral wave develops. In this case, the wave almost blocks on its tail on the first rotation, but barely manages to continue rolling up. Conditions for this case result in wave instability, causing break-up into complex VF.

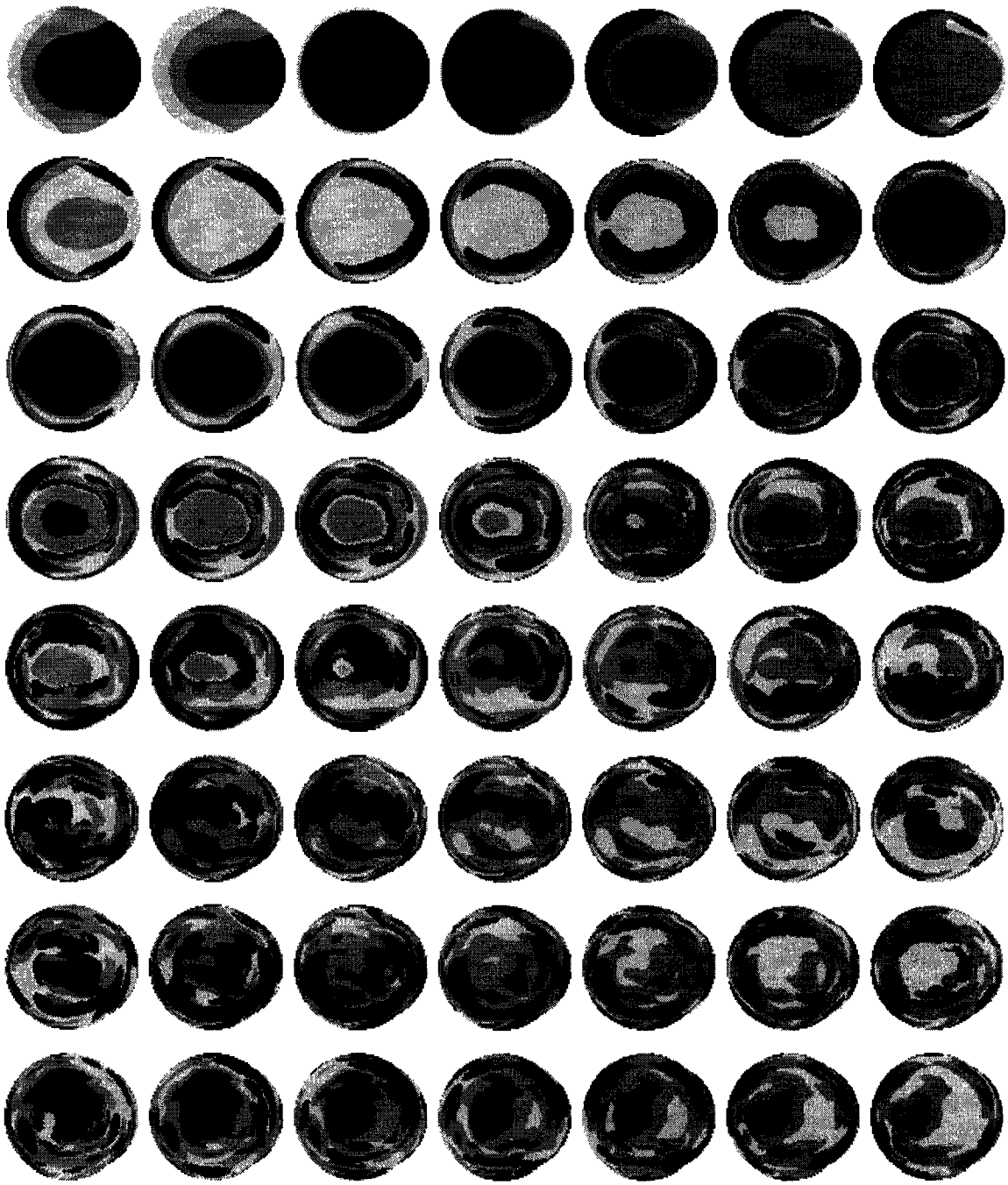

Figure 12.7(b). Apical views of the same case as above. The apical shock is applied in the third frame from left in the top row, resulting in two counter-rotating spiral waves located on each side of the heart. These waves are unstable, and subsequently degenerate to VF.

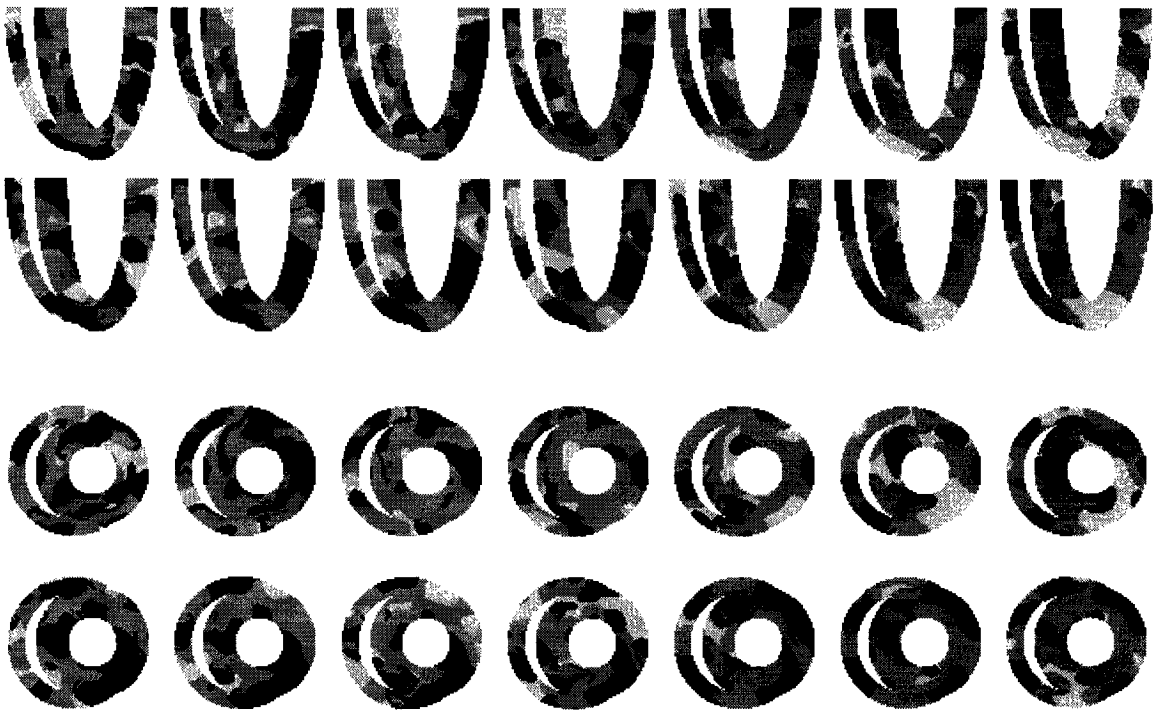

Figure 12.7(c). Frontal (top) and transverse (bottom) sections through the heart during the above case of VF. It is possible to discern regions of reentry within the ventricular wall.

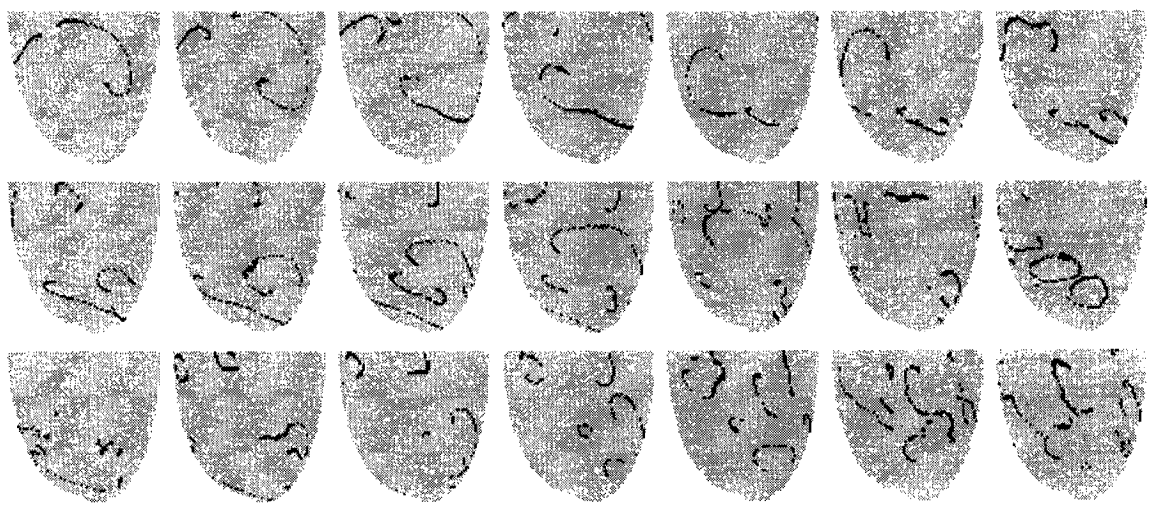

Figure 12.7 (d). Anterior epicardial views of the same VF case filtered to show only the leading edge of activation wave fronts. Spiral waves can be seen to merge and break. Regions of epicardial breakthrough, with radiating rings, can be seen in frame 14. These dynamics resemble those seen in experimental mapping studies using optical dyes [550].

Table 12.1 Experimental VF Frequency Characteristics

Freq (Hz)	Species	Reference
7 - 11	dog	[392]
9 - 14	dog	[419]
5 - 14	dog	[200]
9 - 11	dog	[58]
6 - 8	dog	[251]
7 - 10	rabbit	[208]
12 - 16	rabbit	[81]
14 - 17	rabbit	[440]
14 - 17	rabbit	[82]
7 - 10	rabbit	[253]
5 - 9	sheep	[569]
13 - 14	mouse	[494]
7 - 10	swine	[56]
12 - 14	swine	[337]
3 - 6	human	[48]
12 - 15	human	[49] Immediate
7 - 9	human	[49] After 1 minute
3 - 7	human	[358]
4 - 6	human	[89]

Table 12.2. Cell Parameters for Model Test Cases

Case	g_{Na}	g_{Ca}	g_K^*	g_X	g_{to}	V_{uo}	τ_u
1	8.0	0.02	0.80 - 0.85*	0.20	0.1 - 1.0*	25	400
2	13.0	0.06	1.30 - 1.50	1.00	0.0	75	80
3	13.0	0.06	1.30 - 1.50	1.00	0.0	75	40
4	13.0	0.02	1.30 - 1.50	1.00	0.0	75	400
5	8.0	0.02	0.80 - 0.85	0.20	0.1 - 1.0	25	400
6	13.0	0.08	0.80 - 0.85	0.20	0.0	75	50

* denotes gradient across ventricular wall

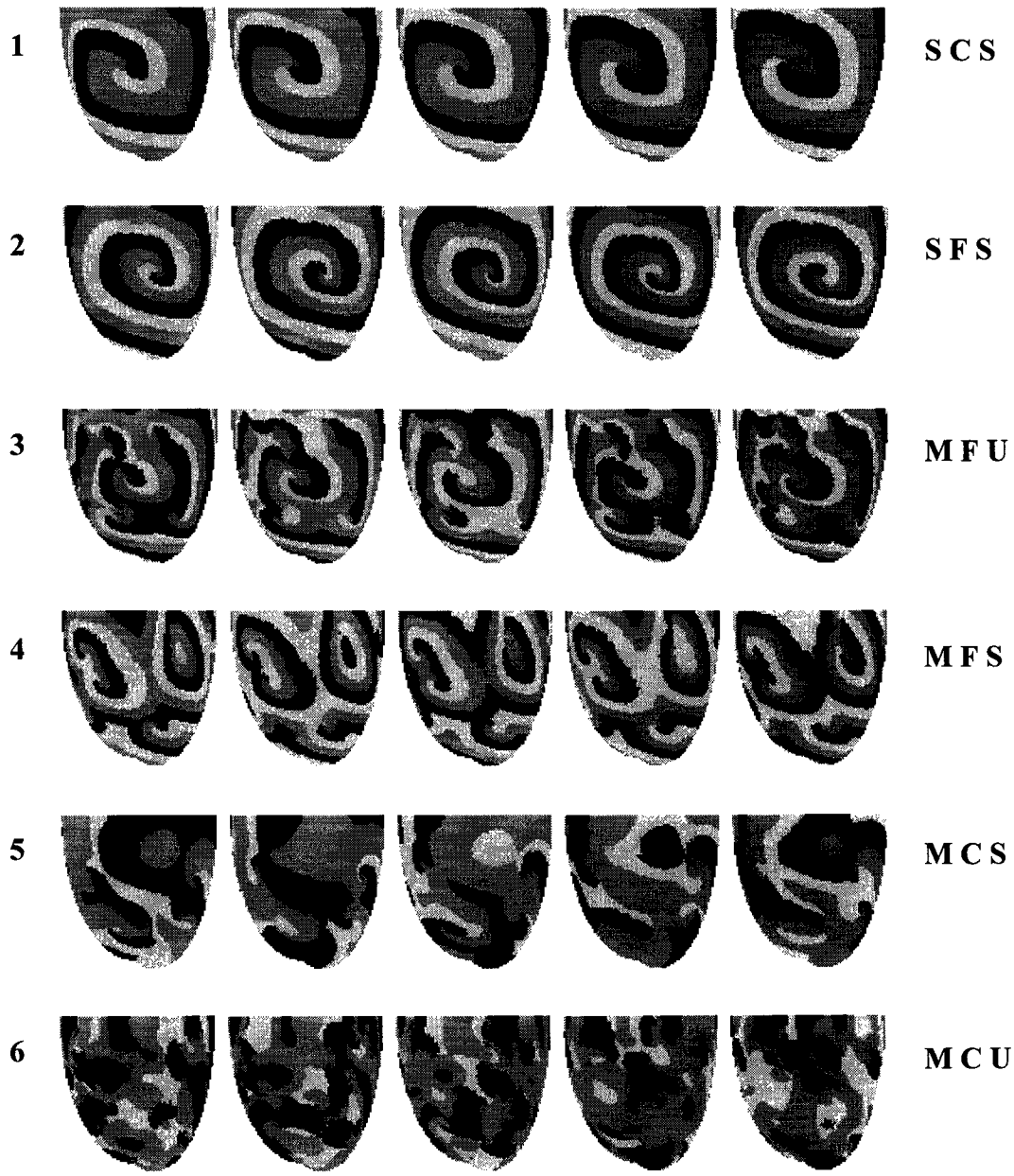

Figure 12.8. Comparison of six subtypes of VF. The classification is based on the three-component nomenclature shown at right: the first letter indicates the number of reentrant circuits: S = solitary, M = multiple. The second letter indicates thickness or spatial size of waves: C = coarse, F = fine. The third letter indicates the spatiotemporal stability or relative repeatability of the pattern: S = stable, U = unstable. Reference numbers for each case are shown at left.

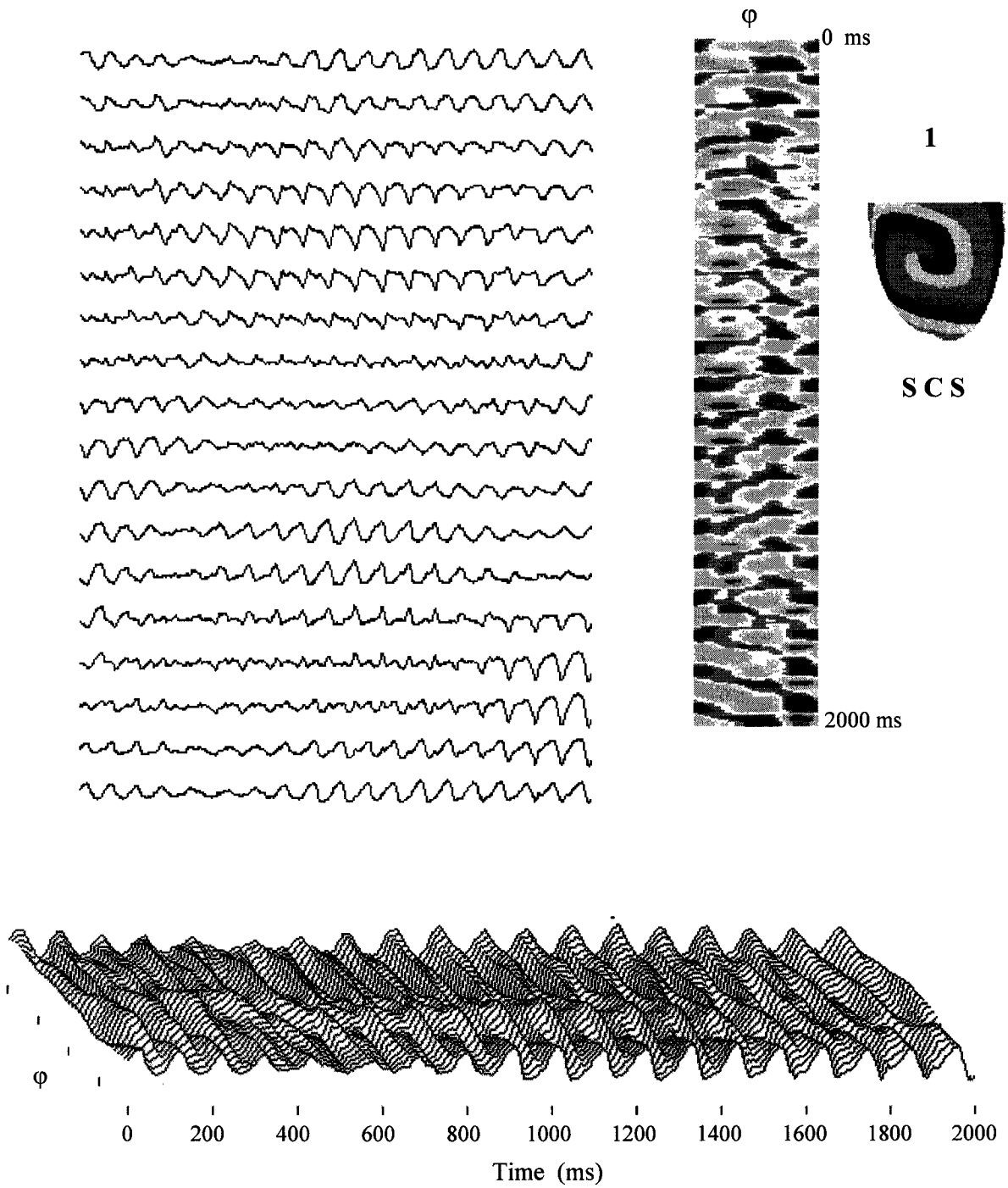

Figure 12.9(a). Body surface ECGs of 2000-ms activity for VF type SCS (case 1). Leads are shown at 20-degree intervals around the equator at upper left, and on a contour surface at bottom. The space-time plot V(φ, t) of 36 leads, at 10-degree intervals around the body surface sphere, is shown at upper right. Dark shades represent highest positive or negative voltages.

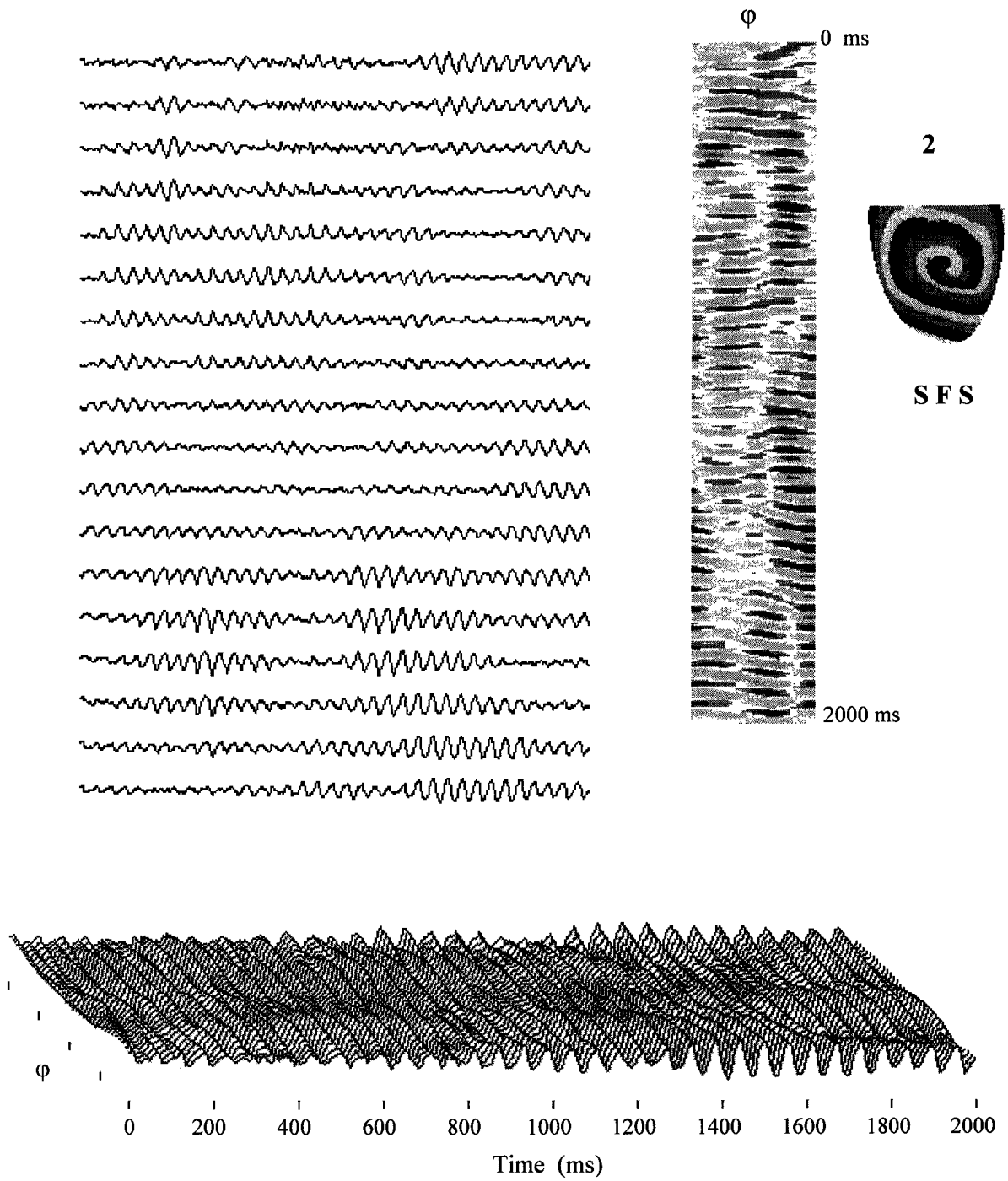

Figure 12.9(b). Body surface ECGs of 2000-ms activity for VF type SFS (case 2).

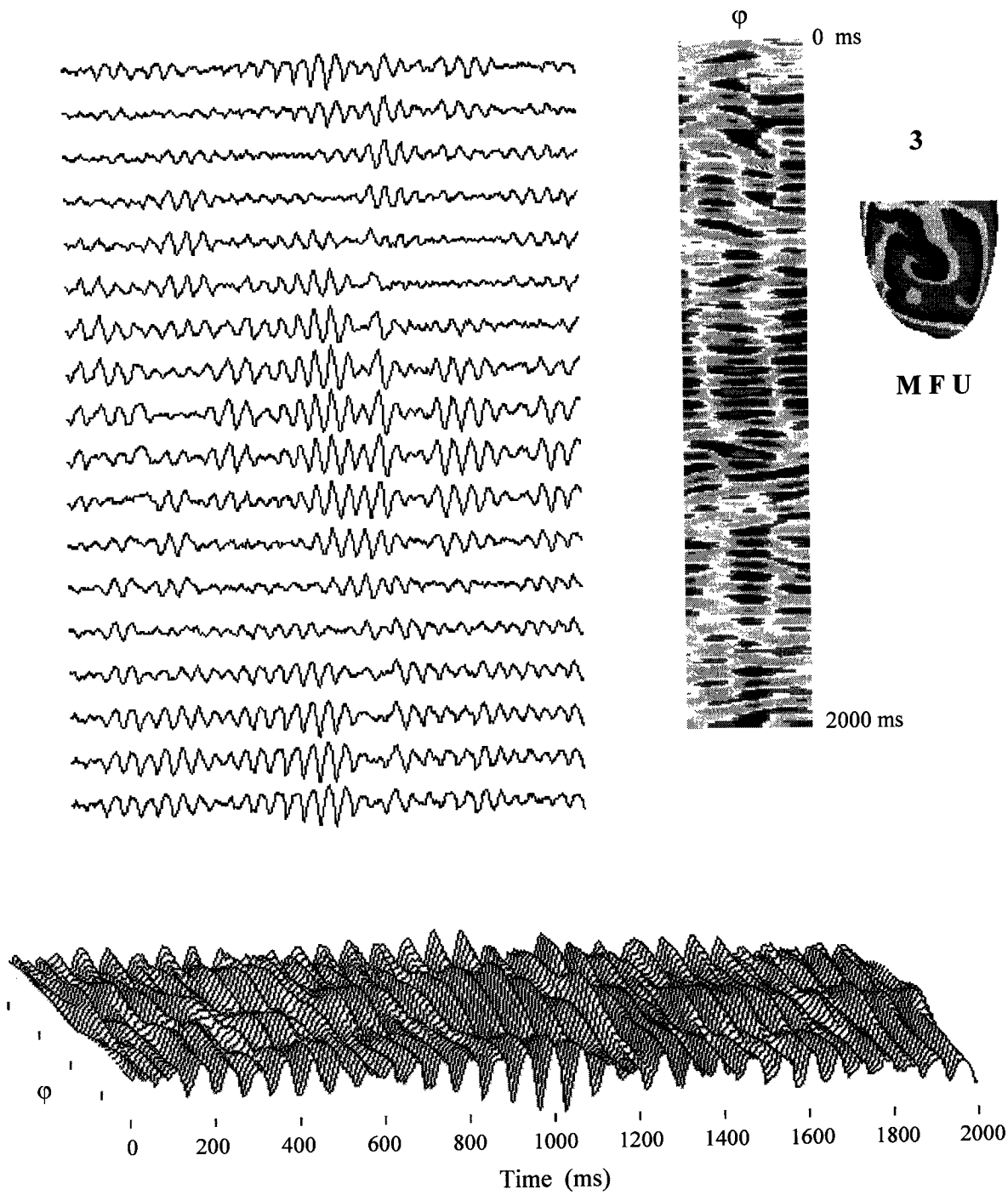

Figure 12.9(c). Body surface ECGs of 2000-ms activity for VF type MFU (case 3).

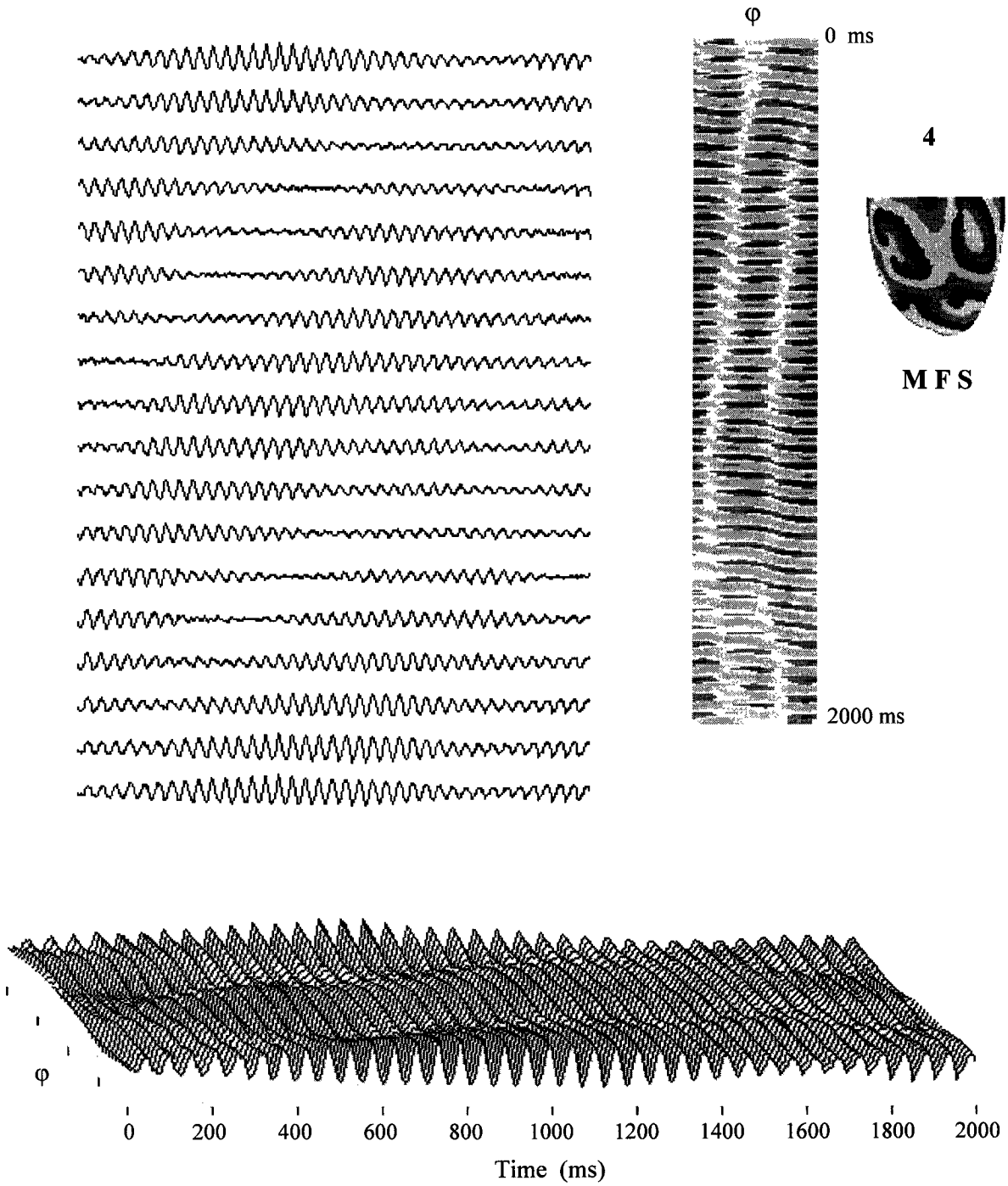

Figure 12.9(d). Body surface ECGs of 2000-ms activity for VF type MFS (case 4).

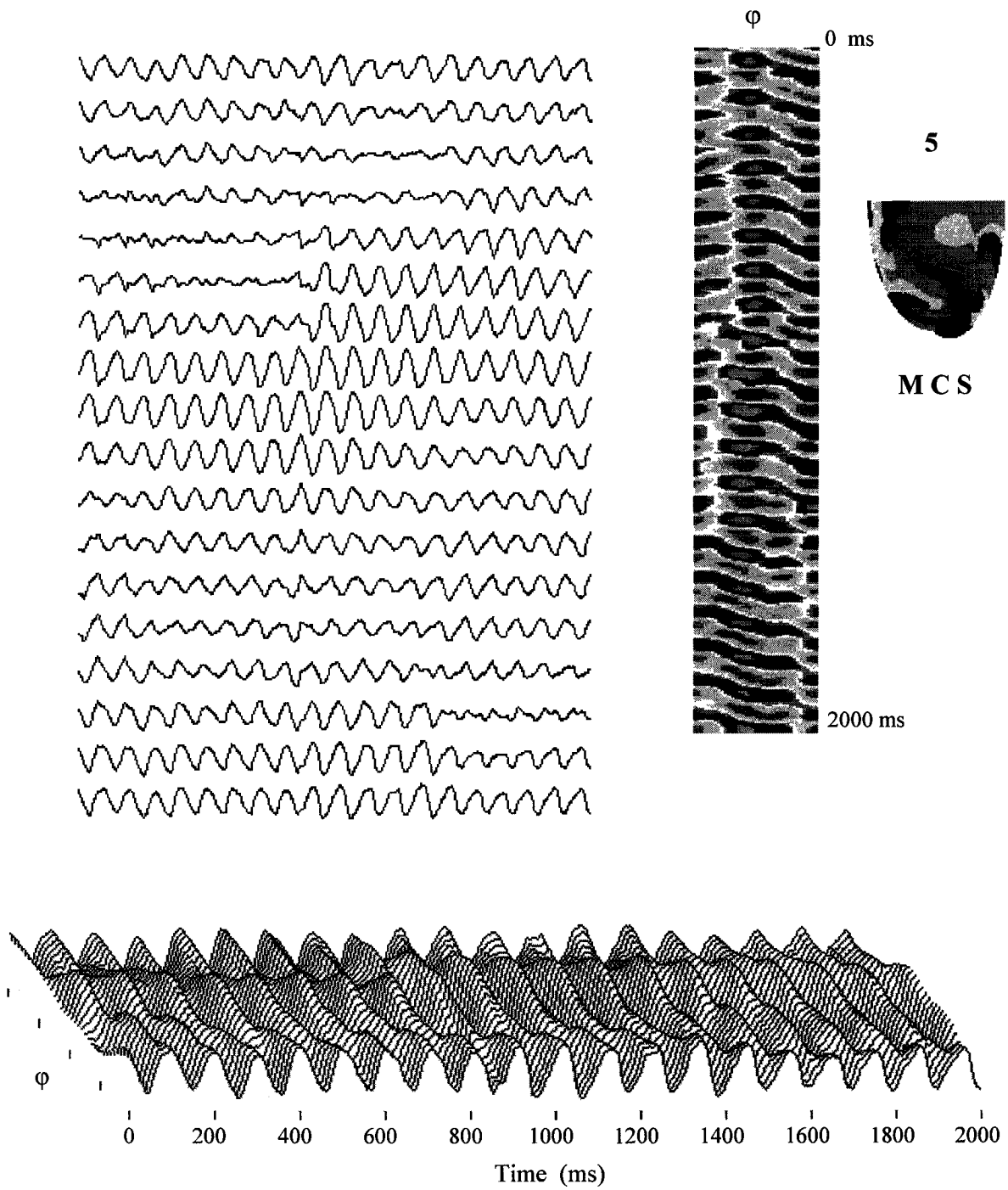

Figure 12.9(e). Body surface ECGs of 2000-ms activity for VF type MCS (case 5).

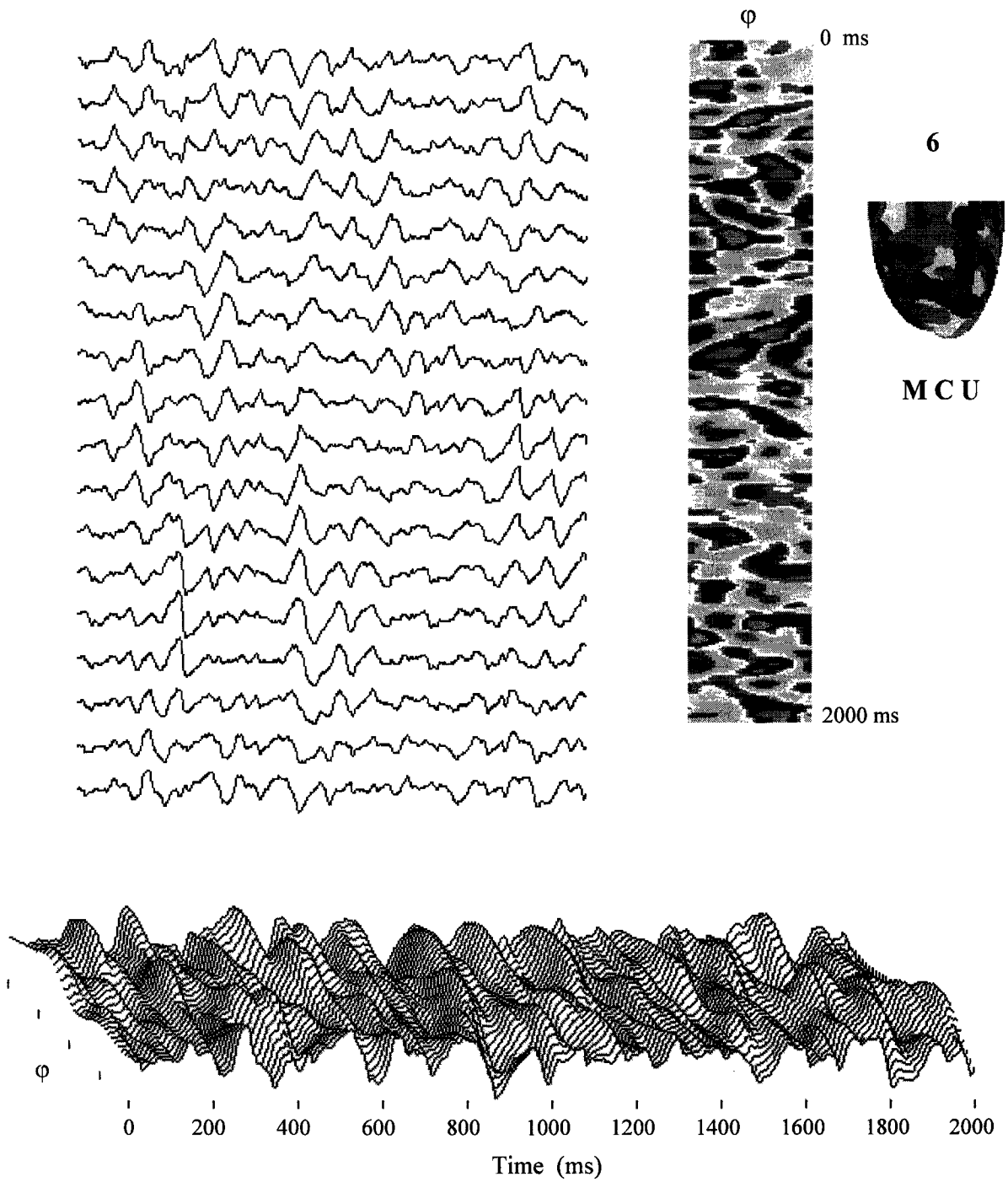

Figure 12.9(f). Body surface ECGs of 2000-ms activity for VF type MCU (case 6).

Figure 12.9 shows the electrocardiograms for each of the six cases. Individual leads are shown at 20° intervals around the heart equator for 2000 ms of activity. The same data is also shown as contour plots along the bottom, and vertically as space-time plots at higher resolution, where dark shades are higher body surface voltages. The differences in ECG characteristics between these six cases are obvious. It is interesting to refer back to the actual VF subtypes measured in the patient of Figure 1.5 to see that we now have a powerful tool to study the spatiotemporal structure of VF in three-dimensions, and the resultant ECG signals.

Figure 12.10 compares space-time plots of epicardial activity against the corresponding body surface ECG maps. Epicardial maps V(i) are generated by monitoring a horizontal aperture of the anterior surface at the heart equator. It is immediately apparent that complexity of epicardial activity is similar to complexity of the ECG patterns, although mathematical tools are needed to formally quantify these patterns. A few examples of epicardial space-time plots, obtained using voltage-sensitive dyes, have been reported in the literature [419, 550].

Frequency spectra of these cases calculated for all 36 leads, both individually and averaged, are shown in Figure 12.11. Case 1 has the lowest FrD of about 7 Hz, while case 4 is highest at about 14 Hz. This range is consistent with that in Table 12.1. Most cases have a relatively fixed and periodic epicardial pattern, which gives rise to distinct spatial peaks in the frequency spectra, the highly dynamic case 6 being the notable exception. The "stable" cases (1, 2, 4, 5), with a third letter S, are narrow-banded, while the "unstable" cases (3, 6) are broad-banded. Case 5 has the largest characteristic epicardial wave size, which is associated with spectral energy peaks of highest amplitude.

Figure 12.12 shows event histograms of DI, APD, and CL for each VF case. The APD restitution curves are shown at right, along with the p(DI) histogram. The dot cluster above shows that each APD is not determined exactly from the restitution curve, but deviates somewhat, likely due to electrotonic load from neighbouring cells that shorten or prolong APD, especially in regions of high wave front or tail curvature. The three

"coarse" cases (1, 5, 6) have relatively wide histograms and long mean APD, while "fine" cases (2, 3, 4) are narrow with short mean APD. The cycle lengths are largely determined by APD, which in turn determine the dominant frequency. There appears to be good correlation between 1/FrD and peak CL for experimental VT and VF [81, 440]. The "fine" cases have relatively high dominant frequency FrD > 10 Hz, while the coarse cases have lower dominant frequency FrD < 10 Hz. These statistical measures are summarized in Table 12.3. Entropies for DI, APD, and CL are calculated using the Boltzmann equation (4.5), and are highest for "coarse" cases having the widest distributions. It is noteworthy that these dynamical statistics cannot distinguish between cases with solitary (S) and multiple (M) reentrant circuits having similar control parameters. For example, SCS (case 1) is statistically similar to MCS (case 5), and SFS (case 2) is similar to MFS (case 4).

Action potentials sampled at an epicardial cell are shown in Figure 12.13 for each VF subtype. Case 6 exhibits the most irregular CL and APD. Although it has been suggested that cells fire in VF as soon as they become excitable [484], such that there is virtually no diastolic interval and CL is equal to ERP, most studies show the existence of a significant excitable gap (EG), ranging from means of 20% [6, 69, 397] to 50% [116]. Figure 12.14 shows changes in the excitable gap fraction for VF cases 1 and 6. The large excitable gaps in these simulations range from about 20% to 40%, consistent with the above studies. Tables 12.4 and 12.5 show that case 6 has both the smallest EG of 21%, and the steepest restitution slope of 2.13, resulting in the most vigorous wave-break and greatest variability in EG. This high level of activity is also reflected in the largest relative volume of wave front at 3.48%, suggesting that this case has the greatest total length of vortex filament. Characteristic wave size is related to the volume of activated cells divided by the surface area of the wave front, and is calculated as L = (100 – EG) / WF, where EG is the percent of excitable gap, and WF is the number of cells on the wave front. Case 1 has the largest relative wave size, while case 6 has the smallest, consistent with subjective estimates by visual inspection of Figure 12.8. The correlation between the reciprocal of the ECG dominant frequency 1/FrD and the mean cycle length CL is very good, as shown in Figure 12.15, consistent with experimental findings [81, 440]

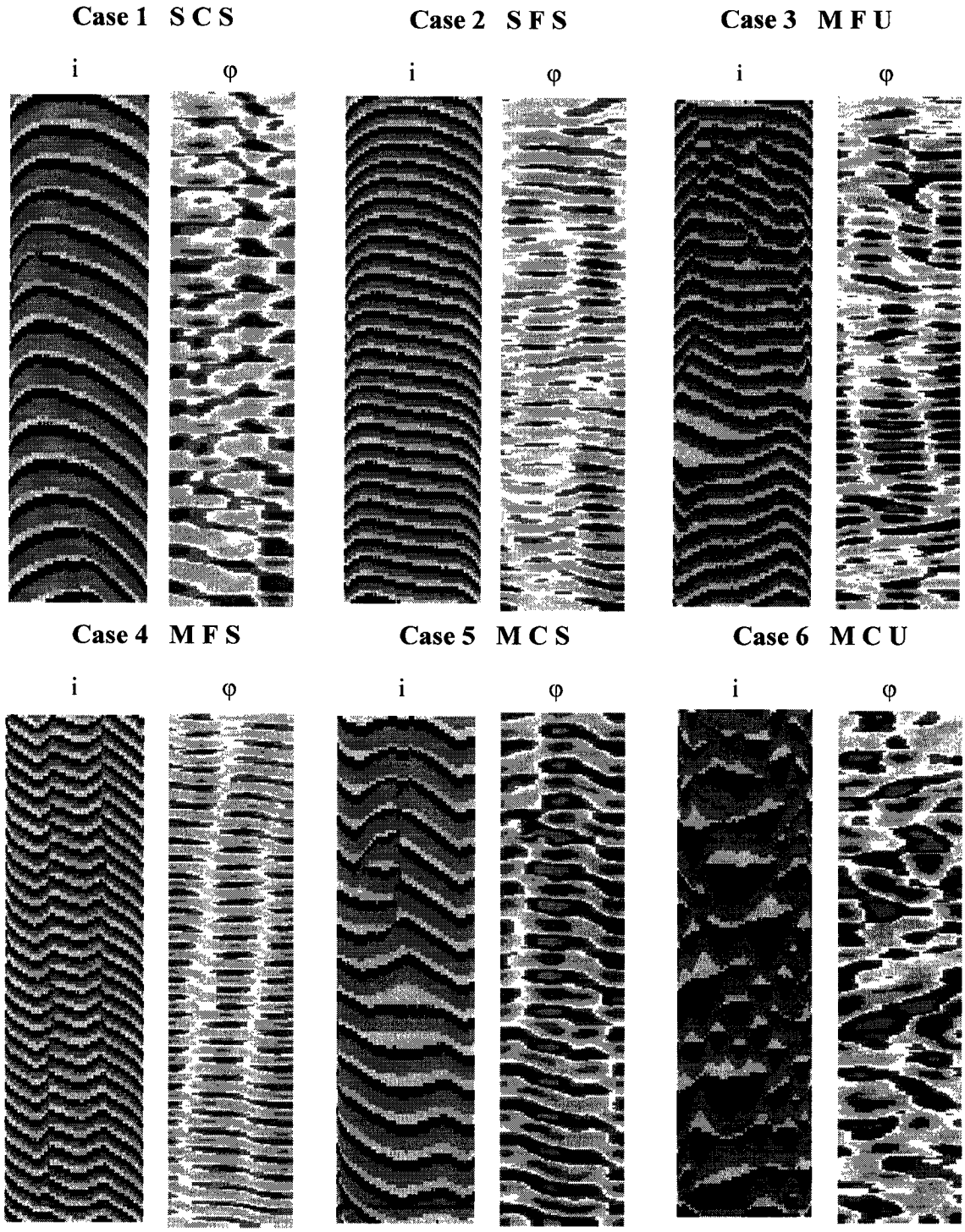

Figure 12.10. Correspondence between epicardial space time plots V(i, t) at left, and the body surface equatorial ECGs V(φ, t) at right, for each of the six cases of VF patterns. The qualitative complexity of ECG patterns is similar to the complexity of the epicardial patterns. Epicardial plots are produced from a horizontal slice of the anterior surface. ECG plots are circumferential around the body sphere equator. The time span is 1500 ms.

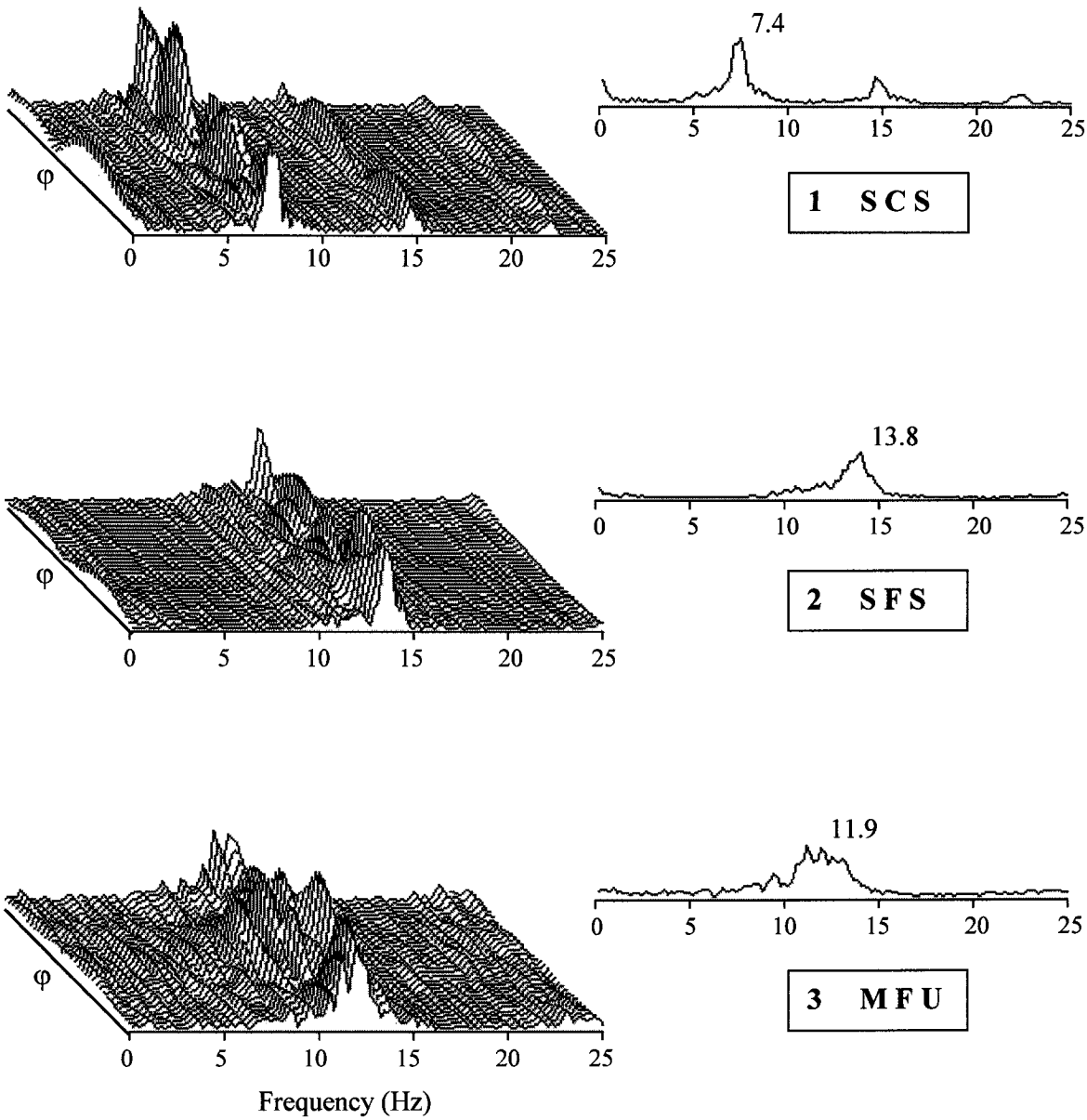

Figure 12.11(a). Frequency spectra of VF ECG amplitudes, measured at the 36 equatorial sites φ at 10-degree intervals, for cases 1 to 3. Individual leads are shown at left, and the mean of all leads is shown at right.

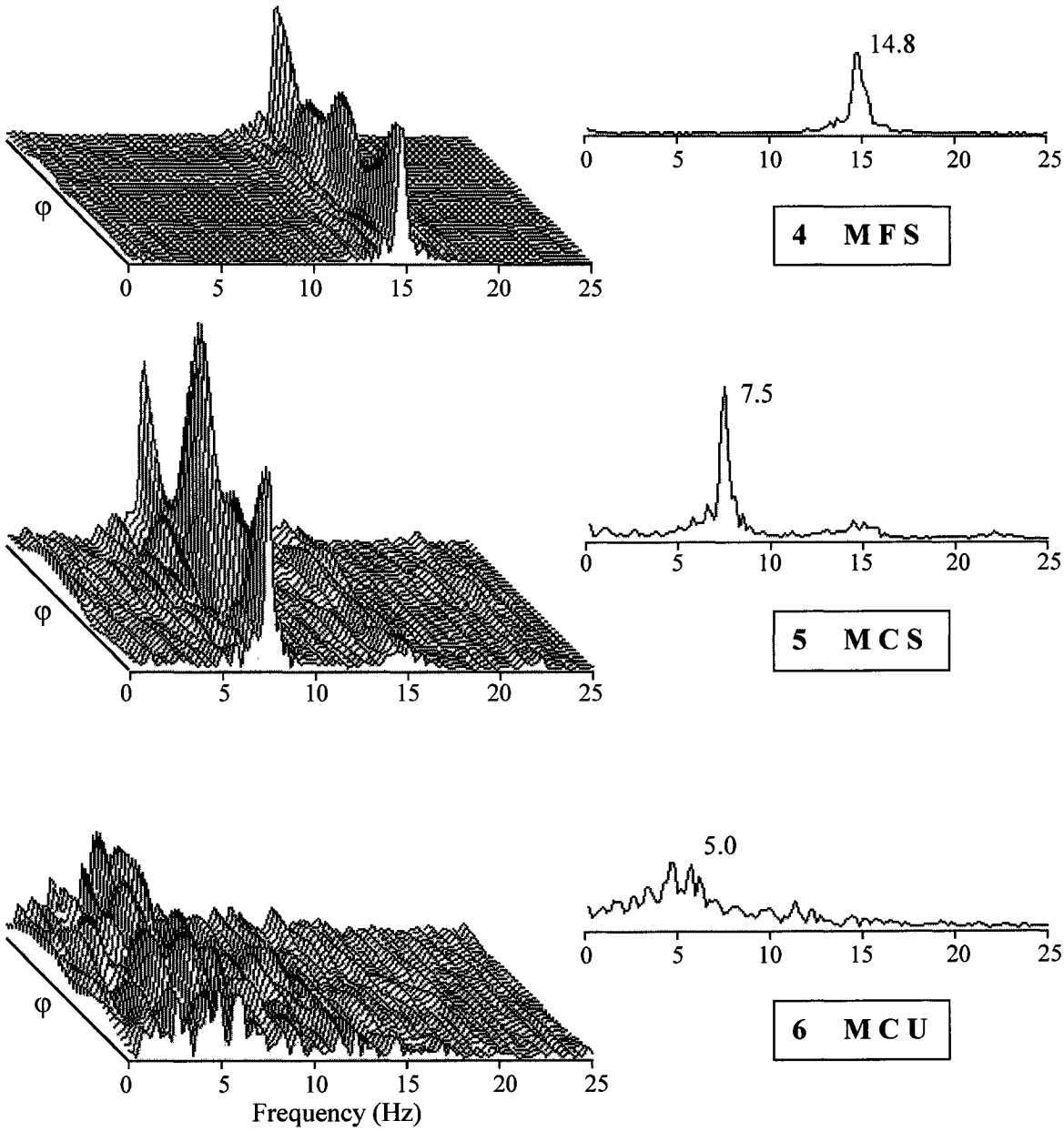

Figure 12.11(b). Frequency spectra of VF ECG amplitudes for cases 4 to 6.

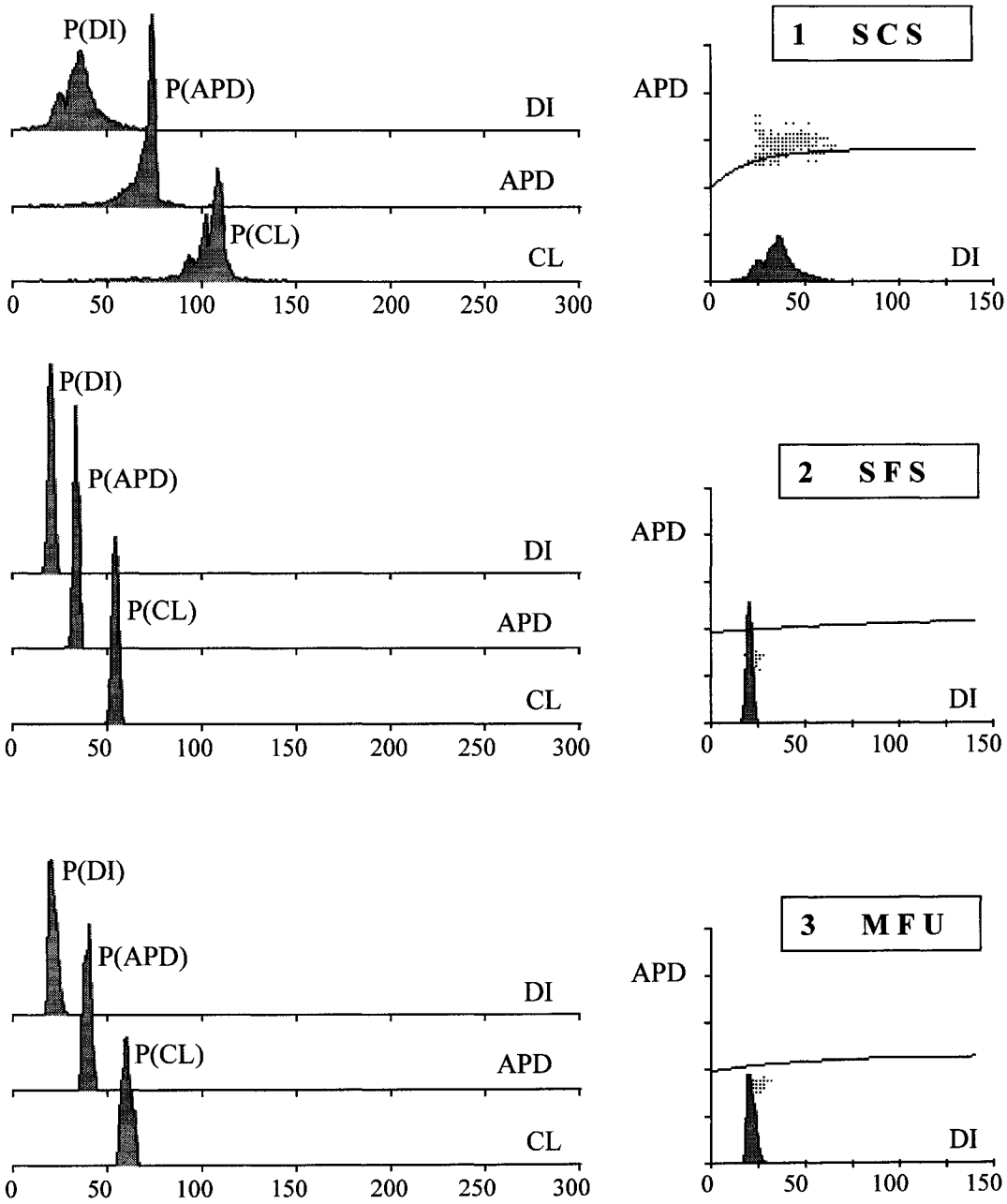

Figure 12.12(a). Event histograms for DI, APD, and CL for different cases of VF. A transmural section of the ventricular wall was monitored for 800 ms to generated these statistics. The APD restitution curve is calculated for a single epicardial SHV cell with the same cell parameters used in the three-dimensional simulation. The DI histogram p(DI) determines the APD distribution. Units are milliseconds. The dot cluster shows sampled events; departures from the curve are likely due to electrotonic interactions in three dimensions.

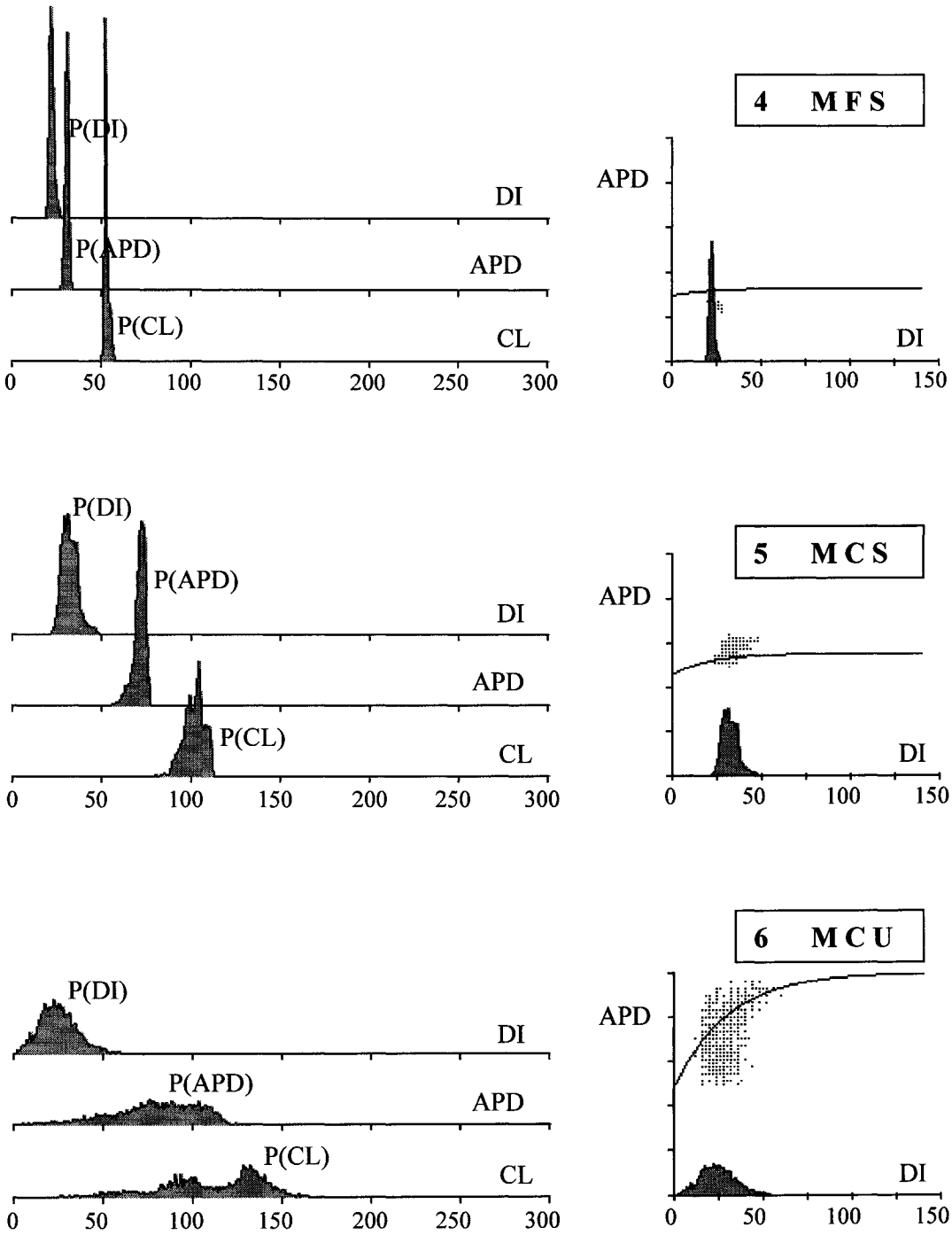

Figure 12.12(b). Event histograms for DI, APD, and CL for each case of VF.

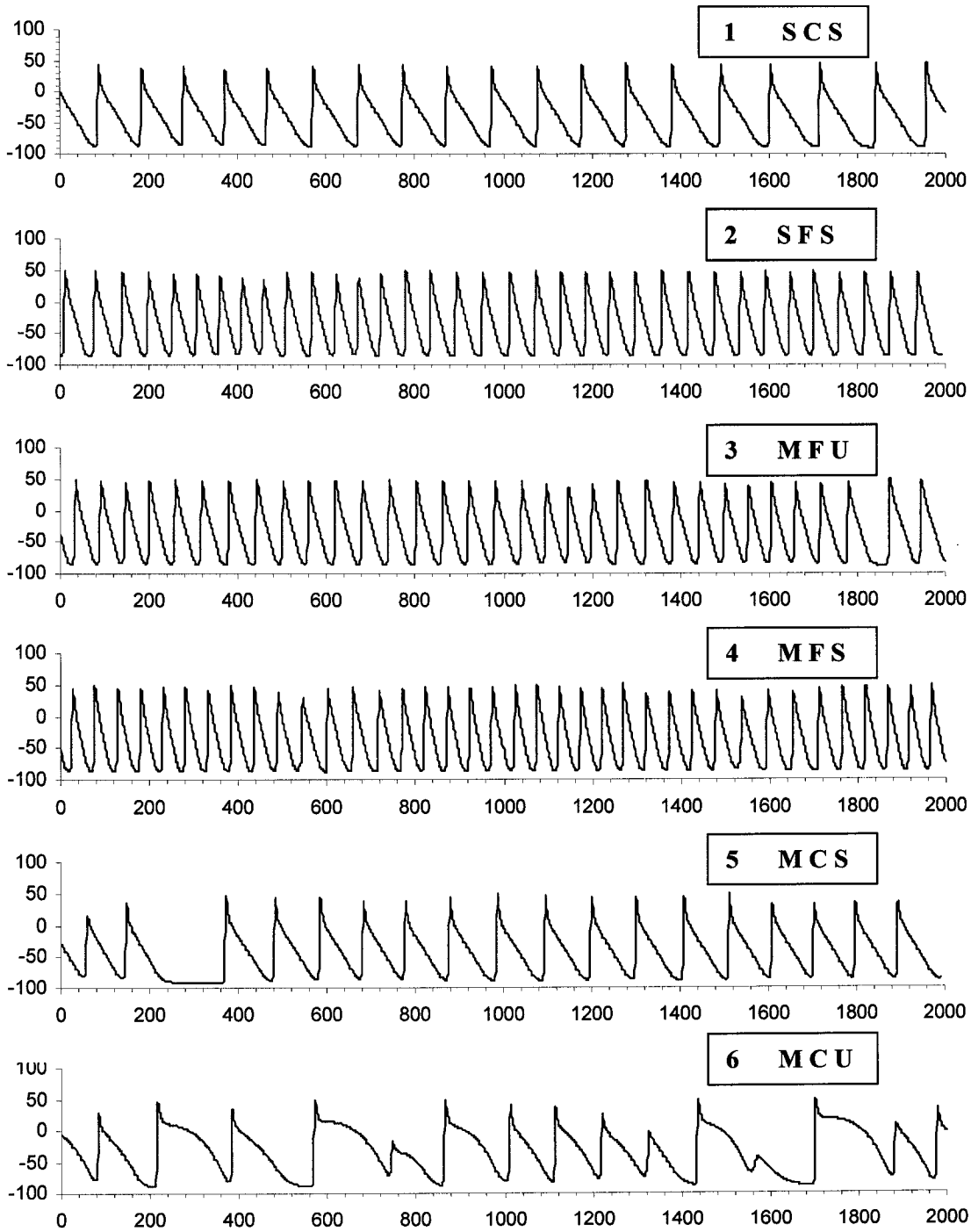

Figure 12.13. Epicardial action potentials V(t) for each of the six VF cases. The cases of fine VF (2, 3, 4) have relatively short APDs, while the cases of coarse VF (1, 5, 6) have longer APDs. The action potential trains are most regular for the stable cases (1, 2, 4, 5), while unstable coarse VF (case 6) has the most irregular APD history.

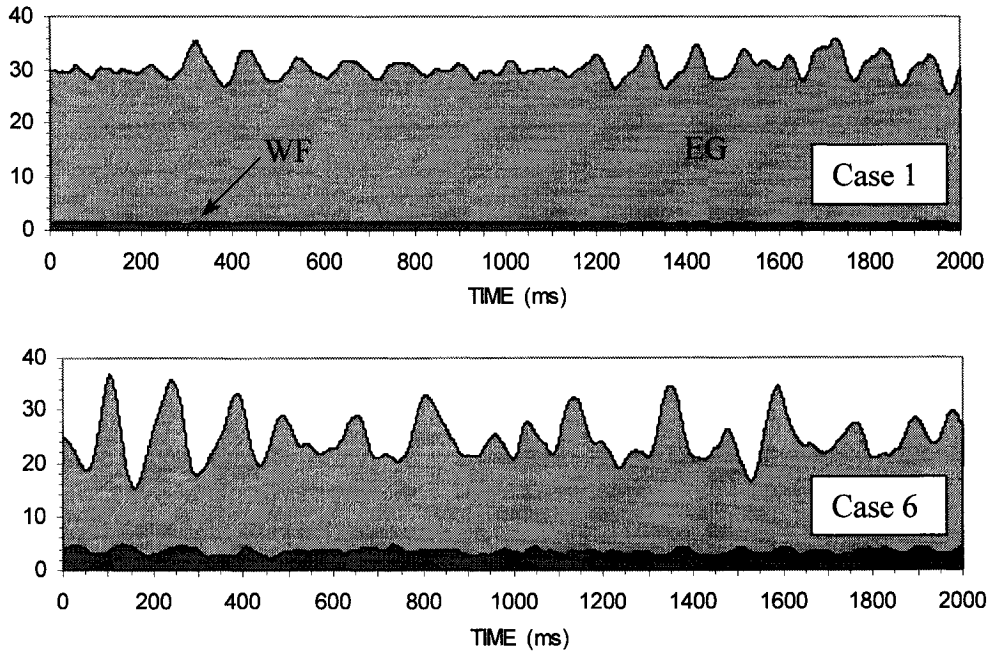

Figure 12.14. Fluctuations in the volume of the excitable gap (grey) and wave front (black) for cases 1 and 6. Case 6 has both largest relative volume of wave front and the greatest variability, suggesting the greatest total length of scroll wave filament. Case 1 has the smallest excitable gap, and consequently the largest spatial scale of waves.

Table 12.3. Statistical Measures of VF Test Cases

Case	DI	APD	CL
1 SCS	35.1 (9.6) *3.62*	68.4 (10.5) *3.22*	102.0 (14.1) *3.59*
2 SFS	20.2 (1.4) *1.77*	33.4 (1.3) *1.68*	54.0 (1.6) *1.87*
3 MFU	21.1 (2.1) *2.08*	39.0 (1.8) *1.96*	60.0 (2.5) *2.72*
4 MFS	22.0 (1.3) *1.60*	30.5 (1.0) *1.38*	52.7 (1.2) *1.35*
5 MCS	32.1 (4.5) *2.85*	70.9 (3.4) *2.49*	101.4 (5.6) *3.08*
6 MCU	24.7 (10.3) *3.72*	78.8 (23.8) *4.51*	109.4 (28.6) *4.62*

Mean values (ms), standard deviation in brackets, entropy in italics

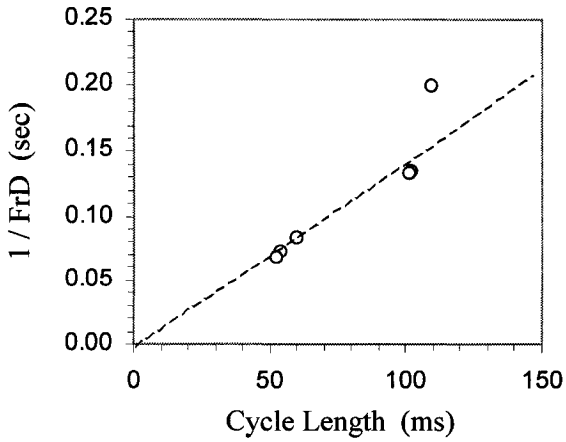

Figure 12.15. Mean cycle length (CL) is highly correlated with the reciprocal of ECG dominant frequency (FrD). The highest point, case 6, departs from the linear relationship because both the CL histogram and the frequency spectrum are most broad-banded, with a relatively indistinct dominant frequency.

Table 12.4. Spatial Statistics of VF Test Cases

Case	Wave Front [%]	Excitable Gap [%]	Wave Size
1 SCS	1.38 (.14)	28.98 (1.95)	51.28
2 SFS	2.01 (.14)	34.36 (1.07)	32.67
3 MFU	2.15 (.16)	33.44 (2.37)	30.90
4 MFS	1.96 (.13)	38.96 (2.11)	31.08
5 MCS	1.60 (.15)	28.49 (2.99)	44.59
6 MCU	3.48 (.55)	21.30 (4.32)	22.64

Mean values (%), standard deviation in brackets, dimensionless wave size

Table 12.5. Stability Measures From VF Test Cases

Case	Slope at DI=0	Lyap Exp
1 SCS	1.02	−1.76
2 SFS	0.08	−2.73
3 MFU	0.16	−2.25
4 MFS	0.20	−2.71
5 MCS	0.60	−2.11
6 MCU	2.47	+0.08

The Lyapunov exponent λ quantifies the degree of periodicity or chaos in a dynamic flow, as previously discussed. While it can be calculated for continuous dynamics using a relatively complex algorithm [553], λ is easier to calculate for a time series of discrete events using equation (4.9). We can replace the time series DI_i with its probability distribution p(DI), and use the slope of the restitution curve. A difficulty arises, however, because electrotonic load on the action potentials alter their durations, and APD can be perturbed off the restitution curve that would be obtained for a single isolated cell. This effect is seen in the dot clusters of Figure 12.12. We can approximate λ for the six VF cases as shown in Table 12.5. These values are calculated based on equation (4.9) using the distribution p(DI) and slope dAPD/dDI shown in Figure 12.12. The restitution curve slope is taken from the SHV model for a single cell without electrotonic load. Cases 1 and 6 have segments with slope $m > 1$, but only case 6 produces a positive Lyapunov exponent by this equation, because there is a sufficient number of reentry cycles that have a low enough DI to fall under the steepest part of the curve.

The subtypes of VF can be more formally quantified in the phase diagram of Figure 12.16, where the definitions of coarse and fine are based on ECG dominant frequency, and stability is defined in terms of the sign and magnitude of the Lyapunov exponent. Under this schema, case 3 is actually not considered unstable, because λ is negative. It is

also interesting that the dots for each case all appear to fall below a hyperbolic line that avoids the "fine unstable" subtype. While the *FU subtype is probably not forbidden, the achievement of fine unstable fibrillation requires both steep restitution and short APD, requiring a very short minimum APD at the intercept.

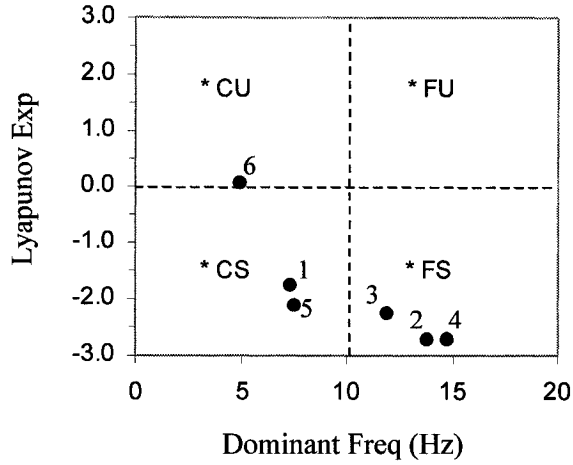

Figure 12.16. Phase diagram of VF subtypes based on ECG dominant frequency (FrD) and Lyapunov exponent λ calculated from p(DI). Each quadrant corresponds to the three-letter type-code. * denotes the first letter, either S (solitary reentry) or M (multiple reentry). C denotes "coarse" fibrillation for FrD < 10 Hz, and F denotes "fine" for FrD > 10 Hz. S denotes "stable" for negative λ, and U denotes "unstable" for positive λ. Each of the six VF subtypes discussed in this chapter are shown as labelled dots.

The subtypes of VF examined here were chosen to accentuate the specific characteristics discussed, without reference to physiological mechanisms responsible for their existence. Differences in VF characteristics in real hearts must arise from three main influences: underlying disease substrate, ischemia, and drug effects. The main dynamical variables, or model outcomes, are frequency and spatiotemporal complexity. Of the six cases discussed, case 6 (MCU) is probably closest to VF in a normal heart, since the parameter set in Table 12.2 is unaltered from the nominal SHV values in Table 8.2, except for shortening of the time constant τ_u to 50 ms to enhance instability. In the next chapter, we will use this case to investigate the role of various ionic channel manipulations to simulate drug effects on established VF, and look at the effects of defibrillating shocks.

Chapter 13

DRUGS AND DEFIBRILLATION

13.1 Drug Effects

Drugs remain the preferred therapy for VF prevention, due to their relative ease of use, and also serve as adjuncts for cardiac resuscitation [153]. There is mounting evidence, however, that many antiarrhythmic drugs in common use today are largely ineffective [500], and may be proarrhythmic [65, 365]. It has become clear that traditional concepts of antiarrhythmic drug actions are in need of critical re-examination. Theoretical models may be useful test-beds for new drugs, and may help define the essential properties that an ideal drug should possess. In this section, we will look at the effects of drugs in the model, in terms of how various ion channel manipulations alter the spatiotemporal characteristics of VF.

The period or cycle length of a reentrant circuit depends largely on conduction velocity and core size. Sodium channel blockade increases the critical radius of curvature [54], which forces increase of core size and prolongation of cycle length. Chorro et al. found that flecainide decreased conduction velocity and increased the functional refractory period, thereby increasing wavelength, or circuit size, and decreasing the dominant frequency (FrD) of VF [81]. Figure 13.1(a) shows VF case 6 described previously, with Figure 13.1(b) showing the effect on VF of reducing sodium conductance g_{Na} in the model from 13.0 to 6.0. Tables 13.1 to 13.3 summarize statistical measures. Wave size is

increased, likely due to slower conduction and a larger critical curvature. Wave front volume, related to vortex filament length, is significantly reduced, corresponding with an increase in the excitable gap. The longer mean diastolic interval shifts dynamics to the right along the restitution curve, such that the mean APD and cycle lengths are both slightly longer. This has the effect of reducing the dominant ECG frequency from 4.98 Hz to 3.74 Hz. Stability is relatively unchanged, as measured by the Lyapunov exponents, which remain weakly positive.

Chorro et al. found verapamil had little effect on conduction velocity, but shortened circuit length, and thereby increased the dominant frequency of VF [81]. Samie et al. [440], however, found that verapamil decreased the VF peak frequency in rabbit hearts, from 16.2 Hz to 13.5 Hz, as a consequence of the core area increasing from 4.5 to 9.2 mm^2. ERP was reduced by about 9%. Verapamil also decreased wave fractionation, and resulted in a 3-fold reduction of phase singularity (PS) density. Six PS on the anterior epicardium, of density 1.04 PS/cm^2, condensed to one solitary PS. Remarkably, all hearts in this study converted from VF to VT after 10 to 20 minutes, with dominant frequencies of 17.0 Hz and 11.6 Hz, respectively. Rapid stimulation induced monomorphic VT rather than VF in rabbit hearts exposed to verapamil [440].

Figure 13.1(c) shows the effect on VF of reducing calcium conductance g_{Ca} from 0.08 to 0.04, as would occur in the presence of verapamil. Epicardial waves clearly become more coherent with fewer surface rotors, as reflected by the larger characteristic wave size and much smaller wave front volume. Mean DI and mean CL are both longer, yet the dominant frequency of the ECG is not significantly different, changing from 4.98 Hz to 5.08 Hz, although the spectral peak is much more narrow. Despite its apparent anti-fibrillation properties, however, verapamil is probably not an appropriate drug for VF treatment, due to its negative inotropic effect.

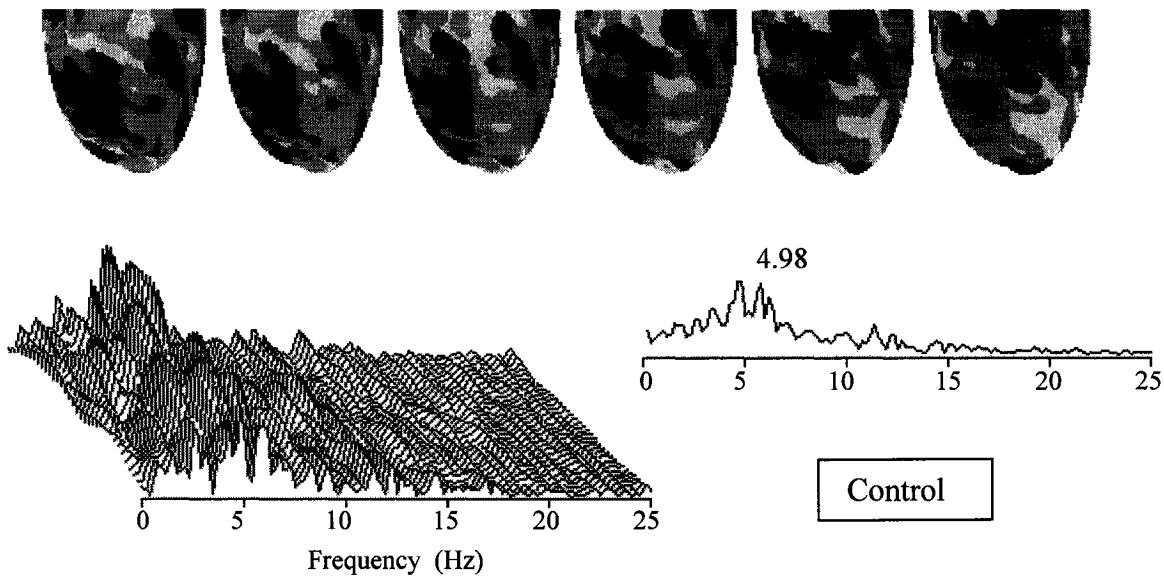

Figure 13.1(a) Drug effects are simulated in the model by partially blocking various ion channels. Case 6 VF, previously discussed and shown here, is used as a baseline control.

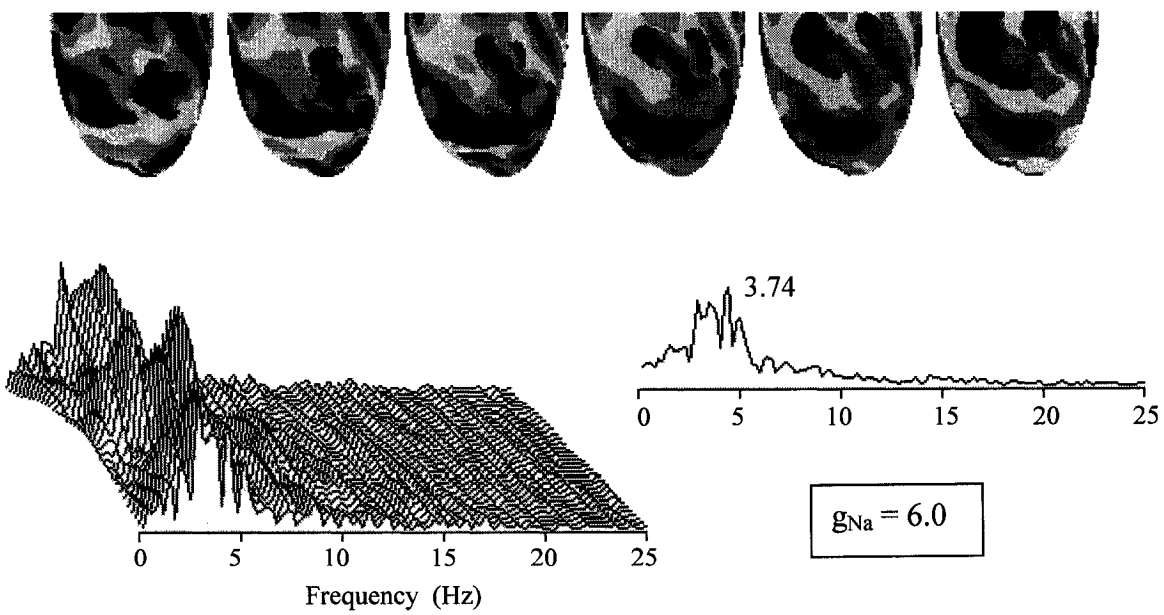

Figure 13.1(b) Effect of reduced sodium conductance g_{Na} = 6.0 on epicardial map and ECG frequency spectra for VF case 6. The excitable gap is slightly larger. Dominant ECG frequency is slightly lower.

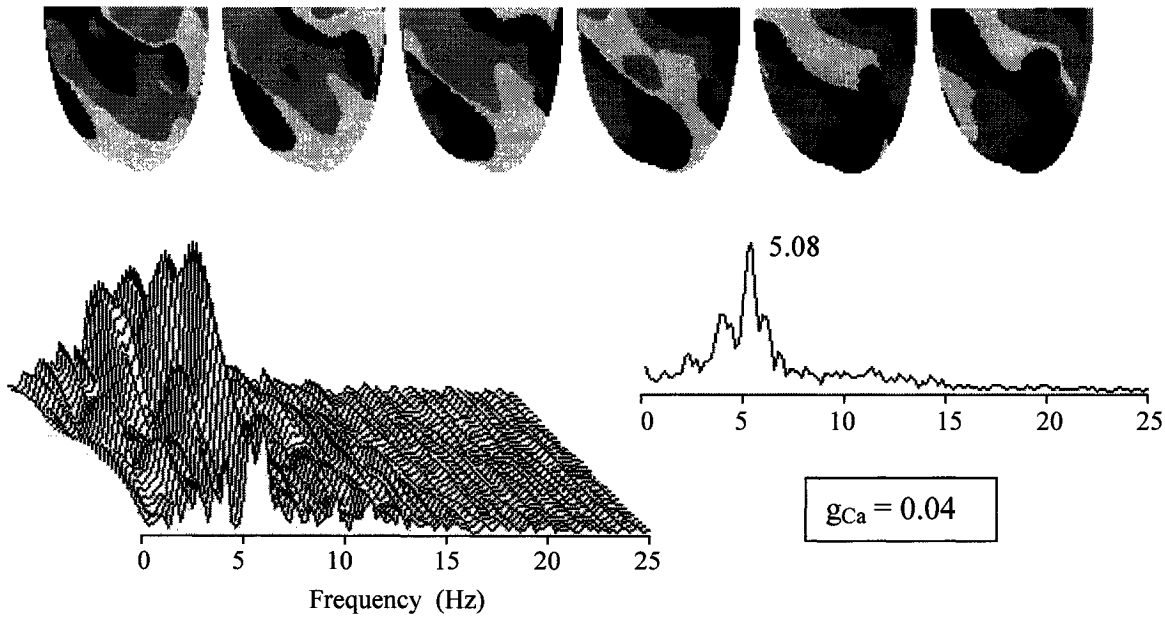

Figure 13.1(c) Effect of reduced calcium conductance g_{Ca} = 0.04 on Case 6 VF epicardial map and ECG frequency spectra. Wave activity is much more coherent, and of larger spatial scale. Dominant ECG frequency is unchanged, but the spectrum is more narrow-banded.

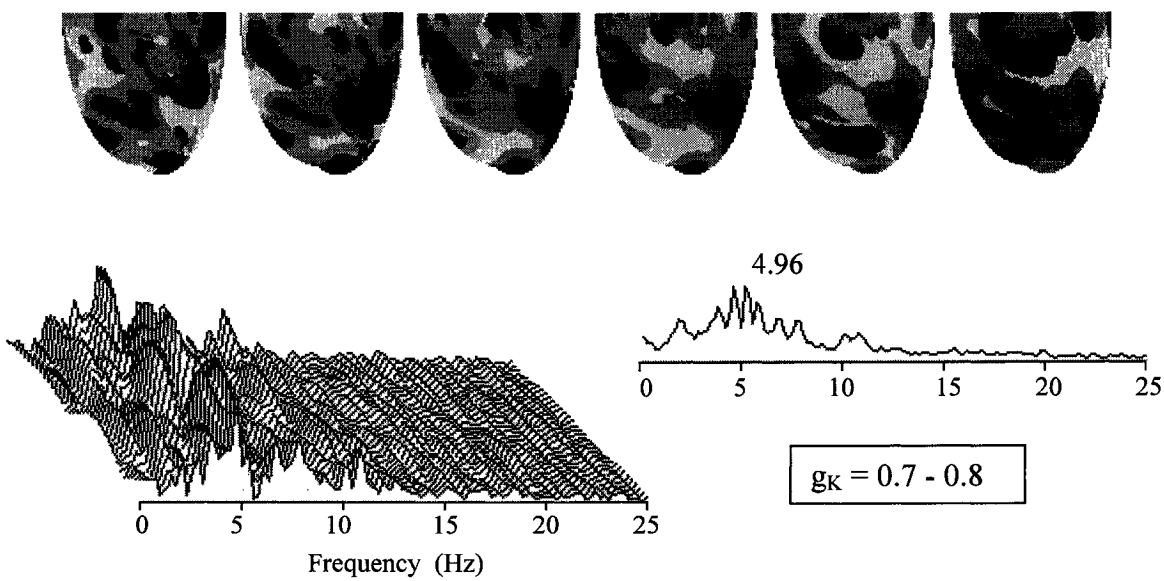

Figure 13.1(d) Effect of reduced potassium conductance g_K = 0.70 - 0.80 on Case 6 VF epicardial map and ECG frequency spectra. Wave activity subjectively does not appear much different from the control case. Dominant ECG frequency is essentially unchanged. The insignificance of changes may be due to the relatively small alteration in g_K.

Potassium channel openers, such as cromakalin and acetylcholine [492], shorten the effective refractory period (ERP), increase vulnerability to reentry, and increase VF frequency. Tedisamil blocks I_K and I_{to} causing prolonged APD and increased VF regularity [137]. Dofetilide blocks I_K, increasing APD and ERP, and slowing or suppressing VT [27]. Sotalol also prolongs APD by blocking outward potassium channels [444], and similarly prolongs FRP, decreases velocity, thereby increasing wave length and decreasing ECG frequency [81]. Figure 13.1(d) shows the effect, in the model, of reducing the potassium rectifier current I_K, by reducing conductance g_K from its baseline of 0.80 - 0.90 across the wall, to 0.60 - 0.70. Mean APD and CL are both prolonged, and the dominant ECG frequency decreases to 4.30 Hz.

Procainamide (PA) is a class I drug that blocks inactivated sodium channels and reduces upstroke velocity. Kim et al. found PA in the pig heart to decrease the number of waves and the size of the cores during VF. APD was prolonged by about 20 percent at all DI, and the minimum diastolic intervals increased to about 40 ms [282], essentially keeping the operating points on a relatively flat part of the restitution curve. Kwan et al. also found PA decreased the density of wavelets [297]. We simulated the effect of procainamide on VF in the heart model by reducing the sodium conductance from 13 to 8, and slowing the sodium channel recovery time constant τ_h to a baseline of 20 ms at resting potential. Figure 13.3 shows the result on VF case 6. Activity condenses from a complex state, with multiple reentrant circuits, to a stable state with about three relatively fixed spiral waves. Despite the apparent success of these changes in this model, the transition from VF took over 20 minutes in the pig experiment, and clinical success in patients treated with PA has been rather poor [479]. There is further evidence that procainamide might actually be proarrhythmic and increase mortality [353].

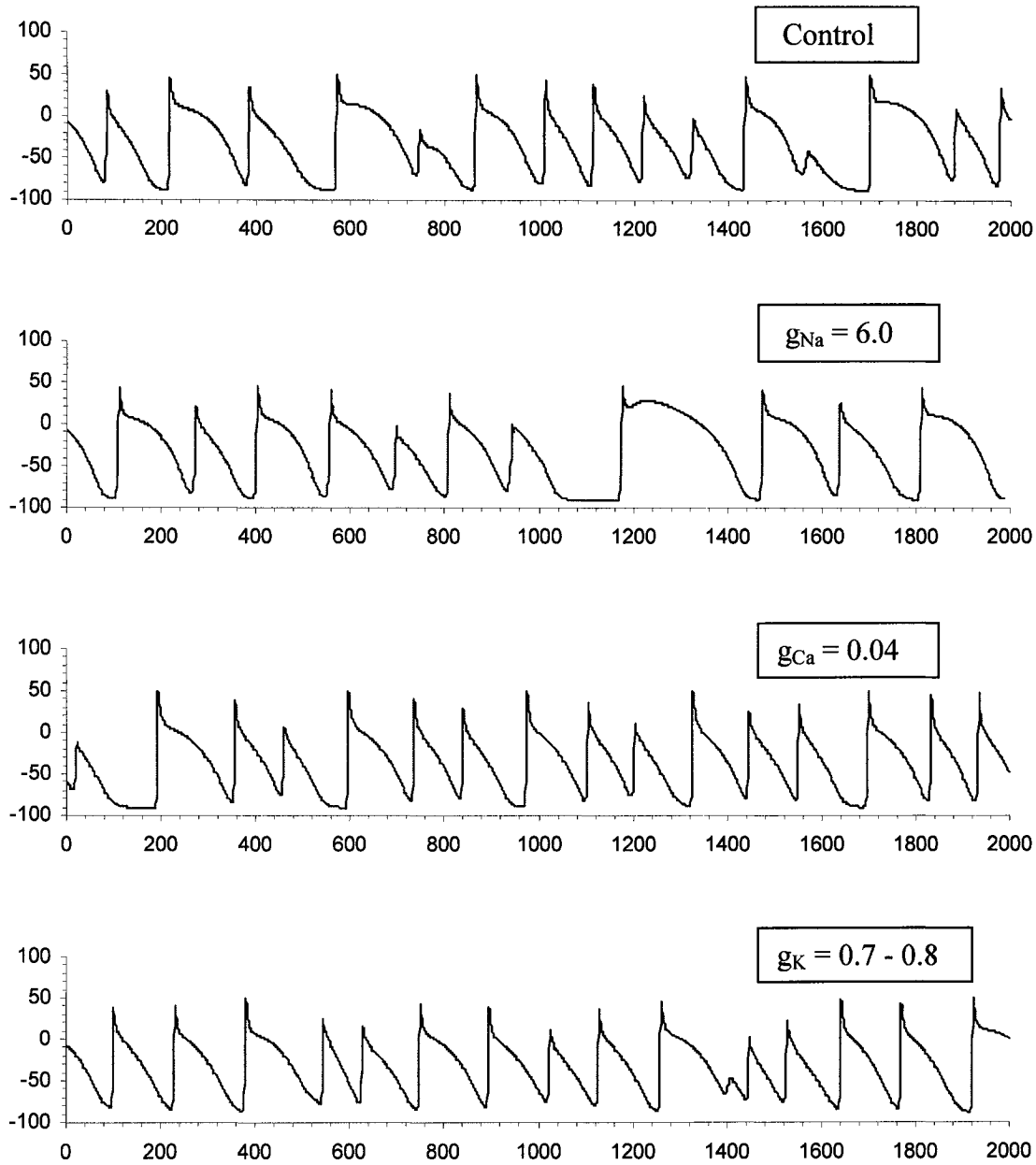

Figure 13.2. Epicardial action potentials sampled under partial blockade of various ionic channels. Control case at top is VF case 6 (MCU) previously discussed. The second case has decreased g_{Na}; longer diastolic intervals give longer APD. The third case with decreased g_{Ca} has flatter restitution of APD, and more uniform APD. The fourth case has reduced transmural g_K.

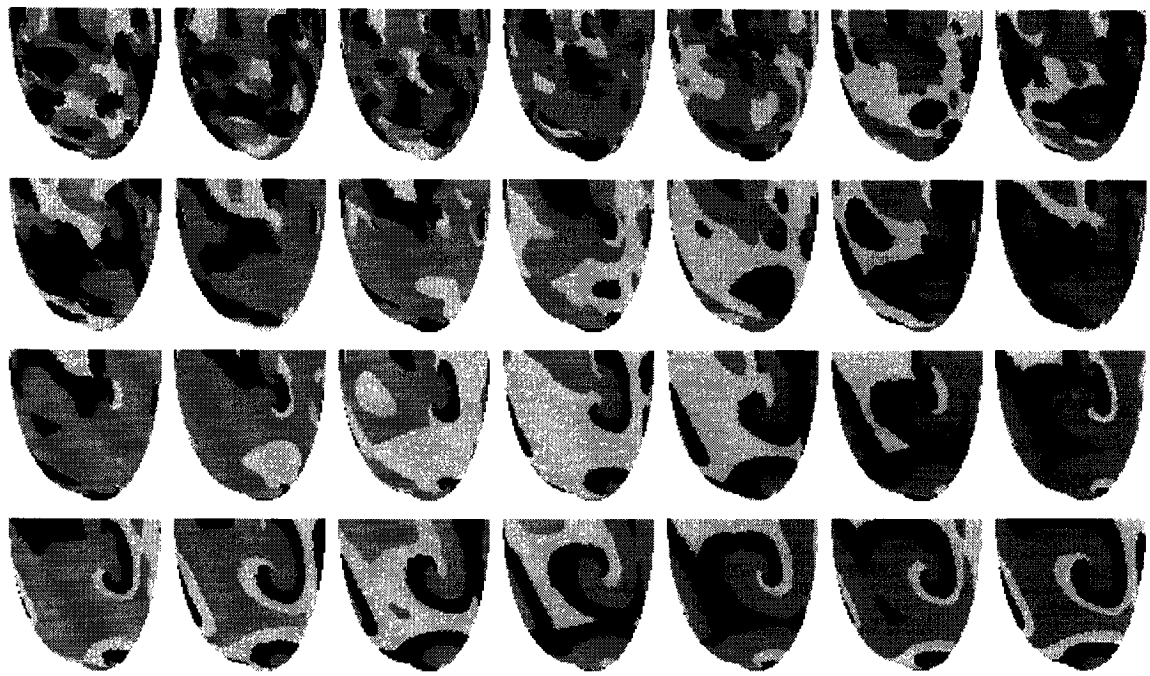

Figure 13.3. Condensation of VF type MCU (case 6), with multiple complex unstable reentrant circuits, into type MCS (case 5), having only a few stable circuits. This transition is achieved in the model by flattening the APD restitution curve, by gradually raising the intercept over the time span shown. The number of reentrant circuits, which can be seen as relatively stationary spiral waves, decreases because the characteristic size of each becomes larger, such that less waves fit in the available space.

Table 13.1. Effect of Drugs on Statistical Measures of VF

Case	DI	APD	CL
Control	24.7 (10.3) *3.72*	78.8 (23.8) *4.51*	109.4 (28.6) *4.62*
↓ g_{Na}	38.7 (17.5) *4.21*	96.5 (40.4) *5.03*	140.5 (45.5) *5.10*
↓ g_{Ca}	34.8 (18.2) *4.15*	87.2 (25.1) *4.36*	124.7 (32.6) *4.43*
↓ g_{K}	26.1 (11.0) *3.77*	84.3 (22.7) *4.48*	110.5 (26.4) *4.57*

Mean values (ms), standard deviation in brackets, entropy in italics

Table 13.2. Effect of Drugs on Spatial Statistics of VF Test Cases

Case	Wave Front [%]	Excitable Gap [%]	Wave Size
Control	3.48 (.55)	21.30 (4.32)	22.64
↓ g_{Na}	2.57 (.51)	26.17 (5.40)	28.69
↓ g_{Ca}	1.73 (.37)	26.05 (8.97)	42.63
↓ g_{K}	4.02 (.73)	20.11 (5.97)	19.87

Mean values (%), standard deviation in brackets, dimensionless wave size

Table 13.3. Effect of Drugs on Stability Measures From VF Test Cases

Case	Slope at DI=0	Lyap Exp
Control	2.47	+0.08
↓ g_{Na}	2.47	+0.05
↓ g_{Ca}	0.90	−1.27
↓ g_{K}	2.65	+0.11

13.2 Pharmacological Defibrillation

An effective means of pharmacological defibrillation has long been desired. The simple injection of a drug, if one existed and was available, to dying patients in cardiac arrest would no doubt save many lives without the need for an electrical defibrillator. Such a drug might also prevent recurrence of VF after successful resuscitation. One possible pharmacological mechanism of defibrillation involves prolongation of the APD, such that the excitable gap becomes entirely filled by a wider action potential wave. This would force all advancing wave fronts to block against their preceding tails, essentially reducing

all reentrant circuits to a size below their critical ring length. At the present time there is no such drug in practice that will do this, although amiodarone is probably the closest candidate, since it prolongs refractoriness [354, 434] and appears to facilitate electrical defibrillation [136, 295]. Figure 13.4 shows the effect of prolonging APD during VF in the heart model, achieved by reducing the rectifier potassium current. Wave fronts rapidly block everywhere, and all electrical activity is extinguished.

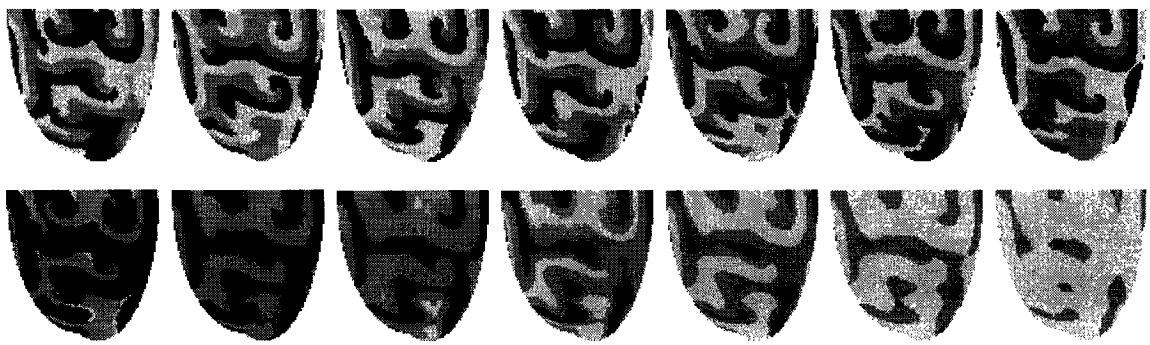

Figure 13.4. VF Case 3 is defibrillated by gradually lowering the potassium current I_{K1}. The APD is prolonged until the excitable gap is completely activated, following which all cells recover to quiescence. Any intervention to ionic channels that sufficiently prolongs APD will achieve a similar result.

Drugs that prolong APD can do so by either enhancing inward currents or reducing outward currents. Since it is generally easier to block a current that to enhance one, most anti-arrhythmic drugs developed so far have been designed to act primarily as channel blockers [533]. It is not possible, however, to discount other secondary effects that may be beneficial or detrimental, including overlapping of specificity for other channels or receptors. Recent drug targets are the various potassium channels which, when blocked, beneficially prolong APD and reduce heterogeneity. These drugs, however, also reduce the firing threshold, potentially precipitating spontaneous depolarization [93], and prolong calcium influx, causing triggered activity as seen in the long QT syndrome [152]. Antiarrhythmic drug development declined somewhat after negative outcomes in the CAST trial [57], but has resurged more recently in a search for highly selective class III

drugs inspired by the apparent success of amiodarone [295, 311]. Theoretical modelling of drug effects in the heart must account for changes in APD restitution, firing threshold, safety factor, anisotropy, and substrate heterogeneity. These effects can all be simulated in computer models, with better predictive performance to be expected in the future with higher-resolution representations. Other modifying effects, such as ischemia, autonomic influences, and electromechanical feedback, will eventually need to be incorporated into these idealized models.

13.3 Electrical Defibrillation

VF and pulseless VT are lethal unless recognized promptly and reversed by defibrillation. Delays of even a few minutes contribute to reduced myocardial viability, progressive brain anoxia, and decreased probability of survival. Although spontaneous defibrillation does occur in small hearts [289, 431], it is a rare event in large mammalian hearts [88]. In practice, the only effective means of defibrillation is an electric shock, delivered either by external transthoracic paddles, internal electrodes, or epicardial patches or catheter leads driven by battery-powered implanted defibrillators. Novel electrical methods, such as programmed spatiotemporal stimulation, may yet remain to be discovered. Resuscitation drugs attempt to facilitate "chemical defibrillation", but these agents are presently used only as adjuncts to electrical defibrillation [153]. Recent evidence highlights the ineffectiveness of many traditional drugs [153]. Mechanical defibrillation, in response to a "precordial thump", is sometimes successful [348], but no other means of achieving defibrillation are presently known. None of these methods are without potentially negative consequences. Weak shocks are ineffective and wasteful of valuable time and battery energy, while strong shocks can damage myocardium [135], and are less effective at high strength [244]. Drugs can have undesirable side effects, including pro-arrhythmic properties [365]. Drugs must also be delivered in adequate concentrations to poorly perfused myocardium during circulatory arrest, assisted by external chest compressions, which are marginally adequate at best [174].

In clinical practice, most defibrillation is achieved by transthoracic shocks delivered by external paddles. Implantable cardioverter-defibrillator (ICD) devices are increasingly being used in patients who have survived VF [357], and have provided a major impetus for defibrillation research over the past decade. Much of the effort has been directed toward signal analysis for automatic VF detection, and efficient electrode configurations and design for minimizing successful shock energy [293].

Despite successful clinical application, the electrophysiological mechanisms underlying defibrillation are not well understood. Continuous mapping and recording of small myocardial signals during VF, while simultaneously applying large current shocks, is technically difficult using existing electrode systems [552]. Optical recordings of action potentials, using voltage-sensitive dyes, have recently been obtained during shocks [157], and are helping to elucidate basic mechanisms. Several theories of defibrillation have been proposed [515, 273]:

(1) The total extinction hypothesis. Wiggers suggested that defibrillation depolarized the excitable gaps between wandering waves, resulting in total extinction of activity, thereby allowing sinus rhythm to return [538]. According to this theory, shocks below a threshold strength are unsuccessful because they fail to halt all wave fronts.

(2) The critical mass hypothesis. The observation that small hearts are difficult to fibrillate and tend to spontaneously defibrillate, while large hearts fibrillate more easily, led Garrey to propose the critical mass hypothesis in 1914 [191]. This idea gained further support when Garrey demonstrated that fibrillation terminated when 75% of the dog heart mass was serially sectioning away. Zipes selectively injected KCl into dog coronary arteries during VF, and found activity terminated when about 75% of tissue mass was depolarized [575].

(3) The upper limit of vulnerability hypothesis. Fabiato found that VF had a threshold strength for induction, yet could not be induced above a certain shock strength, referred to as the upper limit of vulnerability (ULV) [77]. The ULV is highly correlated with the

shock strength of the defibrillation threshold (DFT). Controversy continues regarding the mechanism underlying shocks that fail to defibrillate, in particular, whether wave fronts persist in regions of weak shock current density, or new wave fronts are induced by the shock, perhaps after brief quiescence [76, 519].

The simulations described in this dissertation run in a monodomain model. This means that the extracellular space is considered to have zero resistance, so the transmembrane potential is equal to the intracellular potential. The main motivation for this simplification is the ability to use forward-stepping explicit integration, with reduction of computational storage. One possible limitation of a monodomain model is loss of accurate simulation of membrane response to external stimulation. Bidomain theory, incorporating intracellular and extracellular resistance, predicts that a stimulus delivered by an electrode does not produce a simple region of depolarization at the site of application, but rather induces a spatial pattern involving regions of both depolarization and hyperpolarization [451]. These individual regions within the pattern are called "virtual electrodes", and resemble a dog-bone pattern of shock potential around the stimulus site, that is oriented along the fibre direction in anisotropic tissue [145]. Solution of the bidomain equations in one-, two-, or three-dimensional media requires more sophisticated implicit numerical integration. Analysis using this method is beyond the scope of the models presented in this dissertation.

Defibrillation shocks delivered to a reentrant circuit simulating VF in a one-dimensional cable provide some insight into the basic mechanisms at the cellular level. A monodomain model is quite acceptable if we assume the distribution of applied transmembrane current *a priori*. Figure 13.5 shows an SHV action potential propagating around a cable ring, simulating a reentrant circuit. Defibrillation shocks, of various stimulus current strengths and 5-ms duration, are applied uniformly to the ring. The degree of local depolarization depends on the membrane input impedance, which itself depends on excitability or firing threshold. The greatest response should theoretically occur where the threshold is lowest. For low or normal extracellular potassium concentration $[K^+]_o$, there is a supernormal window, as previously discussed, where the

current threshold at the action potential is lower than that of resting tissue. A relatively weak shock causes a small degree of membrane depolarization, which first appears within the supernormal window, but fails to reach threshold. This shock leaves a brief, relatively inexcitable patch behind the action potential tail, causing slight retardation of the approaching wave front, but otherwise has no significant effect. A slightly stronger shock causes this same region to depolarize a bit more, and for a slightly longer time, to the point where it can almost block the advancing wave front. If the shock strength is increased further, the supernormal region reaches its threshold and fires. A new depolarized wave is born, lying within the excitable gap, however, it experiences unidirectional block by the mechanism described earlier, involving a critical gradient of h(x) recovery. In this case, only the retrograde front survives, and propagates back to meet the original oncoming front. The collision annihilates both waves, and defibrillation is successful. At higher $[K^+]_o$, there is no supernormal window, but the mechanism of defibrillation is essentially the same. The only difference is that the new wave generated appears at its site of lowest threshold, which is now just in front of the approaching wave. This gives the appearance of the advancing front being suddenly accelerated to meet the tail, resulting in block. According to this simple model, defibrillation is facilitated when cells have low thresholds.

The foregoing analysis assumes that the excitable gap is relatively narrow. If the reentrant circuits are larger, with wider excitable gaps, another mechanism comes into play on the cable ring. Since subthreshold depolarizing shocks can advance the upstroke, and thereby shorten the excitable gap, the upstroke can catch-up and block, as if the critical ring length has suddenly been shortened. If sodium conductance g_{Na} is reduced, stronger shocks are required to defibrillate. Sufficiently strong hyperpolarizing shocks suppress the upstroke, and can also extinguish activity by this alternate mechanism. Milder shocks shorten APD, resulting in a wider excitable gap, which allows longer recovery. The subsequent APD is then longer, causing the critical length to be exceeded, resulting in termination.

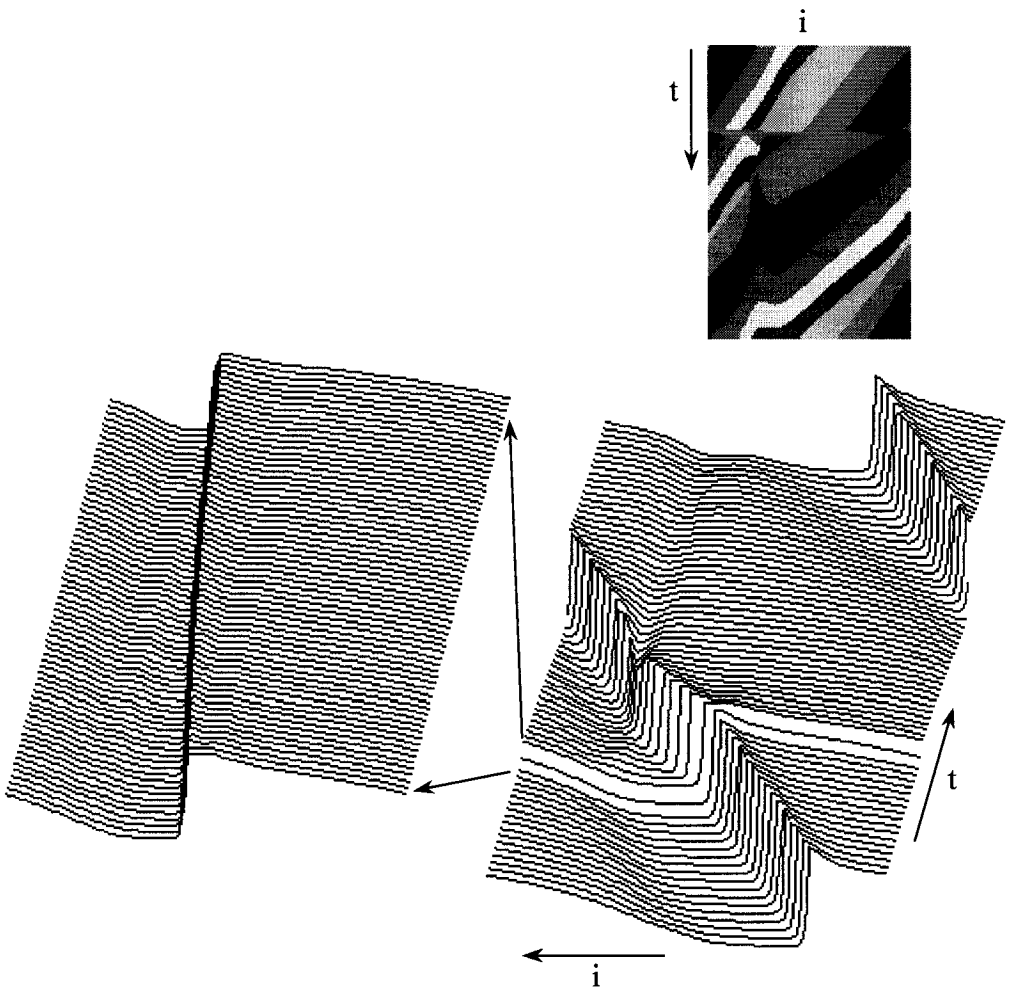

Figure 13.5(a). A wave propagating on a cable is given a relatively weak depolarizing shock over its entire length. The effect is to advance the wave front slightly by bringing it to threshold sooner. The supernormal region, within the excitable gap, depolarizes only subtly, but establishes a brief barrier that momentarily retards the wave front, but is not significant enough to cause block. The space-time plot is shown at upper right, with perspective views below. The left frame is a magnification of the time interval around the shock window indicated by the arrows. $[K^+]_o = 4.0$ for this case.

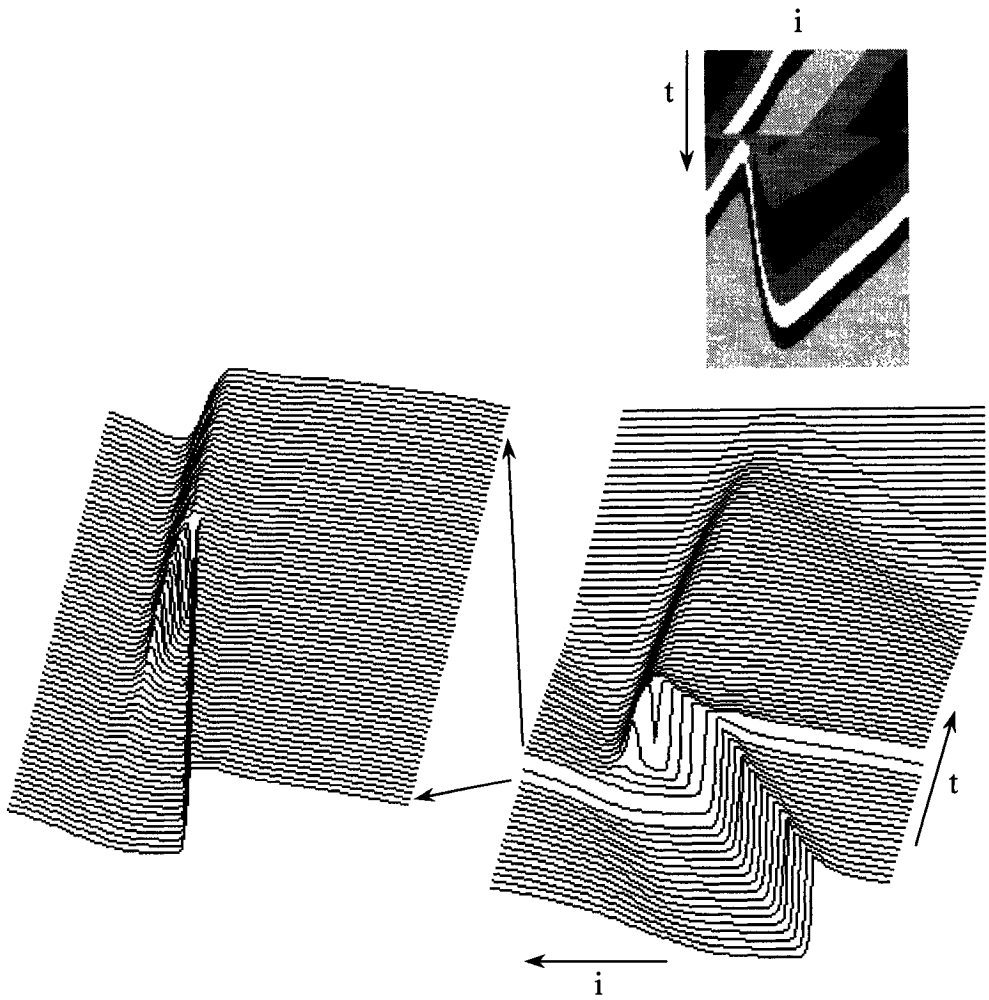

Figure 13.5(b) The depolarizing shock is stronger than in the previous case, causing the supernormal window to fire. This gives birth to a small wave in the excitable gap that blocks in the anterograde direction, yet propagates retrogradely. The oncoming wave front is annihilated, and defibrillation is successful. $[K^+]_o = 4.0$.

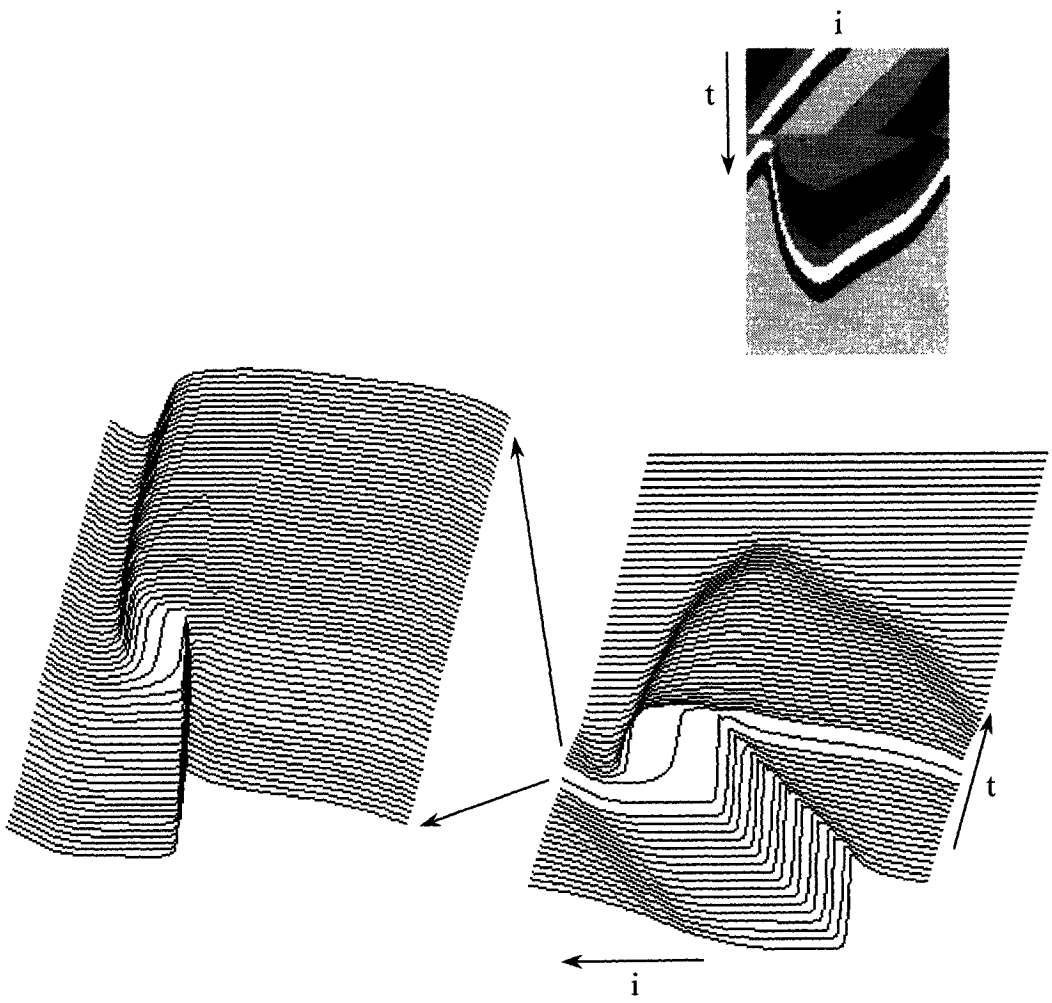

Figure 13.5(c). The same conditions apply as in the previous figure, but $[K^+]_o = 7.0$, such that there is no supernormal window. The shock now causes earliest depolarization to occur at the foot of the wave front. This causes immediate abrupt advancement of the wave front, which depolarizes the entire excitable gap, causing block on the preceding action potential tail.

13.3.1 Uniform Shocks

Although finite element or boundary element methods can be used to calculate more realistic three-dimensional current densities throughout the heart during a shock [87, 349], assuming homogeneous myocardial conductance, we will instead assume, for simplicity, that the transmembrane current density is spatially uniform throughout the heart during an external shock [121, 216]. In reality, the current density is probably high in some regions, especially close to the defibrillating electrodes. Although actual shock profiles decay exponentially in time, due to the combined capacitance of the defibrillator and body, shock profiles in the model will be assumed to be rectangular with one or two phases, as shown in Figure 13.6. Figure 13.7 shows the effect of a rectangular depolarizing (positive) shock delivered to the solitary spiral wave of VF Case 1, discussed in the previous chapter; this being the simplest type of reentry. The weakest subthreshold shock of strength I = 1 causes mild prolongation of the action potential wave, but has little effect otherwise, except to shift the core point slightly to the left. A stronger shock of strength I = 2 produces an interesting result. The wave is again widened and the front is advanced, such that wave front block occurs over a partial segment, giving rise to two new rotors. If we number the free ends 1, 2, and 3 from the centre outward, then the distal two rotors 1 and 2 cancel after about one revolution, leaving the new core point 3 to survive in a shifted position, and become the new solitary core point. It is noteworthy that the segment of block occurs where the wave front is travelling transversely to the fibre orientation, suggesting the existence of a lower safety factor of conduction in this direction. The stronger suprathreshold shock I = 5 successfully excites all cells, causing block along the entire wave front, followed by recovery to quiescence. The defibrillation threshold (DFT) is therefore about 5 units for this case. The mechanism of defibrillation seen here is consistent with Wiggers' total extinction hypothesis [538].

Biphasic truncated-exponential shocks are known to defibrillate with lower energy and less damage to the myocardium than corresponding monophasic shocks [260]. The reason for this relative efficiency is unknown, but might relate to reduced induction of post-shock arrhythmias that regenerate VF [260], or better enhancement of refractoriness. The

charge-burping theory proposes that the change in shock polarity removes excess charge from the membrane [292]. Although predictions from this theory, in terms of shock phase durations, correlate with shock efficacy [485], the underlying mechanism has not been satisfactorily demonstrated in any ionic model. Indeed, this theory was based on subthreshold behaviour. Triphasic shocks might be even more efficient [243], but there is presently no theory to account for this finding, nor to allow derivation of the optimal shock profile.

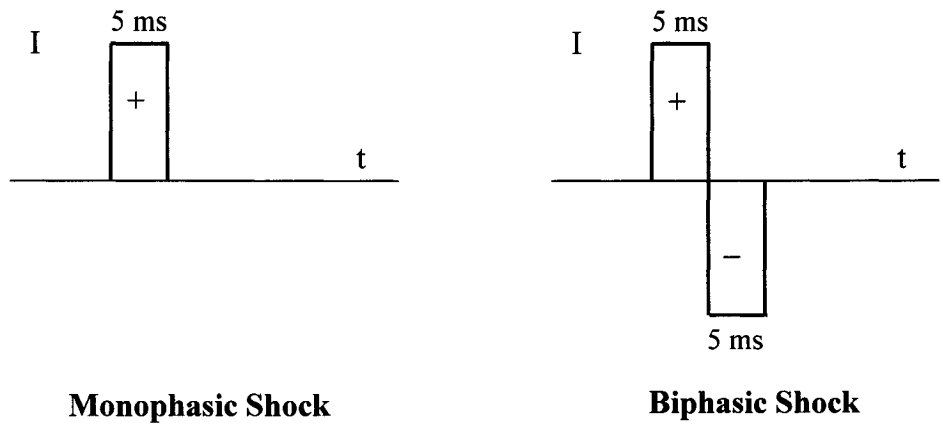

Figure 13.6. Defibrillation shock profiles applied to the model are either monophasic or biphasic. Each phase is assumed of constant magnitude for a duration of 5 ms.

Biphasic shocks are applied to the spiral wave of Case 1 in Figure 13.8. A 5-ms I = 3 depolarizing (positive) shock is followed immediately by a 5-ms I = –2 hyperpolarizing (negative) phase. The response is remarkably similar to that seen with the I = +2 monophasic shock, suggesting that the negative phase does little except partially negate the stronger preceding positive phase. Reversing the order of polarity to I = –3, followed by I = +2, is largely ineffective. It is not clear why these biphasic shocks are less effective than the monophasic shocks in this model. We have not yet explored the detailed cellular responses during these shocks. The reason might relate to a fundamental limitation of the monodomain model in capturing realistic transmembrane behaviour, or it might be due to

the specific choice of VF characteristics used here. In any case, it underscores the need to seek better theories to explain shock efficacy and improve optimization of defibrillation shock waveforms.

Figures 13.9 and 13.10 show defibrillation of multiple spiral wave VF Case 3. A weak depolarizing shock I = 2 prolongs action potentials, causing the waves to widen. This is followed by a period of APD and excitable gap oscillation, induced by the steeper restitution for this case, manifesting as thickening and thinning of the waves. Defibrillation is unsuccessful, since the core points are unaffected, and VF persists. The stronger shock, with I = 4, depolarizes most of the excitable gap, but leaves a few small segments of wave front to survive, like seeds that grow back into spiral waves. The defibrillation threshold (DFT) shock of I = 6 is successful, since it extinguishes all wave fronts. The hyperpolarizing shock of I = – 6 transiently shortens APD, but fails to defibrillate since there is very little induced interaction between the wave fronts and their tails. Defibrillation of Case 6 is shown in Figure 13.11. The subthreshold shock with I = 2 fails to defibrillate, while I = 4 is successful. It not yet clear why the DFT of 4 is substantially lower than that of the previous cases. The explanation might relate to this particular case of VF having a smaller volume of excitable gap (21.3%), or smaller characteristic wave size (22.64) than the other cases, as was summarized in Table 12.5.

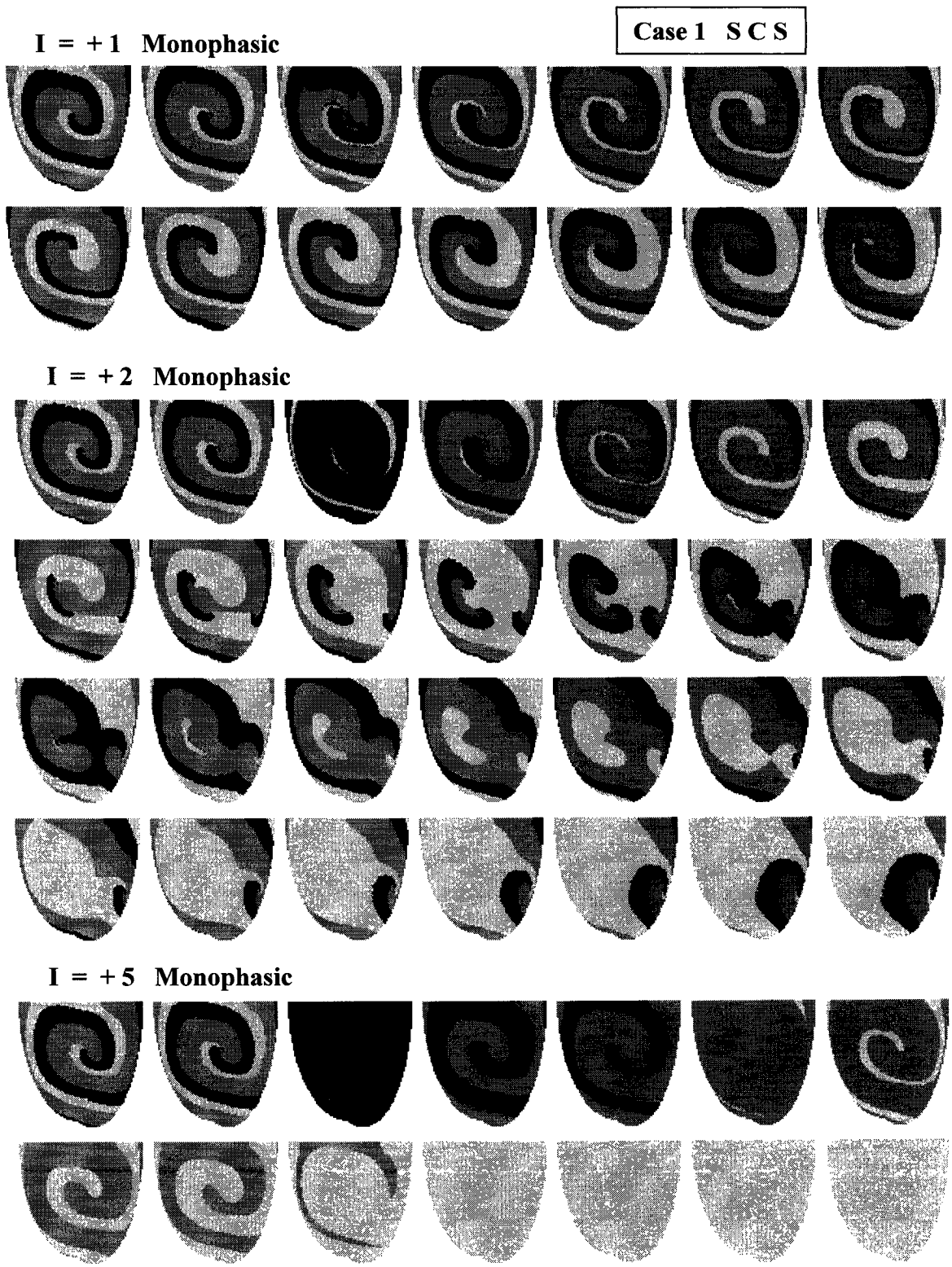

Figure 13.7. Defibrillation of Case 1 solitary spiral wave with 5-ms uniform monophasic rectangular shocks shown in 10-ms frames. Positive currents I above are depolarizing. The defibrillation threshold for this case is DFT = 5. See text for further discussion.

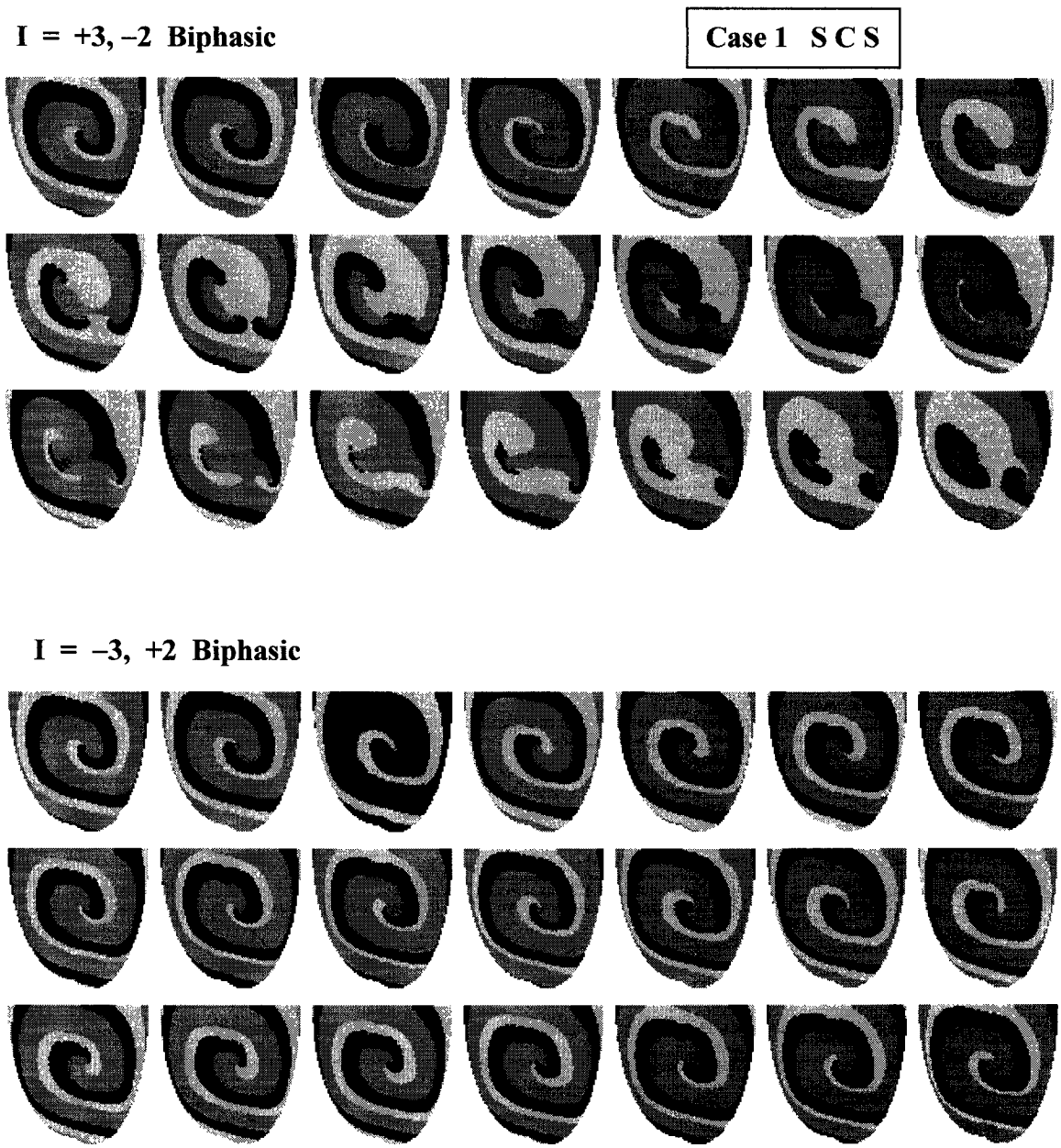

Figure 13.8. Defibrillation of Case 1 solitary spiral wave with uniform biphasic rectangular shocks. The current shown above has two 5-ms components. Positive current is depolarizing, and negative current is hyperpolarizing. Negative current shocks are largely ineffective in this model. There is a tendency for the opposing components to negate each other. Defibrillation is unsuccessful at these levels. See text for discussion.

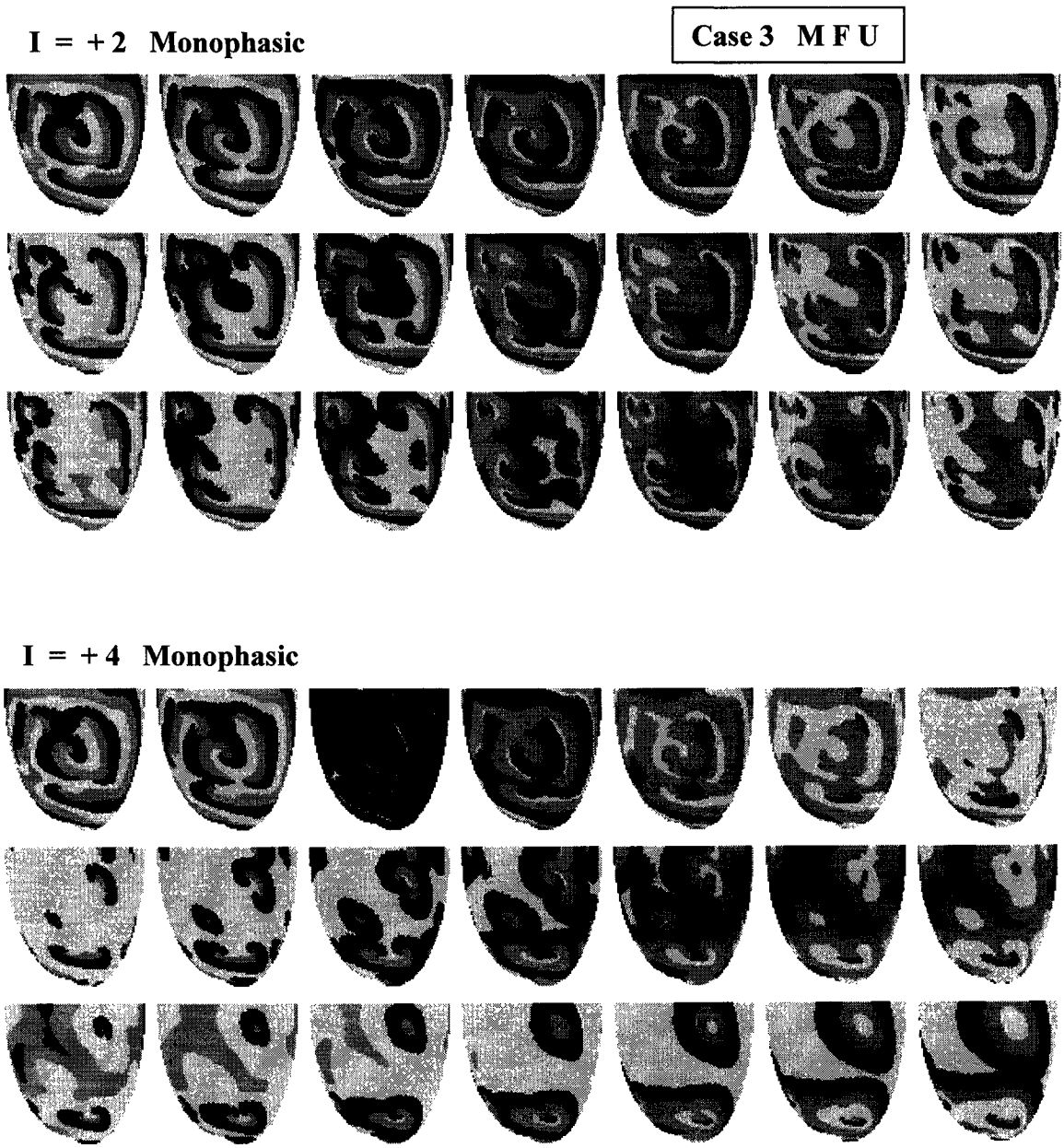

Figure 13.9. Defibrillation of Case 3 (multiple spiral waves) with a monophasic uniform 5-ms rectangular shock. Defibrillation is unsuccessful at these levels. Several small seeds of surviving wave front roll up into reentrant circuit pairs, and re-establish fibrillation. See text for discussion.

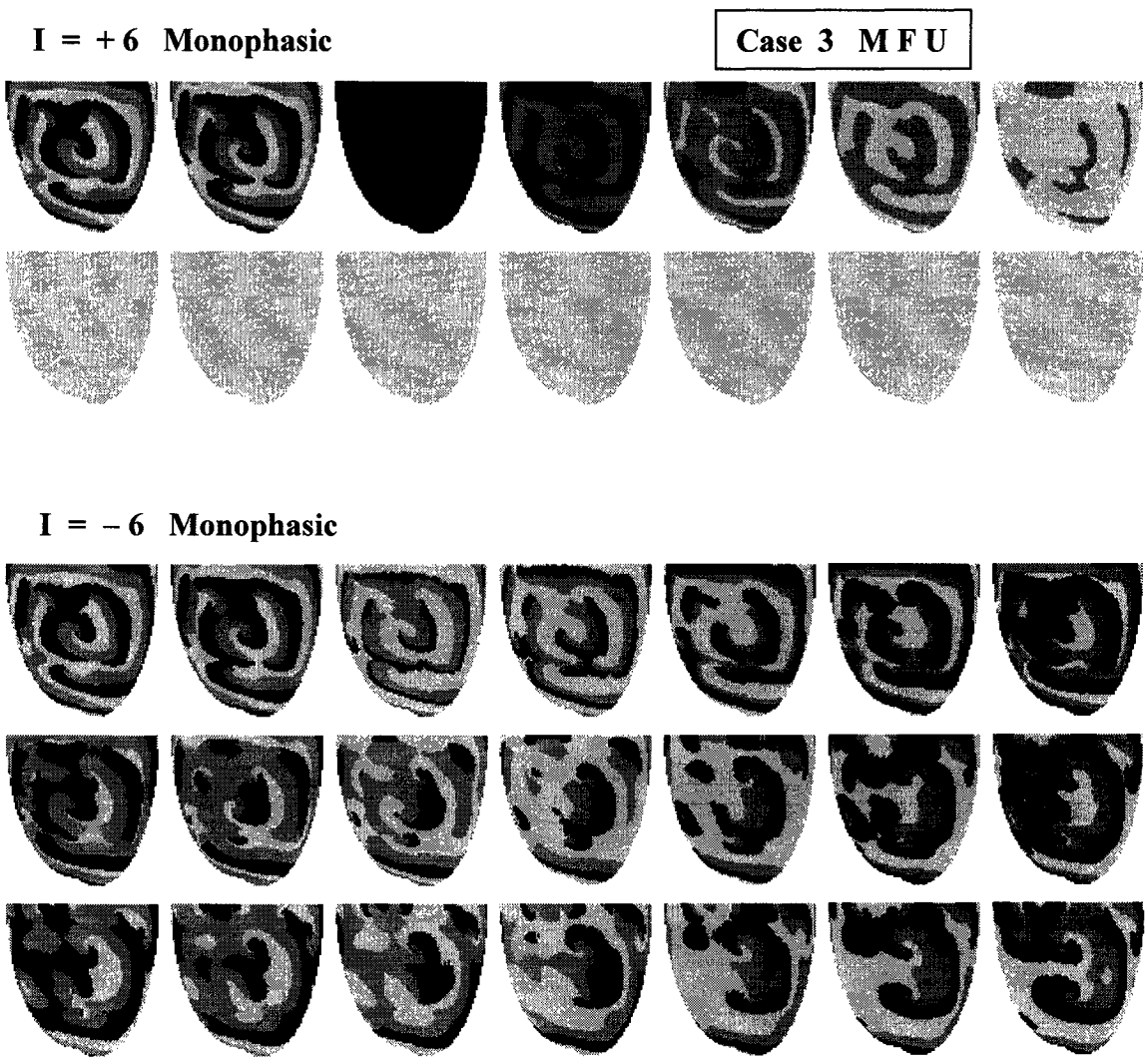

Figure 13.10. Defibrillation of Case 3 is successful at I = +6. A strong hyperpolarizing shock I = –6 shortens APD, causing waves to become narrow initially. Restitution in this case introduces subsequent oscillation of APD, which stabilizes to persistent VF. This hyperpolarizing shock is ineffective for defibrillation.

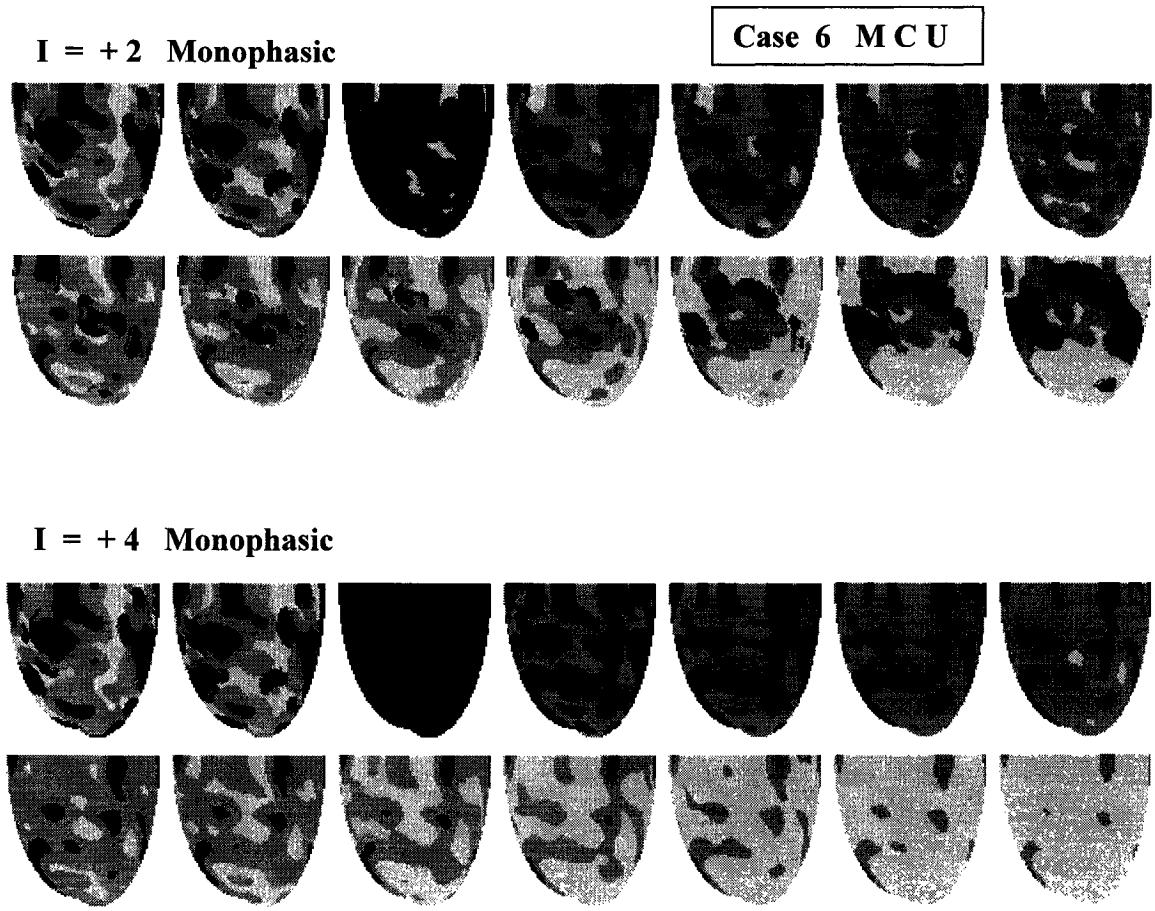

Figure 13.11. Defibrillation of Case 6. The subthreshold uniform shock I = 2 extinguishes only the apical region. The successful shock I = 4 depolarizes the entire excitable gap, causing complete wave front block throughout the heart.

13.3.2 Nonuniform Shocks

The current density throughout the myocardium from a defibrillation shock cannot be expected to be perfectly uniform. If defibrillation is simply a consequence of halting all wave fronts to terminate sustaining propagation, a shock just below the DFT should fail, due to persistence of at least one surviving segment of wave front. Intuitively, this should occur in the region of lowest current density if there is a nonuniform shock field. This situation can be simulated by applying the defibrillating shock to the heart apex, and giving it a spatially decaying current density. The apex should defibrillate cleanly, but regions toward the base, where current density is lower, might not extinguish.

Figure 13.12 shows VF Case 6 defibrillated with a 5-ms shock of spherically decaying current density $I(r) = I_m \exp(-r / \lambda_D)$, where I_m is the central maximum value. λ_D is the space constant of density decay, assumed to be constant for all cases, and arbitrarily assigned to be 30 mm, in the absence of a validated value. A relatively weak shock with $I_m = 20$ extinguishes the apical region as expected, while a strong shock of $I_m = 60$ cleanly defibrillates the whole heart. The intermediate case of $I_m = 40$ appears to be just below the DFT, as activity within a small subregion of myocardium near the RV base survives, and subsequently spreads over the heart to re-establish VF. The statistical plots in Figure 13.13 are consistent with defibrillation by the total extinction hypothesis.

The solitary spiral wave of Case 1, subject to the nonuniform decaying apical shock, is examined in Figure 13.14. A relatively weak shock of $I_m = 20$ defibrillates the core region, but leaves a critical point on the LV free wall that re-establishes a new spiral wave. A second critical point on the opposite side of the heart gives rise to another new spiral wave, creating a counter-rotating pair. The stronger shock $I_m = 60$ has a similar effect, but the critical points are pushed toward the base, such that one moves off the boundary. It is noteworthy that his case demonstrates that a shock can give rise to new reentrant circuits. This did not occur with more complex fibrillation in Case 6, likely because both the characteristic wave size and the excitable gap were smaller, leaving less room for new circuits to develop.

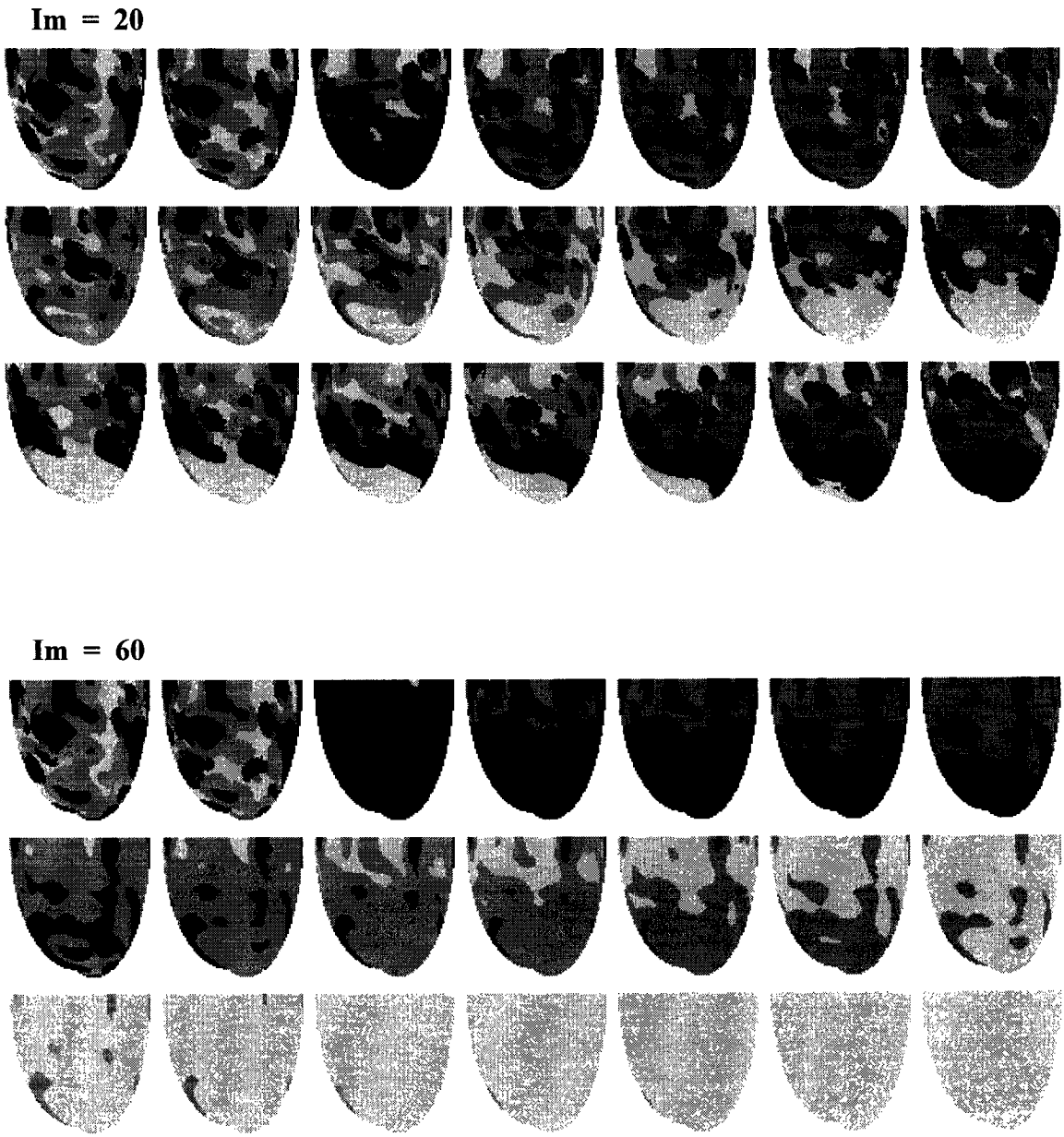

Figure 13.12(a). A subthreshold nonuniform shock applied to VF Case 6 with I_m = 20 halts activity only in the apical region where current density is highest. A suprathreshold shock of I_m = 60 defibrillates by firing the entire excitable gap. The defibrillation threshold lies between these two extremes. The shock is delivered in the third frame of this 10-ms series.

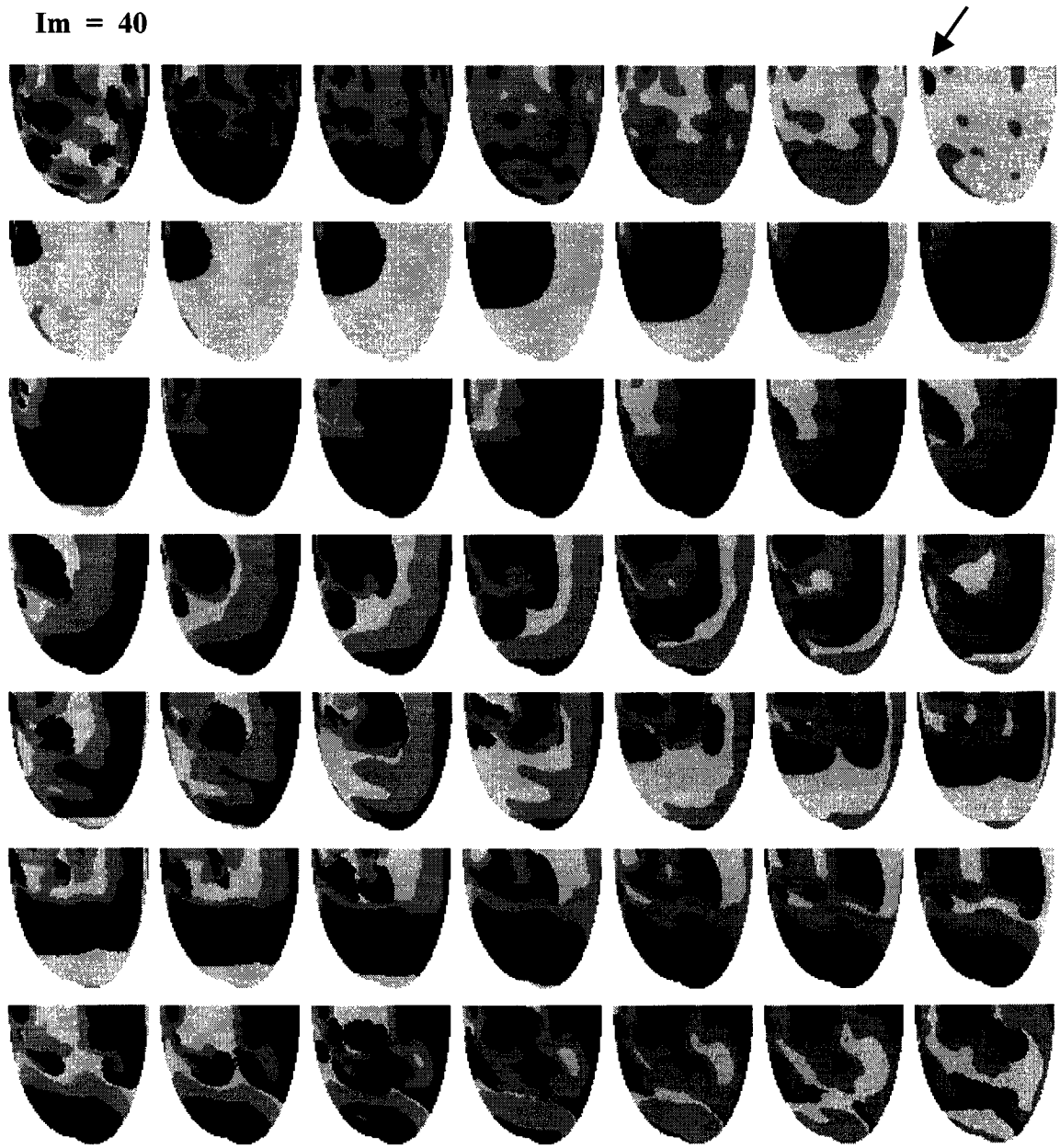

Figure 13.12(b). A nonuniform shock of I_m = 40 to VF Case 6, delivered in the second frame, is just below the defibrillation threshold. A very small remnant of wave front survives at the RV base, shown by the arrow. This gives rise to a coherent radiating wave that passes across the heart, leaving in its wake a small region that grows back into fully-developed fibrillation within about half a second. Frames are 20 ms apart. The sequence spans about 1000 ms.

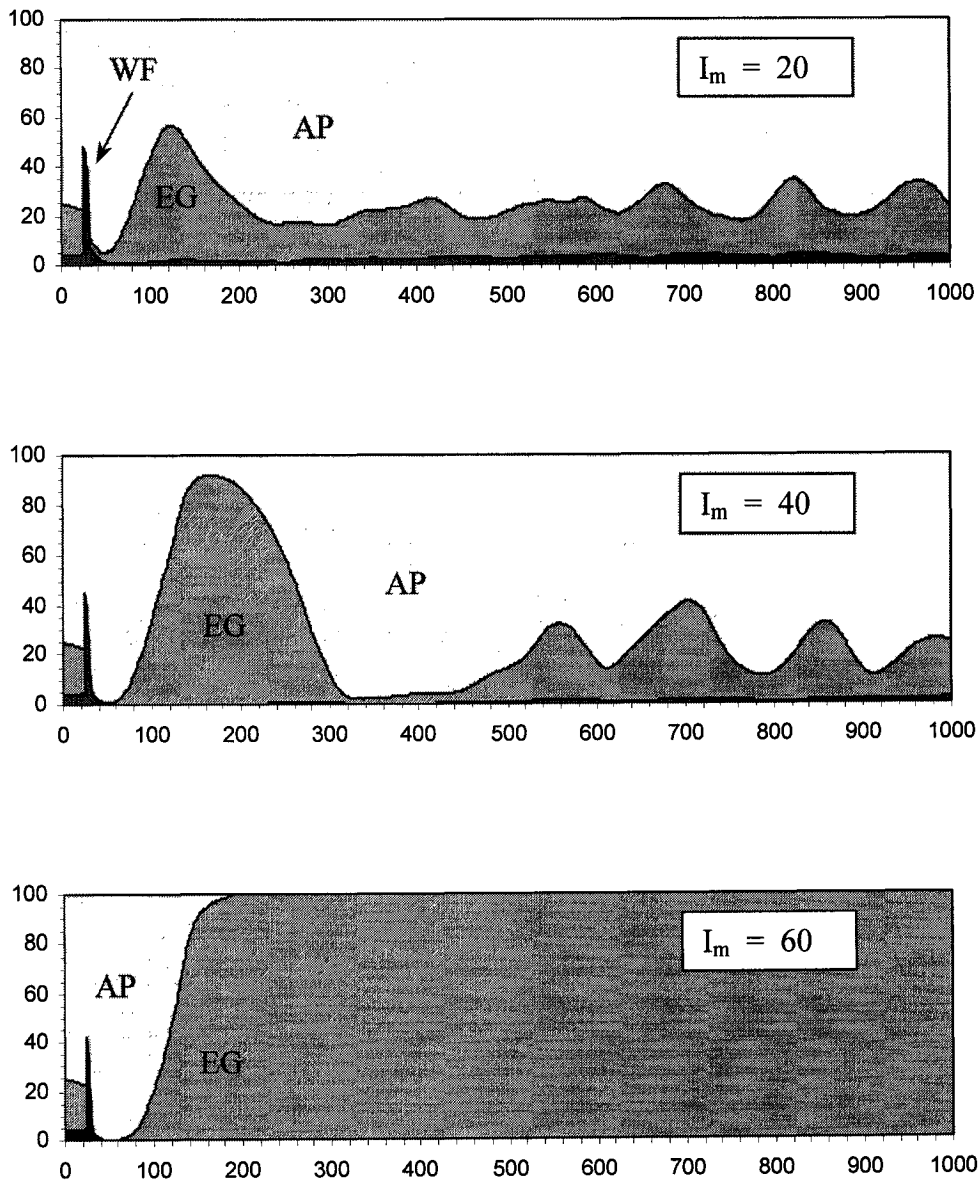

Figure 13.13. Post-shock activation of the heart for Case 6. The spatially decaying apical shock is delivered between t = 25 and 30 ms. Volume percentages of action potential wave (AP), wave front (WF), and excitable gap (EG) are shown for nonuniform shock strengths I_m = 20, 40, and 60. The black spike shows that about 45% of elements are activated by the shock. Successful defibrillation occurs only if the excitable gap is completely abolished, and wave front volume drops to zero, consistent with the total extinction hypothesis.

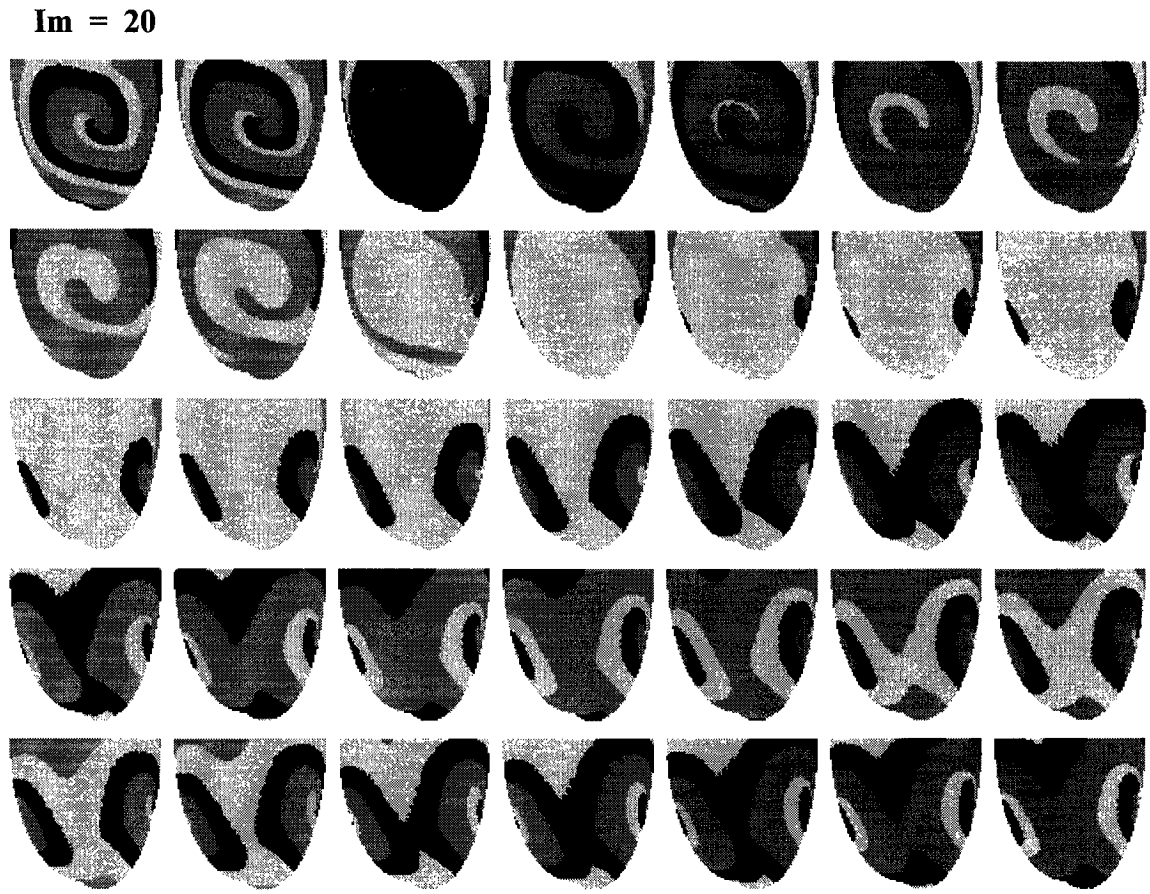

Figure 13.14(a). Nonuniform apical shock is applied to VF Case 1 with $I_m = 20$. The core of the solitary spiral wave is largely destroyed, but a critical point is established at the right-hand margin in the LV free wall, just visible in the eighth frame. This grows back into a spiral wave. A critical point is also created on the posterior side of the heart that manifests as a second mirror-image spiral wave, producing a counter-rotating pair. This case demonstrates that a shock can give rise to new reentrant circuits.

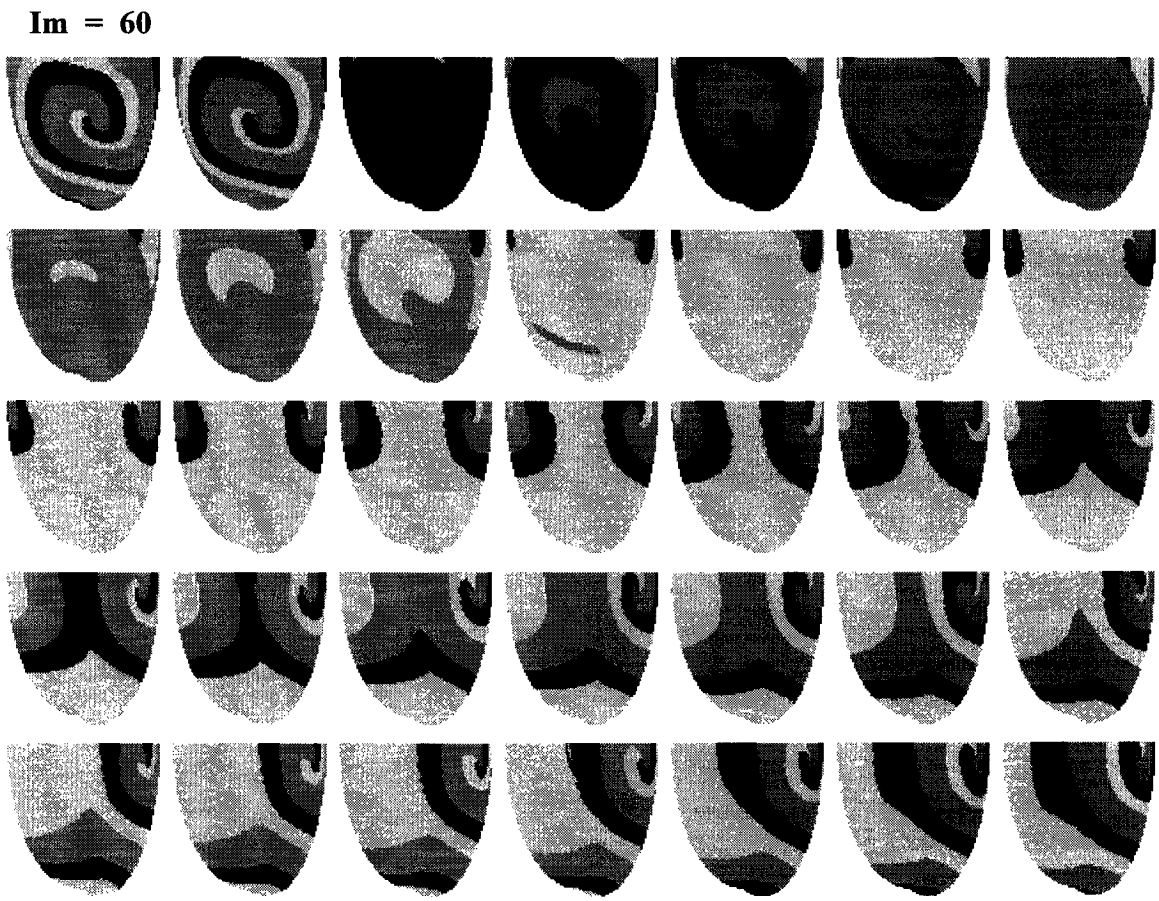

Figure 13.14(b). Nonuniform apical shock is applied to VF Case 1 with I_m = 60. The outcome is similar to the previous case, however, the stronger shock pushes the anterior and posterior critical points farther toward the base. The new spiral wave appearing on the right-hand side barely survives due to its proximity to the boundary. The core on the opposite side migrates off the basal boundary and annihilates, leaving only one spiral wave.

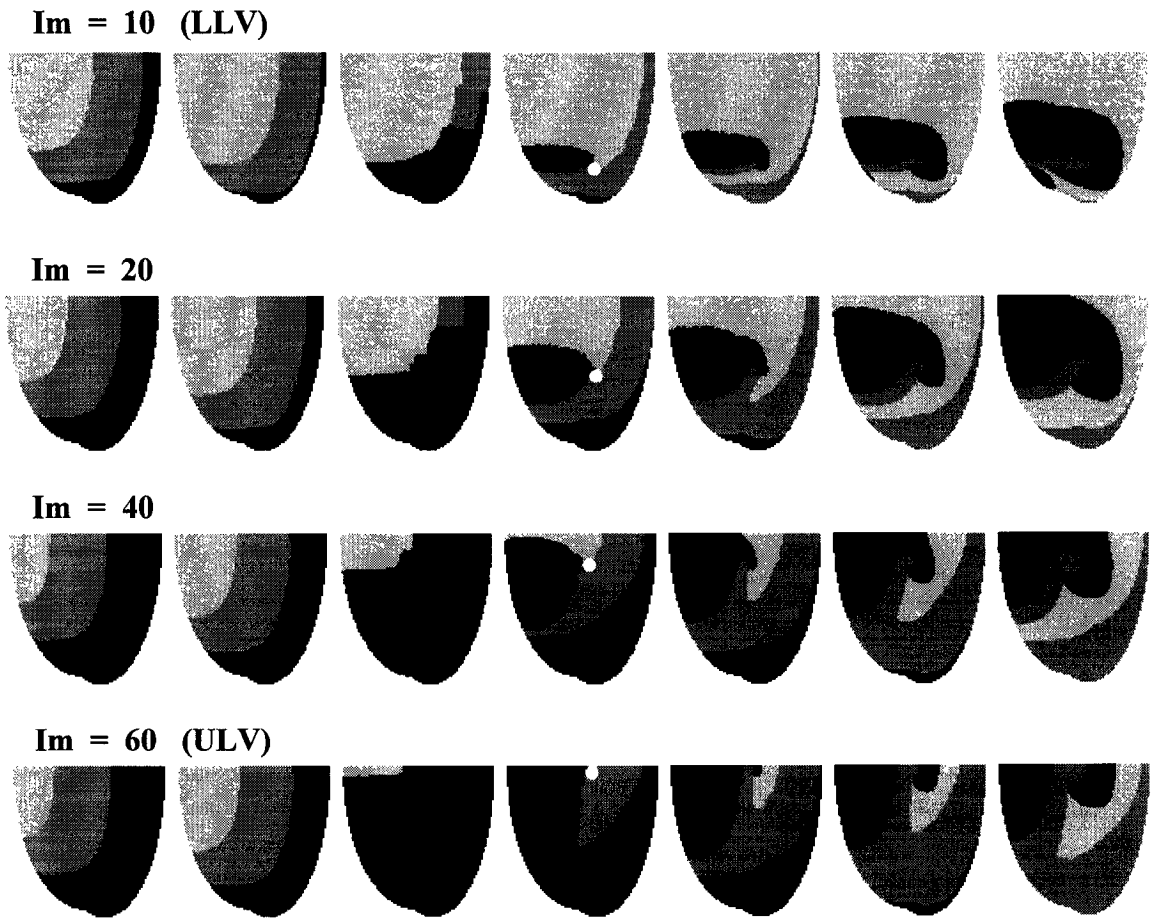

Figure 13.15. Demonstration of the upper limit of vulnerability hypothesis for VF-induction. An initial stimulus S_1 applied to the RV base causes an action potential wave to move across the heart, as shown from left to right. A spatially decaying S_2 shock is applied to the apex in the third frame of each row. A spiral wave develops at a critical point where the shock front intersects with the refractory tail (white circle). Stronger shocks push the critical point farther away from the apex. The lower limit of vulnerability (LLV) and the upper limit of vulnerability (ULV) are the minimum and maximum shock strengths needed to induce reentry by this mechanism. These values are determined by the condition that the location of the critical point must be within the heart boundaries, and allow enough space for the free end to roll up. In this case, LLV is about $I_m = 10$, and ULV is about $I_m = 60$. The ULV corresponds closely to the DFT because a defibrillating shock must abolish activity without creating any new critical points. Above the ULV and DFT, any shock-induced critical points are off the heart domain

13.4 Model Limitations

This chapter is not intended to be an exhaustive treatise on the theoretical mechanisms of defibrillation, but rather a demonstration of some of the model capabilities in simulating basic responses, assuming that fibrillation involves reentrant circuits. The mechanisms underlying successful and unsuccessful defibrillation shocks continue to be debated. Krinsky [291] suggested that if the medium is homogeneous, current density should decay rapidly away from shock electrodes, with the space constant being as low as the Weidmann value of only 1 mm [528]. Since this is obviously not the case in real tissue, high resistance gap junctions between myocytes at the cellular level might be responsible for concentrating transmembrane current at the ends of each cell, allowing the firing threshold to be reached in many cells over much longer distances. Theoretically, the shock-induced transmembrane potential at the cellular level should have a saw-tooth distribution through the syncytium [372, 573]. Superimposed on this profile would be a much longer effective space constant of voltage decay dependent on the rate of current attenuation in bulk myocardium. Empirical measurements of field strength from shocks have so far been limited to surface voltage gradients, the critical value for defibrillation appearing to be about 6 V/cm [532, 574]. It is not possible, at this time, to directly relate these values to actual transmembrane current densities without some sort of interpretative model, and detailed knowledge of the tissue properties [402, 427]. Nevertheless, the anisotropic monodomain model used here can still provide reasonable and useful approximations of three-dimensional responses to external shocks, provided the current density field of the shock is predefined. The spherically decaying exponential function $I_m(r)$ used here is probably reasonable, and produces results consistent with epicardial mapping experiments [23, 75]. Better insight into the spatial distribution of shock fields at the cellular level will likely follow from further development of anisotropic bidomain models of syncytial tissue that include gap junctions.

We have assumed that VF is due to multiple wandering reentrant circuits, which are essentially meandering filaments in three dimensions, similar to those seen in other recent tissue models [16, 164, 409]. There is evidence to suggest that focal activity might also

contribute to at least some cases of VF regeneration after failed shocks [74], perhaps due to large perturbation of the intracellular ionic mileau, giving rise to instability with early or delayed afterdepolarizations [64]. Focal reactivation would explain the relatively long delays seen before VF reappears in some experiments, particularly after strong shocks [74]. While the present model does not account for spontaneous depolarizations as a contributing factor in VF, modifications to the cellular ionic model can be added to include this possibility.

It might be possible to control or stabilize fibrillation by delivering low energy electrical impulses weaker than those needed to defibrillate. A early "protective zone" appears to exist, within which stimuli can prevent VF from developing if given immediately shortly induction [43, 506]. Biktashev and Holden demonstrated how the core of a model spiral wave can be directionally-steered by appropriately timed stimuli, a phenomenon they call resonant drift [40], and proposed this as the basis of a novel type of defibrillator [39]. Interest has grown in techniques of chaos control after the landmark algorithm outlined by Ott, Grebogi, and Yorke [383]. This model-independent OGY method involves monitoring the dynamics to identify the eigenvectors of saddle points upon which unstable trajectories can be stabilized by nudging a substrate property. Garfinkel et al. used this idea to stabilize drug-induced ectopic VT in rabbit hearts [190]. More recent attention has focussed on the more challenging task of controlling spatiotemporal chaos with many degrees of freedom [14, 520]. Theoretical models will remain central to the development of novel arrhythmia control techniques.

Chapter 14

CONCLUSIONS

14.1 Summary

This dissertation describes a journey through a landscape of mathematical theory in an attempt to understand cardiac fibrillation. We have gone from the clinical level of a dying patient experiencing complex heart rhythms to the primitive level of binary strings and entropy, and attempted to bridge this gulf with a scaffold of theory. The heart can clearly exhibit complex electrical dynamics, and shift between multiple modes of behaviour. The ability to remain within a stable subset of dynamics determines life span. The heart has been idealized here as a three-dimensional coupled network of interacting computing elements, each programmed with physical laws at a local level. Simulations of global behaviour represent emergent phenomena of potentially profound complexity.

Much of the early work in this project focussed at an intermediate level of representation by developing theoretical ionic cellular models of action potentials that propagated in two- and three-dimensional blocks of tissue. The initial objective was the simulation of complex tachyarrhythmias within a whole heart and the resultant electrocardiograms. The large scale heart model indeed reached a satisfactory level of performance using the developed ionic model, but it soon became apparent that, while the large simulations were visually spectacular and intriguing, the results were often too complex to answer

some basic questions at the foundation of inquiry into the nature of VT and VF. It therefore became necessary to retreat from the complex model and develop a simpler coupled map lattice model. This formulation has served as an insightful test bed for exploring some of the basic dynamics of excitable tissue subject to refractoriness and restitution of APD. The rapid computational speed and versatility of the simple CML model allowed a broad spectrum of fibrillation spatiotemporal wave dynamics and electrocardiograms to be investigated.

There already exists a considerable body of published literature on the behaviour of solitary spiral waves in various types of excitable reaction-diffusion media, however very little work has been done examining spatial interactions within groups of multiple spiral waves, such as those that appear to be important in fibrillation. The CML model was developed to simulate both focal wave sources and fields of multiple spiral waves, spanning the spectrum of complexity from simple solitary spirals to near-random chaos. The strength of this model is the simplicity of APD restitution, and the ability to easily change and control the restitution curve to examine the effects on spatiotemporal dynamics. Bifurcations in APD were seen with changes in cycle lengths, and were dependent on the slope of the APD restitution curve. Disparities between neighbouring cells were suppressed at shallow restitution, but increased at steep restitution. The latter manifested an instability, giving rise to wave front block and proliferation of wave-break into VF through roll-up of the free ends. Measures of complexity including entropy and Lyapunov exponents were monitored, and found to increase with restitution slope.

It was possible to control transitions from VT to VF by manipulating the restitution curve slope. The transitions between solitary-spiral VT and multiple-spiral VF were plotted on a phase diagram relating core number N_c, restitution steepness as APD_o, and threshold V_{th} in order to conceptualise the structure of pertinent attractors underlying the dynamics of these distinct rhythms. In this model, a restitution curve slope $m > 1$ is a necessary, but not sufficient, condition for wave break progressing to fibrillation. Wave break occurs below a specific value of APD_o corresponding to a maximum slope greater than one. Above this critical APD_o, the number of waves N_c settles to a fixed value dependent on

initial conditions. Below this APD_0, the number of waves is highly dynamic and variable, suggesting a competition between wave break and coalescence that is particularly vigorous at the steepest restitution slopes. The former situation suggests the presence of a relatively simple stable attractor, while the latter suggests a complex strange attractor. The topology of dynamics at the transition is less clear. A macroscopic thermodynamic potential, governing changes in core number, was derived from a simple microstate stochastic model of wave break and coalescence. The transition from VT to VF resembles a second order phase transition.

A second major objective of this work was to study the body surface ECG signals originating from VT and VF, and determine the degree to which intracardiac dynamics might be inferred from these remote signals. Both the CML and ionic models show that ectopic and reentrant forms of VT can be difficult to distinguish using ECG signals alone. This is because dipole contributions to the ECG signals and body surface maps are dominated by similar spatial wave activity away from cores of the respective sources. Quantitative measures of spatiotemporal complexity of wave activity in two-dimensional tissue were applied to simulations of the simple CML model. It was hoped that these measures of complexity could be correlated with those derived from the corresponding ECG signals, and that inferences could be made about the underlying dynamics. The simplest correlation analysed was that between the dominant frequency of the ECG and the peak cycle length of the reentrant circuits. The correlation was not strong, however, largely because the ECG frequency spectra were not narrow-banded, but contained considerable energy dispersed at other frequencies, perhaps from harmonics related to the action potential shapes. The cycle length histograms were also quite broad-banded at steeper APD restitution. The most apparent difference in ECG features between VT and VF were the ranges of ECG amplitudes, as sampled around the heart on an equatorial ring. Amplitudes of VF were highly variable, but this variability was more evenly spread around the ECG leads, whereas VT amplitudes were generally higher, but the maxima and minima were more localized.

As the APD restitution curve was gradually steepened, by lowering the intercept APD_0 as a control parameter, abrupt transitions were seen in the dynamics of action potential trains at specific bifurcation points where there was a change in the periodicity or quasiperiodicity of APD. We were hopeful that these bifurcations in APD, dependent on restitution slope, would manifest in the spatiotemporal wave dynamics in the tissue, and that these transitions would also be detectable in the ECG patterns. Although evident in single cells in the CML model, clear abrupt transitions were not seen in the two-dimensional dynamics, despite the model being stripped to its simplest form in order to identify these critical points. These bifurcation points are probably quite sensitive to small changes or imperfections, particularly in regions susceptible to chaotic dynamics. It is still possible that bifurcation points might be identified in body surface ECG's under ideal conditions, but a continuous ionic model with higher time resolution will be required to help resolve this issue. Velocity restitution, missing in the CML model, may be important to instability, since it should compound wave front irregularities that are largely controlled by APD variability. It remains to be seen if ionic models can better show these transitions in the ECG. High-resolution body surface maps might contain features of these transitions that can be extracted by more powerful pattern analysis techniques, such as eigenvalue decomposition. Further work is needed to resolve these important issues.

While spiral waves are unstable at steep restitution slopes and break into VF, they can be stabilized if there is an inexcitable obstacle at the core. The introduction of an obstacle, however, changes the period of rotation, which becomes dependent on the obstacle circumference rather than the natural dynamics of the wave front at the core. Since this scenario represents one possible model of monomorphic VT, we were interested to see if decreasing the obstacle size could shorten the cycle length sufficiently to induce a bifurcation in APD, which would cause the regular spiral wave to become irregular. There might then be a transition to polymorphic VT in the ECG. Such a bifurcation in APD did occur at the tissue level, but the overall effect on the ECG was quite minimal. The dipole contributions from the irregular central region were evidently insufficient to

manifest over the stronger contributions from the regular wave behaviour beyond the core region. Polymorphic VT could not be produced by this mechanism.

Since the APD restitution curve appears to be a major determinant of cardiac stability, it would be highly desirable to have a means of measuring the restitution curve in patients in clinic or at the bedside. If techniques were available to do this noninvasively, the implications would be quite profound. It might become possible to quantify susceptibility to fibrillation in any given individual at any given time. The choice of antiarrhythmic drugs could be customized to individual patients, and the risk of fibrillation could be assessed and followed like a time series. Unfortunately there is not yet any means to determine this curve at the bedside. High resolution ECG's and body surface maps might contain information useful to this objective, but this problem has not been addressed.

A five-current ionic model of human ventricular cells was developed, and used to study ventricular fibrillation in a three-dimensional anisotropic heart model. This model proved to be an especially versatile computational tool, capable of simulating a variety of VF subtypes through manipulation of ionic conductances and time constants. Six specific cases of VF were examined by characterizing epicardial maps, ECG frequency spectra, wave size, and Lyapunov exponents. A classification scheme of VF was proposed based on wave stability and dominant ECG frequency. Sodium channel partial blockade was associated with larger wave size through prolongation of the mean diastolic interval. Calcium channel blockade flattened APD restitution, lowered dominant frequency of the ECG, and sharpened the frequency spectra. Potassium channel blockade prolonged APD, and caused wave condensation to more coarse VF. We were also able to simulate successful and unsuccessful monodomain electrical defibrillation, the mechanisms of which were consistent with Wiggers' total extinction hypothesis. The upper limit of vulnerability of shock strength was dependent on the location of critical points inducing rotors, the locations of which were dependent on the spatially decaying shock field.

Since this work is one of theoretical modelling and computer simulation, without corresponding experiments in real hearts, it is natural to question the validity of model

results. Since the heart is highly nonlinear, and therefore subject to sensitivity to initial conditions, it is not realistic to expect accurate time-domain prediction of activity. The prediction interval should depend on the magnitude of Lyapunov exponents, much like numerical weather prediction. Simulations are most useful in terms of qualitative results, and elucidation of dynamical mechanisms. Nevertheless, epicardial maps and space-time plots from the heart model were very similar to those reported in the literature, as obtained by using optical dyes. ECG frequency spectra of VF and the effects of drugs were also consistent. We are confident that the model predictions are reasonable, given the underlying assumptions, parameter sets involved, limited resolution, and idealized nature of the cellular elements and heart geometry.

Another criticism of the approach taken here might be that we did not attempt a formal inverse solution from VF electrocardiograms. In other words, given a set of body surface ECG signals of VF, we did not reconstruct the underlying intracardiac sources by formulating the transfer matrix and inverting it. It will be important to pursue this task to determine the degree to which VF activity can be resolved by ECGs alone, but at the present time there is no multiple lead ECG data of VF available suitable to this task. Animal models can provide this essential data.

14.2 Future Work

Future research will be focussed in several areas:

(1) Thermodynamic Model of Fibrillation. The mechanisms underlying wave break at steep APD restitution have been described in the CML model, but more work is needed to understand exactly how wave break is influenced by the spatial configuration of adjacent waves, and what features of these wave patterns are most important, in terms of propagation instability. Wave coalescence is also dependent on the spatial distribution and proximity of core points. A better theoretical description of coalescence is needed, related to more specific details of the probability distribution of core spacing and the

contributory role of core point meander. Mathematical methods or tools are needed for quantifying spatial patterns and spatiotemporal complexity beyond those described in this work, some of which have been recently developed in other fields of statistical physics. There is still considerable scope to advance the application of statistical mechanics to describing state changes, transient and equilibrium phenomena, and phase transitions in excitable media. All of these concepts can, in principle, be applied to ionic models of cardiac tissue, with the hope of achieving better resolution of these phenomena and improved physiological interpretation.

(2) Realistic Heart Geometry. The ionic model described here runs in a three-dimensional heart synthesized from truncated and smoothed ellipsoidal shells. This basic model remains useful for most theoretical purposes, but comparison of model simulations with experimentally measured high-resolution electrocardiograms and body surface potential maps will require that the model be run in a more realistically shaped human heart enclosed by a realistically shaped torso with accurate volume conductance properties. Such human heart and torso geometries already exist on file, and are readily accessible. Investigations involving sinus rhythm, bundle branch block, and intraventricular conduction defects will also require the addition of a His-Purkinje conduction system, the existence of which might also be a contributing factor to fibrillation induction. A network model of fibre geometry is presently available on file for installation, but will require relatively simple modifications to the SHV ionic model for application to Purkinje fibres.

(3) Repolarization Dynamics and T Wave Genesis. Repolarization phenomena are probably important determinants of cardiac stability. There are currently no whole-heart simulations employing ionic cellular models that produce satisfactory T waves, although simple models employing automata or Huygens propagation have been reported. As already demonstrated, the heart model described in this work is ideally suited to studying T waves, and a few examples have been simulated. More work is needed to determine the best combination of regional cellular ionic parameters, electrical coupling, and cell-type spatial distribution, including M cells, across the ventricular wall and throughout the myocardium. Faster exploration of candidate configurations and M cell distributions can

be carried out with the hybrid automaton model, and then applied to the ionic model when satisfactory configurations are found. There is no doubt that better T waves can be achieved with further work on this model. This objective should be pursued, particularly because there is sufficient theoretical reason to believe that subtle T wave changes might be important markers of incipient dysrhythmias or instability.

(4) Reentrant Dysrhythmias. One major advancement achieved by the ventricular model described here is the ability to simulate a variety of simple and complex reentrant dysrhythmias, including subtypes of VT and VF. It is difficult to experimentally validate these modelled phenomena because useful intracardiac mapping data appropriate for this purpose is relatively scarce. Body surface potential map libraries do exist for VT, and will need to be compared with the corresponding maps derived from model simulation. Recent innovations in clinical mapping technologies, such as basket and balloon electrode catheters, might also provide new data for improved model validation and calibration.

(5) Initiation of Dysrhythmias. VT and VF have been induced in the heart model by artificially-applied and contrived initial conditions, mainly for the pragmatic purpose of obtaining an established rhythm with minimal computation of transient behaviour. The tremendous flexibility of the model described here, in terms of ionic current control and substrate heterogeneity, make it ideally suited to simulating arrhythmogenic substrates. Little attention has been paid to studying the mechanistic routes taken to arrive at VT or VF physiologically, largely due to experimental difficulties. Perhaps of greatest practical importance, from a modelling point of view, is that ischemia can be simulated without difficulty by modifying external potassium concentrations, excitability, and intracellular coupling. The effect of these changes on the electrocardiograms, and the ability to induce dysrhythmias, will need to be explored.

(6) Spatiotemporal Complexity. Mathematical methods for measuring and quantifying wave patterns in space and time have been explored in this dissertation, having been applied mainly to the CML model, but also demonstrated in the whole-heart ionic model.

These metrics, which include entropy, correlation, frequency spectra, and Lyapunov exponents, can in principle be applied to a greater extent to the analysis of wave patterns in the three-dimensional heart model. The numerical algorithms will obviously be more complicated owing to the three dimensional irregular geometry, and fibre anisotropy. Other mechanisms of wave instabilities might also become apparent, the discovery of which will require innovative mathematical perspectives and advanced computer graphics to aid in visualization and comprehension.

(7) Pharmacological Effects. Drugs remain the main tools in practice for preventing lethal dysrhythmias. The role of simulated drug effects that modify ionic currents will need to be explored further, specifically in terms of how spatiotemporal complexity of VT and VF are pharmacologically modified. To a certain extent, drugs act directly on the parameters of the mathematical equations pertaining to ionic channels. Progress in developing effective anti-arrhythmic drugs suitable for human use has been slow, with very few impressive pharmacological developments surviving to the clinical level within the past decade. This difficulty is probably due in part to the lack of a satisfactory coherent theory of what constitutes appropriate targets to prevent arrhythmogenesis. Theoretical models, such as those reported here, can play an important role in determining the essential characteristics that ideal drugs should have to be effective in the presence of various substrate properties.

(8) Restitution Dynamics. As described earlier, the APD restitution curve appears to play an important role in the transitions between VT and VF. We need to determine if and how the restitution curve can be measured clinically, and ideally do so with noninvasive body surface potential mapping. The effort invested in this pursuit will be considerable but, if successful, the rewards will be great if fibrillation susceptibility can be predicted or measured at the bedside or in clinic. It is not yet clear how this vital problem is best approached, but all of the modelling efforts described in this dissertation will be relevant as a theoretical foundation. Spontaneous or induced premature beats might provide one window into restitution dynamics at relatively short diastolic intervals. A combination of body surface mapping, signal averaged ECG's, advanced spatiotemporal pattern analysis,

nonlinear dynamics, and large-scale theoretical heart modelling will be required. Other theoretical concepts and technologies will need to be developed, or will be inspired according to the nature of the essential information required.

(9) Experimental Mapping. Electrocardiographic data on human ventricular fibrillation is typically confined to a few leads captured fortuitously during unexpected cardiac arrest. High-resolution body surface mapping over the torso has not been conducted during fibrillation in humans because VF cannot be predicted beforehand, and BSPM equipment is not generally available for clinical monitoring. It might be possible to obtain human data of VF in multiple leads during routine testing at the time of implantable defibrillator insertion. An experimental animal model, such as piglet or swine, would allow full body surface potential mapping to be conducted, along with some degree of intracardiac mapping during induced fibrillation and pharmacological manipulation. Such data is essential to calibrate theoretical heart models.

There is tremendous scope and exciting prospects for applying electrical heart models to many clinical problems, and there is grounding for optimism that practical solutions can be obtained. These theoretical models, and yet more powerful computer simulations that will evolve, will continue to play important roles in the quest to understand and reduce sudden cardiac deaths.

BIBLIOGRAPHY

1. Abildskov JA. The sequence of normal recovery of excitability in the dog heart. Circ 52:442-445; 1975

2. Abildskov JA, Burgess MJ, Millar K, Wyatt R, Baule G. The primary T wave - A new electrocardiographic waveform. Am Heart J 81:242-249; 1971

3. Adam DR, Smith JM, Akselrod S, Nyberg S, Powell AO, Cohen RJ. Fluctuations in T wave morphology and susceptibility to ventricular fibrillation. J Electrocardiol 17:209-218; 1984

4. Ahlers G, Behringer R. Evolution of turbulence for the Rayleigh-Bénard instability. Phys Rev Lett 40:712-721; 1978

5. Aidley DJ. The Physiology of Excitable Cells. 3rd Edition. Cambridge Univ. Press, 1989

6. Akiyama T. Intracellular recording of in situ ventricular cells during ventricular fibrillation. Am J Physiol 240:H465-H471; 1981

7. Akhtar M. Clinical spectrum of ventricular tachycardia. Circ 82:1561-1573; 1990

8. Aliev RR, Panfilov AV. Modeling of heart excitation patterns caused by a local inhomogeneity. J Theor Biol 181:33-40; 1996

9. Allen DG, Kentish JC. The cellular basis of the length-tension relation in cardiac muscle. J Mol Cell Cardiol 17:821-840; 1985

10. Allessie MA, Bonke FIM, Schopman FJG. Circus movement in rabbit atrial muscle as a mechanism of tachycardia. III The "leading circle" concept. Circ Res 41:9-18; 1977

11. Amos G, Wettwer E, Metzger F, Li Q, Mimmel HM, Ravens U. Differences between outward currents of human atrial and subepicardial ventricular myocytes. J Physiol 491:31-50; 1996

12. Antzelevitch C, Sicouri S. Clinical relevance of cardiac arrhythmias generated by afterdepolarizations: role of M cells in the generation of U waves, triggered activity, and torsade de pointes. J Am Coll Cardiol 23:259-277; 1994

13. Antzelevitch C, Sicouri S, Litovsky SH, Lukas A, et al. Heterogeneity within the ventricular wall: Electrophysiology and pharmacology of epicardial, endocardial, and M cells. Circ Res 69:1427-1449; 1991

14. Aranson I, Levine H, Tsimring L. Controlling spatiotemporal chaos. Phys Rev Lett 72:2561-2564; 1994

15. Arisi G, Macchi E, Baruffi S, Spaggiara S, Taccardi. Potential fields on the ventricular surface of the exposed dog heart during normal excitation. Circ Res 52:706-715; 1983

16. Ashihara T, Namba T, Ito M, Kinoshita M, Nakazawa K. The dynamics of vortex-like reentry wave filaments in three-dimensional computer models. J Electrocardiol 32(Suppl):129-138; 1999

17. Ashihara T, Suzuki T, Namba T, Inagaki M, et al. Simulated electrocardiogram of spiral wave reentry in a mathematical ventricular model. In: Yamaguchi T (Ed.). Clinical Application of Computational Mechanics to the Cardiovascular System. Springer, 2000.

18. Aste T, Szeto KY, Tam WY. Statistical properties and shell analysis in random cellular structures. Phys Rev E 54:5482-5492; 1996

19. Bak P. How Nature Works. Springer, New York. 1996

20. Baker GL, Gollub JP. Chaotic Dynamics: An Introduction. Cambridge Univ Press, 1996.

21. Baker LC, London B, Choi BR, Koren G, Salama G. Enhanced dispersion of repolarization and refractoriness in transgenic mouse hearts promotes reentrant ventricular tachycardia. Circ Res 86:396-407; 2000

22. Bailly P, Mouchoniere M, Benita JP, Camillera L, Vassort G, Lorente P. Extracellular K^+ dependence of inward rectification kinetics in human left ventricular cardiomyocytes. Circ 98:2753-2759; 1998

23. Banville I, Gray RA, Ideker RE, Smith WM. Shock-induced figure-of-eight reentry in the isolated rabbit heart. 85:742-752; 1999

24. Bar M, Eiswirth M. Turbulence due to spiral break up in a continuous excitable medium. Phys Rev E 48:R1635-R1637; 1993

25. Bardou AL, Auger PM, Birkui PJ, Chasse JL. Modeling cardiac electrophysiological mechanisms: From action potential genesis to its propagation in myocardium. Crit Rev Biomed Eng 24:141-221; 1996

26. Bardy GH, Ungerleider RM, Smith WM, Ideker RE. A mechanism of torsades de pointes in a canine model. Circ 67:52-59; 1983

27. Bashir Y, Thomsen PE, Kingma JH, et al. Electrophysiologic profile and efficacy of intravenous dofetilide (UK-68,798), a new class III antiarrhythmic drug, in patients with sustained monomorphic ventricular tachycardia. Am J Cardiol 76:1040-1044; 1995

28. Bayes de Luna A, Coumel P, Leclercq JF. Ambulatory sudden cardiac death: mechanisms of production of fatal arrhythmia on the basis of data from 157 cases. Am Heart J 117:151-159; 1989

29. Bayly PV, KenKnight BH, Rogers JM, Johnson EE, Ideker RE, Smith WM. Spatial organization, predictability, and determinism in ventricular fibrillation. Chaos 8:103-115; 1998

30. Bayly PV, Johnson EE, Wolf PD, Greenside HS, Smith WM, Ideker RE. A quantitative measurement of spatial order in ventricular fibrillation. J Cardiovasc Electrophysiol 4:533-546; 1993

31. Beaumont J, Davidenko N, Davidenko JM, Jalife J. Spiral waves in two-dimensional models of ventricular muscle: Formation of a stationary core. Biophys J 75:1-14; 1998

32. Beeler GW, Reuter H. Reconstruction of the action potential of ventricular myocardial fibres. J Physiol 268:177-210; 1977

33. Berenfield O, Jalife J. Purkinje-muscle reentry as a mechanism of polymorphic ventricular arrhythmias in a 3-dimensional model of the ventricles. Circ Res 82:1063-1077; 1998

34. Bernus O, Wilders R, Zemlin CW, Verschelde H, Panfilov AV. A computationally efficient electrophysiological model of human ventricular cells. Am J Physiol 282:H2296-H2306; 2003

35. Bers DM, Perez-Reyes E. Ca channels in cardiac myocytes: Structure and function in Ca influx and intracellular Ca release. Cardiovasc Res 42:339-360; 1999

36. Best E. Null space in the Hodgkin-Huxley equations; a critical test. Biophys J 27:87-104; 1979

37. Beuckelmann DJ, Nabauer M, Erdmann E. Characteristics of calcium current in isolated human ventricular myocytes from patients with terminal heart failure. J Mol Cell Cardiol 23:929-937; 1991

38. Beuckelmann DJ, Nabauer M, Erdmann E. Alterations of K^+ currents in isolated human ventricular myocytes from patients with terminal heart failure. Circ Res 73:379-85; 1993

39. Biktashev VN, Holden AV. Design principles of a low voltage cardiac defibrillator based on the effect of feedback resonant drift. J Theor Biol 169:101-112; 1994

40. Biktashev VN, Holden AV. Reentrant waves and their elimination in a model of ventricular tissue. Chaos 8:48-56; 1998

41. Bing RJ (Ed.). Cardiology: The Evolution of the Science and the Art. Harwood Acad. Publ., Switzerland, 1992.

42. Bollacker KD, Alferness CA, Smith WM, Ideker RE. A cellular automata model of electrical propagation in cardiac tissue. Proc. Computers in Cardiology, IEEE 1990

43. Bonometti C, Hwang C, Hough D, Lee JJ, Fishbein MC, Karagueuzian HS, Chen PS. Interaction between strong electrical stimulation and reentrant wave fronts in canine ventricular fibrillation. Circ Res 77:407-416; 1995

44. Bosch RF, Gaspo R, Busch AE, Lang Hj, Li GR, Nattel S. Effects of the chomanol 293B, a selective blocker of the slow component of the delayed rectifier K^+ current on the repolarization in human and guinea pig ventricular myocytes. Cardiovasc Res 38:441-450; 1998

45. Boyett MR, Jewell BR. A study of the factors responsible for rate-dependent shortening of the action potential in mammalian ventricular muscle. J Physiol 285:359-380; 1978

46. Braaksma B, Grasman J. Critical dynamics of the Bonhoeffer-Van der Pol equation and its chaotic response to periodic stimulation. Physica D 68:265-280; 1993

47. Brown C, Griffin R, Ligten PV. Median frequency - a new parameter for predicting defibrillation success rate. Ann Emerg Med 20:787-789; 1991

48. Brown C, Dzwonczyk R. Signal analysis of the human electrocardiogram during ventricular fibrillation: Frequency and amplitude parameters as predictors of successful countershock. Ann Emerg Med 27:184-188; 1996

49. Brown C, Dzwonczyk R, Martin DR. Physiologic measurement of the ventricular fibrillation ECG signal: estimating ventricular fibrillation duration. Ann Emerg Med 22:70-74; 1993

50. Brugada J, Boersma L, Kirchhof C, Zetelaki Z, Abdollah H, Konings K, Allessie M. Sustained monomorphic ventricular tachycardia: A single electrocardiographic expression of different patterns of reentry. PACE 14:1943-1946; 1991

51. Burgess MJ, Green LS, Millar K, Wyatt R, Abildskov JA. The sequence of normal ventricular recovery. Am Heart J 84:660-669; 1972

52. Burton FL, Cobbe SM. Dispersion of ventricular repolarization and refractory period. Cardiovasc Res 50:10-23; 2001

53. Bustamante JO, McDonald TF. Sodium currents in segments of human heart cells. Science 220:320-321; 1983

54. Cabo C, Pertsov AM, Baxter WT, Davidenko JM, Gray RA, Jalife J. Wave-front curvature as a cause of slow conduction and block in isolated cardiac muscle. Circ Res 75:1014-1028; 1994

55. Cabo C, Pertsov AM, Davidenko JM, Baxter WT, Gray RA, Jalife J. Vortex shedding as a precursor of turbulent electrical activity in cardiac muscle. Biophys J 70:1105-11; 1996

56. Callaway CW, Sherman LD, Scheatzle MD, Memegazzi. Scaling structure of electrocardiographic waveform during prolonged ventricular fibrillation in swine. PACE 23:180-191; 2000

57. Cardiac Arrhythmia Suppression Trial (CAST) Investigators. Preliminary report: Effect of encainide and flecainide on mortality in a randomized trial of arrhythmia suppression after myocardial infarction. NEJM 321:406-412; 1989

58. Carlisle EJF, Allen JD, Bailey A, Kernohan WG, Anderson J, Adgey AAJ. Fourier analysis of ventricular fibrillation and synchronization of DC countershocks in defibrillation. J Electrocardiol 21:337-343; 1988

59. Carlisle E, Allen J, Kernohan W. Fourier analysis of ventricular fibrillation of varied etiology. Eur Heart J 11:173-181; 1990

60. Carmeliet E. Cardiac ionic currents and acute ischemia: From channels to arrhythmias. Physiol Rev 79:917-1017; 1999

61. Casti JL. Complexification: Explaining a Paradoxical World Through the Science of Surprise. HarperCollins Publishers, 1995

62. Chang CM, Wu TJ, Zhou S, Doshi RN, Lee MH, Ohara T, et.al. Nerve sprouting and sympathetic hyperinnervation in a canine model of atrial fibrillation produced by prolonged right atrial pacing. Circ 103:22-25; 2000

63. Chapman RA, Fry CH. An analysis of the cable properties of frog ventricular myocardium. J Physiol (Lond) 283:263-282; 1978

64. Chattipakorn N, Rogers JM, Ideker RE. Influence of post-shock epicardial activation patterns on initiation of ventricular fibrillation by upper limit of vulnerability shocks. Circ 101:1329-1336; 2000

65. Chaudhry GM, Haffajee CI. Antiarrhythmic agents and proarrhythmia. Crit Care Med 28 (Suppl):N158-N164; 2000

66. Chen PS, Shibata N, Dixon EG. Activation during ventricular defibrillation in open-chest dogs: evidence of complete cessation and regeneration of ventricular fibrillation after unsuccessful shocks. J Clin Invest 77:810-823; 1986

67. Chen PS, Wolf PD, Dixon WE, Danieley ND, Frazier DW, Smith WM, Ideker RE. Mechanism of ventricular vulnerability to single premature stimuli in open-chest dogs. Circ Res 62:1191-1209; 1988

68. Chorro F, Guerroro J, Canoves J, Martinez-Sober M. Quantification of the modification in the dominant frequency of ventricular fibrillation under ischemia and perfusion: An experimental study. PACE 21:1716-1723; 1998

69. Cha YM, Birgersdotter-Green U, Wolf PL, Peters BB, Chen PS. The mechanism of termination of reentrant activity in ventricular fibrillation. Circ Res 74:495-506; 1994

70. Chay TR, Lee YS. Phase resetting and bifurcation in the ventricular myocardium. Biophys J 47:641-651; 1985

71. Chay TR, Rinzel J. Bursting, beating, and chaos in an excitable membrane model. Biophy J 47:357-366; 1985

72. Chen PS, Chen LS, Cao JM, Sharifi B, Karagueuzian HS, Fishbein MC. Sympathetic nerve sprouting, electrical remodeling and the mechanisms of sudden cardiac death. Cardiovasc Res 50:409-416; 2001

73. Chen PS, Garfinkel A, Weiss JN, Karagueuzian HS. Computerized mapping of fibrillation in normal ventricular myocardium. Chaos 8:127-136; 1998

74. Chen PS, Shibata N, Dixon EG, Wolf P, Danieley ND, Smith WM, Ideker RE. Activation during ventricular defibrillation in open-chest dogs. Evidence of complete cessation and regeneration of ventricular fibrillation after unsuccessful shocks. J Clin Invest 77:810-823; 1986

75. Chen PS, Wolf PD, Dixon EG, Danieley, Smith WM, Ideker RE. Mechanism of ventricular vulnerability in open-chest dogs. Circ Res 62:1191-1209; 1988

76. Chen PS, Wolf PD, Ideker RE. Mechanism of cardiac defibrillation: a different point of view. Circ 84:913-919; 1991

77. Chen PS, Shibata N, Dixon EG, Martin RO, Ideker RE. Comparison of the defibrillation threshold and the upper limit of ventricular vulnerability. Circ 73:1022-1028; 1986

78. Chialvo DR, Jalife J. Non-linear dynamics of cardiac excitation and impulse propagation. Nature 330:749-752; 1987

79. Chialvo DR, Michaels DC, Jalife J. Supernormal excitability as a mechanism of chaotic dynamics of activation in cardiac Purkinje fibres. Circ Res 66:525-545; 1990

80. Childers RJ. New and neglected aspects of atrial depolarization and repolarization. 30: Suppl 44; 1998

81. Chorro FJ, Canoves J, Guerrero J, Mainar L, Sanchis J, Such L, Lopez-Merino V. Alteration of ventricular fibrillation by flecainide, verapamil, and sotalol: an experimental study. Circ 101:1606-1615; 2000

82. Chorro FJ, Guerrero J, Canoves J, et al. Quantification of the modifications in the dominant frequency of ventricular fibrillation under conditions of ischemia and reperfusion. PACE 21:1716-1723; 1998

83. Chorro FJ, Sanchez-Munoz JJ, Sanchis J, Cortina J, Bataller M, Guerrero J, Espi J, Ruiperez JA, Lopez-Merino V. Modifications in the evolution of the dominant frequency in ventricular fibrillation induced by amiodarone, diltiazem, and flecainide: an experimental study. J Electrocardiol 29:319-26; 1996

84. Chudin E, Goldhaber J, Garfinkel A, Weiss JN, Kogan B. Intracellular Ca^{++} dynamics and the stability of ventricular fibrillation. Biophys J 77:2930-2941; 1999

85. Chung TH, Kim S. Spatio-temporal dynamics in a locally coupled Ginzburg-Landau oscillator chain with time delay. In: Kim S, Lee KJ, Sung W (Eds.) Stochastic Dynamics and Pattern Formation in Biological and Complex Systems. American Institute of Physics, 2000

86. Clancy CE, Rudy Y. Linking a genetic defect to its cellular phenotype in a cardiac arrhythmia. Nature 400:566-569; 1999

87. Claydon FJ, Pilkington TC, Tang ASL, Morrow MN, Ideker RE. A volume conductor model of the thorax for the study of defibrillation fields. IEEE Trans Biomed Eng 35:981-992; 1988

88. Clayton R, Higham D, Murray A, Campbell R. Self-terminating ventricular fibrillation. J Am Coll Cardiol 19:265A(abstr.); 1992

89. Clayton R, Murray A, Campbell W. Changes in the surface electrocardiogram during the onset of spontaneous ventricular fibrillation in man. Eur Heart J 15:184-188; 1994

90. Clayton R, Murray A, Campbell W. Analysis of the body surface ECG measured in independent leads during ventricular fibrillation in humans. PACE 18:1876-1881; 1995

91. Clements CJ. Nonlinear wave propagation in an anisotropic medium. M.Sc. Thesis. Dalhousie University, 1996.

92. Clerc L. Directional differences of impulse spread in trabecular muscle from mammalian heart. J Physiol (Lond) 255:335-346; 1976

93. Colatsky TJ, Follmer CH, Starmer CF. Channel specificity in antiarrhythmic drug action: mechanism of potassium channel block and its role in suppressing and aggravating cardiac arrhythmias. Circ 82:2235-2242; 1990

94. Colatsky TJ, Tsien RW. Sodium channels in rabbit cardiac Purkinje fibres. Nature 278:265-8; 1979

95. Colli Franzone P, Guerri L, Tentoni S. Mathematical modeling of the excitation process in myocardial tissue: influence of fibre rotation on wave front propagation and potential field. Math Biosci 101:155-235; 1990

96. Cooley JW, Dodge FA. Digital computer solutions for excitation and propagation of the nerve impulse. Biophys J 6:583-599; 1966

97. MacFarlane PW, Lawrie, TDV (Eds.). Comprehensive Electrocardiology: Theory and Practice in Health and Disease. Pergamon Press, New York.

98. Coraboeuf E, Nargeot J. Electrophysiology of human cardiac cells. Cardiovasc Res 27:1713-1725; 1993

99. Coullet P, Gil L, Lega J. Defect-mediated turbulence. Phys Rev Lett 62:1619-1622; 1989

100. Courtemanche M. Complex spiral wave dynamics in a spatially distributed ionic model of cardiac electrical activity. Chaos 6:579-600; 1996

101. Courtemanche M, Ramirez RJ, Nattel S. Ionic targets for drug therapy and atrial fibrillation-induced electrical remodeling: Insights from a mathematical model. Cardiovasc Res 42:477-489; 1999

102. Courtemanche M, Skaggs W, Winfree AT. Stable three-dimensional action potential circulation in the FitzHugh-Nagumo model. Physica D 41:173-182; 1990

103. Cowan JC. Epicardial repolarisation sequence and T wave configuration. Br Heart J 59:85; 1988

104. Cox Jl, Jacquiss RD, Schuessler RB, Boineau JP. Modification of the maze procedure for atrial flutter and atrial fibrillation. J Thorac Cardiovasc Surg 110:485-495; 1995

105. Cranefield PF. Action potentials, afterpotentials, and arrhythmias. Circ Res 41:415-423; 1977

106. Creamer JE, Nathan AW, Camm AJ. The proarrhythmic effects of antiarrhythmic drugs. Am Heart J 114:397-406; 1987

107. Cressie N. Statistics of Spatial Data. Wiley and Sons, New York. 1993

108. Cross MC, Hohenberg PC. Pattern formation outside of equilibrium. Rev Mod Phys 65:851-1091; 1993

109. Cummins RO, Austin D. The frequency of occult ventricular fibrillation masquerading as a flat line in prehospital cardiac arrest. Ann Emerg Med 17:813-817; 1988

110. Dahl CF, Ewy GA, Warner ED. Myocardial necrosis from direct current countershock: Effect of paddle size and time interval between discharge. Circ 50:956-961; 1974

111. Daido H. Strange waves in coupled-oscillator arrays: mapping approach. Phys Rev Lett 78:1683-1687; 1997

112. D'Alnoncourt CN, Zierhut W, Luderitz B. Torsades de pointes tachycardia: Reentry or focal activity? Br Heart J 48:213-216; 1982

113. Damle RS, Kanaan NM, Robinson NS, Ge YZ, Goldberger JJ, Kadish AH. Spatial and temporal linking of epicardial activation directions during ventricular fibrillation in dogs: Evidence for underlying organization. Circ 86:1547-1558; 1992

114. Damle R, Robinson N, Ge Y. Electrical activation during ventricular fibrillation in the subacute and chronic phases of healing canine myocardial infarction. Circ 92:535-545; 1995

115. Dangman KH, Danilo P, Hordof AJ, Mary-Rabine L, Reder RF, Rosen MR. Electrophysiologic characteristics of human ventricular and Purkinje fibres. Circ 65:362-368; 1982

116. Davidenko JM, Kent PF, Chialvo DR, Michaels DC, Jalife J. Sustained vortex-like waves in normal isolated ventricular muscle. Proc Natl Acad Sci 87:8785-8789; 1990

117. Davidenko JM, Levi RJ, Maid G, Elizari MV, Rosenbaum MB. Rate dependence and supernormality in excitability of guinea pig papillary muscle. Am J Physiol 259:H290-299; 1990

118. Davidenko JM, Pertsov AM. Understanding ventricular fibrillation by quantifying the complexity of activation patterns. J Cardiovasc Electrophysiol 11:1372-1374; 2000

119. Davidenko JM, Pertsov AV, Salomonsz R, Baxter WT, Jalife J. Stationary and drifting spiral waves of excitation in isolated cardiac muscle. Nature 355:349-351; 1992

120. Davidenko JM, Pertsov AV, Salomonsz R, Baxter WT, Jalife J. Spiral waves of excitation underlie reentrant activity in isolated cardiac muscle. Circ Res 72:631-650; 1993

121. Deale OC, Lerman BB. Intrathoracic current flow during transthoracic defibrillation in dogs. Circ Res 67:1405-1419; 1990

122. DeBakker JM, VanCapelle FJ, Janse MJ, VanHemel NM. Macroreentry in the infarcted human heart: The mechanism of ventricular tachycardias with a "focal" activation pattern. J Am Coll Cardiol 18:1005-1014; 1991

123. DeBoer, S. On the fibrillation of the heart. J Physiol 54:400-409; 1921

124. Decker W, Pesch W, Weber A. Spiral defect chaos in Rayleigh-Bénard convection. Phys Rev Lett 73:648-651; 1994

125. Delgado C, Steinhaus B, Delmar M, Chialvo DR, Jalife J. Directional differences in excitability and margin of safety for propagation in sheep ventricular epicardial muscle. Circ Res 67:97-110; 1990

126. Denton TA, Diamond GA, Helfant RH, Khan S, Karagueuzian HS. Fascinating rhythm: A primer on chaos theory and its application to cardiology. Am Heart J 120:1419-1440; 1990

127. Denton TA, Diamond GA. Can the analytic techniques of nonlinear dynamics distinguish periodic, random and chaotic signals? Comput Biol Med 21:243-264; 1991

128. Dessertenne F. La tachycardie ventriculaire a deux fovers opposes variables. Arch Mal Coeur 59:263-272; 1966

129. Dewdney AK. The hodgepodge machine makes waves. Sci Am: 104-107; Aug 1988

130. DiDiego JM, Sun ZQ, Antzelevitch C. Ito and action potential notch are smaller in left versus right ventricular epicardium. Am J Physiol 271:H548-H561; 1996

131. DiFrancesco D, Noble D. A model of cardiac electrical activity incorporating ionic pumps and concentration changes. Phil Trans R Soc Lond B 307:353-398; 1985

132. DiFrancesco D, Zaza A. The cardiac pacemaker current I_f. J Cardiovasc Electrophysiol 3:334-344; 1992

133. Dillon S, Morad M. A new laser scanning system for measuring action potential propagation in the heart. Science 214:453-456; 1981

134. Ditto WL, Rauseo SN, Spano ML. Experimental control of chaos. Phys Rev Lett 65:3211-3213; 1990

135. Doherty PW, McLaughlin PR, Billingham M. Cardiac damage produced by direct current countershock applied to the heart. AM J Cardiol 43:225-232; 1979

136. Dorian P, Cass D, Schwartz B, Cooper R, Gelaznikas R, Barr A. Amiodarone as compared with lidocaine for shock-resistant ventricular fibrillation. NEJM 346:884-890; 2002

137. Dorian P, Newman D. Tedisamil increases coherence during ventricular fibrillation and decreases defibrillation energy requirements. Cardiovasc Res 33:485-494; 1997

138. Dorian P, Philippon F. The management of acute ventricular tachycardia and fibrillation. In: The Canadian Cardiovascular Society Consensus Conference on Prevention of Sudden Death from Ventricular Arrhythmia. October 1999

139. Downar E, Harris L, Mickelborough LL, Shaikh N, Parson ID. Endocardial mapping of ventricular tachycardia in the intact human ventricle: evidence for a reentrant mechanism. J Am Coll Cardiol 11:783-791; 1988

140. Downar E, Saito J, Doig JC, Chen TC, et. al. Endocardial mapping of ventricular tachycardia in the intact human ventricle: III. Evidence of multi-use reentry with spontaneous and induced block in portions of reentrant path complex. J Am Coll Cardiol 25:1591-1600; 1995

141. Draper MH, Mya-Tu M. A comparison of the conduction velocity in cardiac tissues of various mammals. Q J Exp Physiol 44:91-109; 1959

142. Drouhard JP, Roberge FA. Revised formulation of the Hodgkin-Huxley representation of the sodium current in cardiac cells. Comput Biomed Res 20:333-350; 1987

143. Durrer D, van Dam RT, Freud GE, Janse MJ, Meijler FL, Arzbaecher RC. Total excitation of the isolated human heart. Circ :899-912; 1970

144. Ebihara L, Johnson EA. Fast sodium current in cardiac muscle: A quantitative description. Biophys J 32:779-790; 1980

145. Efimov IR, Aguel F, Cheng Y, et al. Virtual electrode polarization in the far field: implications for external defibrillation. Am J Physiol H1055-H1070; 2000

146. Efimov IR, Krinsky VI, Jalife J. Dynamics of rotating vortices in the Beeler-Reuter model of cardiac tissue. Chaos Solitons Fract 5:513-526; 1995

147. Eisenberg MS, Horwood BT, Cummins RO, Reynolds-Haertle R, Hearne TR. Cardiac arrest and resuscitation: a tale of 29 cities. Ann Emerg Med 19:179-186; 1990

148. Eisenberg M, Mengert TJ. Cardiac resuscitation. NEJM 344:1304-1313; 2001

149. Ehlert FA, Goldberger JJ. Cellular and pathophysiogical mechanisms of ventricular arrhythmias in acute ischemia and infarction. PACE 20:966-974; 1997

150. Einthoven W. The galvanometric registration of the human electrocardiogram, likewise a review of the use of the capillary electrometer in physiology. Pfleugers Arch 99:472-480; 1903

151. Elharrar V, Surawicz B. Cycle length effect on restitution of action potential duration in dog cardiac fibres. Am J Physiol 244:H782-H792; 1983

152. El-Sherif N, Turitto G. The long QT syndrome and torsade de pointes. PACE 22:91-110; 1999

153. Guidelines for Cardiopulmonary Resuscitation and Emergency Cardiovascular Care: International Consensus on Science. Circ 102(Suppl):I-1 - I-384; 2000

154. Ermentrout GB, Edelstein-Keshet L. Cellular automata approaches to biological modeling. J Theor Biol 160:97-133; 1993

155. Escande D, Coloumbe A, Faives J, Deroubaix E, Coraboeuf E. Two types of transient outward currents in adult human atrial cells. Am J Physiol 21:H142-H148; 1987

156. Euler DE. Cardiac alternans: mechanisms and pathological significance. Cardiovasc Res 42:583-590; 1999

157. Evans FG, Ideker RE, Gray RA. Effect of shock-induced changes in transmembrane potential on reentrant waves and outcome during cardioversion of isolated rabbit hearts. J Cardiovasc Electrophysiol 13:1118-27; 2002

158. Ewy GA, Dahl CF, Zimmerman M, Otto C. Ventricular fibrillation masquerading as ventricular standstill. Crit Care Med 9:392; 1981

159. Fast VG, Kleber AG. Role of wave front curvature in propagation of cardiac impulse. Cardiovasc Res 33:258-271; 1997

160. Feder J. Fractals. Plenum Press, New York, 1988.

161. Fei H, Hanna MS, Frame LH. Assessing the excitable gap in reentry by resetting.: Implications for tachycardia termination by premature stimuli and antiarrhythmic drugs. Circ 94:2268-2277; 1996

162. Feigenbaum MJ, Quantitative universality for a class of nonlinear transformations. J Stat Phys 19:25-52; 1978

163. Feng J, Yue L, Wang Z, Nattel S. Ionic mechanisms of regional action potential heterogeneity in the canine right atrium. Circ Res 83:541-551; 1998

164. Fenton F, Karma A. Fibre-rotation-induced vortex turbulence in thick myocardium. Phys Rev Lett 81:481-484; 1998

165. Fenton F, Karma A. Vortex dynamics in three-dimensional continuous myocardium with fibre rotation: Filament instability and rotation. Chaos 8:20-47; 1998

166. Fermini B, Wang Z, Duan D, Nattel S. Differences in rate dependence of transient outward current in rabbit and human atrium. Am J Physiol 263:H1747-1754; 1992

167. Fernandez-Teran MA, Hurle JM. Myocardial fibre architecture of the human heart ventricles. Anat Rec 204:137-147; 1982

168. Firek L, Giles WR. Outward currents underlying repolarization in human atrial myocytes. Cardiovasc Res 30:31-38; 1995

169. Fishler MG, Thakor NV. A computer model study of the ventricular fibrillation vulnerable window: Sensitivity to regional conduction depressions. Ann Biomed Eng 22:610-621; 1994

170. FitzHugh R. Thresholds and plateaus in the Hodgkin-Huxley nerve equations. J Gen Physiol 43:867-886; 1959

171. FitzHugh R. Impulses and physiological states in theoretical models of nerve membrane. Biophys J 1:455-466; 1961

172. Flegel, KM. From delirium cordis to atrial fibrillation: Historical development of a disease concept. Ann Intern Med 122:867-873; 1995

173. Flowers NC, Horan LG. Body surface potential mapping. In: Zipes D, Jalife J (eds.) Cardiac Electrophysiology: From Cell to Bedside. 2nd Ed., WB Saunders, Philadelphia 1995

174. Fodden DI, Crosby AC, Channer KS. Doppler measurement of cardiac output during cardiopulmonary resuscitation. J Accid Emerg Med 13: 379-82; 1996

175. Fox CC, Hutchins GM. The architecture of the human ventricular myocardium. Johns Hopkins Med J 130:289-299; 1972

176. Fox JJ, McHarg JL, Gilmour RF. Ionic mechanics of electrical alternans. Am J Physiol 282:H516-H530; 2002

177. Frame LH, Simson MB. Oscillations of conduction, action potential duration, and refractoriness; a mechanism of spontaneous termination of reentrant tachycardias. 78:1277-1287; 1988

178. Franz MR. Long-term recording of monophasic action potentials from human endocardium. Am J Cardiol 51:1629-1634; 1983

179. Franz MR, Bargheer K, Costard-Jackle A, Miller C, Lichtien P. Human ventricular repolarization and T wave genesis. Prog Cardiovasc Dis 33:369-384; 1991

180. Franz MR, Bargheer K, Rafflenbeul W, Haverich A, Licthlen PR. Monophasic action potential mapping in human subjects with normal electrocardiograms: direct evidence for the genesis of the T wave. Circ 75:379-386; 1987

181. Franz MR, Burkhoff D, Yue DT, Sagawa K. Mechanically induced action potential changes and arrhythmia in isolated and in situ canine hearts. Cardiovasc Res 23:213-223; 1989

182. Franz MR, Swerdlow CD, Liem LB, Schaefer J. Cycle length dependence of human action potential duration in vivo. J Clin Invest 82:972-979; 1988

183. Frazier DW, Wolf PD, Wharton JM, Tang ASL, Smith WM, Ideker RE. Stimulus-induced critical point: Mechanisms for electrical initiation of reentry in normal canine myocardium. J Clin Invest 83:1039-1052; 1989

184. Freudenberg J, Schiemann T, Tiede U, Hohne KH. Simulation of cardiac excitation patterns in a three-dimensional anatomical heart atlas. Comput Biol Med 30:191-205; 2000

185. Furukawa T, Kimura S, Furukawa N, Bassett AL, Myerberg RJ. Potassium rectifier currents differ in myocytes of endocardial and epicardial origin. Circ Res 70:91-103; 1992

186. Furukawa T, Rozanski JJ, Nogami A. Time-dependent risk of and predictors for cardiac arrest recurrence in survivors of out-of-hospital cardiac arrest with chronic coronary artery disease. Circ 80:599-608; 1989

187. Garrey WE. The nature of fibrillary contraction of the heart - its relation to tissue mass and form. Am J Physiol 33:397-414; 1913

188. Gaiser J. Future catheter designs for interventional electrophysiology. In: Singer I (Ed.) Interventional Electrophysiology. Williams and Wilkins, Baltimore. 469-542; 1997

189. Garfinkel A, ChenPS, Walter DO,Karagueuzian HS, Kogan B. Quasiperiodicity and chaos in cardiac fibrillation. J Clin Invest 99:305-314; 1997

190. Garfinkel A, Spano ML, Ditto WL, Weiss JN. Controlling cardiac chaos. Science 257:1230-1235; 1992

191. Garrey WE. The nature of fibrillary contraction of the heart - its relation to tissue mass and form. Am J Physiol 33;397-414; 1914

192. Gerhardt M, Schuster H, Tyson JJ. A cellular automaton model of excitable media including curvature and dispersion. Science 247:1563-1566; 1990

193. Geselowitz DB, Schmitt OH. Electrocardiography. In: Biological Engineering. Schwan HP (Ed). McGraw-Hill, 333-390; 1969

194. Gettes LS, Morehouse N, Surawicz B. Effect of premature depolarization on the duration of action potentials in Purkinje and ventricular fibres of the moderator band of the pig heart. Circ Res 30:55-66; 1972

195. Gilmour RF, Heger JJ, Prystowsky EN, Zipes DP. Cellular electrophysiologic abnormalities of diseased human ventricular myocardium. Am J Cardiol 51:137-144; 1983

196. Giroud SD, Pastore JM, Laurita KR, Gregory KW, Rosenbaum DS. Optical mapping in a new guinea pig model of ventricular tachycardia reveals mechanisms for a multiple wavelengths in a single reentrant circuit. Circ 93:603-613; 1996

197. Glass L, Hunter P, McCulloch A. Theory of Heart. Springer-Verlag, New York, 1991

198. Glass L, Mackey MC. From Clocks to Chaos: The Rhythms of Life. Princeton Univ Press, 1988.

199. Gleick J. Chaos: Making A New Science. Penguin, 1988

200. Goldberger AL, Bhargava V, West BJ, Mandell AJ. Some observations on the question: is ventricular fibrillation chaos? Physica D 19:282-289; 1986

201. Gollub JP, Benson SV. Many routes to turbulent convection. J Fluid Mech 100:449-470; 1980

202. Gonnella G, Orlandini E, Yeomans JM. Spinodal decomposition to a lamellar phase: effects of hydrodynamic flow. Phys Rev Lett 78:1695-1698; 1997

203. Gollub JP, Brunner TO, Danly BG. Periodicity and chaos in coupled nonlinear oscillators. Science 200:48-50; 1978

204. Goryachev A, Kapral R. Structure of complex-periodic and chaotic media with spiral waves. Phys Rev E 54:5469-5481; 1996

205. Grassberger P, Procaccia I. Measuring the strangeness of strange attractors. Physica 9D:189-208; 1983

206. Grassberger P, Procaccia I. Estimation of Kolmogorov entropy for a chaotic signal. Phys Rev A 28:2591-2599; 1983

207. Gray RA, Jalife J. Self-organized drifting spiral waves as a mechanism for ventricular fibrillation. Circ 94:Suppl I-48; 1996

208. Gray RA, Jalife J, Panfilov A. Mechanisms of cardiac fibrillation. 270:1222-1223; 1995

209. Gray RA, Jalife J, Panfilov A, Baxter WT, Cabo C, Davidenko JM, Pertsov AM Nonstationary vortexlike reentrant activity as a mechanism of polymorphic ventricular tachycardia in the isolated rabbit heart. Circ 91:2454-2469; 1995

210. Gray RA, Pertsov AM, Jalife J. Spatial and temporal organization during ventricular fibrillation. Nature 392:75-78; 1998

211. Gray WA, Capone RJ, Most AS. Unsuccessful emergency medical resuscitation - are continued efforts in the emergency department justified? NEJM 325:1393-1398; 1991

212. Greenberg JM, Hastings SP. Spatial patterns for discrete models of diffusion in excitable media. SIAM J Appl Math 34:515-523; 1978

213. Greenbaum RA, Ho SY, Gibson DG, Becker AE, Anderson RH. Left ventricular fibre architecture in man. Br Heart J 45:248-263; 1981

214. Guevara MR, Glass L. Phase locking, period doubling bifurcation and chaos in a mathematical model of a periodically driven oscillator: A theory for the entrainment of biological oscillators and the generation of cardiac dysrhythmias. J Math Biol 14:1-23; 1982

215. Guevara MR, Glass L, Shrier A. Phase locking, period-doubling bifurcations, and irregular dynamics in periodically stimulated cardiac cells. Science 214:1350-1353; 1981

216. Guha SK, Khan MR, Tandon SN. Electrical field distribution in the human body. Phys Med Biol 18:712-720; 1973

217. Han J, Moe GK. Nonuniform recovery of excitability in ventricular muscle. Circ Res 14:44-50; 1964

218. Harris L, Downar E, Shaikh N, Parson ID. Activation sequence of ventricular tachycardia: Endocardial and epicardial mapping studies in the human ventricle. J Am Coll Cardiol 10:1040-1047; 1987

219. Harrison L, Ideker RE, Smith WM, Klein GJ, Kasell J, Wallace AG, Gallagher JJ. The sock electrode array: A tool for determining global epicardial activation during unstable arrhythmias. PACE 3:531-535; 1980

220. Harumi K, Burgess MJ, Abildskov JA. Theoretic model of the T wave. Circ 34:657-668; 1966

221. Hastings HM, Fenton FH, Evans SJ, Hotomaroglu O, Geetha J, Gittelson K, Nilson J, Garfinkel A. Alternans and the onset of ventricular fibrillation. Phys Rev E 62:4043-4048; 2000

222. Hartman H, Tamayo P. Reversible cellular automata and chemical turbulence. Physica D 45:293-306; 1990

223. Haverkamp W, Breithardt G, Camm JA, Janse MJ. The potential for QT prolongation and pro-arrhythmia by non-anti-arrhythmic drugs: clinical and regulatory implications. Cardiovasc Res 47:219-233; 2000

224. Hayashi C. Nonlinear Oscillations in Physical Systems. McGraw-Hill, New York, 1964

225. Henriquez CS. Simulating electrical behaviour of cardiac tissue using the bidomain model. Crit Rev Biomed Eng 21:1-77; 1993

226. Henriquez CS, Plonsey R. Simulation of propagation along a cylindrical bundle of cardiac tissue - I: Mathematical formulation. IEEE Trans Biomed Eng 37:850-860; 1990

227. Heidbuchel H, Vereecke J, Carmiliet E. The electrophysiological effects of acetylcholine in single human atrial cells. J Mol Cell Cardiol 19:1207-1219; 1987

228. Hering HE. Analysis of pulsus irregularis perpetuus. Prag Med Wocenschr. 28:377-81; 1903

229. Hodgkin AL, Huxley AF. A quantitative description of membrane current and its application to conductance and excitation in nerve. J Physiol 117:500-544; 1952

230. Hoffman BF, Rosen MR. Cellular mechanisms for cardiac arrhythmias. Circ Res 49:1-15; 1981

231. Hofstadter DR. Gödel, Escher, Bach: An Eternal Golden Braid. Basic Books, 1999

232. Holden AV (Ed.) Chaos. Princeton Univ. Press, 1986.

233. Holden AV, Poole MJ, Tucker JV. An algorithmic model for the mammalian heart: propagation, vulnerability, re-entry and fibrillation. Int J Bifurcation Chaos 6:1623-1636; 1996

234. Holmes P. Poincaré, celestial mechanics, dynamical systems, and chaos. Phys Rep 193:137-163; 1990

235. Horacek BM, Clements JC. The inverse problem of electrocardiography: A solution in terms of single and double-layer sources on the epicardial surface. Math Biosci 144:119-154; 1997

236. Hoyt RH, Cohen ML, Saffit JE. Distribution and three-dimensional structure of intercellular junctions in canine myocardium. Circ Res 64:565-574; 1989

237. Hren R. A realistic model of the human ventricular myocardium: Application to the study of ectopic activation. Ph.D. Thesis. Dalhousie University, 1996

238. Huang K. Statistical Mechanics. 2nd Ed. Wiley and Sons, New York. 1987

239. Huikuri HV, Castellanos A, Myerburg RJ. Sudden death due to cardiac arrhythmias. NEJM 345:1473-1482; 2001

240. Hunter PJ, McNaughton PA, Noble D. Analytical models of propagation in excitable cells. Prog Biophys Molec Biol 30:99-144; 1975

241. Hutchins GM, Bulkley BH, Moore GW, Piasio MA, Lohr FT. Shape of the human cardiac ventricles. Am J Cardiol 41:646-654; 1978

242. Huzar RJ. Basic Dysrhythmias: Interpretation and Management. C.V. Mosby, St. Louis, 1988

243. Hwang J, KenKnight BH, Rollins DL, Smith WM, Ideker RE. Ventricular defibrillation with triphasic waveforms. Circ 101:1324-1328; 2000

244. Ideker RE, Hillsley RE, Wharton JM. Shock strength for the implantable defibrillator: Can you have too much of a good thing? PACE 15:841-844; 1992

245. Ikeda T, Yashima M, Uchida T, et al. Attachment of meandering reentrant wave fronts to anatomical obstacles in the atrium: role of the obstacle size. Circ Res 81:753-764; 1997

246. Inoue H, Murakawa Y, Toda I. Epicardial activation patterns of torsades de pointes in canine hearts with quinidine-induced long QT interval but without myocardial infarction. Am Heart J 111:1080-1087; 1986

247. Iost N, Virag L, Opincariu M, Szecsi J, Varro A, Papp JG. Delayed rectifier potassium current in undiseased human ventricular myocytes. Cardiovasc Res 40:508-515; 1998

248. Irvine LA, Jafri MS, Winslow RL. Cardiac sodium channel Markov model with temperature dependence and recovery from inactivation. Biophys J 76:1868-1885; 1999

249. Ito H, Glass L. Spiral break-up in a new model of discrete excitable media. Phys Rev Lett 66:671-674; 1991

250. Ivanchenko YM, Lisyansky AA. Physics of Critical Fluctuations. Springer-Verlag, New York, 1995

251. Jacobson JT, Johnson D, Horvath G, Goldberger J, Kadish A. Effect of underlying heart disease on the frequency content of ventricular fibrillation in the dog heart. PACE 23:243-252; 2000

252. Jalife J. Ventricular fibrillation: mechanisms of initiation and maintenance. Ann Rev Physiol 62:25-49; 2000

253. Jalife J, Gray RA, Morley GE, Davidenko JM. Self-organization and the dynamical nature of ventricular fibrillation. Chaos 8:79-93; 1998

254. Jais P, Haissaguerre M, Shah DC, Chouairi S, Gencel L, Hocini M, Clementy J. A focal source of atrial fibrillation treated by discrete radiofrequency ablation. Circ 95:572-576; 1997

255. Janicki JS, Weber KT, Gochman RF, Shroff S, Geheb FJ. Three-dimensional myocardial and ventricular shape: a surface representation. Am J Physiol 241:H1-H11; 1981

256. Janse MJ. The premature beat. Cardiovasc Res 26:89-100; 1992

257. Janse MJ. Vulnerability to ventricular fibrillation. Chaos 8:149-156; 1998

258. January CT, Chau V, Makielski JC. Triggered activity in the heart: cellular mechanisms of early after-depolarizations. Eur Heart J (Suppl) 12:4-9; 1991

259. Jensen JH, Christiansen PL, Scott AC. Chaos in the Beeler-Reuter system for the action potential of ventricular myocardium. Physics D 13:269-277; 1984

260. Jones JL, Jones RE. Improved defibrillator wave from safety factor with biphasic waveforms. Am J Physiol 245:H60-H65; 1983

261. Joyner RW, Westerfield M, Moore JW, Stockbridge N. A numerical method to model excitable cells. Biophys J 22:155-170; 1978

262. Kac M. Can we hear the shape of a drum? Am Math Mon 73-II:1-23; 1966

263. Kaneko K. Pattern dynamics in spatiotemporal chaos: Pattern selection, diffusion of defect and pattern competition intermittency. Physica D 34:1-41; 1989

264. Kaneko K. Spatiotemporal chaos in one and two dimensional coupled map lattices. Physica D 37:60-82; 1989

265. Kaneko K. Spatiotemporal intermittency in coupled map lattices. Prog Theor Phys 74:1033-1044; 1985

266. Kaneko K. Lyapunov analysis and information flow in coupled map lattices. Physica D 23:436-447; 1986

267. Kaneko K, Akutsu Y. Phase transitions in two-dimensional stochastic cellular automata. J Phys A 19:L69-L75; 1986

268. Kannel WB, Abbott RD, Savage DD. Epidemiological features of chronic atrial fibrillation: the Framingham Heart Study. NEJM 306:1018-1022; 1991

269. Kaplan DT. The dynamics of cardiac electrical instability. Ph.D. Thesis. Harvard University, 1989.

270. Kaplan DT, Smith JM, Saxberg BEH, Cohen RJ. Nonlinear dynamics in cardiac conduction. Math Biosci 90:19-48; 1988

271. Kapral R. Pattern formation in two-dimensional arrays of coupled, discrete-time oscillators. Phys Rev A 31:3868-3879; 1985

272. Kapral R, Oppo GL. Competition between stable states in spatially-distributed systems. Physica D 23:455-463; 1986

273. Karagueuzian HS, Chen PS. Fibrillation and defibrillation: the odd couple. J Cardiovasc Electrophysiol 11:642-644; 2000

274. Karma A. Spiral break up in model equation of action potential propagation in cardiac tissue. Phys Rev Lett 71:1103-1106; 1993

275. Karma A. Electrical alternans and spiral wave break up in cardiac tissue. Chaos 4:461-472; 1994

276. Kasmacher-Leidinger H, Schmid-Schonbein H. Complex dynamic order in ventricular fibrillation. J Electrocardiol 27:287-299; 1994

277. Keane D, Zhou L, Ruskin J. Catheter ablation for atrial fibrillation. Semin Intervent Cardiol 2:251-265; 1997

278. Keener JP. The effect of gap junction distribution on defibrillation. Chaos 8:175-187; 1998

279. Kleber AG. Resting membrane potential, extracellular potassium activity, and intracellular sodium activity during acute global ischemia in isolated perfused guinea pig hearts. Circ Res 52:442-450; 1983

280. Kleber AG, Fast V. Molecular and cellular aspects of re-entrant arrhythmias. Basic Res Cardiol 92: Suppl I:111-119; 1997

281. Kim S, Lee KJ, Sung W (Eds.). Stochastic Dynamics and Pattern Formation in Biological and Complex Systems. American Institute of Physics. Melville, N.Y. 1999

282. Kim YH, Yashima Y, Wu TJ, Doshi R, Chen PS, Karagueuzian HS. Mechanism of procainamide-induced prevention of spontaneous wave break during ventricular fibrillation. Circ 100:666-674; 1999

283. Klevecz RR, Bolen J, Duran O. Self-organization in biological tissues: analysis of asynchronous and synchronous periodicity, turbulence and synchronous chaos emergent in coupled chaotic arrays. Int J Bifurc Chaos 2:941-953; 1992

284. Kodama I, Kamiya K, Toyama J. Amiodarone: ionic and cellular mechanisms of action of the most promising class III agent. Am J Cardiol 84:20R-28R; 1999

285. Kogan BY, Karplus WJ, Billett BS, Pang AT, Karagueuzian HS, Khan SS. The simplified FitzHugh-Nagumo model with action potential duration restitution: effects on 2D wave propagation. Physica D 50:327-340; 1991

286. Koller ML, Riccio ML, Gilmour RF. Dynamic restitution of the action potential during electrical alternans and ventricular fibrillation. Am J Physiol H1635-1642; 1998

287. Konarzewska H, Peeters GA, Sanguinetti MC. Repolarizing K^+ currents in nonfailing human hearts. Circ 92:1179-1187; 1995

288. Koumi S, Backer CL, Arentzen CE. Characterization of inwardly rectifying K^+ channel in human cardiac myocytes. Circ 92:164-174; 1995

289. Kralios FA, Millar CK, Kralios AC. Role of heart mass in the developmental changes of ventricular fibrillation threshold and spontaneous defibrillation in young dogs. J Dev Physiol 19:119-124; 1993

290. Kramer JB, Saffitz JE, Witkowski FX, Corr PB. Intramural reentry as a mechanism of ventricular tachycardia during evolving canine myocardial infarction. Circ Res 56:736-754; 1985.

291. Krinsky V, Pumir A. Models of defibrillation of cardiac tissue. Chaos 8:188-203; 1998

292. Kroll MW. A minimal model of the single capacitor biphasic defibrillation waveform. PACE 17:1782-1792; 1994

293. Kroll MW, Lehmann MH. Implantable Cardioverter Defibrillator Therapy: The Engineering-Clinical Interface. Kluwer Acad Publ. Norwell, Mass. 1996

294. Kuck KH, Ernst S, Cappato R. Nonfluoroscopic endocardial catheter mapping of atrial fibrillation. J Cardiovasc Electrophysiol 9:S57-S62; 1998

295. Kudenchuk PJ, Cobb LA, Copass MK. Amiodarone for resuscitation after out-of-hospital cardiac arrest due to ventricular fibrillation. NEJM 341:871-878; 1999

296. Kuo CS, Munakata K, Reddy CP, Surawicz B. Characteristics and possible mechanism of ventricular arrhythmia dependent on the dispersion of action potential durations. Circ 67:1356-1367; 1983

297. Kwan YY, Fan W, Hough D. The effects of procainamide on the characteristics of functional reentry in canine ventricular fibrillation. 97:1828-1836; 1998

298. Lacroix D, Extramiana F, Delfaut P, Adamantidis M. Factors affecting epicardial dispersion of repolarization: a mapping study in the isolated porcine heart. Cardiovasc Res 41:563-574; 1999

299. Lammers WJ, Schalij MJ, Kirchhof CJ, Allessie MA. Quantification of spatial inhomogeneity in conduction and initiation of reentrant atrial arrhythmias. Am J Physiol 259:H1254-H1263; 1990

300. Landau DP, Binder K. A Guide to Monte Carlo Simulations in Statistical Physics. Cambridge Univ Press, 2000

301. Lander P, Berbari EJ. Principles and signal processing techniques of the high-resolution electrocardiogram. Prog Cardiovasc Dis 35:169-188; 1992

302. Langton CG. Computation at the edge of chaos: phase transitions and emergent computation. Physica D 42:12-37; 1990

303. Larsen MP, Eisenberg MS, Cummins RO, Hallstrom AP. Predicting survival from out-of-hospital cardiac arrest: A graphic model. 22:1652-1658; 1993

304. Lauwerier HA. One-dimensional iterative maps. In: Holden AV (Ed.) Chaos. Princeton Univ Press, 1986.

305. LeGrand B, Hatem S, Deroubaix E, Couetil JP, Coraboeuf E. Depressed transient outward and calcium currents in dilated human atria. Cardiovasc Res 28:548-556; 1994

306. Lee JJ, Kamjoo K, Hough D, Hwang C, Fan W, Fishbein MC, Bonometti C, Ikeda T, Karagueuzian HS, Chen PS. Reentrant wave fronts in Wiggers' stage II ventricular fibrillation: characteristics and mechanisms of termination and spontaneous regeneration. Circ Res 78:660-675; 1996

307. Lee RJ, Liem LB, Cohen TJ, Franz MR. Relation between repolarization and refractoriness in the human ventricle: cycle length dependence and effect of procainamide. J Am Coll Cardiol 19:614-618; 1992

308. Leon LJ, Horacek BM. Computer model of excitation and recovery in the anisotropic myocardium. I. Rectangular and cubic arrays of excitable elements. J. Electrocardiol 24:1-16; 1991

309. Leon LJ, Horacek BM. Computer model of excitation and recovery in the anisotropic myocardium. II. Excitation in the simplified left ventricle. J. Electrocardiol 24:17-31; 1991

310. Leon LJ, Roberge FA. Directional differences of action potential propagation in cardiac muscle: a model study. Circ Res 69:378-395; 1991

311. Levine JH, Massumi A, Scheinman MM. Intravenous amiodarone for recurrent sustained hypotensive ventricular tachyarrhythmias. J Am Coll Cardiol 27:67-75; 1996

312. Lewis T. Notes upon the alternation of the heart. Q J Med 4:141-144; 1911

313. Lewis T. Observations upon flutter and fibrillation IV. Impure flutter: theory of circus movement. Heart 7:293-346; 1920

314. Lewis TJ, Guevera MR. Chaotic dynamics in an ionic model of the propagated cardiac action potential. J Theor Biol 146:407-432; 1990

315. Li GR, Feng J, Yue L, Carrier M, Nattel S. Evidence for two components of delayed rectifier K^+ current in human ventricular myocytes. Circ Res 78:689-696; 1996

316. Li GR, Nattel S. Properties of human atrial I_{Ca} at physiological temperatures and relevance to action potential. Am J Physiol 272:H227-H235; 1997

317. Li GR, Yang B, Feng J, Bosch RF, Carrier M, Nattel S. Transmembrane I_{Ca} contributes to rate-dependent changes of action potentials in human ventricular myocytes. Am J Physiol 276:H98-H106; 1999

318. Li H,Easley A, Windle J, Samoil D, D, Barrington W. The mean ventricular fibrillation cycle length: A potentially useful parameter for programming implantable cardioverter defibrillators. PACE 21:1789-1794; 1998

319. Li W, Packard NH, Langton CG. Transition phenomena in cellular automata rule space. Physica D 45:77-94; 1990

320. Lind DA. Applications of ergodic theory and sofic systems to cellular automata. Physica 10D:36-44; 1984

321. Lindblad DS, Murphey CR, Clark JW, Giles WR. A model of the action potential and underlying membrane currents in a rabbit atrial cell. Am J Physiol 271:H1666-H1696; 1996

322. Litovsky SH, Antzelevitch C. Transient outward current prominent in canine ventricular epicardium but not endocardium. Circ Res 62:116-126; 1988

323. Liu DW, Gintant GA, Antzelevitch C. Ionic bases for electrophysiological distinctions among epicardial, midmyocardial, and endocardial myocytes from the free wall of the canine left ventricle. Circ Res 72:671-687; 1993

324. Liu DW, Antzelevitch C. Characteristics of the delayed rectifier current (I_{Kr} and I_{Ks}) in canine ventricular epicardial, midmyocardial, and endocardial myocytes. Circ Res 76:351-365; 1995

325. Liu S, Rasmusson RL. Hodgkin-Huxley and partially coupled inactivation models yield different voltage dependence of block. Am J Physiol 272:H2013-2022; 1997

326. Lorenz EN. Deterministic nonperiodic flow. J Atmosph Sci 20:130-141; 1963

327. Lorz U. Statistics for the Poisson-Voronoi tesselation. In: Titterington DM (Ed) Complex Stochastic Systems and Engineering. Clarendon Press, Oxford, 1995

328. Lukas A, Antzelevitch C. Differences in the electrophysiological response of canine ventricular epicardium and endocardium to ischemia: role of the transient outward current. Circ 88:2903-2915; 1993

329. Luo CH, Rudy L. A model of the ventricular cardiac action potential. Circ Res 68:1501-1526; 1991

330. Luo CH, Rudy L. A dynamic model of the cardiac ventricular action potential. I. Simulations of ionic currents and concentration changes. Circ Res 74:1071-1096; 1994

331. Luo CH, Rudy L. A dynamic model of the cardiac ventricular action potential. II. Afterdepolarizations, triggered activity, and potentiation. Circ Res 74:1097-1113; 1994

332. Malik M, Camm AJ. Possible pathophysiology of torsades evaluated by a realistic heart computer model. Cardiovasc Res 20:436-444; 1986

333. Mandapati R, Asano Y, Baxter WT, Gray R, Davidenko J, Jalife J. Quantification of effects of global ischemia on dynamics of ventricular fibrillation in isolated rabbit heart. Circ 98:1688-1696; 1998

334. Mandelbrot BB. Fractal Geometry in Nature. W.H. Freeman, 1982

335. Markus M, Hess B. Isotropic cellular automaton for modelling excitable media. Nature 347:56-58; 1990

336. Marmont G. Studies on the axon membrane: I. A new method. J Cell Comp Physiol 34:351-382; 1949

337. Martin D, Brown C, Dzwonczyk R. Frequency analysis of the human swine electrocardiogram during ventricular fibrillation. Resuscitation 22:85-91; 1991

338. May RM. Simple mathematical models with very complicated dynamics. Nature 261:459-467; 1976

339. Mayer AG. Rhythmic pulsation in Scyphomedusae - II. Papers from the Tortugas Laboratory. Washington DC. 1908

340. McAllister RE, Noble D, Tsien RW. Reconstruction of the electrical activity of cardiac Purkinje fibres. J Physiol 251:1-59; 1975

341. McCoy BM, Wu TT. The Two-Dimensional Ising Model. Harvard Univ Press, 1973

342. McCullough JR, Baumgarten CM, Singer DH. Intra and extracellular potassium activities and the potassium equilibrium potential in partially depolarized human atrial cells. J Mol Cell Cardiol 19:477-486; 1987

343. McDonald JL. Coarse ventricular fibrillation presenting as asystole or very low amplitude ventricular fibrillation. Crit Care Med 10:790-791; 1982

344. McWilliam JA. Fibrillar contractions of the heart. J Physiol 8:296-310; 1887

345. Mecke KR. Morphological characterization of patterns in reaction-diffusion systems. Phys Rev E 53:4794-4800; 1996

346. Mewes T, Ravens U. L-type calcium currents of human myocytes from ventricle of non-failing and failing hearts and from atrium. J Mol Cell Cardiol 26:1307-1320; 1994

347. Miller WT, Geselowitz DB. Simulation studies of the electrocardiogram: I. The normal heart. Circ Res 43:301-314; 1978

348. Miller J, Tresch D, Horwitz L, Thomson BM. The precordial thump. Ann Emerg Med 13:791-794; 1984

349. Min X, Mehra R. Finite element analysis of defibrillation fields in a human torso model for ventricular defibrillation. Prog Biophys Mol Biol 69:353-386; 1998

350. Mines GP. On dynamic equilibrium in the heart. J. Physiol 46:349-383; 1913

351. Mitchell RH, Bailey AH, Anderson J. Cellular automaton model of ventricular fibrillation. IEEE Trans BME 39:253-259; 1992

352. Moe GK, Reingholdt WC, Abildskov JA. A computer model of atrial fibrillation. Am Heart J 67:200-220; 1964

353. Moosvi AR, Goldstein S, Medendorp SV. Effect of empiric antiarrhythmic therapy in resuscitated out-of-hospital cardiac arrest victims with coronary artery disease. Am J Cardiol 65:1192-1197; 1990

354. Morady F, DiCarlo LA, Kroll RB, Baerman JM, deBuitleir MB. Acute and chronic effects of amiodarone on ventricular refractoriness, intraventricular conduction and ventricular tachycardia induction. J Am Coll Cardiol 7:148-157; 1986

355. Morgan JM, Cunningham D, Rowland E. Electrical restitution in the endocardium of the intact human right ventricle. Br Heart J 67:42-46; 1992

356. Morris JJ, Entman M, North WC, Kong Y, McIntosh H. The changes in cardiac output with reversion of atrial fibrillation to sinus rhythm. Circ 31:670-676; 1965

357. Moss AJ, Hall WJ, Cannom DS. Improved survival with an implantable defibrillator in patients with coronary disease at high risk for ventricular arrhythmias. NEJM 335:1933-1940; 1996

358. Murray A, Campbell RWF, Julian DG. Characteristics of the ventricular fibrillation waveform. Computers in Cardiology, IEEE Computer Society, Los Angeles, 1985

359. Muzikant AL, Henriquez CS. Validation of three-dimensional conduction models using experimental mapping: Are we getting closer? Prog Biophys Mol Biol 69:205-223; 1998

360. Myerburg RJ, Gelband H, Nilsson K, Castellanos A. et al. The role of canine superficial ventricular muscle fibres in endocardial impulse distribution. Circ Res 42:27-35; 1978

361. Myerburg RJ, Kessler KM, Castellanos A. Sudden cardiac death: epidemiology, transient risk, and interventional assessment. Ann Intern Med 119:1187-1197; 1993

362. Nabauer M, Beukelmann DJ. Regional differences in current density and properties of the transient outward current in human ventricular myocytes. Circ 88:Suppl I:I-89; 1993

363. Nabauer M, Beukelmann DJ, Erdmann E. Characteristics of transient outward current in human ventricular myocytes from patients with terminal heart failure. Circ Res 73:386-394; 1993

364. Nabauer M, Beukelmann DJ,Uberfurh P, Steinbeck G. Regional differences in current density and rate-dependent properties of the transient outward current in subepicardial and subendocardial myocytes of human left ventricle. Circ Res 93:168-177;1996

365. Naccarelli GV, Wolbrette DL, Luck JC. Proarrhythmia. Med Clin North Am 85:503-526; 2001

366. Nattel S. Antiarrhythmic drug classification. A critical appraisal of their history, present status, and clinical relevance. Drugs 41:672-701; 1991

367. Nattel S. Atrial electrophysiological remodeling caused by rapid atrial activation: Underlying mechanisms and clinical relevance to atrial fibrillation. Cardiovasc Res 42:298-308; 1999

368. Neilsen PMF, LeGrice IJ, Smaill BH, Hunter PJ. Mathematical model of geometry and fibrous structure of the heart. Am J Physiol 260:H1365-H1378; 1991

369. Nenonen J, Edens JA, Leon JL, Horacek BM. Computer model of propagated excitation in the anisotropic human heart: I. Implementation and algorithms. Comp in Cardiol, IEEE Computer Society Press, Los Alamitos, CA, 1991.

370. Nenonen J, Edens JA, Leon JL, Horacek BM. Computer model of propagated excitation in the anisotropic human heart: II. Simulation of extracardiac fields. Comp in Cardiol, IEEE Computer Society Press, Los Alamitos, CA, 1991.

371. Newman D, Dorian P, Feder-Elituv R. Isoproterenol antagonizes drug-induced prolongation of action potential duration in humans. Can J Physiol Pharmacol 71:755-760; 1993

372. Newton JC, Knisley SB, Zhou X, Pollard AE, Ideker RE. Review of mechanisms by which electrical stimulation alters the transmembrane potential. J Cardiovasc Electrophysiol 10:234-243; 1999

373. Nicolis G, Prigogine I. Exploring Complexity: An Introduction. W.H. Freeman, New York, 1989

374. Nikolic GR, Bishop RL, Singh JB. Sudden death recorded during Holter monitoring. Circ 66:218-225; 1982

375. Noble D. The surprising heart: A review of recent progress in cardiac electrophysiology. J Physiol 353:1-50; 1983

376. Noble D, Cohen IS. The interpretation of the T wave of the electrocardiogram. Cardiovasc Res 12:13-27; 1978

377. Nolasco JB, Dahlen RW. A graphic method for the study of alternation in cardiac action potentials. J Appl Physiol 25:191-196; 1968

378. Nygren A, Fiset C, Firek L, Clark JW, Lindblad DS, Clark RB, Giles WR. Mathematical model of an adult human atrial cell: The role of K^+ currents in repolarization. Circ Res 82:63-81; 1998

379. Ohara T, Ohara K, Cao JM, Lee MH, Fishbein MC, Mandel WJ, Chen PS, Karagueuzian HS. Increased wave break during ventricular fibrillation in the epicardial border zone of hearts with healed myocardial infarction. Circ 103:1465-1472; 2001

380. Olshausen KV, Witt T, Pop T, et. al. Sudden cardiac death while wearing a Holter monitor. Am J Cardiol 67:381-386; 1991

381. Okajima M, Fujino T, Kobayashi T, Yamada K. Computer simulation of the propagation process in excitation of the ventricles. Circ Res 23:203-211; 1968

382. Omichi C, Zhou S, Lee MH, Naik A, Chang CM, Garfinkel A, Weiss JN, Lin SF, Karagueuzian HS, Chen PS. Effects of amiodarone on wave front dynamics during ventricular fibrillation in isolated swine right ventricle. Am J Physiol 282:H1063-H1070; 2002

383. Ott E, Grebogi C, Yorke JA. Controlling chaos. Phys Rev Lett 64:1196-1199; 1990

384. Ouyang Q, Li R, Li G, Swinney HL. Dependence of Turing pattern wavelength on diffusion rate. J Chem Phys 102:2551-2555; 1995

385. Packard N, Wolfram S. Two-dimensional cellular automata. J Stat Phys 38:901-946; 1985

386. Packer DL, Munger TM, Johnson SB, Cragun KT. Mechanism of lethal proarrhythmia observed in the Cardiac Arrhythmia Suppression Trial: role of adrenergic modulation of drug binding. PACE 20:455-67; 1997

387. Panfilov AV. Modelling of reentrant patterns in an anatomical model of the heart. In: Panfilov AV and Holden A (Eds.) Computational Biology of the Heart. John Wiley and Sons 259-276; 1997.

388. Panfilov AV, Holden A (Eds.) Computational Biology of the Heart. John Wiley and Sons, 1997.

389. Panfilov AV. Spiral breakup as a model of ventricular fibrillation. Chaos 8:57-64; 1998

390. Panfilov A, Keener J. Re-entry in an anatomical model of the heart. Chaos 5:681-689; 1995

391. Pastore JM, Rosenbaum DS. Role of structural barriers in the mechanism of alternans-induced reentry. Circ Res 87:1157-1163; 2000

392. Patwardhan A, Moghe S, Wang K, Leonelli F. Frequency modulation within electrocardiograms during ventricular fibrillation. Am J Physiol 279:H825-H835; 2000

393. Pepe PE, Levine RL, Fromm RE, Curka PA, Clark PS, Zachariah BS. Cardiac arrest presenting with rhythms other than ventricular fibrillation: Contribution of resuscitative efforts toward total survivorship. Crit Care Med 21:1838-1843; 1993

394. Pereon V, Demolombe S, Baro I, Drouin E, Charpentier F, Escande D. Differential expression of KvLQT1 isoforms across the human ventricular wall. Am J Physiol 278:H1908-H1915; 2000

395. Pertsov AM, Davidenko JM, Salomonsz R, Baxter WT, Jalife J. Spiral waves of excitation underlie reentrant activity in isolated cardiac muscle. Circ Res 72:631-650; 1993

396. Pertsov AM, Ermakova EA, Panfilov AV. Rotating spiral waves in a modified FitzHugh-Nagumo model. Physica 14D:117-124; 1984

397. Peters NS, Coromilas PJ, Hanna MS, Josephson ME, Costeas C, Wit AL. Characteristics of the temporal and spatial excitable gap in anisotropic reentrant circuits causing sustained ventricular tachycardia. Circ Res 82:279-293; 1998

398. Peterson I. Newton's Clock: Chaos in the Solar System. W.H. Freeman, New York. 1993

399. Pieper CF, Pacifico A. Observations on the epicardial activation of the normal human heart. PACE 15:2295-2307; 1992

400. Pierce JR. An Introduction to Information Theory: Symbols, Signals, and Noise. Dover Publ., New York 1984.

401. Pinto JMB, Boyden PA. Electrical remodeling in ischemia and infarction. Cardiovasc Res 42:284-297; 1999

402. Plonsey R, Barr RC. A critique of impedance measurements in cardiac tissue. Ann Biomed Eng 14:307-322; 1986

403. Pogwizd SM, Corr PB. Reentrant and nonreentrant mechanisms contribute to arrhythmogenesis during early myocardial ischemia: results using three-dimensional mapping. Circ Res 61:352-371; 1987

404. Pogwitz SM, Hoyt RH, Saffitz JE, Corr PB, Cox JL, Cain ME. Reentrant and focal mechanisms underlying ventricular tachycardia in the human heart. Circ 86:1872-1887; 1992

405. Pratt CM, Francis MJ, Luck CR, Wyndham RR. Analysis of ambulatory electrocardiograms in 15 patients during spontaneous ventricular fibrillation with special reference to preceding arrhythmic events. J Am Coll Cardiol 2:789-797; 1983

406. Priebe L, Beuckelmann DJ. Simulation study of cellular electrical properties in heart failure. Circ Res 82:1206-1223; 1998

407. Prigogine I, Stengers I. Order Out of Chaos: Man's New Dialogue With Nature. Bantam Books, Toronto 1984.

408. Qu Z, Garfinkel A, Chen PS, Weiss JN. Mechanisms of discordant alternans and induction of reentry in simulated cardiac tissue. Circ 102:1664-70; 2000

409. Qu Z, Kil J, Xie F, Garfinkel A, Weiss JN. Scroll wave dynamics in a three-dimensional cardiac tissue model: roles of restitution, thickness, and fibre rotation. Biophys J 78:2761-2775; 2000

410. Qu Z, Weiss JN, Garfinkel A. Spatiotemporal chaos in a simulated ring of cardiac cells. Phys Rev Lett 78:1387-1390; 1997

411. Qu Z, Weiss JN, Garfinkel A. From local to global spatiotemporal chaos in a cardiac tissue model. Phys Rev E 61:727-732; 2000

412. Qu Z, Weiss JN, Garfinkel A. Cardiac electrical restitution properties and stability of reentrant spiral waves: a simulation study. Am J Physiol 276:H269-H283; 1999

413. Quan W, Rudy Y. Unidirectional block and reentry of cardiac excitation: a model study. Circ Res 66:367-382; 1990

414. Raeder EA, Rosenbaum DS, Bhasin R, Cohen RJ. Alternating morphology of the QRST complex preceding sudden death. NEJM 326:271-272: 1992

415. Ramanathan C, Rudy Y. Electrocardiographic imaging I: Effect of torso inhomogeneities on body surface electrocardiographic potentials. J Cardiovasc Electrophysiol 12:229-240; 2001

416. Rayleigh, Baron. The Theory of Sound. Reprinted. Dover, New York, 1945

417. Reek S, Klein HU, Ideker RE. Can catheter ablation in cardiac arrest survivors prevent ventricular fibrillation recurrence? PACE 20:1840-1859; 1997

418. Restivo M, Yin H, Caref EB, Patel AI. Reentrant arrhythmias in the subacute infarction period: the proarrhythmic effect of flecainide acetate on functional reentrant circuits. Circ 91:1236-1246; 1995.

419. Riccio ML, Koller ML, Gilmour RF. Electrical restitution and spatiotemporal organization during ventricular fibrillation. Circ Res 84:955-963; 1999

420. Roberts DE, Hersh LT, Scher AM. Influence of cardiac fibre orientation on wave front voltage, conduction velocity, and tissue resistivity in the dog. Circ Res 44:701-712; 1979

421. Rogers JM, Huang J, KenKnight BH, Smith WM, Ideker RE. Stationary reentrant circuits are rare during ventricular fibrillation in pigs. Circ 94:I-48; 1996

422. Rogers JM, Huang J, Pedoto RW, Walker RG, Smith WM, Ideker RE. Fibrillation is more complex in the left ventricle than in the right ventricle. J Cardiovasc Electrophysiol 11:1364-1371; 2000

423. Rogers JM, Huang J, Smith WM, Ideker RE. Incidence, evolution, and spatial distribution of functional reentry during ventricular fibrillation in pigs. Circ Res 84:945-954; 1999

424. Rosen MR, Cohen IS, Danilo P, Steinberg SF. The heart remembers. Cardiovasc Res 40:469-482; 1998

425. Rosenbleuth A, Garcia-Ramos J. Studies on flutter and fibrillation: influence of artificial obstacles on experimental auricular flutter. Am Heart J 33:677-684; 1947

426. Rosenbaum DS, Jackson LE, Smith JM, Garan H, Ruskin JN, Cohen RJ. Electrical alternans and vulnerability to ventricular arrhythmias. NEJM 330:235-241; 1994

427. Roth BJ. Electrical conductivity values used with the bidomain model of cardiac tissue. IEEE Trans Biomed Eng 44:326-328; 1997

428. Roth BJ, Krassowska W. The induction of reentry in cardiac tissue. The missing link: how electric fields alter transmembrane potential. Chaos 8:204-219; 1998

429. Rudy Y, Oster HS. The electrocardiographic inverse problem. CRC Crit Rev Biomed Eng 20:25-46; 1992

430. Rudy Y, Quan WL. A model study of the effects of the discrete cellular structure on electrical propagation in cardiac tissue. Circ Res 61:815; 1987

431. Ruiz E, Valentinuzzi ME. Heart weight affects spontaneous defibrillation but not ventricular fibrillation threshold. PACE 17: 2255-62; 1994

432. Ryder KM, Benjamin EJ. Epidemiology and significance of atrial fibrillation. Am J Cardiol 84:131R-138R; 1999

433. Sager PT, Nademanee K, Antimisiaris M, Pacifico A, Pruitt C, Godfrey R, Singh BN. Antiarrhythmic effects of selective prolongation of refractoriness. Circ 88:1072-1082; 1993

434. Sager PT, Uppal P, Follmer C, Antimisiaris M, Pruitt C, Singh BN. Frequency-dependent electrophysiological effects of amiodarone in humans. Circ 88:1063-1071; 1993

435. Sakakibara Y, Furukawa T, Singer DH, Jia H, et al. Sodium current in isolated human ventricular myocytes. Am J Physiol 265:H1301-H1309; 1993

436. Sakakibara Y, Wasserstrom JA, Furukawa T, Jia H, Arentzen CE, Hartz RS, Singer DH. Characterization of the sodium current in single human atrial myocytes. Circ Res 71:535-546; 1992

437. Sakmann B, Trube G. Conductance properties of single inwardly rectifying potassium channels in ventricular cells from guinea pig heart. J Physiol (Lond) 347:641-657; 1984

438. Salama G, Kanai AJ, Huang D, et al. Hypoxia and hypothermia enhance spatial heterogeneities of repolarization in guinea pig hearts: analysis of spatial autocorrelation of optically recorded action potential durations. J Cardiovasc Electrophysiol 9:164-183; 1998

439. Samet P. Hemodynamic sequelae of cardiac arrhythmias. Circ 47:399-405; 1973

440. Samie FH, Mandapati R, Gray RA, Watanabe Y, Zuur C, Beaumont J, Jalife J. A mechanism of transition from ventricular fibrillation to tachycardia: effect of calcium channel blockade on the dynamics of rotating waves. Circ Res 86:684-691; 2000

441. Sanguinetti MC, Jurkiewicz NK. Two components of cardiac delayed rectifier K^+ current. J Gen Physiol 96: 195-215; 1990

442. Sano T, Takayama N, Shimamoto T. Ventricular fibrillation studied by the microelectrode method. Circ Res 6:262-267; 1959

443. Sano T, Takayama N, Shimamoto T. Directional differences of conduction velocity in the cardiac ventricular syncytium studied by microelectrodes. Circ Res 6:41-46; 1958

444. Savino GV, Romanelli L, Gonzalez DL, Piro O, Valentinuzzi ME. Evidence for chaotic behaviour in driven ventricles. Biophys J 56:273-280; 1989

445. Schalij MJ, Lammers WJ, Rensma PL, Allessie MA. Anisotropic conduction and reentry in perfused epicardium of rabbit left ventricle. Am J Physiol 263:H1466-H1478; 1992

446. Schalij MJ, van Rugge P, Siezenga M, van der Velde ET. Endocardial activation of ventricular tachycardia in patients: First application of a 32-site bipolar mapping electrode catheter. Circ 98:2168-2179; 1998

447. Schmitt C, Brachmann J, Karch M, Waldecker B, et al. Reverse use-dependent effects of sotalol demonstrated by recording monophasic action potentials of the right ventricle. Am J Cardiol 68:1183-1187; 1991

448. Schroeder M. Fractals, Chaos, and Power Laws: Minutes From and Infinite Paradise. W.H. Freeman, New York, 1991

449. Schuster HG. Deterministic Chaos: An Introduction. 3rd Ed.VHC Publ. New York 1995

450. Selvester RH, Wagner NB, Wagner GS. Ventricular excitation during percutaneous transluminal angioplasty of the left anterior descending coronary artery. Am J Cardiol 62:1116-1121; 1988

451. Sepulveda NG, Roth BJ, Wikswo JP. Current injection into a two-dimensional anisotropic bidomain. Biophys J 55:987-999; 1989

452. Shaw RM, Rudy Y. Ionic mechanisms of propagation in cardiac tissue: Roles of the sodium and L-type calcium currents during reduced excitability and decreased gap junction coupling. Circ Res 81:727-741; 1997

453. Shibata N, Chen PS, Dixon WE, Wolf PD, Danieley ND, Smith WM, Ideker RE. Influence of shock strength and timing on induction of ventricular arrhythmias in dogs. Am J Physiol 255:H891-H901; 1988

454. Schlichting H. Boundary Layer Theory. McGraw-Hill, New York. 1979

455. Shimizu W. T wave alternans: from cell to clinical. J Cardiovasc Electrophysiol 12:428-430; 2001

456. Shrier A, Dubarsky H, Rosengarten M, Guevera MR, Nattel S, Glass L. Prediction of complex atrioventricular conduction rhythms in humans with use of the atrioventricular nodal recovery curve. Circ 76:1196-1205; 1987

457. Singh BN. Overview of trends in the control of cardiac arrhythmias: past and future. Am J Cardiol 84:3R-10R; 1999

458. The Sicilian Gambit: A new approach to classification of antiarrhythmic drugs based on their actions on arrhythmogenic mechanisms. Circ 84:1831-1851; 1991

459. Siregar P. An interactive 3D anisotropic cellular automata model of the heart. Comput Biomed Res 31:323-347; 1998

460. Siregar P. A cellular automata model of the heart and its coupling with a qualitative model. Comput Biomed Res 29:222-246; 1996

461. Smith JM, Cohen RJ. Simple finite-element model accounts for wide range of cardiac dysrhythmias. Proc Natl Acad Sci 81:233-237; 1984

462. Smith WM, Gallagher JJ. "Les torsades de pointes" an unusual ventricular arrhythmia. Ann Int Med 93:278-284; 1980

463. Snyders DJ. Structure and function of cardiac potassium channels. Cardiovasc Res 42:377-390; 1999

464. Solé R, Goodwin B. Signs of Life: How Complexity Pervades Biology. Basic Books, New York. 2000.

465. Solomon JC, Selvester RH. Simulation of measured activation sequence in the human heart. Am Heart J 85:518-524; 1973

466. Spach MS, Barr RC. Analysis of ventricular activation and repolarization from intramural and epicardial potential distributions for ectopic beats in the intact dog. Circ Res 37:830-843; 1975

467. Spach MS, Barr RC. Origin of epicardial ST-T wave potentials in the intact dog. Circ Res 39:475-487; 1976

468. Spach MS, Kootsey JM. The nature of electrical propagation in cardiac tissue. Am J Physiol 244:H3-H22; 1983

469. Spach MS, Miller WT, Geselowitz DB, Barr RC, et al. The discontinuous nature of propagation in normal canine cardiac tissue. Circ Res 48:39-54; 1981

470. Spear JF, Moore EN. The effect of changes in rate and rhythm on supernormal excitability in the isolated Purkinje system of the dog. Circ 50:1144-1149; 1974

471. Sperelakis N. Propagation mechanisms in heart. Ann Rev Physiol 41:441-457; 1979

472. Starmer CF. The cardiac vulnerable period and reentrant arrhythmias: targets of anti- and proarrhythmic processes. PACE 20:445-454; 1997

473. Starmer CF, Biktashev VN, Romashko DN, et al. Vulnerability in an excitable medium: analytical and numerical studies of initiating unidirectional propagation. Biophys J 65:1775-1787; 1993

474. Stevenson WG, Kha H, Sager P, Saxon LA. Identification of reentry circuit sites during catheter mapping and radiofrequency ablation of ventricular tachycardia late after myocardial infarction. Circ 88:1647-1670; 1993

475. Stoyan D, Stoyan H. Fractals, Random Shapes and Point Fields. Wily and Sons, New York. 1994

476. Streeter DD. Gross morphology and fibre geometry of the heart. In: Handbook of Physiology. The Cardiovascular System. Bethesda MD. Am Physiol Soc. Vol 1:61-112; 1979

477. Streeter DD, Hanna WT. Engineering mechanics for successive states in canine left ventricular myocardium. Circ Res 33:656-664; 1973

478. Streeter DD, Spotnitz HM, Patel DP, Ross J, Sonnenblick EH. Fibre orientation in the canine left ventricle during diastole and systole. Circ Res 24:339-347; 1969

479. Steill IG, Wells GA, Hebert PC, Laupacis A, Weitzmann BN. Association of drug therapy with survival in cardiac arrest: limited role of advanced cardiac life support drugs. Acad Emerg Med 2:264-273; 1995

480. Surawicz B. Ventricular Fibrillation. J Am Coll Cardiol 5:43B-54B; 1985

481. Surawicz B. Electrophysiological substrate of torsades de pointes: Dispersion of repolarization or early afterdepolarizations? J Am Coll Cardiol 14:172-184; 1989

482. Suzuki R. Electrochemical neuron model. Adv Biophys 9:115-156; 1976

483. Svozil K. Constructive chaos by cellular automata and possible sources of an arrow of time. Physica D 45:420-427; 1990

484. Swartz JF, Jones JL, Fletcher RD. Characterization of ventricular fibrillation based on monophasic action potential morphology in the human heart. Circ 87:1907-1914; 1993

485. Swerdlow CD, Fan W, Brewer JE. Charge-burping theory correctly predicts optimal ratios of phase durations for biphasic defibrillation waveforms. Circ 94:2278-2284; 1996

486. Taneja T, Goldberger J, Parker M. Reproducibility of ventricular fibrillation characteristics in patients undergoing implantable cardioverter defibrillator implantation. J Cardiovasc Electrophysiol 8:1209-1217; 1997

487. Tchou PJ, Lehmann MH, Dongas J, Mahmud R, Denker ST, Akhtar M. Effect of sudden acceleration on the human His-Purkinje system adaptation to refractoriness in a damped oscillatory pattern. Circ 73:920-929; 1986

488. Toledano JC, Toledano P. The Landau Theory of Phase Transitions. World Scientific, New Jersey, 1987

489. Thompson JMT, Stewart HB. Nonlinear Dynamics and Chaos. Wiley, New York, 1986

490. Toffoli T, Margolus N. Cellular Automata Machines. MIT Press, Cambridge, Mass. 1987

491. Tyson JJ, Keener JP. Spiral waves in a model of myocardium. Physica 29D:215-222; 1987

492. Uchida T, Yashima M, Gotoh M, Qu Z, Garfinkel A, Weiss JN, Fishbein MC, Mandel WJ, Chen PS, Karagueuzian HS. Mechanism of acceleration of functional reentry in the ventricle: effects of ATP-sensitive potassium channel opener. Circ 99:704-712; 1999

493. Uzunov DI. Introduction to the Theory of Critical Phenomena. World Scientific, New Jersey, 1993

494. Vaidya D, Morley GE, Samie FH, Jalife J. Reentry and fibrillation in the mouse heart: A challenge to the critical mass hypothesis. Circ Res 85:174-181; 1999

495. Valderrábano M, Kim YH, Yashima M, Wu TJ, Karagueuzian HS, Chen PS. Obstacle-induced transition from ventricular fibrillation to tachycardia in isolated swine right ventricles. J Am Coll Cardiol 36:2000-2008; 2000

496. Van Capelle FJL, Durrer D. Computer simulation of arrhythmias in a network of coupled excitable elements. Circ Res 47:454-466; 1980

497. Van der Pol B. On relaxation oscillations. Phil Mag 2:978-992; 1926

498. Van der Pol B, Van der Mark J. The heart beat considered as a relaxation oscillation, and an electrical model of the heart. Phil Mag 6;763-775;1928

499. Van Wagoner DR, Pond AL, Lamorgese M, Rossie SS, McCarthy PM, Nerbonne JM. Atrial L-type Ca^{2+} currents and human atrial fibrillation. Circ Res 85:428-436; 1999

500. Van Walraven C, Stiell IG, Wells GA, Herbert PC, Vandemheen K. OTAC Study Group. Do advanced cardiac life support drugs increase resuscitation rates from in-hospital cardiac arrest? Ann Emerg Med 32:544-553; 1998

501. Varro A, Nanasi PP, Lathrop DA. Potassium currents in isolated human atrial and ventricular cardiocytes. Acta Physiol Scand 149:133-142; 1993

502. Vassallo JA, Cassidy DM, Kindwall KE. Nonuniform recovery of excitability in the left ventricle. Circ 78:1365-1372; 1988

503. Veldkamp MW. Is the slowly activating component of the delayed rectifier current I_{Ks} absent from undiseased human ventricular myocardium? Cardiovasc Res 40: 433-435; 1998

504. Veldkamp MW, van Ginneken ACG, Opthof T, Bouman LN. Delayed rectifier channels in human ventricular myocytes. Circ 92:3497-3504; 1995

505. Verkerk AO, Veldkamp MW, deJonge N, Wilders R, VanGinneken A. Injury current modulates afterdepolarizations in single human ventricular cells. Cardiovasc Res 47:124-132; 2000

506. Verrier RL, Brooks WW, Lown B. Protective zone and the determination of vulnerability to ventricular fibrillation. Am J Physiol 234:H592-H596; 1978

507. Vichniac G. Simulating physics with cellular automata. Physica 10D:96-115; 1984

508. Vichniac GY, Tamayo P, Hartman H. Annealed and quenched inhomogeneous cellular automata. J Stat Phys 45:875-879; 1986

509. Vinet A, Roberge FA. The dynamics of sustained reentry in a ring model of cardiac tissue. Ann Biomed Eng 22:568-591;1994

510. Virag N, Blanc O, Kappenberger L. (Eds.) Computer Simulation and Experimental Assessment of Cardiac Electrophysiology. Futura Publ., Armonk, N.Y. 2001

511. Viswanathan PC, Rudy Y. Pause induced early afterdepolarizations in the long QT syndrome: A simulation study. Cardiovasc Res 42:530-542; 1999

512. Viswanathan PC, Shaw RM, Rudy Y. Effects of I_{Kr} and I_{Ks} heterogeneity on action potential duration and its rate dependence: A simulation study. Circ 99:2466-2474; 1999

513. Volders PG, Sipido KR, Carmeliet E, Spatjens RL. Repolarizing K^+ currents I_{to1} and I_{KS} are larger in right than left canine ventricular midmyocardium Circ 99:206-210; 1999

514. Volders PGA, Vos MA, Szabo B, et al. Progress in understanding of cardiac early afterdepolarizations and torsades de pointes: time to revise current concepts. Cardiovasc Res 46:376-392; 2000

515. Walcott GP, Knisley SB, Zhou X, Newton JC, Ideker RE. On the mechanisms of ventricular defibrillation. PACE 20:422-431; 1997

516. Waldo AL. Experimental models of atrial fibrillation - What have we learned? Semin Intervent Cardiol 2:195-201; 1997

517. Waldo AL, Camm AJ, deRuyter H. Effect of d-sotalol on mortality in patients with left ventricular dysfunction after recent and remote myocardial infarction. Lancet 348:416; 1996

518. Waller I, Kapral R. Spatial and temporal structure in systems of coupled nonlinear oscillators. Phys Rev A 30:2047-2055; 1984

519. Wang NC, Lee MH, Ohara T, Okuyama Y, Fishbein GA, Lin SF, Karagueuzian HS, Chen PS. Optical mapping of ventricular defibrillation in isolated swine right ventricles: demonstration of a postshock isoelectric window after near-threshold defibrillation shocks. Circulation 104:227-33; 2001

520. Wang PY, Xie P. Eliminating spatiotemporal chaos and spiral waves by weak spatial perturbations. Phys Rev E 61:5120-5123; 2000

521. Wang Z, Fermini B, Nattel S. Delayed rectifier outward current and repolarization in human atrial myocytes. Circ Res 73:276-285; 1993

522. Wang Z, Fermini B, Nattel S. Rapid and slow components of delayed rectifier current in human atrial myocytes. Cardiovasc Res 28:1540-1546; 1994

523. Watanabe M, Otani NF, Gilmour RF. Biphasic restitution of action potential duration and complex dynamics in ventricular myocardium. Circ Res 76:915-921; 1995

524. Watanabe M, Koller ML. Mathematical analysis of dynamics of cardiac memory and accommodation: theory and experiment 282:H1534-H1547; 2002

525. Watanabe Y, Gray RA, Mandapati R, Asano Y, Jalife J. Verapamil converts ventricular fibrillation into sustained monomorphic tachycardia in the isolated rabbit heart. PACE 20:1136; 1997

526. Waterman MS. Some applications of information theory to cellular automata. Physica 10D:45-51; 1984

527. Weaire D, Rivier N. Soap, cells, and statistics - random patterns in two dimensions. Contemp Phys 25:59-99; 1984

528. Weidmann S. The electrical constants of Purkinje fibres. J Physiol 118:348-360; 1952

529. Weiss JN, Garfinkel A, Karagueuzian HS, Qu Z, Chen PS. Chaos and the transition to ventricular fibrillation: A new approach to antiarrhythmic drug evaluation. Circ 99:2819-2826; 1999

530. Weiss JN, Garfinkel A, Spano ML, Ditto W. Chaos and chaos control in biology. J Clin Invest 93:1355-1360; 1994

531. Wettwer E, Amos G, Posival H, Ravens U. Transient outward current in human ventricular myocytes of subepicardial and subendocardial origin. Circ Res 75:473-482; 1994

532. Wettwer E, Amos G, Gath J, Zerkowski HR. Transient outward current in human and rat ventricular myocytes. Cardiovasc Res 27:1662-1669; 1993

533. Whalley DW, Wendt DJ, Grant AO. Basic concepts in cellular cardiac electrophysiology: block of ion channels by antiarrhythmic drugs. PACE 18:1686-1704; 1995

534. Wharton JM, Wolf PD, Smith WM, Ideker RE. Cardiac potential and potential gradient fields generated by single, combined, and sequential shocks during ventricular defibrillation. Circ 85:1510-1523; 1992

535. Wiener N, Rosenblueth A. The mathematical formulation of the problem of conduction of impulses in a network of connected excitable elements, specifically in cardiac muscle. Arch Inst Cardiol Mexico 16:205-265; 1946

536. Wijffels MC, Kirchhof CJ, Dorland R, Allessie MA. Atrial fibrillation begets atrial fibrillation. A study in awake chronically instrumented goats. Circ 92:1954-1968; 1995

537. Wiggers CJ. Studies on ventricular fibrillation produced by electric shock. II Cinematographic and electrocardiographic observations on the natural process in the dog's heart. Am Heart J 5:351-365; 1930

538. Wiggers CJ. On the mechanism and nature of ventricular fibrillation. Am Heart J 20:399-412; 1940

539. Wiggers CJ. The physiologic basis for cardiac resuscitation for ventricular fibrillation: method for serial defibrillation. Am Heart J 20:413-428; 1940

540. Wiggers CJ, Wegria R. Ventricular fibrillation due to single localized induction and condenser shocks applied during the vulnerable phase of ventricular systole. Am J Physiol 128:500-505; 1940

541. Winfree AT. The Geometry of Biological Time. Springer-Verlag, New York, 1980

542. Winfree AT. When Time Breaks Down. Princeton Univ Press. 1987

543. Winfree AT. Electrical instability in cardiac muscle: Phase singularities and rotors. J Theor Biol 138:353-405; 1989

544. Winfree AT. Estimating the ventricular fibrillation threshold. In: Glass L, Hunter P, McCulloch A (Eds.) Theory of Heart. Springer-Verlag, New York, 1991

545. Winfree AT. Electrical turbulence in three-dimensional heart muscle. Science 266:1003-1006; 1994

546. Winfree AT. A spatial scale factor for electrophysiological models of myocardium. Prog Biophys Mol Biol 69:185-203; 1998

547. Winfree AT. Various ways to make phase singularities by electric shock. J Cardiovasc Electrophysiol. 11:286-9; 2000

548. Wit AL, Allessie MA, Bonke FIM, Lammers W, Smeets J, Fenoglio JJ. Electrophysiologic mapping to determine the mechanism of experimental ventricular tachycardia initiated by premature impulses. Am J Cardiol 49:166-185; 1982

549. Witkowski FX, Kavanagh KM, Penkoske PA,Plonsey R, Spano ML, Ditto WL, Kaplan DT. Evidence for determinism in ventricular fibrillation. Phys Rev Lett 75:1230-1233; 1995

550. Witkowski FX, Leon LJ, Penkoske PA, Giles WR, Spano ML, Ditto WL, Winfree AT. Spatiotemporal evolution of ventricular fibrillation. Nature 392:78-82; 1998

551. Witkowski FX, Leon LJ, Penkoske PA, Clark RB, Spano ML, Ditto WL, Giles WR. A method for visualization of ventricular fibrillation: Design of a cooled fibreoptically coupled image intensified CCD data acquisition system incorporating wavelet shrinkage based adaptive filtering. Chaos 8:94-102; 1998

552. Witkowski FX, Penkoske PA, Plonsey R. Mechanism of cardiac defibrillation in open-chest dogs using unipolar DC-coupled simultaneous activation and shock potential recordings. Circ 82:244-252; 1990

553. Wolf A, Swift JB, Swinney HL, Vastano JA. Determining Lyapunov exponents from a time series. Physica 16D:285-317; 1985

554. Wolf M, Seroppian E, Lown B, Temte J, Garfein A, Verrier RL. Protective zone for ventricular fibrillation. Am J Cardiol 29:298; 1972

555. Wolff GA, Veith F, Lown B. A vulnerable period for ventricular tachycardia following myocardial infarction. Cardiovasc Res 2:111-121; 1968

556. Wolfram S. Statistical mechanics of cellular automata. Rev Mod Phys 55:601-642; 1983

557. Wolfram S. Cellular automata as models of complexity. Nature 341:419-424; 1984

558. Wolfram S. Universality and complexity in cellular automata. Physica 10D:1-35; 1984

559. Wolfram S. A New Kind of Science. Wolfram Media Inc. 2002

560. Wooters WK, Langton CG. Is there a sharp phase transition for deterministic cellular automata? Physica D 45:95-104; 1990

561. Wu G, Littmann L, Svenson RH, Nanney GA, et al. Computerized three-dimensional activation mapping study of spontaneous ventricular arrhythmias during acute myocardial ischemia in dogs. J Electrocardiol 28:115-130; 1995

562. Wu TJ, Ong JJC, Hwang C, Lee JJ, Fishbein MC, et. al. Characteristics of wave fronts during ventricular fibrillation in human hearts with dilated cardiomyopathy: Role of increased fibrosis in the generation of reentry. J Am Coll Cardiol 32:187-196; 1998

563. Xi H, Gunton JD, Vinals J. Spiral defect chaos in a model of Rayleigh-Bénard convection. Phys Rev Lett 71:2030-2033; 1993

564. Xu A, Guevera MR. Two forms of spiral wave reentry in an ionic model of ischemic ventricular myocardium. Chaos 8:157-174; 1998

565. Yan GX, Antzelevitch C. Cellular basis for the electrocardiographic J wave. Circ 93:372-379; 1996

566. Yan GX, Antzelevitch C. Cellular basis for the normal T wave and the electrocardiographic manifestations of the long QT syndrome. Circ 98:1928-1936; 1998

567. Yamamoto Y, Hughson RL. Extracting fractal components from time series. Physica D 68:250-264; 1993

568. Yeomans J. Statistical Mechanics of Phase Transitions. Oxford Univ Press, 1993.

569. Zaitsev AV, Berenfeld O, Mironov SF, Jalife J, Pertsov AM. Distribution of excitation frequencies on the epicardial and endocardial surfaces of fibrillating ventricular wall of the sheep heart. Circ Res 86:408-417; 2000

570. Zeeman EC. Catastrophe theory. Sci Am 234:65-83; 1976

571. Zeng J, Rudy Y. Early afterdepolarizations in cardiac myocytes: mechanism and rate dependence. Biophys J 68:949-964; 1995

572. Zhou X, Huang J, Ideker RE. Transmural recording of monophasic action potentials. Am J Physiol 282:H855-H861; 2000

573. Zhou X, Rollins DL, Smith WE, Ideker RE. Responses of the transmembrane potential of myocardial cells during a shock. J Cardiovasc Electrophysiol 6:252-263; 1995

574. Zhou X, Daubert JP, Wolf PD, Smith WM, Ideker RE. Epicardial mapping of ventricular defibrillation with monophasic and biphasic shocks in dogs. Circ Res 72:145-160; 1993

575. Zipes DP, Fischer J, King RM, Nicoll A, Jolly WW. Termination of ventricular fibrillation in dogs by depolarizing a critical amount of myocardium. Am J Cardiol 36:37-44; 1975

576. Zipes DP, Jalife J (Eds.). Cardiac Electrophysiology: From Cell to Bedside. 3rd Ed. W.B. Saunders, 2000

577. Zipes DP, Wellens HJ. Sudden cardiac death. Circ 98:2334-2351; 1998